AD-A205 816

Proceedings of the

1981

ANTENNA APPLICATIONS

SYMPOSIUM

Sponsored by

DEPUTY FOR ELECTRONIC TECHNOLOGY
ROME AIR DEVELOPMENT CENTER
ELECTRONIC SYSTEMS DIVISION
AIR FORCE SYSTEMS COMMAND
AND
ELECTROMAGNETICS LABORATORY
UNIVERSITY OF ILLINOIS
URBANA-CHAMPAIGN, ILLINOIS 61801

September 23, 24, 25, 1981
Robert Allerton Park
University of Illinois

PROCEEDINGS OF THE

1981

ANTENNA APPLICATIONS SYMPOSIUM

Sponsored by

DEPUTY FOR ELECTRONIC TECHNOLOGY

ROME AIR DEVELOPMENT CENTER

ELECTRONIC SYSTEMS DIVISION

AIR FORCE SYSTEMS COMMAND

and

ELECTROMAGNETICS LABORATORY

UNIVERSITY OF ILLINOIS

URBANA-CHAMPAIGN, ILLINOIS 61801

September 23, 24, 25, 1981

Robert Allerton Park

University of Illinois

PROGRAM FOR
1981 ANTENNA APPLICATIONS SYMPOSIUM

WEDNESDAY, SEPTEMBER 23, 1981

MILLIMETER WAVE ANTENNAS

Welcome

† "Millimeter Wave Technology and Applications," J. Wiltse, Georgia Institute of Technology, Atlanta, GA

"Millimeter Wave Integrated Circuits and Systems," N. Deo* and R. Mittra**, *Epsilon Lambda Electronics Corp., Geneva, IL and **University of Illinois, Urbana, IL

"Recent Developments in Millimeter-Wave Antennas," S. Ray, R. Mittra, T. Trinh and R. Paleta, University of Illinois, Urbana, IL

"A Beam Waveguide Linearly Polarized KU Band Feed System," J. B. Flannery, Sylvania Systems Group, GTE, Needham Heights, MA

"An Ellipsoidal Frequency Selective Surface," M. J. Dick, Cubic Corp., San Diego, CA

"Shaped Lens Antennas," J. J. Lee and R. L. Carlise, Rockwell International, Anaheim, CA

ANTENNA THEORY AND MEASUREMENTS

† "Spherical and Cylindrical Near Field Testing of Electrically Large Antennas," S. Sanzgiri and Kang Lee, Texas Instruments, Dallas, TX

"Phased Array Alignment with Planar Near-Field Scanning," W. T. Patton, RCA, Moorestown, NJ

† *Not included*

† "Array Antenna Phase Functions for Simultaneous Multiple Beams," R. P. Gray, Jr. and J. L. Armitage, Westinghouse, Baltimore, MD

"Small Array Illuminations for Pattern Nulling with Sidelobe Level Control," C. F. Winter, Raytheon, Wayland, MA

"Study of Antenna Patterns with Null Constraints," H. Steyskal, Rome Air Development Center, Hanscom Air Force Base, MA

"Interference Sources and Degrees of Freedom in Adaptive Nulling Antennas," A. J. Fenn, Lincoln Laboratory, MIT, Lexington, MA

"Cross-Polarized Retrodirective Arrays," H. E. Schrank, Westinghouse, Baltimore, MD (ABSTRACT)

"An Investigation of a Six-Port Microwave Measurement System," B. Hiben, Motorola, Schaumburg, IL

THURSDAY, SEPTEMBER 24, 1981

ANTENNA DESIGN

"Multibeam Phased Array for Surveillance Radar," C. E. Grove, J. C. McDade and Y. R. LaCourse, General Electric, Utica, NY

"A Geodesic Lens Antenna for 360-Degree Azimuthal Coverage," J. L. McFarland and R. P. Savage, Lockheed, Sunnyvale, CA

"A Common-Aperture S- and X-Band Four-Function Feedcone," J. R. Withington and W. F. Williams, Jet Propulsion Laboratory, California Institute of Technology, Pasadena, CA

"The Confocal Reflector," D. G. Killion, Cubic Defense Systems, San Diego, CA

"Techniques for Low Sidelobe, High Efficiency Offset Dual Reflector Antennas," C. J. Sletten, Solar Energy Technology, Bedford, MA

"New Advances in Wide Band Dual-Polarized Antenna Elements for EW Applications", G. Monser, Raytheon, Goleta, CA

"A Rapid-Tuning High-Power POD-Mounted VHF Antenna System," B. Hodgson, American Electronic Labs, Montgomeryville, PA

"Omnidirectional Transmitter Combining Antenna," A. L. Davidson, Motorola, Schaumburg, IL

ANALYSIS AND MEASUREMENT

"Multimode Planar Spiral for DF Applications," D. D. Connell and B. J. Lamberty, Boeing Aerospace, Seattle, WA

"A Network Formulation for Phased Arrays - Application to Log-periodic Arrays of Monopoles on Curved Surfaces," R. J. Coe and D. E. Young, Boeing Aerospace, Seattle, WA

"The Impedance of the Guyed Quarter Wave Monopole," S. M. Wright*, P. W. Klock* and J. D. Jubera**, *University of Illinois, Urbana IL and **Harris Corp., Quincy, IL

"Alternate Formulas for Near-Field Computation," P. E. Mayes, University of Illinois, Urbana, IL

"Efficient Numerical Evaluation of Electromagnetic Fields Due to Rectangular Patches of Electric Current," P. W. Klock, D. Sall and P. E. Mayes, University of Illinois, Urbana, IL

"Simple Formulas for Transmission Through Periodic Metal Grids or Plates," S. W. Lee and G. Zarrillo, University of Illinois, Urbana, IL

"An Algebraic Synthesis Method for RN^2 Multibeam Matrix Network," G. G. Chadwick, W. Gee, P. T. Lam and J. L. McFarland, Lockheed, Sunnyvale, CA

"Optimization of the Directivity of a Parabolic Reflector Antenna," R. A. Gilbert and Y. T. Lo, University of Illinois, Urbana, IL

FRIDAY, SEPTEMBER 25, 1981

MICROSTRIP ANTENNAS

"Advances in Microstrip Antenna Technology," R. E. Munson, Ball Aerospace Systems Division, Boulder, CO

"An Analysis of Annular, Annular Sector, and Circular Sector Microstrip Antennas," J. D. Ou*, W. F. Richards* and Y. T. Lo**, *University of Houston, Houston, TX and **University of Illinois, Urbana, IL

"Microstrip Dipoles on Cylindrical Structures," N. G. Alexopoulos*, P. L. E. Uslenghi** and N. K. Uzunoglu***, *University of California at Los Angeles, **University of Illinois at Chicago Circle, Chicago, IL, and ***National Technical University of Athens, Athens, Greece

"Design of Microstrip Linear Array Antennas," M. Campi, Harry Diamond Laboratories, Adelphi, MD

"Conformal and Small Antenna Designs," H. S. Jones, Jr., Harry Diamond Laboratories, Adelphi, MD

MILLIMETER WAVE INTEGRATED CIRCUITS AND SYSTEMS

Naresh Deo and Raj Mittra

Epsilon Lambda Electronics Corporation
Geneva, IL
and
University of Illinois, Urbana, IL

ABSTRACT

The last decade has seen significant advances in the area of millimeter wave integrated circuits and this frequency band has emerged as a serious contender for use in commmunication radar, missile guidance and other systems. In this paper we emphasize the integration aspects of millimeter wave systems and begin by discussing dielectric waveguide structures which form the building block for circuit integration. This is followed by a description of different integration schemes and a discussion of a number of problems in the design and fabrication of mm-ICs that must be resolved in the future. Finally, illustrative examples based on some existing integrated components and systems are given, and a prognosis for future trends in the millimeter wave integrated circuits is included.

INTRODUCTION

Recent advances in the field of millimeter-waves have opened up exciting new possibilities, but have also created novel challenges for the circuit and system designer. Millimeter-wave integrated systems, after being fully developed, are expected to perform many of the same functions as conventional microwave and optical systems, such as communication, radar, remote sensing, radiometry and weapon guidance. However, since millimeter-waves fall approximately midway between microwave and optical spectra, the design methods and technologies of both are often applicable to this intermediate frequency range, and hence the term 'quasi-optical'. In addition, millimeter-wave systems can potentially combine the advantageous features of microwaves and optical systems while eliminating some of their major drawbacks, which result in systems that are superior in performance to both.

In comparison to conventional microwave systems, the millimeter-wave conterparts offer smaller size, and hence reduced weight, improved angular resolution or tracking accuracy, resistance to jamming and lower clutter. At the same time, compared to optical or infrared systems, they provide better penetration in adverse weather conditions, and lesser vulnerability to smoke, dust and rocket plumes. In addition, due to the presence of narrow bands of high and low atmospheric absorption (windows) in their propagation characteristics, some unique applications, such as covert operation and secure communication are possible.

From the viewpoint of space and airborne applications, millimeter waves are extremely attractive, as they offer significantly reduced size and weight. Although the standard or integrated millimeter-wave systems today are very expensive, it is predicted that the emerging integration techniques will permit cost reduction to a point where they become competitive with microwave systems having comparable performance. In fact the viability of many of these systems relies heavily upon achieving the reduced weight and lower cost afforded by integrated circuit techniques. In spite of the fact that research in this direction was initiated several decades ago, certain technological barriers have inhibited their progress. The development of high-power, high-frequency solid state sources and other active devices during the last few years has removed one critical barrier, and the evolution of dielectric-based integration leading to low-cost mass-production has brightened the future prospects. Millimeter-wave and quasi-optical integrated circuits are expected to attain a mature state and economic viability in the not too distant future. Consequently, dramatic changes in the world of communication and defense electronics are anticipated within this decade.

MILLIMETER-WAVE TRANSMISSION MEDIA AND SYSTEMS

Having established the usefulness and potential of millimeter waves, we turn our attention to a comparison of various conventional and integrated systems. Conventional millimeter-wave systems utilize standard rectangular metal waveguides and components much like the microwaves, except for a dimensional scaling in proportion to the decrease in wavelength. On the other hand, newly emerging millimeter-wave and quasi-optical integrated circuits generally employ a dielectric-based waveguide or transmission line (including the printed circuit types), and the entire circuit is built in an integrated fashion by appropriate manipulations of this basic guiding structure —— the planar dielectric waveguide.

Since conventional metal waveguides have dimensions only on the order of a few millimeters, extremely tight dimensional and surface tolerance requirements must be imposed in machining and other manufacturing processes. In addition, the standard components are not very amenable to integration and mass production techniques, since they have to be individually fabricated, assembled and implemented in a complete system. Both of these factors significantly contribute to the high cost of conventional millimeter-wave systems, which tend to be substantially larger and heavier in comparison to dielectric-based systems. A strong trend away from conventional systems and toward dielectric-based circuits is primarily prompted by these considerations. However, in some applications, a sacrifice in performance may have to be tolerated with the use of dielectric-based systems. Consequently, at the present time, when extremely high performance is essential, standard metal waveguide implementation is reverted to.

INTEGRATION SCHEMES FOR MILLIMETER WAVE CIRCUITS

Essential to any successful integration is the development of a transmission medium from which most of the active and passive elements are derived by appropriate modifications. The guiding structure thus serves as the basic building block for all the circuit components. Considerable research interest has been generated in the development of new transmiision media suitable for circuit integration. Some of the basic considerations and problem area in the selection of guiding structures and integration techniques are:

(a) Transmission losses
(b) Compatibility with solid-state devices (packaged, chip, beam-lead or whisker-contacted)
(c) Dispersion and multimoding effects
(d) Adaptability to fabricate ferrite and other non-reciprocal devices
(e) Radiation losses
(f) Fabricational ease; suitability for mass production
(g) Frequency range of interest, complexity of the circuit
(h) Availability of design data and theoretical formulations and results
(i) Desired performance characteristics
(j) Cost, size, weight, and environmental requirements

An evaluation of the existing and proposed guides must be made on the basis of these considerations. Table 1 shows the comparison of various popular waveguides along these lines. We next describe some of the proposed schemes of integrating millimeter-wave circuits.

TABLE I: WAVEGUIDE COMPARISON

	METAL WAVEGUIDE	MICROSTRIP	IMAGE LINE [PLANAR DIELECTRIC WAVEGUIDES]	FIN LINE
TRANSMISSION LOSS.	LOWEST	RELATIVELY HIGH	POTENTIALLY LOW. LOWER THAN MICRO-STRIP.	MODERATE LOSS
SIZE, WEIGHT	LARGE, HEAVY	SMALL, LIGHT. OFTEN TOO SMALL FOR MANUFACTURING.	INTERMEDIATE, LIGHT	LARGE, HEAVY
DISPERSION, MULTIMODING.	LOW DISPERSION. NORMALLY SINGLE-MODED.	DISPERSIVE POTENTIALLY MULTIMODED.	DISPERSIVE OFTEN HEAVILY MULTIMODED.	DISPERSIVE. POTENTIALLY MULTIMODED.
SOLID-STATE DEVICE COMPAT-ABILITY AND INTEGRABILITY	UNSUITABLE FOR INTEGRATION.	GOOD / FAIR. PLANAR DEVICES MORE SUITABLE.	GOOD / FAIR. STILL UNDER INVESTIGATION.	FAIR. SUITED FOR BEAM-LEAD DIODES.
USEFUL FREQUENCY RANGE.	ALL FREQUENCY RANGE. SIZE TOO SMALL. ABOVE 130 GHz.	UP TO 60 GHz. UNSUITABLE BEYOND.	> 60 GHz. ALSO GOOD BELOW.	30 - 95 GHz.
COST.	VERY EXPENSIVE.	LOW COST.	MODERATE COST.	LOW-COST.
COMMENTS.	DESIGN INFO. AVAILABLE. VERY HIGH PERFORMANCE.	DESIGN INFO. AVAILABLE. SHIELDING MAY BE REQUIRED.	LACK OF ADEQUATE THEORY. RADIATION PROBLEMS.	CIRCUIT INTER-ACTS WITH HOUSING. SOME DESIGN DATA AVAILABLE.

1. Totally integrated monolithic circuits: The ideal goal for millimeter-wave and quasi-optical IC's is a completely monolithic design using Si, GaAs or some other substrate. In such a scheme, all the components, active or passive, as well as the interconnections are fabricated by diffusion, ion implantation, metallization and other processing steps similar to low frequency IC technology. The rapid development of Molecular Beam Epitaxy (MBE) and other techniques is likely to accelerate the progress of this scheme. Use of concepts from the fast growing area of intecrated optics is made in implementation using this design technique. Monolithic GaAs integrated circuits have recently been developed for microwave frequencies (up to about 10 GHz), attaining Medium Scale Integration complexity. In the very near future, complete receivers and some digital circuits on a single chip will be available for microwave frequencies. Even though considerable research efforts have been expended, no complete advanced millimeter-wave ICs of this type are expected to merge in the near future. However, in the far infrared, progress has been made to a point when prototypes will soon appear on the scene.

2. Dielectric waveguide integrated circuits (DWICs): These employ a dielectric-based waveguide, such as an image or insular guide as the primary building block for the circuit. Discrete active devices are individually mounted in the prefabricated circuit block, which is backed by a metallic ground plane to provide heat-sink and d.c.bias ground. Fabrication of such circuit can be done by one or more of the available techniques, e.g., injection molding, precision milling, laser cutting, etc. At the present time this scheme seems to enjoy considerable popularity,[1-4] particularly those using image guides. A number of critical problems associated with integration in a dielectric environment remain to be solved. These will be discussed later together with some existing systems of this kind.

3. Combinational techniques: By far the most prevalent, these techniques combine or hybridize standard waveguide methods and printed circuit technology, According to some researchers[5] circuits constructed by using a combination of various guides such as microstrip, suspended stripline, fin-line and dielectric waveguides will be the most cost-effective solution to the design of advanced millimeter-wave systems. Several existing systems use standard metal waveguide-type modules or components to perform certain functions. These and other dielectric-based modules are then interconnected by open dielectric guides. This is obviously a compromise between the standard implementation and an all-dielectric realization. On the other hand, the well established waveguide integrated package (WIP) techniques[5] utilizes standard waveguides for providing

interconnections while the actual functions are generated by means of dielectric guide-based modules, which typically employ suspended striplines. In the lower millimeter-wave bands the most common design technique is still a microstrip or stripline circuit with standard rectangular metal waveguides for input-output and selected processing.

CURRENT PROBLEMS IN MMIC DESIGN

Millimeter-wave ICs have not reached a technologically mature state yet, and many problems still remain to be solved. Some of the problems in the design and fabrication of both active and passive components are:

(a) Active components
   1. Radiation from discontinuities near active devices
   2. Complexity of mounting active devices in a compatible fashion
   3. Lack of proper matching and biasing networks
   4. Highly diminished device size
   5. Increased parasitics and attenuation
   6. Lack of adequate theory and design data

(b) Passive components (in addition to some of the above)
   1. Dispersion and multimoding
   2. Radiation from bends, etc.
   3. Absence of ferrite and other non-reciprocal devices

It has been demonstrated that open dielectric guides suffer from radiation losses. Substantial loss occurs in the vicinity of active components, sources and other discontinuities. Shielding, use of properly designed transitions, and avoidance of abrupt discontinuities are helpful in minimizing radiation losses. Also, certain configurations are more likely to radiate than others. One additional problem created by radiation is that of cross-talk in a compact circuit.

Complexity of mounting solid state active devices in an integrated circuit depends a great deal on the package of the device, and on the guiding medium. Planar technology, which often utilizes a suspended stripline or microstrip, is very suitable for mounting planar devices, e.g., beam-lead diodes. Whisker contacted diodes are considered labor intensive and hard to mount. Availability of a ground plane/heat sink for mounting solid state sources is essential. In addition, the circuit configuration must accommodate biasing networks and filters as an integral part of the active component. Even today, one of the major problems in fabricating dielectric-based integrated circuits is the difficulty of mounting active devices in a compatible manner.

Design and construction of matching network or shorts, particularly the movable type, present considerable difficulty at these wavelengths in an open waveguide environment. The lack of a good theory to account for parasitic and other effects forces one to design on a cut-and-trial basis. Substantial analytic as well as emperical work is needed before design algorithms for such circuits become available.

As the frequency of operation goes up, the active and passive component size goes down proportionately. The design process increases in its complexity, and fabrication becomes more difficult with increasing frequency. For example, above 130 GHz, beam-lead diodes are not usable; hence, whisker-contacted mixer wafers must be used. Apart from being extremely difficult to mount and unsuitable for assembly-line-type production, they are somewhat unreliable in a rugged environment. Specialized equipment and expert handling are essential for most circuits designed to operate above 130 GHz.

Accurate design computations are not possible due to the absence of adequate models and characterization of circuit elements associated with active components. Cavities, posts, transitions, and actual solid-state devices must all be accurately characterized in terms of impedance and frequency-dependent parameters to facilitate design of high-performance components in accordance with specifications. This problem is particularly complicated in an open dielectric environment for which few analytic results exist.

Most dielectric-based waveguides and components exhibit higher attenuation than their standard metal waveguide counterparts. Also, as the frequency of operation increases, parasitic effects begin to have pronounced influence on the performance of active components. Severe degradation can result from these factors.

The problems of multimoding and radiation from bends are encountered frequently in the design of some passive components. In general, any attempt to solve these problems results in complicating the design and fabrication procedure, which eventually makes mass production less attractive. In case of many dielectric waveguides, the dimensions become prohibitively small to achieve single-mode operation. The radiation from bends and transitions can and must be minimized by proper shielding and design modifications. Small and yet low-loss transitions between various components and their interconnections are being studied extensively. Most advanced millimeter wave integrated systems require high performance dielectric-based ferrite devices, such as isolators, circulators and modulators. At the present time, there just are not any high-performance integrable ferrite components in the upper millimeter-wave bands.

EXAMPLES OF DIELECTRIC BASED INTEGRATED SYSTEMS

We now describe briefly some existing millimeterwave components and the integrated systems in which they have been used. We begin by describing the active circuits, such as oscillators and mixers, and then continue with passive components, e.g., filters, couplers and antennas.

The dramatic improvements in the past decade in solid-state sources and other devices have significantly enhanced their performance capabilities. In fact, millimeter-wave integrated systems heavily capitalize on the advantages of the recently developed solid-state devices. Significant progress in the output power and efficiency has been made with Impatt diodes in the 30-300 GHz range. This is true for both CW and pulsed mode of operation.[5] Mixers have undergone a similar advancement in their performance at the high-frequency end. Beam-lead diodes that are very suitable for planar circuit integration have only recently been made commercially available for frequencies in excess of 30 GHz, with cut-off frequencies higher than 1000GHz. Beam-lead diodes eliminate the costly and labor intensive whisker contacting procedures used so far, and yet provide performance comparable to standard implementation. These advances have been critical for the progress and survival of millimeter-wave ICs.

Integration involving the use of image guides is very popular primarily because they are easy to fabricate. Figure 1 shows the schematic of a dielectric-based, integrated receiver developed at the University of Illinois. It comprises an Impatt local oscillator and a beam-lead diode mixer. The Impatt diode is mounted in the ground plane, which also serves as a heat sink. A cylindrical pin attached to a metal plate on top of the dielectric guide contacts the diode to provide the dc bias. For the mixer, a metal post attached to the ground plane passes through a hole drilled in the dielectric waveguide. Next, a diamond-shaped metal plane is deposited around the post on the top surface of the dielectric such that the metal post is electrically isolated from it. A GaAs beam-lead diode is mounted in the small airgap between the post and the deposited plate, which serves as the common terminal for bias and IF output. Mechanical tuning for the Impatt oscillator as well as the mixer is provided by movable metal shorts. This scheme works very satisfactorily and shows potential for successful integration of large systems.

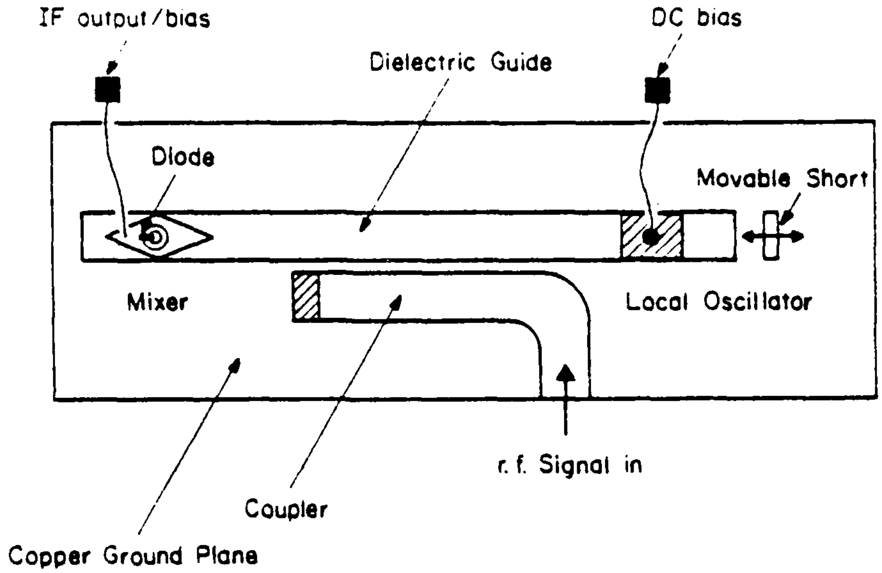

Figure 1. Dielectric-based integrated receiver developed at the University of Illinois.

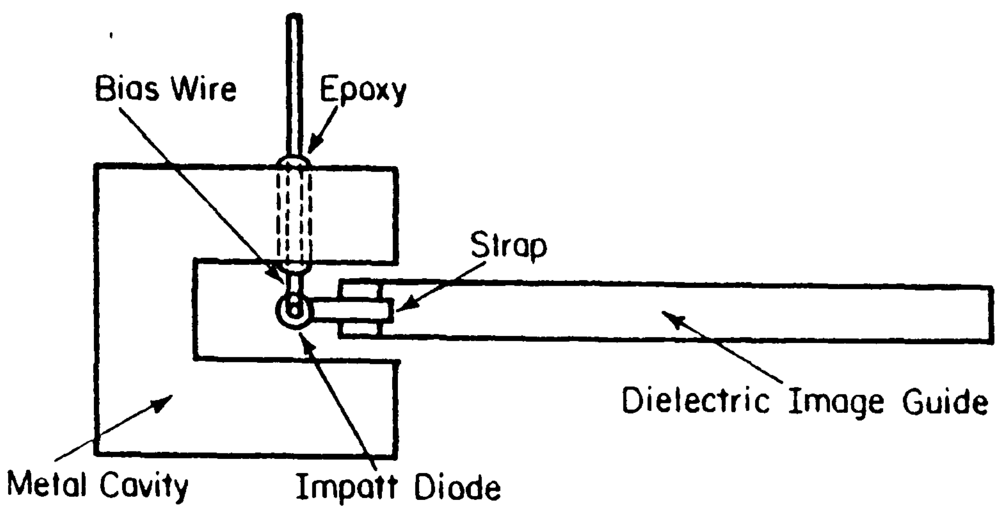

Figure 2. Bo.on Nitride Image Guide Oscillator developed by Hughes Aircraft Company.

Figure 2 shows a view of the Boron Nitrade image guide oscillator developed at Hughes Aircraft Company.[2] A metal cavity is employed around the diode, but the generated power is fed into an image guide with a metal strap employed as a transition. Bias is provided by means of an insulated wire that passes through the cavity wall. Complete enclosure is achieved by the use of a top plate. Many modifications of this basic type are possible. Hughes (using identical construction) has developed detectors and balanced mixers at 70 GHz and beyond. One advantage of this scheme is the obvious reduction of radiation losses near the impatt which occur in an open dielectric waveguide realization. High performance of this type of device can be attributed to metal cavity use. Another example of a prototype transceiver circuit[7] constructed by ERA Technology, UK is shown in Figure 3 Notice the twopole band pass ring filter and the balanced mixer configuration. Another very popular class of integrated circuits uses the printed circuit technology by combining a variety of transmission lines which are integrated on a single substrate suspended in the E-plane of a split rectangular metal waveguide housing. An example of such an integrated receiver is seen in Figure 4. Here the filters and the matching networks are realized using fin-lines, coplanar lines and microstrips - all produced by standard printed circuit techniques. This type of design is well-suited for frequencies up to 100 Ghz, beyond which printed circuits are considered inappropriate. Balanced mixers at 94 GHz have been built with a typical noise figure of 8 dB, which includes the IF amplifier contributions. At Bell Laboratories a similar technique has been used[8] with standard waveguides providing the inputs through transitions. This is well-integrated, easy to implement, relatively inexpensive, and has adequate design information (or theoretical results).

Passive devices for the integrated circuits have to be compatible with the rest of the circuit elements. In general, they are made by modifying or manipulating dielectric transmission lines which provide the interconnections. Once again, image guides are most popular at higher frequencies, viz., 60 GHz and above, and striplines (printed circuits) in the lower frequency range. Although the performance of these components is certainly inferior to their metal waveguide counterparts, the other advantages compensate for the deficit.

Finally, a very essential part of many systems is the antenna. From an integrability standpoint, dielectric or microstrip antennas are ideal for most applications and can be built as an integral part of the system. The usefulness of antennas in millimeter-wave and FIR stems from the fact that optical techniques can be combined with conventional circuit techniques. However, if very high gain or extreme-

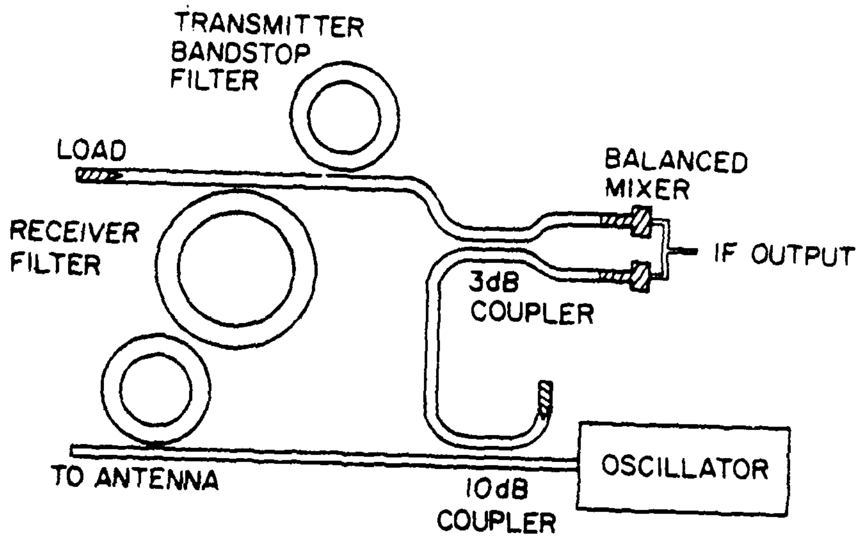

Figure 3. Prototype Transceiver Circuit constructed by ERA Technology, England.

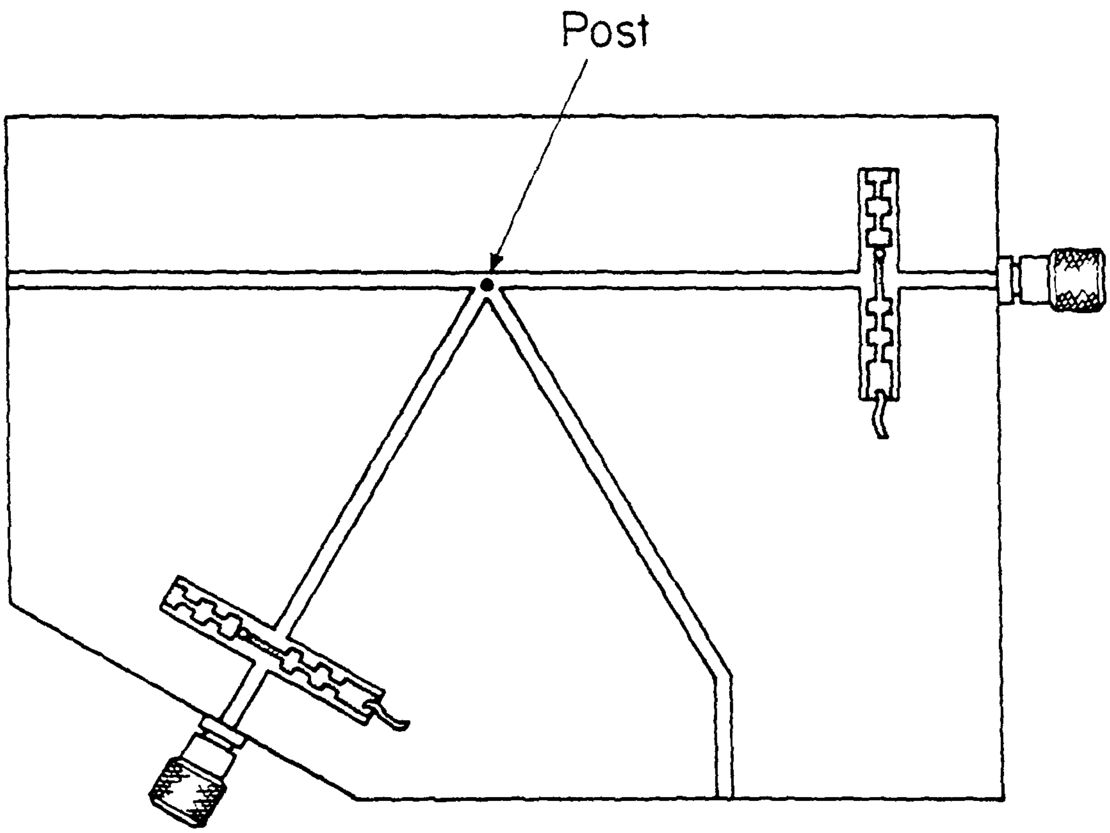

Figure 4 .94 GHz balanced mixer using suspended substrate technology developed by TRG division, Alpha Industries.

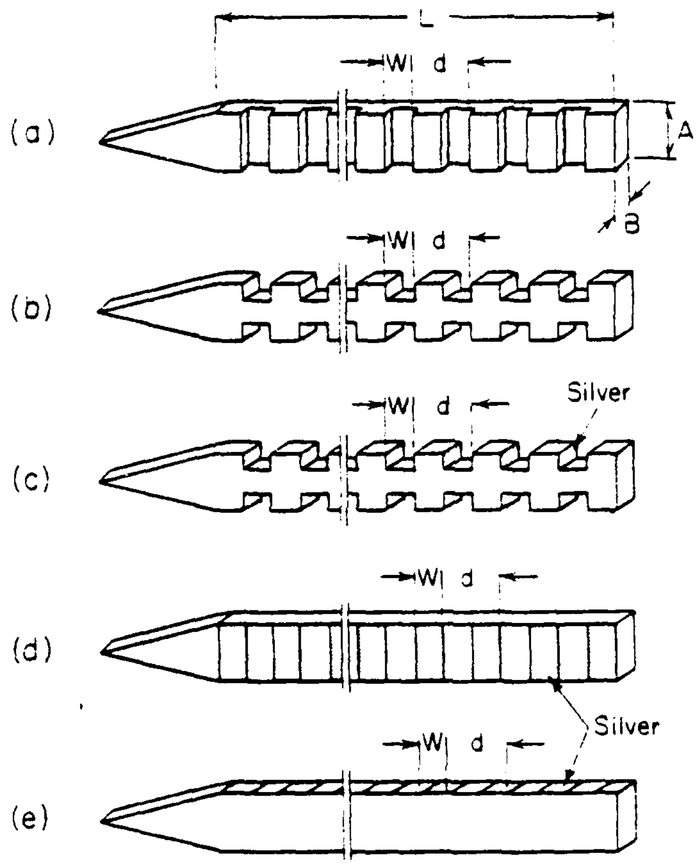

Figure 5. Examples of Dielectric Antennas.

ly narrow beamwidths are required, use of conventional parabolic or other reflectors is still the best choice. Dielectric antennas (including the printed-circuit type) at millimeter wavelengths are sometimes classified into two groups, viz., surface-wave and leaky-wave types, although strictly speaking both of them continuously leak energy as a mechanism for radiation. The surface-wave types, which are usually uniform or tapered rods, are usually end-fire, while the leaky-wave antennas radiate off broadside and are frequency scannable. Figure 5 depicts some of the typical antennas. Two subjects of current interest are phased arrays and feeds using dielectric-type antenna elements.

CONCLUSIONS

It is fairly evident at this time that in spite of a slow and somewhat problematic start, millimeter-wave technology and, in particular, the mmICs and QOICs have begun to find a multitude of important applications. The many advantages offered by them over conventional microwaves or optical systems will ensure their continued development and use. It is projected that combinational methods of integration will continue to prevail for some time. They are commercially available today. Fully integrated monolithic far infrared and some microwave circuits are expected to emerge into production stage during this decade, while mmICs will slowly head in that direction. Dielectric-based integration techniques have already established their feasibility though further work on some aspects, such as non-reciprocal devices, is needed. A quest for better, low-loss dielectric materials also continues. At the present stage, mmICs have not attained the state of maturity and economic viability that microwave systems have reached. However, as research activities throughout the industry progress new technologies and schemes of integration are expected to emerge. There is little doubt about their cost-effectiveness, and according to most experts in the area, the 1980's will see mmICs go through a phase of strong challenges, critical tests, and tremendous advancements.

REFERENCES

(1) R. M. Knox, "Dielectric Waveguide Microwave Integrated Circuits -- An Overview," IEEE Trans. Microwave Theory Tech., vol. MTT-24, no. 11, Nov. 1976, pp. 806-814.

(2) J. A. Paul and Y.W. Chang, "Millimeter-Wave Image Guide
c Integrated Passive Devices," IEEE Trans.Microwave Theory Tech., vol. MTT-26, no. 10, Oct. 1978 pp. 751-754

(3) J. E. Kietzer, A.R. Kaurs and B.J. Levin, "A V-Band Communication Transmitter and Receiver System Using Dielectric Waveguide Integrated Circuits," IEEE Trans. Microwave Theory Tech., vol. MTT-24, no. 11, Nov. 1976, pp. 797-803

(4) Millimeter-Wave Integrated Circuits Session, Session L, International Microwave Symposium, 1979, Orlando, Florida, May 1, 1979

(5) A. G. Cardiasmenos, "Planar Devices Make Production Practical," Microwave Systems News, vol. 9, no. 5, May 1979

(6) T. A. Midford and R. L. Bernick, "Millimeter-Wave CW Impatt Diodes and Oscillators," IEEE Trans. Microwave Theory Tech., vol. MTT-27, no. 5, May 1979, pp. 483 - 491.

(7) M. J. Aylward and N. Williams, "Feasibility Studies of Insular Guide Millimeter Wave Integrated Circuits," AGARD Conference Proceedings, no. 24, Millimeter and Submillimeter Wave Propagation and Circuits Symposium, Munich, 1979

(8) E. R. Carlson, M.V. Schneider and T. F. McMaster, "Subharmonically Pumped Millimeter-Wave Mixers," IEEE Trans. Microwave Theory Tech., vol. MTT-26, no. 10, Oct. 1978, pp. 706-715

RECENT DEVELOPMENTS IN MILLIMETER-WAVE ANTENNAS

S. Ray, R. Mittra, T. Trinh, and R. Paleta
University of Illinois
Urbana, Illinois

ABSTRACT

Several types of antennas for use at millimeter-wave frequencies are presented. The first is a leaky-wave structure consisting of a rectangular dielectric rod with metallic strips on one side. This structure radiates a fan-shaped beam in the near-broadside range and can be frequency scanned. A modification of this antenna is the horn-image guide antenna. This antenna consists of a leaky-wave structure, as described above, that is mounted in a metal trough. A metal flare is added along the trough for increased beamwidth control and directivity. This antenna produces a beam which is narrow in both planes and has substantially higher gain than the leaky-wave antenna alone. A particular advantage of both these types of antennas is their integrability with a dielectric waveguide integrated circuit.

I. INTRODUCTION

Currently, a great deal of interest has been placed in the development of integrated circuits for millimeter-wave frequencies. Dielectric waveguides of rectangular cross-section provide one of the most attractive technologies for the realization of this objective. Dielectric waveguides exhibit many important characteristics in this frequency range including low loss, low cost and relatively low manufacturing tolerances. For this reason, we have investigated a number of antenna structures which consist of appropriately modified rectangular guides. These antennas would be readily integrable with a dielectric waveguide based system.

The antennas discussed are of the leaky-wave variety. The basic structure consists of a periodically perturbed rectangular waveguide. Perturbations commonly used are notches or metallic strips. As metallic strips have been shown to be superior [1], this report uses metallic strips exclusively. This antenna radiates essentially broadside. Since the propagation constant along the structure is frequency dependent, the beam is frequency scannable.

II. UNIFORM STRIP WIDTH ANTENNAS - THEORY

The leaky-wave antenna (LWA) with uniform metallic strips has been studied extensively by several investigators [2],[3]. These antennas are strictly periodic. The distance between the strips and the size of the strips are constants. A typical antenna of this type is shown in Figure 1 with its related coordinate system. For experimental purposes the antenna has been fed with a rectangular metal waveguide fitted with an optimally designed feed horn [4]. Thus, the feed end of the dielectric waveguide is tapered for matching purposes. The metallic strips of width W are placed along one broad-wall. D, the spacing between elements is chosen to be on the order of a guided wavelength. This allows the structure to support a slow traveling wave, $Re[k_z] > k_o$. This wave attenuates along the guide due to energy "leaking" away from the antenna in the form of radiation. As is typical of traveling wave antennas, this antenna is many wavelengths long in the wave propagation or z direction. Due to the high frequency employed, the antenna is physically quite short.

For moderate strip size, this antenna can be described in terms of simple linear array theory. By ignoring such effects as mutual coupling, backward reflections at discontinuities, and interaction with the feed, the strips can be considered as the elements of a linear array. The elements are identical, have constant spacing D, and are excited by a traveling wave with a complex propagation constant k_z.

Given k_z, the array factor, AF, is given by

$$AF = A_0 \frac{\sin N\Psi/2}{\sin \Psi/2} \tag{1}$$

where N is the number of elements, A_0 is a constant, and Ψ is the complex quantity

$$\Psi = k_0 D \cos\theta - k_z D \tag{2}$$

The condition for a field maxima (position of a main beam) is that $Re[\Psi]=2n\pi$, $(n=0,\pm1,\pm2,\ldots)$, or

$$90^\circ - \theta = \theta' = \sin^{-1}\left[\frac{\lambda_0}{\lambda_g} + \frac{n\lambda_0}{D}\right] \tag{3}$$

where λ_0 is the free space wavelength, and λ_g is the guided wavelength given by

$$\lambda_g = \frac{2\pi}{Re[k_z]} \tag{4}$$

Antennas are generally designed to have only one main beam in the visible region. In a suspended guide mode of operation, this means one beam in the upper half space, $180 \geq \theta \geq 0$, and its mirror image in the lower half space. To insure the existence of only one main beam, care must be taken to insure that the argument of the inverse sine function in Equation (3) have absolute value less than unity for only one integer value of n.

Determination of the element pattern requires precise knowledge of the current on a given strip. As this is unknown, a complete analytical description of the radiation pattern is impossible. Conveniently, the element pattern is a slowly varying function of angle whereas the array factor is rapidly varying. Thus the E-plane (the plane which contains the guide axis) far-field pattern is given accurately by the array factor. The 3 dB beamwidths are given by solving Equation (1) for the half power points. Since the propagation constant is complex, the beamwith depends critically on the imaginary portion of k_z, instead of depending simply on the number of strips.

The above discussion presupposes knowledge of the propagation constant. Mittra and Kastner [5], have recently developed a spectral domain solution for k_z. A more convenient method is to assume that the real portion of the propagation constant is identical to the propagation constant of the unperturbed guide. This can be found via the Effective Dielectric Constant method [6]. Although this method gives no information on the imaginary portion of k_z and hence the beamwidth, this assumption has been found to be useful and valid for strips of small to moderate size. Experimental techniques can then be used to determine the beamwidth, gain, and the characteristics in the H-plane, the plane transverse to the guide axis. Sidelobe and endfire radiation levels also depend on feed and termination effects. These are unaccounted for in our simple linear array theory and must thus be measured.

III. UNIFORM STRIP WIDTH ANTENNAS-EXPERIMENT

This section discusses the validity of the above approximation and studies the relationship between various parameters, the complex propagation constant, and the far-field characteristics. To this end, eight identical antennas were constructed varying only the strip-width, W. These antennas were constructed of polyethelyne, $\epsilon_r = 2.33$, and had cross-sectional dimensions of 3.2 x 1.6 mm. Each antenna had 15 strips of constant width separated by D = 3.0 mm = 0.992 λ_g. The first strip was located approximately 20 mm from the feed to minimize feed interaction. From antenna to antenna the ratio W/D ranged from 0.142 to 0.733. Throughout this report, the fixed frequency measurements were made at 31.5 GHz

Far-field and near-field measurements were made on each of the antennas. From this data the complex propagation constant for each antenna was determined. Figure 2 shows $\beta_z = Re[k_z]$ as a function of the ratio W/D, determined from far and near-field data. Both methods show that for moderate strip sizes, $_z$ remains virtually identical to the unperturbed waveguide case, $\beta_z = 2.03$ mm. The far-field data shows that the real portion of k_z increases for larger strip sizes. Due to basic imprecision in the measurements, we have assumed the far-field data to be more reliable than the near-field data.

Examination of the far-field radiation patterns shows significant pattern degradation for strips larger than $W/D > 0.5$, i.e., sidelobe and endfire radiation levels are greatly increased. This is most likely due to mutual coupling and matching effects. Undoubtedly the transition from open guide to leaky-wave structure is more severe when the strip size is large, resulting in increased radiation. Hence we see that approximating the real portion of k_z with the propagation constant of an unperturbed guide is valid over the range of useful strip-widths.

Figure 3 shows $\alpha_z = \mathrm{Im}[k_z]$ as a function of W/D. The imaginary portion of k_z is seen to depend strongly on this ratio. The beamwidths display similiar behavior. Antennas with narrow strips have small α_z's and correspondingly narrow beams. The drawback of these antennas is that a large number of strips are required to radiate all the incident power in the broadside direction. An insufficient number of strips will result substantial endfire radiation. This was evidenced in these experiments. The antenna with the narrowest strips ($W/D = 0.112$) had endfire radiation which exceeded the main beam power level, in spite of having 16 strips. Building longer antennas increases manufacturing tolerances and are thus more difficult to realize.

Figure 3 shows that an optimal radiator exists for $W/D \sim 0.6$. Use of this strip-width should allow construction of the shortest possible antenna. This antenna would also have the widest beam. As discussed above though, antennas with large strip-widths are not practical. Optimization in the sense of minimizing endfire and sidelobe radiation levels and in maximizing gain occurs for $W/D \sim 0.4$.

Figure 4 shows a typical E-plane radiation pattern for an antenna with $W/D = 0.392$. Here we see the characteristic narrow beams at $\pm 90^\circ$. Interestingly, the gain is higher on the nonmetallized side of the antenna. The beamwidth is approximately 4.5, while the gain is 17 dB. The H-plane pattern is given in Figure 5. Here the beams are quite broad. The 3 dB beamwidths are 39° and 120° on the nonmetallized and metallized sides respectively.

Scanning characteristics were studied over the frequency range from 76 to 86 GHz. The scanning characteristics closely follow the results predicted via the dispersion relation of the unperturbed guide. The main beam scanned approximately 9° over this range of frequencies with little degradation in radiation characteristics. The use of higher dielectric constants would allow wider scanning ranges

IV. TAPERED STRIP-WIDTH ANTENNAS

The previous section discussed an antenna which was strictly periodic. Both D and W were constants. In this section the condition that W be constant is relaxed and significantly better antennas are designed and tested. It has been shown that varying W within a rather large range affects only the imaginary portion of k_z and not the real part. This allows the design of an antenna with varying strip-widths.

Motivation for this approach is the tradeoff found in the last section between beamwidth and antenna length. With the present scheme, narrow strips can be used at the initial portion of the antenna where the bulk of the power is radiated. This insures a narrow beam. The later strips can then be wider to efficiently radiate the power before the antenna termination.

Added benefits of this design scheme are reduced mutual coupling and feed interaction effects since the initial strips are small. Also, the transition from unperturbed guide to leaky-wave structure is gradual, yielding a better match.

Several strip-width variation schemes have been investigated. As is to be expected from the above discussion, the best antenna patterns were produced by antennas which tapered the strip-width as a function of distance. The first strip was chosen to be extremely narrow. Each consecutive strip is then made larger by some factor until W reaches some convenient size. The strip size is then maintained until most of the power is radiated and the antenna is terminated. By proper design of the taper function, the aperture distribution can be held virtually constant for 10-20 strips. The rest of the distribution is characterized by an increasing rate of exponential decay. Near-field measurements show this to be the case.

Tapering the length of the strips has a similiar effect on the propagation constant. This effect is somewhat weaker than the effect of width tapering. Combining both strip-width and strip-length tapering gives greater control over the aperture distribution. A longer effective aperture is more easily produced.

Such an antenna was built and tested with very good results. This antenna has cross-sectional dimensions of 3.16 x 1.62 mm, an overall length of 161 mm, and 41 strips which span the last 130 mm of the antenna. The strip spacing is one guided wavelength, $D = \lambda_g = 3.05$ mm. The shorter strips are placed symmetrically along the guide axis. The width, W_n, and the length, L_n, of the nth strip are given by:

$$W_n = \begin{cases} .175+.05n \quad (\mathrm{mm}) & 1 \leq n \leq 26 \\ 1.475 \quad (\mathrm{mm}) & 26 \leq n \leq 41 \end{cases} \tag{5a}$$

$$L_n = \begin{cases} 1.0+.11n \quad (\mathrm{mm}) & 1 \leq n \leq 20 \\ 3.2 \quad (\mathrm{mm}) & 20 \leq n \leq 41 \end{cases} \tag{5b}$$

The far-field radiation of this antenna is given in Figure 6. This antenna has main beams at $\pm 90^\circ$. The beams are very narrow with 3 dB beamwidths of 3.9° and 6.7° on the metallized and nonmetallized sides respectively. Compared with an antenna with constant W (see Figure 4), this antenna shows marked improvement. The improvement is not only in the beamwidth, which was expected, but also in endfire suppression, sidelobe levels, and roll-off past the 3 dB point. The 20 dB beamwidth is only slightly wider than the 10 dB beamwidth. The highest sidelobes are less than the detection level of 25 dB below the main beam power level. The main lobes are remarkably free from shoulders and other perturbations. Directive gain of this antenna is 17.5 dB, approximately 0.5 dB higher than the uniform case. As expected, the scanning characteristics and the H-plane pattern are very similiar to those of antennas with constant V.

V. HORN IMAGE-GUIDE LEAKY-WAVE ANTENNA

The previously described antennas operate in a suspended guide mode of operation. The extension to image guide is straight forward. The antenna is simply mounted in a ground plane. This has the effect of substantially increasing the antenna gain by eliminating the back lobe and subsequently increasing the power in the front lobe. For many applications though, this antenna has the drawback of producing a very wide beam in the plane transverse to the guide axis.

To reduce the beamwidth in the transverse plane an antenna was built which consisted of an antenna as described in section IV, embedded in a rectangular trough with a metal flare attached on the side [7]. This antenna is shown in Figure 7. With this arrangement, the antenna behaves like a linear array in the longitudinal (or E) plane while the radiation pattern resembles that of a horn in the transverse (or H) plane.

The dielectric rod used in this antenna had cross-sectional dimensions of 3.4 x 1.4 mm. The antenna had 32 tapered strips separated by a guided wavelength. The trough depth was chosen arbitrarily to be 3.4 mm. The flare length was chosen to be 40 mm. By modeling the H-plane characteristics with an H-plane sectoral horn, an optimum flare angle of $\alpha = 14$ was chosen. This angle was experimentally observed to maximize the gain.

The far-field E and H-plane radiation patterns are given in Figure 8. The 3 dB beamwidths in the E-plane is 4°, similiar to that of the tapered strip LWA. The H-plane half power beamwidth is 13°. This is significantly better than leaky-wave antennas without the flare. The gain of this antenna is 26 dB. The sidelobe levels are at least 25 dB below the main beam. Scanning characteristics were similiar to the previous cases.

VI. CONCLUSION

A leaky-wave antenna consisting of a periodically perturbed rectangular dielectric waveguide and several of its variants have been studied at millimeter-wavelengths. The relationship between various parameters and the radiation characteristics were investigated. This study motivated the design of antennas with tapered strip-widths to better control the aperture distribution. Strip-length variations were also studied. A combination of these two methods yielded an antenna with very narrow beams and -25 dB sidelobes. Drawbacks of this antenna are its relatively low gain, 17.5 dB, and the broad beamwidth in the plane transverse to the guide axis. The horn-image guide antenna overcomes these two difficulties by mounting the leaky-wave structure in a metal trough and by using a metal flare for increased beam control.

VII. REFERENCES

[1] S. KOBAYASHI, R. LAMPE, N. DEO, and R. MITTRA, "A study of millimeter-wave dielectric antennas," 1979 IEEE Antennas and Propagation Symposium Digest, June 1979, pp. 408-411

[2] K.L. KLOHN, R.E. HORN, H. JACOBS, and E. FREIBERGS, "Silicon waveguide frequency scanning linear array antenna," IEEE Trans. Microwave Theory Tech., vol. MTT-26, no. 10, pp. 764-773, October 1978.

[3] T. ITOH, "Application of gratings in a dielectric waveguide for leaky-wave antennas and band-reject filters," IEEE Trans. Microwave Theory Tech., vol. MTT-25, no. 12, December 1977, pp. 1134-1138.

[4] T.N. TRINH, J.A.G. MALHERBE, and R. MITTRA, "A metal-to dielectric waveguide transition with application to millimeter-wave integrated circuits," 1980 IEEE, MTT-S International Symposium Digest, pp. 205-207, May 1980.

[5] R. MITTRA and R. KASTNER, "On the solution of the complex propagation constant describing the wave propagation along a leaky-wave structure," 1980 IEEE Antennas and Propagation Symposium Digest, June 1980, pp. 35-38.

[6] R.M. KNOX and P.P. TOULIOS, "Integrated circuits for the millimeter through optical frequency range," Proceedings of the Symposium on Submillimeter Waves, Polytechnic Institute of Brooklyn, New York:1970, pp. 497-516.

[7] T.N. TRINH, R. MITTRA, and R.J. PALETA, Jr., "Horn image-guide leaky-wave antenna," 1981 IEEE, MTT-S Symposium Digest, June 1981.

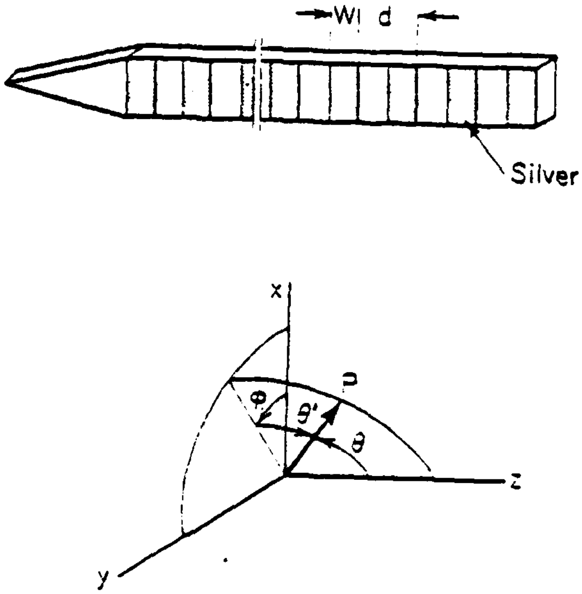

Figure 1. leaky-wave antenna and coordinate reference system

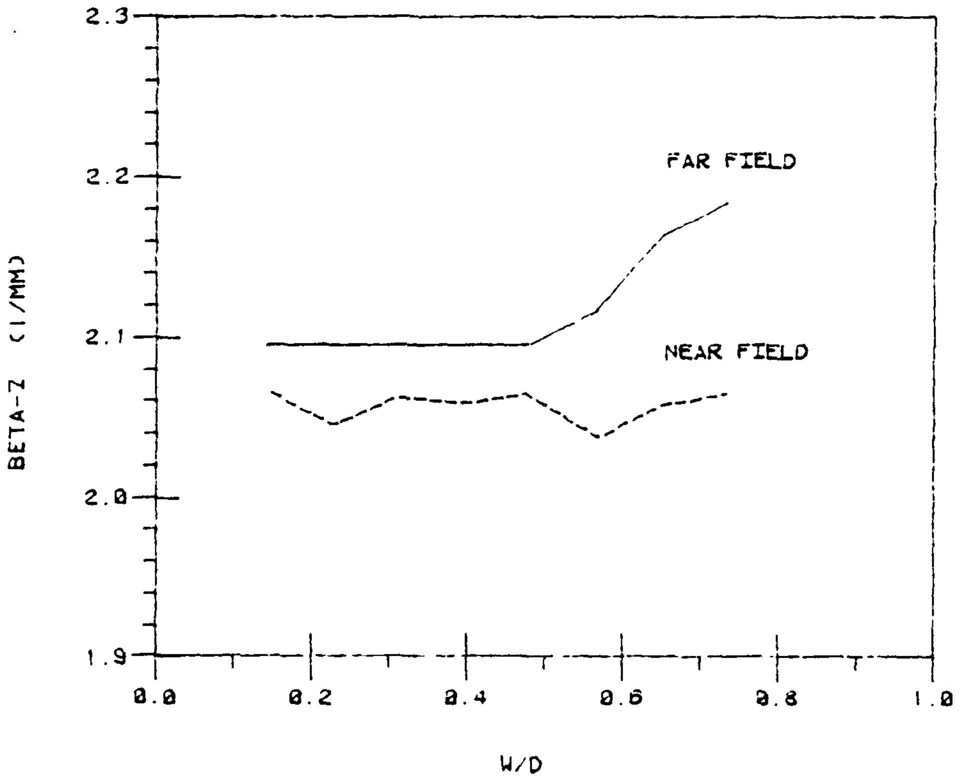

Figure 2. β_z vs. W/D

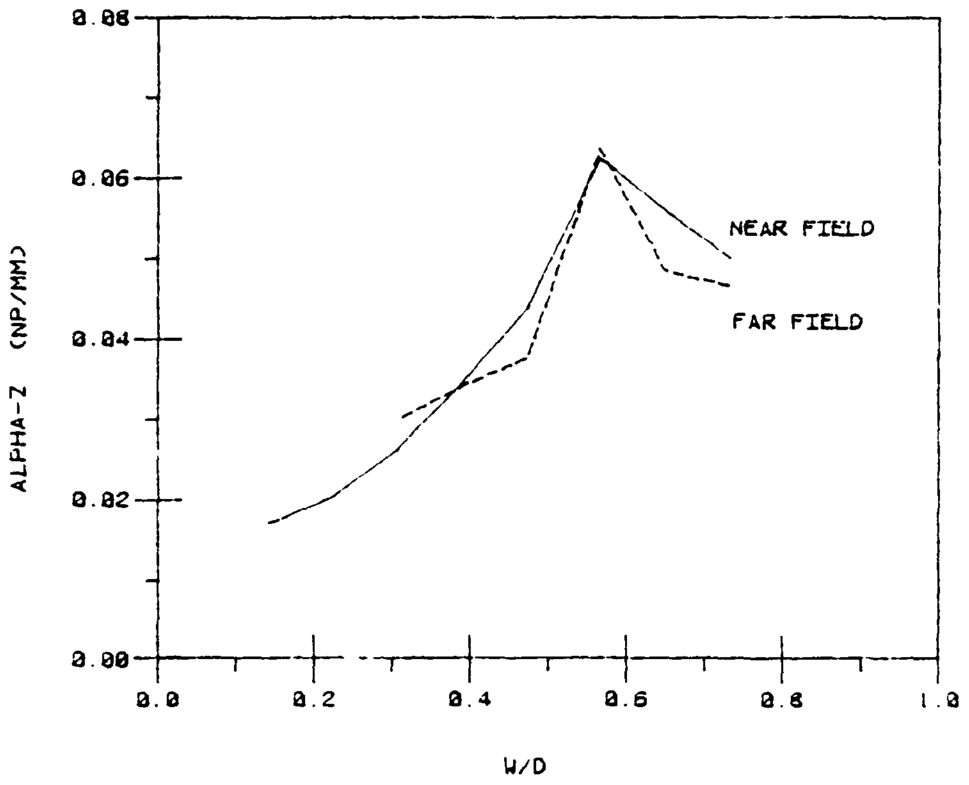

Figure 3. α_z vs. W/D

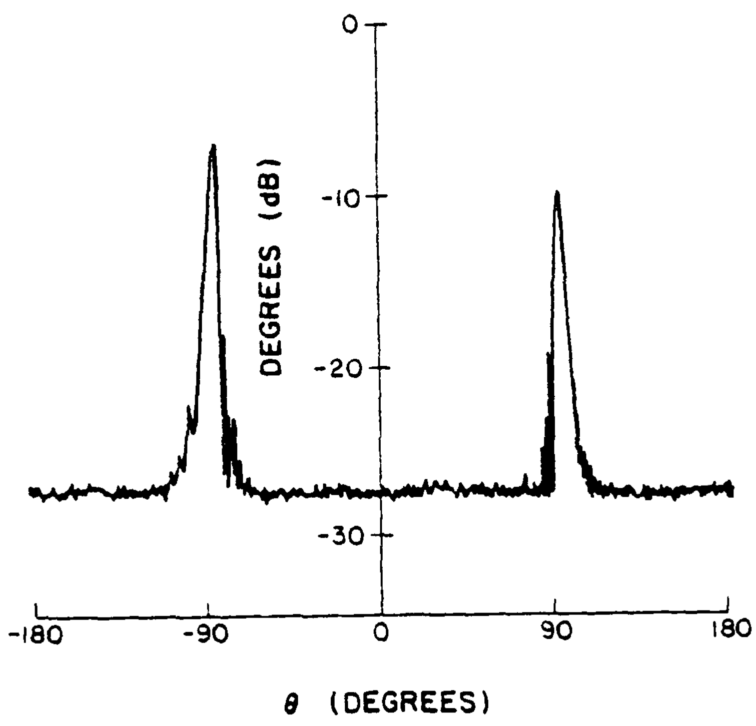

Figure 4. E-plane radiation pattern for uniform strip-width antenna

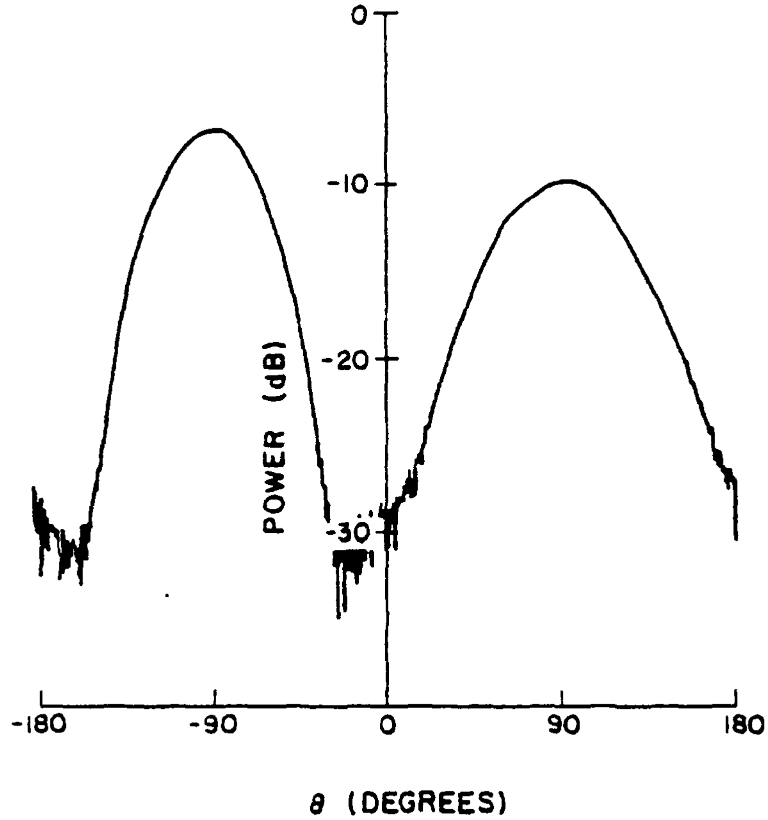

Figure 5. H-plane radiation pattern for uniform strip-width antenna

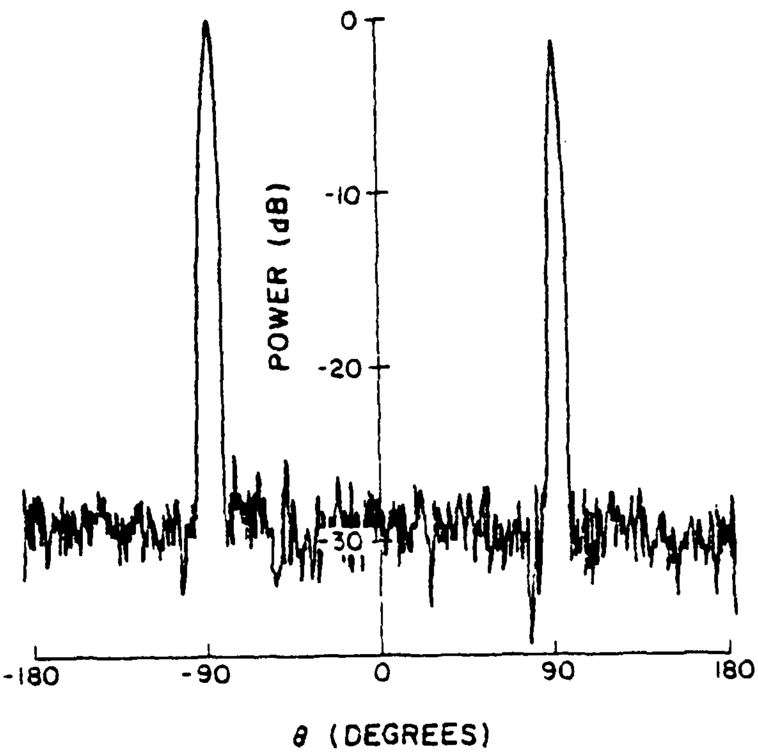

Figure 6. E-plane radiation pattern for tapered stripwidth antenna

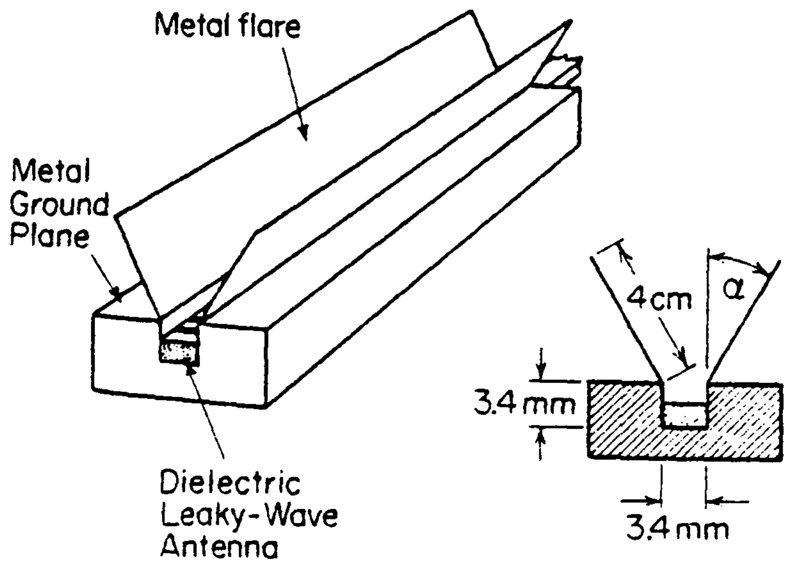

Figure 7. Geometry of horn image-guide antenna

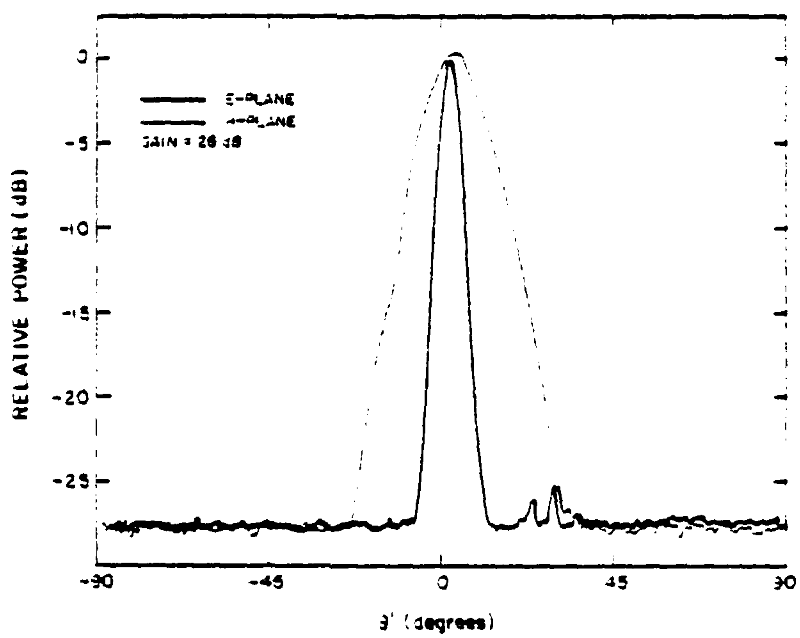

Figure 8. E and H-plane patterns of horn image-guide antenna

A Beam Waveguide Linearly Polarized KU Band Feed System

John. B. Flannery

Sylvania Systems Group
Communication Systems Division
GTE Products Corporation
77 A Street
Needham Heights, Mass. 02194

Introduction

This paper provides a description and theory of operation for the GTE linearly polarized KU band Beam Waveguide Feed System. The feed is designed for use with large Cassegrain antennas typical of those associated with satellite communications earth stations. The beam waveguide technique permits fixed ground installations of the transmitters and low noise receivers and eliminates the large equipment room usually mounted behind the reflector vertex.

The feed was originally developed for the INTELSAT Standard "C" ground terminal antenna. Though not originally designed for frequency reuse applications, its cross-polarization performance is compatible with this requirement. Therefore, with the simple addition of filters to provide two orthogonal ports in both receive and transmit, the design also satisfies the frequency reuse requirements of the EUTELSAT (European Telecommunications Satellite) programs.

The feed system shown in Figure 1 consists of a tapered corrugated wall horn, a matching network, a TE21 mode coupler, three differential phase shifters, a choke coupled rotatable, motor driven orthogonal mode transducer (OMT), a transmit rotary joint, a receive rotary joint, a drive motor and a servo amplifier system incorporated in the control panel subassembly. The rotary joints and the choke coupled orthogonal mode transducer allow the feed polarization to be aligned with any orientation of the satellite antenna system.

The basic KU band feed has provision for automatic closed loop tracking by means of a TE21 mode coupler shown in Figure 2. This TE21 Difference Mode Coupler provides the required linearly polarized tracking capability in the 11 GHz band. To do this, two orthogonal TE21 difference modes, excited by the coupler, are combined in a quadrature hybrid, the outputs

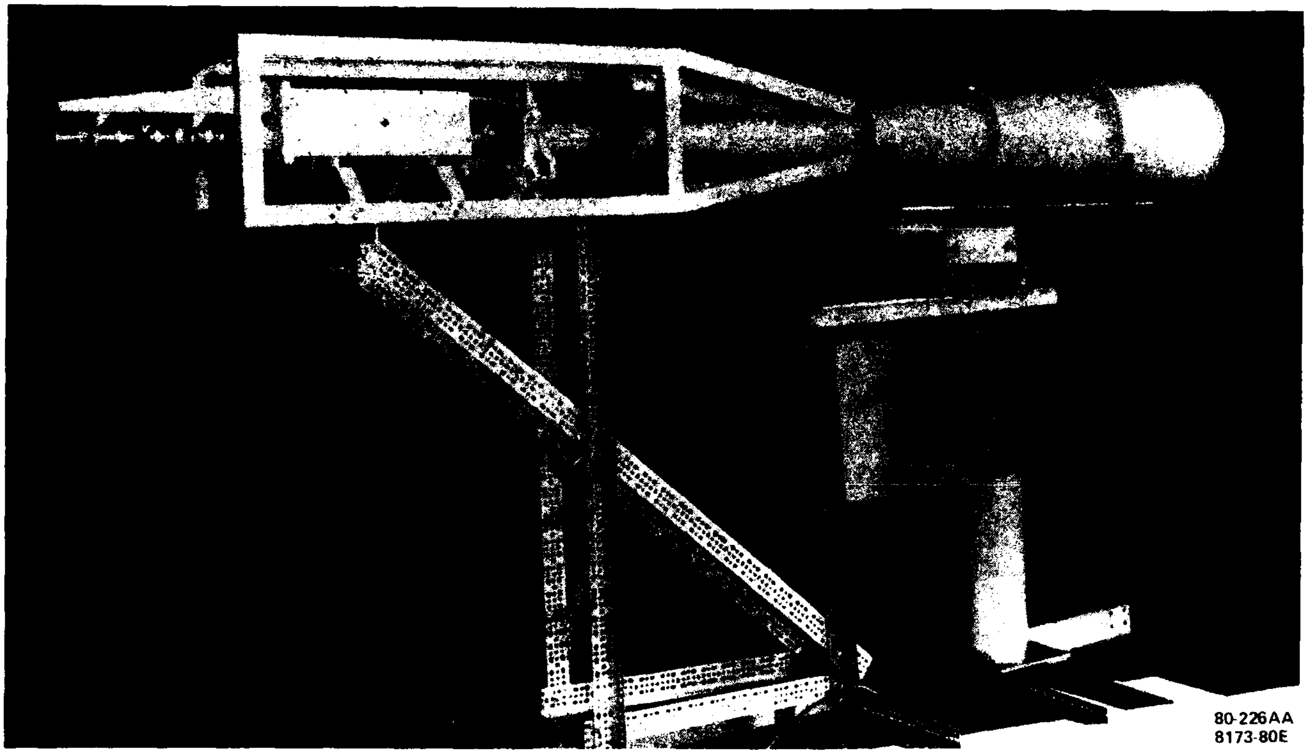

Figure 1.   Photo Of Feed Assembly

Figure 2.   TE21 Difference Mode Coupler

of which are left- and right-hand circularly polarized difference signals. As a circularly polarized tracking device, it will receive a linearly polarized tracking signal of any polarization orientation.

For simplicity, the operation is described as though the coupler were operating in the transmit mode. However, by reciprocity the same field configuration exists in receive. The device shown is actually two TE21 mode couplers interlaced around the circumference of the centrally located circular waveguide.

Coupler No. 1 excites the TE21 mode field configuration shown in Figure 3. By inspection, it is apparent that this mode radiates a horizontally polarized elevation plane difference pattern, and a vertically polarized azimuth difference pattern. On the other hand, coupler no. 2 which is rotated 45° relative to No. 1, radiates a vertically polarized elevation plane difference pattern, and a horizontally polarized azimuth difference pattern. Since the two field patterns are in space quadrature, exciting them simultaneously through a quadrature hybrid results in circularly polarized tracking difference patterns. We next address the basic design of the tracking system which employs this type of higher order mode tracking coupler.

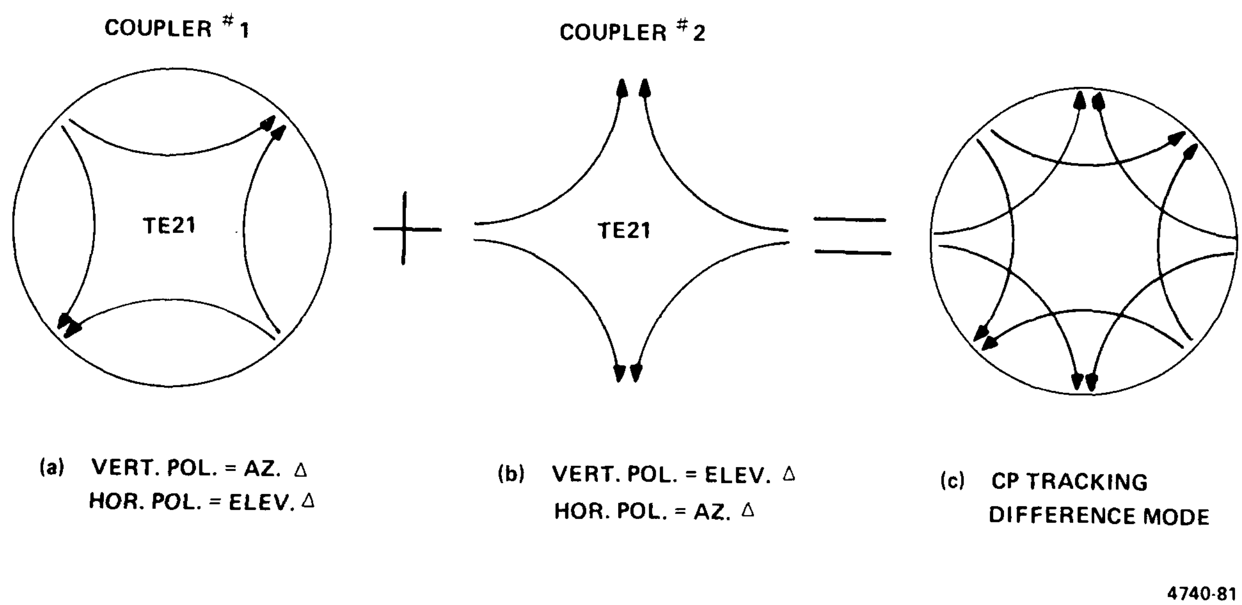

Figure 3. TE21 Mode Coupler Operation

Tracking System Theory of Operation

Consider the system in receive. If a linearly polarized signal is received directly on the RF bore sight axis of the antenna, only the TE_{11} mode is excited in the feed horn. Figure 4 shows the decoupling of the TE11 mode to the output terminal, so there is no effective signal to the tracking receiver.

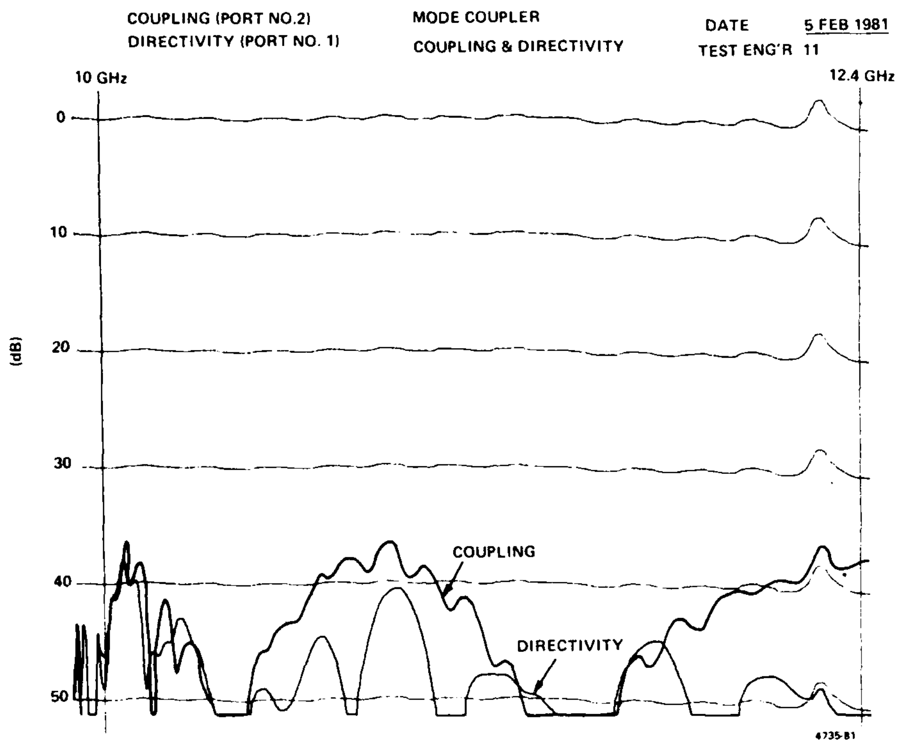

Figure 4. Mode Coupler TE11 Coupling and Directivity

If now, the received signal is off axis a TE21 mode is excited in the horn. Figure 5 shows the effective coupling of the TE21 energy to the receive terminal. The magnitude of this TE21 mode is proportional to the angle off axis within a restricted segment; its phase, for any given polarization orientation, is determined by the direction off axis.

Assume the receive signal arrives off axis only in elevation. Assume further that it is above the bore sight axis of the antenna. The excited TE21 mode will be coupled out of the tracking mode coupler and processed to the input of the tracking receiver. At this point, its phase is adjusted to be the same as that of the sum channel signal at the tracking frequency.

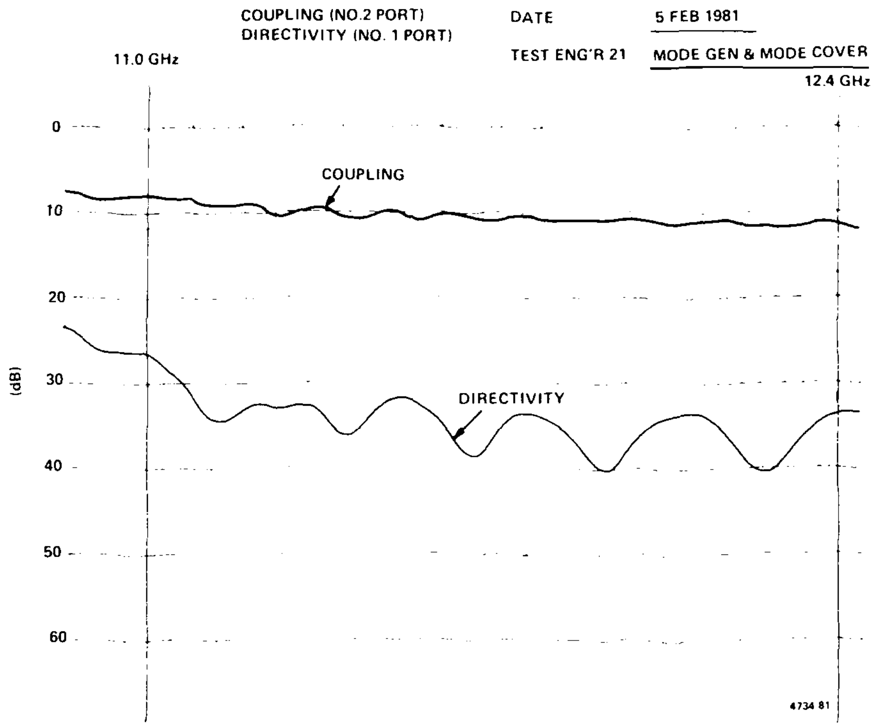

Figure 5. TE21 Mode Coupling and Directivity

If now, the signal is received from some other direction, its phase at the receiver input will vary accordingly. Thus, from the magnitude and phase of the difference signal arriving at the tracking receiver, error signals are generated to bring the RF axis of the antenna in line with the source. Figure 6 is a dual antenna pattern showing a sum pattern at the receive beacon frequency and a difference TE21 mode at the output of the quadrature hybrid port No. 1.

Horn Description

The feed horn transmits at power levels up to 2.5 KW CW in the 14 to 14.5 GHz frequency band and simultaneously receives in the 10.95 to 11.7 GHz band. The design consists of a conical horn with its wall corrugated by chokes, resulting in equal tapers in the E&H planes. The choke depth is selected to be between one quarter and one half over the receiver bands. The choke spacing, while not critical, requires a uniform periodicity. The resultant propogating mode in both the 14 GHz and 11 GHz frequency bands is equivalent to the sum of the TE11 and TM11 modes. Combining the dominant and higher order modes results in field radiation patterns with extremely low side lobes and near perfect symmetry about the horn axis.

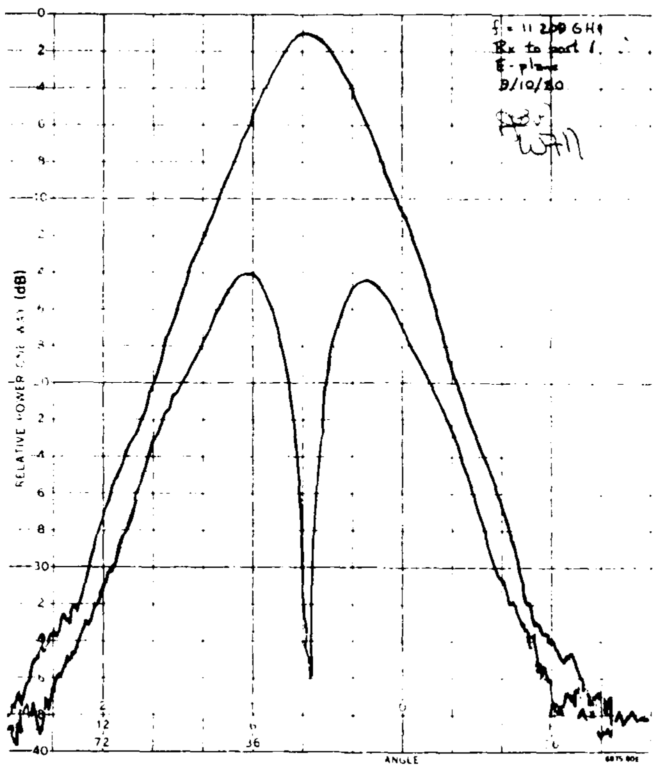

Figure 6. Antenna Pattern Receive and Port #1

(Mode Coupler) E-Plane and Difference f = 11.20 GHz

The horn length and aperture size are selected to minimize beam width variations with frequency across both bands by incorporating a phase error of 90° to 100° at 11.5 GHz in the horn aperture. As frequency is increased, the phase error increases, thereby broadening the beam in a manner to partially compensate for the electrically larger aperture. Typically the beam width remains constant over the 11.5 to 14 GHz bands to within 10 percent.

Beam Waveguide Description

As pointed out previously, the beam waveguide mirror system as shown in Figure 7 directs the energy to and from the feed horn and the Cassegrain antenna subreflector. The configuration utilized is based on optical techniques, though corrected for diffraction effects by using slightly elliptical curved mirrors. It refocuses the energy for proper shaping and positioning of the waveguide mirrors. The configuration consists of two flat mirrors and two curved mirrors, the size and shape of which are designed to reduce spillover and increase efficiency. Reflectors B&C are approximately 83 feet from each other. Thus, the energy travelling from mirror B to mirror C, for example, initially converges toward that focus point, as suggested in Figure 7. This is the correction for diffraction effects mentioned previously. These effects

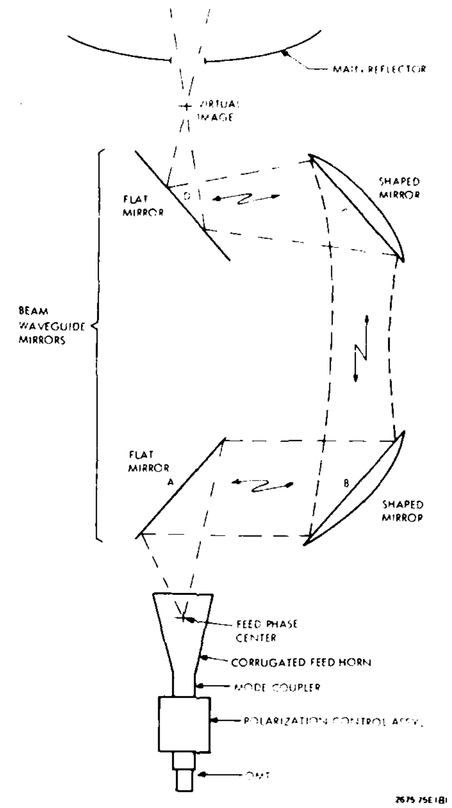

Figure 7. Optical Ray Path of Beam Waveguide Feed

cause the energy to spread as it approaches mirror B, as shown in Figure 7. A similar situation exists for energy travelling from mirror C to B in receive. Reflectors A&D are planar. In operation, reflectors A, B, C, and D move as a unit where the azimuth platform rotates. Reflector D is on the elevation axis and rotates also when the disk is steered in elevation. In this way the energy from the beam waveguide is always directed through the hole in the main reflector vertex.

As part of our system, GTE supplies the subreflector. This unit is shaped in such a way as to optimize the power illumination of the main reflector. Since this results in distortion of phase, shaping coordinates of the main reflector are supplied to the customer. The shaping program contributes approximately .5 dB of system gain.

The corrugated horn generates a spherical wave front at reflector B, the apparent center of radiation being near the throat of the horn, and almost frequency independent. Reflector A serves as a right-angle bend between the horn and shaped reflector B. Reflector C focuses the incident planar wave front to a point which, when imaged by reflector D, appears near the vertex of the large dish.

Polarization Control

In a linearly polarized satellite communications system, it is necessary to align the polarization of the ground station antenna with that of the received satellite signal. This capability must be provided in the feed.

To provide this capability, it is necessary to rotate the orthomode transducer which is used to combine the receive and transmit rectangular waveguides into the circular waveguide of the feed proper. The two outputs of the OMT are connected to the low, noise, amplifiers and high power combining network by means of waveguide rotary joints. The circular output of the OMT is connected to the field proper by means of a choke coupled rotary section. This operation is automated and controlled by an operator from a control panel.

When these components are assembled and measured as a unit the first test is swept VSWR in both the receive and transmit bands. Figures 8 & 9 show good compliance with specifications in both bands. The multiple traces are for different polarization orientations as represented by different settings of the rotary joints and the OMT.

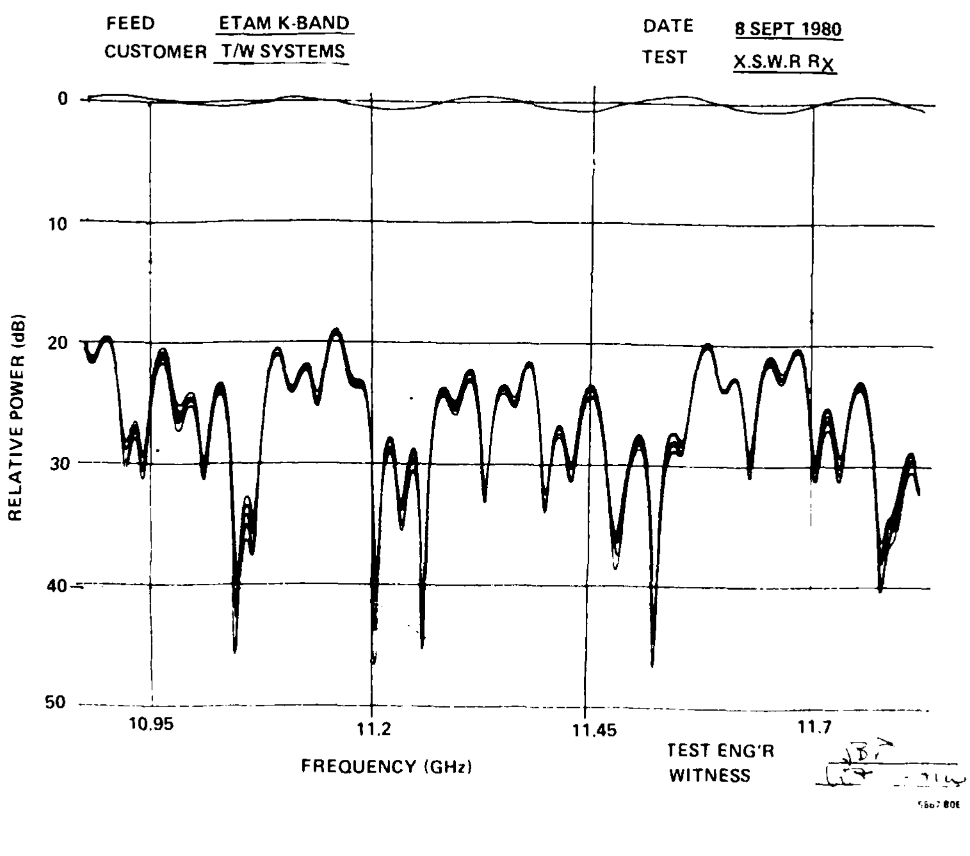

Figure 8. VSWR Receive

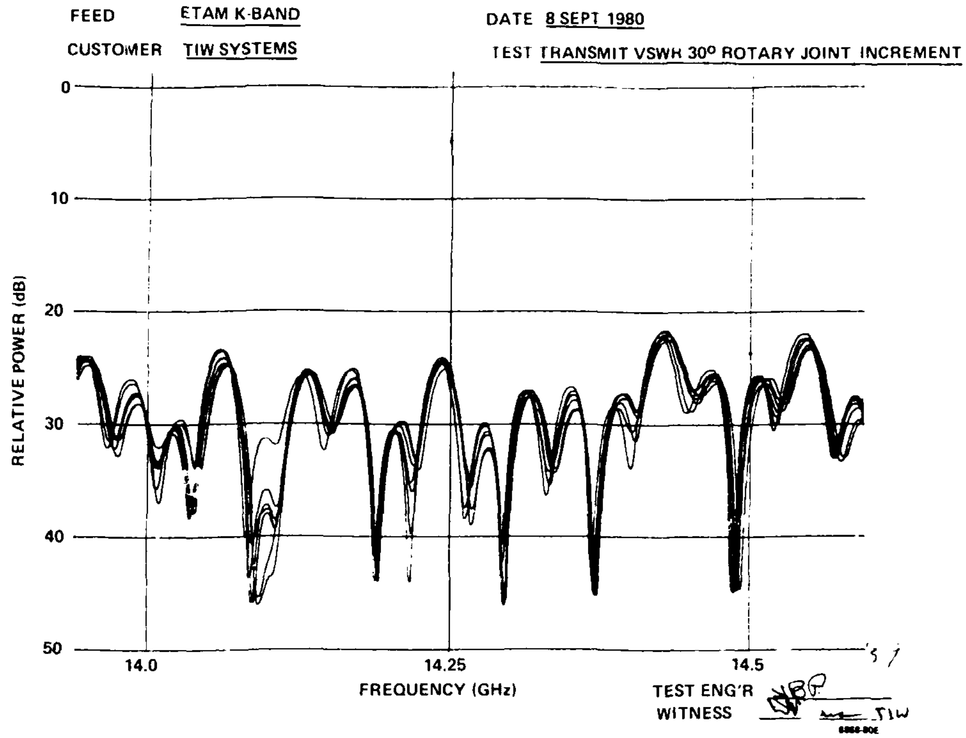

Figure 9. VSWR Transmit

To meet the requirements of axial ratio it is necessary to tune three different Δ phi sections. The application of these differential phase shifters compensates for elepticities in the horn matching section and TE21 mode coupler. Figures 10 & 11 show the final tuned results.

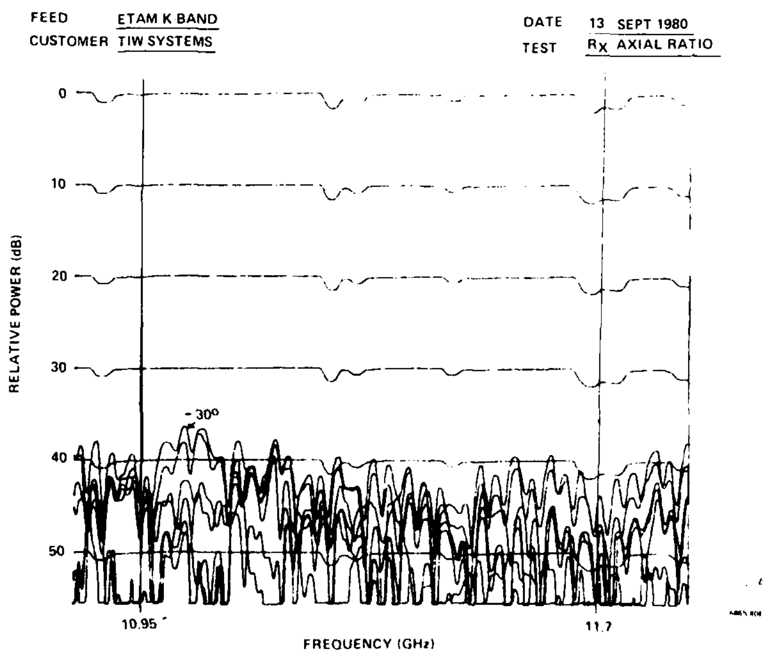

Figure 10. Axial Ratio Receive

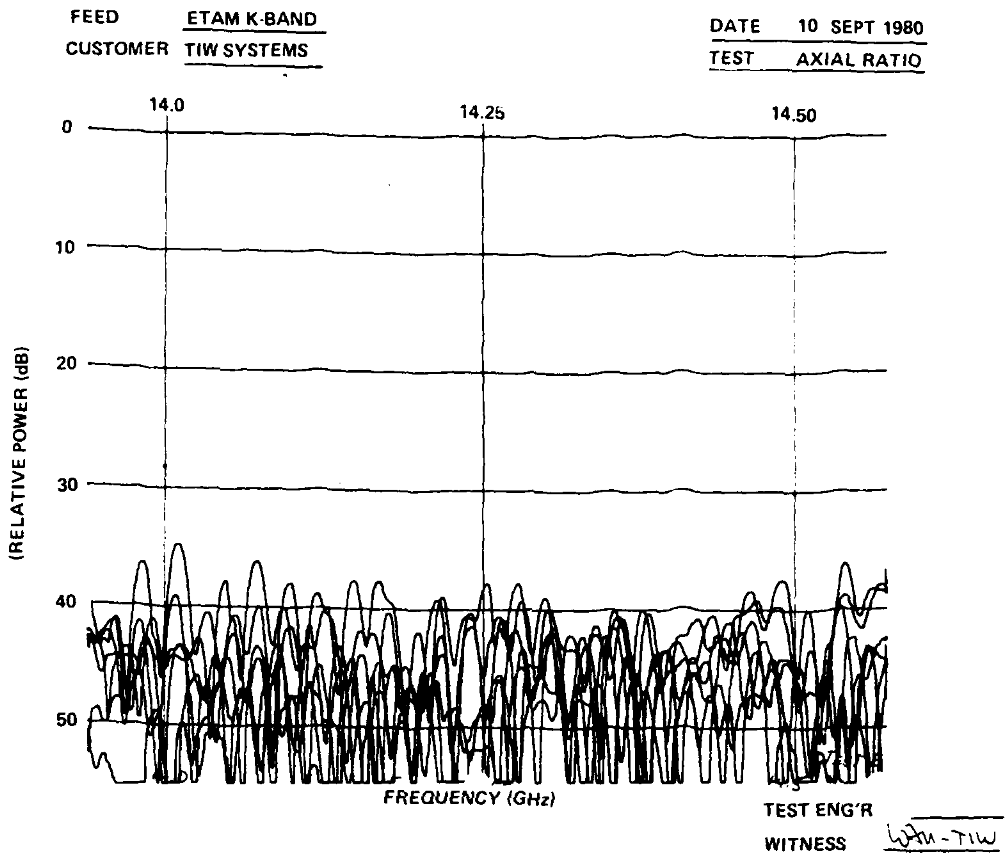

Figure 11. Axial Ratio Transmit

4699-81

This configuration works very well for linear polarized transmit and orthogonal receive stations. To modify for frequency reuse it is necessary to add a diplexing filter and broadband OMT as shown in Figure 12. Because of the waveguide size we are operating in (.922 inch diameter), a multiplicity of modes can propogate with a deleterious effect on VSWR. To help compensate a symmetrical excitation at the ortho port is used.

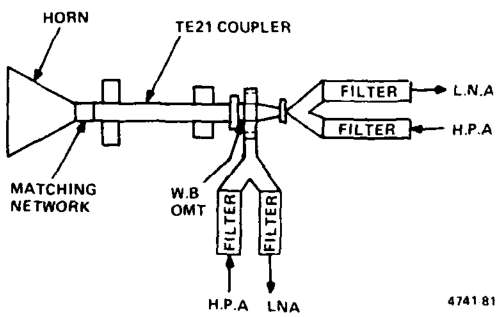

Figure 12. Frequency Reuse

Figures 13, 14, 15 & 16 show the excellent isolation characteristics between ports.

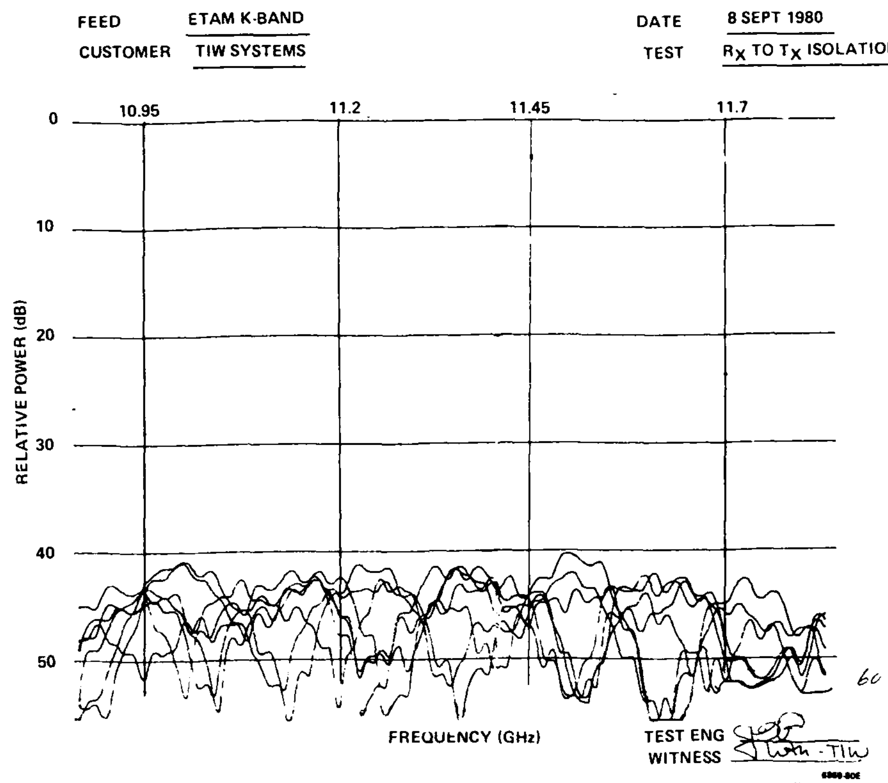

Figure 13. Isolation Measurement Receive To Transmit

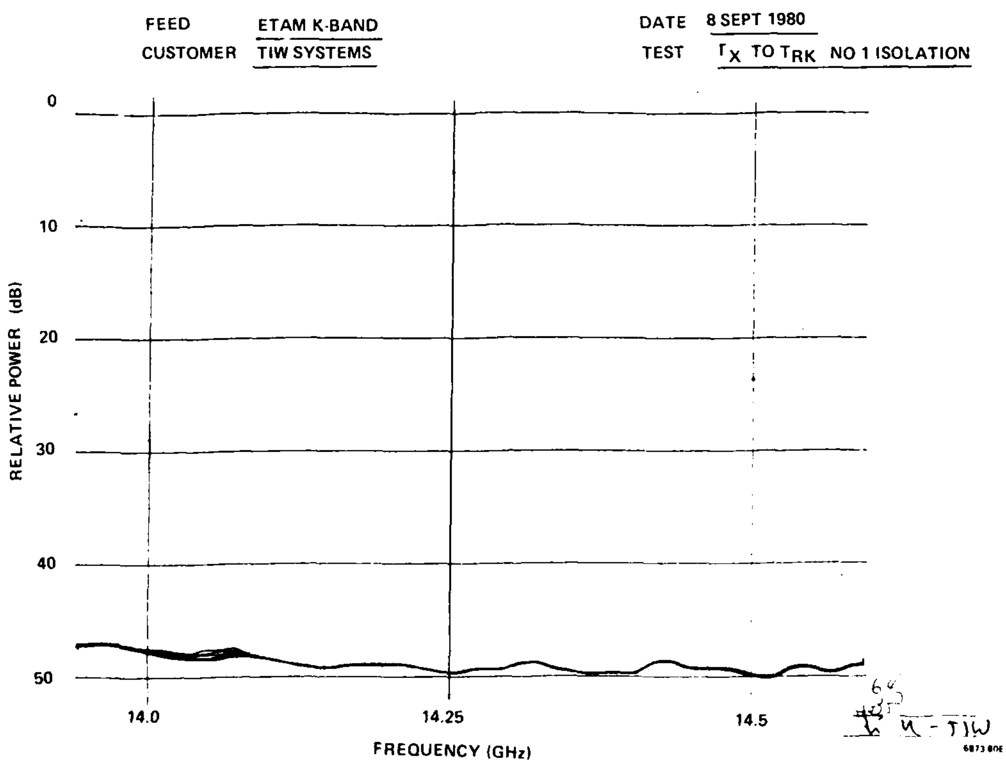

Figure 14. Isolation Measurement Transmit To Tracking Channel 1

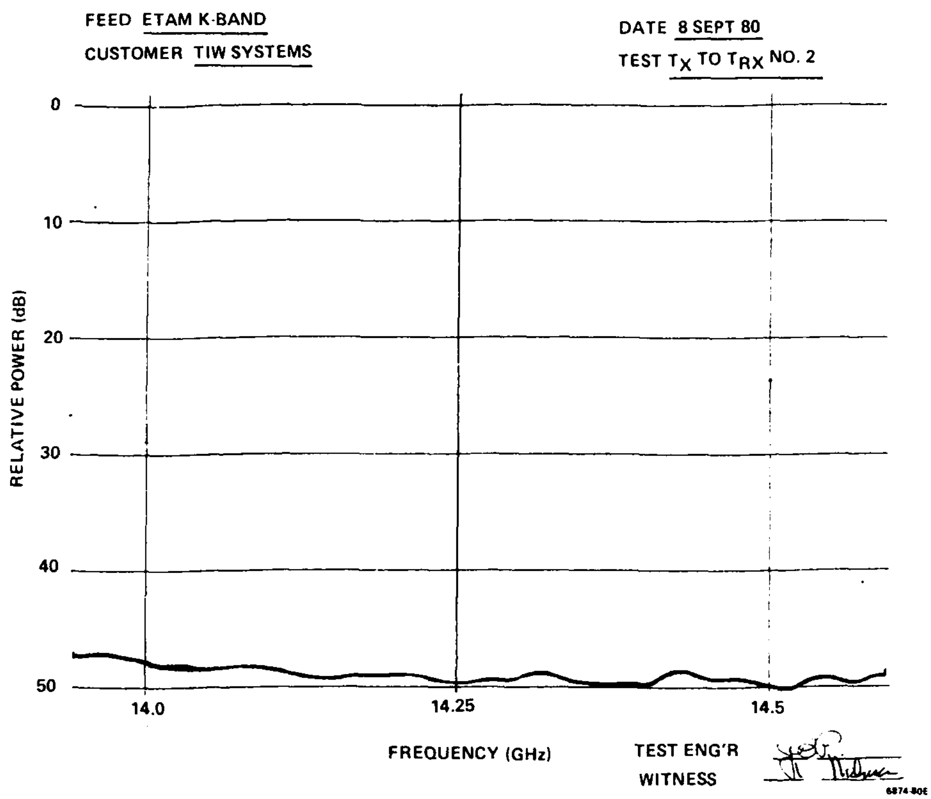

Figure 15. Isolation Measurement Transmit ToTracking Channel 2

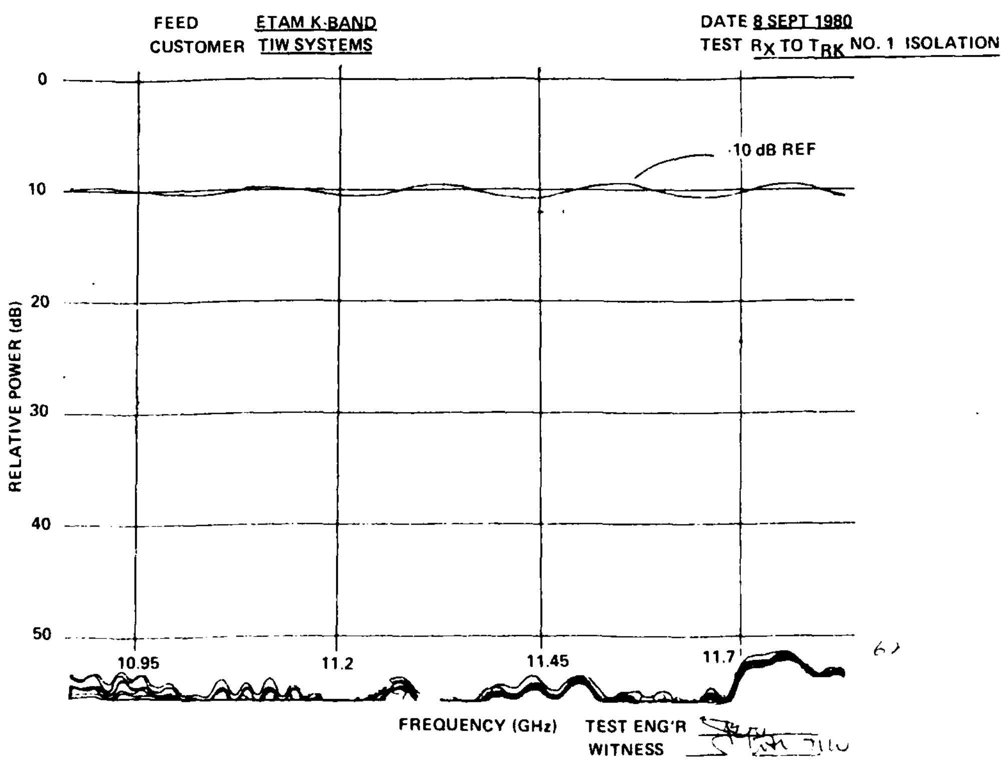

Figure 16. Isolation Measurement Receive To Tracking Channel 1

R-81014

AN ELLIPSOIDAL FREQUENCY SELECTIVE SURFACE

Michael J. Dick

Cubic Corporation

San Diego, California

ACKNOWLEDGEMENTS

The author wishes to thank D. Killion, R. Stevenson, W. McNaul, P. Eberhardt and Dr. R. Justice for their valuable help in working on this project.

1.0 INTRODUCTION

The frequency selective surface (FSS) described herein reflects radio waves within a small frequency band, but it is nearly transparent to radio waves outside this band. This ellipsoidal FSS is an ordered arrangement of dipole - like elements on an elliptical surface. The design and testing of an elliptical FSS requiring a highly curved geometry to be taken into account during the design process, is the topic of this paper.

The basic requirements of this ellipsoidal FSS are to be reflective in a band centered at roughly 9 GHz and to be relatively transparent at frequencies above 10.5 GHz and below 7.5 GHz. More specific requirements are given in a companion paper by D. Killion to be presented at this symposium. That paper describes the use intended for the ellipsoidal FSS in the APS-80 radar.

A literature search revealed that most of the previous FSS work involved surfaces much less curved than the surface required for this project. Nevertheless, Schenum's[1] presentation of the effects of element length and element separation on FSS performance provided excellent starting point dimensions for the experimental design.

2.0 THEORY

A radio wave of any wavelength striking a reflector causes surface currents to flow in that reflector. These surface currents re-radiate the wave.

A polarized radio wave of wavelength λ striking a sheet of elements of length $\lambda/2$ excites these elements as if they were resonant dipoles (Figure 1). These dipoles, if they are oriented parallel to the E field, re-radiate the wave.

Should the length of the elements be much different from $\lambda/2$, the elements will not be strongly excited and these dipole elements will be more nearly transparent to the radio wave. Similarly, if the dipole elements are not nearly parallel to the polarization of the incident wave, the surface becomes more transparent.

A current element can be considered as an infinitesimal dipole. The composition of a current can be considered to be a combination of current elements of any length. Therefore, a solid reflector, being equivalently composed of dipoles of any length, will "reflect" any wavelength radio wave. Whereas a sheet of dipoles of length $\lambda/2$ oriented parallel to the E field will reflect only wavelengths in the neighborhood of $\lambda/2$(or $n\lambda/2$, n=1, 2, 3, ...).

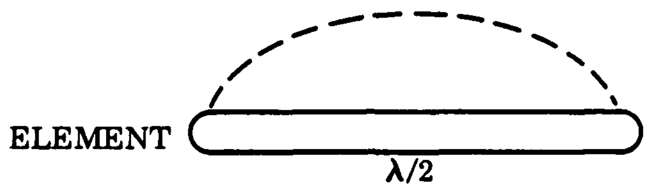

NOTE: DASHED LINE REPRESENTS CURRENT VS. DISTANCE ALONG THE ELEMENT. THIS PLOT IS CHARACTERISTIC OF A HALF WAVE DIPOLE.

Figure 1. Excited Element of Length $\lambda/2$

3.0 APPROACH

- Build an FSS on a simple flat surface.

- Experiment with various fabrication techniques such as electrodag silk screening, electrodag painting, and copper tape.

- Experiment with various dimensions on the FSS which deviate from those used by Schenum. Test to see if the reflective bandwidth requirements are met.

- Project a selected flat FSS design onto the more complex curved surface (ellipsoid).

- Adjust parameters on the curved surface FSS to meet specified reflective bandwidth requirements, testing after each parametric adjustment.

- Make E and H plane-pattern tests comparing the performance of the FSS with that of a solid reflector.

4.0 PROCEDURE

4.1 FLAT SURFACE FSS

Various techniques were examined for fabricating the flat surface FSS. These techniques placed reflective element strips on thin plastic by either silk screening with eletrodag, painting with electodag, or using small strips of reflective tape. Silk screening proved to be a poor technique for fabricating the FSS. The eletrodag did not easily go through the silk screen. When it did go through, it smeared. Another material besides eletrodag could have been used for silk screening. However, the experience with the eletrodag coupled with the projected difficulty of eventually having to silk screen onto a curved surface (for the final product) led to the abandonment of the silk screening technique.

The second method (painting with electrodag), was more successful. Masks made of scotch tape kept the electrodag from smearing. With extreme care, the worker could round off the ends of the electrodag elements and avoid the high voltage breakdown expected in pointed tipped elements.

The third method, using reflective tape strips on the thin plastic sheet, also proved to be practical.

Estimations for good dimensions for the element length, element gap (end to end) and element separation (broad side) were based on the results of Schenum. The dimensions (Figure 2) chosen for fabrication appear in the Table below. These FSS's were tested for frequency dependence of reflection and transmission in the small chamber illustrated in Figure 3.

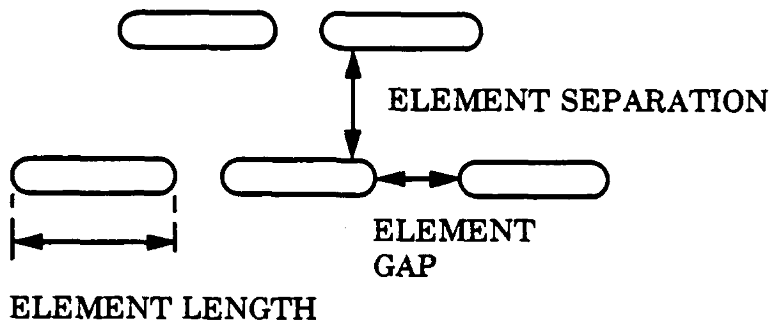

Figure 2. Pictorial Definition of Demensions

	ELEMENT LENGTH	GAP	SEPARATION
#1	.42"	.11"	.57"
#2	.52"	.11"	.38"
#3	.62"	.11"	.38"

Table: Dimensions of Flat Surface FSS's Fabricated

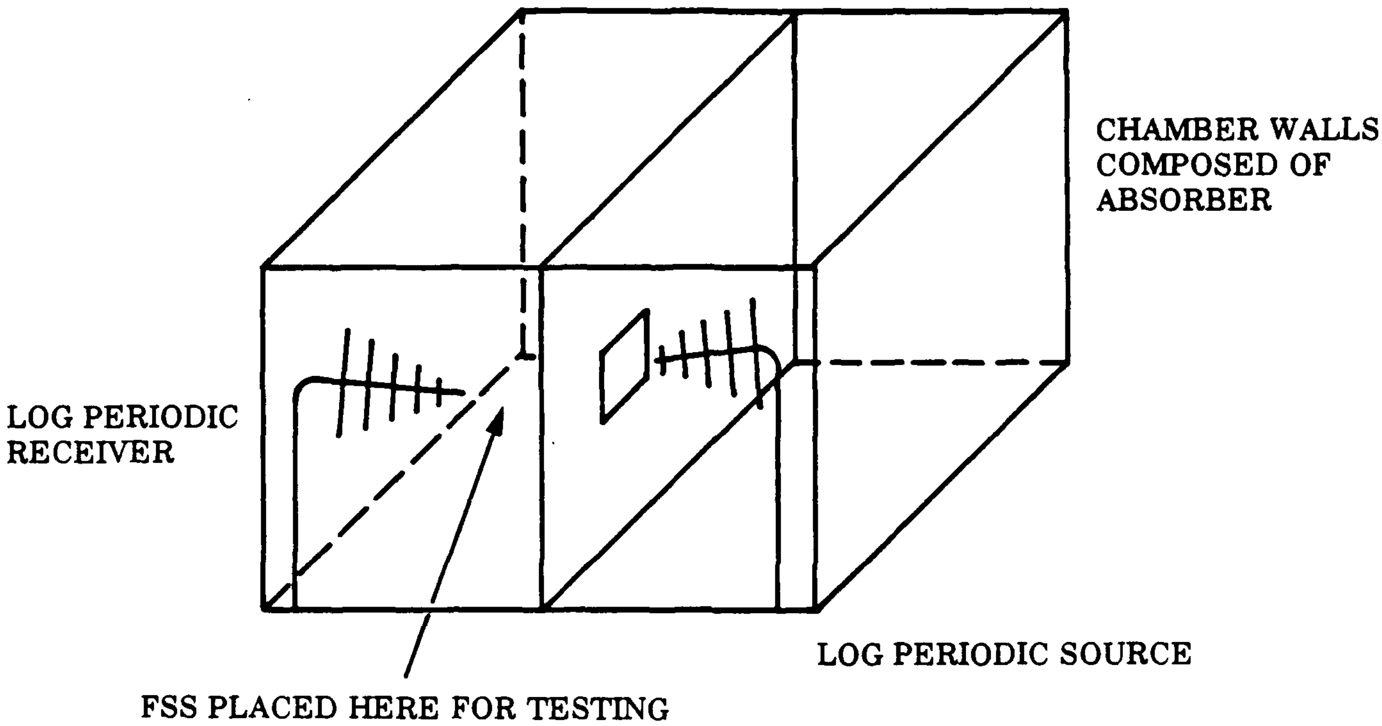

Figure 3. Test Chamber

4.2 CURVED SURFACE

After a design for the flat FSS was developed, it had to be transferred to the ellipsoidal curved surface. Designs employing techniques which only slightly modified broadside element spacing to compensate for the difference between the flat and curved surface did not yield the required reflection band.

The successful technique was to project a flat FSS vertical spacing onto the curved elliptical surface in the manner shown in Figure 4. Each row of elements is projected toward the focus of the ellipse where the transmitting source is to be located. One could view this design as a point source at the focus transmitting to each row of the flat surface. Where the lines of transmission intersect the ellipse is the projection of the flat surface FSS element broadside spacing onto the ellipse.

The successful dimensions in order to obtain a reflective band between approximately 7.5 GHz and 10.5 GHz which is centered near 9 GHz are: flat surface vertical separation = .75" (this dimension was projected onto ellipse as shown in Figure 4), element gap = .07", element length = .625" The width of each element was .15"

The semi-major axis of the ellipse used is a = 2.12".
The semi-minor axis of the ellipse used is b = 1.82".

The curved FSS was placed in the chamber (Figure 3) and tested. Element length and gap parameters were finely adjusted to meet the reflective band requirements. The band test results of the final design are given in Figure 6 (presented in the results section of this paper).

E and H Plane tests compared the FSS patterns to those of a solid elliptical reflector. For both the FSS and the solid reflector, waveguide feed was centered at the focus F_1 (Figure 5). Sample E and H plane test results are presented in the results section.

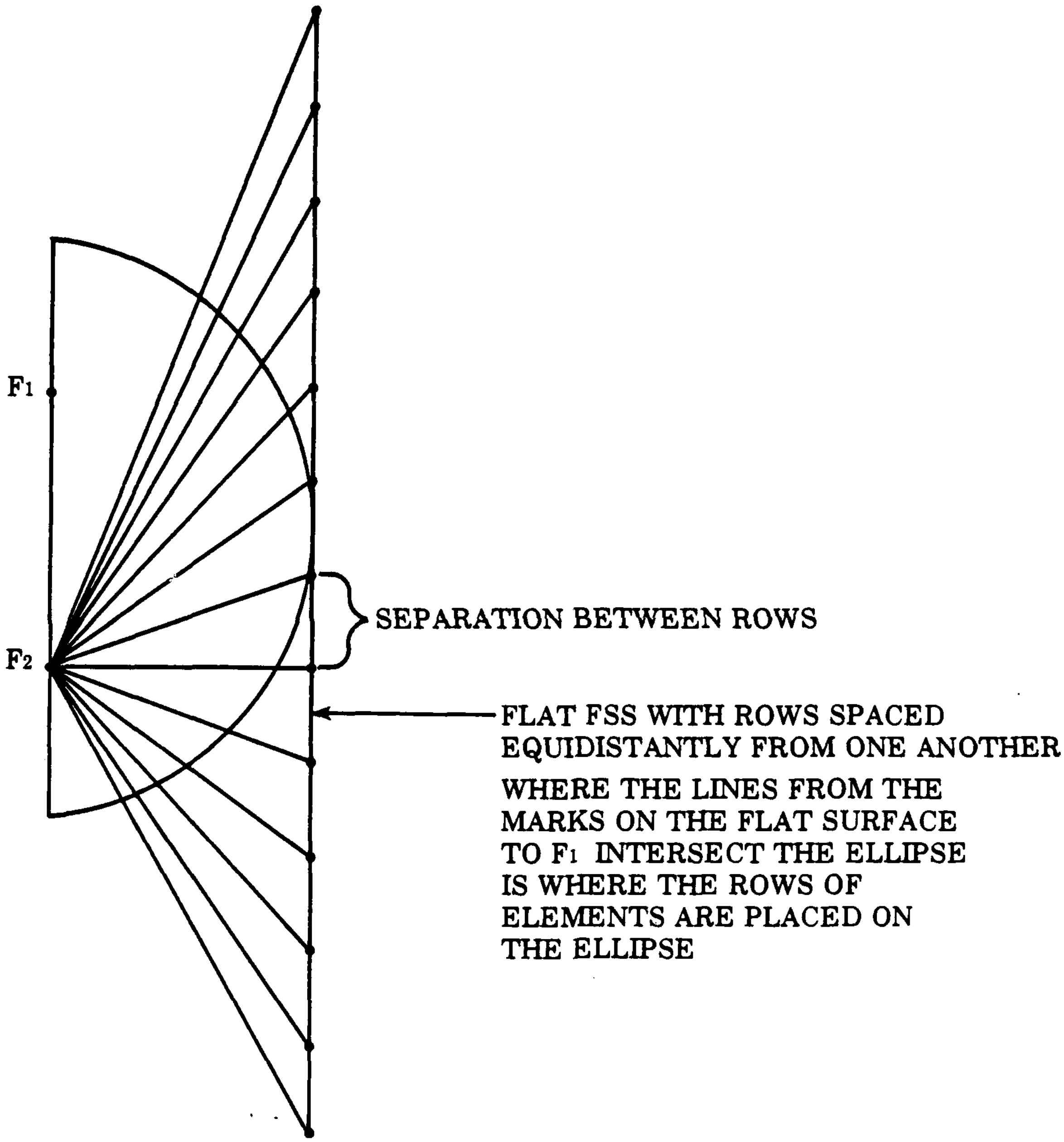

Figure 4. Projecting The Flat Surface FSS Onto The Ellipse

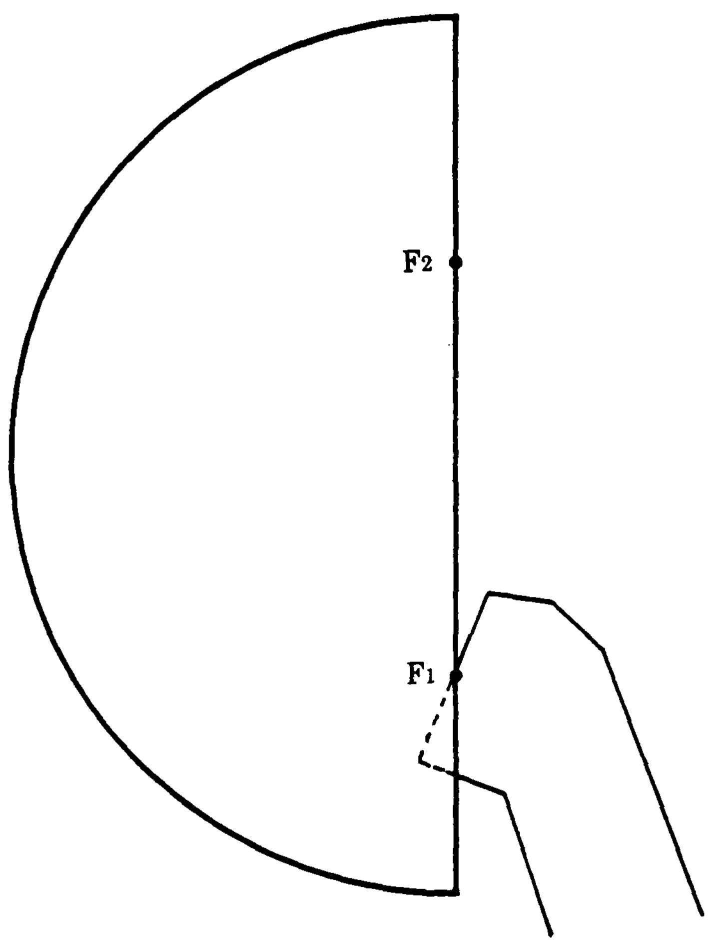

Figure 5. Positioning of Waveguide Feed With Respect To The Ellipse

5.0 RESULTS

The test results referenced in section 4.0 do indeed indicate the satisfaction of design requirements alluded to in section 1.0: high reflectivity near 9.0 GHz and relative transparency above 10.5 GHz and below 7.5 GHz.

The frequency-selective response of the FSS, as tested in the chamber illustrated in Section 4, is depicted below in Figure 6. This shows the FSS is highly reflective near 9 GHz and is relatively transparent above 1.05 GHz and below 7.5 GHz.

The results of tests comparing the ellipsoidal FSS and a solid perfectly reflecting ellipse appear in Figure 7. The patterns were made with the waveguide feed centered at one focus of the reflector (Figure 5).

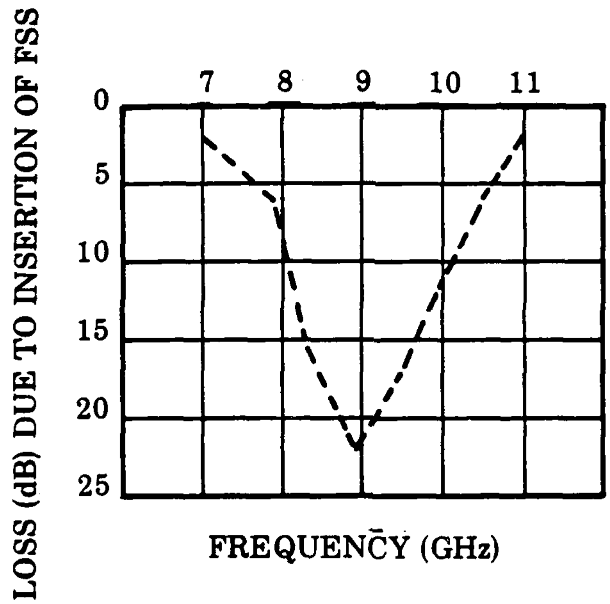

Figure 6. Frequency Selective Responses of FSS

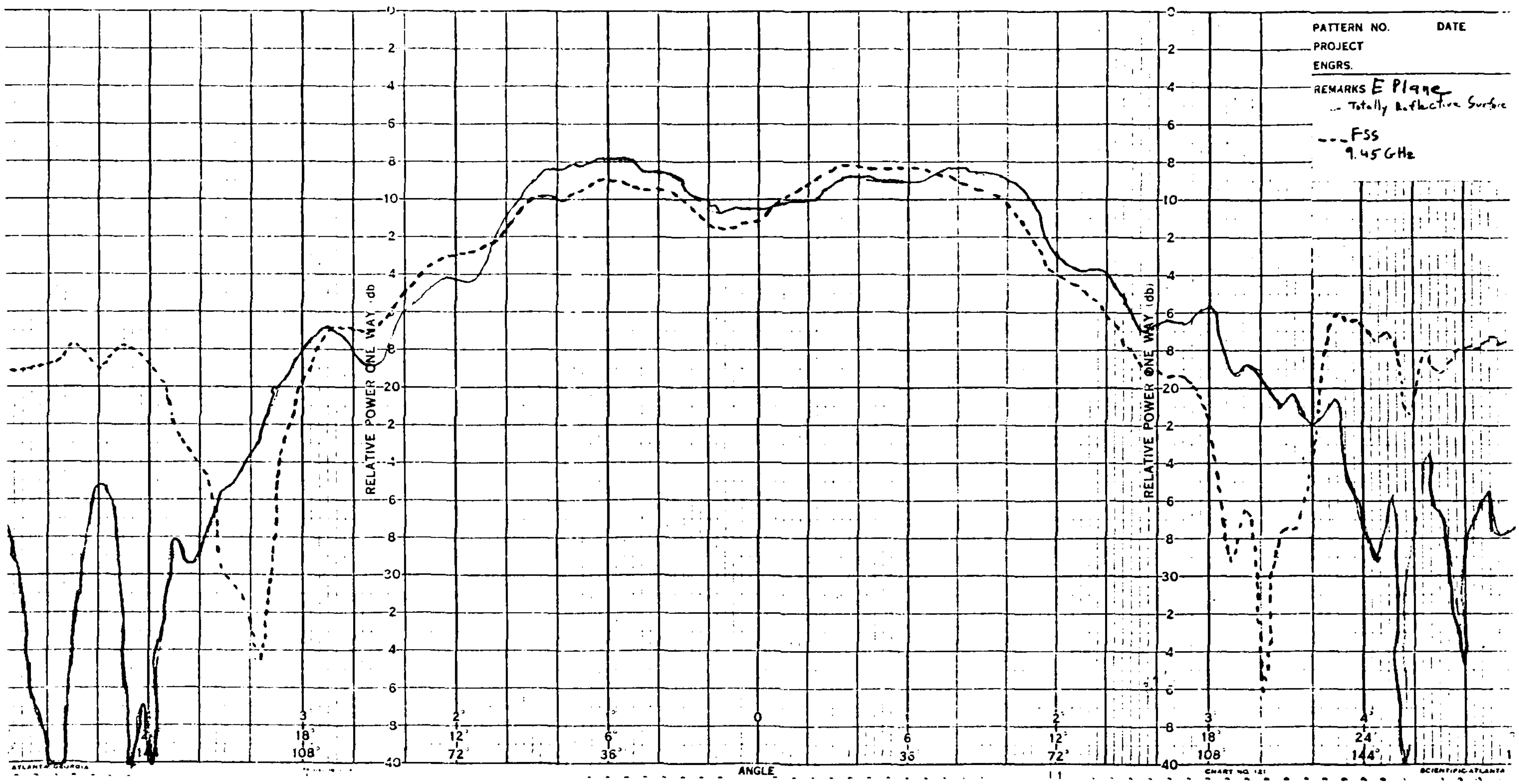

FIGURE 7a   E PLANE 9.45 GHz (WITHIN REFLECTIVE BAND)

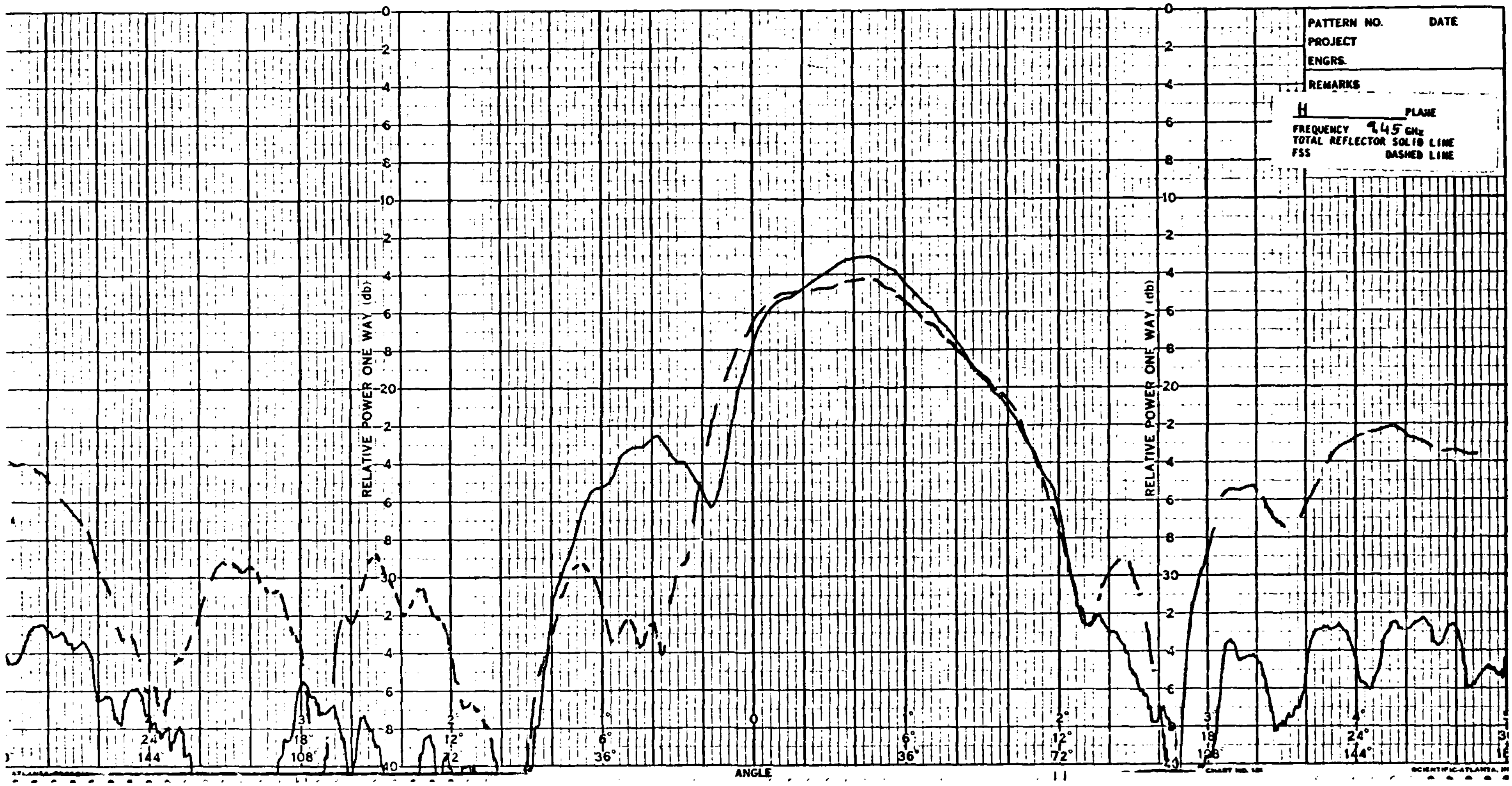

FIGURE 7b H PLANE 9.45 GHz (WITHIN REFLECTIVE BAND)

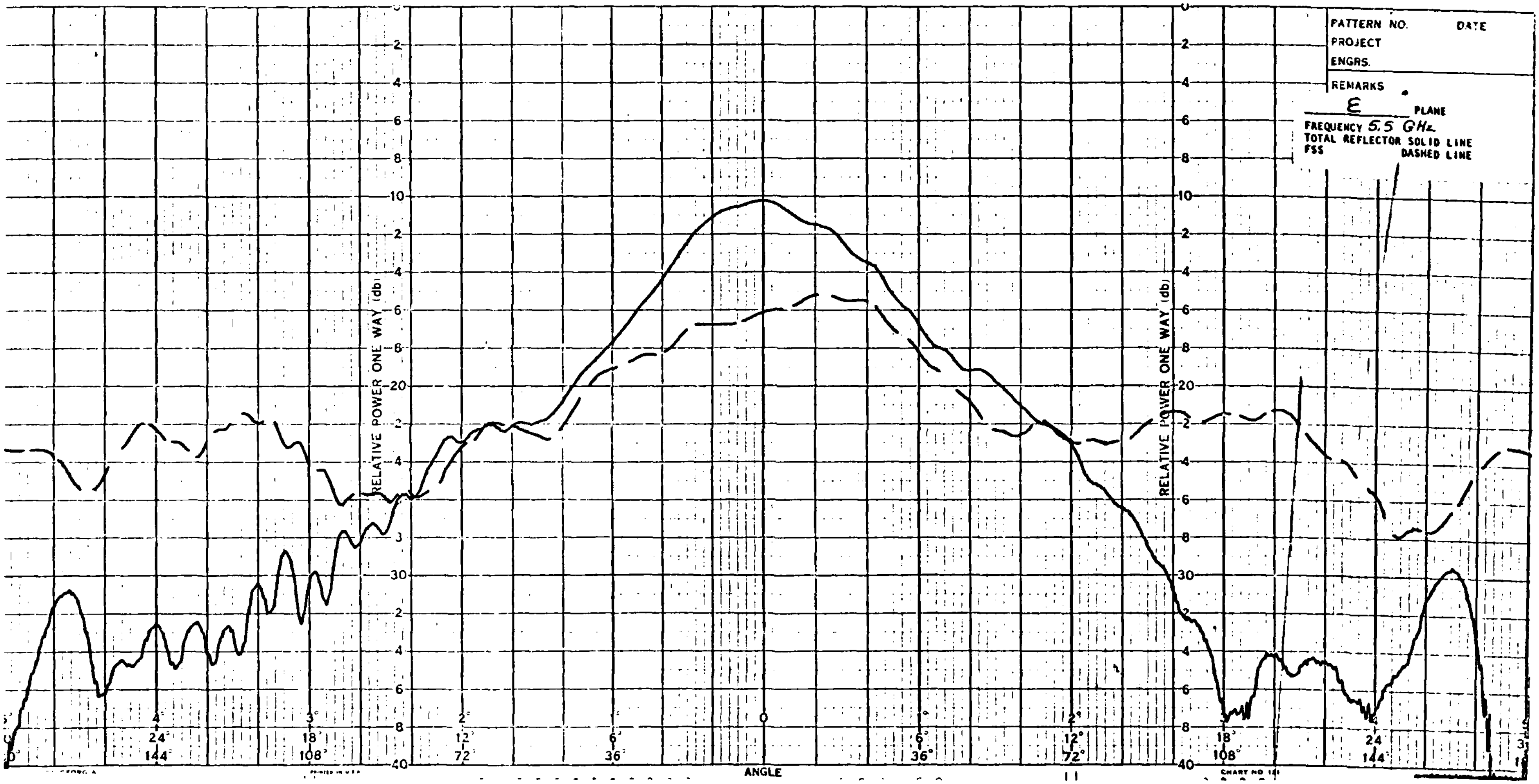

FIGURE 7c E PLANE 5.5 GHz (OUTSIDE REFLECTIVE BAND)

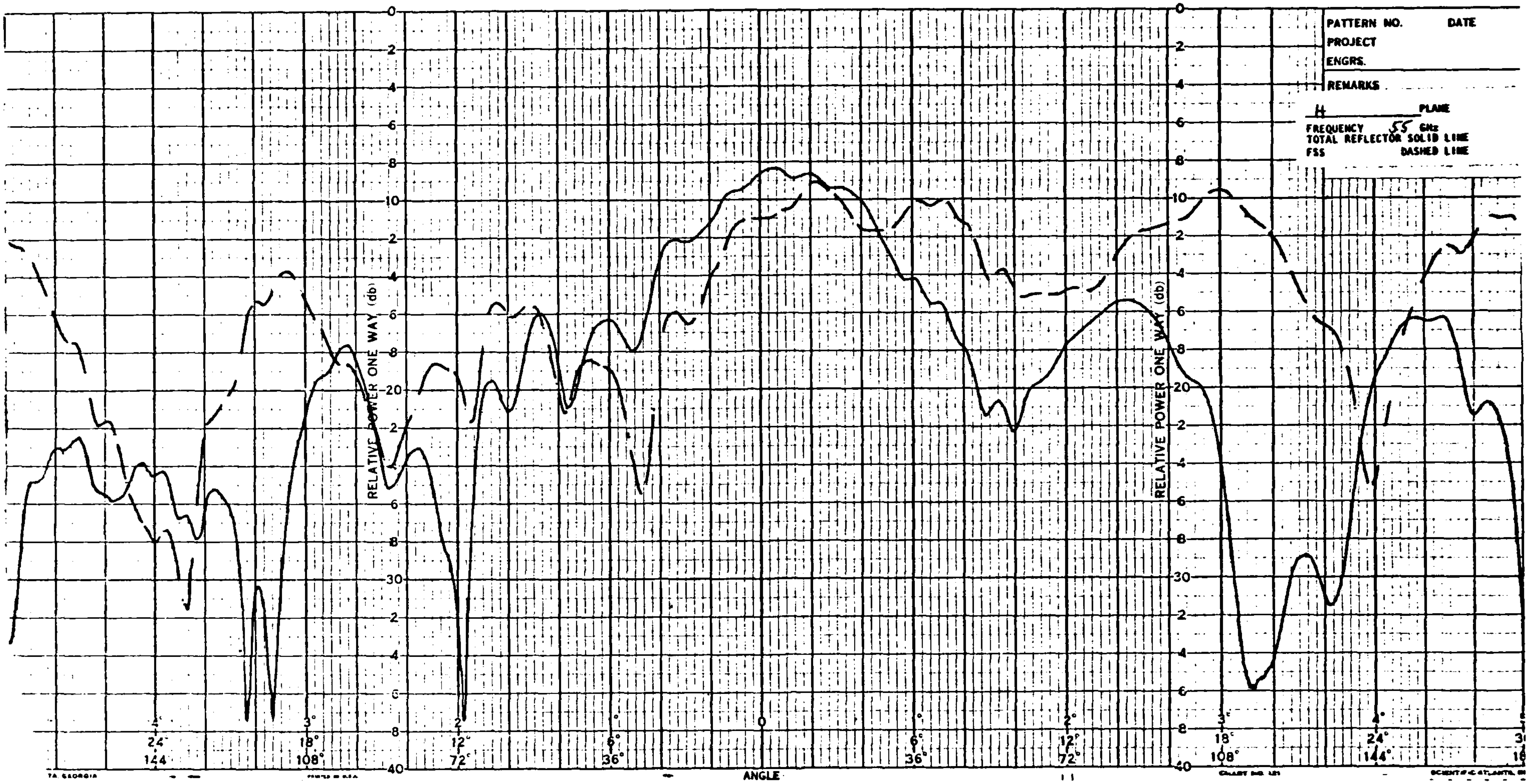

FIGURE 7d H PLANE 5.5GHz (OUTSIDE REFLECTIVE BAND)

6.0 CONCLUDING COMMENTS

Should one desire to build a curved surface FSS with reflective frequency requirements different from the ones described for this project, the following suggestions should be helpful.

(1) The element length should be approximately $\lambda/2$ (λ being the wavelength of the center frequency of the reflected band).

(2) Small consistent deviations in gap length do not seem to affect the frequency reflective band significantly. In the example described in this paper, the reflective properties of the FSS met the prescribed requirements both when all gaps were .07" and when all gaps were .10."

(3) The vertical separation of elements should follow the pattern depicted in Figure 4. Note that shifting the projected plane surface either up or down produces an acceptable projection onto the ellipse. An HP 25 program for producing the projection is printed in the Appendix.

FOOTNOTES

[1]G.H. Schenum, "Frequency Selective Surfaces for Multiple Frequency Antennas," Microwave Journal, May 1973, pp. 74-76.

BIBLIOGRAPHY

Agrawal, Vishwavy D. and William A. Imbraile, "Experimental and Theoretical Design of Dicrhoic Surface for a Spacecraft Antenna," IEEE Antenna and Propogation Society International Symposium Proceedings, 1976.

Cohn, Seymour B. "Microwave Measurements on Metallic Delay Media," Proceedings of the I.R.E, 1953.

Schenum, G.H., "Frequency-Selective Surfaces for Multiple Frequency Antennas," Microwave Journal, 1973.

APPENDIX
HP 25 Program

This program determines the vertical position (y coordinate on the diagram) where rows of elements should be placed on the FSS ellipsoid.

Variable List

Inputs

m = slope = n (.75) $n = \pm 1, \pm 2, \pm 3$, ie., m is the slope of the line from focus F_1 to a given marking on the vertical line (from which the projection is being made)

Q = - focal length (measured from center of ellipse)

a^2/b^2 = (semi-major axis / semi-minor axis)^2

a^2 = (semi-major axis)^2

Outputs

x, y (point of intersection of line with the ellipse)

Register	1	2	3	4	5	6	7	0
Start	m	Q	$\frac{a^2}{b^2}$	a^2	$\frac{a^2}{b^2} + m^2$			
Finish						$\frac{mQ}{\frac{a^2}{b^2} + m^2}$	$\left[\left(\frac{mQ}{\frac{a^2}{b^2} + m^2}\right)^2\right.$	$\left.\left(\frac{mQ}{a^2/b^2} + m^2\right)^2 \left(-\frac{Q^2 - a^2}{\frac{a^2}{b^2} + m^2}\right)\right]$

Step #	Command	X register	Y register
1	Recall 1	m	
2	gx^2	m^2	
3	Recall 3	a^2/b^2	m^2
4	+	$a^2/b^2 + m^2$	
5	STO 5	$a^2/b^2 + m^2$	
6	Recall 1	m	$a^2/b^2 + m^2$
7	Recall 2	Q	m
8	x	mQ	
9	Recall 5	$a^2/b^2 + m^2$	mQ
10	÷	$mQ/(a^2/b^2 + m^2)$	
11	STO 6	$mQ/(a^2/b^2 + m^2)$	
12	$g\ x^2$	$(mQ/(a^2/b^2 + m^2)^2$	
13	STO 7	$(mQ/(a^2/b^2 + m^2)^2$	

Step #	Command	X register	Y register
14	Recall 2	Q	
15	gx^2	Q^2	
16	Recall 4	a^2	Q^2
17	-	Q^2-a^2	
18	Recall 5	$a^2/b^2 + m^2$	$Q^2 - a^2$
19	÷	$(Q^2 - a^2) / (a^2/b^2 + m^2)$	
20	Recall 7	$(mQ/(a^2/b^2 + m^2))^2$	
21	-	$(mQ/(a^2/b^2 + m^2))^2 - (Q^2 - a^2)/(a^2/b^2 + m^2)$	
22	gABS	$\lvert(mQ/(a^2/b^2 + m^2))^2 - (Q^2 - a^2)/(a^2/b^2 + m^2)\rvert$	
23	$f\sqrt{}$	$\lvert(mQ/(a^2/b^2 + m^2))^2 - (Q^2 - a^2)/(a^2 + m^2)\rvert^{½}$	
24	STO 0	$\lvert(mQ/(a^2/b^2 + m^2))^2 - (Q^2 - a^2)/(a^2/b^2 + m^2)\rvert^{½}$	$\lvert(mQ/(a^2/b^2 + m^2))^2 - (Q^2 - a^2)/(a^2/b^2 + m^2)\rvert^{½}$
25	Recall 6	$mQ(a^2/b^2 + m^2)$	
26	-	$\lvert(mQ/(a^2/b^2 + m^2))^2 - (Q^2 - a^2)/(a^2/b^2 + m^2)\rvert^{½} - mQ/(a^2/b^2 + m^2)$	
27	R/S	This is the x position	
28	Recall 1	m	$\lvert(mQ/(a^2/b^2 + m^2))^2 - (Q^2 - a^2)/(a^2/b^2 + m^2)\rvert^{½} - mQ/(a^2/b^2 + m^2)$
29	x	$m(\lvert(mQ/(a^2/b^2 + m^2))^2 - (Q^2 - a^2)/a^2/b^2 + m^2\rvert^{½} - mQ/(a^2/b^2 + m^2)$ This is the y position	

SHAPED LENS ANTENNAS*

J. J. Lee and R. L. Carlise

Defense Electronics Operations

Rockwell International

Anaheim, CA 92803

INTRODUCTION

As the demand for EHF technology increases along with the recent advances in the development of low loss dielectric materials and numerically controlled machines, dielectric lenses have become viable candidates for EHF antennas. For the design of low cost, light weight and high performance lens antenna systems, lens shaping is a powerful technique.

Shaping techniques can be applied to design dielectric lenses for different applications. The constraint of aperture power distribution can be imposed to control the main beam shape and sidelobe level. For excellent scanning capabilities the lens can be designed to be coma free by imposing the Abbe sine condition. For multibeam systems where low sidelobes and high crossover in gain between overlapping beams are required, a combination of aperture control and coma correction can be implemented.

Based on these different requirements, three different lenses were designed and fabricated. Preliminary test results were obtained and are reported here.

SPECIAL SHAPED LENS

The first lens designed and fabricated was shaped to transform a standard sin u/u pattern into a Taylor type distribution.

---

*This work was supported by NAVELEX under contract N00039-79-C-0207.

However this is by no means a limiting case. The transformation can be applied to any reasonable aperture distribution. As an example, the lens can be shaped to produce the well known $J_1(u)/u$ pattern for earth coverage with maximum efficiency, or any other aperture distribution which meets specific requirements.

The lens was designed to operate at 44 GHz with a Taylor type aperture distribution achieving both amplitude and phase control. The computed far field pattern was for a beamwidth of 3.0 degrees and -40 db first sidelobes. The lens is 43 λ in diameter with a focal length of 46 λ and horn aperture of 2.85 λ. The horn illumination is transformed by both the first and second lens surface to produce the desired aperture distribution as depicted in Figure 1. The measured far field pattern of this lens at 44 GHz is shown in Figure 2. The measured gain is 34.5 dbi with a 3 db beamwidth of 2.9 degrees. Note that the beamwidth for a cosine illuminated aperture of 43 λ would be 1.5 degrees. The first sidelobe is seen to be on the order of 32 db below the peak while the design goal was 40 db. This sidelobe degradation is believed to result from the surface mismatch of the lens. Also it was later found that a small portion of the first sidelobes of the feed horn pattern was intercepted by the lens. It is anticipated that with surface matching and feed control the sidelobes would be well below -32 db as predicted.

As expected the scanning characteristics of the special shaped lens were very poor. The adverse effect of cubic phase errors for off axis beams are manifested by high coma lobes and main beam distortion. As the offset angle increases, the beam deteriorates even more, making the special shaped lens unacceptable for scan applications. This requirement led to the development of the second lens for wide scanning capabilities.

WIDE SCANNING LENS

The second lens was designed and fabricated to meet the Abbe sine condition for wide angle scans. In this case no special transformation on the aperture distribution can be made. The distribution was basically the sin u/u horn pattern in amplitude, but modified in phase by the lens. This means, of course, that the sidelobe would not be as low as -40 db, but still at an acceptable level. The configuration of the lens is shown in Figure 3. The measured patterns are shown in Figure 4. As can be seen, there is no coma or main beam distortion with scan. The wide angle scanned beam has almost identical characteristics as the beam on axis. Again, the lens surfaces are not matched, but it has very little differential effects on the sidelobes of -23 db as the beam scans. The mismatch would indeed be a critical factor if the sidelobe were on the order of -40 db.

For multibeam systems, the horn phase centers were displaced off axisat intervals of one horn width (horns touching each other) to maintain the desired beam configuration. However the horn size is usually too small to have a proper lens illumination for low sidelobes. But if the horn size were increased, the crossover level would decrease. These conflicting requirements led to the development of the third lens configuration, which scans well and encompasses low sidelobes with good beam crossover levels.

SHAPED MULTIBEAM LENS

The third type of lens is a combination of the special shaped lens and the wide scanning lens. As well known, the Abbe sine condition basically requires that the lens be spherically concaved in contour to be coma free. This is the principle used in the second lens. The first lens has a pronounced convex surface, therefore, zonning is introduced in N λ increment to force an approximation of the Abbe sine condition. However the highly convex profile of the first surface of the special shaped lens deviates so much from the circular arc that too many zones would be required to satisfy this condition of coma correction.

To make the lens profile more practical, a less severe taper given by $E(r) = [1-(r/1.05)^2]^3$ with a uniform phase was specified. In this case, the lens is shaped for -36 db sidelobes with a 3° beam width at 44 GHz. For 36 db directivity, this lens is smaller in diameter, only 30 λ , because the aperture efficiency in this case is higher, about 48 percent.

When coma correction is applied along with shaping, the cross section of the lens becomes zig-zag shaped as shown in Figure 5.

Figure 6 shows the measured patterns of the overlapping beams at 44 GHz. These results were obtained by offsetting the feed horn from the axis with one horn size each step. As predicted, the lens collimates very well to form a high quality beam despite the ostensibly erratic surface zoned for coma reduction. The first sidelobe level of the central beam is -30 db, not as low as predicted, yet considered to be remarkable for an unmatched lens. The sidelobe level can be anticipated to be well below -30 db when the surfaces of the lens are perfectly matched with quarter-wavelength layers of proper dielectric material.

For off axis scans, it can be seen that the coma distortion of the main beam is almost completely eliminated, and the sidelobe degradation is correctably small. Again, substantial improvements can be made by careful surface matching. A smaller step size in the discontinuity jump of zoning would also lower the sidelobes, because the scattering loss is expected to be further reduced for off axis scans. In addition, the intrinsic cubic phase error would decrease because a better approximation to the Abbe sine condition is achieved, leading to even lower coma lobes.

Note that the beam crossover level is only 4 db below the peak, a feature not easily attainable with -30 db sidelobes by single horn feed. On an expanded scale, the 3 db beamwidth was measured to be 3.4 degrees, slightly larger than the predicted value of 3.1 degrees. This discrepancy is possibly due to the phase errors of the feed pattern and the diffraction of the zone ridges. It was found that the ratio of scan angle to the incident offset angle of the feed is very close to one.

The measured peak gain of the prototype multibeam lens antenna is 33.3 db. The computed directivity is 36.3 db. Thus, the total loss is about 3 db which accounts for the spillover of the horn, surface mismatch, diffraction, dielectric loss and horn copper loss. With surface matching and a smaller step size in zoning, the loss can be somewhat reduced to about 2 db.

From these preliminary test results, the superior features of the shaped lens with coma correction are clearly demonstrated.

The experiments also successfully verify the accuracy of the theoretical analyses and predictions.

SUMMARY

Three different lenses are reviewed, each with its own application. Each design can have many configurations, depending on the requirements of the various systems. A more detailed design analysis will be the subject of a forthcoming paper; however, it is hoped that this information will stimulate a renewed interest in the design of dielectric lenses.

Acknowledgement

The authors would like to thank Dr. H. E. Foster for his enlightening discussions and Mr. George H. Campbell for his valuable assistance in carrying out the experiments.

SPECIAL SHAPED LENS

LENS CONTROLS BOTH AMPLITUDE
AND PHASE DISTRIBUTION ON
THE APERTURE

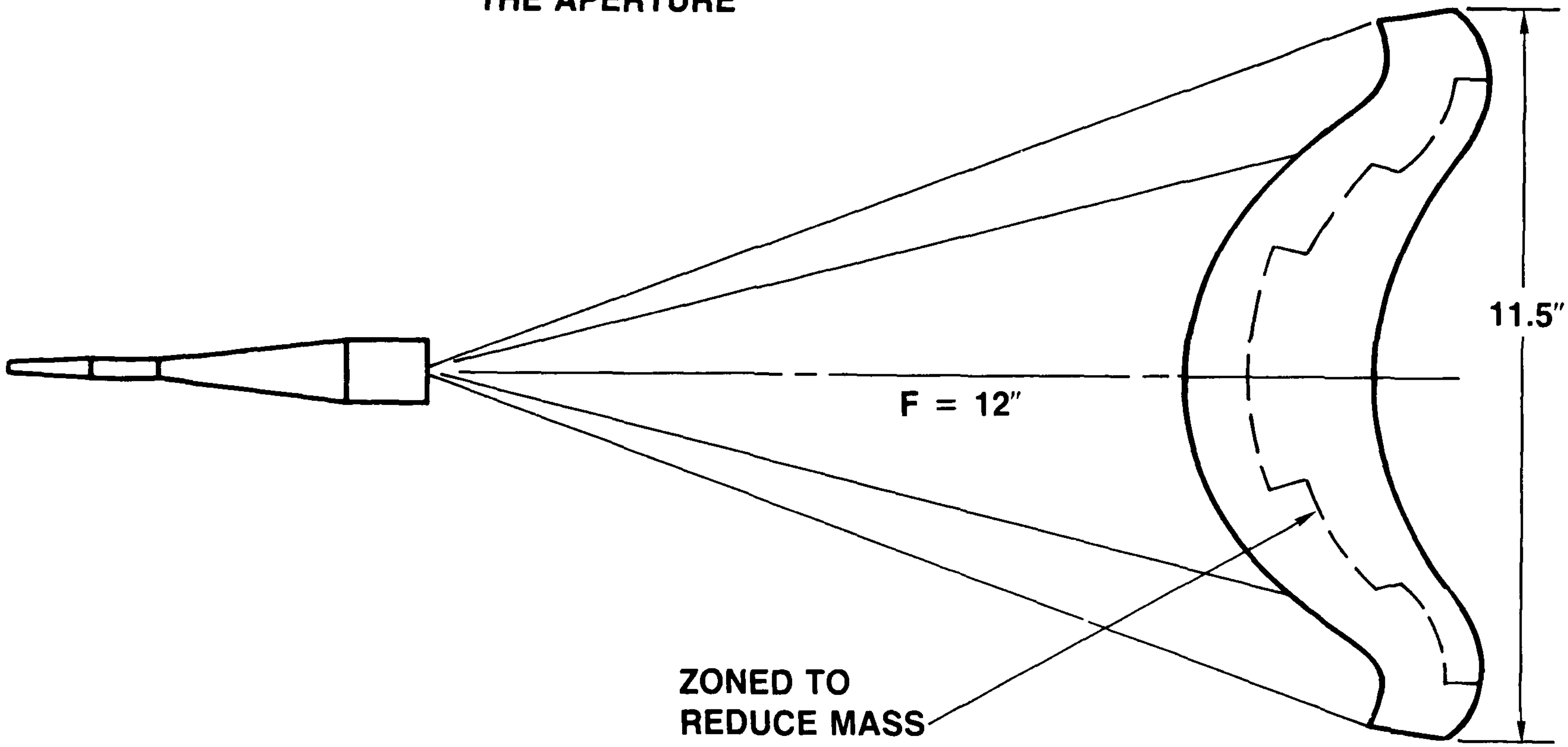

FIGURE 1

Rockwell International

SHAPED LENS

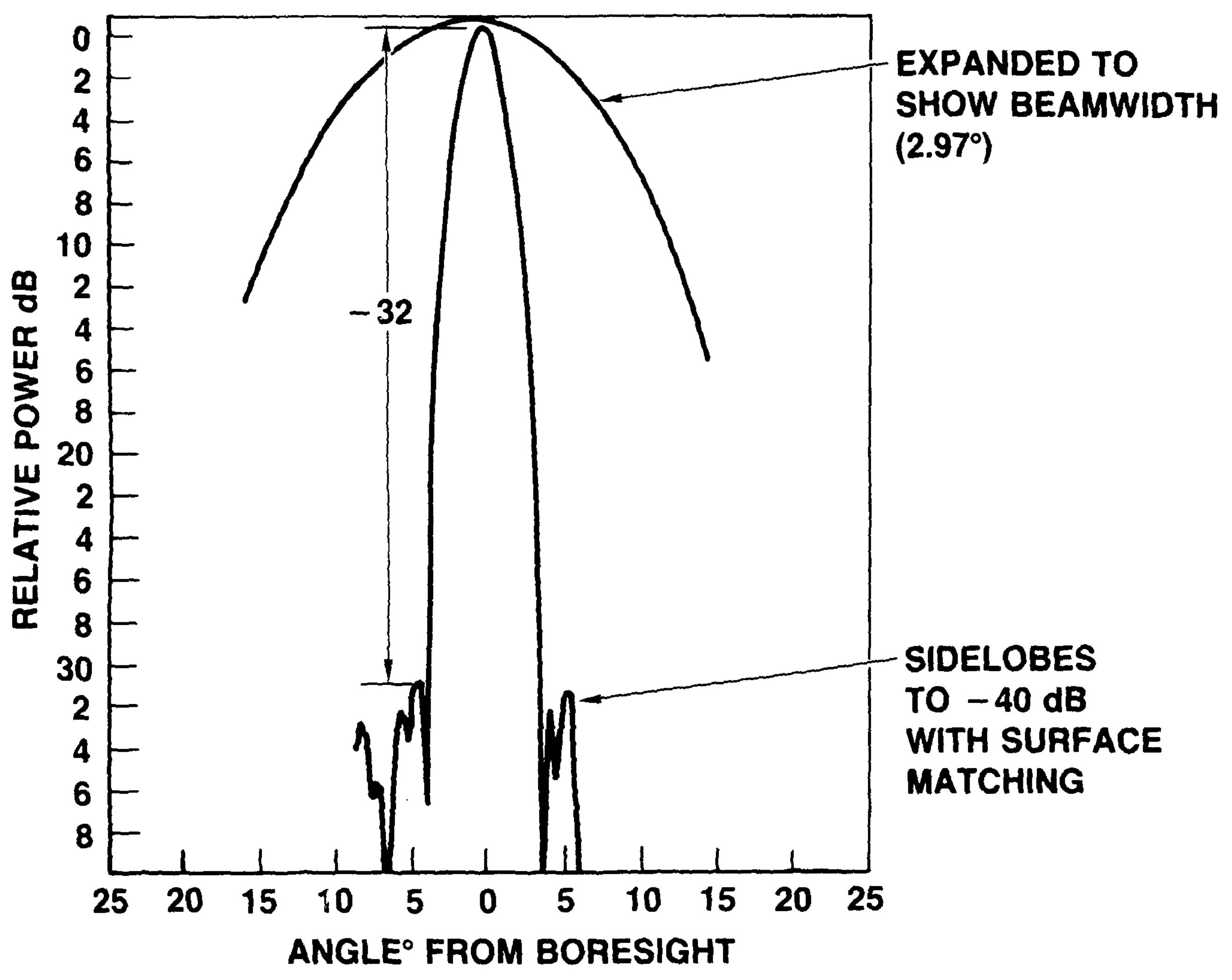

Rockwell International

FIGURE 2

WIDE SCAN ANGLE ERROR FREE LENS

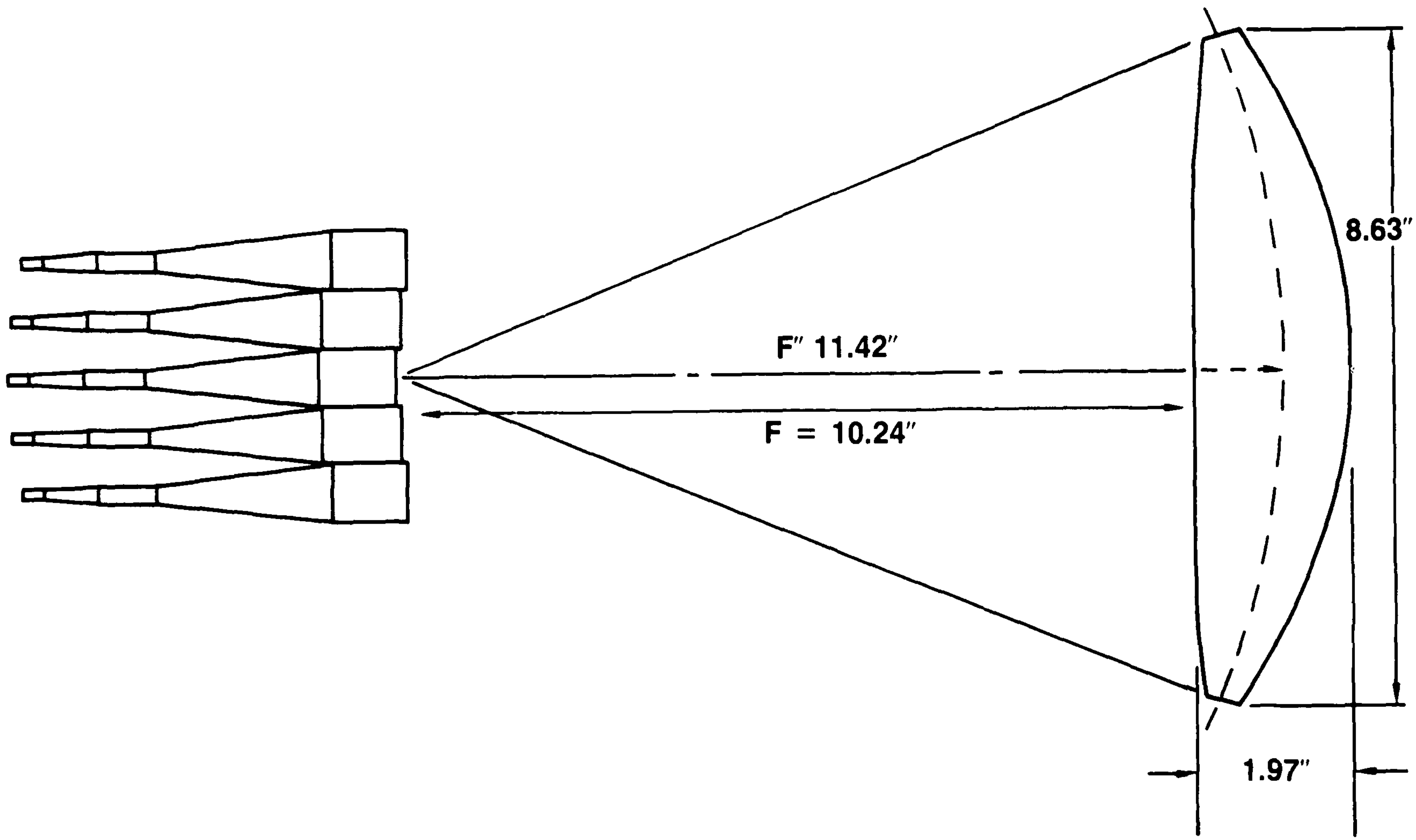

FIGURE 3

Rockwell International

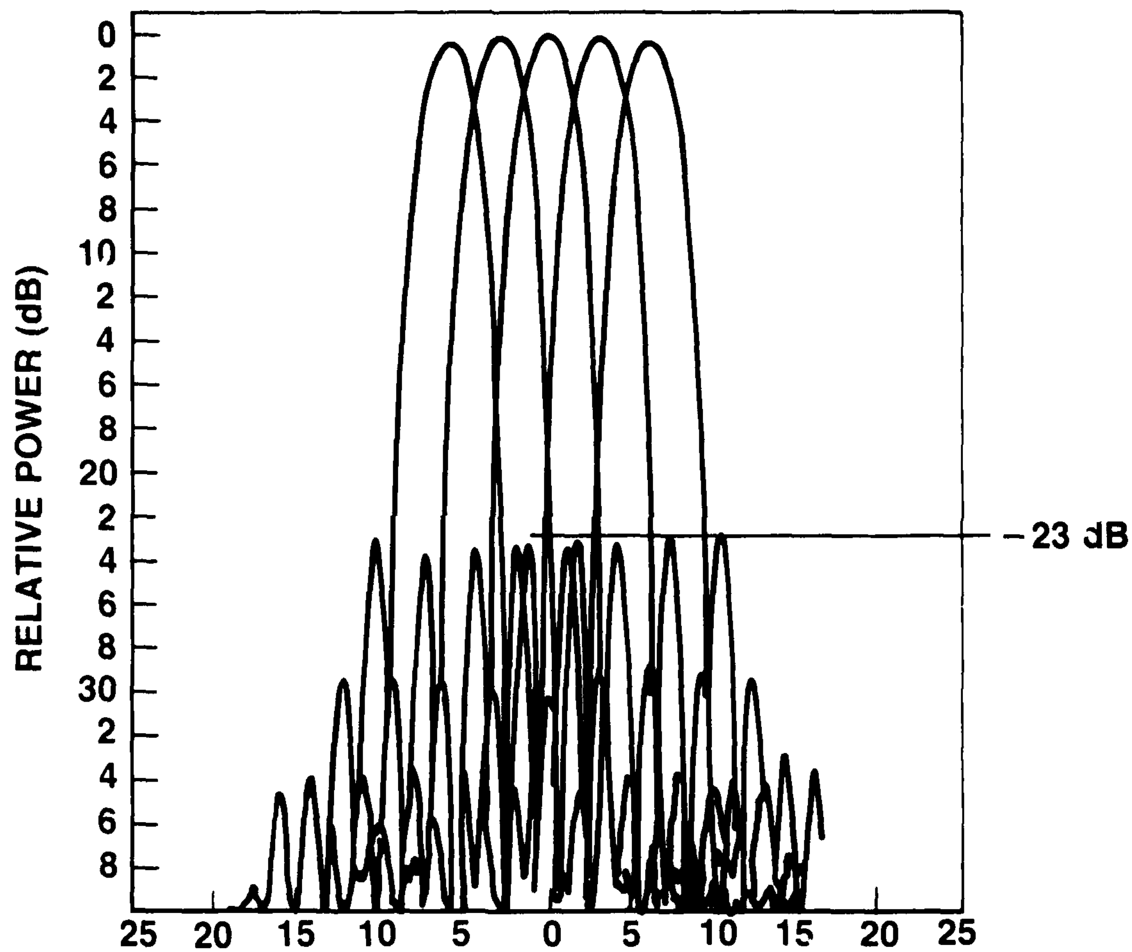

FIGURE 4

Rockwell International

- SHAPED FOR APERTURE DISTRIBUTION PANEL
- FOUR-STEP ZONED FOR COMA CORRECTION

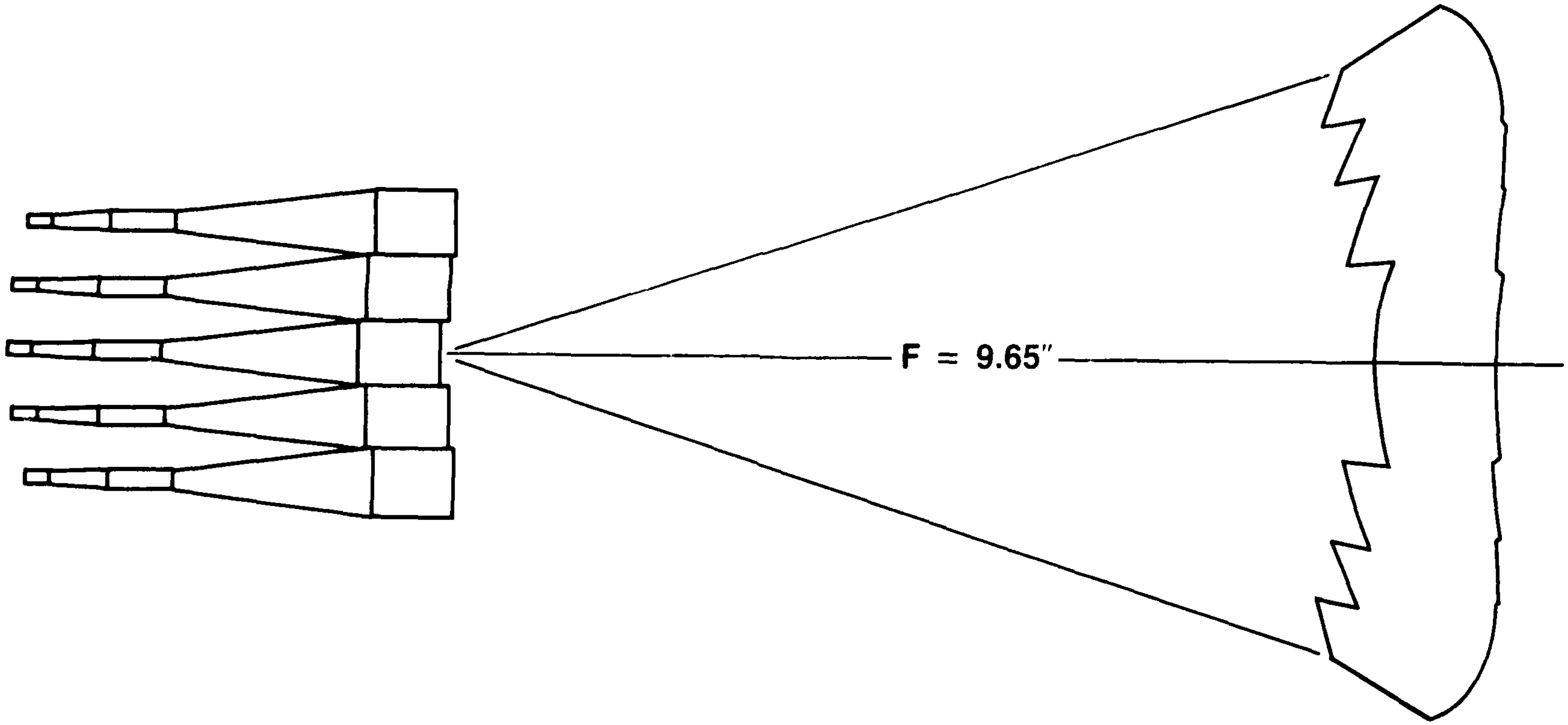

FIGURE 5

Rockwell International

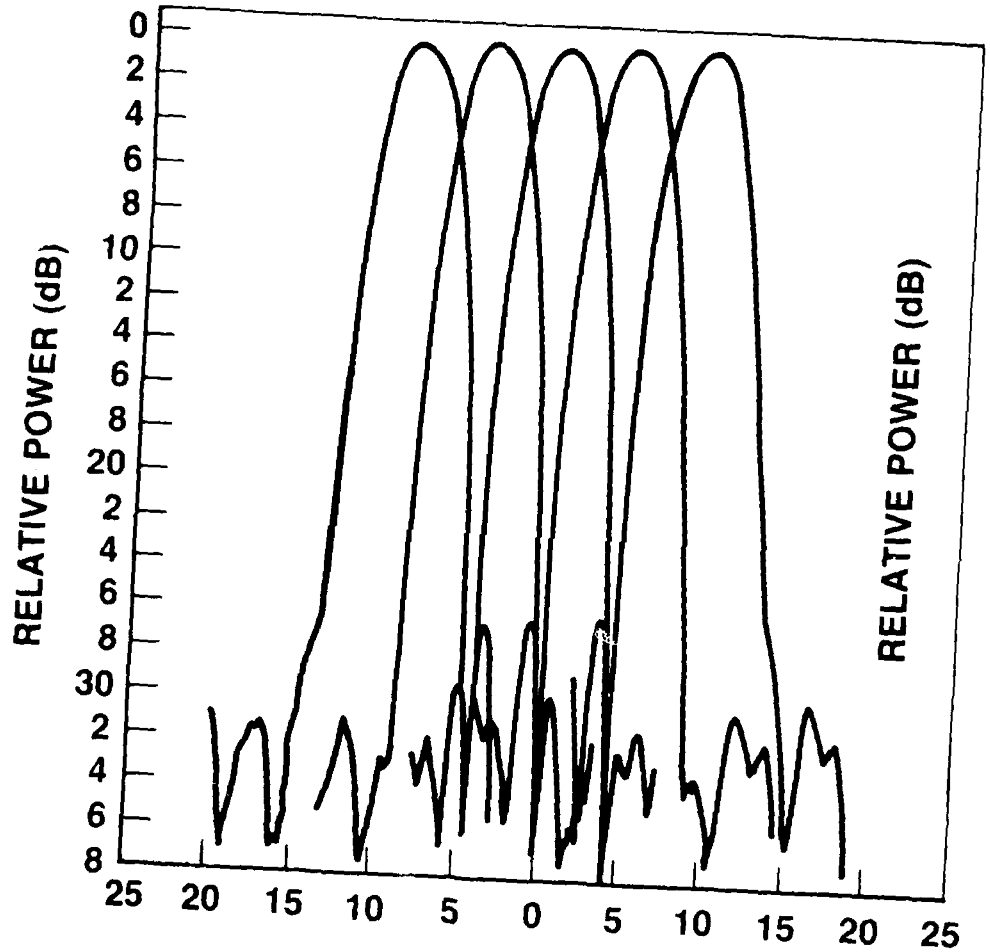

FIGURE 6

Rockwell International

PHASED ARRAY ALIGNMENT WITH
PLANAR NEAR-FIELD SCANNING
OR
DETERMINING ELEMENT EXCITATION FROM
PLANAR NEAR-FIELD DATA

W.T. Patton

1. INTRODUCTION

The usual function of a near-field antenna test facility is to determine the far-field pattern of the antenna. The far-field pattern is that part of the angular spectrum of the antenna which has wave numbers less than the characteristic wave number of free space corresponding to the operating frequency. This part of the antenna's angular spectrum is frequently called the visible spectrum.[1] Perhaps a more significant use of such a facility is in aligning the antenna. An example of this is the use of a near-field facility to align the beamformer of a phased array antenna for a tactical radar system, where the area of the array controlled by each beamformer port consists of 64 elements. The conditions and methods required to extend this technique to the alignment of individual elements of the array will be considered below.

2. SPECTRAL DOMAIN RELATIONSHIPS

Some of the fundamental relationships between the antenna aperture and the far-field pattern can be illustrated using an array of 9 identical elements such as that shown in Figure 1.

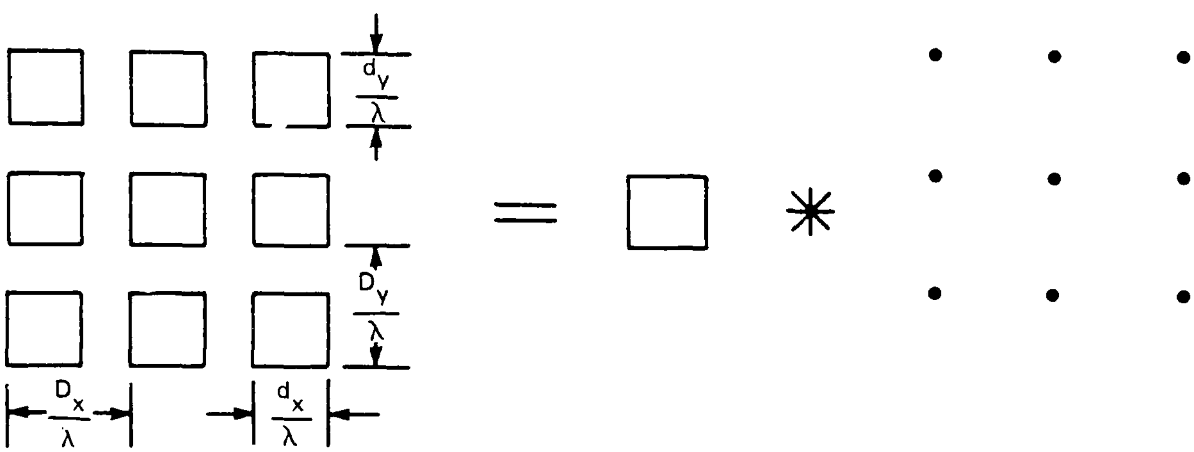

Figure 1. Nine Element Array - Aperture Diagram

It is convenient, in the analysis that follows, to represent the array distribution as a convolution operation between the aperture function of a typical element and an array of delta distributions with the amplitude and phase imposed on the array by the beamforming network. It is just this amplitude and phase information that we will seek to recover from the far-field spectrum of the array.

The angular spectrum is the Fourier transform of the aperture function. In this case it will be the product of the spectrum of the element supported on the rectangular area d_x/λ x d_y/λ with the spectrum of the array supported at nine discrete points. This is illustrated in Figure 2.

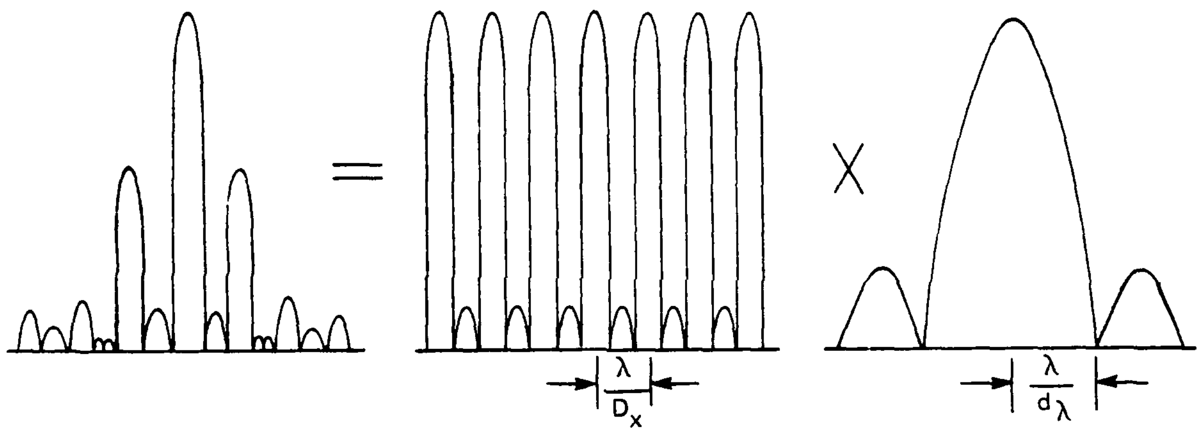

Figure 2. Nine Element Array - Angular Spectra Diagram

Two important features of the angular spectrum are apparent in this figure. First, to recover the angular spectrum of the array it is necessary to remove the spectrum of the element. This may be done either by using a priori data on the element spectrum or by using data gathered by the near-field facility using the procedure discussed in Section 3 below. Second, the array spectrum is periodic. In this case it has a period λ/D_x in the u direction and λ/D_y in the v direction. Thus all necessary information about the aperture function of the nine point-source array is contained in a rectangular section of the u-v space of dimension λ/D_x x λ/D_y as illustrated in Figure 3. In fact because of the periodic nature of this angular spectrum, all the information .bout the angular spectrum of an array of point-sources with any number of elements having this same inter-element spacing will be contained within the same region of the u-v space.

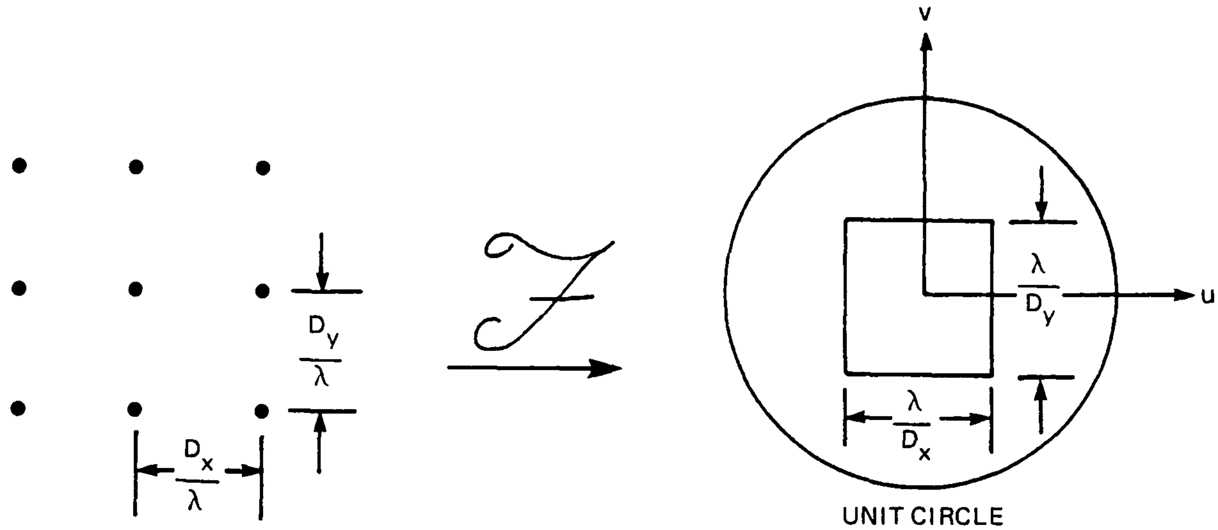

Figure 3. Angular Spectral Domain of an Array

The angular spectrum of the nine element array can be written as

$$S(u,v) = f_e(u,v) \sum_{m=-1}^{1} \sum_{n=-1}^{1} a_{m,n}\, e^{j 2\pi \left(m \frac{D_x}{\lambda} u + n \frac{D_y}{\lambda} v \right)} \tag{1}$$

where f_e is the Fourier transform of the element aperture function.

From this expression and the well-known orthogonality relations of Fourier it is clear that the array coefficients can be recovered from the angular spectrum by the operation

$$a_{m,n} = \frac{D_x D_y}{\lambda^2} \int_{\frac{-\lambda}{2 D_x}}^{\frac{\lambda}{2 D_x}} \int_{\frac{-\lambda}{2 D_y}}^{\frac{\lambda}{2 D_y}} \frac{S(u,v)}{f_e(u,v)}\, e^{-j 2\pi \left(m \frac{D_x}{\lambda} u + n \frac{D_y}{\lambda} v \right)} du dv \tag{2}$$

We note that this operation makes use of two elements of special knowledge about the array and its spectrum: the element spectrum and the interelement spacing. It can be easily extended to an array with any number of elements merely by extending the range of the indices m and n.

In applying equation (2) to an array spectrum obtained from a near-field test facility, we must first properly align our phase centers. Implicit in (1) is the location of the phase center at the central element of the array. The phase center used in computing the angular spectrum from a planar near-field measurement plane is typically some distance in front of the array aperture and also laterally displaced from the array center. Therefore an appropriate[2] transformation of the computed angular spectrum must be made to shift the phase center to one of the elements in the array aperture before (2) is used.

Another important condition that must be considered if we are to recover the array excitation coefficients is that all the data be accessible in visible space. This requirement is easily satisfied in the case of a rectangular element grid if

$$\left(\frac{\lambda}{D_x}\right)^2 + \left(\frac{\lambda}{D_y}\right)^2 < 4 \qquad (3)$$

In a case where $D_x = D_y$ the above condition gives $D_x > \lambda/\sqrt{2}$.

This restriction is quite innocuous for a non-scanning array. Unfortunately for a scanning array, it is not compatible with the requirement to prevent grating lobes of the array from entering visible space for any angle of scan. However, the fact that the array can be scanned offers a solution to the dilemma. Remembering that a linear phase distribution over the array aperture is equivalent to a translation of the angular spectrum with respect to the unit circle and the element pattern, we can determine the entire array spectrum by shifting it so that in two or more scan positions all parts of the fundamental period of the array spectrum are brought into visible space. In this way the necessary data for most arrays of practical interest can be recovered and used to determine the array excitation function.

3. ELEMENT PATTERN

The angular spectrum of the radiating element can also be determined by scanning the array. This follows since a linear phase distribution is a translation of the array spectrum with respect to the element spectrum as noted above. The variation of the peak spectral value (main beam) with scan is due to, and an indication of, the element spectrum. In principle then, it is necessary to scan the array to each point at which the element pattern is to be evaluated and perform a full near-field scan. This process would be extremely slow and costly if the same number of data points were taken in each scan as required to determine the array spectrum. However, since the elements are small, the element spectrum is generally slowly varying and therefore can be evaluated with relatively few scanned sets of data in the measurement plane. Rapidly steering the array during the measurement will allow many points of the element pattern to be obtained with a single planar scan.

The density of the points at which the element spectrum must be determined is controlled by the length "L" of the effective scanner motion in both the X and Y directions. The spacing between such points is numerically equal to

$$\Delta u = \lambda / L_x, \text{ and}$$
$$\Delta v = \lambda / L_y \tag{4}$$

respectively. L_x and L_y are generally made enough larger than the array to insure covering the larger amplitude region in the near-field at the extreme scan limits. They may even be larger than the physical scanner motion, when zero padding of the measurement plane is employed. The array should be steered to each direction formed by all combinations of multiples of Δu and Δv to evaluate the element pattern there. The number of scan positions can, however, be reduced by a factor of 5 by using knowledge of the array beam shape near its peak to estimate the value of the element spectrum at positions adjacent to the scan position. Such techniques to reduce data collection time are important since the complete element spectrum must be evaluated for each frequency at which the array is to be aligned.

The amount of data required to evaluate the element spectrum can be further reduced by reducing the density of sampling points in the measurement plane associated with a particular scan position and frequency. The data-point density must be large enough to filter out the higher-order array spectra or to prevent it from folding into the lower-order spectrum contaminating the element spectrum data. When the array itself has extremely low sidelobe levels, there is little incentive for making the sample density greater than that required to cover the main beam of the array out to the first null. This can usually be done satisfactorily with from four to eight sample points in each direction, depending on the size of the measurement plane relative to that of the array.

4. DATA PRECISION REQUIREMENTS

An analysis of errors introduced in the measurement process can be performed in the same manner as an analysis of the effect of array errors themselves. In the following analysis we will treat errors as random noise which contaminates the measurements and therefore the spectrum that we are trying to determine. We are concerned about the level of the this noise, both with respect to the total array output or the peak of the spectrum, and with respect to the amplitude of a single array element or a single near-field measurement. The processing of the data generally provides some gain in the signal-to-noise ratio of the data, limited by the extent and coherency of the data. For example, if all measurements taken in the measurement plane were approximately equal, the gain in signal-to-noise power ratio would equal the total number of sample points. The actual gain is less than this to the extent that the amplitude of the measured field decays rapidly when the probe moves away from the aperture of the antenna under test. A useful estimate of the gain in signal-to-noise power ratio is transforming between aperture or measurement plane and the angular spectrum is given by

$$\text{Forward Processing Gain} \approx n_a \; N_e \; \frac{A_e}{A_s} \tag{5}$$

where

n_a = aperture efficiency of the array excitation,

N_e = number of elements in the array,

A_e = area occupies by an element, and

A_s = sample cell area.

An error introduced in the data in the spectral domain due to round-off error will not be significantly reduced in transforming back to the aperture plane because most of the spectral data of significant amplitude are restricted to relatively few spectral points. An estimate of the reverse processing gain is given by

$$\text{Reverse Processing Gain} \approx \frac{L_x \; L_y}{n_a \; A} \tag{6}$$

where

$L_x \; L_y$ is the area of the measurement plane, and

$n_a \; A$ is the effective area of the antenna under test.

We can see from (5) and (6) that, if we are dealing with a small array of a small number of elements, the forward processing gain can be expected to be small while the reverse gain is large. The product of forward and reverse processing gains, however, equals the number of sample points processed. The process of transforming data from the measurement plane to the aperture plane should have a gain given by

$$\text{M-A processing gain} \approx \frac{\left[\sum\limits_{n,m} \dfrac{m_{n,m} \, e^{-j \frac{2\pi}{\lambda} \sqrt{z^2 + (n D_x)^2 + (m D_y)^2}}}{\sqrt{z^2 + (n D_x)^2 + (m D_y)^2}} \right]^2}{\sum\limits_{n,m} \dfrac{m^2_{n,m}}{z^2 + (n D_x)^2 + (m D_y)^2}} \tag{7}$$

This will usually differ insignificantly from unity.

5. SPECIFIC EXAMPLE

As a specific example, consider a circular array of 4350 elements with an element spacing of 1.06λ in each row with the adjacent rows displaced 0.53λ along the row and 0.293λ vertically. The array has an aperture distribution designed for peak sidelobe levels of -50 dB with an aperture efficiency of -2.1 dB.

The element configuration and angular spectrum are illustrated in Figure 4.

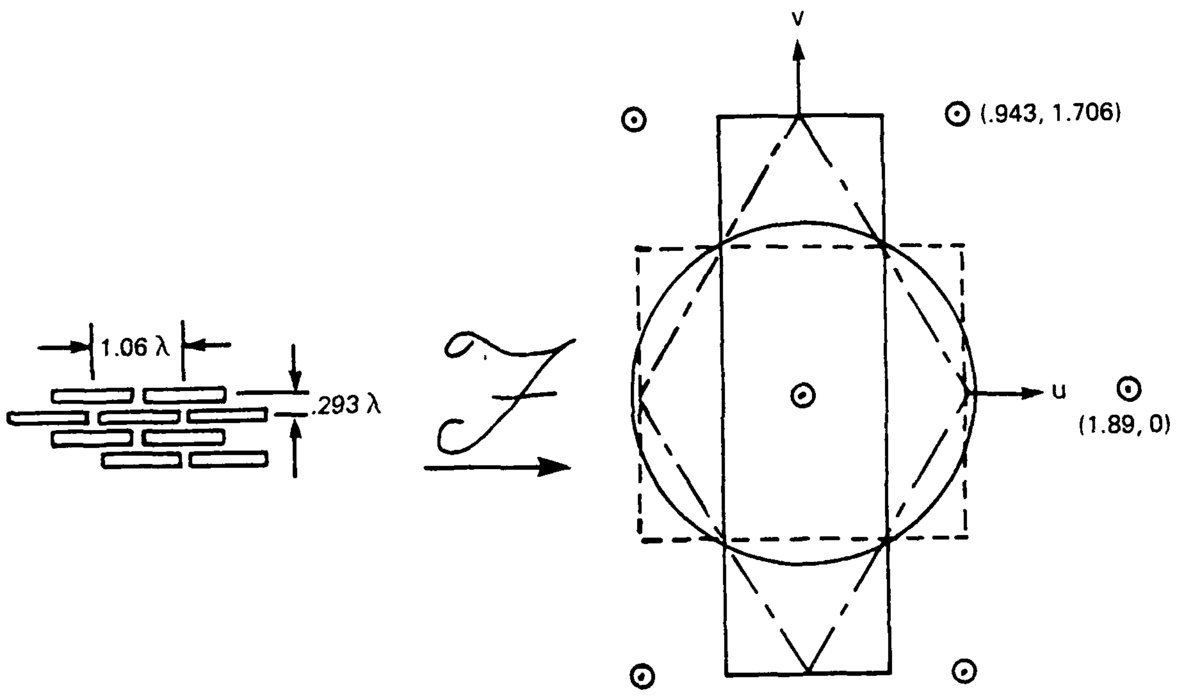

Figure 4. Angular Spectral Domain of a Triangular Grid Array

Here we see a triangular grid in the aperture domain that can be viewed as a rectangular grid 1.06λ x 0.586λ with a similar rectangular grid place in the center of the cell. These transform to the angular spectrum as a rectangular grid of grating lobes 1/1.06 x 1/0.586 with a similar grid of grating lobes located at the center of this cell. There are three choices for the shape of the support of the periodic angular spectrum illustrated in Figure 4. Two of these are rectangular in shape with different aspect ratios and one is romboidal. None of these shapes fits entirely within the unit circle. Therefore it will take at least two scans to cover the entire spectrum. The tall, thin shape is the only one that can be covered in two scans. This is done by steering the array up and then down by an angle whose sine is 1.706/2 or 0.853. This will allow half of the spectrum to fit within the unit circle since $0.853^2 + 0.472^2 = 0.926 < 1$.

If the measurement plane grid is 3 cm x 3 cm, or 1.4 square inches, we can estimate the forward processing gain using (5) to be

$$\text{FPG} = 10 \log 4350 \frac{3.56}{1.4} - 2.1 = 38.3 \text{ dB}$$

Thus an RMS measurement error of -32 dB is adequate to achieve a spectral error of less than -70 dB RMS, which will produce an error of less than 1 dB at the -50 dB sidelobe level with 90% probability. However, when the measurement is being used to align the array, a measurement error becomes part of the error allocation of the array, so that even greater precision must be provided.

The allocation of array errors to the measurement process must be shared between the various error sources. We must distinguish between error sources that are independent from sample to sample, like roundoff error and receiver noise, and those that are correlated over large segments of the array, like probe sway in the scanner due to its alignment, or motion-induced phase variation in the probe-receiver RF path. To insure that a correlated error will not cause more than 1 dB increase in the array sidelobe level, its effect must be more than 18 dB below that level of at -68 dB for a -50 dB design sidelobe level. This is an amplitude error of approximately 398 in 10^6. This error can be produced by a periodic phase error of 0.8 milliradian or a peak harmonic probe position error (z) of 0.00045 inch.

An important source of error in the spectral domain comes from the process of removing the probe pattern and the array element pattern. If the total number of data points processed is 12^{16}, a total processing gain of 48 dB is available. With 38 dB gain expected in the forward direction, we can expect only 10 dB gain in the reverse direction. Thus probe calibration precision must be better than -20 dB RMS to achieve a -30 dB error allocation to the test facility. A precision of -25 dB would consume 1/3 of this allocation. The measurement error in the array element pattern starts first with the ability to shift phase in the array. Using 6-bit phase shifters this amounts to -30.8 dB rms error. If we take eight sample points in each direction or use a measurement grid 48 x 48 cm, our forward gain is reduced to 38.3-24 = 14.3 dB. This process gives an RMS error of -45 dB in the spectral representation of the array element pattern, which is independent at each spectral point (scan angle). Since the array element pattern is slowly varying, we can expect large processing gain (36 dB) in transforming these errors to the aperture plane, giving a residual effect of -81 dB. This error is negligible relative to other sources of error.

6. DATA COLLECTION RATES

The total number of data points required to define the element pattern in the area of the array pattern support can be estimated by

$$N = \frac{1.706 \times 0.943}{(2.857)^2} \times 2^{16} = 0.197 \times 2^{16}$$

If we can estimate five pattern points for each scan position, then

$$N_s \approx \frac{2^{16}}{26}$$

If there are 16 horizontal moves per data point, then $N_{sv} = \frac{2^{12}}{26}$, and data collection time at 2 ms/beam position is

$$T_f = \frac{2 \times 10^{-3} \times 2^{12}}{26} = 0.315 \text{ sec}$$

Time to collect data at 10 frequencies is

$$T = 10 \times (0.015 + 0.315) = 3.3 \text{ sec},$$

where 15 ms is the time required to change frequency.

If the distance between data points in one data set is 48 cm, the scan velocity can be as high as 14.5 cm/sec.

Since this rate is near the nominal (15 cm/sec) scan rate of the scanner used for acceptance testing of the array, we can conclude that the entire data set for element coverage can be obtained in a single nominal scan of the measurement plane.

The time required to collect data for array alignment can be estimated from the requirement to obtain two beam positions and 10 frequencies. This time will be

$$T = 10 \times (15 + 2) = 170 \text{ ms}.$$

With data required every 3 cm, the scan rate can be

$$V = 3/0.17 \cong 18 \text{ cm/sec}.$$

This is greater than the nominal scan rate, indicating that this data also can be acquired in a single scan.

7. REFERENCES

1. P.L. Ransom and R. Mittra, "A Method of Locating Defective Elements in Large Phased Arrays", Phased Array Antennas, Artech House, 1972.

2. David Staiman, "Automated Near Field Antenna Test Set for Phased Array Production", Proceedings of 1979 Antenna Applications Symposium, The University of Illinois, 1979.

SMALL ARRAY ILLUMINATIONS FOR PATTERN NULLING WITH SIDELOBE LEVEL CONTROL

Charles F. Winter
Microwave/Antenna Department
Radar Systems Laboratory
RAYTHEON COMPANY
Wayland, MA 01778

ABSTRACT

An iterative procedure is described for determining the discrete element excitation amplitudes of a small (in-phase) linear array that will generate a directional beam antenna pattern having a wide null at a preassigned far-field angle away from the beam peak direction and having all of its pattern sidelobes at or below a preassigned sidelobe level envelope. The wide null involved is created by causing two adjacent single-valued zeroes of the directional beam pattern to become coincident at the desired far-field angle. Antenna patterns of this nature can be useful in narrowband interference-reduction applications whenever the angular relationship between the peak direction and the null position remains constant.

The problem of scanning the double-valued null position throughout the antenna pattern sidelobe region is evaluated with respect to two types of feed networks for the array. One feed network contains variable power dividing components such that the array element excitation amplitudes can be adjusted to properly position the double-valued pattern null. The other network contains an orthogonal multiple-beam-forming device as well as variable power dividing components such that the beam weighting amplitudes can be adjusted to properly position the pattern null. Patterns of this nature can be useful in applications where the angular relationship between the beam peak direction and the null position varies in some predictable manner.

Prepared for presentation at the
1981 Antenna Applications Symposium
Allerton Park, Monticello, Illinois
September 23-25, 1981

SMALL ARRAY ILLUMINATIONS FOR PATTERN NULLING WITH SIDELOBE LEVEL CONTROL

Charles F. Winter
Microwave/Antenna Department
Radar Systems Laboratory
RAYTHEON COMPANY
Wayland, MA 01778

I. INTRODUCTION

There are applications for directional beam antenna patterns that have a deep null region occurring in the sidelobe structure at some specified far-field angle measured away from the pattern main beam peak. Various objectives for optimizing the properties of a nulled antenna pattern have been reported [1]-[5]. Tseng [5], in particular, has shown how the Taylor distribution [6] impressed on a continuous line source or a large linear array aperture can be generalized such that the resulting antenna pattern will have a deep null region centered at a preassigned angular position. For Tseng's purposes, a large aperture is required in order that a sufficient number of zeros in the pattern will be available for controlling (to a large extent) the sidelobe level characteristics of the complete pattern. Tseng also showed that the null region might be scanned by varying the relative amplitudes of only the outermost elements in a large array.

The antenna pattern for a small linear array does not possess a sufficient number of zeros to permit such a generalized approach toward establishing a null region. This report is concerned with the specific problem of positioning a small array pattern double-null at a preassigned location with respect to the main beam peak while constraining all of the sidelobes that occur in the far-field pattern to be at least a preassigned dB level down from the main beam peak. The pattern double-null will be created by causing two adjacent single-valued zeros of the pattern to become coincident at the desired location. The angular width of the region in the neighborhood of a double-null position is shown below to be greater than that of a single-valued null, particularly if the levels at the sidelobe peaks on each side of a null of each type are essentially equal. For some narrowband applications, the width of this double-null characteristic may be satisfactory. The introduction of more than one double-null point into the antenna pattern will not be considered in this report, since the primary intent is to describe a method of controlling the pattern sidelobe levels when a double-null exists.

Since a pattern double-null as just defined is a sidelobe which has 'disappeared', modification to a previously described technique [7] are discussed for controlling the remaining sidelobes of the antenna pattern at desired suppression levels. As in this reference, the antenna pattern will be approximated by its array factor. The array factor will be restricted to be a real-valued voltage pattern such that its directional beam peak is broadside to the array axis and its sidelobes are always formed between two adjacent zero crossings of the voltage pattern expression.

II. BACKGROUND

Consider a small linear array of N equally-spaced elements having an illumination A_n of the form

(1) $$A_n = \sum_{i=0}^{I} T_i \cos(2\pi i d_n)$$

where the series coefficients T_i are real valued and normalized such that $T_o = 1.0$. Let the axial coordinates d_n of the array elements be ordered by index n such that

(2) $$d_n = \frac{2n-N-1}{2N} \qquad \text{for } 1 \leq n \leq N.$$

With this symmetry*, the array factor R(z) can be written as

(3) $$R(z) = \sum_{n=1}^{N} A_n \cos(2\pi d_n z)$$

where

(4) $$z = N(\frac{d}{\lambda}) \sin \Theta$$

---

* The symmetry of the array factor expression means that, when a double-null occurs at a positive z-value, one also occurs at the corresponding negative z-value. When the element spacing is taken larger than 0.5 λ, additional double-null points within the array factor period may appear in real space. To avoid the former situation, the use of a complex illumination function in place of (1) would be required. Adapting the remaining expressions used in this report to handle complex forms appears to be straightforward provided attention is paid to monitoring the directional beam pointing direction as non-zero phase terms are introduced.

relates the array factor variable z to the far-field angle Θ of real space depending upon an element-spacing-to-wavelength ratio.**

The array factor (3) is an even function and its absolute value is periodic in N. When the T_i-coefficients of the aperture illumination (1) are appropriately selected, the array factor will have N-1 zeros and N-2 sidelobe peaks within one period. Because of the pattern symmetry, however, both the zeros and the sidelobe peaks within the period must be paired off (counting away from the directional beam peak) such that the number of independent positions for either is given by the integer part of the expression (N-1)/2. Should I in (1) be taken equal to IP [(N-1)/2], any combination of I zeros and/or sidelobe peaks can be independently manipulated by the selection of the T_i-coefficients. Note here that an (N =) even numbered element array will have an array factor with odd symmetry about the point z = N/2. At least a single-valued zero position must therefore occur at this point. An odd numbered array has even symmetry about the point z - N/2 and a slope reversal point (i.e., a pattern minimum or maximum value) will thus exist at this point.

Taylor [6] showed that the T_i-coefficients in (1) for $1 \leq i \leq I$ (in the notation used here) are equal to twice the normalized array factor (3) values at the matching integers for $1 \leq z \leq I$. Altering any single T_i-coefficient will change the pattern sidelobe structure somewhat, thereby causing a movement of a pattern zero. A zero occurs in the array factor, of course, whenever a value of z (say z_d) makes the right-hand side of (3) equal to zero. For such a zero to be double-valued, the derivative of (3) with respect to z must also be equal to zero when evaluated at the point $z = z_d$.

(5) $$\left.\frac{dR}{dz}\right|_{z = z_d} = 0 = \sum_{n=1}^{N} d_n A_n \sin (2\pi d_n z).$$

** While this report employs an aperture normalized variable z in the discussion, it must be emphasized that the far-field angle Θ is dependent upon the free-space wavelength. The frequency bandwidth of the results presented herein are therefore limited.

For the array illumination (1) under consideration, it is necessary to use two of the independent T_i-coefficients in creating a double-null at a specified pattern point in order to satisfy both (3) and (5) simultaneously. The remaining I-2 T_i-coefficients are thus available for controlling pattern sidelobe levels. Noting that both a pattern double-null and a sidelobe peak are slope reversal points in the voltage array factor, it is apparent that I-1 conditions might be imposed on (5) and one condition on (3). The resulting set of I equations could be solved for the I T_i-coefficients provided an appropriate means of selecting the z-values for each of the slope reversal points was at hand. One sidelobe level, of course, would remain uncontrolled under this situation.

This report describes an iterative method for determining both an appropriate selection of the slope reversal z-values and a suitable choice of the sidelobe left uncontrolled. Results are presented showing that an array factor can often be obtained which has a preassigned double-null position with all of its sidelobes at or below a preassigned envelope level.

III. AN INITIAL PATTERN

In order to evaluate the nulling technique discussed in this report, comparisons are made with the initial array factur shown in dB down form in Figure 1. A small (N=) 20-element linear array where the aperture illumination uses (I = IP[19/2]=) 9 T_i-coefficients is involved. The T_i-coefficients listed in Figure 1 were derived [7] to meet the arbitrary 20/30 dB down sidelobe envelope shown. The illumination taper across one-half of the array elements is also plotted. The aperture efficiency for this excitation (0.314 dB) was calculated using the (power) definition.

$$\eta = \frac{\left[\sum_{n=1}^{N} An\right]^2}{N \sum_{n=1}^{N} A_n^{\,2}} \tag{6}$$

The sidelobe behavior of this initial pattern is plotted in voltage form in Figure 2. Its 9 independent voltage zero-crossings and its 9 sidelobe peak positions are noted by their z-coordinates. Recall this pattern was derived by specifying 9 sidelobe levels meeting the 20/30 dB envelope. The same procedure [7] can be used to create a double-null pattern by

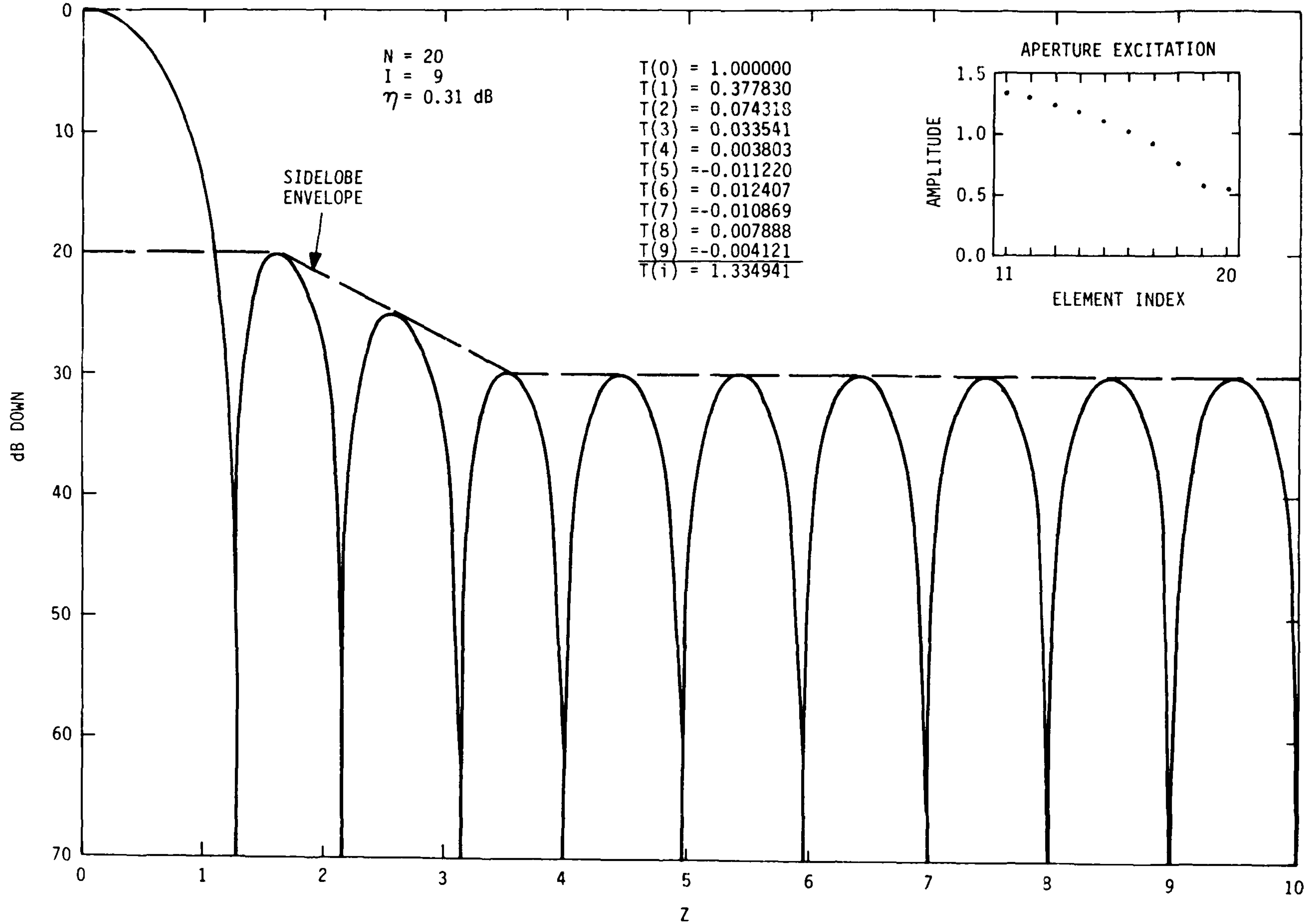

FIGURE 1. ARRAY FACTOR FOR INITIAL 20/30 dB SIDELOBE ENVELOPE

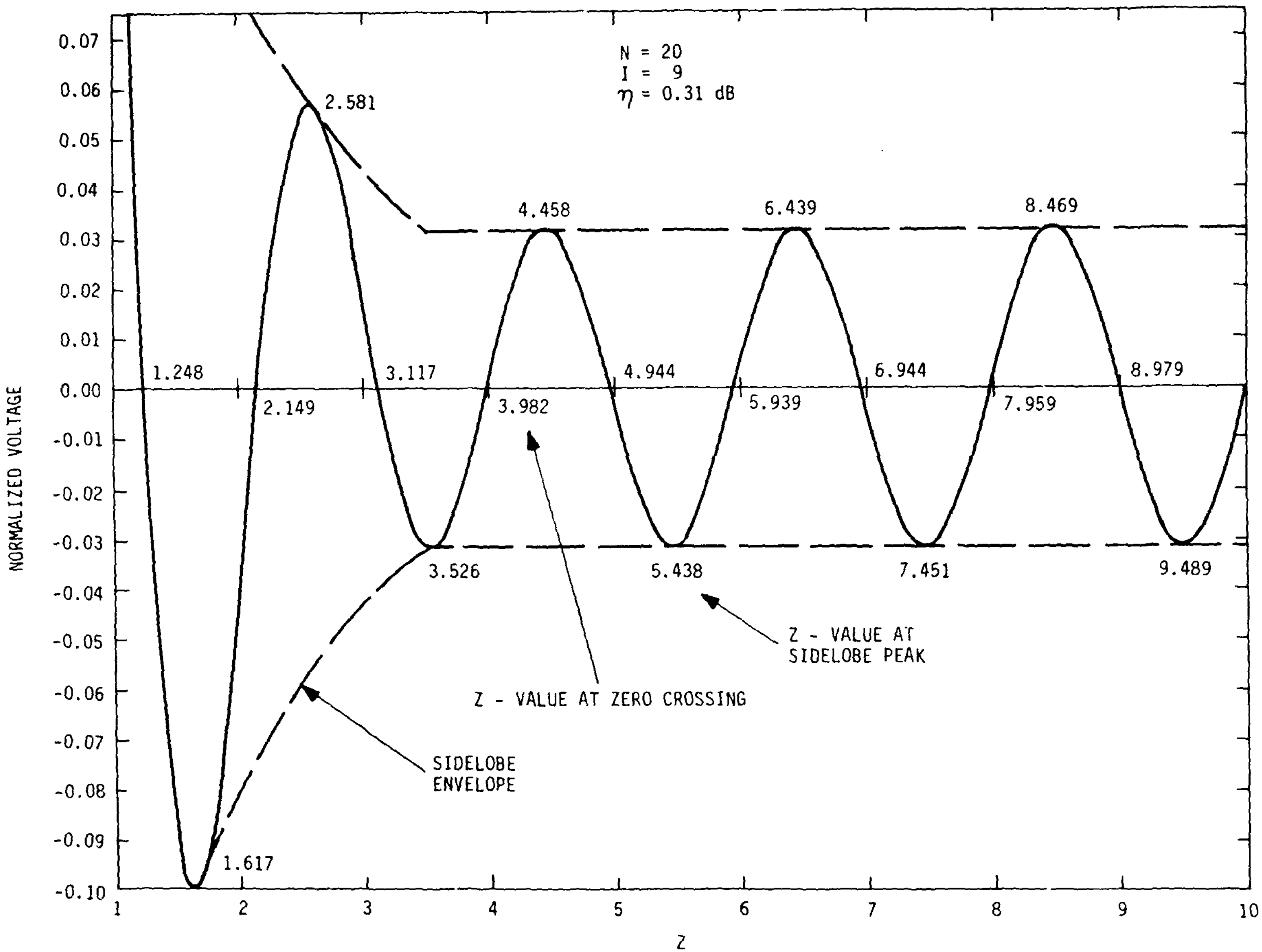

FIGURE 2. SIDELOBE BEHAVIOR OF INITIAL VOLTAGE ARRAY FACTOR.

specifying one particular sidelobe at ∞ dB down (i.e., $R(z) = 0$) with the other eight sidelobes at the envelope values. Of course, no control on the position of the double-null point exists with this technique. That is, for the 20/30 dB envelope the first sidelobe will disappear at $z = 1.708$, the second at 2.633, the third at 3.556, the fourth at 4.463, the fifth at 5.445, the sixth at 6.451, the seventh at 7.472, and the eighth at 8.511 respectively. The ninth sidelobe will disappear at $z = 10.0$ where the pattern null is actually triple-valued because the number of array elements happens to be even.

Figure 3 compares array factors of the pattern having a double-null at $z = 3.556$ and the initial pattern. As the third and fourth zeros of the initial pattern moved into coincidence at $z = 3.556$ in the double-null pattern, the remaining zeros shift very slightly. Of importance, observe that the angular width of the double-null region at the 40 dB down level is at least three times as wide as the region of either nearby single-valued null in the initial pattern. At the 60 dB level the ratio is approximately eight to one.*

IV. DOUBLE-NULL POSITION CONTROL

One means of introducing a controlled position double-null into the array factor (3) generated by the aperture illumination (1) is to alter the two T_i-coefficients which match up with the integral z-values bounding the z-value of the desired double-null position. That is, by letting $T_j = T_j' + \Delta_j$, $T_{j+1} = T_{j+1}' + \Delta_{j+1}$, and $z = z_d$ in (3) and (5) respectively, two equations in two unknowns result.

(7a) $$C_{11}\Delta_j + C_{12}\,\Delta_{j+1} + C_{13} = 0$$

(7b) $$C_{21}\Delta_j + C_{22}\,\Delta_{j+1} + C_{23} = 0$$

---

* It is recognized that a still wider null region could be obtained if the two zeros did not actually become coincident but were allowed to remain separated by an amount such that a sidelobe existed in between the two zeros having its peak value exactly equal to the dB down level at which the angular measurement was being made.

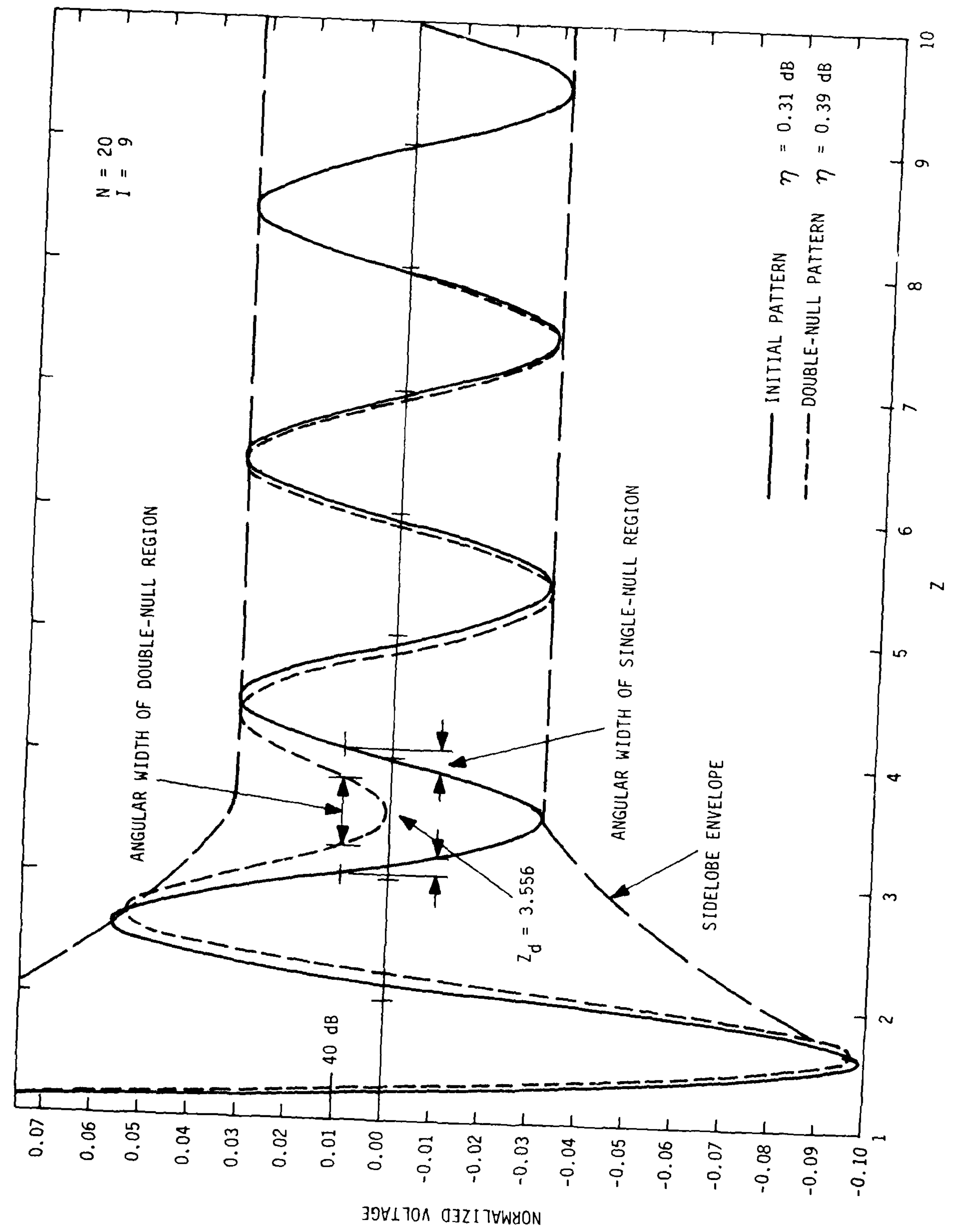

FIGURE 3. COMPARISON OF THE INITIAL PATTERN AND A DOUBLE-NULL PATTERN

where

(8a) $$C_{11} = \sum_{n=1}^{N} \cos(2\pi d_n z_d) \cos(2\pi d_n j)$$

(8b) $$C_{12} = \sum_{n=1}^{N} \cos(2\pi d_n z_d) \cos[2\pi d_n (j+1)]$$

(8c) $$C_{13} = \sum_{n=1}^{N} A_n \cos(2\pi d_n z_d)$$

(8d) $$C_{21} = \sum_{n=1}^{N} d_n \sin(2\pi d_n z_d) \cos(2\pi d_n j)$$

(8e) $$C_{22} = \sum_{n=1}^{N} d_n \sin(2\pi d_n z_d) \cos[2\pi d_n (j+1)]$$

(8f) $$C_{23} = \sum_{n=1}^{N} d_n A_n \sin(2\pi d_n z_d)$$

Solving (7) for the T_i-coefficient adjustments Δ_j and Δ_{j+1}, is straightforward using Cramer's rule.

The desirability of having control on the pattern sidelobe behavior as the position of a double-null point is varied is shown by Figure 4. Here the voltage array factors of the pattern having a double-null at $z = 3.556$ and a pattern having a double-null at $z = 3.250$ are compared. The latter pattern was obtained using (7) with $j = 3$ and the T_i-coefficients of the former pattern. Note both array factors have the same R-value at all integral z-points other than $z = 3$ and $z = 4$ in agreement with Taylor's observation relative to the T_i-coefficients.

The sidelobe behavior of the two patterns, however, is quite different. In shifting the double-null position from $z = 3.556$ to $z = 3.250$, the first two sidelobes have dropped below the 20/30 dB envelope while the other six have risen above the envelope. The fourth sidelobe (counting by slope reversal points) is only 21.734 dB down, i.e., well above the desired 30 dB level.

Figure 4 illustrates the modifications that have been made to a least-squares-error iterative technique [7] for controlling sidelobe levels when the requirement to also control the position of a double-null point is

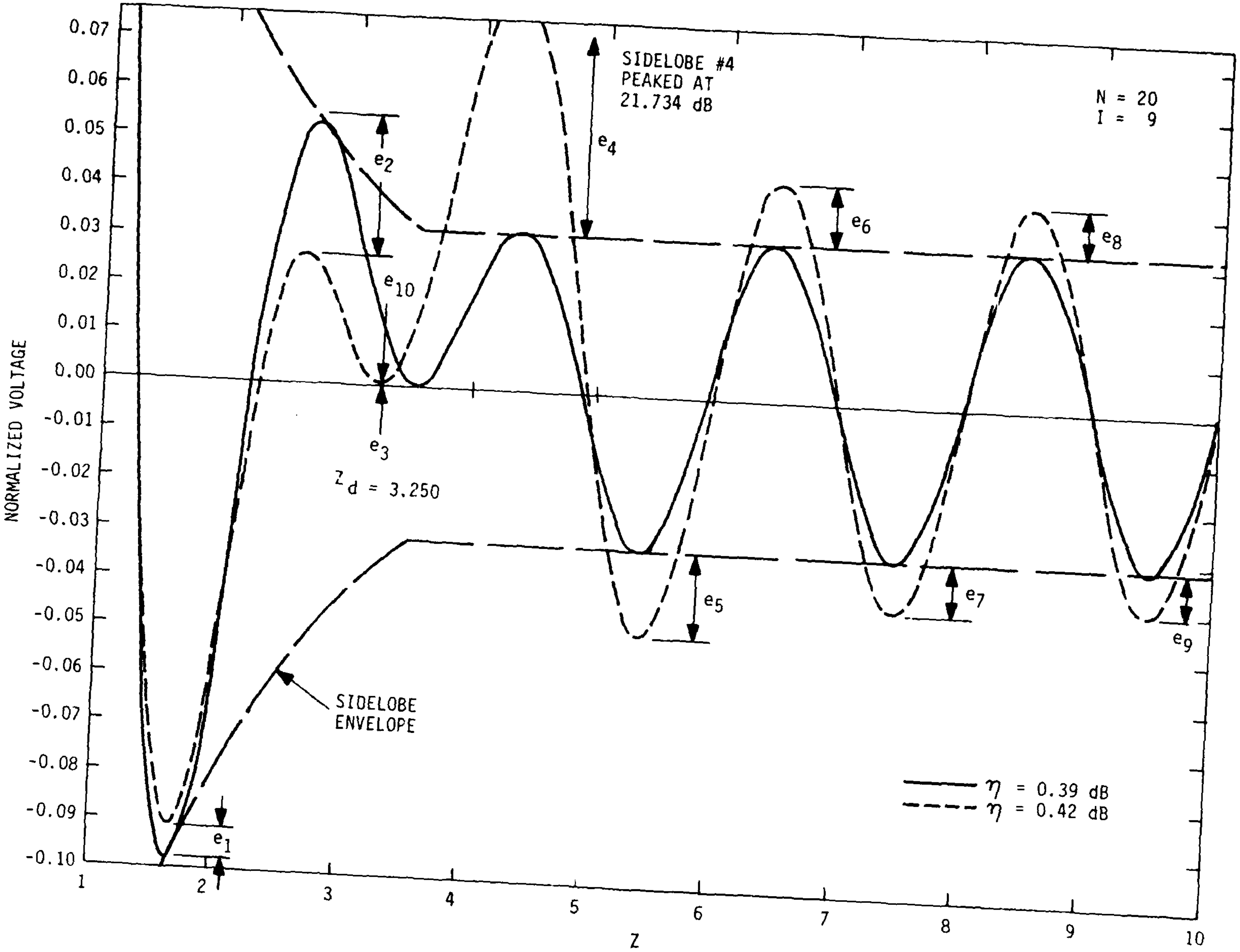

FIGURE 4. COMPARISON OF DOUBLE-NULL PATTERNS IN MEETING SIDELOBE ENVELOPE.

introduced. Ten errors are shown in the figure which may be used to contribute terms to the error function being minimized. Eight of these errors are the deviations of the sidelobe peaks of an approximating pattern from the desired sidelobe envelope. The ninth error (i.e., e_3 here) is the deviation from zero of the approximating pattern slope reversal point intended to be the double-null point. The tenth error is the deviation from zero of the approximating pattern value at the desired double-null point.

Obviously, ten errors involving nine variables will generally only minimize the value of the error function. An example is shown in Figure 5 where the desired double-null point was z = 3.250 and the desired sidelobe levels were the 20/30 dB envelope. Using equal weighting on each of the ten error terms leaves large errors in the e_3 and e_{10} terms (probably those of the most importance) when the error function reaches its minimum value. While it is possible that some weighting scheme could be devised to reduce these important errors, the following alternative was adopted.

Note in both Figures 4 and 5 that at least one of the approximating pattern sidelobes was at a level lower than the desired envelope. The iterative procedure as modified for the purpose of this report does not include any contribution from the error existing at one of the sidelobes adjacent to the desired double-null position. Thus, the error function sums nine terms with nine variables and the function value converges to zero (when it converges). Of course, the uncontrolled sidelobe may have risen above the desired sidelobe envelope when convergence occurs.

For the case of a desired double-null point at z = 3.250 leaving the second sidelobe out of the error function gives the array factor of Figure 6. The second sidelobe level has dropped to 51.951 dB down, well below the assigned sidelobe envelope. Thus, the price for meeting the objective of a desired double-null position having all sidelobes at or below a preassigned level would seem to be a slight dimunition in the available antenna gain of the pattern. A possible trade-off situation exists in that the angular width of this pattern null (at 40 dB down) is quite large.

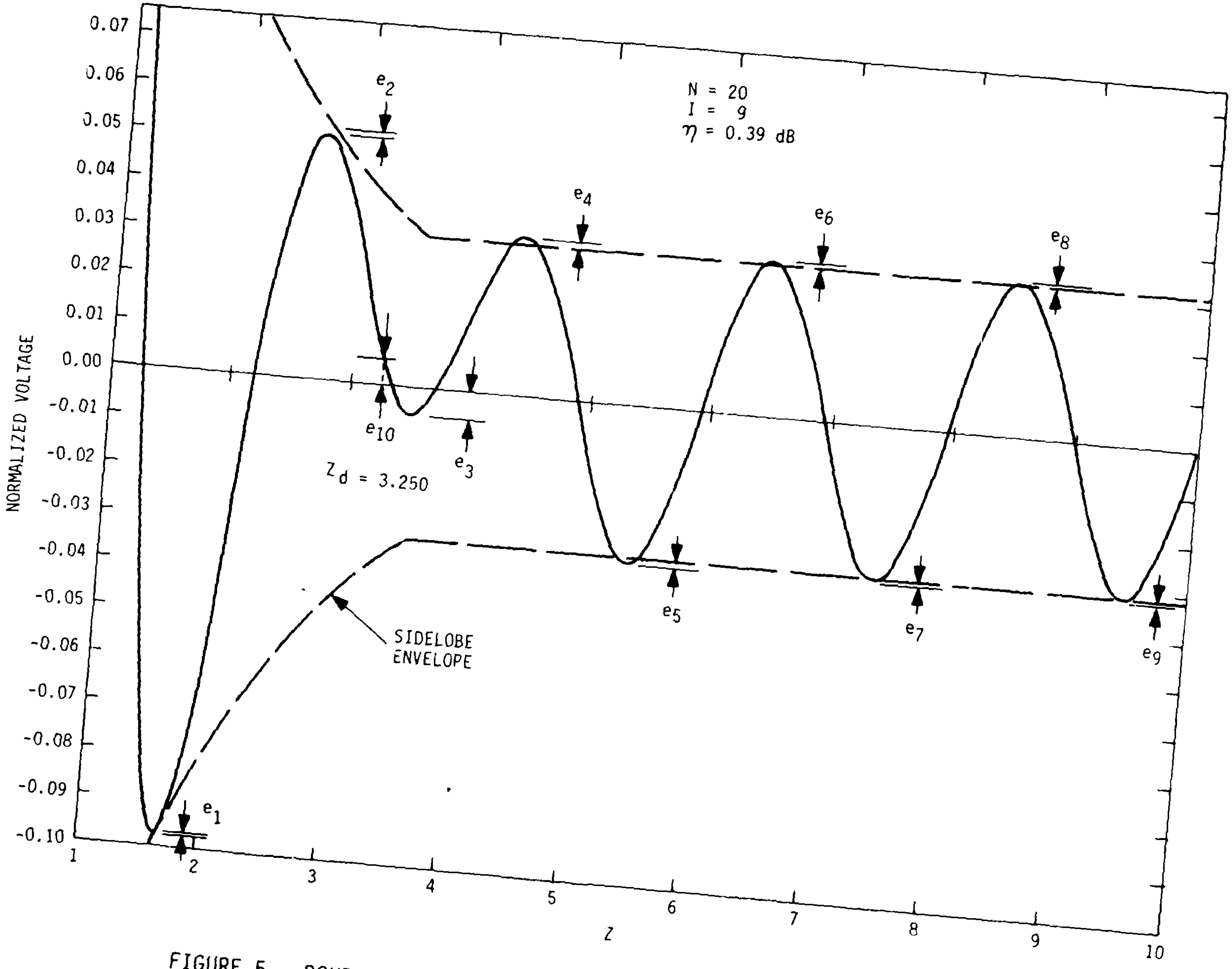

FIGURE 5. DOUBLE-NULL PATTERN WITH EQUAL ERROR TERM WEIGHTING.

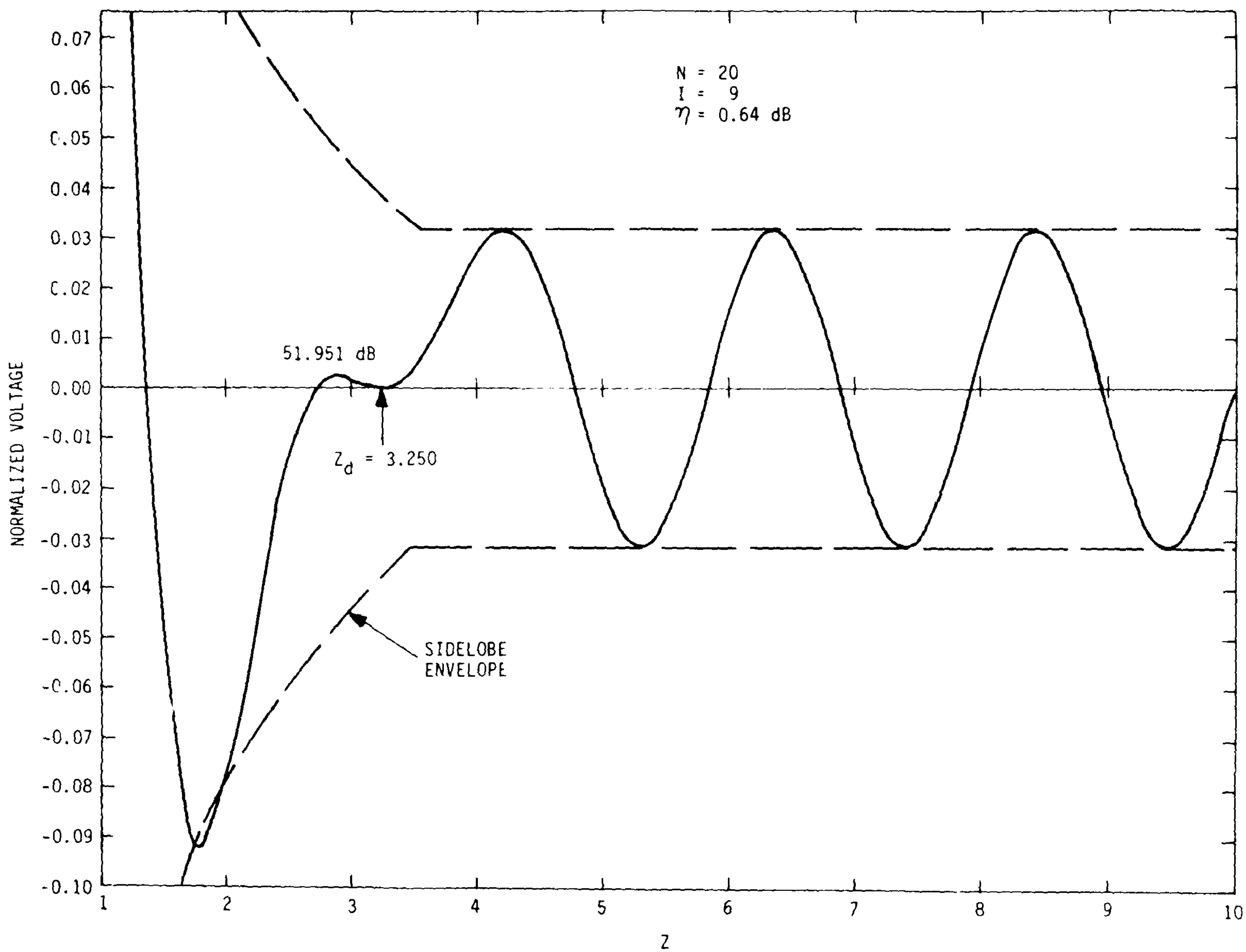

FIGURE 6. DOUBLE-NULL PATTERN WITH MODIFIED ERROR TERM WEIGHTING

V. ITERATIVE CONTROL PROCEDURE

The procedure devised to control the position of a pattern double-null point and to constrain the pattern sidelobe levels is summarized as follows:

a. Choose the desired sidelobe level envelope $R_e(z)$.

b. Select an initial set of $I(=IP[(N-1)/2])T_i$-coefficients.

c. Calculate the excitation amplitudes (1) for N elements located at the aperture points (2).

d. Calculate the voltage array factor (3) at a grid of z-points suitable for determining each slope reversal point z_{rj} and each zero crossing point z_{ck} of the pattern.

e. Select the desired double-null point z_d and its associated i-index i_d based upon the j and k index counts of step d.

f. Adjust the T_i-coefficients by (7) for $i = i_d$ and $i_d + 1$ to obtain an aperture illumination that will generate the double-null point at z_d.

g. Calculate an approximating array factor (3) and determine the array factor values $R_a(z_{rj})$ at its slope reversal points and the array factor value $R_a(z_d)$ at the desired double-null point.

h. Calculate an error function of the form

$$E(T_i) = [R_a(z_d)]^2 + \sum_{i=1}^{I} [R_a(z_i) - R_e(z_i)]^2 \tag{9}$$

where $R_e(z_i) = R_a(z_{ri})$ for the index $i = i_u$ of the single sidelobe chosen to be uncontrolled and $R_e(z_i) = 0$ for the index $i = i_d$ of the sidelobe chosen to 'disappear'.

i. Minimize the error function (9) by the Newton-Raphson method [8] applied to the I simultaneous equations.

$$\frac{\partial E(T_i)}{\partial T_j} = 0, \qquad j = 1, 2, \ldots, I. \tag{10}$$

j. Using the new set of T_i-coefficients from step i, return to step g until the error function (9) converges to its minimum value.

The computer program devised to carry out the iterative procedure is considered proprietary and is not presented herein. It is noted, however, that maintaining the proper ordering of all the slope reversal points $R_a(z_r)$ from iteration to iteration is essential for successful use of the procedure. For this reason it is desirable to return to step f instead of step g occasionally during the iteration process. That is, continuously forcing the double-null point to exist tends to prevent the disappearance of any slope reversal point.

For some of the cases examined, the double-null point turned out to be essentially a triple-null point. Specifically, the sidelobe chosen to have its own calculated level replace the envelope level also 'disappeared' to more than 80 dB down. Figure 7 is a plot of the sidelobe region of the voltage array factor for a desired double-null position $z_d = 6.000$ with the fifth sidelobe uncontrolled. For the scale of this plot, it is impossible to determine whether the pattern behavior near $z = 6.000$ behaves as an exact triple-null position or as a double-null position with a single-null close by.

VI. RESULTS

A large number of array factors have been computed for double-null patterns as z_d was varied between 1.708 and 10.000. Three important results have been extracted from these computations.

Figure 8 shows how the aperture efficiency (6) varies for the range $1.750 \leq z_d \leq 10.000$ by 0.25 increments in z_d. The efficiency degrades significantly only when a double-null point is positioned such that the first sidelobe of the pattern turns out to be the sidelobe controlled at its calculated value instead of the desired envelope value. It is conjectured that the array illuminations derived by this iterative technique will represent a near-optimum compromise between narrow antenna beamwidth and sidelobe suppression when a double-null point is required to be present in the antenna pattern. Note that the minimum loss values occur at the points where the double-null position was uncontrolled while the maximum losses are at the points where triple-nulls exist.

Figure 9 shows how the array element excitations vary for the range $1.750 \leq z_d \leq 10.000$ by 0.25 increments in z_d. The relative amplitudes plotted here have been normalized to unity power across the array elements

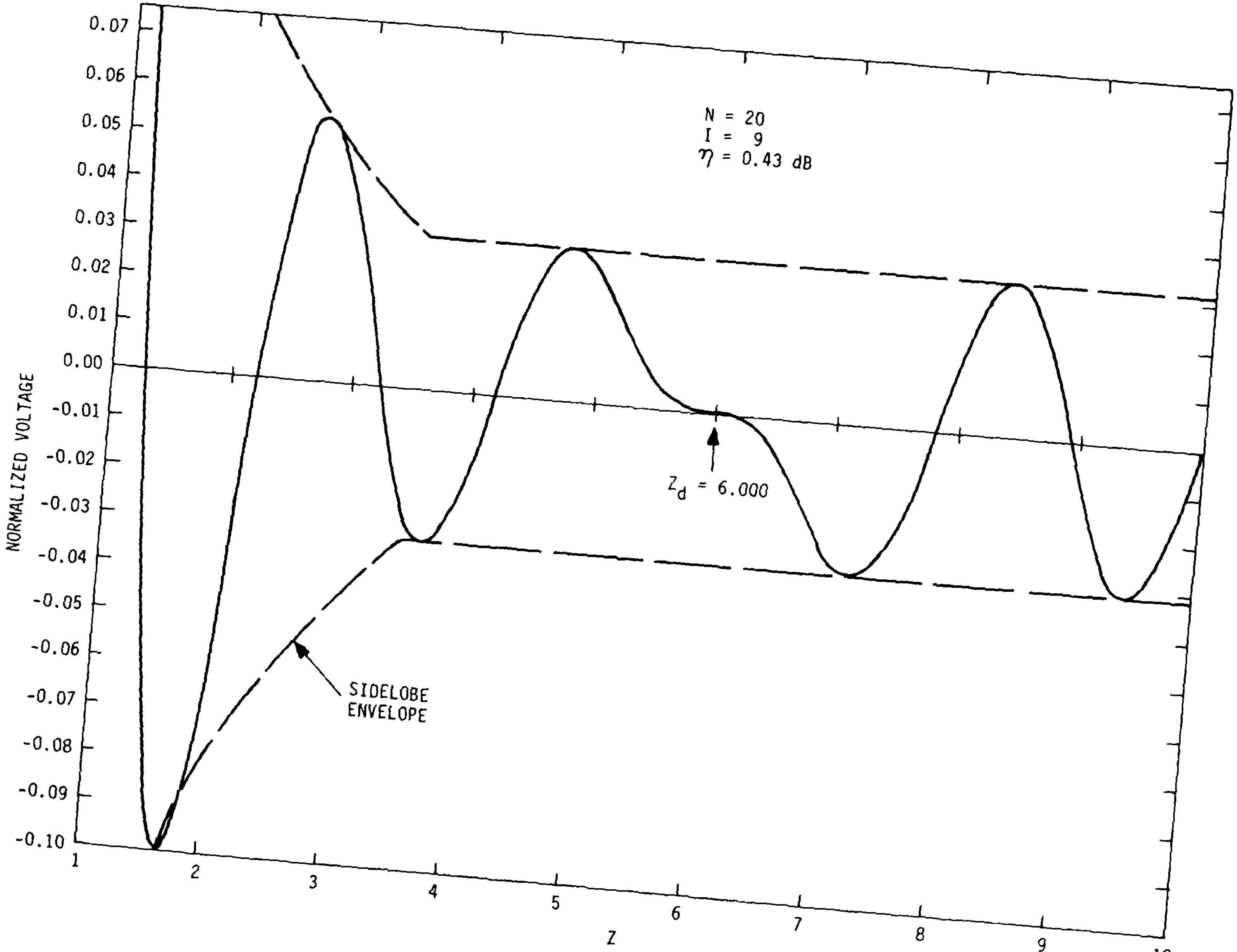

FIGURE 7. TRIPLE-NULL PATTERN USING MODIFIED ERROR TERM WEIGHTING.

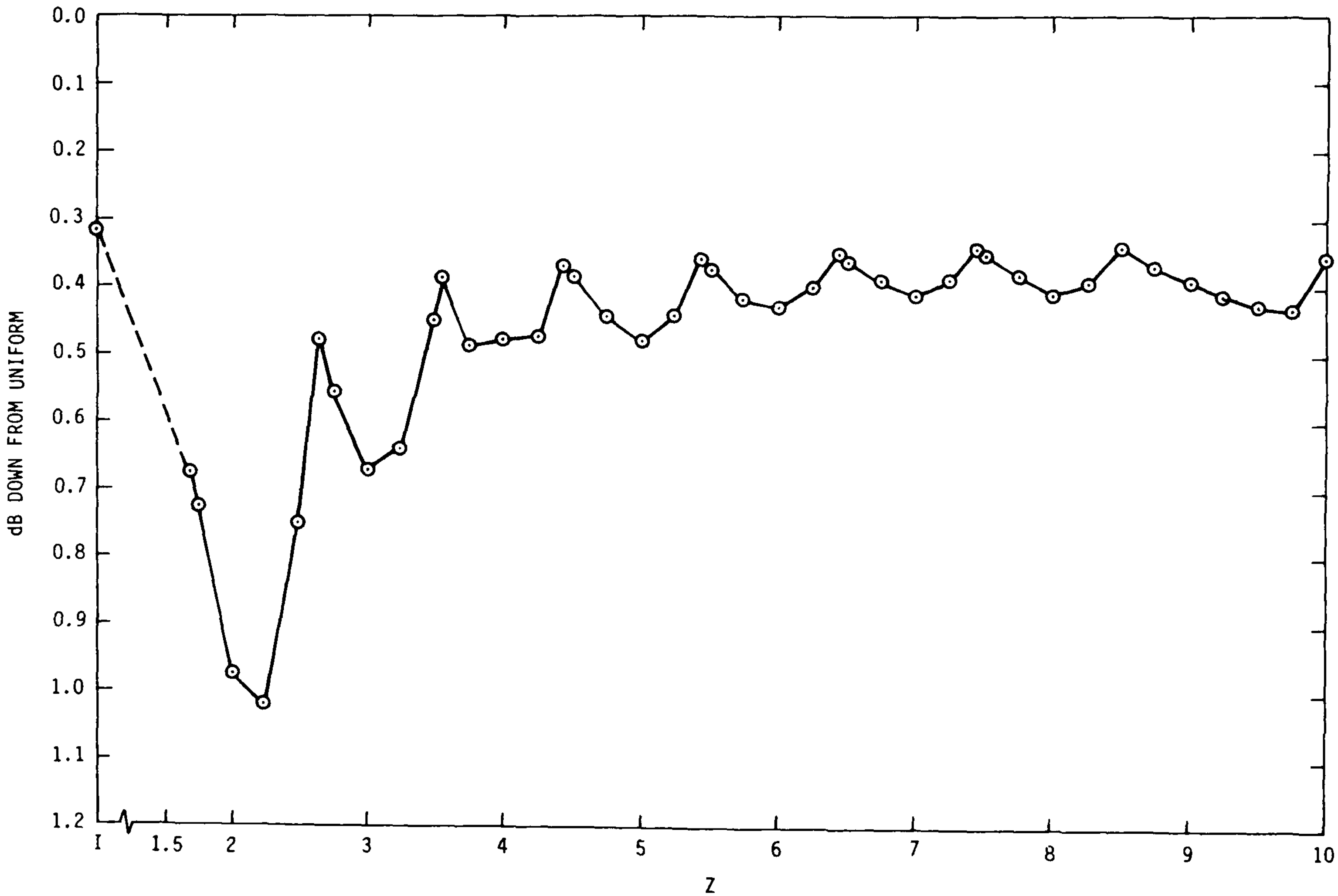

FIGURE 8. APERTURE ILLUMINATION EFFICIENCY VS. DOUBLE-NULL POSITION.

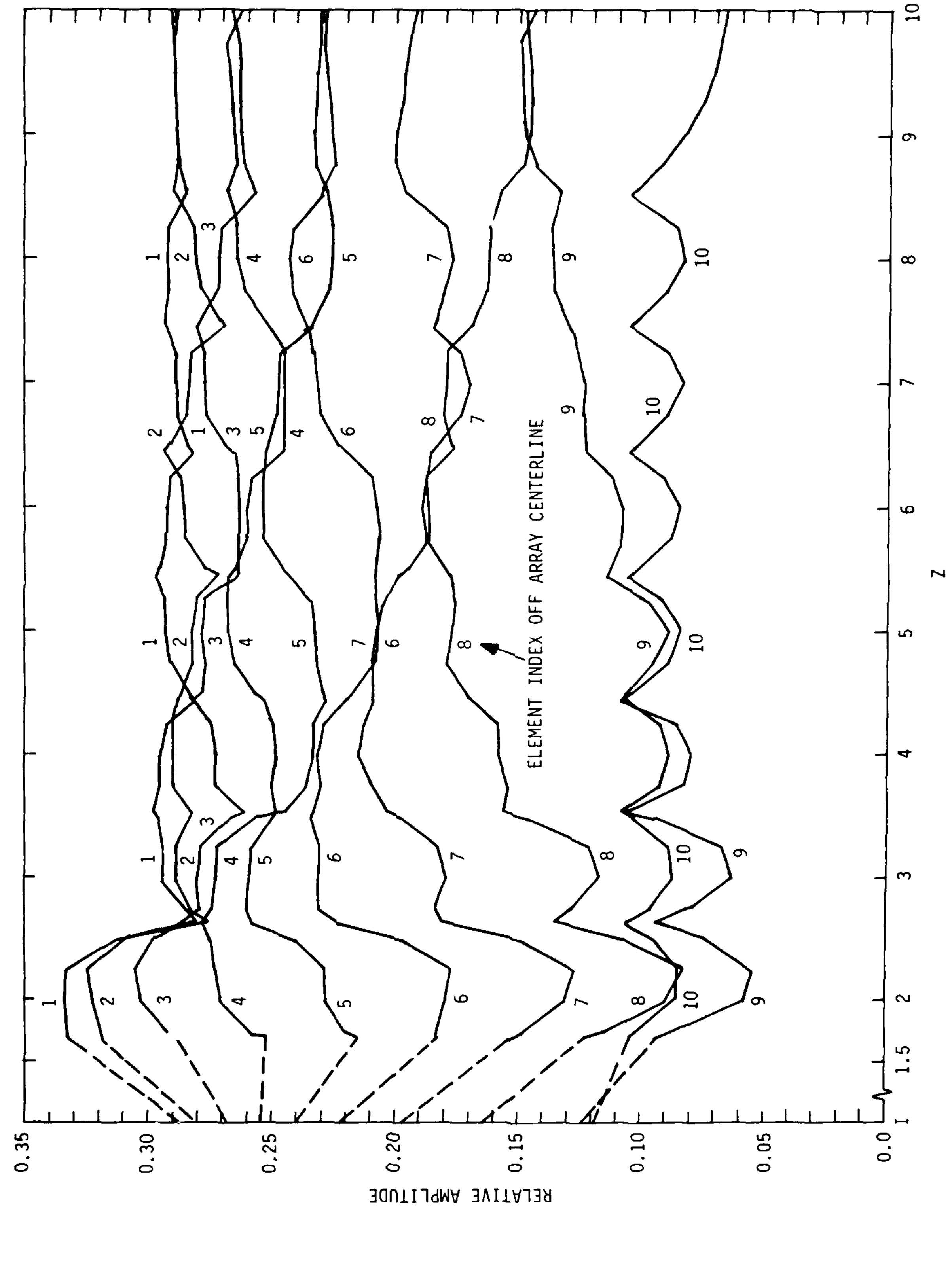

FIGURE 9. ARRAY ELEMENT AMPLITUDE VARIATION VS. DOUBLE-NULL POSITION.

to assist in evaluating the requirements that would be placed on various feed network configurations for producing double-null patterns. For example, to scan the position of a double-null point throughout the sidelobe region of an antenna pattern by means of a variable power divider network directly feeding the array elements, it is apparent that all elements in a small array will probably require amplitude adjustments. The accuracy required at each power dividing junction of the feed network appears to be just within the state-of-the-art. Note again the cusp-type behavior of each curve occurs at the points where the double-null position was uncontrolled.

Figure 10 shows how the T_i-coefficients vary for the range $1.750 \leq z_d \leq 10.000$ by 0.25 increments in z_d. The relative values of these coefficients have been normalized to unity power in order to investigate the possibility of designing a variable power divider feed network capable of electronically scanning the double-null position across the pattern sidelobe region. Here the network would feed the beam ports of an orthogonal multiple (sin x/x) beam-forming device connected to the array elements. It is apparent that all ports of the variable power divider will require substantial output level changes. The change in sign of the T_i-coefficients for $2 \leq i \leq I$, of course, means that a 180^0 phase reversal at that output port is necessary. The accuracy needed at each power dividing junction of the feed network, however, may well be somewhat beyond the state-of-the-art since many of the output values must be more than 40 dB down. Once more the cusp-type behavior occurs at the uncontrolled double-null positions.

It is worth noting that one additional result was found in using this iterative procedure. The range of desired double-null positions reported above was $1.708 \leq z \leq 10.000$. Figure 11 shows now a typical pattern result when the desired double-null position is taken at a point $z_d < z = 1.708$. For this case the first sidelobe of the initial pattern was selected to 'disappear' with the second sidelobe left uncontrolled. The desired double-null position was $z_d = 1.625$. Observe that the uncontrolled sidelobe rises higher (to 19.856 dB down) than the desired envelope. Trials with other choices for the uncontrolled sidelobe behaved similarly. It is conjectured, therefore, that a desired double-null position cannot be

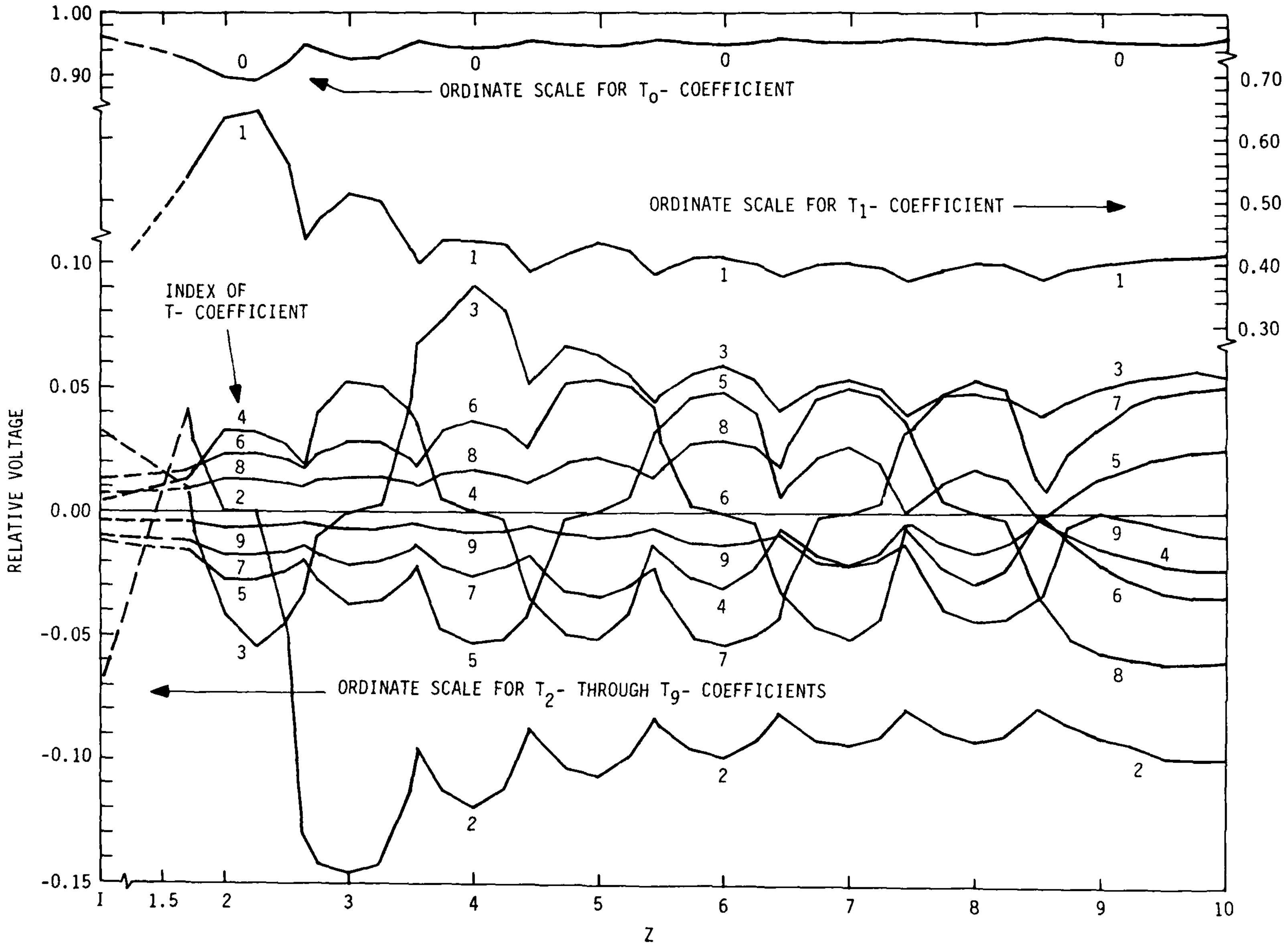

FIGURE 10. T_i - COEFFICIENT VARIATION VS. DOUBLE-NULL POSITION.

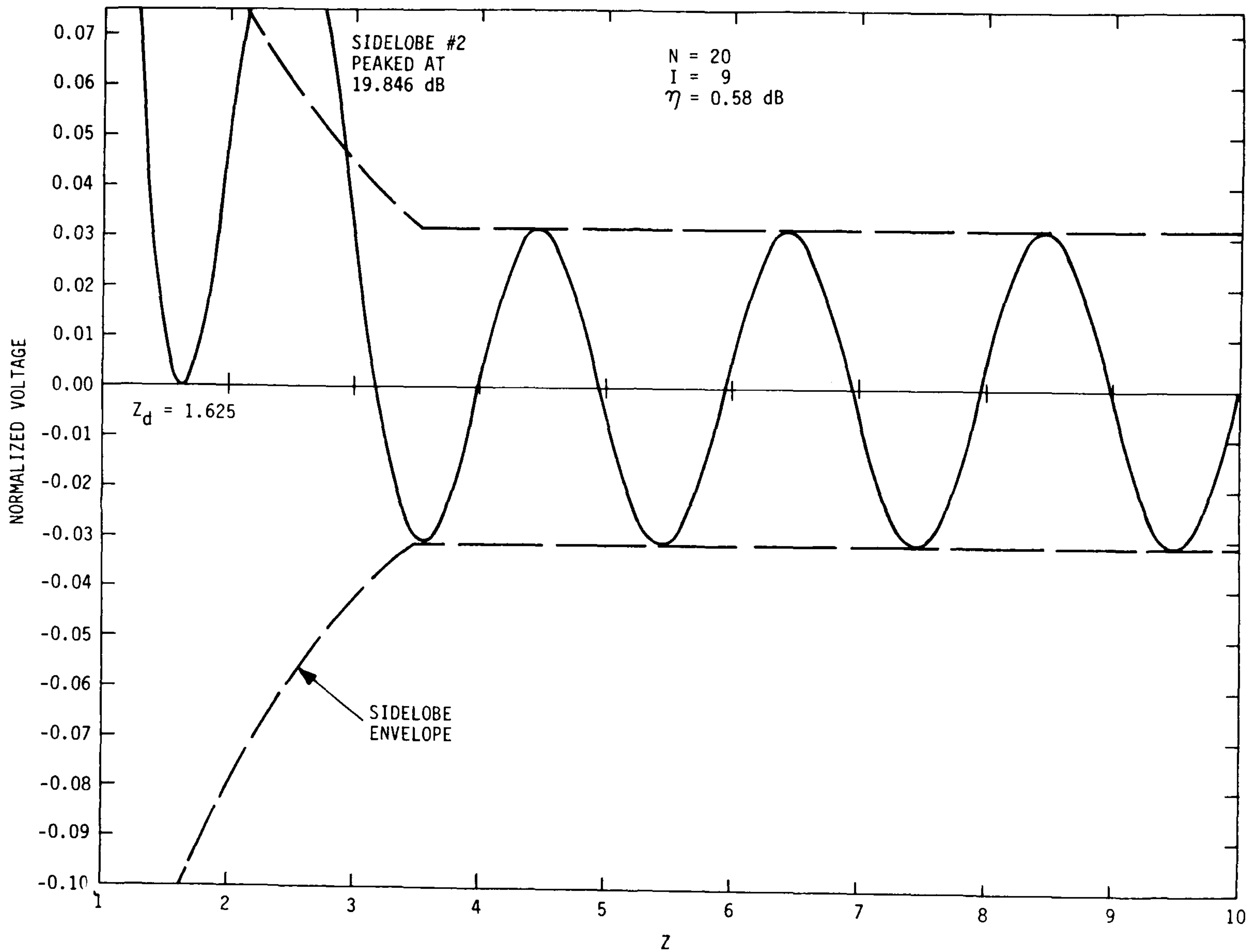

FIGURE 11. DOUBLE-NULL PATTERN FOR DESIRED POSITION $Z_d < Z = 1.708$.

located at a point closer to the directional beam peak direction than the point halfway between the first two nulls of the initial pattern (setting a desired sidelobe envelope) and also meet the desired envelope levels with a resulting double-null pattern.

VII. CONCLUSION

A procedure has been described which was shown to establish a theoretical aperture illumination for a small discrete-element linear array that will generate an antenna pattern having both a wide (double-valued) null located at a preassigned angle measured away from the pattern's directional beam peak and sidelobe characteristics meeting a preassigned sidelobe level envelope. While this procedure uses an aperture-normalized angular variable, converting the results to a real-space far-field angle is straightforward. The array element pattern has been neglected but this effect could easily be taken into account by the selection of the arbitrary sidelobe envelope should a known element pattern exist.

It is intended to extend the aperture illumination derivation technique to handle those cases where multiple double-null positions are involved and where complex aperture excitations can be employed.

VIII. REFERENCES

[1] D. E. N. Davies, 'Independent Angular Steering of Each Zero of the Directional Pattern for a Linear Array', IEEE Trans. Antennas Propagat., Vol. AP-15, pp. 296-298, March 1967.

[2] C. Drane and J. McIlvenna, 'Gain Maximization and Controlled Null Placement Simultaneously Achieved in Aerial Array Systems', Radio Electron. Eng., Vol. 39, pp. 49-57, January 1970.

[3] P. J. D. Gething, 'Linear Antenna Arrays with Broadened Nulls', Proc. IEE, Vol. 121, pp. 165-168, March 1974.

[4] S. Prasad, 'Linear Antenna Arrays with Broad Nulls with Application to Adaptive Arrays', IEEE Trans. Antennas Propagat., Vol. AP-27, pp. 185-190, March 1979.

[5] F. I. Tseng, 'Design of Array and Line-Source Antennas for Taylor Patterns with a Null', IEEE Trans. Antennas Propagat., Vol. AP-27, pp. 474-479, July 1979.

[6] T. T. Taylor, 'Design of Line-Source Antennas for Narrow Beamwidth and Low Sidelobes', IEEE Trans. Antennas Propagat., Vol. AP-3, pp. 16-28, January 1955.

[7] C. F. Winter, 'Using Continuous Aperture Illuminations Discretely', IEEE Trans. Antennas Propagat., Vol. AP-25, No. 5, pp. 695-700, September 1977.

[8] P. A. Stark, Introduction to Numerical Analysis, New York: MacMillan, 1970, pp. 130-133.

STUDY OF ANTENNA PATTERNS WITH NULL CONSTRAINTS

Hans Steyskal

Electromagnetic Sciences Division
Rome Air Development Center
Hanscom AFB, MA

ABSTRACT

The least mean square pattern synthesis method is extended to include constraints such as pattern nulls at a given set of angles. The problem is formulated as a constrained approximation problem which is solved exactly and a clear geometrical interpretation of the solution in a multidimensional vector space is given. The relation of the present method to those of constrained gain-maximization and signal-noise ratio maximization is discussed and conditions for their equivalence stated.

For a linear uniform N-element array it is shown that, when M single nulls are imposed on a given "quiescent" pattern, the optimum solution for the constrained pattern is the initial pattern and a set of M weighted (sin Nx)/sin x-beams. Each beam is centered exactly at the corresponding pattern null, irrespective of its relative location. Several illustrative examples of patterns with imposed nulls are included. In addition, curves are derived, which allow an estimate of the number of nulls required to suppress the sidelobes within a given sector, or alternatively, an interference source of given bandwidth, to a desired level.

1. Introduction

The problem of forming nulls in the radiation pattern of an antenna, in order to suppress interference from certain directions, presently receives much attention. Most work is in the area of adaptive nulling systems, as discussed by Applebaum [1] where a performance index such as the signal-to-noise ratio is maximized. In the case where jammers are the dominant noise source this process automatically places pattern nulls in the directions of the jammers. A seemingly different approach is that of Drane-McIlvenna [2] where another index, antenna gain, is maximized, subject to a set of null constraints on the pattern. In both methods the performance index is the quantity of prime interest, whereas the role of the antenna pattern is not too clear, which - to an antenna engineer - is unsatisfactory.

The purpose of this paper is to show that the problem can be formulated as a direct pattern synthesis problem which includes the pattern nulls. The method is based on least mean square or Gaussian approximation [3] which allows an attractive geometrical interpretation in a multi-dimensional vector space. It will be shown that under certain conditions the present approach yields the same result as the methods of constrained gain maximization and as SNR maximization. The least mean square error criterion with single null constraints has been lucidly discussed [4] in very general terms and as applied to satellite multiple-beam antennas. In contrast, we will study the classic problem of pattern synthesis for a linear array of isotropic elements, which leads to a slightly different formulation and some complementary viewpoints and results.

2. Formulation of the Problem

We consider a situation where an array antenna is being illuminated by desired signals and also by highly dominant interference signals from certain, discrete directions. The optimum antenna pattern for this case is reasonably defined as the desired pattern in the absence of the jammers, the so called quiescent pattern, suitably modified so as to form pattern nulls in the interference directions. The degrees of freedom available in the antenna pattern are thus used in first place to form the pattern nulls, with remaining degrees of freedom being used for approximation of the quiescent pattern.

The corresponding antenna pattern synthesis problem consists of determining the closest approximation p_a to a given, quiescent pattern p_o, subject to a set of null constraints. The solution of this problem requires a definition of "distance" between two patterns and this will be defined in Gauss' sense as the mean square difference between the patterns. This particular metric provides an over-all measure of approximation, and, in contrast to, for instance, the Chebyshev approximation places no explicit bound on the maximum deviation from the desired function at any particular point. However, it is the only metric that allows the approximation problem to be solved with any sense of generality.

For simplicity we consider a linear array of N isotropic antenna elements with uniform, half-wavelength spacing. Setting $u = \sin\theta$ where θ is defined in Fig. 1, the antenna far-field pattern is described by the array factor

$$p(u) = \sum_{1}^{N} x_n e^{-in\pi u} \tag{1}$$

where x_n denotes the complex excitation of the n:th array element.

The synthesis problem can now be stated mathematically: Find the pattern $p_a(u)$, such that the mean-square difference

$$\mathcal{E}(p_a) = \tfrac{1}{2} \int_{-1}^{1} | p_o(u) - p_a(u)|^2 \, du = \text{minimum} \tag{2a}$$

subject to the constraints

$$p_a(u_m) = 0, \qquad m = 1,\ldots,M \tag{2b}$$

where $\{u_m\}_1^M$ denotes the angular location of the M interference sources.

We assume that the desired, quiescent pattern is given as a sum of N harmonics, as represented by (1). For the general case, where $p_o(u)$ has any functional form, p_o may be simply approximated by the first N terms of its Fourier-series expansion. Although the synthesis procedure then involves two subsequent approximations, it can be shown to lead to the correct least-mean-square approximation of the initial pattern.

3. Method of Solution

The synthesis problem posed above is most conveniently formulated in a multi-dimensional vector space, where each point represents one array excitation, which allows a clear geometrical interpretation of the approximations involved. From the solution for the array excitation the desired pattern is then simply given by (1). The underlying principle for this equivalence between array excitation and radiation pattern is of course Parseval's theorem.

We introduce an N-dimensional excitation space X, in which the array excitation $\{x_n\}_1^N$ is represented by the vector $\bar{x} = (x_1,..,x_N)$. The inner product of two vectors we define as $(\bar{x},\bar{y}) = \Sigma x_n y_n^*$, where *denotes complex conjugate, and the norm $\|\bar{x}\| = (\bar{x},\bar{x})^{1/2}$.

In order to express the mean square error ε in terms of the array excitation we substitute (1) in (2a) and obtain after integration

$$\varepsilon = \tfrac{1}{2}\int_{-1}^{1} |p_o - p_a|^2 du = \sum_{n=1}^{N} |x_{on} - x_{an}|^2 = \|\bar{x}_o - \bar{x}_a\|^2 \qquad (3)$$

where $\bar{x}_o$ and $\bar{x}_a$ are the excitation vectors corresponding to the patterns p_o and p_a, respectively. Likewise the pattern constraints (2b) can be expressed as constraints on the array excitation. The mathematical expressions simplify somewhat if we first multiply the pattern function p by a phase factor $\exp(i\psi u)$, where

$$\psi = \frac{N+1}{2} \tag{4}$$

which shifts the phase center of the pattern to the array center. Substituting this new function in (2b), we find, in view of (1), that a null at $u = u_m$ requires

$$\sum_{1}^{N} x_n \, e^{i(\psi - n\pi)u_m} = 0. \tag{5}$$

Defining constraint vectors $\bar{y}_m$ by

$$\bar{y}_m = e^{-i\psi}\left(e^{i\pi u_m}, \ldots, e^{iN\pi u_m} \right) \tag{6}$$

finally let us write (5) as orthogonality conditions on the array excitation

$$(\bar{x}, \bar{y}_m) = 0, \qquad m = 1, \ldots, M. \tag{7}$$

Note that we now have characterized each jammer direction u_m by one constraint vector.

In view of (3) and (7) the synthesis problem as expressed by (2) now becomes

$$\varepsilon = \| \bar{x}_o - \bar{x}_a \|^2 = \min. \tag{8a}$$

$$(\bar{x}_a, \bar{y}_m) = 0, \qquad m = 1, \ldots, M \tag{8b}$$

where x_o and $\bar{x}_a$ denote the unconstrained and constrained array excitation, respectively.

Equation (8) shows that the desired solution $\bar{x}_a$ is orthogonal to the constraint vectors $\{\bar{y}_m\}_1^M$. A geometrical interpretation of this relation is obtained if the excitation space X is divided into an M-dimensional sub-space

Y, spanned by the vectors $\{\bar{y}_m\}_1^M$ and its (N-M)-dimensional orthogonal complement Z. Any vector $\bar{x}$ now has a unique decomposition [5]

$$\bar{x} = \bar{y} + \bar{z} \tag{9}$$

where $\bar{y} \in Y$, $\bar{z} \in Z$, $\bar{z} \perp Y$, and due to this orthogonality

$$\|\bar{x}\|^2 = \|\bar{y}\|^2 + \|\bar{z}\|^2 \tag{10}$$

Using this decomposition for $\bar{x}_o$ and $\bar{x}_a$ we get from (8), (9) and (10)

$$\varepsilon = \|\bar{y}_o - \bar{y}_a\|^2 + \|\bar{z}_o - \bar{z}_a\|^2 = \min. \tag{11a}$$

$$(\bar{x}_a, \bar{y}_m) = (\bar{y}_a, \bar{y}_m) = 0, \qquad m = 1,\ldots,M\ . \tag{11b}$$

Equation (11b) yields

$$\bar{y}_a \equiv 0, \tag{12}$$

and therefore ε in (11a) is minimized by setting $\bar{z}_a = \bar{z}_o$ leading to the sought constrained excitation

$$\bar{x}_a = \bar{x}_o - \bar{y}_o \tag{13}$$

and the least mean square error

$$\varepsilon_{min} = \|\bar{x}_o - \bar{x}_a\|^2 = \|\bar{y}_o\|^2 \tag{14}$$

Equation (13) and (14) constitute the mathematical solution to the posed problem. Its properties will now be discussed from various points of view.

The method of solution is illustrated in Figure 2. The excitation $\bar{x}_o$, which is to be approximated, has the projections $\bar{y}_o$ and $\bar{z}_o$ in subspaces

Y and Z. Equation (8b) implies that the approximation $\bar{x}_a$ is orthogonal to the constraint vector set $\{y_m\}_1^M$ which spans Y, and therefore $\bar{x}_a$ is confined to the subspace Z. Under these circumstances the best approximation to $\bar{x}_o$ is obtained by setting $\bar{x}_a = \bar{z}_o$, since of all elements $\bar{z} \varepsilon Z$ this point is closest to $\bar{x}_o$.

Returning to the solution for the constrained excitation as given by (13) we note that $\bar{y}_o$ is a linear combination of the vectors $\bar{y}_m$ and therefore $\bar{x}_a$ may be written

$$\bar{x}_a = \bar{x}_o - \sum_1^M \alpha_m \bar{y}_m \tag{15}$$

where the coefficients α_m will be determined later. Presently, we infer from (15) that the sought excitation $\bar{x}_a$ is composed of the quiescent excitation $\bar{x}_o$ and a weighted sum of the vectors $\bar{y}_m$. Note the dual role of these vectors: initially they characterized a constraint, now they represent an array excitation.

As for the resultant antenna pattern, it follows from (15) and the linear relation between the array excitation and the pattern, that the constrained pattern $p_a(u)$ will be the quiescent pattern $p_o(u)$ with M beams superimposed. The beam corresponding to the excitation $\bar{y}_m$ we call a cancellation beam, denoted by $q_m(u)$, and it is easily shown by using (6) in (1) that

$$q_m(u) = \frac{\sin N\pi(u-u_m)/2}{\sin \pi(u-u_m)/2} \tag{16}$$

For the case of M nulls in the pattern the constrained pattern becomes

$$p_a(u) = p_o(u) - \sum_1^M \alpha_m \frac{\sin N\pi(u-u_m)/2}{\sin \pi(u-u_m)/2} \tag{17}$$

When N is large (17) can be approximated as

$$p_a \simeq p_o - N \sum_{1}^{M} \alpha_m \operatorname{sinc} [N\pi(u-u_m)/2] \ . \qquad (18)$$

Thus the pattern p_o is simply given by the quiescent pattern p_o and M superimposed sinc-beams. This result agrees with the single-jammer case considered in [1] and the general conclusion in [4].

The M cancellation beams represent M degrees of freedom and clearly it should be possible to realize M pattern nulls with these. However, it is noteworthy that each of these beams is centered exactly on the corresponding null, irrespective of their relative location and that the beam shape, given by $\sin(N\pi u/2)/\sin(\pi u/2)$, is fixed, regardless of how much the individual beams overlap. Similar observations hold for the cancellation beams corresponding to higher order pattern derivatives. These properties are consequences of the isotropic array elements and the least-mean-square approximation we have adopted.

The present synthesis method with single null constraints can be shown [6] to yield the same pattern as does SNR maximization [1] in the limiting case, where the jammers become infinitely strong. This latter condition forces the optimum SNR-pattern to maintain true nulls, rather than shallow dips, in the jammer directions and then the two methods are comparable, as shown in the appendix. Further, we also find equivalence with constrained gain maximization [2] in the special case where p_o is a maximum gain pattern, on which a set of nulls is imposed. Minimizing the pattern change ε then simultaneously minimizes the gain cost, and thus the constrained least mean square pattern coincides with the constrained maximum gain pattern.

Compared to these methods, however, the pattern synthesis method is a more direct and therefore conceptually more appealing approach, which provides valuable insight into fundamental pattern properties.

4. The Synthesized Pattern

The pattern p_a, which satisfies the desired null constraints is given by (17) where, however, the coefficients α_m so far are unknown. They may be determined from (15) and (11b) which leads to the following system of equations:

$$\begin{pmatrix} (\bar{y}_1, \bar{x}_o) \\ \cdot \\ \cdot \\ \cdot \\ (\bar{y}_M, \bar{x}_o) \end{pmatrix} = \begin{pmatrix} (\bar{y}_1, \bar{y}_1) & (\bar{y}_1, \bar{y}_2) & \cdots & (\bar{y}_1, \bar{y}_M) \\ (\bar{y}_2, \bar{y}_1) & (\bar{y}_2, \bar{y}_2) & & \\ \cdot & \cdot & \cdots & \cdot \\ (\bar{y}_M, \bar{y}_1) & (\bar{y}_M, \bar{y}_2) & & (\bar{y}_M, \bar{y}_M) \end{pmatrix} \begin{pmatrix} \alpha_1 \\ \cdot \\ \cdot \\ \cdot \\ \alpha_M \end{pmatrix}^* \quad (19)$$

Applying Cramer's rule and substituting into (18) yields

$$\bar{x}_a = \bar{x}_o - \frac{1}{G} \sum_{1}^{M} D_m^* \bar{y}_m \quad (20)$$

where the Gram determinant $G = G(\bar{y}_1, \ldots, \bar{y}_M)$ is the coefficient matrix in (19), see [5], and D_m is the determinant of the same matrix with the m:th column replaced by the column vector $((\bar{y}_1, \bar{x}_o), \ldots, (\bar{y}_M, \bar{x}_o))$. Note that there are only as many equations as there are constraints and usually therefore (19) will represent a small system of equations, which will be easy to invert.

To illustrate the synthesis method we have programmed (20) on a digital computer and calculated a few actual patterns. We considered "sinc-patterns" defined by the function $\sin(N\pi u/2)/N\sin(\pi u/2)$ and Chebyshev patterns, since they are in a sense complementary - the former have sidelobes of constant width and varying height, the latter have sidelobes of varying width but constant height.

In the first example we chose the original pattern p_o to be a sinc-pattern with three single nulls located at $u_1 = 0.21$, $u_2 = 0.22$, $u_3 = 0.23$. Figure 3 shows that in this case we do achieve 36 dB sidelobe cancellation over this sector. In the next two examples the unconstrained pattern is a 40 dB Chebyshev pattern in which we place 4 single nulls over a narrow sector (0.22, 0.28) and 8 single nulls over a wider sector (0.22, 0.36), respectively. In both cases the nulls are equally densely spaced $\delta u = 0.02$ apart. The resultant patterns, given in Fig. 4 and 5, show a sidelobe cancellation of 30 dB and 51 dB, resp., over the sectors. This is a surprising fact. Intuition would lead us to expect less cancellation for the wider sector, which contains a larger number of nulls, i.e., a larger number of superimposed sinc-beams, whose uncontrolled sidelobes we might expect to add up to a relatively higher average sidelobe level between the nulls.

Finally, we show a sinc-pattern and a 20 dB Chebyshev pattern in Figs. 6 and 7, again with 4 single nulls equispaced over the interval (0.22, 0.28). The sidelobe cancellation in this case is 34 dB and 32 dB resp., which is of roughly the same magnitude as the 30 dB obtained for the 40 dB Chebyshev pattern above. This indicates that it takes as many degrees of freedom to suppress the sidelobe level for example from 20 dB to 60 dB as from 40 dB to 80 dB.

5. Wideband Sidelobe Cancellation

A jammer located at a fixed direction u_j, with a fractional bandwidth $B = \Delta f/f$, will, in the antenna pattern, appear to cover a finite angular sector, centered at u_j and of width

$$\Delta u = Bu_j \tag{21}$$

due to the frequency dependence of the antenna. A problem of practical interest concerns the number of pattern nulls required to suppress the sidelobes to a desired level in this sector (or bandwidth). This question will be addressed below.

We limit ourselves to cases where the M nulls are spaced equidistantly over the nulling sector Δu, such that u_1 and u_M coincide with the left and right end-points of the sector. The spacing between the nulls is therefore

$\delta = \Delta u/(M-1) = (u_M - u_1)/(M-1)$. As a measure for how well we suppress the original pattern p_o over the desired nulling sector Δu, we define the power cancellation ratio

$$C = \frac{\max\limits_{u \varepsilon \Delta u} p_a(u)^2}{\max\limits_{u \varepsilon \Delta u} p_o(u)^2} \tag{22}$$

To investigate how the cancellation ratio depends on the pattern p_o, the array element number N, the sector Δu, and the number of nulls M, we calculated several patterns with imposed nulls. Typical results appear in Fig. 8 which shows $C = C(M, N = 41)$, with Δu as a parameter. The location of the nulling sector is rather arbitrary, although for the case $\Delta u = 0.025$, we had to distinguish whether Δu is symmetrically located over a sidelobe maximum or over a pattern null. The reason for this is that when we have only 2 or 3 nulls, symmetry conditions may create the effect of an extra null. This effect disappears with an increasing number of nulls. Several interesting conclusions can be drawn from Fig. 8:

— the sidelobe cancellation is relatively independent of the type of original pattern p_o, (sinc- or Chebyshev pattern)

— the cancellation is relatively independent of the actual sidelobe level

— the cancellation increases faster with M than it decreases with Δu. In other words, doubling the nulling sector requires less than doubling the number of nulls to maintain the same cancellation.

These results indicate that the main feature which determines the cancellation is the ripple rate of the sidelobes. The rate depends almost solely on the array element number and is approximately the same over most of the sidelobe region of all practical patterns. (Exceptions are the one or two sidelobes near the main beam of a Chebyshev pattern). This then suggests that we can model the sidelobe pattern by a simple sinusoid and that the cancellation obtained for this case provides a good estimate for the sidelobe cancellation of the general pattern.

We have evaluated such a simple model, where the sidelobes are approximated by the function $\sin(N\pi u/2)$ and have calculated the cancellation versus M, the number of nulls on the sector $0 \leq u \leq \Delta u$. This corresponds to a nulling sector adjacent to a natural pattern null. To allow for a possible difference when the nulling sector is close to a sidelobe maximum, we also placed the sector at $\pi/2 \leq u \leq /2 + \Delta u$, and chose the lower cancellation value of the two cases. The results are summarized in Fig. 9 which shows sidelobe cancellation as a function of the variable $N\Delta u = NBu_j$. Given the array element number N, the jammer direction u_j, and bandwidth B, we can thus, from these curves determine the number of nulls required to achieve a desired cancellation.

6. Summary and Conclusion

We have extended the general method of least mean square pattern synthesis [3] to include null constraints on the pattern. The problem has been posed as a constrained approximation problem and an exact solution has been obtained. The relation to other methods to achieve pattern nulls under mathematically well-defined conditions has been indicated. For a linear uniform array we have shown that when M single nulls are imposed on a pattern the constrained pattern is the sum of the original pattern and M weighted sinc-beams. Each beam is centered on the corresponding null, irrespective of how closely spaced they are or how much the beams overlap. Several illustrative examples of patterns with imposed nulls are given.

In addition, we have derived a set of curves which allow a simple estimate of the number of pattern nulls required to suppress the sidelobes to a desired level in a given sector. For adaptive antennas, these curves thus give an estimate of the number of adaptive loops required to suppress an interference source of given bandwidth.

Finally, it is worth noting that, although we have formulated the constrained synthesis method for a linear array with isotropic, half-wavelength spaced elements, it is not limited to these cases. It can readily be formulated in more general terms, in which case any desired linear passive beamforming network may be included in the antenna. It is hoped that this approach can contribute to an understanding of the fundamental properties and limits of an adaptive antenna.

7. Acknowledgement

The author wishes to thank Dr. Robert Mailloux for suggesting the problem and Ms. Yelena Gersht and Dr. Robert Shore for the computer programming.

8. References

[1] S. Applebaum, "Adaptive Arrays", IEEE Trans. Antennas Propagation, Vol. AP-24, pp. 585-598, Sep. 1976.

[2] C. Drane, J. McIlvenna, "Gain Maximization and Controlled Null Placement Simultaneously Achieved in Aerial Array Patterns", The Radio and Electronic Eng., Vol. 39, No. 1, pp. 49-57, Jan. 1970. [3] A. Schell,

[3] A.Schell, A. Ishimaru, "Antenna Pattern Synthesis", in Collins and Zucker (ed.): "Antenna Theory", Part I, McGraw-Hill, 1969.

[4] J.Mayhan, "Nulling Limitations for a Multiple-Beam Antenna", IEEE Trans. Antennas Propagation, Vol. AP-24, pp. 769-779, Nov. 1976.

[5] F. Gantmacher, "The Theory of Matrices", Vol. 1, Chelsea Publication Co., NY, 1959.

[6] H. Steyskal, "Synthesis of Antenna Patterns with Null Constraints", Report RADC-TR-80-402, Jan. 1981.

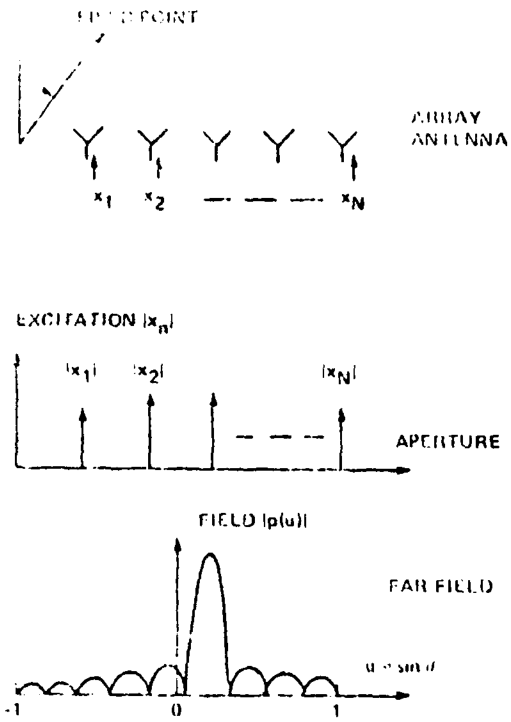

Figure 1. The array antenna, its aperture and far-field.

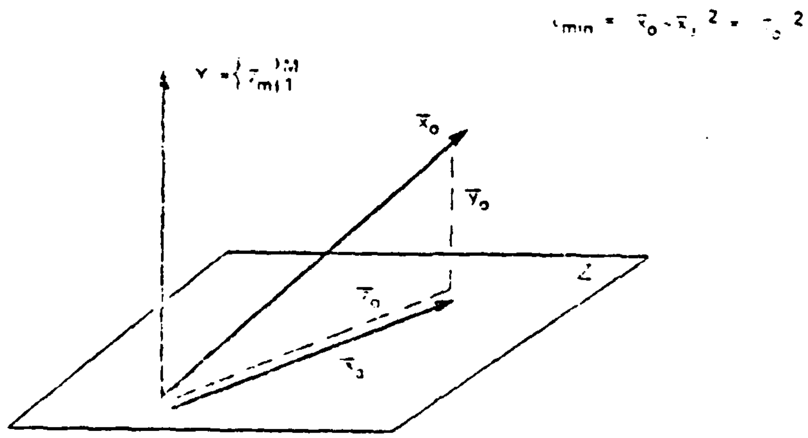

Figure 2. Geometrical illustration of the approximation problem: Desired point = x_o, closest approximation confined to subspace Z is $x_a = z_o$.

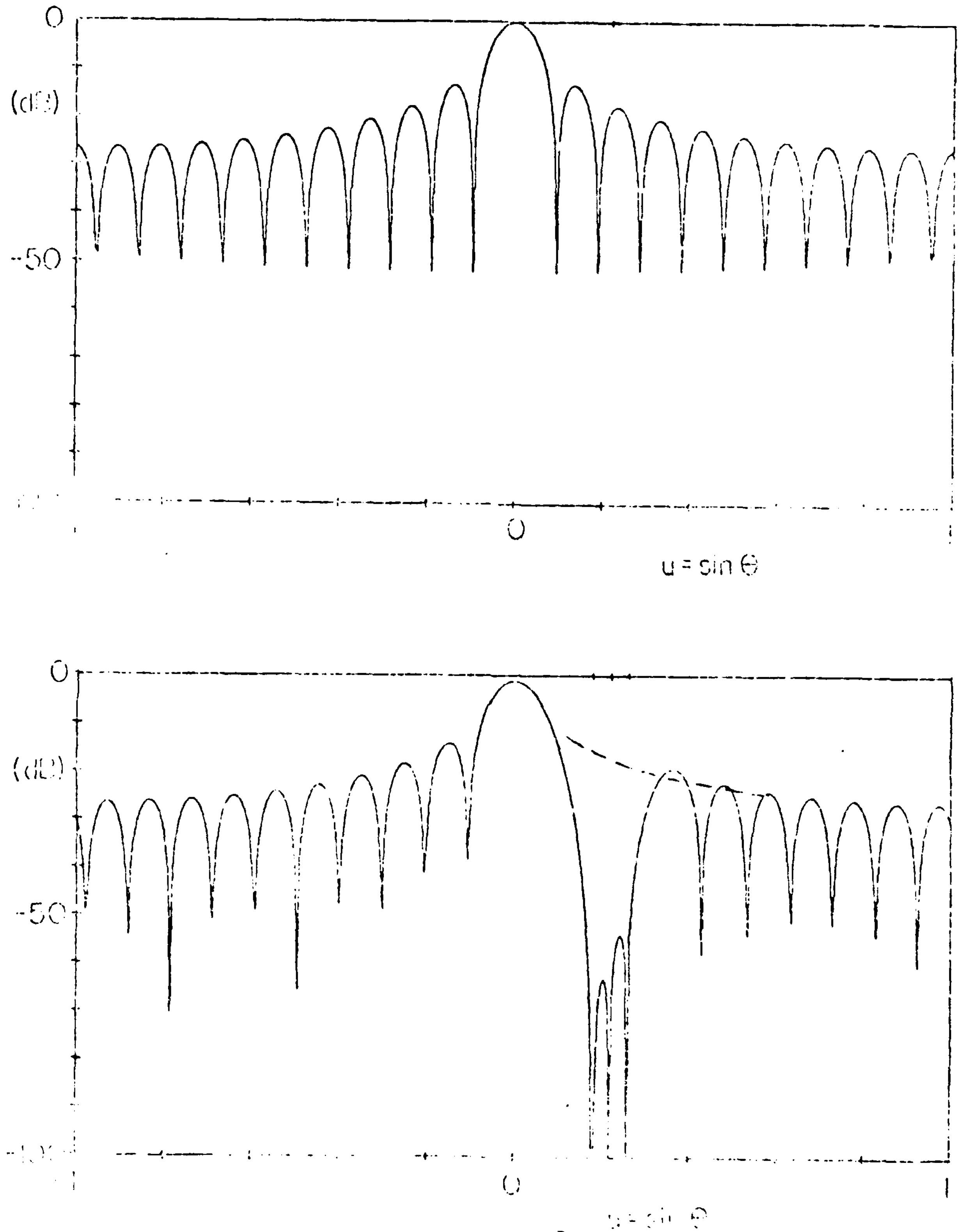

Figure 3. (a) Initial sinc-pattern and (b) pattern with three nulls equispaced over the sector (0.18, 0.26). Sidelobe cancellation = 30 dB, pattern change = 0.12, gain cost = 0.55 dB. 21 array elements.

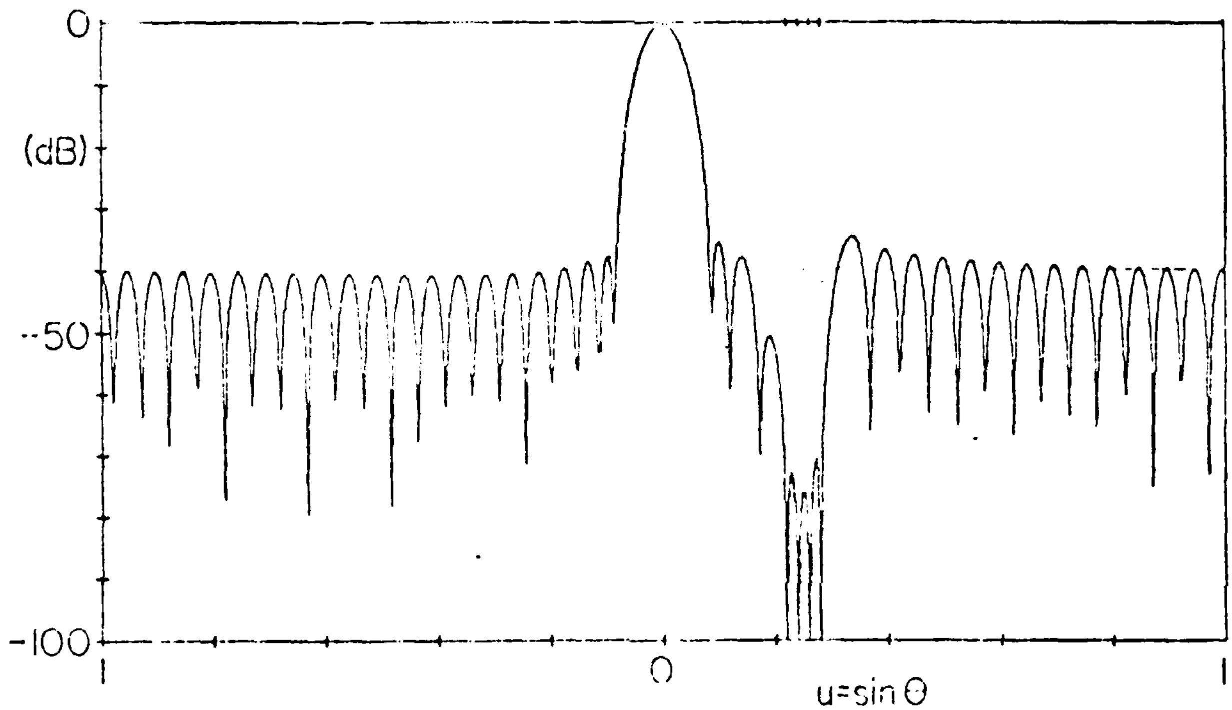

Figure 4. Initial 40 dB Chebyshev pattern with four nulls equi-spaced over the sector (0.22, 0.28). Sidelobe cancellation = 30 dB, pattern change ε = 0.001, gain cost = 0.04 dB. 41 array elements.

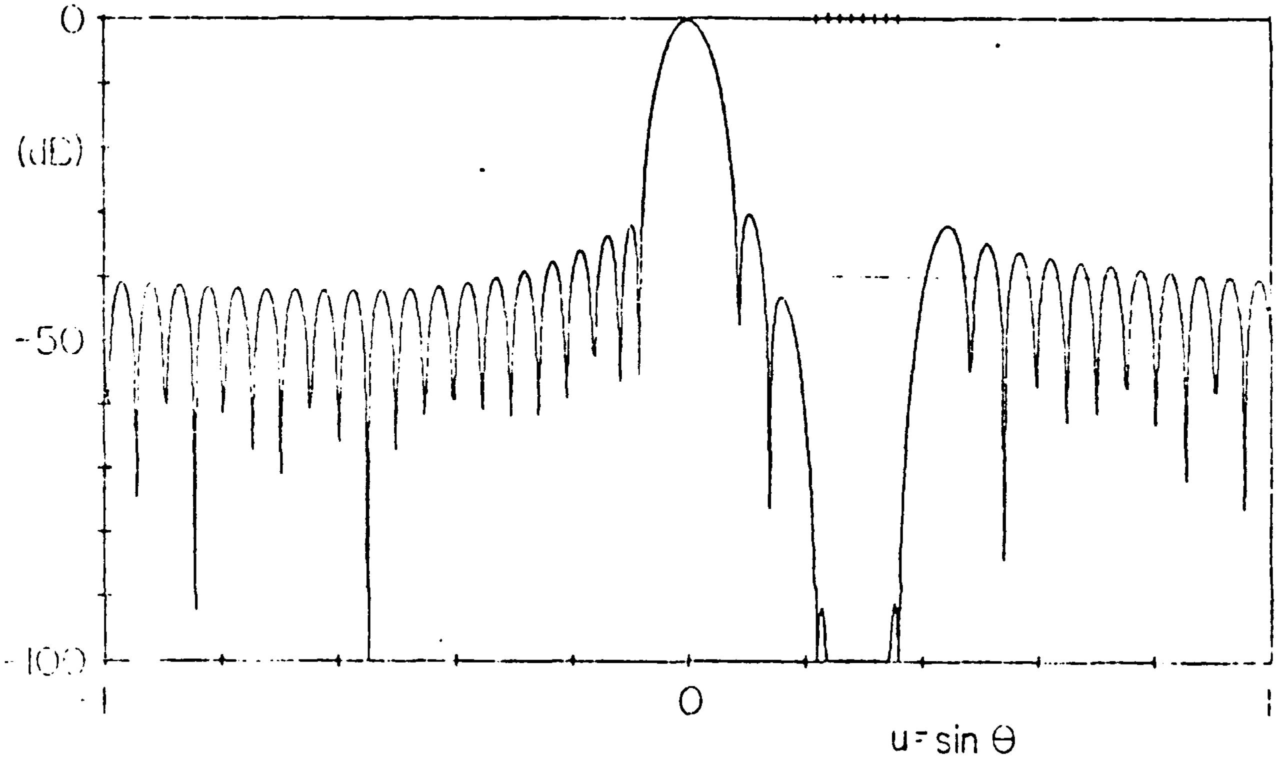

Figure 5. Initial 40 dB Chebyshev pattern with eight nulls equispaced over the sector (0.22, 0.36). Sidelobe cancellation = 51 dB, pattern change ε = 0.004, gain cost = 0.15 dB. 41 array elements.

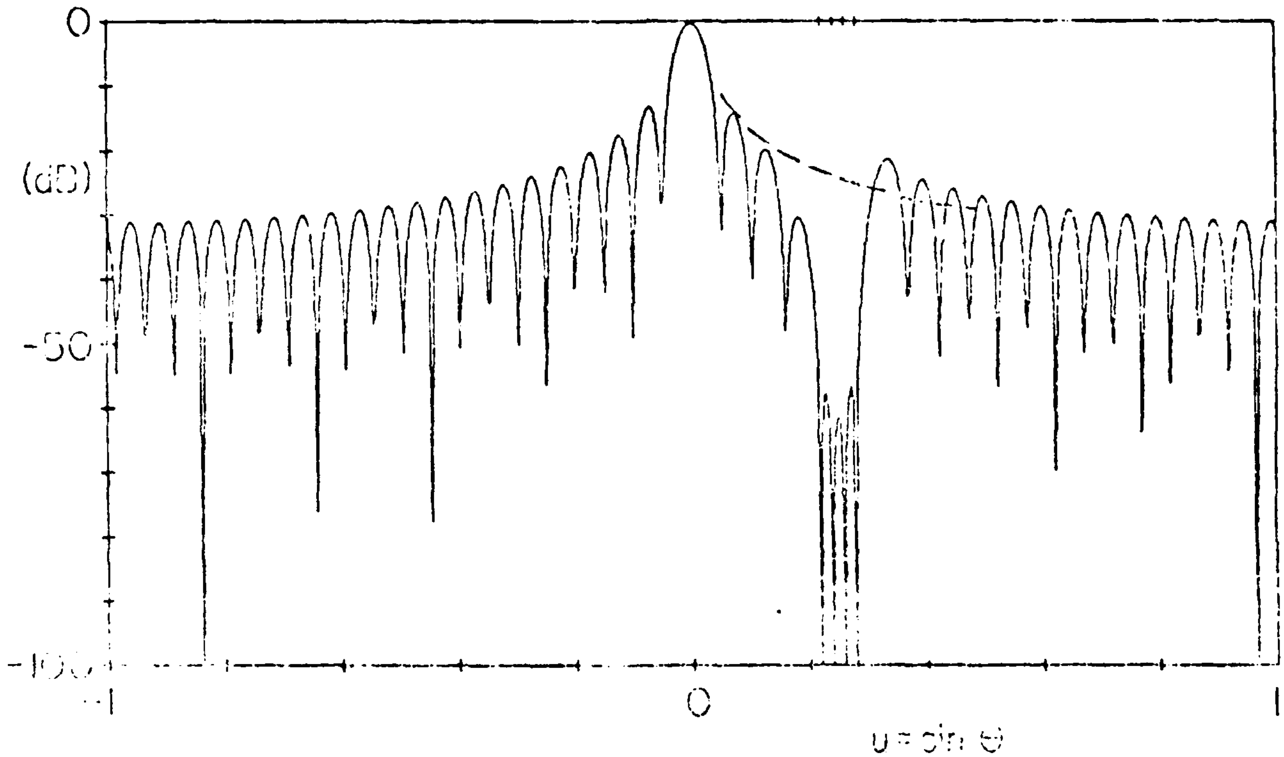

Figure 6. Initial sinc-pattern with four nulls equispaced over the sector (0.22, 0.28). Sidelobe cancellation = 34 dB, pattern change ε =0.03, gain cost = 0.13 dB. 41 array elements.

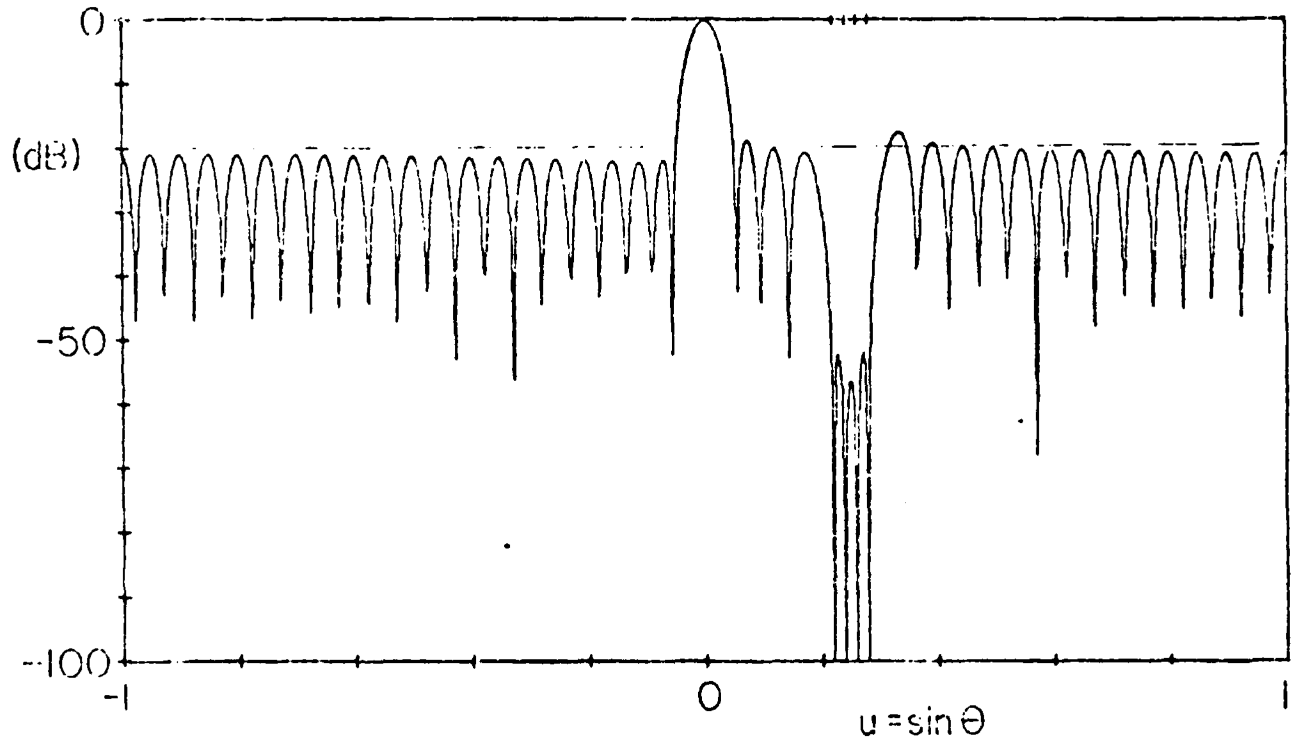

Figure 7. Initial 20 dB Chebyshev pattern with four nulls equispaced over the sector (0.22, 0.28). Sidelobe cancellation = 32 dB, pattern change ε = 0.04, gain cost = 0.03 dB. 41 array elements.

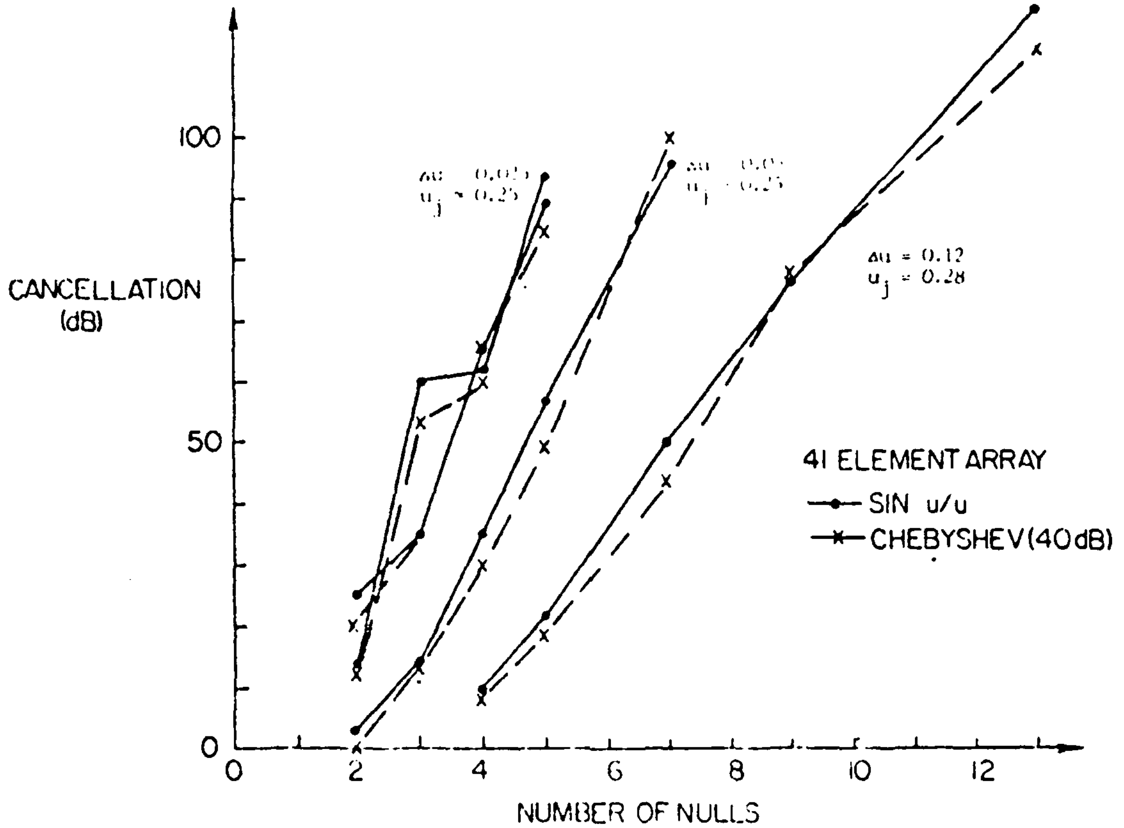

Figure 8. Sidelobe cancellation versus number of pattern nulls for a sinc- and for a 40 dB Chebyshev pattern.

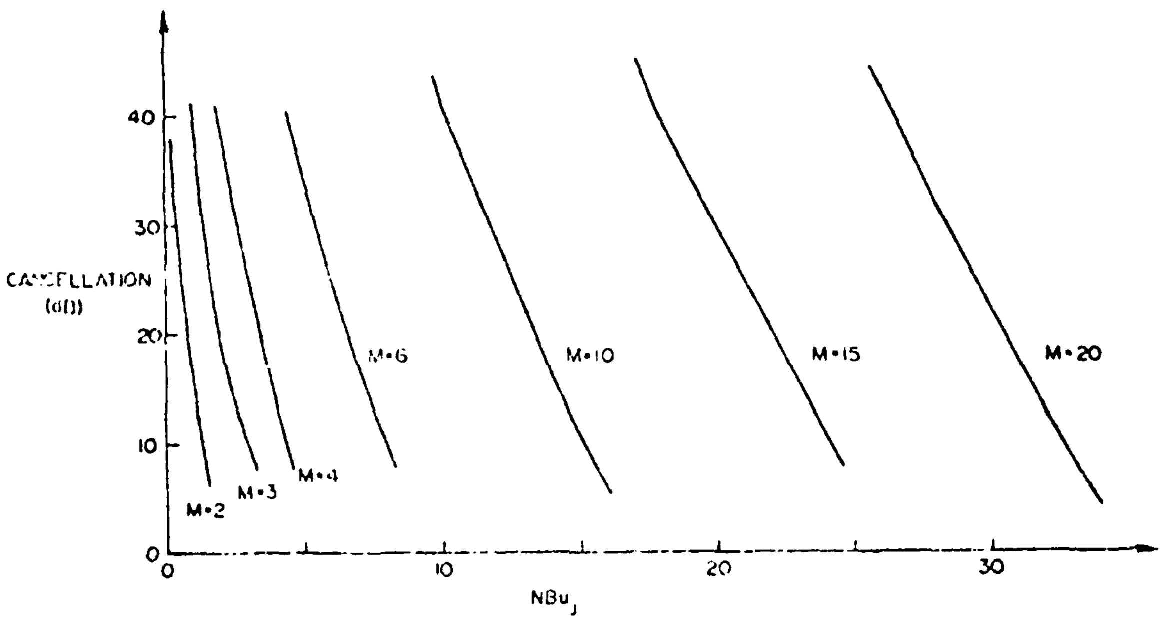

Figure 9. Sidelobe cancellation by equispaced nulls. M = number of nulls, N = number of array elements, B = interference bandwidth, u_j = interference direction.

INTERFERENCE SOURCES AND DEGREES OF FREEDOM IN ADAPTIVE NULLING ANTENNAS*+

Alan J. Fenn
MIT/Lincoln Laboratory
Lexington, Massachusetts 02173

Abstract

It is sometimes desirable to know how many interference sources an N-element array or N-beam multiple-beam antenna can adaptively null. This problem is usually addressed by considering the antenna to have at most N-1 degrees of freedom available for placing nulls on interference sources. However, if some of the N-1 sources are very close together, it is possible that less than N-1 degrees of freedom are used. This paper will quantitatively describe this effect for specific examples by examining the eigenvalue spread of the interference covariance matrix. It is shown in the simple case of two equal-power interference sources in the field of view of a multiple-beam antenna, the two dominant eigenvalues are approximately equal when the source separation exceeds a half-power beamwidth. In other words, two degrees of freedom are used when two interference sources are separated by greater than a half-power beamwidth. This effect is also investigated for an array, and the results are compared against a multiple-beam antenna.

I. INTRODUCTION

A measure of the susceptibility to interference for an adaptive antenna is the spread of the eigenvalues of the covariance matrix, formed by signals received at each antenna port, or the "channel" covariance matrix. The spatial location and strength of the interference source (or sources) affects the eigenvalues and the interference-to-noise ratio prior to adaption. The

*This work performed in this paper was sponsored by the Defense Communications Agency.

+"The U.S. Government assumes no responsibility for the information presented."

quiescent (before adaption) radiation pattern of the adaptive antenna affects the initial value of the interference-to-noise ratio. However, the eigenvalues depend only on the radiation pattern and location of each element of either an adaptive phased array or multiple-beam antenna (MBA). That is, they are independent of scan angle. This is because the channel covariance matrix is formed prior to weighting or beam forming.

It is convenient to think of the eigenvectors corresponding to those eigenvalues which are large compared to receiver noise levels, as representing beams pointed in the direction of a given interference source. Typically a null is created, for a single-lobe eigenvector beam, by setting the amplitude level of the quiescent radiation pattern and the eigenvector beam equal in the direction of the interference source and then combining them 180° out of phase.

Often the number of degrees of freedom used, by an adaptive antenna in any given scenario, is assumed equal to the number of interference sources nulled. This is usually in error. A count of the number of large eigenvalues present in the channel covariance matrix is a very accurate estimate of the degrees of freedom used. It is the intention of this paper to show how the eigenvalues change as the separation between two equal-power interference sources varies. This is investigated for a multiple-beam antenna and a thinned array. The case of more than two interference sources is also addressed.

II. FORMULATION

The adaptive nulling algorithm used in this paper is a modified Applebaum-Howells analog servo-control-loop processor[1,2]. For this algorithm the steady state adapted antenna weight column vector is given by

$$\underline{w} = [\underline{\underline{I}} + \mu \underline{\underline{R}}]^{-1} \underline{w}_o \tag{1}$$

where $\underline{\underline{I}}$ is the identity matrix

$\underline{\underline{R}}$ is the channel covariance matrix

μ is the effective loop gain

$\underline{w}_o$ is a beam steering vector which gives a desired quiescent radiation pattern in the absence of interference sources.

For an N-channel adaptive nulling processor $[\underline{\underline{I}}+\mu\underline{\underline{R}}]$ is an NxN matrix. The covariance matrix elements are defined to be

$$\underline{\underline{R}}_{p,q} = \frac{1}{FBW} \int_{1-\frac{FBW}{2}}^{1+\frac{FBW}{2}} E_p(\omega)\, E_q^{*}(\omega)\, \frac{d\omega}{\omega_o} \tag{2}$$

where FBW is the fractional nulling bandwidth

$E_p(\omega)$, $E_q(\omega)$ are the voltages measured in the pth and qth channels, respectively, over the nulling bandwidth

ω_o is the center frequency

* denotes complex-conjugate.

The covariance matrix is Hermitian (that is, $\underline{\underline{R}} = \underline{\underline{R}}^{\dagger}$ where † *means complex-conjugate-transposed*) which by the spectral theorem can be decomposed in eigenspace as[3]

$$\underline{\underline{R}} = \sum_{k=1}^{N} \lambda_k\, \underline{e}_k\, \underline{e}_k^{\dagger} \tag{3}$$

where λ_k, k=1,2,...,N are the eigenvalues of $\underline{\underline{R}}$

$\underline{e}_k$, k=1,2,...,N are the eigenvectors of $\underline{\underline{R}}$.

The matrix product $\underline{e}_k\, \underline{e}_k^{\dagger}$ is an NxN matrix which represents the projection onto eigenspace for λ_k. Comparing Eqn. (2) and Eqn. (3), it is observed that the eigenvalues have units of voltage squared, that is, the eigenvalues are proportional to power.

Substituting Eqn. (3) in Eqn. (1) and using the orthogonality property of the eigenvectors leads to the following expression for the adapted antenna weight vector,

$$\underline{w} = \underline{w}_o - \sum_{k=1}^{N} \frac{\mu\lambda_k}{1+\mu\lambda_k} \langle \underline{e}_k{}^\dagger, \underline{w}_o \rangle \, \underline{e}_k \qquad (4)$$

where $\langle , \rangle$ means inner product.

Eqn. (4) shows how the quiescent beam steering vector is modified in the presence of interference sources. The vector $\langle \underline{e}_k{}^\dagger, \underline{w}_o \rangle \underline{e}_k$ is the projection of the kth eigenvector on the quiescent antenna weight vector. If, for example, a single interference source (which gives rise to a single eigenvalue λ_1 and eigenvector $\underline{e}_1$) lies on a null of the quiescent pattern, then $\langle \underline{e}_1{}^\dagger, \underline{w}_o \rangle = 0$. This means that no adaption is necessary and $\underline{w} = \underline{w}_o$. However, if a source lies on a sidelobe of the quiescent pattern, the inner product of $\underline{e}_1{}^\dagger$ with $\underline{w}_o$ will be non-zero. This projection is then weighted by the quantity $\mu\lambda_1/(1+\mu\lambda_1)$ and subtracted from $\underline{w}_o$. For a large value of λ_1 corresponding to a strong interference source, the product $\mu\lambda_1$ is much greater than unity. This implies that $\mu\lambda_1/(1+\mu\lambda_1) \cong 1$. Similarly, a weak interference source which has $\mu\lambda_1$ much less than unity results in $\mu\lambda_1/(1+\mu\lambda) \cong 0$. If another source sufficiently separated from the first is added, a second large eigenvalue, λ_2, will occur. Two terms (k=1,2) would then be significant in Eqn. (4).

From the above examples it is clear that strong sources result in a larger change with respect to the quiescent weight vector than do weak sources. Eqn. (4) has been shown to be dependent on both interference source location as well as power level. Basically, the quiescent beam steering vector is modified by removing any projections of interference source eigenvectors on $\underline{w}_o$. This causes the antenna to form a null in the direction of the interference.

In the following section, the eigenvalues of $\underline{\underline{R}}$ are used to describe the degrees of freedom of adaptive antennas. Specific examples of multiple-beam and phased array antennas are given.

III. TWO INTERFERENCE SOURCES

Multiple-Beam Antenna Results

A nineteen-beam MBA was chosen for a demonstration of the eigenvalue spread ($\Delta\lambda$) as a function of separation between two interference sources. The beams are located in a hexagonal grid which is shown in Figure 1. The antenna diameter was chosen to be $D=150\lambda$. With uniform aperture illumination the half-power beamwidth of each beam of the MBA is 0.39°; the composite pattern of all nineteen beams results in the 2° diameter spot indicated in Figure 1.

Standard spherical coordinates are used to represent a far-field point at (θ,ϕ), where θ is the angle measured from boresight and ϕ is the azimuth angle. Two equal-power sources of interference are assumed to be located within the 2° coverage area. Source #1 was chosen to be fixed at the half-power point of beam #1 ($\theta=0.195^{\circ}$, $\phi=0^{\circ}$). Source #2 was allowed to vary in angle from boresight, beginning with $\theta=0.195^{\circ}$ in increments of 0.05° for $\phi=0^{\circ}$ fixed. The nulling bandwidth was assumed to be narrow in order to minimize the effects of bandwidth on the results. Thus, there are only two eigenvalues different from quiescent noise in this case. The two eigenvalues, λ_1 for source #1 and λ_2 for source #2, are shown in Figure 2 as a function of source separation angle $\Delta\theta$. When the two sources are at the same location ($\Delta\theta=0^{\circ}$), only one large eigenvalue appears (one degree of freedom is used) which is 3 dB higher than for a single source. As the second source is moved away, its associated eigenvalue (λ_2) rises from 0 dB and is nearly equal to λ_1 ($\Delta\lambda=1.7$ dB) when the separation angle is equal to the half-power beamwidth of the antenna. (The spread for separations greater than one half-power beamwidth decreases only slightly.) As is expected, λ_1 decreases slowly as the sources move apart since source #1 begins to behave as a single source. Additionally, source #2 was varied in position on a circle with a radius equal to a half-power beamwidth and centered at source #1. It was found that the eigenvalue spread ($\lambda_1-\lambda_2$) was between 1.6 dB to 2.0 dB for twelve positions spaced uniformly about the circle.

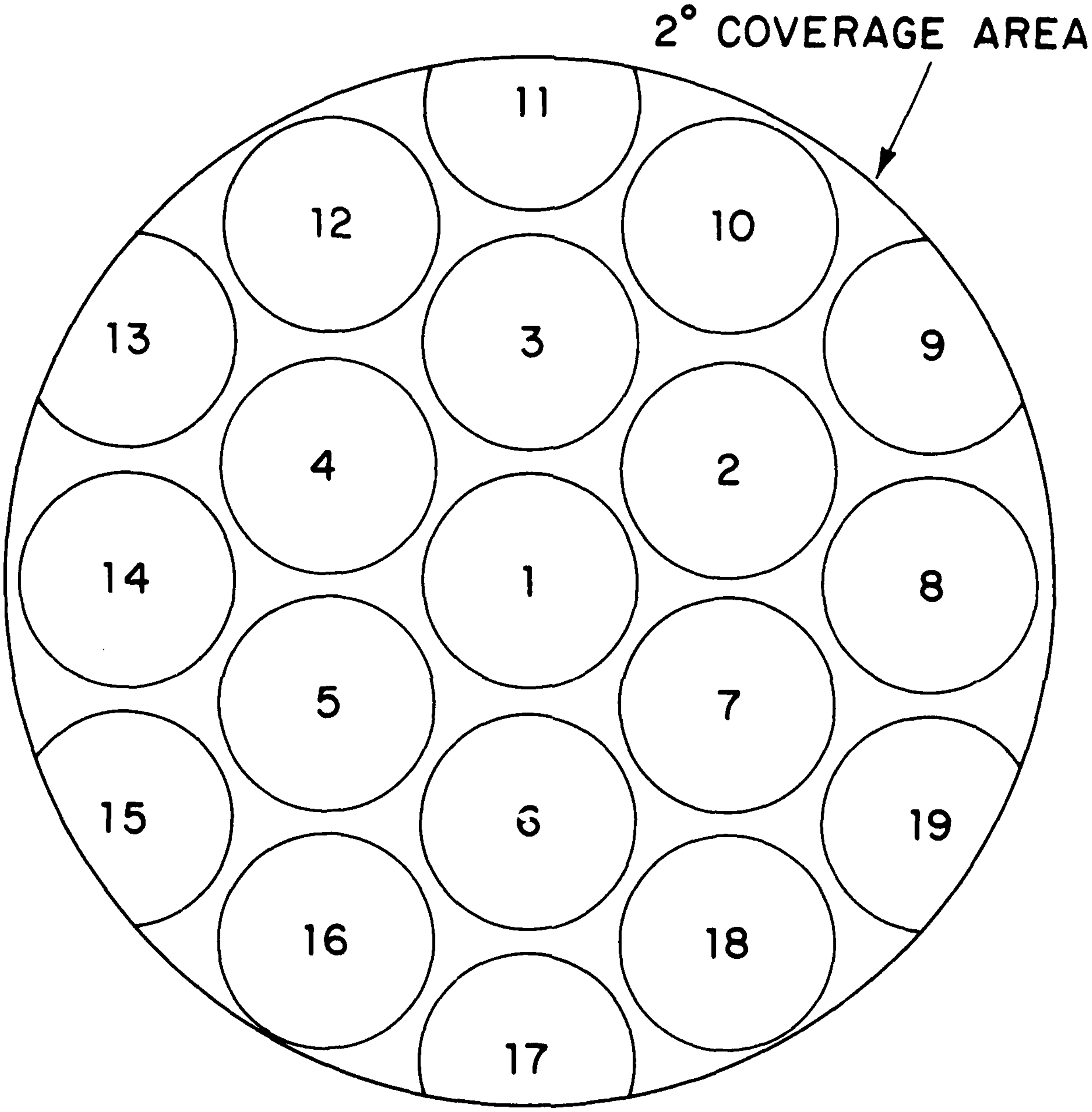

Figure 1. Hexagonal beam positions for a 19-beam multiple beam antenna.

From the above results this implies that a source separation of approximately one-half power beamwidth or larger is required to cause the MBA to use two degrees of freedom. In the following section it is shown that the same criterion applies to an adaptive array.

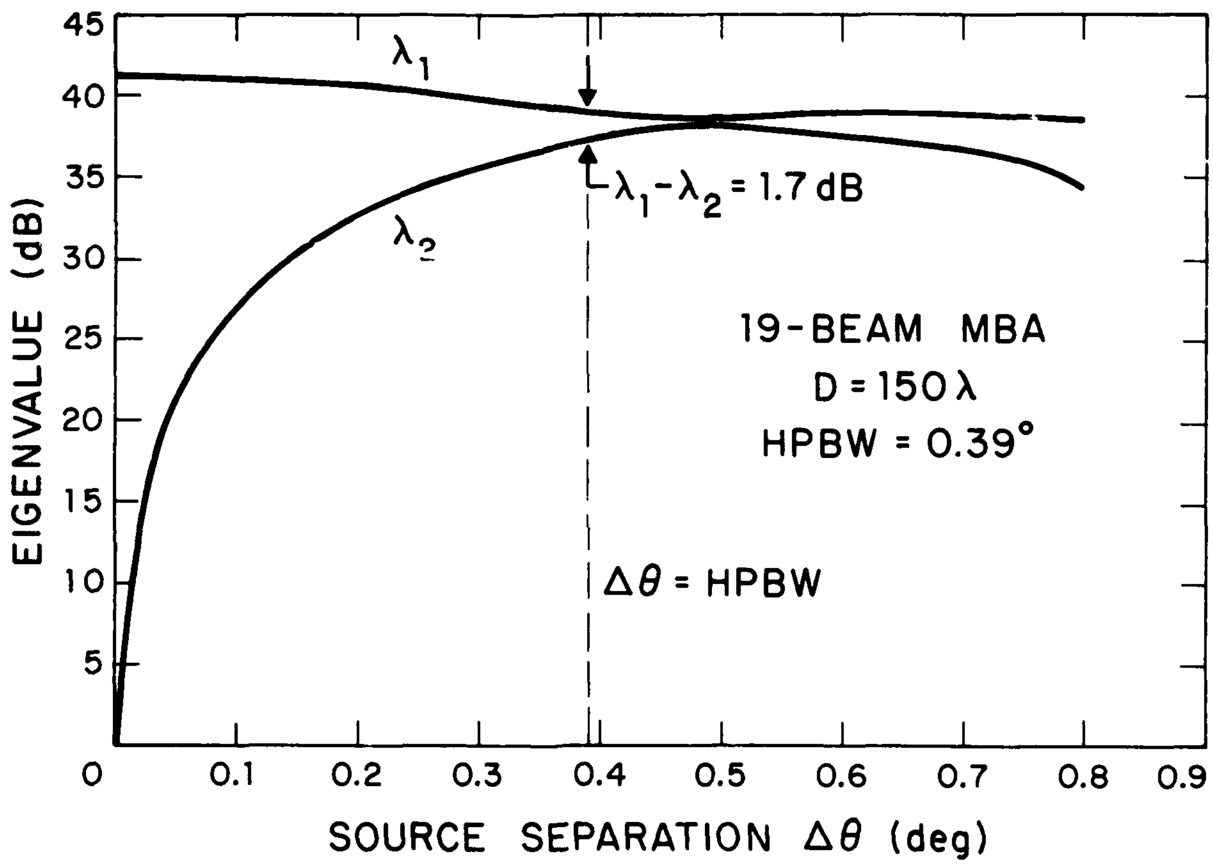

Figure 2. Eigenvalues for two equal-power interference sources as a function of angular separation in the field of view of a 19-beam MBA.

Phased Array Antenna Results

A ten-element uniform circular ring array was chosen for demonstrating the eigenvalue spread for two sources in the field of view of a thinned array. As for the MBA example, the array diameter was chosen to be $D=150\lambda$ and the coverage area is again chosen to be two degrees in diameter. The array elements have a diameter of $D_e=35\lambda$ which produces a half-power beamwidth (rotationally symmetric) that subtends this 2^o diameter coverage area. This array configuration, shown in Figure 3, has the highest resolution (narrowest beamwidth) for a given planar aperture size[4]. For uniform illumination, the ring array half-power beamwidth is related to the aperture diameter by $HPBW \cong 0.72\lambda/D$ radians. The half-power beamwidth for the present example is 0.274^o.

As was done in the MBA example, two sources are assumed to lie within a 2^o coverage area. Source #1 is fixed at the half-power point ($\theta=0.137^o$, $\phi=0^o$). Source #2 varies in position from $\theta=0.137^o$ in increments of 0.05^o for $\phi=0^o$ fixed. There are only two eigenvalues (λ_1, λ_2) different from quiescent noise (again, with narrowband nulling) in this case. These are plotted in Figure 4 as a function of source separation $\Delta\theta$. This behavior is very similar to that for the MBA shown in Figure 2. Eigenvalue λ_1 is reduced in power by approximately 3 dB as the sources separate beyond a half-power beamwidth. A minimum eigenvalue spread (approximately 0.7 dB) occurs at approximately one half-power beamwidth separation. Next, source #2 was moved uniformly for twelve positions on a circle with a half-power beamwidth radius centered at source #1. The eigenvalue value spread ($\lambda_1-\lambda_2$) was between 0.2 dB and 0.5 dB. Thus, like the MBA, two sources of interference separated by a half-power beamwidth or more use two degrees of freedom.

In the next section the eigenvalue spread for three interference sources is examined. A discussion of the case where there are as many interference sources as there are degrees of freedom then follows.

IV. THREE INTERFERENCE SOURCES

MBA and Array Results

With two interference sources the previous sections showed that each source consumes a degree of freedom when the separation between sources is

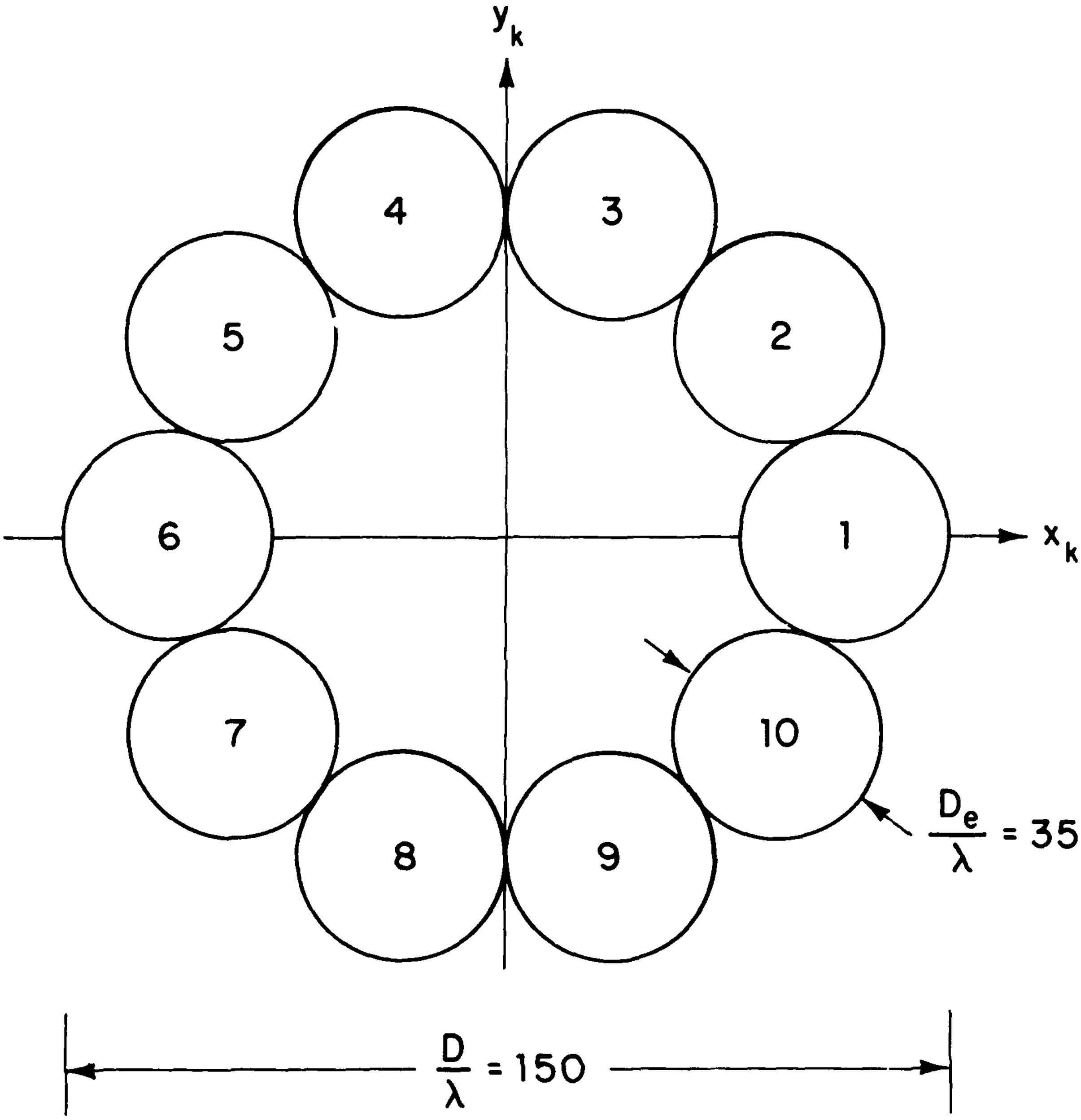

Figure 3. A ten-element circular array designed for a 2^o coverage area.

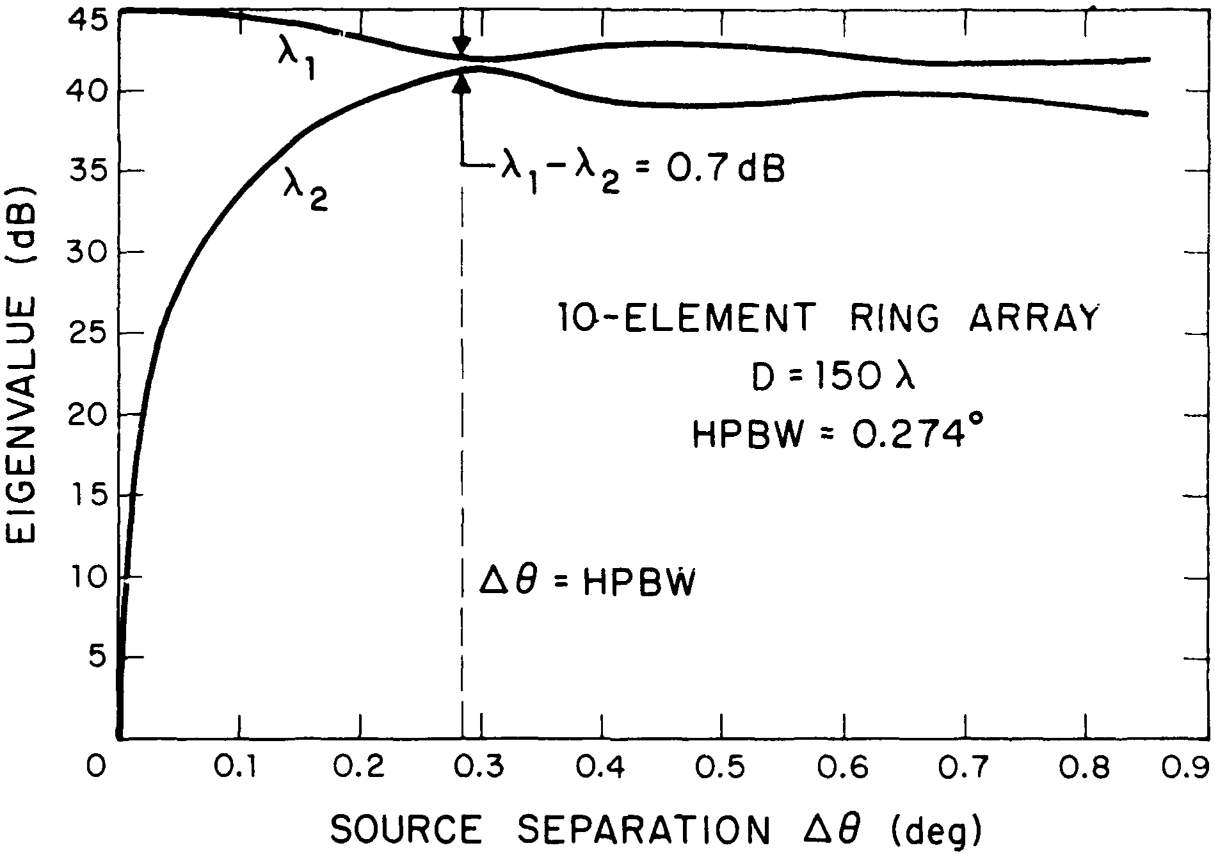

Figure 4. Eigenvalues for two equal-power interference sources as a function of angular separation in the field of view of a 10-element ring array.

greater than the antenna half-power beamwidth. This section examines two simple configurations of three equal-power sources, one is a straight line (constant azimuth angle), the other an equilateral triangle. In each configuration, the sources are separated by a half-power beamwidth.

First, consider the 19-beam MBA shown in Figure 1. For three sources on a straight line (θ=0.195°, 0.585°, 0.975°; ϕ=0°) the three eigenvalues are found to be λ_1=39.1 dB, λ_2=38.2 dB, and λ_3=32.1 dB. This is a spread of

7.0 dB which indicates that three degrees of freedom are not completely used. However, with three sources on an equilateral triangle (each side a half-power beamwidth) the eigenvalues are found to be λ_1=39.7 dB, λ_2=37.2 dB, λ_3=37.1 dB. The spread is 2.6 dB which suggests that three degrees of freedom have been nearly completely used.

The ten-element array (see Figure 3) shows a somewhat different behavior from the MBA. For three sources on a line (θ=0.137°, 0.411°, 0.685°; ϕ=0°) the three eigenvalues are computed to be λ_1=42.4 dB, λ_2=41.4 dB, and λ_3=39.1 dB. The spread is 3.3 dB which implies that three degrees of freedom are almost fully used (this was not true for the MBA). With an equilateral triangle configuration, the eigenvalues are λ_1=41.7 dB, λ_2=41.3 dB, and λ_3=41.1 dB, which is a spread of only 0.6 dB. Again, three degrees of freedom are being used.

From these examples it seems that the equilateral triangle source configuration causes an adaptive antenna to use its degrees of freedom more completely than for three sources on a straight line.

V. DISCUSSION AND CONCLUSIONS

The goal of this paper is to illustrate quantitatively the utilization of antenna degrees of freedom when interference sources are present. This is done by relating the eigenvalue spread to the spacing of the interference sources. It is shown that when two interference sources are spaced less than one-half power beamwidth apart, the covariance matrix possesses only one dominant eigenvalue, indicating that only one degree of freedom is required to null both sources. As the source spacing approaches a half-power beamwidth, a second eigenvalue approximately equal to the first occurs. Thus, for the case with two interference sources, a source spacing of one half-power beamwidth or more is required to cause the antenna to fully utilize two degrees of freedom to null the interference. With three interference sources, the equilateral triangle configuration (with half-power beamwidth spacing) caused the array and the MBA to use three degrees of freedom more completely than did a straight line configuration.

A scenario of interest is the placement of N interference sources in the field of view of an N-port adaptive antenna, such that N-1 degrees of freedom are consumed by N-1 of the sources and the Nth source jams the system by capturing the last remaining degree of freedom. From the previous discussion one might conclude that the eigenvalue spread among the N eigenvalues should be less than 3 dB to insure the use of all degrees of freedom. Based on the results given for two and three sources, a minimum necessary condition to achieve this is to separate the sources such that no two are less than a half-power beamwidth apart. Because the antenna beams represented by the eigenvectors, however, can have complicated patterns when many sources are present (e.g., bifurcated beams), this approach will not necessarily be successful. The exact configuration of the interfering sources affects both the eigenvalues and the interference-to-noise ratio. More research into this problem is clearly required.

REFERENCES

1. J. T. Mayhan, "Bandwidth Limitations on Achievable Cancellation for Adaptive Nulling Systems," Technical Note 1978-1, Lincoln Laboratory M.I.T. (17 February 1978).

2. W. F. Gabriel, "An Introduction to Adaptive Arrays," Naval Research Laboratory, Washington, D. C., NRL Report 7739 (July 1974).

3. G. Strang, Linear Algebra and Its Applications, (Academic Press, Inc., New York, NY, 1976).

4. J. T. Mayhan, "Thinned Array Configurations for Use with Satellite-Based Adaptive Antennas", IEEE Trans. on Antennas and Propagation, AP-28 No. 6, p. 846-856 (November 1980).

ACKNOWLEDGMENT

The author is grateful to Mr. William C. Cummings, Dr. Alan J. Simmons, and Dr. Leon J. Ricardi for their contributions to this study.

CROSS-POLARIZED RETRODIRECTIVE ARRAYS

Helmut E. Schrank
Westinghouse Electric Corporation
Baltimore, Maryland 21203

Abstract

This paper discusses an extension of the Van Atta reflector array principle, allowing an incident RF wave to be reradiated back in the direction of arrival but with the reradiated wave orthogonally polarized relative to the incident polarization. This performance can be achieved for an arbitrarily polarized incident wave (including elliptical) and is done without the use of conjugate phase shifter devices or other adaptive feedback circuits. Instead it is achieved by simple interconnections between radiating elements of the array.

The basic form of this generalized Van Atta reflector is passive, but it could also be extended to an active device by adding amplifiers between each pair of interconnected elements. Another variation is the ability to switch from the disclosed cross-polarized to "flat plate" reradiation, thereby allowing the device to also perform as a conventional Van Atta reflector.

Van Atta devised a method of interconnecting elements of an array of antennas so that incident plane RF waves are reradiated back in the same direction from which they came, i.e., retrodirectively. The principle is extended to planar arrays by interconnecting pairs of elements that are equidistant from the array center with transmission lines of equal electrical length.

The principal advantage of Van Atta reflectors lies in their ability to perform as effective retroreflectors over wider angular regions than either an equivalent size flat plate or a trihedral corner reflector.

One limitation of existing Van Atta reflectors is that their performance is restricted to the polarization and frequency bandwidth of the radiating elements used. For example, a Van Atta array of parallel dipoles can receive and reflect only the linear polarization component of an incident wave corresponding to its dipole orientation, over the limited operating bandwidth of the dipoles.

If circularly polarized elements (such as spiral or helical radiators) are used to form a Van Atta reflector, then only one circular sense of polarization can be received and reflected. Or if (as suggested by Sharp and Diab) a dual polarization Van Atta array is made by arranging half vertically polarized and half horizontally polarized elements "to reflect any polarization", then the array will reradiate incident polarizations the way a flat plate reflects, i.e., linear polarizations are reflected unchanged, circular polarizations are reflected orthogonally, and elliptical polarizations are reflected with ellipse orientation unchanged but with sense reversed. Furthermore, the effectiveness of such an array in terms of radar cross-section is reduced by a factor of four relative to an equal size array with all elements alike.

The extension of Van Atta's principle discussed in this paper not only overcomes most of the limitations of the state-of-the-art Van Atta reflectors, but allows a particular configuration which retroreflects any (and every) incoming polarization with its mathematically-orthogonal polarization.

A generalized Van Atta array is one using dual-mode radiating elements (capable of radiating two independent orthogonal polarizations) with both terminal pairs connected to corresponding elements by equal length transmission lines. The configuration described will receive an incoming plane wave of any polarization and re-radiate a plane wave of the precise orthogonal polarization back in the direction of arrival. This is true for linear polarizations of any oreintation, for circular polarizations of either sense, and for all elliptical polarizations.

An advantage of this technique over existing cross-polarized response systems is that it can be achieved with completely passive components, whereas various existing retroradiating schemes require active phase sensing and conjugating devices, adaptive feedback circuits, and/or phase shifting networks to accomplish orthogonal polarization responses. Another advantage is that both the retrodirectional feature and the cross-polarizing action of this approach are completely automatic and instantaneous, whereas the more complex existing schemes require a finite time interval for sensing, direction finding, adapting, and "settling" before a desired response is formed. Also, the technique is capable of responding simultaneously to multiple incident waves of different directions and polarizations, whereas existing schemes work only in one direction at a time.

AN INVESTIGATION OF A SIX-PORT MICROWAVE MEASUREMENT SYSTEM

by
Brad Hiben

R.F./Antenna Systems Research Laboratory
Motorola, Inc., Schaumburg, Illinois

ABSTRACT A relatively simple and inexpensive method of measuring complex circuit parameters at microwave frequencies is explored. Use is made of the increasingly popular automated instrumentation systems.

INTRODUCTION

In the microwave range of frequencies, accurate measurement of phase has always been more difficult than measurements of the magnitude of a given signal. The introduction of vector-voltmeters and network analyzers in the last 15 years has made it much easier to make phase measurements. However, these instruments are complex and frequency limited.

It has been recognized that a six-port network can be used to measure the complex circuit parameters of active and passive circuits. Using two of the ports as inputs for "reference" and "unknown" signals, power measurements at the remaining four ports, or side-arms, as they will be called, provide sufficient information for the calculaton of the relative amplitude and phase of the "unknown" signal referred to the "reference" signal. In this role, the six-port functions as a network analyzer or vector-voltmeter.

Also, the six-port can be used to determine the absolute power absorbed by a load terminating a transmission line if the "reference" and "unknown" signals are proportional to the signals incident on and reflected from the load, respectively. Figure 1 shows a six-port network which can be used to measure complex circuit parameters.

An outstanding feature of the six-port measurement concept is that phase is not measured directly. Phase is determined from the four scaler power measurements. No frequency conversion or sampling techniques are necessary since power can be measured directly at the test frequency. This allows

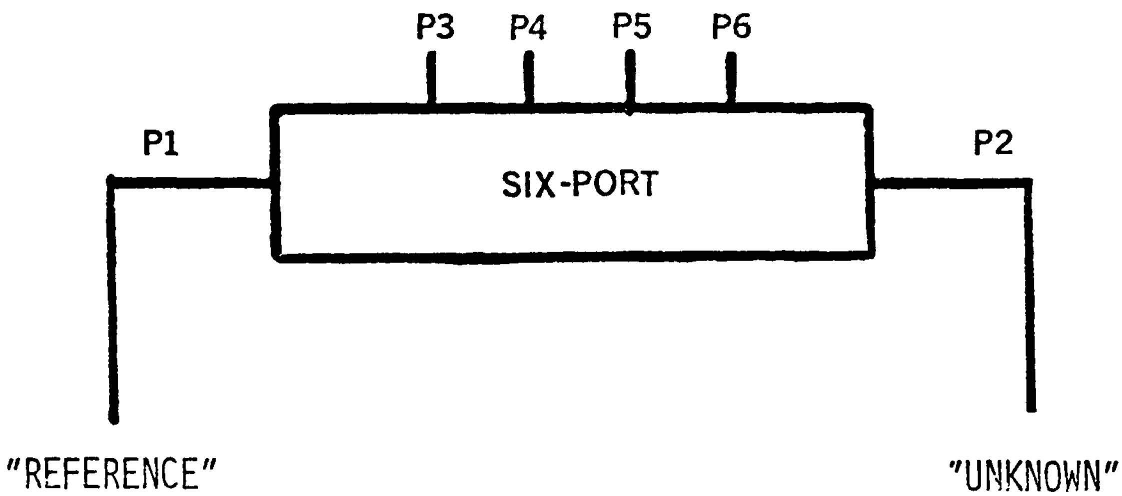

Fig. 1 A six-port network being used as a microwave measurement system.

the frequency of operation of the six-port measurement system to be arbitrarily high.

The plausibility of the six-port technique can be demonstrated as follows. Figure 2 shows a transmission line where A and B are the complex voltage wave functions for the signals incident on and reflected from the termination, Z_1, respectively, and measured at reference plane R. Knowledge of the A and B waves permits the computation of the reflection coefficient and the power absorbed by the termination. Since A and B are complex, they can be written as

$$A = A_x + jA_y = |A| \underline{/\arg A} \tag{1a}$$

$$B = B_x = jB_y = |B| \underline{/\arg B}. \tag{1b}$$

There are four variables to be determined in equation (1) which indicates that a system of four linearly independent equations is sufficient to determine A and B. These equations can be provided by the four side-arm ports of the six-port network. This also indicates that any six-port network can be used as long as the side-arm ports provide linearly independent combinations of the waves A and B.

HISTORY

The six-port technique can be traced to A.L. Samuel [1], who, in 1947, constructed an impedance meter using four probes placed one-eighth wave-length apart on a slotted transmission line, as shown in Figure 3. With A, B, R and Z_1 defined as before, the powers at ports 3-6 are given by

$$P_3 = \frac{1}{Z_0} |A + B|^2 \tag{2}$$

$$P_4 = \frac{1}{Z_0} |A - jB|^2 \tag{3}$$

$$P_5 = \frac{1}{Z_0} |A - B|^2 \tag{4}$$

$$P_6 = \frac{1}{Z_0} |A - jB|^2 \tag{5}$$

where Z_0 is the characteristic impedance of the line. Using the law of Cosines and manipulating a bit renders

$$|AB| \underline{/\theta =} \frac{Z_0}{4} (P_3 - P_5) + j(P_4 - P_6). \tag{6}$$

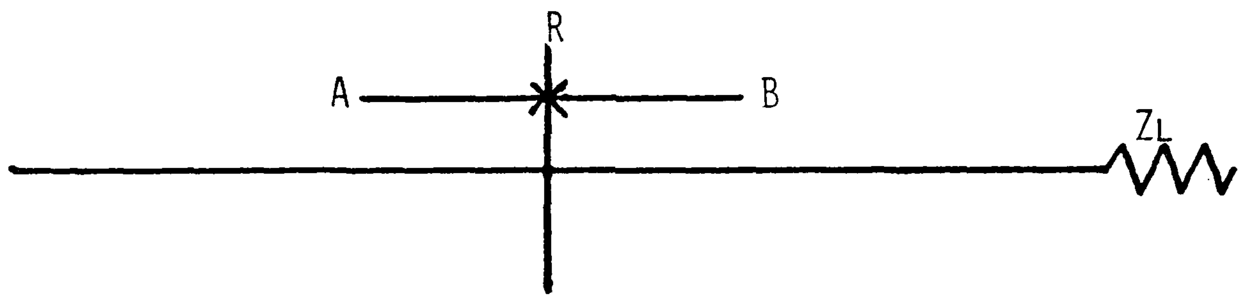

Fig. 2 A transmission line showing forward and reflected voltage wave functions.

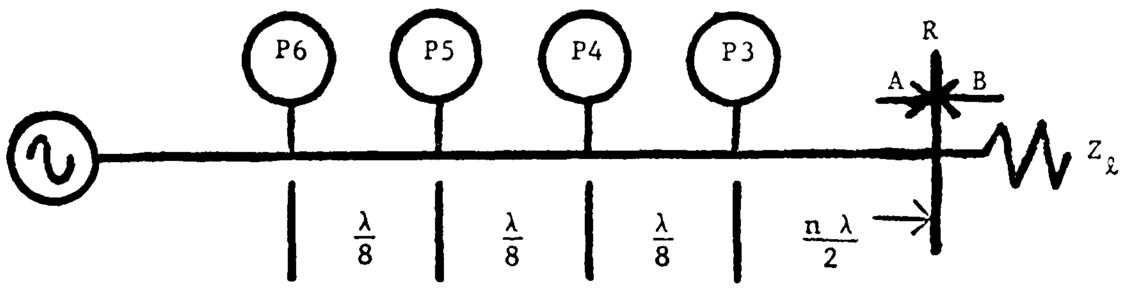

Fig. 3 Samuel's reflectometer

Note that equation (6) is only proportional to reflection coefficient. Upon inspecting equations (2) - (5) more closely, it is realized that they are not a linearly independent set. Any three are linearly independent with the fourth being determinable from the other three. In order to be a legitimate six-port, one more independent linear combination is needed. This can be provided through the use of a leveling loop.

Samuel used an oscilloscope to display the reflection coefficient of the termination. By hooking the detector outputs to the differential inputs of a scope, as shown in Figure 4, the deflection of the beam from center is proportional to the real part of the reflection coefficient. This is because $P_3 - P_5$ is proportional to the real part of the reflection coefficient and $P_4 - P_8$ is proportional to the imaginary part.

In the early 1970's, Cletus Hoer and Glenn Engen of the National Bureau of Standards began an extensive investigation of the six-port measurement tecnique for use in standards applications [2-4]. They realized a six-port system using hybrids so that a wide frequency range could be covered. Also, the magnitude of A, as previously defined, was measured directly using a directional coupler. Doing this

$$\Gamma = \frac{(P_3 - P_5) + j(P_4 - P_8)}{4P_7} \tag{7}$$

$$P_{absorbed} = P_7 \left[1 - \frac{(P_3 - P_5)^2 + (P_4 - P_8)^2}{16P_7^2} \right] \tag{8}$$

are attained where P_7 is the incident power given by $1/Z_0 |A|^2$. The power absorbed by the termination is given by the incident power times the power transmission coefficient of the termination.

Much of Hoer and Engen's work involved the development of methods to calibrate arbitrary six-port networks so that accurate results could be obtained regardless of imperfections in hardware. They have developed calibration schemes that derive a set of network constants which fully describe the imperfect network, taking into account its imperfections. Moreover, in some cases these network constants can be found using no absolute standards. In concept, this property should make possible very accurate measurements using equipment that is not of high quality.

The NBS has, because ultimate accuracy is of prime concern in their work, made their six-port systems out of very high quality components and at great cost. The purpose of this investigation was to build a simple six-port measurement system out of readily available commercial components and make

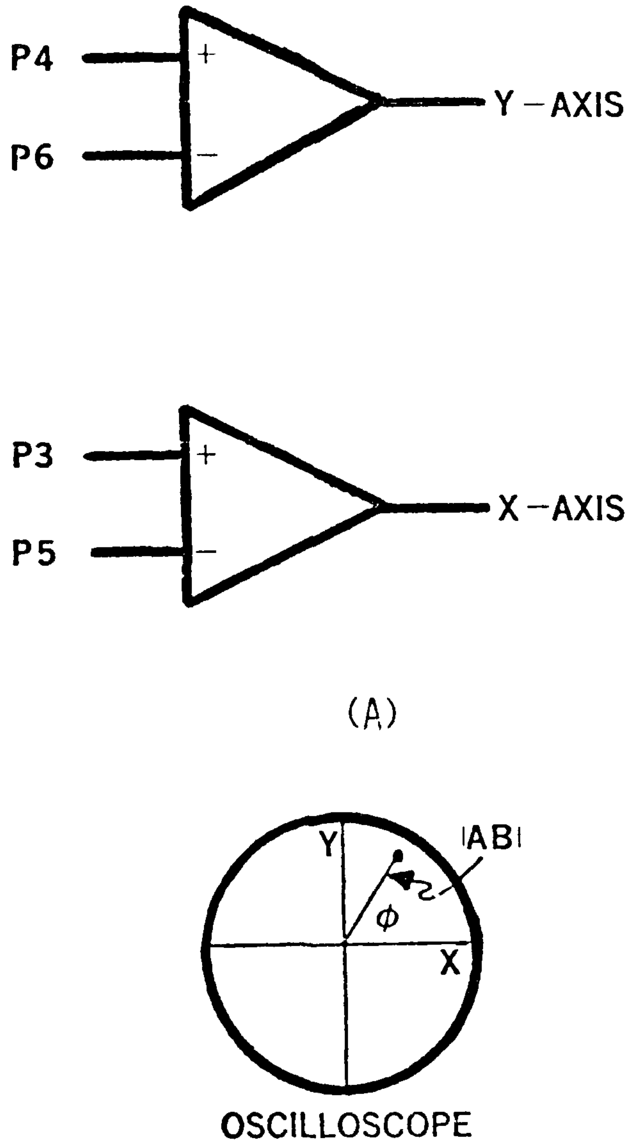

Fig. 4 Using a cathode ray oscilloscope to display reflection coefficient.

performance measurements concerning its operation.

THEORY

This investigation dealt only with reflection measurements, i.e., power absorbed by the termination and reflection coefficient. The principles are the same for transmission measurements.

The six-port power meter was realized using a scheme developed by Hoer and Engen. In general, the power absorbed by a termination is given by

$$P_{absorbed} = P_3Q_3 + P_4Q_4 + P_5Q_5 + P_6Q_6 \tag{9}$$

where the Q's are the network constants mentioned earlier, and the P's are the side-arm powers measured for the given termination. The network constants are merely a set of constants such that when multiplied by the appropriate side-arm power values and summed, render the value of the real power absorbed by the termination. These constants are unique to each six-port and, therefore, must be determined for the particular six-port being used.

The constants are found by placing a termination that absorbs a known amount of power at the test port, such as a standard power meter. Then the powers at the side-arm ports are measured and used to form an equation like equation (9). Then a sliding short is placed at the test port and the powers at the side-arms are measured for three settings of the offset short and three more equations like (9) are formed. This forms a system of equations that can be written:

$$\begin{bmatrix} P^1 \\ 0 \\ 0 \\ 0 \end{bmatrix} = \begin{bmatrix} P_{3,3} & \cdot & \cdot & P_{3,6} \\ \cdot & \cdot & \cdot & \cdot \\ \cdot & \cdot & \cdot & \cdot \\ \cdot & \cdot & \cdot & P_{6,6} \end{bmatrix} \begin{bmatrix} Q_3 \\ Q_4 \\ Q_5 \\ Q_6 \end{bmatrix} \tag{10}$$

where P^1 is the power known to be absorbed by the first termination. Note that the power absorbed by the short is zero and that the offsets of the shorts do not need to be known. The network constants can be solved for by inverting the P matrix.

Note that each side-arm power is associated with a single network constant. This implies that the side-arm power values need not be in absolute power, but merely linearly proportional to power since the network constants are essentially scaling factors. In concept, these network constants ideally describe the six-port. The accuracy will be a function only of how accurately power at the side-arms can be measured. When using crystal detectors the accuracy becomes a function of the linearity of the detector.

The reflectometer was realized using Samuel's scheme as modified by Hoer and Engen. Note that five side-arm power values are used, and, hence, this is actually a seven-port reflectometer. Only four side-arm power measurements are necessary, and, therefore, one of the side-arm power values can be eliminated allowing equation (7) to be rewritten as

$$\Gamma_m = \frac{(P_3 - P_5) + j(2P_4 - P_3 - P_5)}{4P_7} \quad (11)$$

However, the seven-port reflectometer was investigated here since the redundant port increases accuracy.

For best results, an error correction scheme was used. The scheme used here models the non-ideal functions of the measurement system, such as the finite directivity of a directional coupler, as an additional two-port inserted between an ideal reflectometer and the device under test, or DUT [5]. Figure 5 is a signal flow-graph of the error model used here. Γ_1 is the actual reflection coefficient of the DUT. Γ_m is the reflection coefficient that is indicated by the ideal reflector as it looks at the DUT through the error network. Equivalently stated Γ_m is the reflection coefficient of the DUT as indicated by the real reflectometer. Mason's rule can be used to express the signal flow graph as a mathematical relationship for the actual reflection coefficient of the DUT in terms of the measured reflection coefficient and the error parameters. This yields

$$\Gamma_1 = \frac{\Gamma_m - E_{11}}{E_{21}E_{12} + E_{22}(\Gamma_m + E_{11})}. \quad (12)$$

Since E_{21} and E_{12} are a product in equation (12), there are actually three error parameters to be solved for. To determine these, three known loads are sufficient. After solving for the error parameters, the actual reflection coefficient of a DUT can be written in terms of Γ_1, the reflection coefficient as indicated by the real reflectometer, and Γ_0, Γ_s and Γ_a, the reflection coefficients of the matched load, short arbitrary terminations as indicated by the real reflectometer.

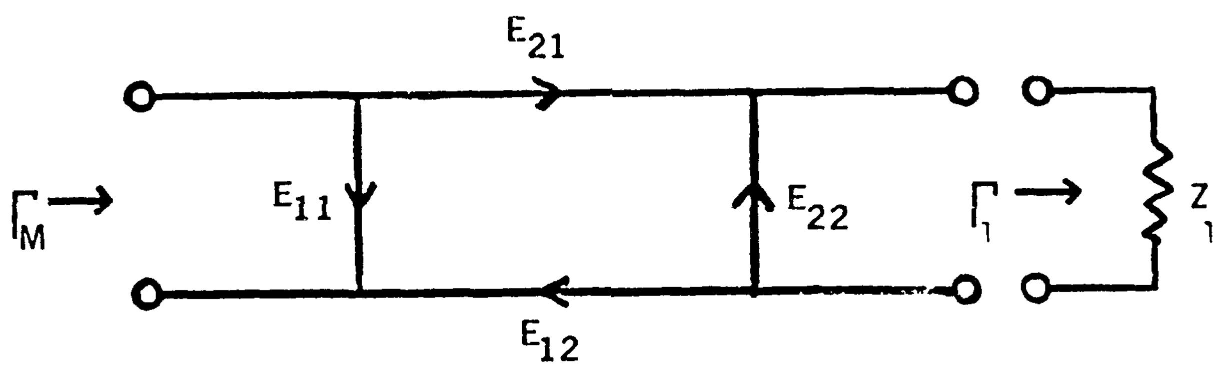

Fig. 5 Signal flow graph of the error correction scheme used with the seven-port reflectometer.

This gives

$$\Gamma_1 = \frac{\Gamma_m \Gamma_s - \Gamma_o \Gamma_s'}{(\Gamma_s \Gamma_a + \Gamma_o (\Gamma_o - \Gamma_s - \Gamma_a))(A + 1) - (\Gamma_m \Gamma_s - \Gamma_o \Gamma_m - \Gamma_o \Gamma_s + r^2 (1 + A))} \quad (13)$$

Equation (13) is only shown to make a point. For each of the reflection coefficients used, five power measurements have to be made. Γ_o, Γ_s, and Γ_a are measured only during calibration, but they should be measured at many (the more, the better) frequencies. Then equation (13) must be solved. It is obvious that the six-port measurement technique is not practical unless an automatic measurement system is used. This is what was done here.

EXPERIMENTAL SETUP

Figure 6 shows the network used to realize the six-port power meter and seven-port reflectometer. It consists of five 180° hybrids, a quadriture hybrid and a Hewlett-Packard reflection test unit. All units are coaxial. The reflection test unit consists of a 20 dB dual directional coupler, a line stretcher and a APC-7 connector at the test port. A and B are the incident and reflected voltage wave functions measured at some reference plane as indicated before. The absolute phase shifts and attenuations of the signal are not shown since the calibration procedure takes care of these. The junction shown has six side-arm ports, even though only four or five are required. The side-arm combinations chosen to realize the measurement systems are somewhat arbitrary since it is only required that four ports render linearly independent combinations of the incident and reflected signals. For this hybrid matrix, one port from each box is required with the fourth port being any of the remaining ports. This guarantees that the side-arms will be independent.

With the hybrids that were available, this network covered the range of 450 MHz to 950 MHz. Each side-arm port was terminated with a crystal detector. When operating in its square-law region, the detector's output voltage was proportional to power.

The automatic data acquisition and processing system that was used was based on the HP-9835A desk-top computer. It was the system controller, and based on inputs from and outputs to peripheral units, controlled the frequency of operation and measurement of detector voltages, processed the collected data and output the results to a CRT, printer and plotter. Programs were written to control all phases of the operation of the six-port power meter and seven-port reflectometer. Data was input to the controller through an HP-3955A digital

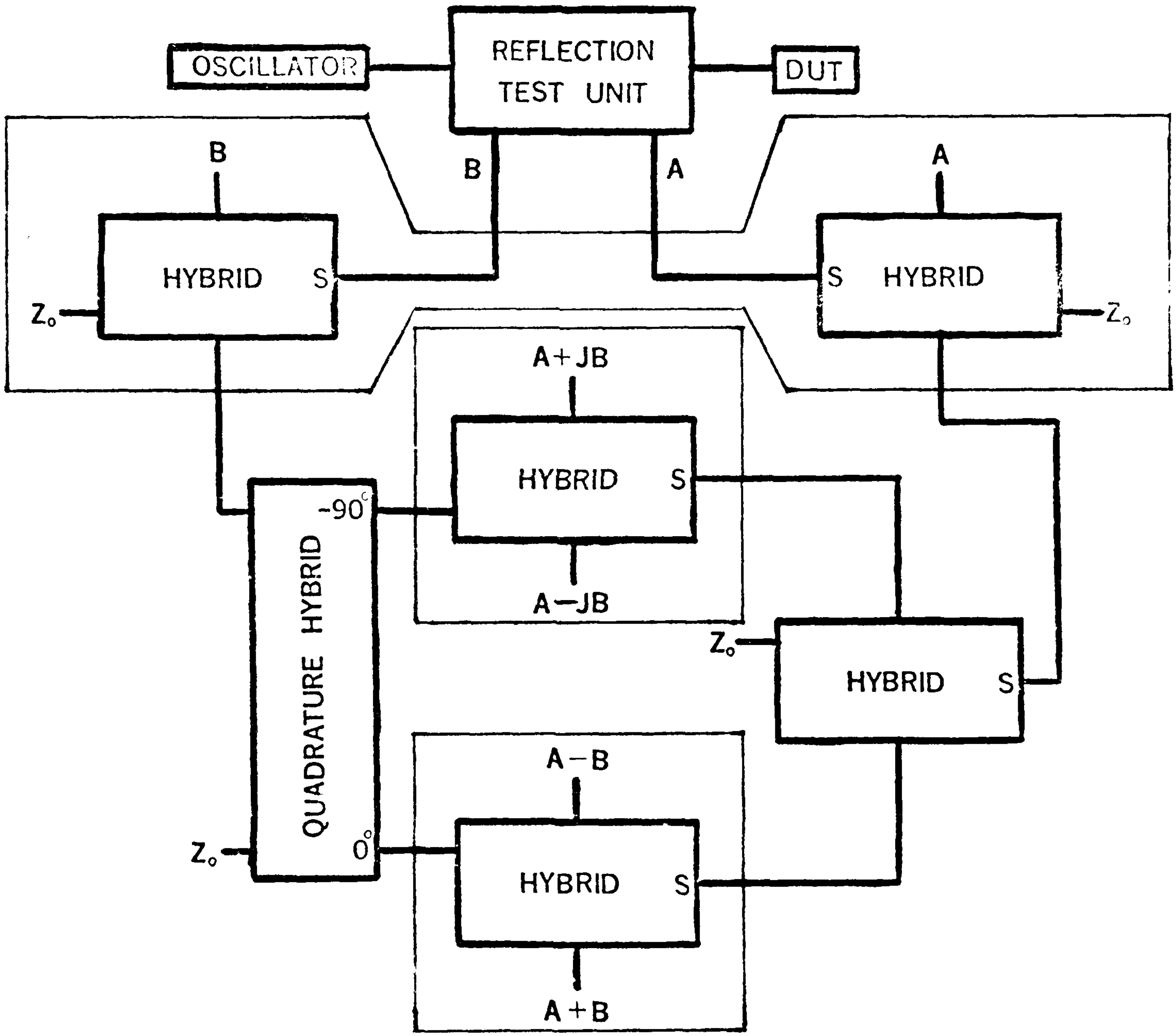

Fig. 6 Hybrid matrix used to realize the six-port power meter and seven-port reflectometer.

voltmeter and an HP-5328A universal counter. The voltmeter was used to measure the detector voltages to 1 micro Volt resolution and the counter was used as a frequency meter. Both units can be interfaced to the controller using the HP-IB bus which is Hewlett-Packard's realization of the IEEE 488-1975 standard. The function each unit is to perform, as well as measured data, can be communicated over the bus. Each detector was switched onto the voltmeter using a computer controlled switch.

A programmable oscillator was not available, but a programmable power supply was. The power supply was used to provide the control voltage for a voltage controlled oscillator. To precisely control the frequency provided by the oscillator, a discrete closed loop feedback system was used as shown in Figure 7. The controller instructed the power supply to output a voltage. The frequency meter would then feedback the oscillator's actual frequency to the controller which adjusted the power supply voltage according to a binary search routine. The resolution of this system was limited to $\pm$400 KHz by the resolution of the power supply, which is 50 mV.

The standard power needed to calibrate the six-port power meter was obtained from a Boonton microwatt meter which outputs a voltage that is proportional to power. The voltage was input to the controller through the voltmeter. The controller scaled the voltage to attain the actual power incident on the power meter. Figure 8 shows the complete automatic set-up.

Unlike the six-port powermeter calibration scheme, the calibration scheme used with the reflectometer required true power to be input. Therefore, it was necessary to convert the detector voltages into true power. Two methods were used to accomplish this and their results were compared. The first approximated the detector response as linear and a single straight line function was used to convert detector voltage to power. This was called the linear detector calibration scheme. The second broke the detector's response into several small straight line approximations. For a given detector voltage, a particular straight-line function was chosen to convert detector voltage to power. This can be called a look-up table method. The two methods are portrayed graphically in Figure 9.

EXPERIMENTATION AND RESULTS

Stepped-frequency measurements were made in the range of 450 MHz - 950 MHz in 10 MHz intervals for the six-port power meter and in 5 MHz intervals for the seven-port reflectometer. Prior to making measurements, the networks were calibrated. Approximately six minutes were required to calibrate the powermeter and nine minutes were required to calibrate the re-

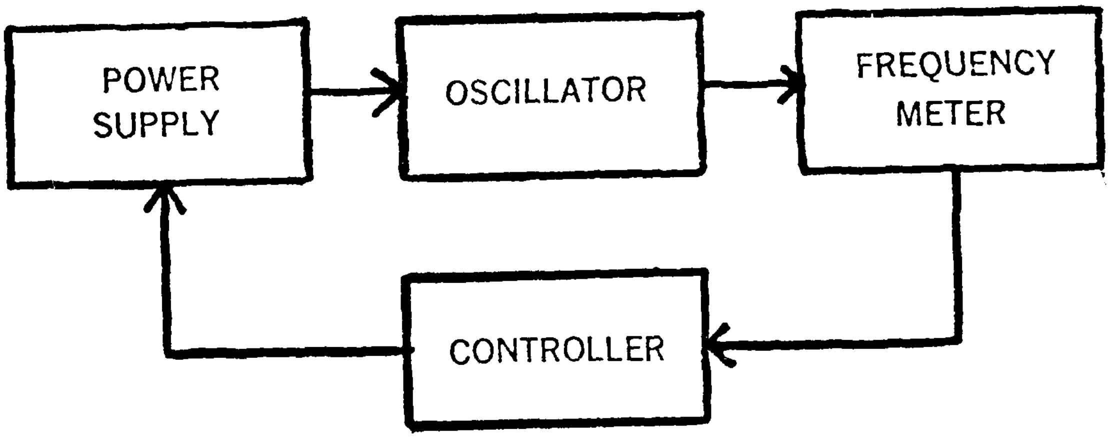

Fig. 7 The discrete closed loop frequency control system.

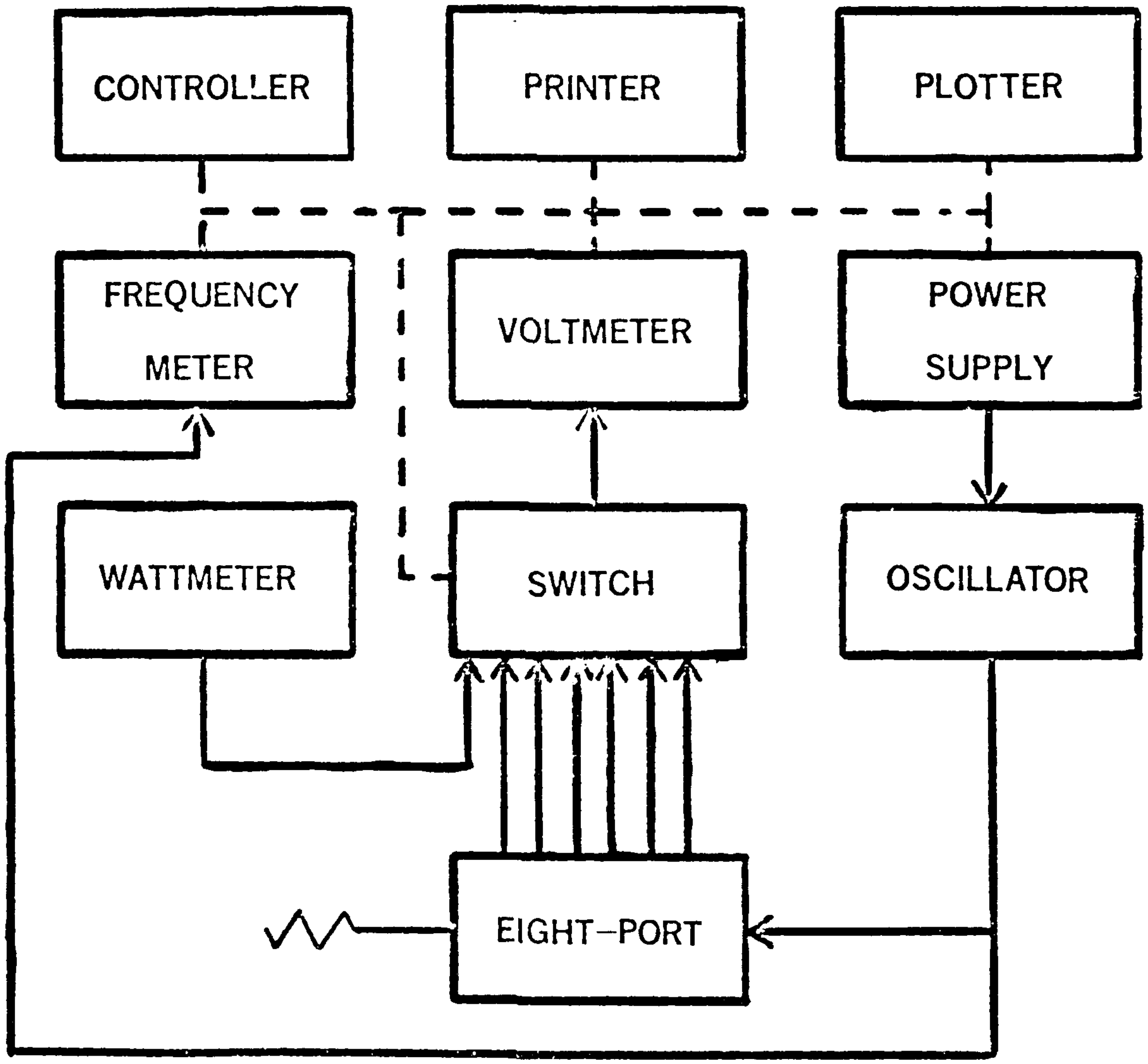

Fig. 8 The automatic data acquisition and processing system used in this investigation. Dashed lines indicate bus lines.

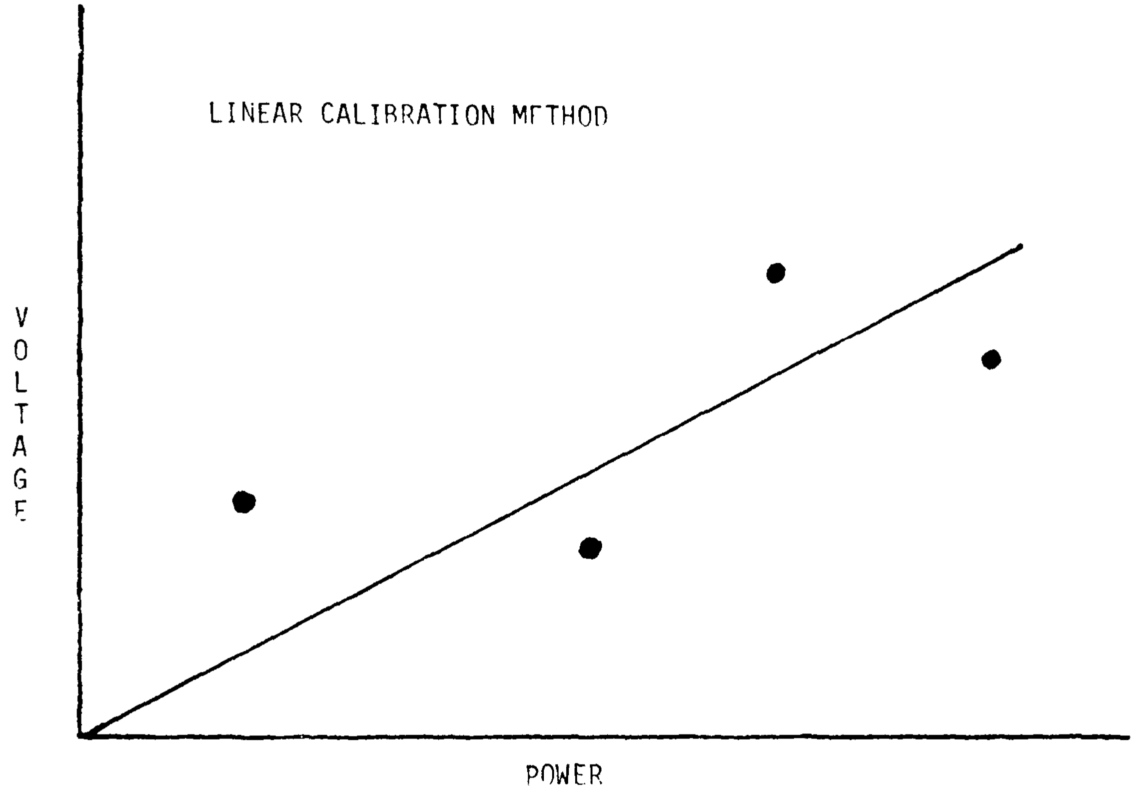

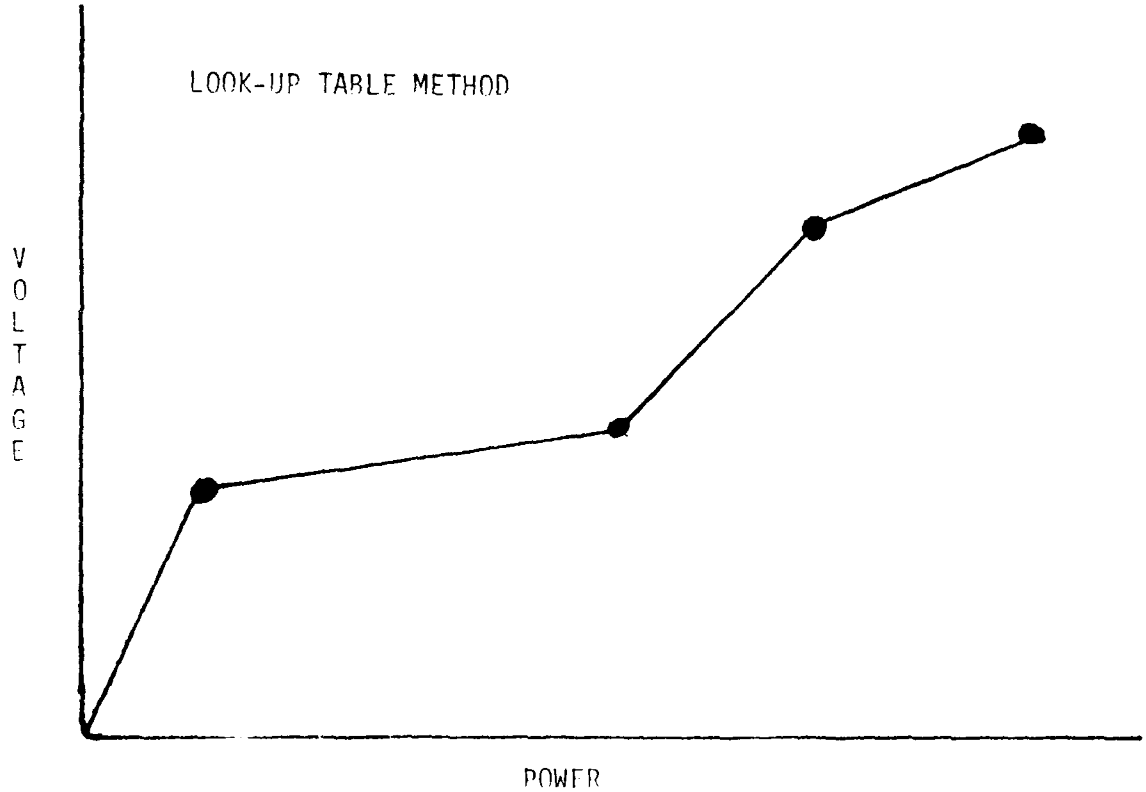

Fig. 9 Comparison of linear calibration method and look-up table method.

flectometer when under computer control.

The accuracy of the six-port meter was tested by placing known terminations at its test-port and then making stepped-frequency measurements using the six-port. Laboratory grade APC-7 and GR-900 terminations were used. The power incident on the termination was known from the calibration procedure described previously. Since the incident power and the impedance of the termination were known, the actual power absorbed by the termination could be computed. For the 50Ω, 100Ω, and 200 Ω terminations used for accuracy testing, the values of absorbed power indicated by the six-port power meter were accurate to within approximately 0.3 dB. Figure 10 is a graph showing the point by point errors between the value of power known to be absorbed by the termination and the power that was indicated absorbed by the six-port.

To roughly determine the dynamic range of the six-port power meter, a matched termination was attached to the test port and the incident, or input, power was varied. For each level of incident power, data was taken at all 51 frequencies from 400 MHz to 950 MHz and the dB errors from the actual values were computed. The absolute values of the errors were averaged and plotted in Figure 11 along with the greatest absolute error for each level of incident power. Figure 10 shows that a worst case error of 0.5 dB was attained for approximately a 15 dB range of input power. The range over which the average error was less than 0.5 dB was greater than 20 dB. Figure 10 indicated that these dynamic range figures may have been higher had greater input power been available.

The seven-port reflectometer was also tested using known loads. Figure 12 is a sample of the output generated by the reflectometer computer program for a 200Ω termination offset by an 8.33 cm air line. The markers are shown, as well as the start and stop frequencies. The solid circle indicates the expected value. It is hard to draw a conclusion concerning the detector calibration schemes since in some cases one worked better than the other and vice-versa. The worst case errors in reflection coefficient for the linear detector calibration method were 0.09 for magnitude and 2.3° while the worst case errors for the look-up table detector calibration method was 0.03 for magnitude and 3.0°. In both cases, the typical errors were less than 0.01 in magnitude and less than 1.0°.

CONCLUSIONS

It was determined that a known detector response was important and that the above figures could be improved. This investigation did indicate that a six-port measurement system which is adequate for many purposes can be constructed out of

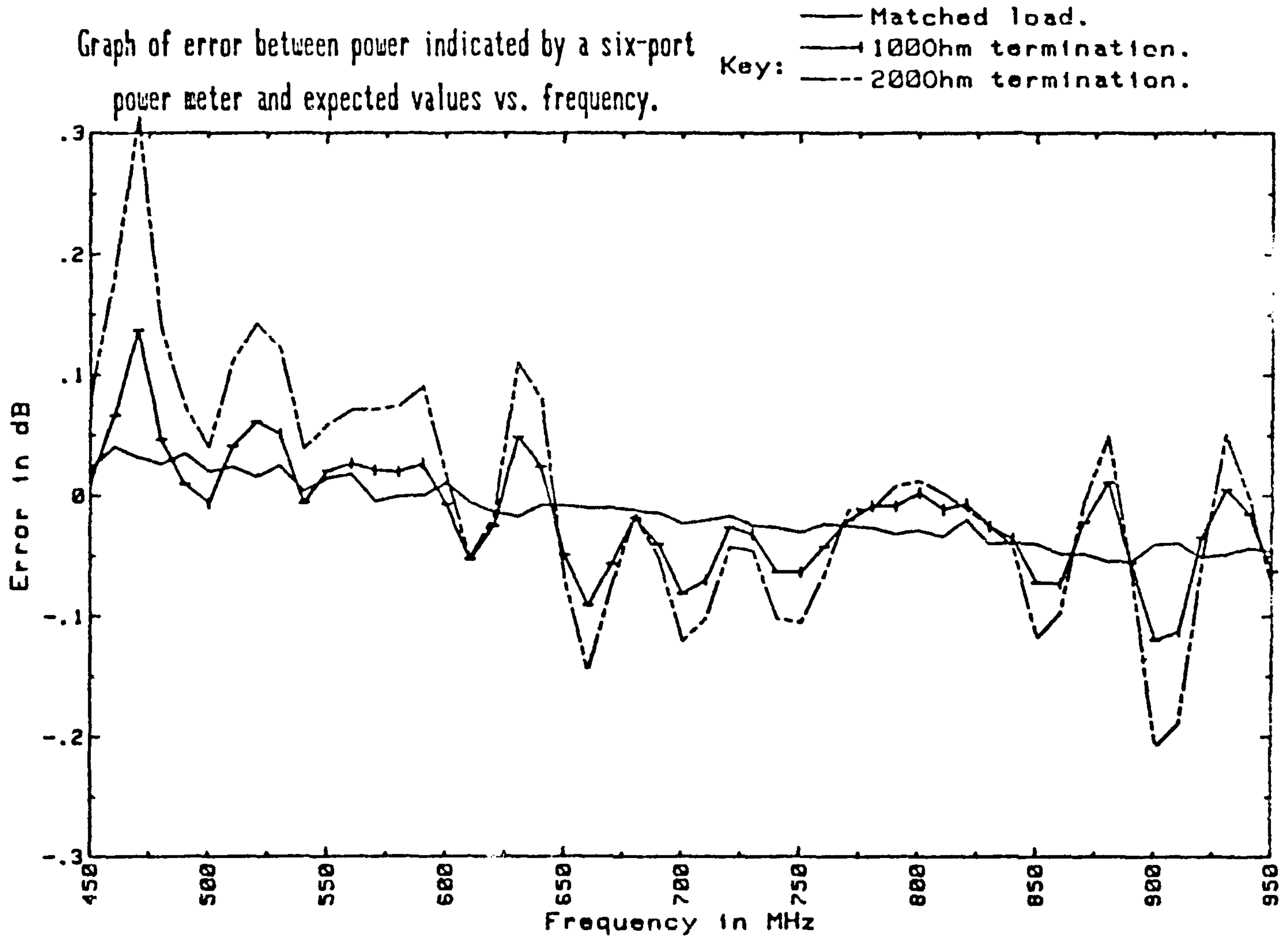

Fig. 10 Graph of the error between power indicated absorbed by a termination and the power actually absorbed.

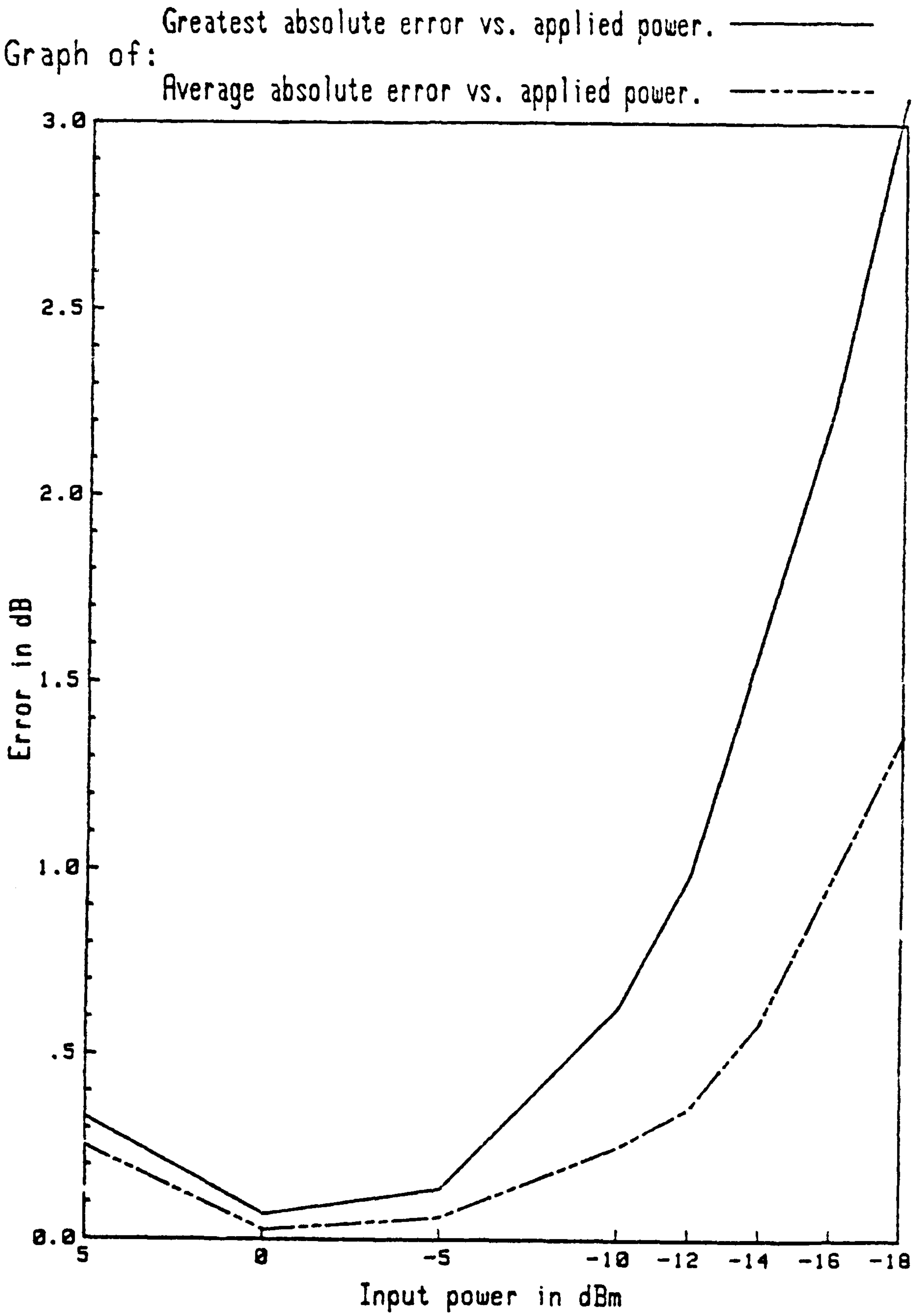

Fig. 11 Graph of the error between the power absorbed by a matched load as indicated by the six-port power meter and the power actually absorbed by the termination as input power is varied.

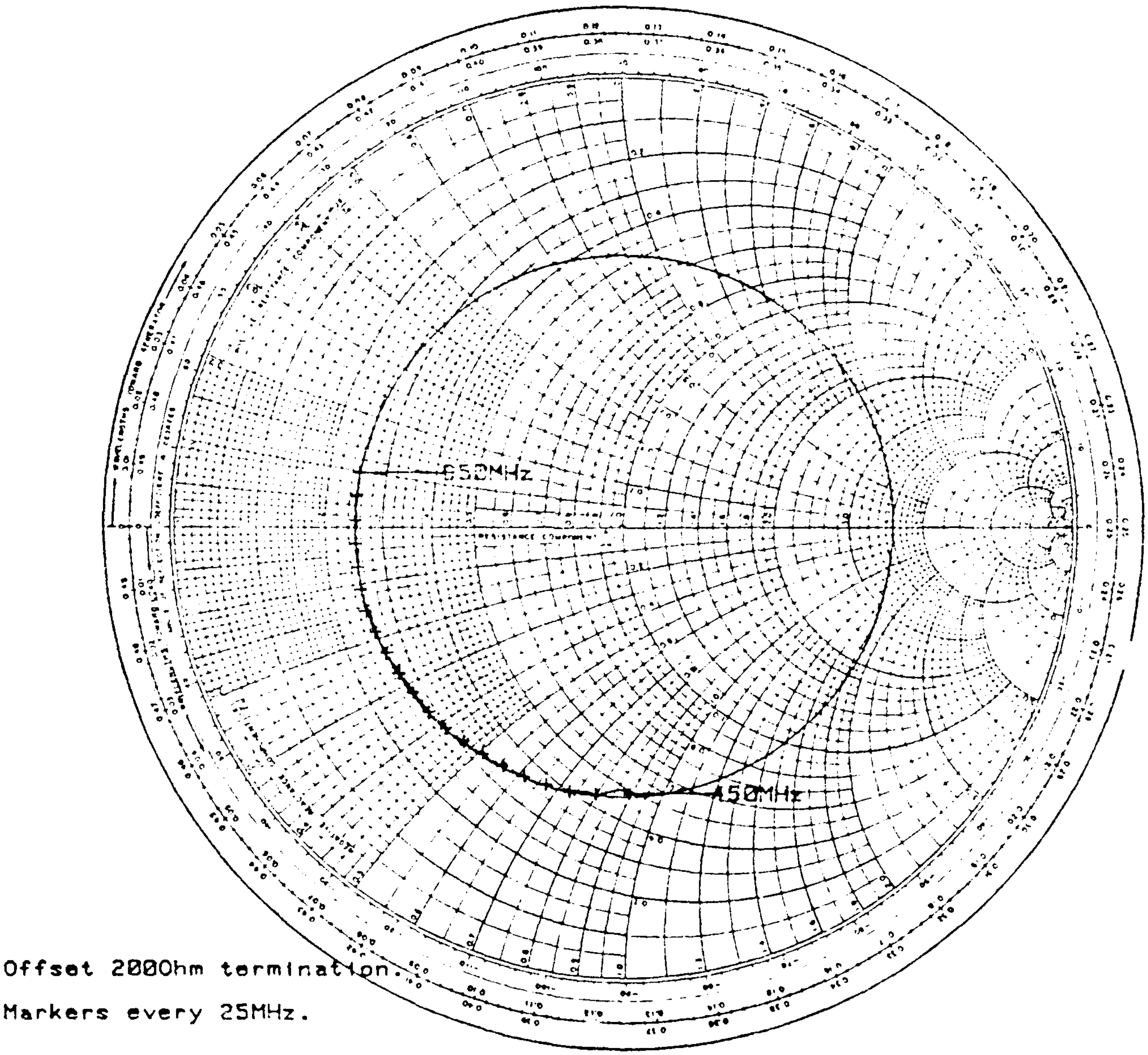

Fig.12 Sample output from the seven-port reflectometer program.

readily available commercially produced components.

ACKNOWLEDGMENT

This work was done under the direction of Professor J.D. Dyson of the University of Illinois Electrical Engineering Department. His guidance was greatly appreciated.

REFERENCES

[1] A.L. Samuel, "An Oscilloscope method of presenting impedances on the reflection coefficient plane," Proc. IRE, vol. 35, pp. 1279-1283, Nov. 1947.

[2] C.A. Hoer and K.C. Roe, "Using an arbitrary six-port junction to measure voltage ratios," IEEE Trans. Microwave Theory Tech., vol. MTT-23, pp. 978-984, Dec. 1975.

[3] G.F. Engen, "The Six-port reflectometer, an alternative network analyzer," IEEE Trans. Microwave Theory Tech., vol. MTT-25, pp. 1075-1080, Dec. 1977.

[4] G.F. Engen, "Determination of phase and amplitude from power measurements," IEEE Trans. Instrm. Meas., vol. IM-25, pp. 414-418, Dec. 1976.

[5] T. Ichino, H. Ohlawara, N. Sugihara, "Vector impedance analysis to 1000 MHz," Hewlett-Packard Journal, vol. 31, pp. 22-32, Jan. 1980.

Lockheed

MISSILES
& SPACE
COMPANY,
INC.

A GEODESIC LENS ANTENNA FOR 360° AZIMUTHAL COVERAGE

J. L. McFARLAND & R. P. SAVAGE
LOCKHEED MISSILES & SPACE CO.
SUNNYVALE, CALIFORNIA

INTRODUCTION

This paper describes a parallel-plate figure-of-revolution geodesic surface that can be used in cojunction with phase shifters and either a fixed or commutating power distribution network to form a high-gain low-sidelobe 360° electronic scanning radiation pattern. Other pattern shapes are electronically selectable; e.g., an omni pattern, and a selectable-width 360° electronic scanning sector pattern, etc. For this application a typical feed would be a multimode radial line fed by either a turnstile junction or 2N port unitary matrix with the appropriate power division/mode selection network. The geodesic surface may also be used to create simultaneous multiple beams over 360° azimuth. In this application, the feed network would be a combination of a 2N port unitary matrix (e.g., Butler Matrix) and fixed phasors in which the matrix outputs are connected directly to the inside circumference of the geodesic structure.

The essence of the geodesic structure is derived from the fact that the electromagnetic field is constrained to follow, in a controlled fashion, geodesic paths between the parallel plates, redistributing itself in a highly advantageous manner prior to radiation into free space. Radiation takes place directly from the parallel plates at the output, shaped in the form of a horn of some sort. An hourglass type reflector may also be used to narrow the elevation beamwidth, if desired. In this case, the geodesic pathes are altered from the case where no reflector is used, but this represents no problem.

The RF energy from all the elements at the input feed are simultaneously phased and spatially distributed to form the radiation pattern, in contradistinction to the conventional circular array. Thus, the statistical population is from 2 to 3 times greater than in a conventional circular array so that lower sidelobes are easier to obtain.

Other conventional approaches include the use of geodesic structures with additional lenses such as the parrallel-plate Luneburg used in conjunction with circulators at every element, or additional phase shifters at every element. Although it may not be obvious, these additional devices at the output (phase shifters, lenses, circulators, radiating elements, etc.) are not needed, using this geodesic approach; consequently much simplification of hardware is realized. In the process, appreciable cost, weight, volume etc. is saved and performance is enhanced at the same time. Other advantages are more subtle; for example, the generation of multiple simultaneous beams does not suffer from the high sidelobe problem associated with the conventional circular array/Butler matrix approach. A cylindrical harmonic modal expansion of the fields will reveal a much improved behavior for this approach compared to the conventional circular array. The net result would undoubtedly be lower sidelobes for this approach.

Since this approach is physically very simple, it is inherently low loss, a common attribute to all parallel plate geodesic structures.

This paper is presented in 3 parts: the first part derives the geodesic structure; the second part addresses applications very briefly, and the third part gives an example of what might be a typical application.

1.0 Derivation of the Geodesic Structure

Figure 1 depicts a generalized figure-of-revolution geodesic structure. Although not shown, the surface is actually the mean surface between parallel plates.

Equations (1) through (9) derive the geodesics for the general case. A special case of interest is the cone, since it is the easiest to manufacture. (9) through (11) are the geodesics for the geodesic cone. From these equations, the geodesic paths are plotted in Figure 2 for a typical set of parameters as shown. Equations (13) through (18) relate the output power, $P(y_o)$, to the power at the input feed circle, $P(\phi_i)$.

For the geodesic cone, Figure 3 is a plot showing M_2 the ratio of the projected radiating aperture size to the output cone diameter, D_o. Obviously, it behooves one to choose parameters that yields a large value for M_2.

To get some idea of the instantaneous bandwidth capability of a geodesic cone design using phase shifters, Figure 4 shows the maximum angle of incidence vs. r_3/r_1. For a given design at center frequency, there is no phase error; however, using phase shifters, an essentially quadratic phase error is introduced at the aperture as frequency changes. Thus, the total instantaneous bandwidth is limited to that shown (in hertz). The example given illustrates that a -50 dB sidelobe level at center frequency would become -47 dB at the frequency extremes for an instantaneous bandwidth of 365 MHz using the parameters given.

2.0 Applications

Figure 5 depicts four different aperture designs and Figure 6 depicts 3 feed approaches. These configurations can be used in any combination, depending upon the application. The simplest configuration would use aperture (A) with feed (E), but low sidelobes are not obtainable. Feed configuration (F) was therefore chosen to be used with aperture configuration (A) for the example to follow, a design that will be reduced to hardware.

3.0 Design Example

Figure 7 shows a cross-sectional view of an antenna being developed at LMSC. It operates in the 3 modes specified. Figure 8 is a plot of the amplitude distribution and Figure 9 its far-field radiation pattern in the pencil beam mode. Figure 10 is a 90° scanning sector pattern. The sector pattern width is selectable between 10° and 360° The omni pattern is not shown but is another mode of operation. Figure 11 is a schematic representation of the feed and mode-selection network. Figure 12 depicts a 360° cut of the geodesic cone using a different set of parameters for another application, illustrating the low sidelobe capability of this lens.

ACKNOWLEDGEMENTS

The authors are indebted to Peter Lam for his mathematical and computer programming help. Thanks is also extended to Rick Beich on this project, who worked with the authors in the earlier phases of this program.

GENERAL FIGURE-OF-REVOLUTION GEODESIC STRUCTURE

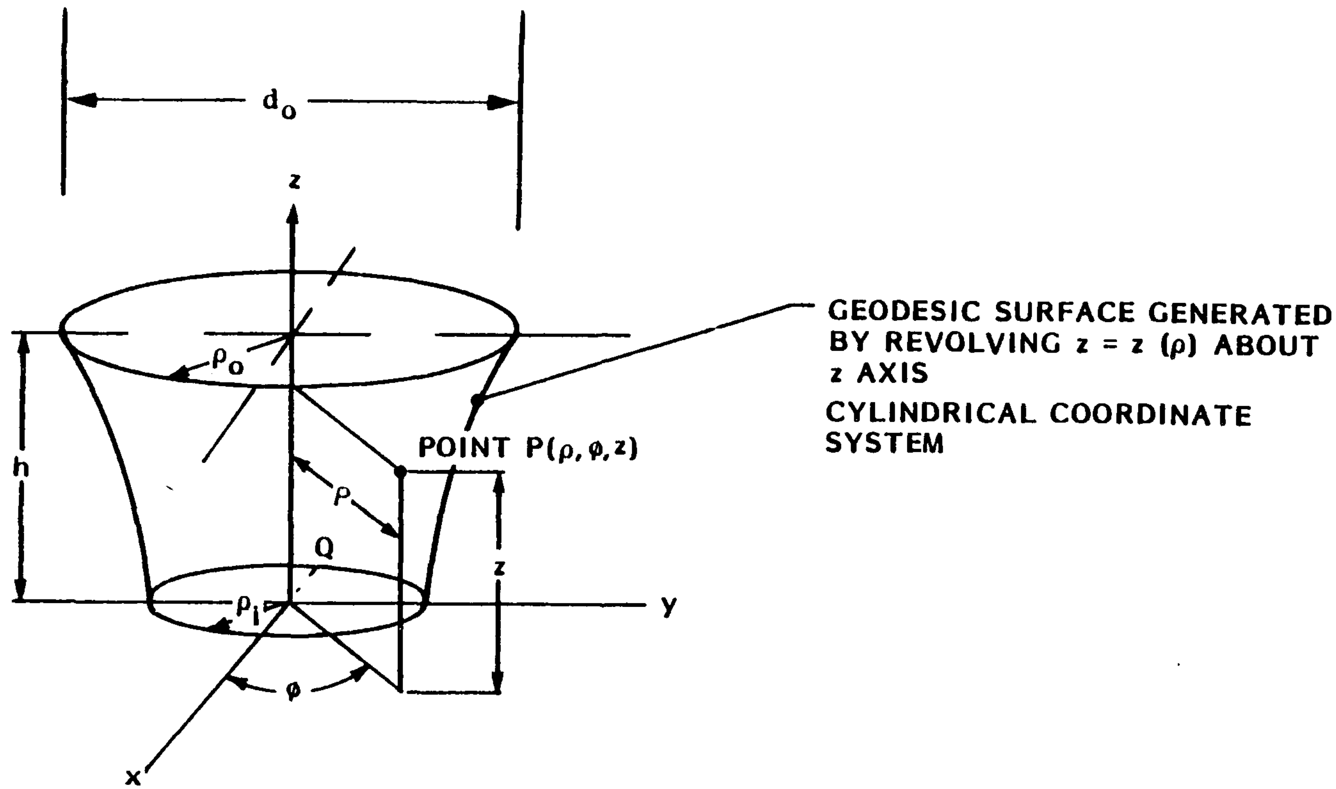

POINT Q IS DEFINED AS THE FEED POINT

FIGURE 1

GENERAL DIFFERENTIAL EQUATION OF GEODESICS

IN CYLINDRICAL COORDINATES, THE DIFFERENTIAL ARC LENGTH IS:

$$ds = \sqrt{(\rho d\phi)^2 + d\rho^2 + dz^2} \qquad (1)$$

THUS

$$S = \int_{\rho_1}^{\rho_2} \sqrt{\rho^2 \dot{\phi}^2 + 1 + \dot{z}^2}\, d\rho = \int_{\rho_1}^{\rho_2} F(\rho, \phi, \dot{\phi})\, d\rho \qquad (2)$$

IN WHICH $\dot{\phi} = \frac{d\phi}{d\rho}$, $\dot{z} = \frac{dz}{d\rho}$

GENERAL DIFFERENTIAL EQUATION OF GEODESICS (CONT)

FROM FERMAT'S PRINCIPLE, S IS STATIONARY, THUS

$$\frac{\partial F}{\partial \phi} - \frac{d}{d\rho}\left(\frac{\partial F}{\partial \dot{\phi}}\right) = 0 \tag{3}$$

THIS REDUCES TO:

$$\phi(\rho) = C_1 \int_{\rho_o}^{\rho} \frac{\sqrt{1 + \dot{z}^2}}{\rho\sqrt{\rho^2 - C_1^2}}\, d\rho + \phi(\rho_o) \tag{4}$$

AND

$$\phi_i = C_1 \int_{\rho_o}^{\rho_i} \frac{\sqrt{1 + \dot{z}^2}}{\rho\sqrt{\rho^2 - C_1^2}}\, d\rho + \phi_o \tag{5}$$

WHERE $\phi_i = \phi(\rho_i)$ and $\phi_o = \phi(\rho_o)$.

GEODESICS ON A CONE

FOCUSSING AT ∞ REQUIRES THE BOUNDARY CONDITION:

$$\tan\phi(\rho_o) = \frac{-\rho_o \dot{\phi}(\rho_o)}{\sqrt{1+\dot{z}^2(\rho_o)}} \tag{6}$$

IT THEN FOLLOWS THAT

$$C_1 = -\rho_o \sin\phi_o \tag{7}$$

BY SUBSTITUTING

$$\rho = -C_1 \csc\alpha,$$

THE GEODESICS BECOME

$$\phi = \int_{\alpha_o}^{\alpha} \csc\gamma \, d\alpha + \phi(\rho_o) \tag{8}$$

IN WHICH

$$\csc\gamma = \sqrt{1+\dot{z}^2} = \textit{constant for a cone} \tag{9}$$

FOR THE GEODESIC CONE, THE GEODESIC PROJECTION IN THE ρ, ϕ PLANE BECOMES (TOP VIEW)

$$\phi = \left(\csc\gamma\right)\left[\arcsin\left(\frac{\rho_o \sin\phi_o}{\rho}\right) - \phi(\rho_o)\right] + \phi(\rho_o) \tag{10}$$

GEODESICS ON A CONE (CONT)

GEODESICS ON A CONE (CONT)

FOR THE SIDE AND FRONT VIEW, THE GEODESICS ARE

$$\frac{x}{\rho_o} = \frac{\rho}{\rho_o} \cos \left[\frac{\arcsin\left(\rho_o \dfrac{\sin \phi_o}{\rho}\right) - \phi_o}{\sin \gamma} + \phi_o \right] \quad \text{(side)} \qquad (11)$$

$$\frac{y}{\rho_o} = \frac{\rho}{\rho_o} \sin \left[\frac{\arcsin\left(\rho_o \dfrac{\sin \phi_o}{\rho}\right) - \phi_o}{\sin \gamma} + \phi_o \right] \quad \text{(front)} \qquad (12)$$

IN WHICH

$\rho = z \text{ TAN } \gamma + \rho_i$

ρ_i = INSIDE RADIUS (FEED)

ρ_o = OUTSIDE RADIUS (RADIATION)

GEODESIC PATHS TAKEN BY THE ELECTROMAGNETIC FIELD FOR THE GEODESIC CONE

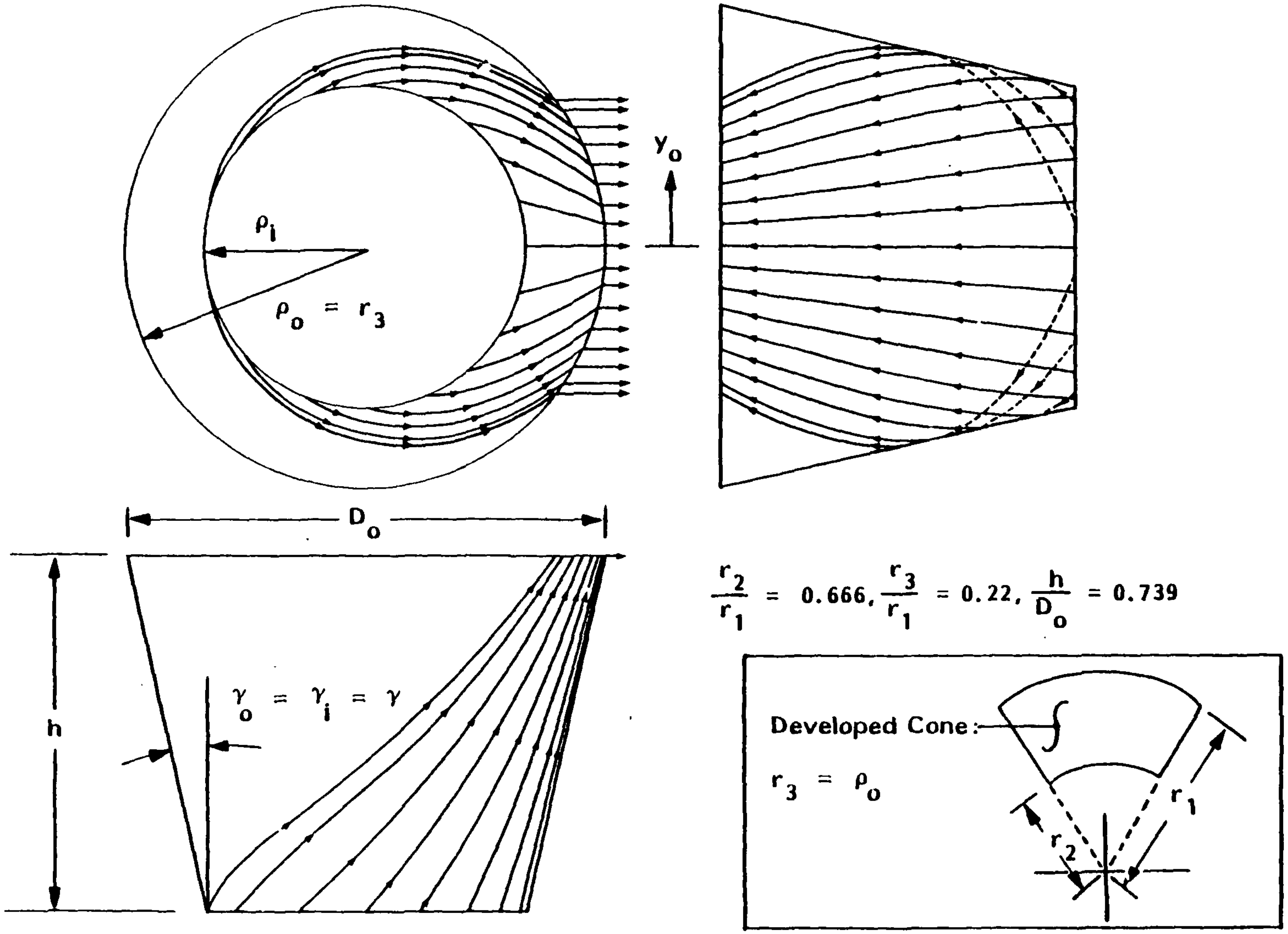

FIGURE 2

OUTPUT DISTRIBUTION DEPENDS UPON $\dot{z}(\rho)$

THE LINEAR APERTURE VARIABLE y_o IS

$$Y_o = \rho_o \sin \phi_o \quad \text{thus,} \tag{13}$$

$$dY_o = \rho_o \cos \phi_o \, d\phi_o \tag{14}$$

FROM CONSERVATION OF ENERGY

$$P(y_o)\, dy_o = P(\phi_i)\, d\phi_i \quad \text{and} \tag{15}$$

$$E(y_o) = \sqrt{P(y_o)} \quad \text{Hence} \tag{16}$$

$$E(y_o) = \left[P(\phi_i) \sec \phi_o \frac{d\phi_i}{d\phi_o} \right]^{1/2} \tag{17}$$

THUS, THE OUTPUT AMPLITUDE DISTRIBUTION IS DETERMINED BY BOTH $P(\phi_i)$ AND $\dot{z}(\rho)$ OF EQUATION (5). TO WITHIN A MULTIPLICATIVE CONSTANT:

$$P(\varphi_i) = \frac{P(y_o) \cos \varphi_o}{1 - \csc \gamma_o + \dfrac{\csc \gamma_i \cos \varphi_o}{\sqrt{(\rho i/\rho_o)^2 - \sin^2 \varphi_o}}} \tag{18}$$

IN WHICH $\gamma_i = \gamma(\rho_i)$ and $\gamma_o = \gamma(\rho_o)$

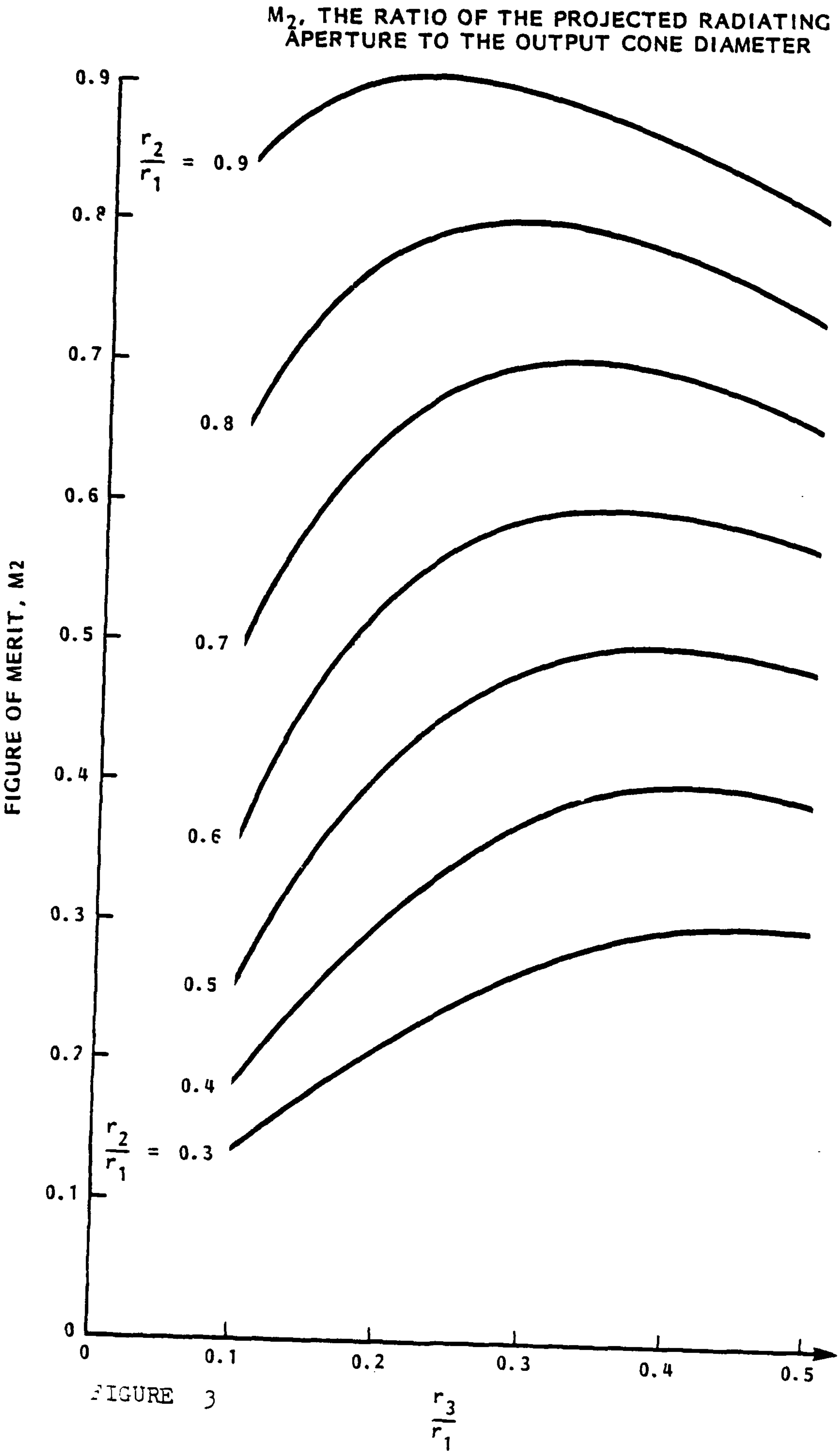

M2, THE RATIO OF THE PROJECTED RADIATING APERTURE TO THE OUTPUT CONE DIAMETER
FIGURE OF MERIT, M2
0.9
0.8
0.7
0.6
0.5
0.4
0.3
0.2
0.1
0
r2/r1 = 0.9
0.8
0.7
0.6
0.5
0.4
r2/r1 = 0.3
0.1
0.2
0.3
0.4
0.5
r3/r1

FIGURE 3

GEODESIC CONE

MAXIMUM ANGLE OF INCIDENCE

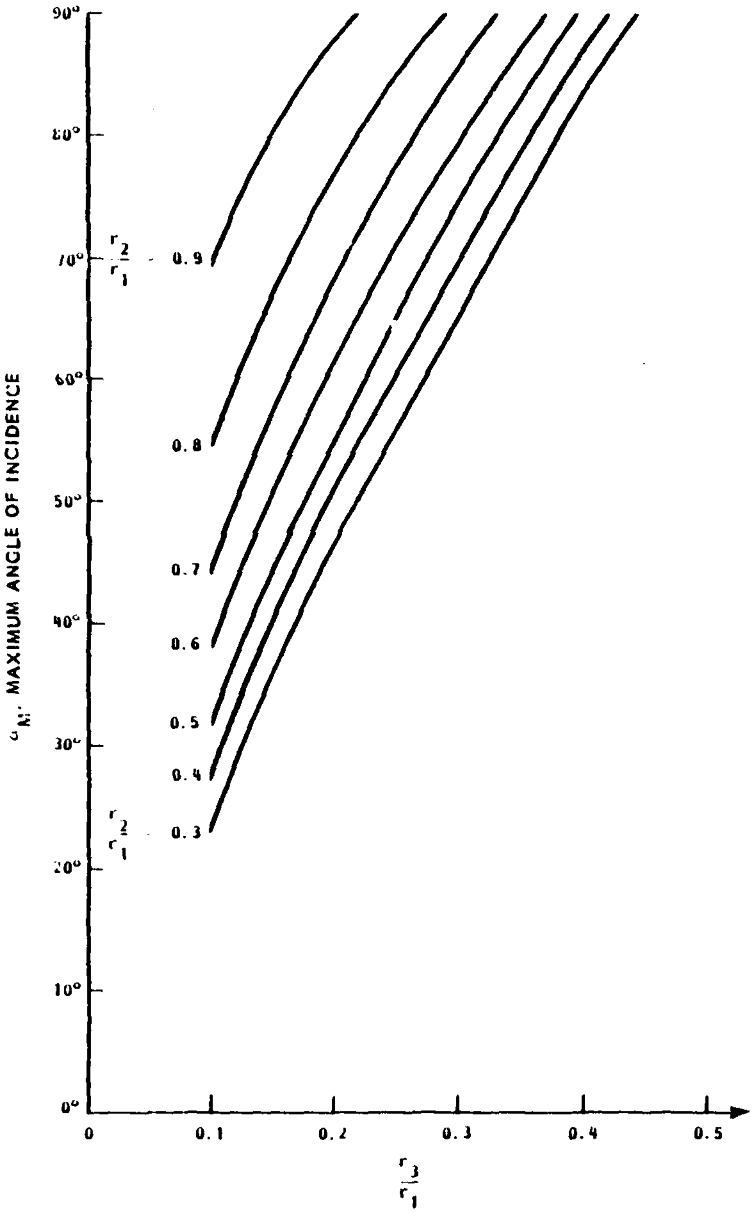

$$\text{TOTAL INSTANTANEOUS BANDWIDTH} = \frac{\Delta_{MAX} C}{\pi \rho_o \left[1 - \sqrt{1 - M_2^2}\right]}$$

WHERE Δ_{MAX} = MAX TOLERABLE QUADRATIC PHASE ERROR (RAD.) FOR A LINEAR APERTURE

C = VELOCITY OF LIGHT

EXAMPLE:

ρ_o = 25 INCHES

M_2 = 0.627

CENTER FREQ SIDELOBE LEVEL = -50 dB

TOLERABLE SIDELOBE DEGRADATION = 3 dB ∴

$\Delta_{MAX} \simeq 30°$

THUS:

INSTANTANEOUS BANDWIDTH = 365 MHz

FIGURE 4

APPLICATIONS

APERTURE:

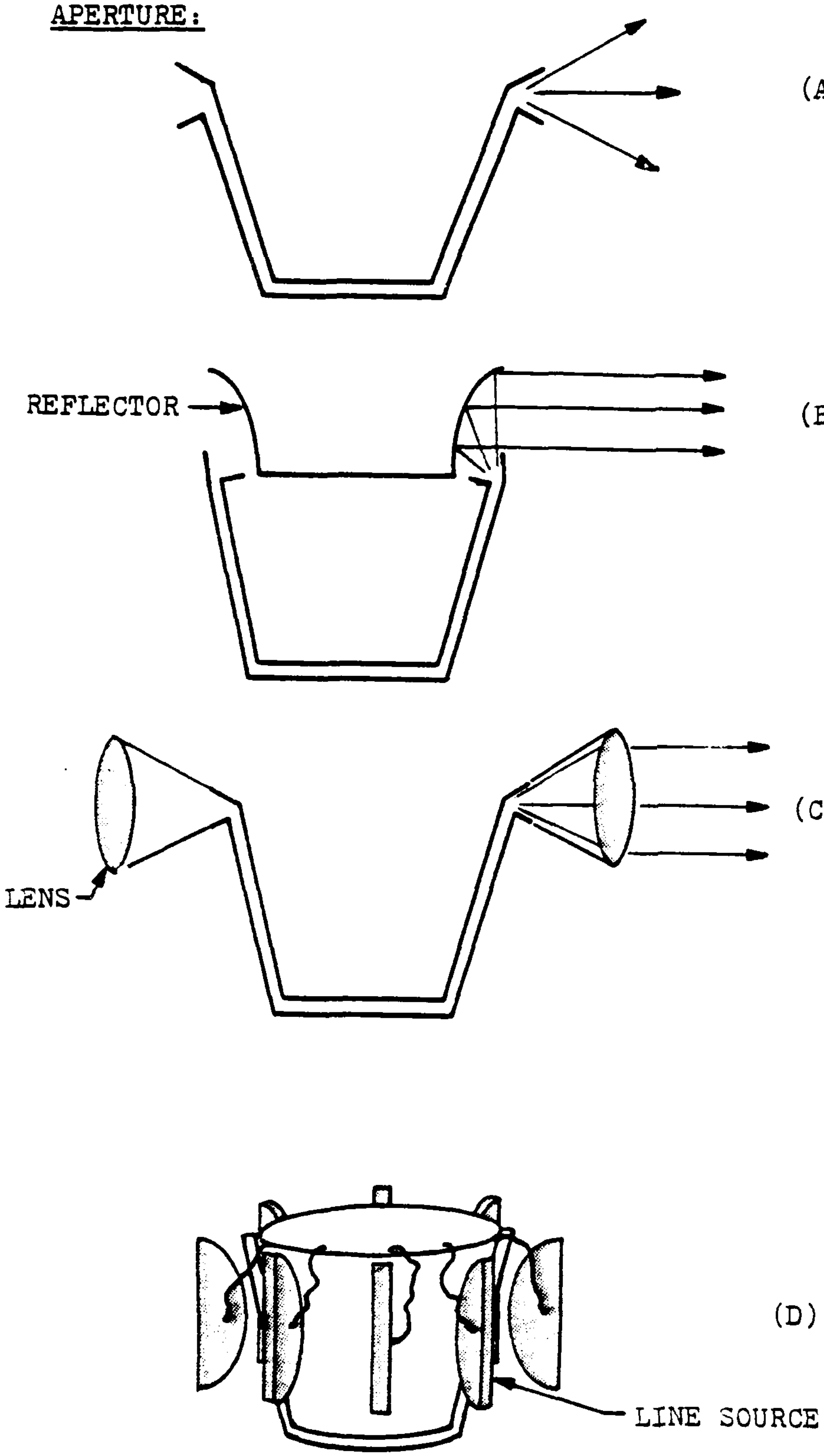

(A) RADIATION FROM HORN

(B) HORN FEEDS REFLECTOR

(C) HORN FEEDS LENS

(D) OUTPUT PROBES FEED LINE SOURCES

FIGURE 5

APPLICATIONS

FEED

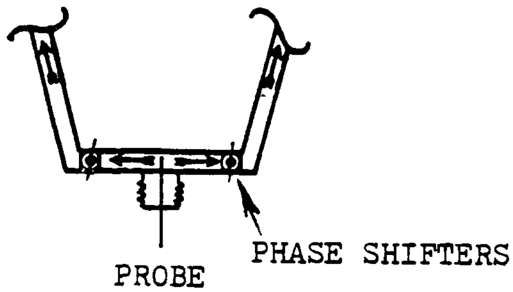

(E) SIMPLE PROBE FEED

- ·10 TO 13 DB SIDELOBES
- ·MULTIMODE CAPABILITY
  - ·PENCIL BEAM
  - ·SECTOR BEAM, VARIABLE WIDTH
  - ·OMNI BEAM

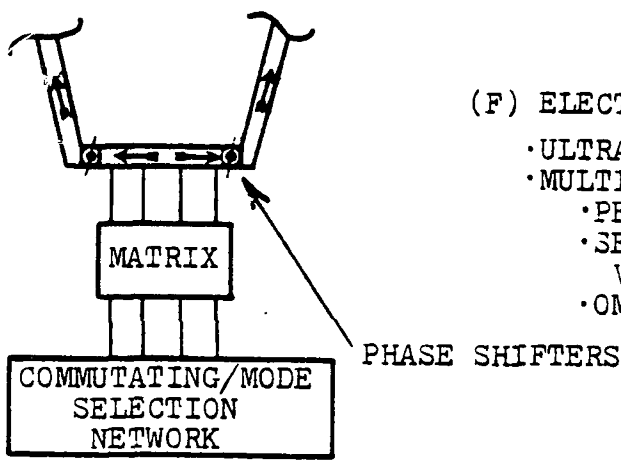

(F) ELECTRONIC COMMUTATING FEED

- ·ULTRA LOW SIDELOBES
- ·MULTIMODE CAPABILITY
  - ·PENCIL BEAM
  - ·SECTOR BEAM, VARIABLE WIDTH
  - ·OMNI BEAM

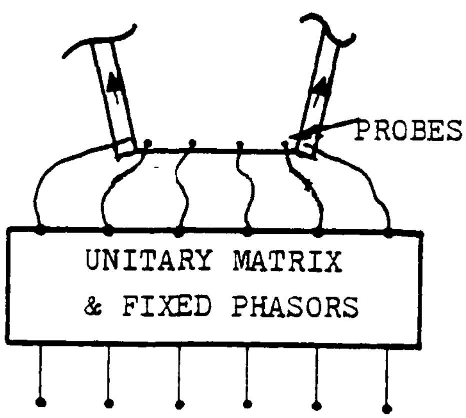

(G) MULTIPLE BEAM MATRIX FEED
(NO PHASE SHIFTERS)

- ·MULTIPLE BEAMS OVER 360° AZIMUTH
- ·REQUIRES LARGER MATRIX THAN (F)

FIGURE 5

SECTIONAL VIEW OF THE GEODESIC ANTENNA

MODES: SCANNABLE PENCIL BEAM
OMNI
SCANNABLE, VARIABLE WIDTH SECTOR BEAM

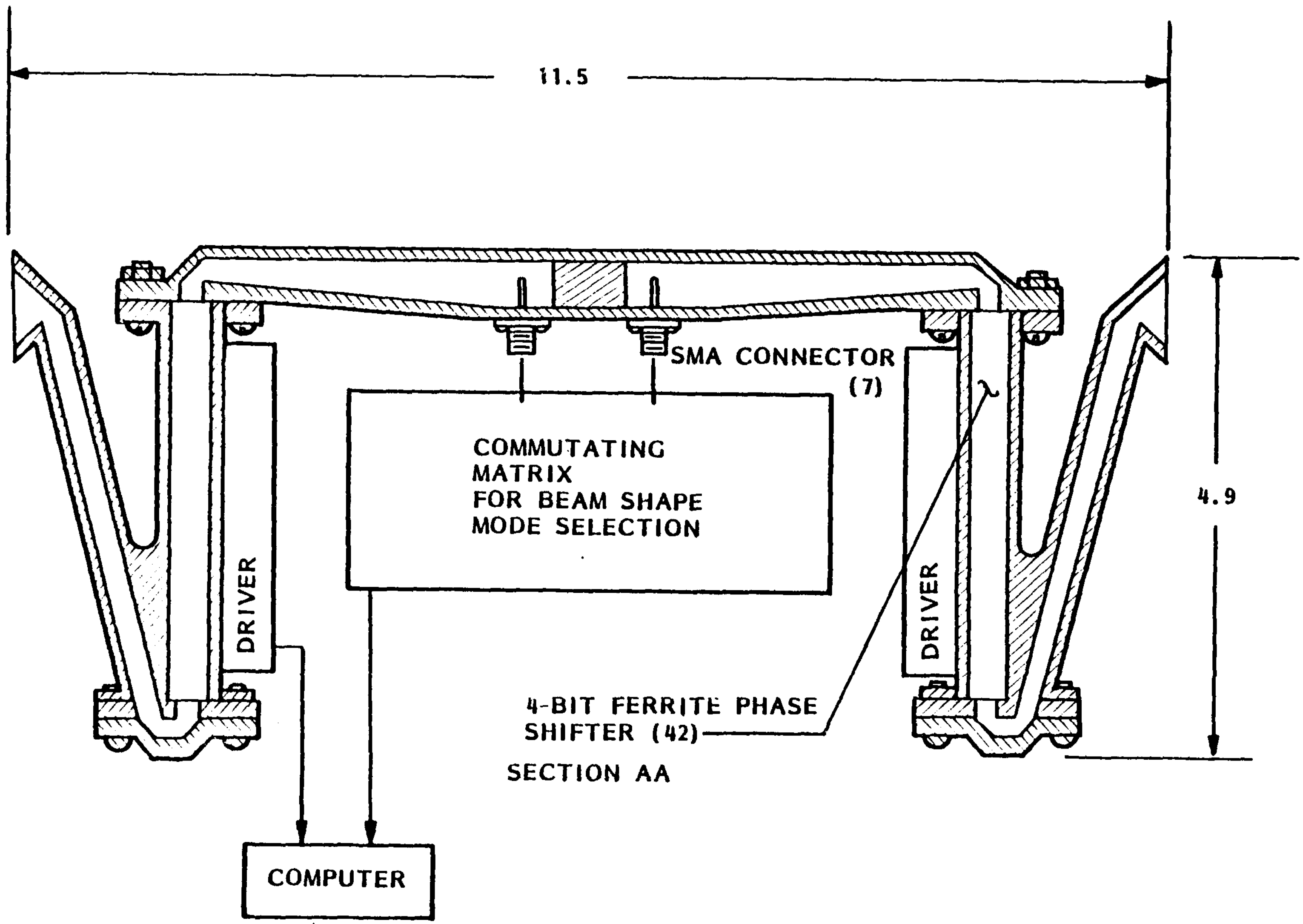

FIGURE 7

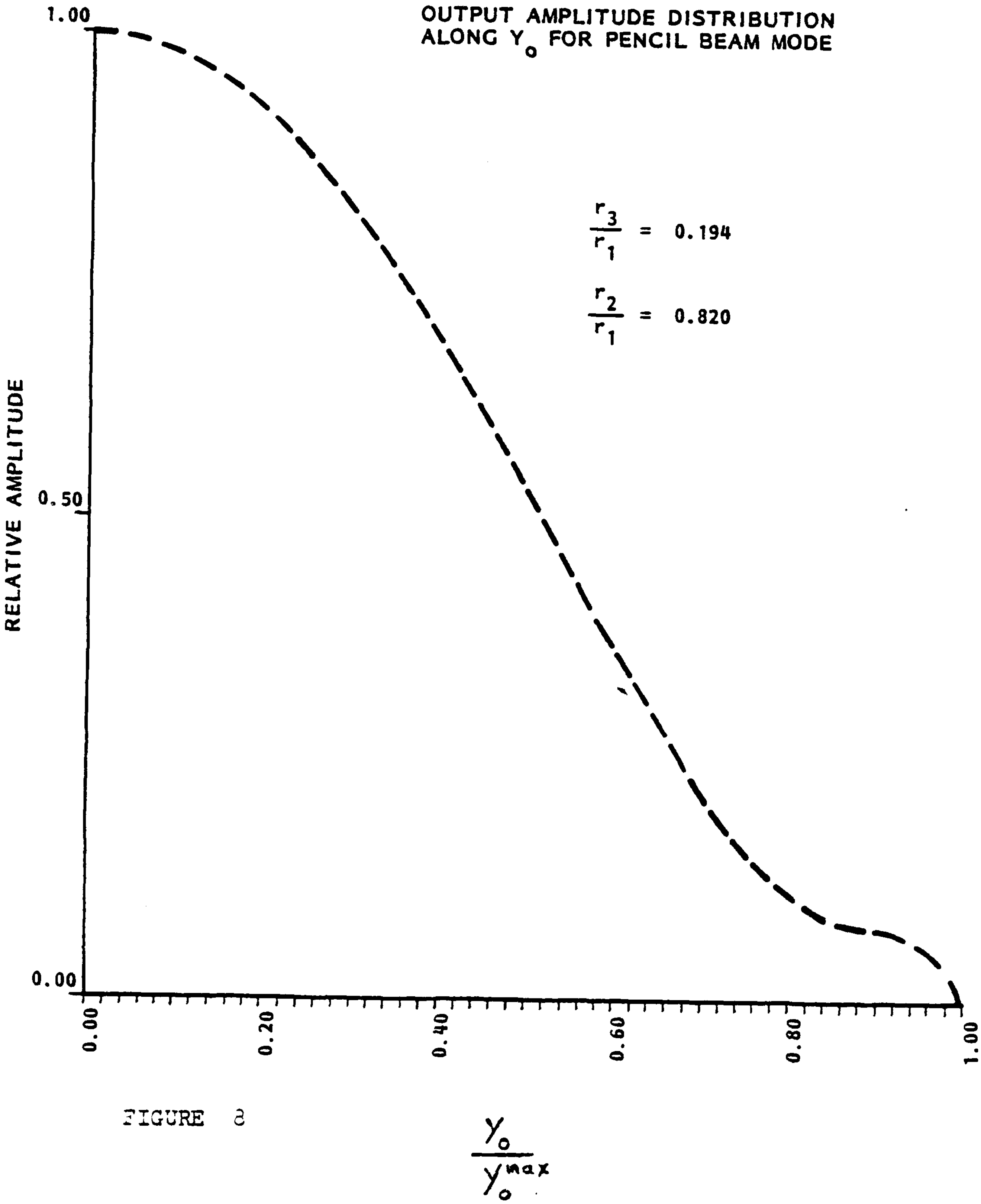
OUTPUT AMPLITUDE DISTRIBUTION
ALONG Y_o FOR PENCIL BEAM MODE
$\frac{r_3}{r_1}$ = 0.194
$\frac{r_2}{r_1}$ = 0.820
RELATIVE AMPLITUDE
1.00
0.50
0.00
0.00
0.20
0.40
0.60
0.80
1.00
$\frac{Y_o}{Y_o^{max}}$

FIGURE 8

FAR-FIELD RADIATION PATTERN FOR
PENCIL BEAM MODE

FIGURE 9

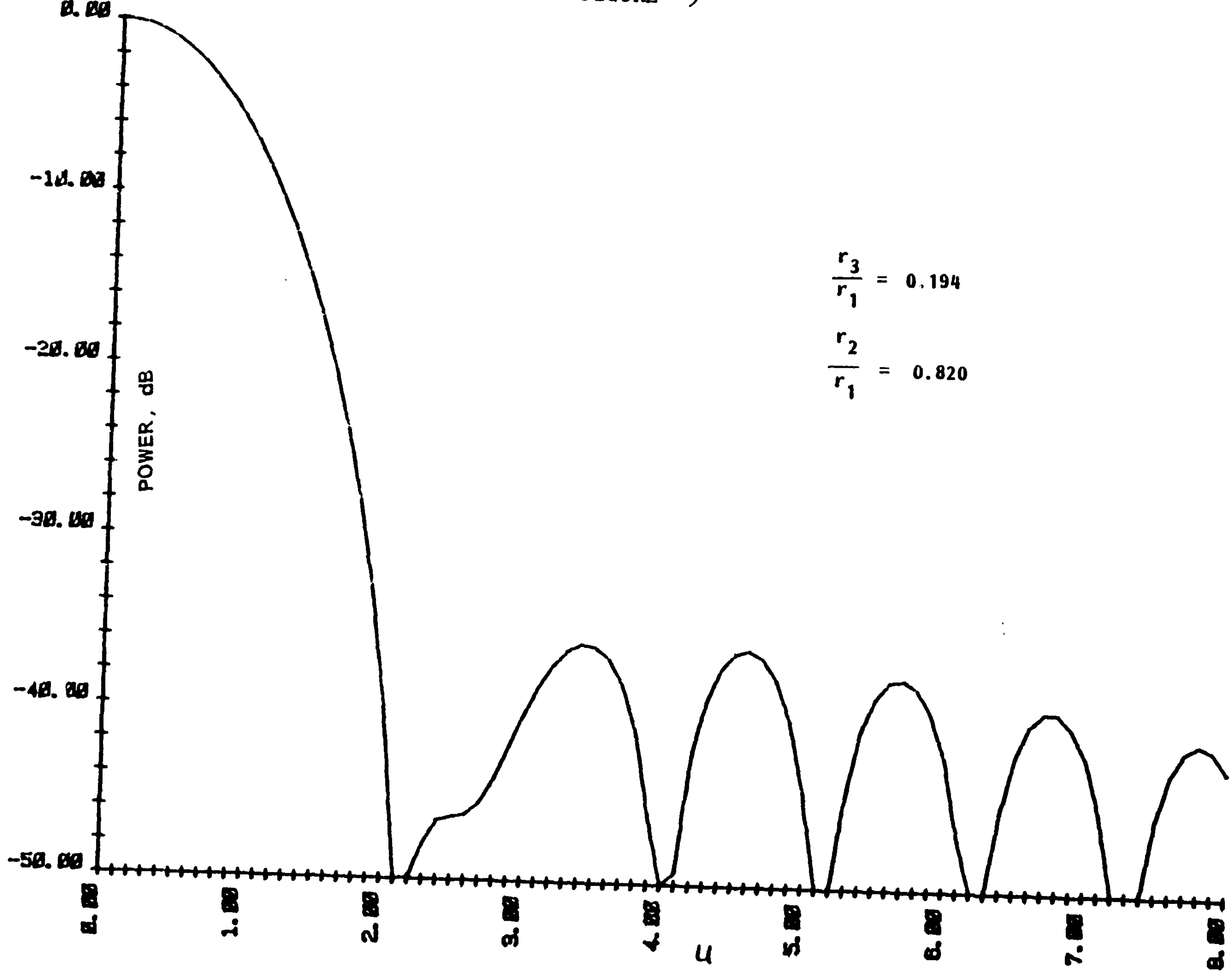

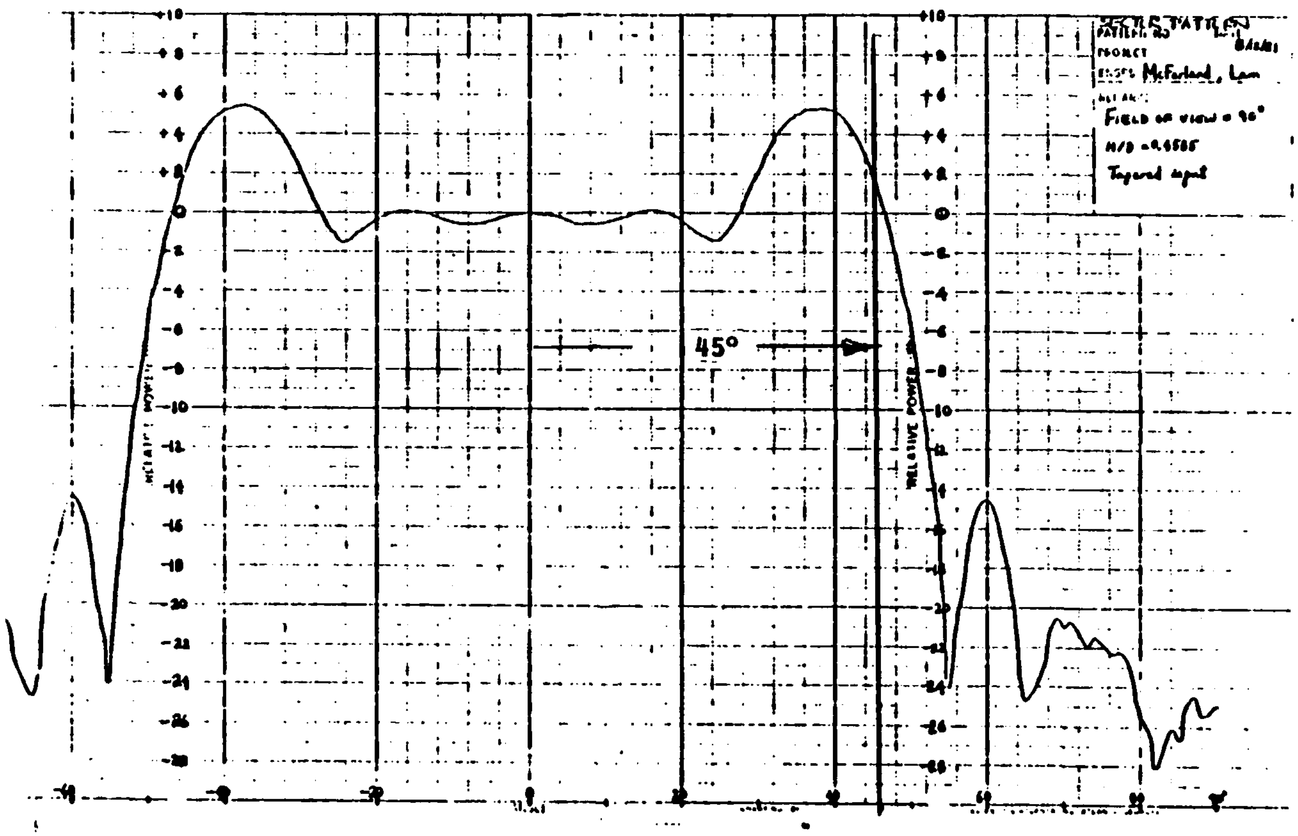

SELECTABLE WIDTH, SCANNING SECTOR PATTERN

FIGURE 10

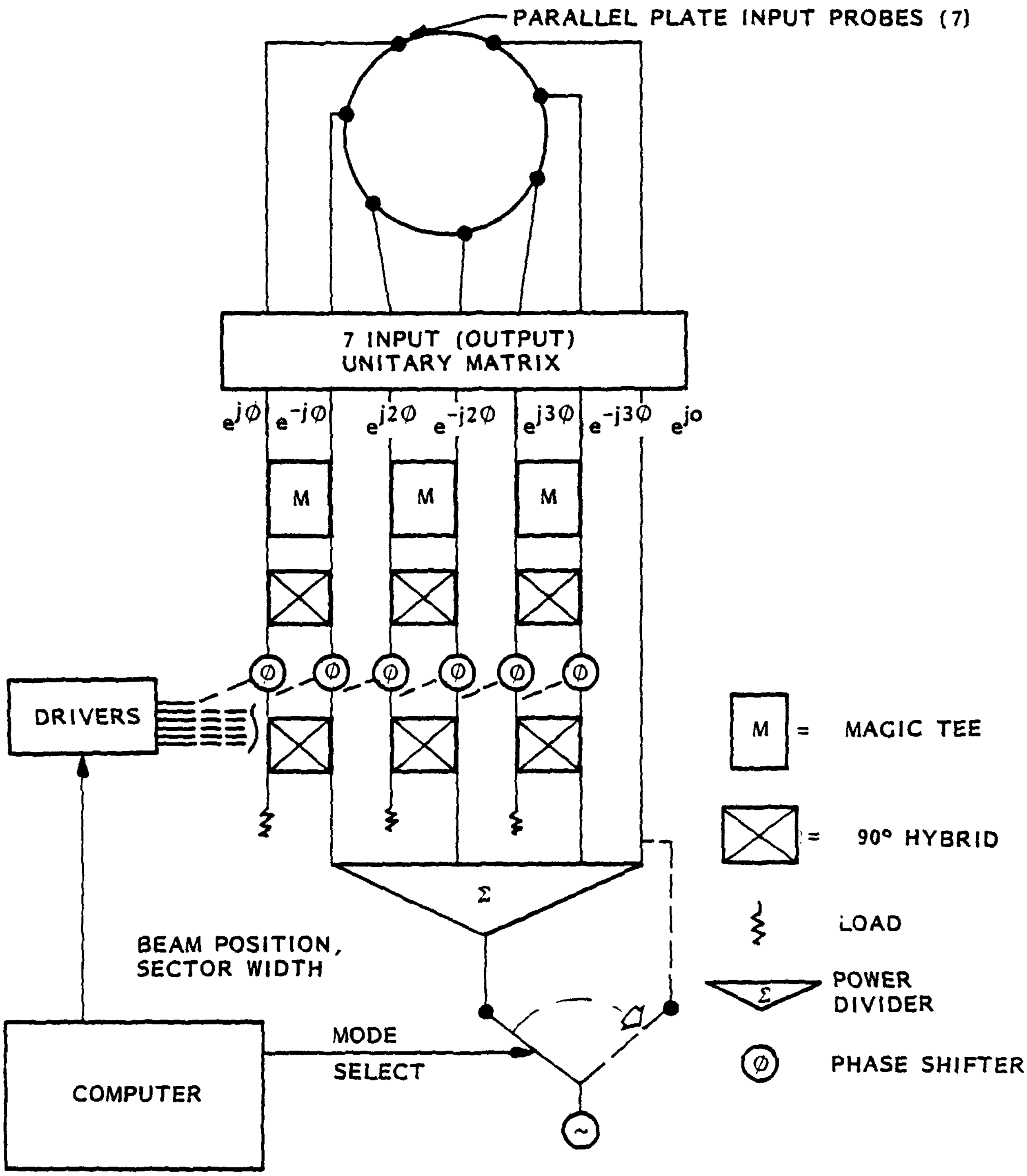

FEED AND MODE SELECTION SCHEMATIC

FIGURE 11

FIGURE 12

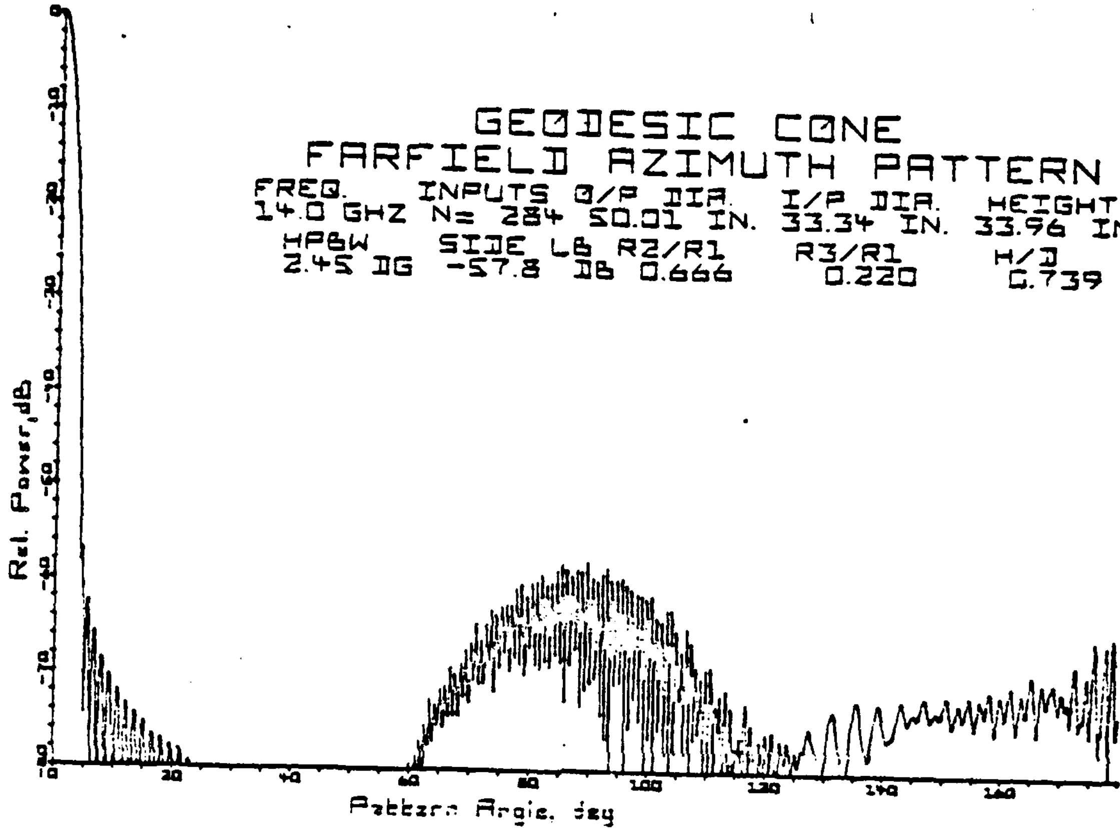
GEODESIC CONE
FARFIELD AZIMUTH PATTERN
FREQ. INPUTS O/P DIA. I/P DIA. HEIGHTH
14.0 GHZ N= 284 50.01 IN. 33.34 IN. 33.96 IN.
HPBW SIDE LB R2/R1 R3/R1 H/D
2.45 DG -57.8 DB 0.666 0.220 0.739
Rel. Power, dB
Pattern Angle, deg

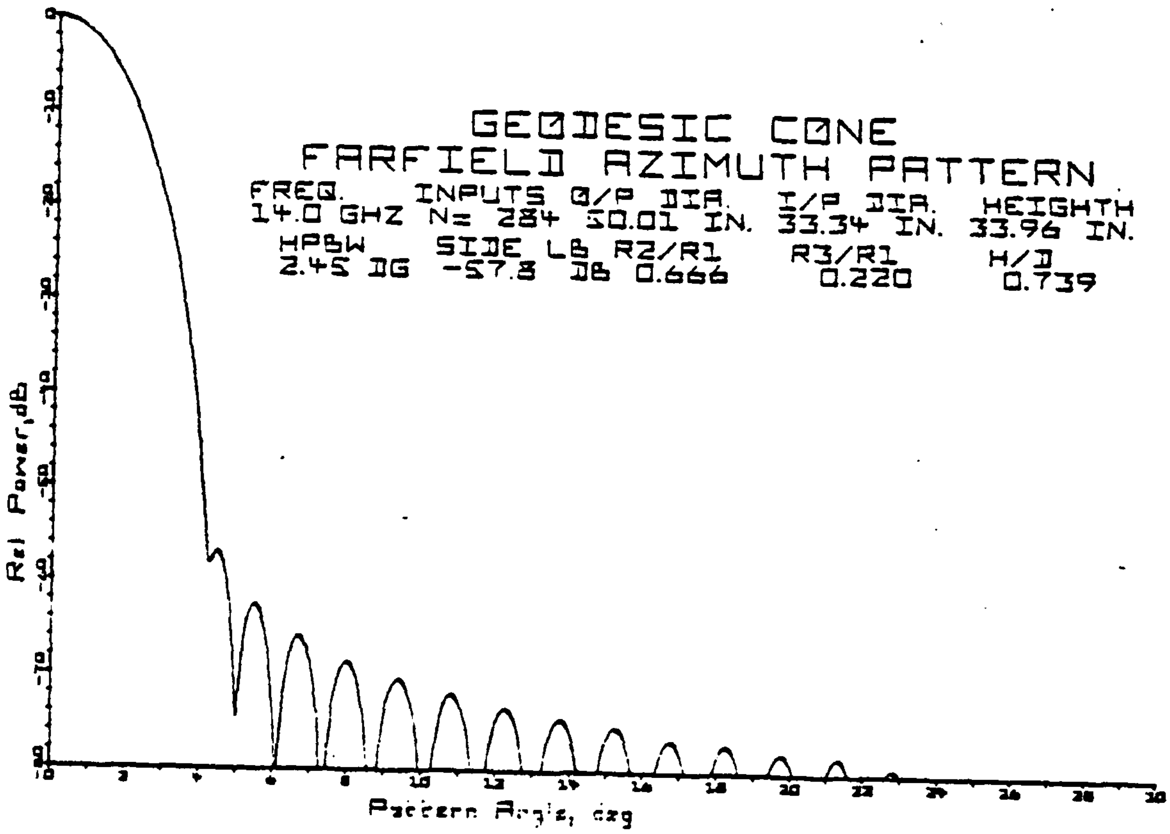
GEODESIC CONE
FARFIELD AZIMUTH PATTERN
FREQ. INPUTS O/P DIA. I/P DIA. HEIGHTH
14.0 GHZ N= 284 50.01 IN. 33.34 IN. 33.96 IN.
HPBW SIDE LB R2/R1 R3/R1 H/D
2.45 DG -57.8 DB 0.666 0.220 0.739
Rel Power, dB
Pattern Angle, deg

A COMMON-APERTURE
S- AND X-BAND FOUR-FUNCTION FEEDCONE

J. R. Withington and W. F. Williams

Telecommunications Science and Engineering Division

Jet Propulsion Laboratory

California Institute of Technology

Pasadena, California

Presented at

The 1981 Antenna Applications Symposium

University of Illinois

Allerton Park

Monticello, Illinois

September 1981

A COMMON-APERTURE X- AND S-BAND FOUR-FUNCTION FEEDCONE

J. R. Withington and W. F. Williams
Jet Propulsion Laboratory
California Institute of Technology

Abstract

A paper discussing a prototype X/S-band feedhorn that enabled simultaneous X-band and S-band reception from a geometrically symmetrical Cassegrain reflector antenna was presented at this symposium in 1979. Since that time, the solutions to problems discussed in that paper were incorporated into a new (second generation) X/S feedhorn and combiner. Included were developments to make the feedhorn/combiner a broadband device at both X- and S-band. The bandwidth is necessary for simultaneous reception/transmission at frequencies widely separated within each band.

A (transmit/receive) feedcone fitted with a second-generation feedhorn is being built. X- and S-band receivers and transmitters in the feedcone and on the antenna will enable the NASA/JPL Deep Space Network to transmit and receive simultaneously from the same common-aperture Cassegrain feed.

Three development areas are considered:

(1) The Horn. Incorporating the findings discussed in the first paper, a new wide groove corrugated horn was designed and built.

(2) The Combiner. In order to handle the much broader bandwidth and power handling capabilities required for the fully diplexed system, a new combiner section was designed and built.

(3) X-Band Component Hardware. An efficient broadband diplexer and a high-performance modified iris polarizer to cover the 1.6-GHz bandwidth X-band requirements were designed and built.

The concluding portions of this paper deal with the feedcone for a highly diversified frequency system and the components that will be used to demonstrate simultaneous X- and S-band uplink/downlink capabilities. Design of new X-band components, feedcone layout, capabilities and performance are discussed.

Introduction

An article discussing a prototype X-S-band feedhorn that enabled simultaneous X- and S-band reception from a Cassegrain antenna was presented at this symposium in 1979 (Ref. 1). That feedcone has quite successfully demonstrated an alternate method to the standard Deep Space Network system of multiple subreflectors and dichroic plate for dual-band reception.

Since JPL is engaged in a Network Consolidation Program, involving centralized control of existing antennas and construction of new reflector antennas, a second-generation feedhorn/combiner was conceived to show that this common-aperture feedhorn system was capable of performing all necessary functions the DSN would be called upon to perform with existing and future X-S-band spacecraft, including not only uplink/downlink operation at S-band but also an X-band system, paralleling the existing S-band system, for simultaneous or separate system uplink/downlink operations. Because no complete X-band system existed for accomplishing this, certain waveguide components, such as an X-band diplexer and a wide-band polarizer, were designed and built. When all of the new and existing S- and X-band components are assembled, we will have for the first time a complete S- and X-band system in one feedcone. Each future S- and X-band feedcone constructed for the DSN network will use only those portions of this design necessary to perform the required task. Once in place, all of these feedcones will have the ability to be easily upgraded to include further sophistication as necessary for future DSN operations.

The Feedhorn Concept

Jeuken and Vokurka (Ref. 2) suggested this technique of feedhorn operation in different frequency bands. The corrugated feedhorn derives its operating characteristics from the fast wave structure of the feedhorn walls, and this characteristic is obtained by grooving the walls perpendicular to power flow so that the surface impedance becomes capacitive. For this to occur, the input grooves must be between $\lambda/4$ and $\lambda/2$ deep (λ = free space wavelength for a conical horn) at the operating frequency, or in the range $\lambda[(2N-1)/4]$ to $\lambda(2N/4)$, where N may assume any integer value. Once this fast wave is established, the grooves may gradually become shallow and inductive and the fast wave will still exist and propagate.

There are two basic degrees of freedom in the design of such a feedhorn:

(1) The groove structure used to create a condition to support multiband operation.

(2) The flare angle and final aperture size to obtain a desired pattern beamwidth.

Because of the periodic behavior of the corrugation impedance in the frequency spectrum, there will be a multiplicity of frequency bands for which any corrugated horn will support the proper fast waves. For instance, a groove depth can be found that is a multiple for the two frequency bands (N = 1,3 for S- and X-band), which presents the correct boundary conditions to support this corrugated hybrid mode.

Now consider the second degree of freedom, the flare angle. As a horn with fixed flare angle becomes longer, the aperture becomes larger and radiation patterns become narrower. A point is reached, however, when additional size does not make the pattern narrower or the feedhorn develop higher gain, generally because of total phase error in the aperture. For this discussion we may call this "gain limit" or "saturated operation." As size is further increased, some change in pattern texture may be detected; however, the pattern remains essentially unchanged. Therefore, flare angle alone determines the final pattern "saturated" beamwidth. For both generations of common aperture feedhorns, this full flare angle is 34.2 degrees. In fact, both feedhorns are the same size overall (1496 mm high with a 1219-mm aperture diameter). Figure 1 is a picture of the new feedhorn and the principal feed components.

Fig. 1 The second-generation X/S horn with the Mod II combiner, S-band bridge assembly X-band polarizer packaging, and X-band diplexer.

One now sees the possibilities. A groove depth can be chosen which satisfies the depth requirements within two (or more) frequency bands for proper corrugated feedhorn operation, and with a sufficiently large aperture to just be "saturated" in the lowest band so that the higher bands would be operating well above this point for nearly equal pattern characteristics. It is therefore possible to illuminate a reflector antenna efficiently at two widely spaced frequency bands using a single corrugated feedhorn. The problem only remains to excite or "combine" the two rather diverse frequency bands (in our case, S- and X-band) in the feedhorn.

The Combiner Concept

The following specifications were the constraints in defining an X-S device to efficiently "combine" S- and X-band.

Frequency-Bandwidth

2.1 to 2.3 GHz at S-band (9.09%)
7.1 to 8.6 GHz at X-band (19.1%)

Receive

S-band, 2.2 to 2.3 GHz; VSWR 1.2:1
X-band, 8.2 to 8.6 GHz; VSWR 1.2:1
X-band, 8.4 to 8.5 GHz; VSWR 1.1:1

Transmit

S-band, 2.11 to 2.12 GHz; VSWR 1.1:1
X-band, 7.145 to 7.235 GHz; VSWR 1.1:1

Dissipative Losses

S-band, < 0.2 dB
X-band, < 0.02 dB (relative to horn without combiner)

Power

S-band, 20 kW CW
X-band, 20 kW CW

The technique chosen to feed S-band into the feedhorn combiner is through a circumferential slot in the side of the feedhorn. The original conception and analysis was assisted by Dr. S. B. Cohn (Ref. 3), and is illustrated in Fig. 2. The radial line slot injection region is within the feedhorn proper at a diameter "d" that, at the desired center frequency, effects the best impedance match in the plane of the slot, i.e., the short reflected back from the X-band input section at S-band. The dimension "b" is chosen to be less than one-half wavelength at the highest X-band frequency. This eliminates any possible X-band propagation within the TM^r_{m0} radial modes, where m = number of $\lambda/2$ variations around the circumference. The TE^r_{20} radial mode is excited by the X-band HE_{11} wave. Therefore, the radial line band stop filter in the slot is designed to stop X-band in the TE^r_{20} radial line mode, and also to present a short circuit looking into the annular opening at X-band.

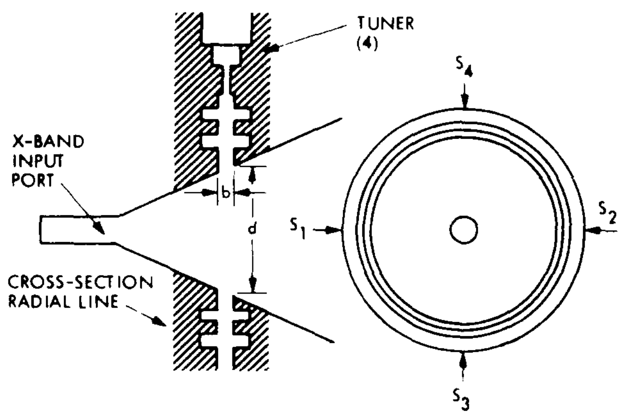

Fig. 2 The combiner concept.

The X-band is conventionally fed through the throat of the combiner, which flares fairly abruptly from the round waveguide input to the diameter of the S-band circumferential slot.

First-Generation Configuration

The X-band throat section of the combiner flares from the WC-137 round waveguide input to the diameter of the S-band slot over some 100 mm, and was corrugated with groove depth on the order of 10.16 mm. A unique concept for this corrugated horn, relative to others that have been used, is the abrupt change in corrugation (groove) depth in the region of the horn where S-band is introduced. Grooves in the feedhorn were 49.40 mm deep, are 0.378 wavelengths at 2.295 GHz (S-band) and 1.392 wavelength deep at 8.45 GHz (X-band), and exhibit the proper corrugated surface boundary conditions for both bands. However, the particular configuration of the X-band chokes in the S-band radial line designed for the combiner did not allow the full groove depths to be used in the input region where only X-band was present. This was in order to allow S-band tuning irises to be placed as near as possible to the slot/feedhorn junction to obtain the maximum possible bandwidth. The resulting abrupt change near the combiner S-band input represents a potential discontinuity in groove impedance for the X-band and will be frequency-dependent (the electrical depth of the two grooves changing at different rates); an exact "match" is only possible at one frequency. This dispersion effect was the primary cause of extraneous moding in this early feedhorn, as was observed initially in the 8.45 GHz X-band radiation patterns (Fig. 3b).

The first-generation combiner slot (see Ref. 4 for photos and a detailed discussion), a thin radial line only 8.89-mm wide, surrounds the horn at a horn diameter of about 119.4 mm. Since grooves of the feedhorn were 3.55 mm wide, this slot width created a pitch ratio (defined as the ratio of groove width to groove period) interruption along the corrugated surface in the feedhorn and resulted in a second moding problem. The very narrow radial line was chosen to help assure that no X-band energy could penetrate the S-band portion of combiner. However, this narrow line also tends to make the S-band passband more limited (as determined by the impedance variation with frequency looking into the combiner). The radial line X-band rejection chokes isolated the X-band so successfully that no X-band noise could be detected as coming from the S-band system. But because the X-band chokes reflected a short to the top of the groove (see Fig. 4 for definition of "top," and "bottom" and "width" of grooves), it represented a third cause of moding in the feedhorn (119.4-mm diameter) was selected for a best impedance match at 2.3 GHz and this resulted in a narrow bandwidth of approximately 50 MHz over which input VSWR was less than 1.2:1.

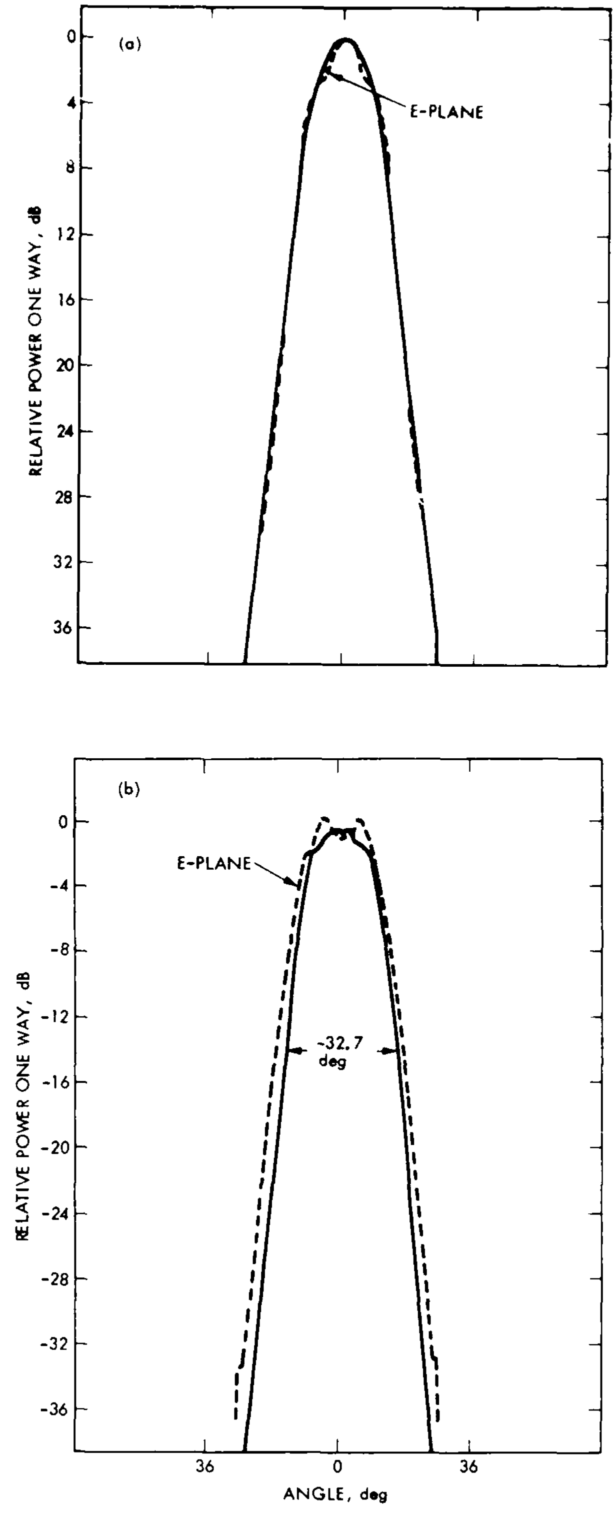

Fig. 3 Radiation patterns at 8.450 GHz, (a) E and H plane patterns of second-generation feedhorn, (b) E and H-plane patterns of first-generation feedhorn.

The Second-Generation Configuration

Because the first-generation horn revealed that the abrupt step impedance discontinuity was the major cause of extraneous X-band moding (indicated by the level of cross-polarization in the 45-degree radiation pattern cut), appropriate groove depths were necessary that both satisfied the fast wave structure of the HE_{11} mode, and gave a groove impedance match at the center of the desired X-band range. This would give the least (symmetrical) impedance mismatch at the band edges for the broadest possible bandwidth. The final model of the full scale, second-generation horn was made with X-band

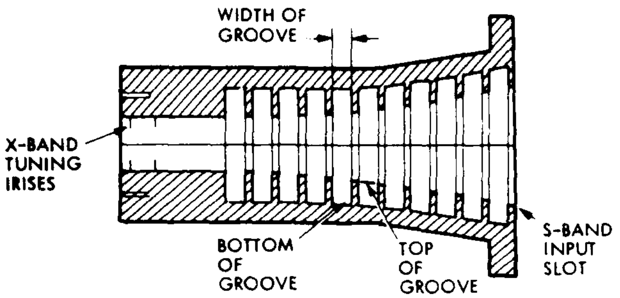

Fig. 4 The Mod II X-band radially tapered input section.

input grooves at 11.43 mm and output grooves at 48.89 mm, giving the ideal match at midband, 7.8 GHz, unfortunately a frequency region of no planned use. At 7.8 GHz, the two groove depths at the abrupt change are 0.297λ (λ = X-band free space wavelengths) and 1.297λ, the "perfect" match. This resulted in measured -43 dB cross polarization, a good result indeed. At 7.1 GHz, the selected depth results in a 0.271λ input groove and a 1.18λ output groove, a mismatch giving rise to a cross-polarization level of -32 dB; however, this is still acceptable. At 8.45 GHz, the selected (7.8 GHz) depth results in a mismatch from 0.322 to 1.405, and similar (-32 dB) cross-polarization levels (Ref. 1,5).

The first-generation X/S-band combiner performed its function well. It extracted the S- and X-band receive signal from the horn at low loss, and there was no interaction of the two frequencies in the combiner to degrade either system; i.e., no additional noise contribution was detectable in either system. Because of this, the basic original design was used for the second-generation combiner. However, this unit was, at S-band, of such narrow bandwidth that it could not be used for simultaneous S-band reception and transmission. Broadening the S-band bandwidth of the earlier combiner so that receive/transmit functions could be included was another major objective of the second-generation development.

In the second-generation combiner, the radial line section was widened to 12.7 mm to increase the S-band performance. So as to have no pitch ratio interruption, this slot width determines the width of the grooves for the rest of the horn. The second-generation feedhorn has 12.7-mm groove width with a 3.55-mm wall for a pitch ratio = 0.78 (Ref. 6). The S-band center is now lower (2.2 GHz), and therefore a new injection horn diameter of 127 mm is used. Four X-band reject radial line chokes are used to maintain the required high X-band isolation and now reflect a short to the bottom of the groove so as to eliminate that wave interruption. As with the first-generation combiner, tuning irises were required to be inserted into the radial line area to achieve an acceptable performance across the S-band. It was convenient to place these irises as metal blocks inserted into portions of the X-band chokes. A disassembled picture of this combiner is shown in Fig. 10. With no pitch ratio nor radial slot interruptions, and only the minor dispersive effects of the groove step discontinuity, acceptable concentric patterns were obtained. Figures 3, 6 and 7 show the patterns of the full-scale first generation and second-generation feedhorn. (Note the significant change in the amplitude patterns at 8.45 GHz.) In Fig. 8 we compare the S-band patterns of both feedhorns. There is basically no difference in the amplitude pattern structure at S-band.

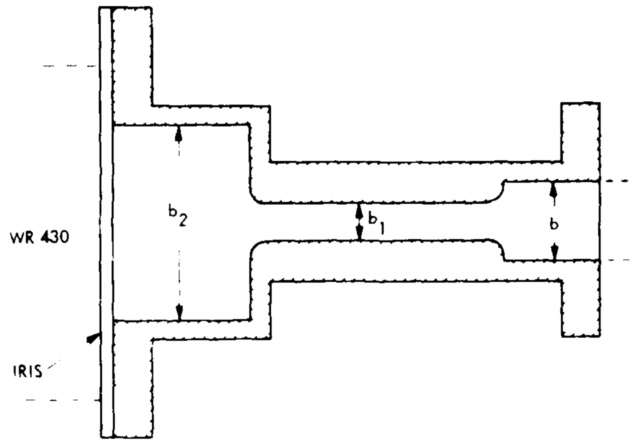

Fig. 5 The S-band tuner section.

S- and X-band Tuning

The combiner along with its four 12.7-mm-wide input waveguide terminals is not matched to standard S-band waveguide. The additional matching must be done with a transformer-tuner that transforms the 12.7 mm waveguide height (b) to the 54.6 mm height of standard S-band (WR-430) waveguide and at the *same time provides the necessary tuning to match* the input impedance over the required bandwidth to a VSWR (voltage standing wave ratio) of less than 1.2:1. The graph shown in Fig. 9 represents the VSWR looking into any one of the four combiner input terminals under two-terminal (diametrically opposite) linear polarization excitation. The requirement on the tuner is to develop a response VSWR of less than 1.2:1 from 2.1 to 2.3 GHz.

The transformer-tuner (Fig. 5) was designed and is fabricated using a three-step, two-section waveguide structure to transform from the 12.7-mm height (b) waveguide combiner input (standard 109.2-mm width) down to a narrow height guide of only 3.12 mm (b_1), increasing to a section of 39.4-mm height (b_2) and then to the full 54.6-mm height of standard WR-430 waveguide. At the final step, an inductive iris is inserted into the 39.4-mm size that tunes the total combination across the required band. The VSWR response of the transformer-tuner and combiner is also shown in Fig. 9. Note that there exists a small region above 2.25 GHz where the VSWR exceeds 1.2:1, but this receive-only region is less critical than the lower or transmit end of the band, and is fully acceptable.

The tuner-combiner is designed to transmit 20-kW CW power, or 5 kW into each tuner port under circular polarization excitation. Calculations of voltage breakdown in the 3.12-mm-height section of waveguide indicate that it has this capability with sufficient safety factor. However, if the transmitter requirement should become 100 kW (possibly future requirements) or more at a later date, there is a serious question about the performance of this particular transformer-tuner design.

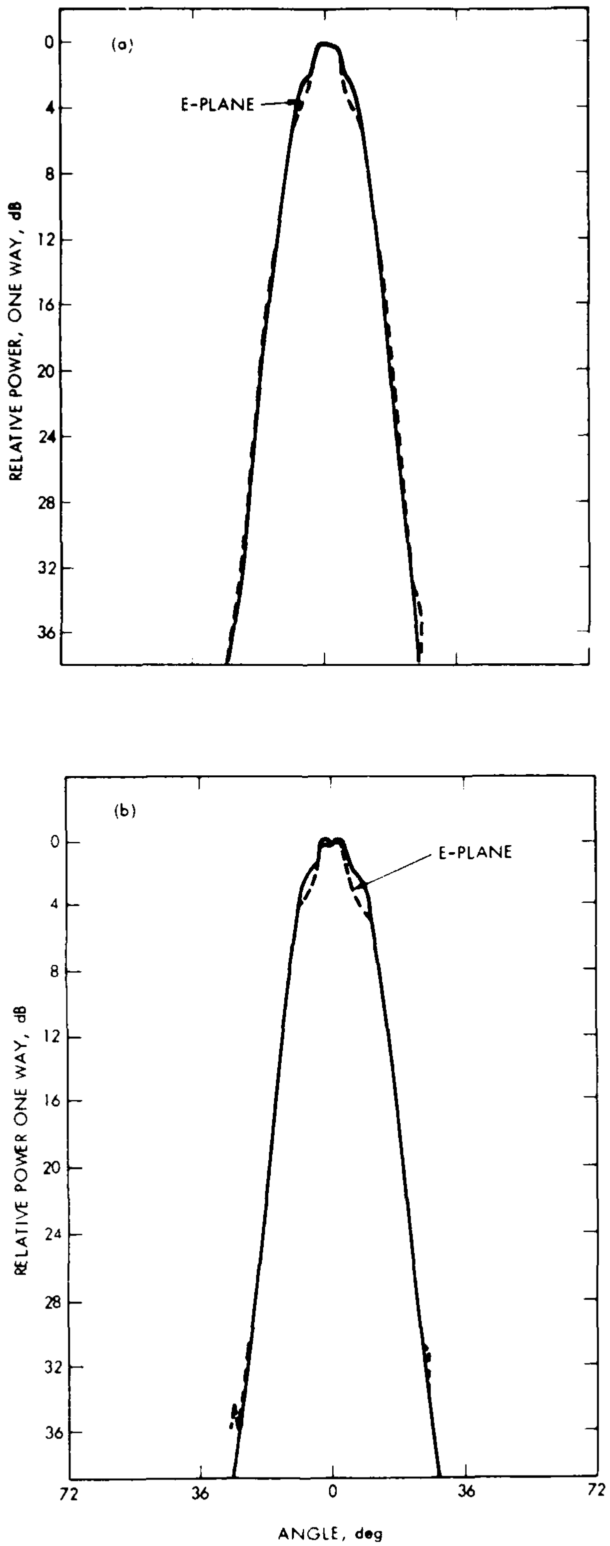

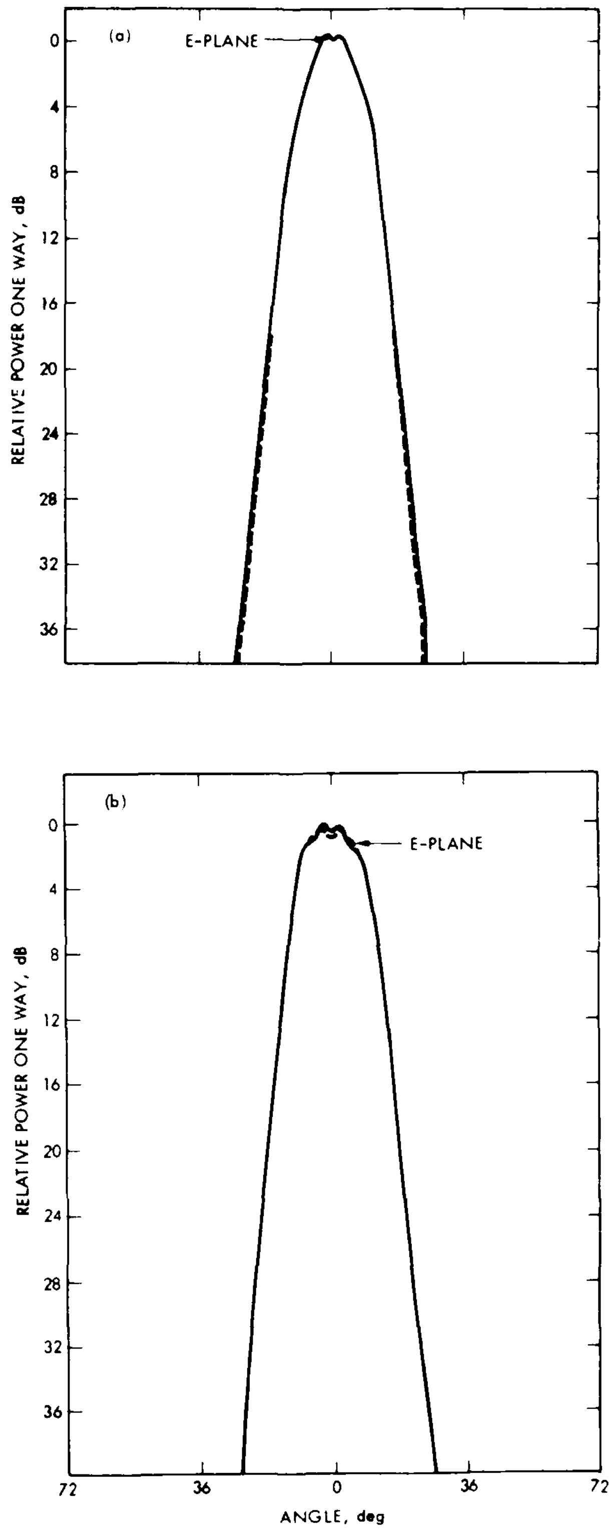

Fig. 6 Radiation patterns at 7.175 GHz, (a) E and H plane patterns of second-generation feedhorn, (b) E and H plane patterns of first-generation feedhor...

Fig. 7 Radiation patterns at 7.800 GHz, (a) E and H plane patterns of second-generation feedhorn, (b) E and H plane patterns of first-generation feedhorn.

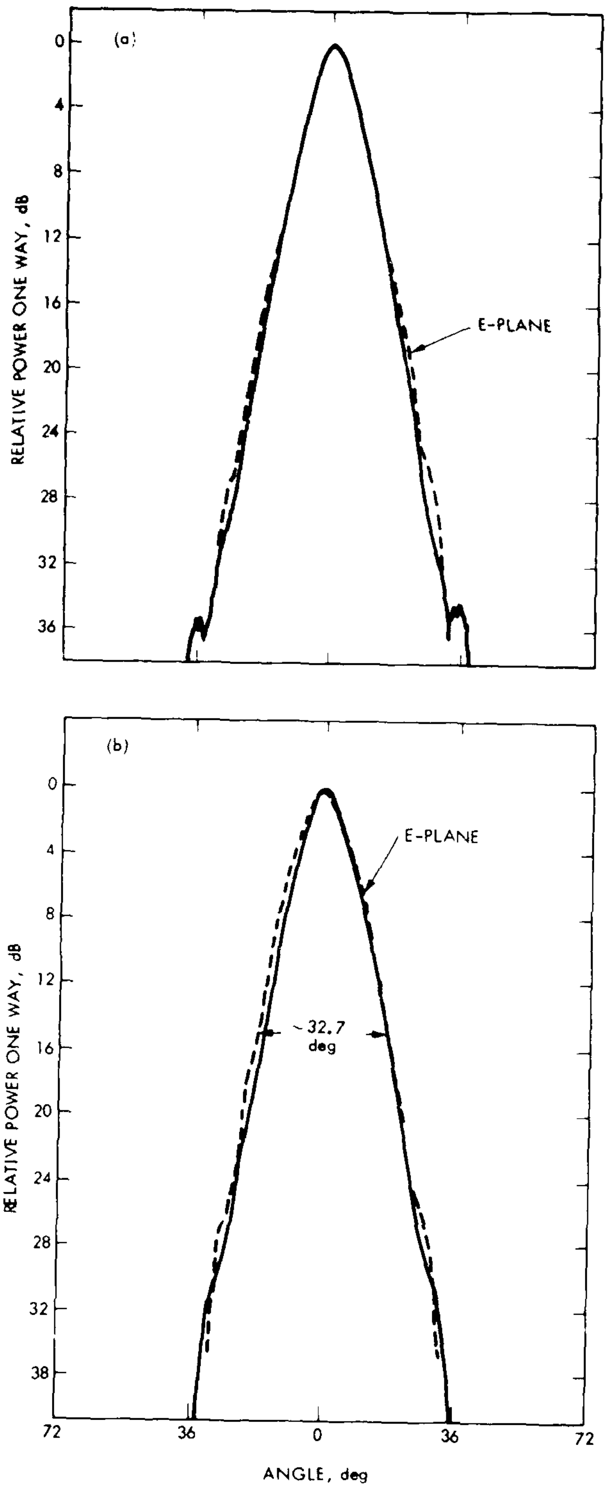

Fig. 8 Radiation patterns at 2.295 GHz, (a) E and H plane patterns of second-generation, (b) E and H plane patterns of first-generation feedhorn.

Early investigations into the causes of X-band moding indicated that the abrupt flare angle change in the throat of the feedhorn could be a source of problems in obtaining the desired X-band bandwidth.

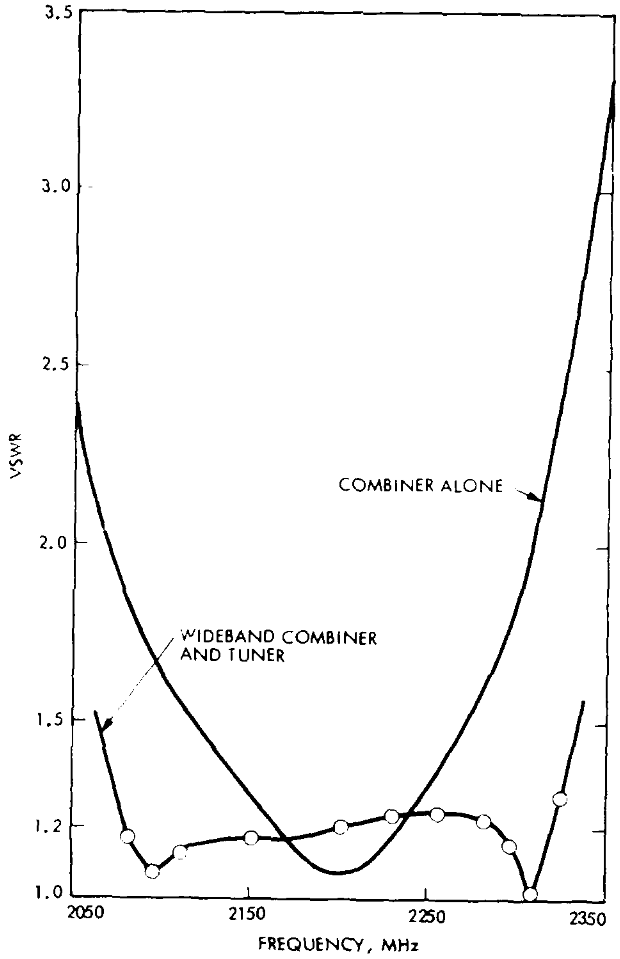

Fig. 9 The VSWR at input to the second-generation combiner and at the tuner input.

It was felt that some improvements could be achieved by building a gradual radial taper from the throat to the 34-degree flare angle and at the same time tapering the groove over the same transition (Fig. 4). Using this method, the best VSWR we could obtain was no better than 1.23:1 over the band (7.1 to 8.6 GHz) with a 1.07:1 VSWR over the receive frequency range of 8.4 to 8.5 GHz. Since a VSWR of 1.23:1 at the transmit band is too high, a pair of irises placed in the WC-137 waveguide input section dropped the transmit band VSWR to 1.05:1. These irises were spaced so as to have little effect on the receive band, which remained at a 1.07:1 VSWR.

A new approach to tapering the depth of the slots is being considered. Instead of linearly tapering the slot depths, we taper them so as to gradually "profile" the hybrid guide wavelength as we move from the throat to the diameter of the S-band input slot. With this idea, as suggested by Dr. A. David Olver at Queen Mary College, England, we hope to be able to remove the tuning irises in the input X-band waveguide and improve the overall performance. This approach holds the promise of minimizing the VSWR as well as any higher order mode effects that may arise in the throat region.

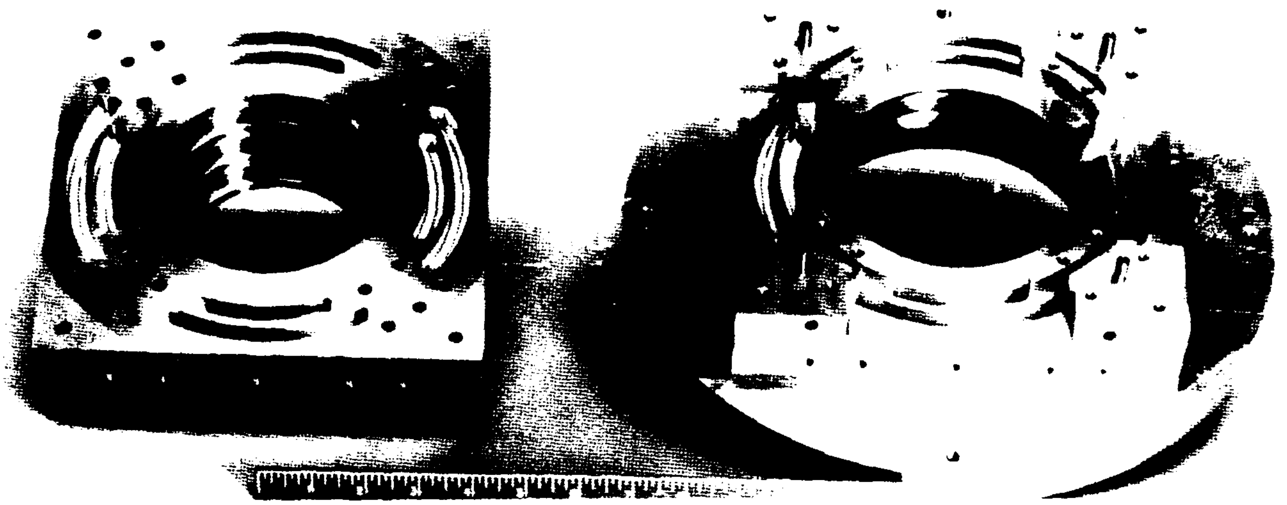

Fig. 10 The Mod II X/S combiner showing S-band ports.

Calculated Performance for DSS 13 Demonstration Application

As in the first-generation case, the measured horn patterns of Figs. 3 and 8 are used in a scattering program with the DSS 13 subreflector (including the vertex plate and outer spillover control flange) to determine the final primary reflector excitation and efficiency for the 26-meter paraboloid at DSS 13, Goldstone, California (Fig. 11).

Two techniques are used to determine these subreflector scattered patterns. In one, the measured pattern is used to determine current excitations on the subreflector and finally the physical optics scattering (Ref. 7). In the other technique, the horn radiation pattern is used to determine its spherical wave coefficients (Ref. 8), and these are then used to determine currents on the subreflector at its unique range from the horn, instead of assuming far field. These techniques agreed to within 0.5 percent, and so the far field approach is used for all calculations herein.

Figure 12 shows the DSS 13 scattered patterns in X- and S-band. One can observe the effect of the S-band designed vertex plate at X-band with a smaller, perhaps modest effect at S-band. Although

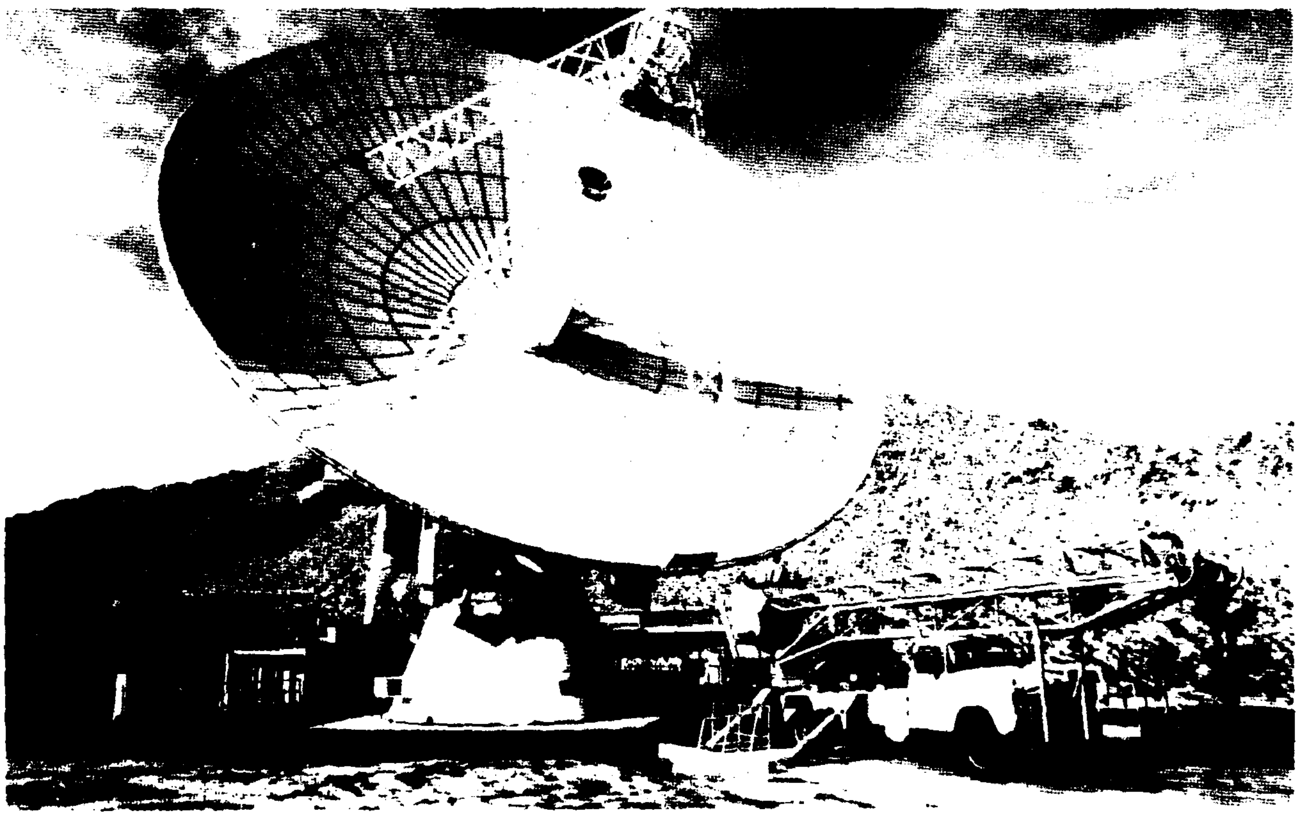

Fig. 11 The X-S common-aperture feedcone, DSS 13, Goldstone, California.

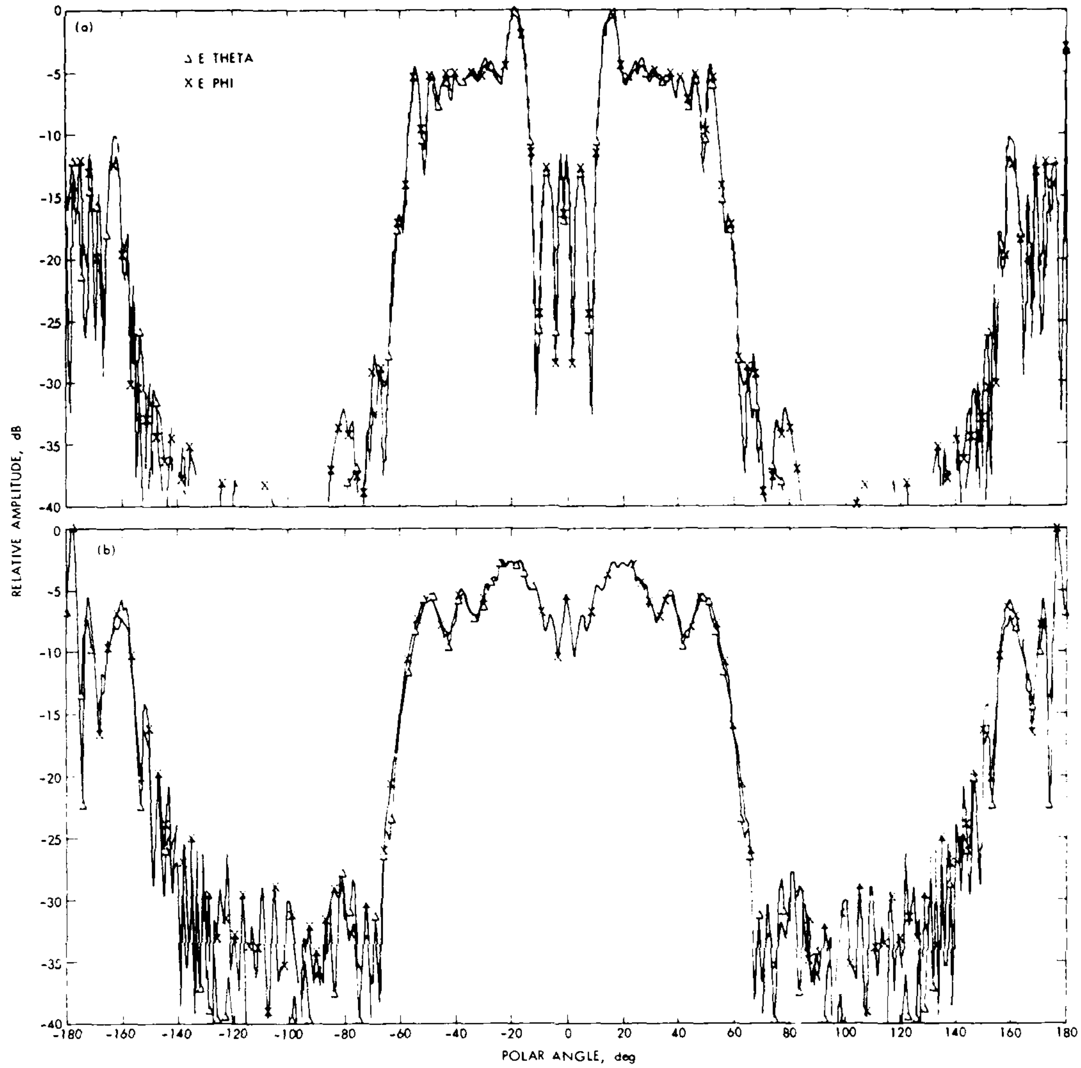

Fig. 12. Subreflector scattering second generation horn from the DSS 13 subreflector: (a) at 8.450 GHz; (b) at 2.295 GHz.

subreflector blockage of radiated power is reduced to essentially zero at X-band, a corresponding X-band loss is noted (relative to S-band) in illumination efficiency and phase efficiency, due to pattern distortions related to the (oversized at X-band) vertex plate.

The efficiencies calculated from these scatter patterns are tabulated in Table 1. The 71.3-percent value at X-band is about 5 percent higher than the heretofore standard DSN (22-dBi gain) feedhorn used, or about +0.3 dB. The efficiencies from the narrowband first-generation horn are included for comparison.

While the performance of the second-generation feedhorn is slightly less than the first (but very acceptable for our demonstration goals using an existing station, DSS 13), it should be pointed out that the especially critical X-band performance can and will be optimized upon other (new) antenna construction. Here the concentricity (therefore minimal cross polarization) in the amplitude patterns gained in the second-generation feedhorn are highly desirable for high-performance (shaped) dual-reflector antenna application.

Planned Capabilities

This new feedcone will transmit 2.11 to 2.12 GHz and receive 2.2 to 2.3 GHz at S-band, and transmit 7.145 to 7.235 GHz and receive 8.2 to 8.6 GHz at X-band. Each function is fully independent and each band diplexed, to allow any combination of functions desired (Fig. 13, Ref. 9).

The S-band waveguide bridge (Fig. 1) design requires the polarization of the S-band signal to be a "hard-wired" function. Right-circular polarization (RCP) will be the one provided. As is standard in JPL/DSN S-band feedcones, the system will consist of a switchable low-noise listen-only path, or a fully diplexed path for simultaneous transmission/reception. The system will have a single S-band maser preamplifier. Because of X-band rejection uncertainty in the new combiner section, a waffle-iron filter is placed in front of the maser for added X-band isolation. This will add 3.4 K to an approximate 24 K (baseline) system noise temperature. It is expected that tests on the antenna will indicate sufficient X-band rejection to warrant its removal. (Ultimately, cryogenic filtering within the amplifiers will be developed.) In the diplexed

Table 1 Illumination and phase efficiencies

	first-generation horn		second-generation horn	
Efficiencies	8.45 GHz X-Band	2.295 GHz S-Band	8.45 GHz X-Band	2.295 GHz S-Band
Forward spillover	0.967	0.887	0.979	0.889
Rear spillover	0.996	0.996	0.997	0.994
Illumination	0.841	0.843	0.811	0.865
Phase	0.898	0.912	0.902	0.925
Blockage	1.000	0.969	1.000	0.972
X-polarization	0.992	0.999	0.993	0.999
	0.721	0.657	0.713	0.686

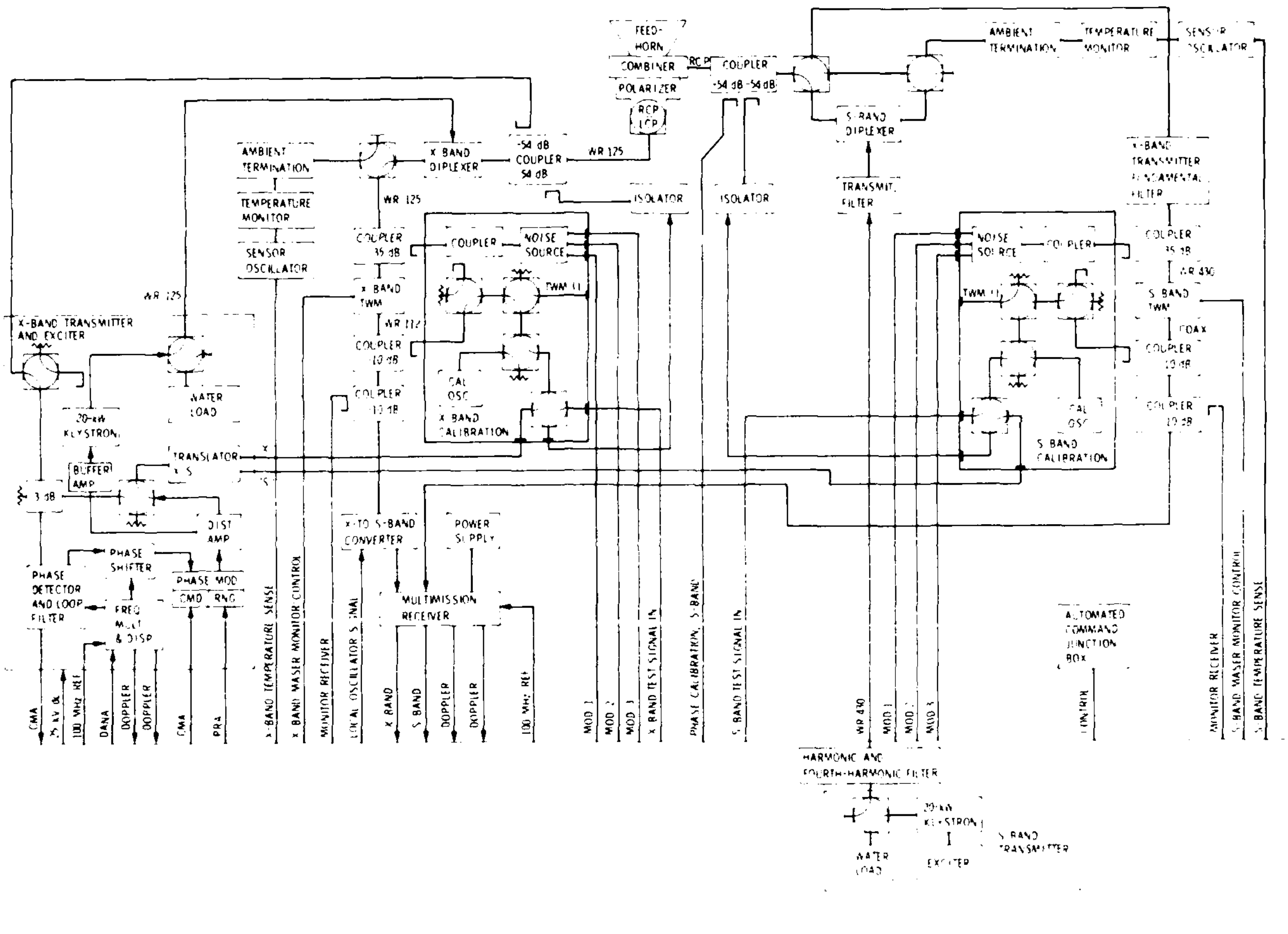

Fig. 13 Second-generation X-S feedcone, block diagram.

position, the additional waveguide and S-band diplexer will add approximately 5 K additional for a total 33 K system noise temperature. These figures are based on performance of the first-generation feedcone and known effects of various S-band components. The output of the S-band maser is fed into the multimission receiver from which down-converted signals are distributed to users. The S-band system is designed to transmit 20-kW, CW, powered by the present transmitter on DSS 13. The S-band transmit filter will reject S-band klystron beam noise that could degrade either the X- or S-band system.

The X-band system will have switchable polarization (LCP or RCP); it will not mirror the S-band switchable low noise listen-only/diplexer receive configuration but will have only the "hard wired" diplexed configuration. This is because the X/X-band diplexer will cover the full proposed receive band (8.2 to 8.6 GHz) with a low noise contribution to the receive system over that band. The receive output of the diplexer is fed directly into a JPL X-band Block II-A maser preamplifier (100 MHz instantaneous bandwidth) that for the present will only monitor the primary receive band of 8.4 to 8.5 GHz. An approximate system noise temperature for that system is 30 K. A listen-only path could conceivably drop this to 27 K or 28 K, but at the same time would degrade the diplexed receive link by 7 K due to an additional waveguide switch and plumbing. This option is of course available if the need ever arises. The output of the X-band maser is fed into an X- to S- downconverter whose S-band output is also fed into the multimission receiver, whose output is distributed to users. A new X-band transmitter system (Refs. 10, 11) located in the feedcone itself will supply the required 20-kW signal for the X-band uplink demonstration.

A dual -54 dB loop coupler at S-band and a dual -54 dB cross-guide coupler at X-band are supplied to monitor the respective transmitter signals, run phase calibration checks, and perform other required microwave tests. Both an X-band and S-band calibration system will be supplied for maser calibration. The calibration system will incorporate noise diodes (three levels), a receive-band signal source, such that the system can be operable as a noise adding radiometer. All microwave switches, the X-band polarizer, and both calibration boxes will be remotely operational. The signal paths, components, and cone interfaces shown in Fig. 13 are those necessary to operate a DSN standard fully operational feedcone. However, in this R&D feedcone some of the X-band transmit functions (doppler extraction, for example) are scheduled for implementation at a later date (Ref. 12).

Planned Feedcone Layout

In keeping with the idea of interchangeability in the consolidation program, the feedcone starts as a standard DSN straight base cone shell to which has been added a 1963 mm cone extension (Fig. 14). The extension was necessary because, since the phase center of the horn moved back into the throat of the horn (as it does in the wide flare angle feedhorn), the aperture and mounting structure of the feedhorn move that much closer to the subreflector. An adapter ring (37.3 mm thick) is used to mount and position the X/S feedhorn/combiner in the cone. A standard DSN X-band polarizer package, consisting of WC-137 spacers, two WC-137 rotary joints, a quarter wave plate type polarizer, and a motor-driven rotating mechanism that orients the polarizer for the desired polarization, is bolted to the bottom of the combiner plate. A new four-section stepped transition from WC-137 to WR-125 and a dual -54 dB cross guide coupler are inserted between the polarizer plate and the WR-125 two-position switch to complete the new polarizer package.

The X/X-band diplexer, a "T" str cture in appearance, is placed with the receive th. ugh arm between the WR-125 two-position switch and the -35 dB calibration coupler on the X-band maser. The transmit arm of the diplexer is joined to the X-band transmitter positioned directly below it on the cone floor by 3660 mm of WR-125 water-cooled waveguide.

The S-band system will employ a waveguide bridge network to feed the combiner (Fig. 1 shows the majority of the waveguide components). The S-band signal is fed through four separate circumferential ports 90 degrees apart on the side of the horn. The phasing at each port is controlled by "equal-length" waveguide runs, two 90-degree hybrids, and a magic "T" (all in the WR-430 waveguide). Coupling the magic "T" to the correct two ports of the two 90-degree hybrids "hard wires" either RCP or LCP operation.

The listen-only low noise path includes a dual -54 dB loop coupler for phase calibration, a WR-430 two-position switch, and approximately 910 mm of WR-430 in front of the waffle-iron filter and S-band maser. In the diplexed mode, the S-band diplexer, 2130 mm of WR-430 and another WR-430 two-position switch are inserted between the first switch and the waffle-iron filter. The second switch is necessary for S-band maser calibration. The S-band transmitter is located outside of the feedcone, below the main reflector in an equipment room.

It was necessary to run some 4270 mm of WR-430 aluminum waveguide between the S-band transmit filter on the floor to the transmitter input part at the top of the S-band diplexer to complete the transmitter waveguide run.

Feedcone Components

This feedcone is basically two separate systems sharing a common feedhorn aperture. Except for the X/S feedhorn/combiner, no new S-band hardware was developed. Much the same thing can be said for the X-band system, except for the aforementioned X/X-band diplexer and the broadband polarizer. The following are excerpts of the more pertinent characteristic of each.

X/X-Band Diplexer

The original analysis and design was done by W. G. Erlinger of Wenzel/Erlinger Associates (Ref. 13). This design consists of three separate components: a center "T" combiner section and two E-plane cavity-type band stop filters (BSF), one each in cascade in the transmit and receive arms of the diplexer for added isolation (Fig. 15).

The "T" combiner section consists of a high-pass filter in the receive arm designed to have a cutoff frequency of 7.44 GHz. This cutoff frequency was computed by minimizing the ratio of dissipation loss per unit length at 8.4 GHz to rejection per unit length at 7.235 GHz. Its length is determined by the required rejection. The transmit arm is realized with an N = 7 Chebyshev bandpass filter, which was necessary to provide approximately 40 dB of transmitter isolation at the receive frequency.

The "T" section combiner was electroformed (copper electrodeposited on an aluminum mandrel), while the two BSFs were constructed of three flat plates, all machined separately, and then pinned and bolted together to give a section of WR-125 waveguide with inductively coupled "E" plane cavities.

A two-cavity BSF used in the receive line was originally designed for 40-dB rejection of the transmit band (7.145 to 7.235 GMHz); a four-cavity BSF used for the transmit line has better than 70-dB rejection of 8.4 to 8.5 GHz. Both prototypes showed signs of moding and overcoupling between the cavities. The design goal of 40-dB isolation for the two-cavity BSF was achieved by respacing the two cavities. However, respacing was not possible with the four-cavity BSF. Here it was necessary to solder a periodic "fish bone" type filter structure

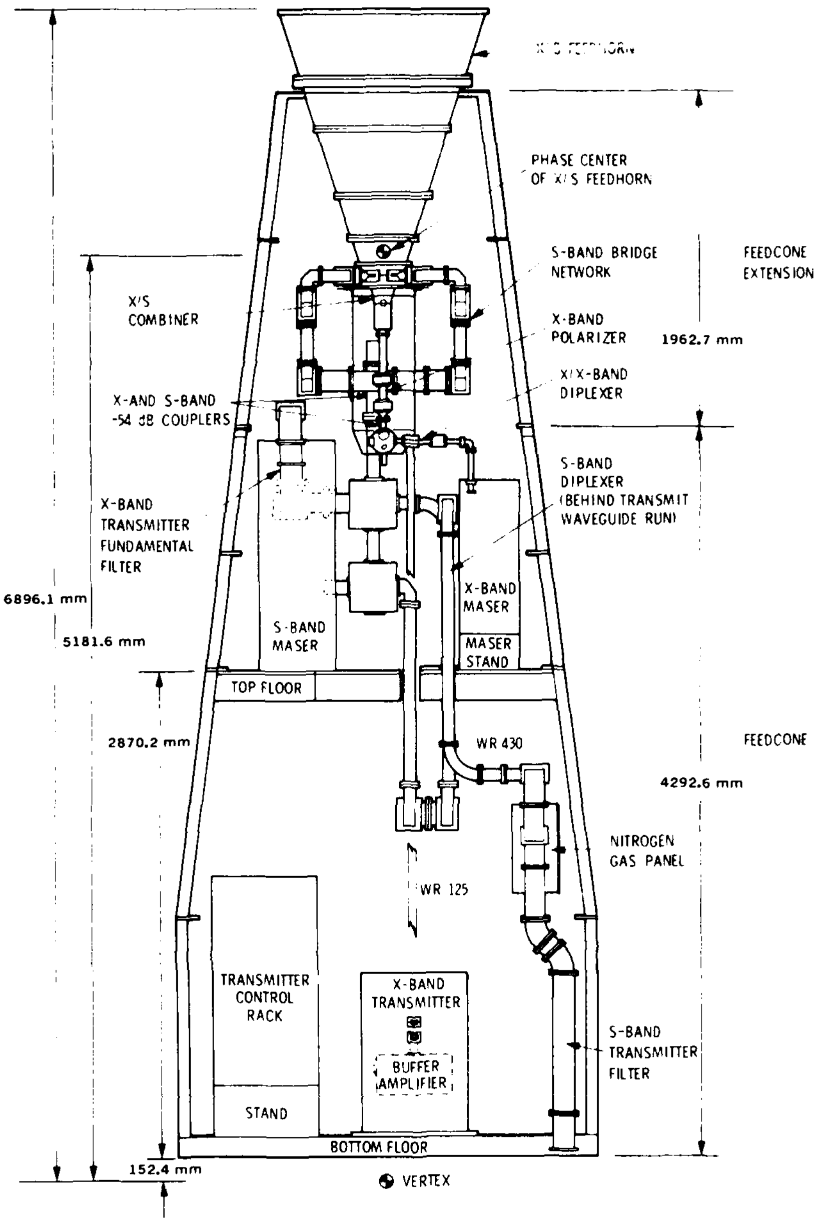

Fig. 14 Second-generation X-S feedcone, general layout.

(0.318 mm high) to the broad wall opposite the four cavities in the filter. This structure effectively controlled the mode coupling in the filter, was well matched, and added little to the dissipation of the network.

The transmit arm of the "T" was tuned in conjunction with the four-cavity BSF, and as such must be used as a single unit. However, the receive arm of the "T" and the two-cavity BSF were matched independently and are meant to be used together or separately depending on the desired isolation. The high-pass receive arm has >33 dB of rejection of the 7.145 to 7.235 GHz band, and the two-cavity BSF added some 40 dB more. The four-cavity filter has over 70 dB of isolation from 8.4 to 8.5 GHz.

Measured performance of the receive arm is as follows:

VSWR (8.2 to 8.6 GHz):	<1.17:1
(8.40 to 8.6 GHz):	<1.07:1
Dissipative loss (combined):	<0.05 dB (<3.0 K)
Isolation/rejection (7.145 to 7.245 GHz):	>73 dB

Measured performance of the transmit arm is as follows:

VSWR: (7.145 to 7.245 MHz)	<1.07:1
Dissipative loss:	<0.08 dB
Isolation/rejection (8.4 to 8.5 GHz):	>110 dB

WC-137 Broadband Polarizer

Our standard polarizer converts a linearly polarized $TE°_{11}$ mode, generated from rectangular TE_{10} by the WR-125 four-step transition, into a circularly

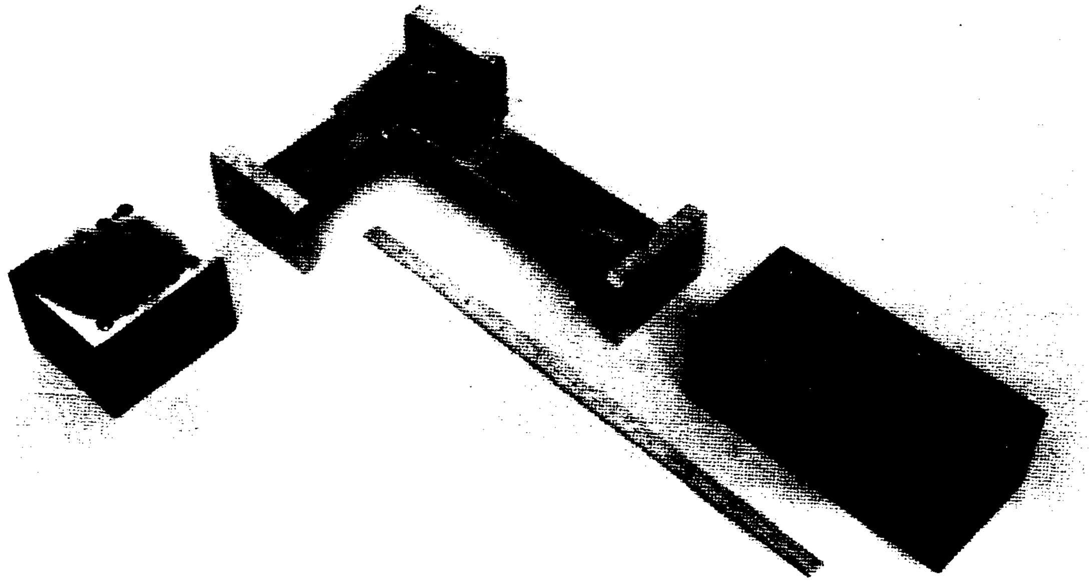

Fig. 15 The X/X-band displexer showing the center "T" section and the two band stop filter sections.

polarized TE°_{11} mode by "quarter-wave plate" action. Because of the wide separation of the transmit and receive bands, the performance over this extended range of the quarter-wave plate is unacceptable and will be replaced with a modified iris-type polarizer (Fig. 16). Individually, the modified irises are thin, rectangular and tooth-shaped. They are used in pairs, placed symmetrically in the guide, and give the effect of two ridges in the round guide. When cascaded with other "tooth" iris pairs of various heights (constant width) both a good match and a phase differential of 90 degrees between the orthogonal waveguide orientation over reasonably large bandwidth are possible. The 90-degree phase differential will give a perfectly circular polarization. We are interested in a broad band (7.0 MHz to 9.0 GHz) but in a waveguide size (WC-137 = 34.77 mm diameter) which will not only support the TE_{11} mode (λ cutoff 5.052 GHz) but will also support the TM_{01} (λ cutoff = 6.604 GHz). Normally there is one optimum-diameter waveguide that will give the broadband response over the frequencies desired. The added degree of freedom resulting from the ability to pick an optimum width iris enabled us to use the standard DSN round waveguide size and still get the desired response. Testing of the modified iris polarizer has shown no adverse effects due to a possible moding problem. The polarizer is 104.5 mm long, uses nine pairs of irises, and was machined from a solid block of copper. The heights of the irises are cosine tapered, for match purposes. The measured performance of the broadband polarizer (7.0 to 9.0 GHz) is: VSWR $< 1.07:1$, and ellipticity < 0.5 dB.

Conclusions

A new Cassegrain feedcone assembly designated the XSU feedcone (for common aperture X- and S-band uplink is being built to replace the previous XSR (for common aperture X- and S-receive only) feedcone presently in use at DSS 13 (Fig. 16). This feedcone is the prototype for six wideband listen-only (SXC designated feedcone) (convertible to XSU) to be implemented throughout the operating DSN network.

Following fabrication and installation, testing will take place at the Microwave Test Facility at DSS 13, Goldstone, California, and will measure system noise, power handling capabilities, and microwave component performance.

This feedcone greatly extends the state of the art in DSN performance and will enhance DSN capabilities in the future.

Acknowledgment

The authors wish to thank Dan Bathker, Harry Reilly, Dave Nixon, Rod Mitchell, Tom Plummer, and Max Rodarte, without whose help none of this could have been possible. The support of the NASA OSTDS is acknowledged.

The research described in this paper was carried out by the Jet Propulsion Laboratory, California Institute of Technology, under contract with the National Aeronautics and Space Administration.

References

1. W. F. Williams and J. R. Withington, "A Common Aperture S- and X-Band Feed for the Deep Space Network," Proceedings of the 1979 Antenna Applications Symposium, University of Illinois, Urbana-Champaign, Illinois, Sept. 26-28, 1979.

2. E. J. Jeuken and V. J. Vokurka, "Multi-Frequency Band Corrugated Conical Horn Antenna," 1973 European Microwave Conference Proceedings, Vol. 2, Sept. 4-7, 1973, Brussels University, Brussels, Belgium.

3. Seymour Cohn Associates, Brentwood, Calif.

4. W. F. Williams, "A Prototype DSN X-S Band Feed DSS 13 Application Status (Second Report)," DSN Progress Report 42-47, Jet Propulsion Laboratory, Pasadena, Calif., July-Aug. 1978.

Fig. 16 The modified iris X-band broadband polarizer in 34.77 mm diameter waveguide (WC-137).

5. W. F. Williams and H. Reilly, "A Prototype DSN X/S-Band Feed: DSS 13 Application Status (Fourth Report)," TDA Progress Report 42-60, September and October 1980, Jet Propulsion Laboratory, Pasadena, Calif.

6. B. M. Thomas, "Design of Corrugated Horns," IEEE Trans. Ant. Prop., Vol. AP-26, No. 2, March 1978.

7. W. V. T. Rusch, Scattering of an Arbitrary Spherical Wave by An Arbitrary Surface of Revolution, Technical Report 32-979, Vol. 1, Jet Propulsion Laboratory, Pasadena, Calif., pp. 31-39, April 1967.

8. Arthur C. Ludwig, "Near-Field Far-Field Transformations Using Spherical Wave Expansions," IEEE Trans. Ant. Prop., Vol. AP-19, March 1971, pp. 214-220.

9. J. R. Withington, "Second-Generation X/S Feedcone: Capabilities, Layout and Components," TDA Progress Report 42-63, March and April 1981, Jet Propulsion Laboratory, Pasadena, Calif.

10. R. Hartop, C. Johns, and R. Kolbly, "X-Band Uplink Ground Systems Development," DSN Progress Report 42-56, March and April 1980, Jet Propulsion Laboratory, Pasadena, Calif.

11. R. B. Kolbly, "20-KW X-Band Uplink Transmitter Development," TDA Progress Report 42-60, September and October 1980, Jet Propulsion Laboratory, Pasadena, Calif.

12. T. Komarek and J. Meeker (Editors), X-Band Uplink Technology Demonstration, Document 900-944, Jet Propulsion Laboratory, Pasadena, Calif., March 1, 1981 (an internal document).

13. Wenzel/Erlinger Associates, Woodland Hills, Calif.

TECHNIQUES FOR LOW SIDELOBE, HIGH EFFICIENCY OFFSET DUAL REFLECTOR ANTENNAS

C. J. Sletten
Solar Energy Technology, Inc.
Bedford, Massachusetts

ABSTRACT: Ideal paraboloidal dish illuminations for -30 to -40 dB sidelobe levels with 70 to 80% aperture efficiencies can be realized using either Cassegrain or ellipsoidal offset subreflectors fed by conical corrugated horns. All antennas are optimally tilted by the Japanese criteria for symmetric beams, low crosspolarization, and no aperture blocking. New techniques for computing the horn near-field patterns on the subreflectors and for correcting the phase center errors of the horn pattern by shaping the subreflector surface are reported.

For generating or scanning multibeams by horn motion the best focal surfaces of the offset dual reflector systems are computed for best azimuth, best elevation and best compromise patterns. These dual reflector systems with high magnifications can produce multibeams with -30 dB sidelobe levels over more than $\pm$ 8^{o} beamwidth intervals. Techniques for computing the diffraction patterns for scanned beams are described. Also, the effects of dish aperture diffraction on pattern bandwidth are presented.

A demonstration model antenna with 8 ft. circular aperture operating in the 12 gHz satellite communications band is being designed and tested by Chu Associates, Inc. based on the techniques presented in this paper. A 12^{o} conical corrugated horn has been constructed to illuminate a shaped Gregorian subreflector about 30" in diameter. This paper will stress new and practical analytical design and present available results.

INTRODUCTION

In sat ellite communications for both ground and satellite borne systems, antennas with very low sidelobe levels and high aperture efficiencies are in demand to reduce microwave interference due to traffic congestion to and from the geostationary satellite orbit. Multiple beam antennas with

---

This work is sponsored by NASA Lewis, Cleveland, Ohio, under Contract NAS 3-22343 with Chu Associates, Inc., Littleton, Mass., with subcontract to Solar Energy Technology, Inc., Bedford, Mass.

sidelobes 30 to 40 dB below main beam peaks are required with aperture efficiencies approaching 80%. Multibeam patterns with these characteristics, scanned more than 4 beamwidths from the on-axis beam, are obtainable with tecnniques presented in this paper. Such limited scanned antennas have applications to military and commercial radars as well as to space communications.

Offset dual reflector antennas[1] (see FIG. 1) designed according to Japanese tilt criteria offer attractive solutions because optimum aperture distributions can be realized without aperture blocking. Also symmetrical beams with very low cross-polarization (and low VSWRs) are achieved. Wide-angle multibeams can be generated because of the high magnifications of dual reflector systems. Conical corrugated horn design and subreflector shaping are used to control the main dish amplitude and phase distributions.

The model antenna chosen to demonstrate the stringent NASA requirements on ground based terminals has the following dimensions and characteristics:

Main Reflector: Offset paraboloidal section of circular aperture 96 inches in diameter; center point 62" above paraboloid axis; focal length 70".

Gregorian Subreflector: Nearly ellipsoidal in shape. Eccentricity 0.538; axis tilt from paraboloid axis, 5.14°; approximate diameter 30"; foci separated 35".

Corrugated Conical Horn: Semiflare angle 12°, length 30".

Antenna Characteristics at 12 gHz (calculated)

$B.W._{\frac{1}{2}\ pwr} = 3/4^{\circ}$ Gain = 48.5 dB_i

Sidelobe levels 1st and 2nd <30 dB others <40 dB

Antenna aperture efficiency = approx. 70%

ANTENNA DESIGN TECHNIQUES

The offset dual reflector configuration was optimized using formulas given in Ref. 1. A Gregorian subreflector was selected over a Cassegrain because lower sidelobes can be obtained without subreflector shaping. The illuminated section of the subreflector has a diameter greater than 15λ. The magnification and f/D are appropriate to scanning a 3° cone by feed horn motion. 100% of the 8 ft. diameter dish is used for all beams.

IDEAL APERTURE DISTRIBUTIONS

The next step in the design is to determine main reflector amplitude distributions on the circular paraboloidal aperture (the aperture phase distribution is assumed to be plane) to achieve -30 dB to -40 dB sidelobe levels with 70% to 80% aperture efficiencies. For circular apertures with continuous field distributions, there is no "best" distribution in the Dolph-Tchebyscheff sense but fortunately "ideal" amplitude distributions derived from Case studies by SET, Inc. and others[2,3] exist which produce beamwidth vs sidelobe characteristics summarized in TABLE I. The important result from these studies is that when the best theoretical data available is compared with Case 2A, computed pattern for 30", 12^{o} flare horn, the dish aperture distribution obtained with the Japanese optimized Gregorian antenna produces the near ideal antenna patterns required by NASA specifications. In FIG. 2, this diffraction pattern calculated from the corrugated conical horn near-field pattern on the subreflector transformed to the main dish aperture is shown. A Fourier transform of the aperture distribution on the 8 ft. dish produces this pattern assuming no aperture phase errors. Case 2B, TABLE I, gives pattern characteristics when phase errors are included.

CORRUGATED CONICAL HORN DESIGN

The analytical procedure of Clarricoats[4], et al, was extended to obtain the near-field patterns of the corrugated conical horn in the region of the subreflector. The important finding in this research work is that on long conical horns with semiflare angles less than 20^{o} the length of the horn (the distance from the horn aperture to the subreflector surface) can be used to control the edge illumination taper on the subreflector. The horn amplitude pattern dependence on horn length is given in FIG. 3. By computing the horn patterns for different separation distances to the subreflector several of the nearly ideal dish aperture distributions of TABLE I can be obtained. Small flare corrugated conical horns have small phase errors (see FIG. 4) however, that can be corrected by subreflector shaping.

A corrugated conical horn approximately 30 inches long with a semiflare angle of 12^{o} was designed based on theory reported here and constructed by Chu Associates for best operation in the 12 gHz band. Experimental measurements of near-field amplitude and phase approximated closely the computed patterns of FIGS. 3 and 4.

SUBREFLECTOR DESIGN

Unfortunately conical corrugated horns with semiflare angles of less than 25^{o} do not have a fixed center of phase point but the center of phase generally moves forward with increasing polar angle, θ, of the horn pattern, depending too on the radial distance, R, from the horn apex. The phase pattern for the 30", 12° conical horn at 47.5" from the horn apex is shown in FIG. 4. On a Gregorian subreflector antenna these phase distribution departures from a true spherical wavefront cause a greater amplitude taper (due to ray direction near edge of horn pattern) on the main dish, producing lower aperture efficiencies and sometimes lower sidelobes (if phase errors are small). A numerical method of subreflector shaping was developed that references the near-field rays from the horn to the paraboloid focus, F_o of FIG. 1. For the horn phase errors of FIG. 4, the shaped subreflector surface varies from that of a true ellipsoid only near the edge of the principal pattern of the horn which produces the z-axis, $\hat{z}$ direction dish pattern. Even at the edge of this central illuminated section of the subreflector, the surface shaping to correct the horn phase errors is only a few tenths of an inch (departure from an ellipsoid).

The computer technique for phase correction by subreflector shaping is similar to the numerical technique reported in Reference 1. The illuminated subreflector aperture should be at least 15 wavelengths in diameter to minimized diffraction caused crosspolarization. The subreflector area was enlarged from that required to produce the phase corrected principal beam with ellipsoidal borders to provide beam scanning out to $\pm$ 3° by horn motion. This border enlarges the subreflector diameter to about 30" and also reduces the small (forward) spillover associated with 15 to 20 dB horn tapers on the subreflector. The phase correction is only fully effective on the principal antenna pattern.

FOCAL SURFACES FOR BEAM SCANNING

A new method for computing the best focal surfaces for locating sources to feed reflector antennas was developed to exploit the wide angle characteristics of high magnification dual reflector antennas. Both the location of a conical horn vertex (center of phase) and the orientation of the horn axis can be determined for the best scanning patterns. The best focal surfaces for azimuth-plane, elevation-plane, and compromise-plane patterns are found by a ray tracing technique that maps a received congruence of rays incident on the dish aperture onto a flat "screen" oriented at right angles to the horn axis. By mathematically focusing (translating) this screen the sharpest traces of the dish edge rays can be displayed. This optical method gives useful information about the beam pointing direction and the magnitude of scanning aberrations. In addition, an aperture diffraction method was then developed to compute sidelobes and beamwidths on scanned beams. In FIG. 5 a diffraction pattern is shown for the 8 ft.

antenna scanned 3° from the $\hat{z}$ axis by conical horn repositioning. These results confirm that the optical raytracing technique gives the correct focal surfaces for best azimuth and elevation plane patterns and that these patterns have acceptable gains and sidelobes at 3° scanning of the $3/4^{\circ}$ beam pattern.

Radiation patterns will vary slightly with frequency due primarily to diffraction from the main aperture. These effects were studied by computing the near-field patterns of the circular paraboloid section in the region of the subreflector surface. Based on these studies, it is expected that the model antenna will perform satisfactorily in both the 12 and 14 gHz satellite communications bands.

REFERENCES

1. C. J. Sletten, "Numerical Technique for Shaping Reflecting Surfaces to Synthesize Antenna Patterns." Proc. IEEE, Vol. 69, No. 3, March 1981, pp 392-393.

2. V. Kouznetov, "Sidelobe Reduction in Circular Aperture Arrays." 1978 European Antenna Conf. Dig. (London, England)

3. P. Jacqinot and B Roizen-Dossier, "Apodisation." Progress in Optics, E. Wolf, Vol. III, 1964, North Holland

4. P. J. B. Clarricoats and P. K. Soha, "Propagation and Radiation Behaviour of Corrugated Feeds Parts I and II." Proc. IEEE, Vol. 118, pp 1167-1176, Sept. 1971.

ILLUSTRATIONS

For: 1981 Antenna Applications Symposium, Monticello, Illinois

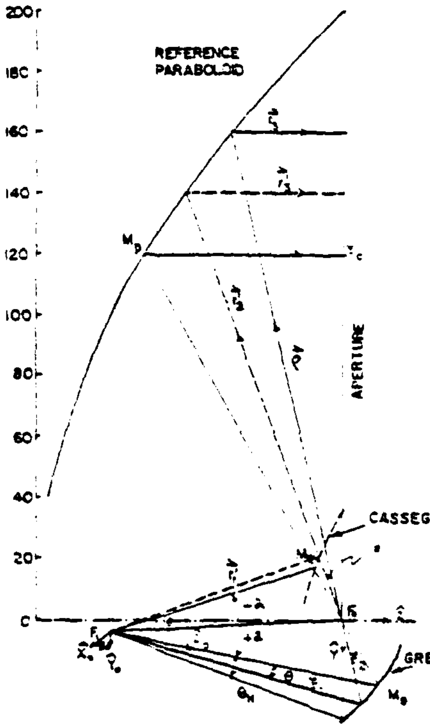

FIG.1 OFFSET DUAL REFLECTOR GEOMETRY FOR REFERENCE SURFACES

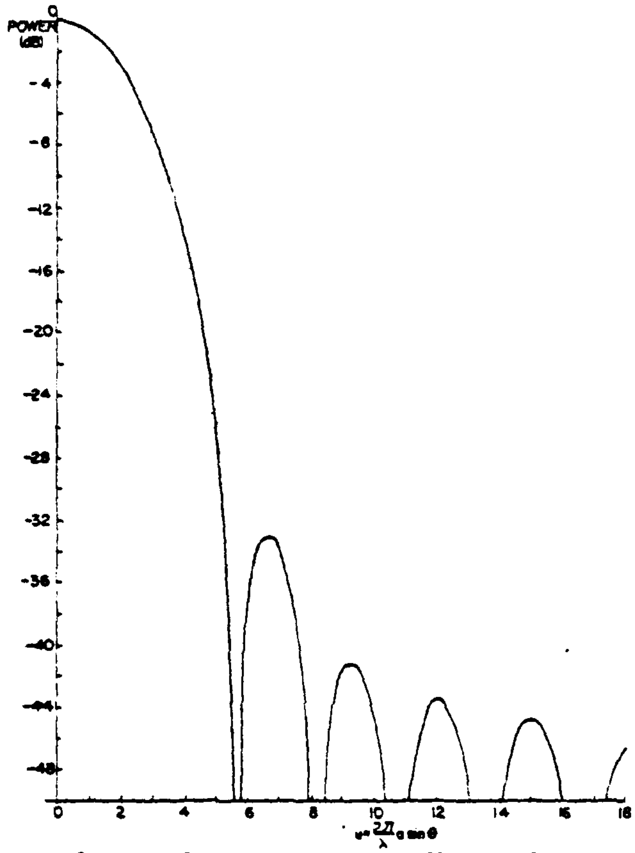

FIG. 2 DIFFRACTION OF CIRCULAR APERTURE ILLUMINATED BY A 30 INCH,12° CORRUGATED HORN– NO PHASE ERROR

HORN PATTERN
POWER TAPERS

Length	Edge power
30"	- 19.98 dB
27"	- 18.09
25"	- 17.26
20"	- 16.77

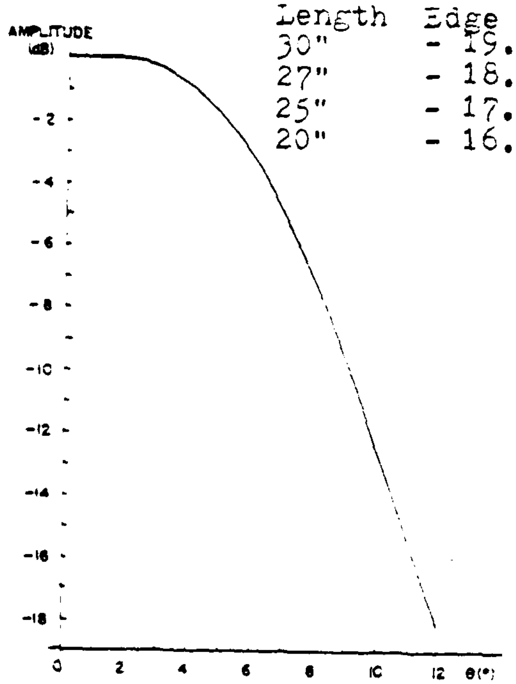

FIG. 3 AMPLITUDE FUNCTION OF 27 INCH,12° CORUGATED HORN

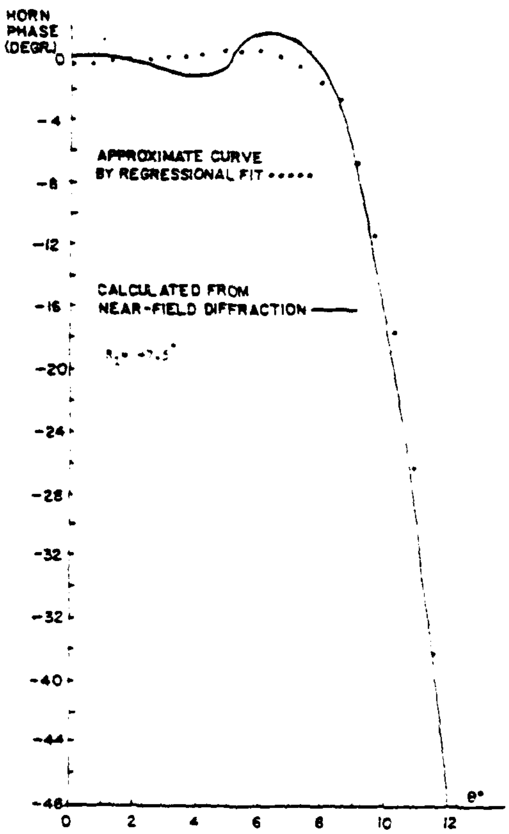

FIG.4 CONICAL HORN PHASE CURVE

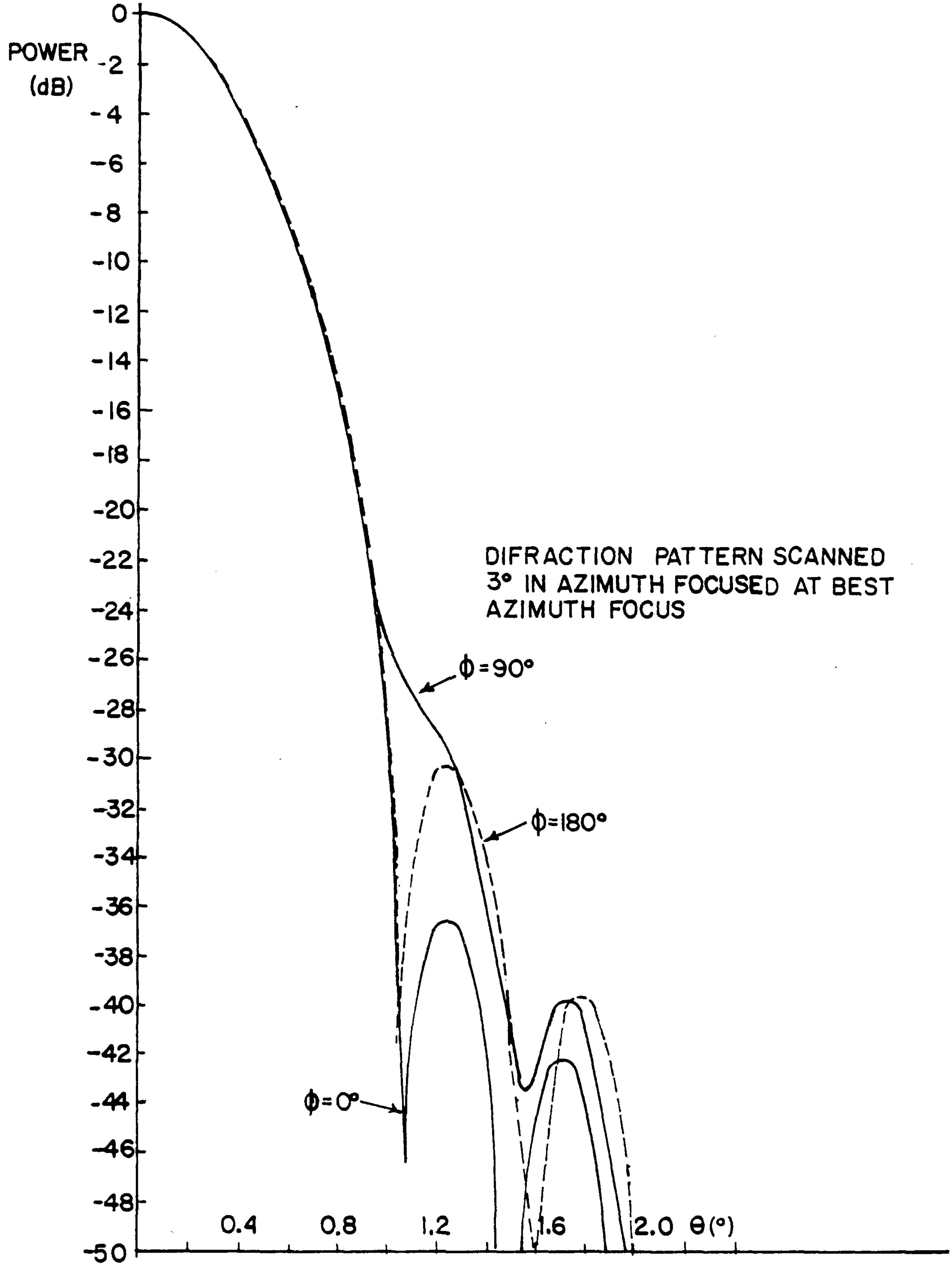
POWER (dB)
0
-2
-4
-6
-8
-10
-12
-14
-16
-18
-20
-22
-24
-26
-28
-30
-32
-34
-36
-38
-40
-42
-44
-46
-48
-50
0.4
0.8
1.2
1.6
2.0
θ(°)
DIFRACTION PATTERN SCANNED 3° IN AZIMUTH FOCUSED AT BEST AZIMUTH FOCUS
ϕ=90°
ϕ=180°
ϕ=0°

FIG.5

TABLE I

APERTURE EFFICIENCY, HALF-POWER POINT, AND SIDELOBES FOR DIFFERENT CIRCULAR APERTURE ILLUMINATION FUNCTIONS

Case	Apt Eff	BW 1/2 Pwr	u_1	S_1	u_2	S_2	u_3	S_3	u_4	S_4	u_5	S_5
(1)	1.00	1.62	5.12	-17.57	8.42	-23.81	11.62	-27.96	14.80	-31.08	17.96	-33.60
(2A)	0.71	2.04	6.66	-33.22	9.33	-41.35	12.08	-43.67	15.07	-44.88	18.17	-46.79
(2B)	0.69	2.06	6.97	-30.96	-	-	11.66	-37.59	15.12	-43.71	18.21	-46.48
(3A)	0.74	2.00	6.51	-34.02	9.06	-39.78	11.86	-41.02	14.89	-42.72	18.02	-44.52
(3B)	0.68	2.08	6.95	-41.31	9.13	-44.99	11.81	-43.46	14.87	-44.67	18.00	-46.35
(4A)	0.81	1.88	5.97	-26.71	8.91	-32.45	11.97	-36.42	15.07	-39.48	18.19	-41.96
(4B)	0.71	2.06	6.72	-34.68	9.35	-39.79	12.26	-43.01	15.32	-45.83	18.38	-48.25
(5A)	0.88	1.82	5.71	-30.77	8.35	-28.38	11.58	-31.75	14.77	-34.71	18.00	-37.18
(5B)	0.84	1.86	5.85	-35.57	8.34	-29.35	11.57	-32.51	14.77	-35.43	17.94	-37.87
(5C)	0.80	1.90	6.03	-45.48	8.31	-30.50	11.55	-33.39	14.76	-36.26	17.94	-38.68
(6A)	0.81	1.91	6.10	-30.01	8.89	-33.18	11.93	-36.92	15.03	-39.88	18.15	-42.31
(6B)	0.71	2.03	6.63	-40.93	8.96	-36.94	12.03	-40.52	15.11	-43.36	18.22	-45.73
(7A)	0.80	1.92	6.18	-30.28	8.79	-38.42	11.65	-35.72	14.84	-39.58	17.97	-40.96
(7B)	0.80	1.92	6.14	-31.83	8.70	-35.95	11.65	-35.49	14.83	-39.03	17.97	-40.55
(7C)	0.80	1.91	6.11	-33.21	8.62	-34.06	11.66	-35.35	14.82	-38.40	17.97	-40.29

$u = \frac{2\pi}{\lambda} a \sin \theta$ S = Sidelobe dB from Beam Peak

NEW ADVANCES IN WIDE BAND DUAL POLARIZED ANTENNA ELEMENTS FOR EW APPLICATIONS

By: George Monser

Raytheon Company
Electromagnetic Systems Division
6380 Hollister Avenue
Goleta, California 93117

7-31-81

1981 ANTENNA APPLICATIONS
SYMPOSIUM
23-25 Sept 1981
Allerton Park
Monticello, Illinois

NEW ADVANCES IN WIDE BAND DUAL POLARIZATION ANTENNA ELEMENTS FOR EW APPLICATIONS

SUMMARY

This paper describes the performance achievements in the design of wide band dual-polarized array element(s) intended for EW applications. Gain tracking, within 4 dB, phase tracking, within 35°, and active match (VSWR) near boresight under 2:1, were realized. Element efficiency, i.e., Gain/Directivity, was typically greater than 75 percent. Parametric design requirements are summarized.

1.0 INTRODUCTION

This paper reports the results of a company-funded effort directed toward achieving multi-octave integrated, dual-polarized, array element(s) for EW array applications.

A requirement existed for wideband, dual-polarized arrays with the following properties:

(1) Greater than 2 octaves of bandwidth with continuous coverage.

(2) Amplitude tracking between orthogonally polarized corresponding elements within the array within ± 3 dB over the band.

(3) Phase tracking between orthogonally polarized corresponding elements within the array within $\pm 20°$ over the band.

(4) Array coverage: 120° (minimum).

(5) Orthogonal coverage: 30° (minimum).

(6) Element efficiency: 75% (minimum).

(7) Small package, ruggedized for tactical airborne applications.

(8) Element power handling: 100 watts (cw).

(9) Cross-polarized content: -20 dB or lower.

In addition, for maximum utility in the selection and application of polarization techniques, each array element should provide independent, orthogonal polarizations within the element.

2.0 STATEMENT OF THE PROBLEM/SOLUTION

To solve the problem, it was first necessary to find two compatible orthogonal array elements with design freedom for providing necessary aperture tapers for similar spatial coverage and gain. For maximum efficiency, uniform illumination was chosen for the array-plane dimension. For the orthogonal plane, the illumination taper was empirically adjusted. By holding circuit losses within the elements, within limits, gain and gain tracking was assured.

The unique requirement for independent polarizations and maximum utility in this respect necessitated the selection of array elements with phase centers close to the aperture plane. Elements exhibiting minimum phase center deviations and/or axial tracking over the band were a must. Similar dispersion characteristics from the input to the aperture plane were required.

For one polarization, TE_{10}, waveguide radiation was provided while for the other polarization, TEM stripline and notch radiation were provided. It had been previously verified that the phase centers for these elements would track or hold constant within the required limits over the band.

3.0 ACHIEVEMENTS

The array developed to satisfy the requirements is shown in the photograph as Figure 1. Observe that eight elements were used for developing polarization parallel to the array, and nine elements were used for developing polarization orthogonal to the array. By this arrangement, the array phase centers for both polarizations were coincident even though the orthogonal elements were offset by half an element width.

16382

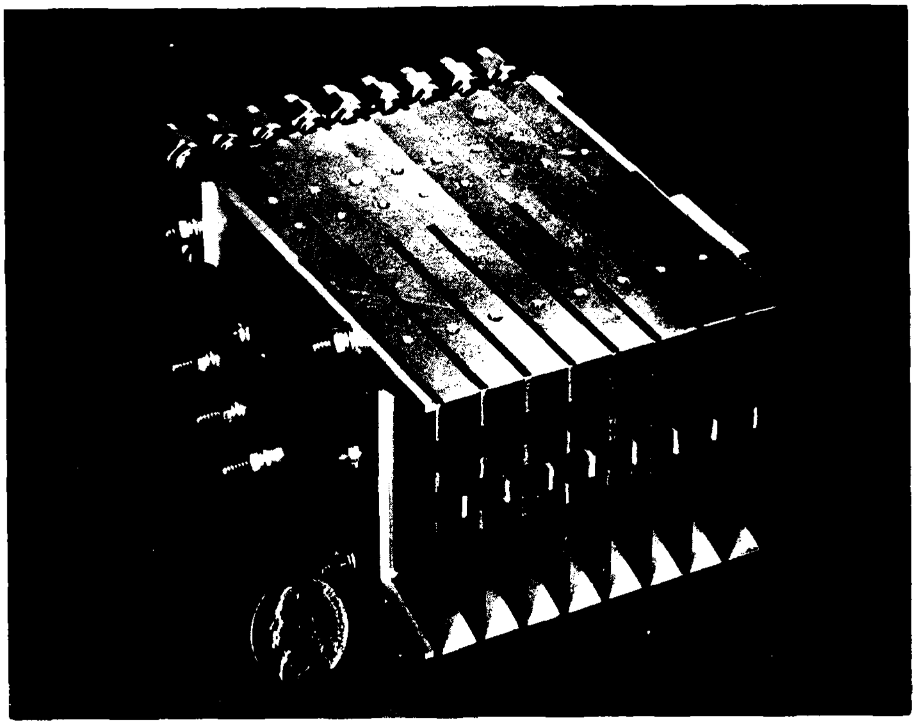

Figure 1. Wide-Band Dual Polarized Array

In Figure 2, gain tracking for several orthogonally polarized elements near the center of the array is presented. Amplitude tracking is well within the ± 3 dB limit over most of the band.

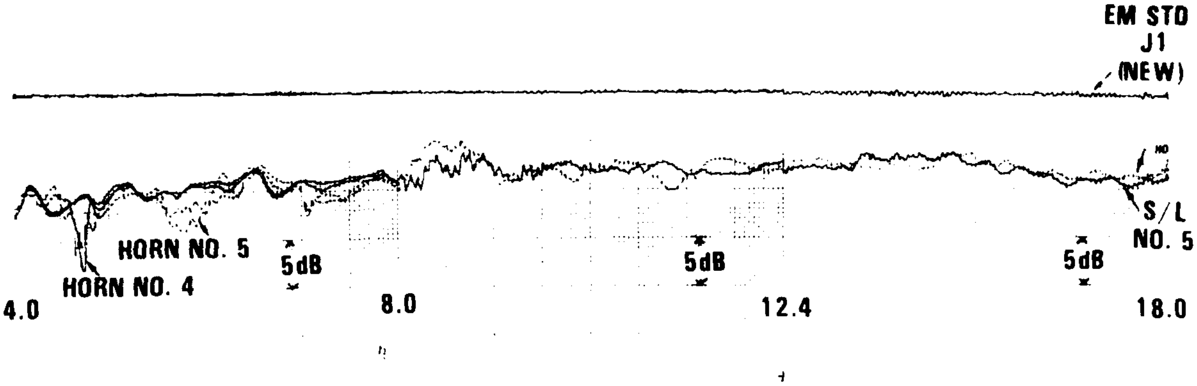

Figure 2. Center Elements Gain Tracking (Vertical and Horizontal Polarizations)

On-axis phase tracking for an orthogonal pair of elements near the center of the array is displayed in Figure 3. Phase tracking is well within $\pm$ 0°, the objective requirement. Below 6 GHz, some dispersion occurs, and the phases depart approaching the $\pm 20°$ design window.

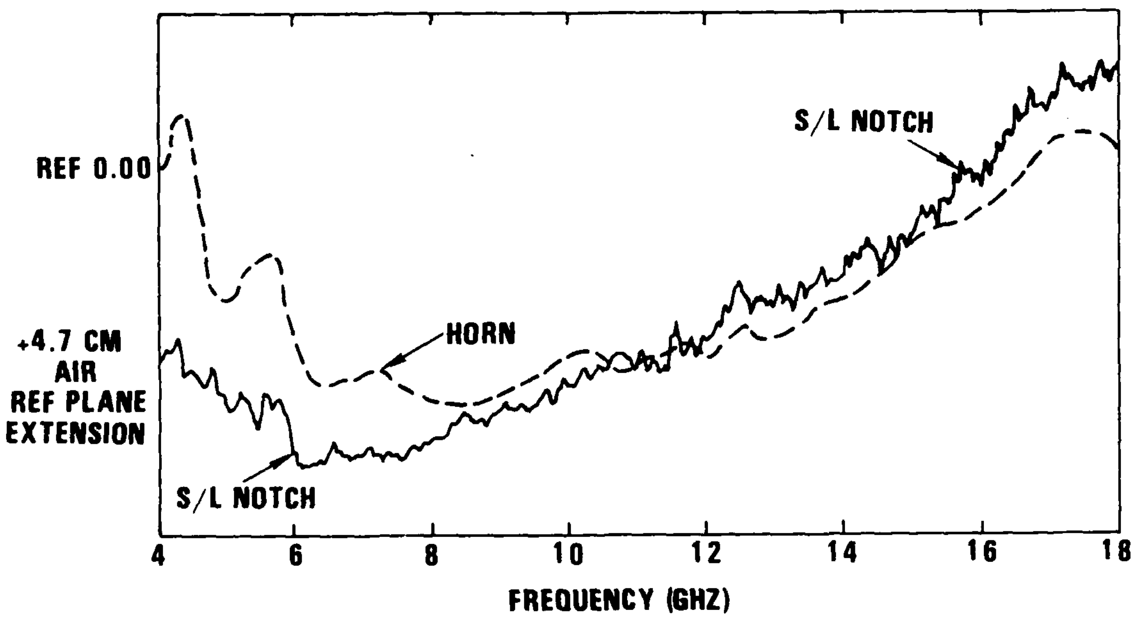

Figure 3. S/L and Horn Elements Relative Phase vs Frequency with Phase Compensated Cables (20 deg/cm)

Figure 4 shows the summed output from a 90° hybrid when two orthogonally polarized, near-center-elements were illuminated by rotating linear polarization. To fill in the envelope, several passes were recorded over the frequency interval using different sweep rates. From 7 GHz upward, the envelope response measured typically less than 3 dB with approximately 5 dB maximum. Below 7 GHz, singular response values on the order of 7 to 8 dB were noted. This test provided an independent check of the results given earlier in Figures 2 and 3. For example, for a point where the gains are equal, a phase difference of 20° from quadrature results in an axial ratio of approximately 3 dB.

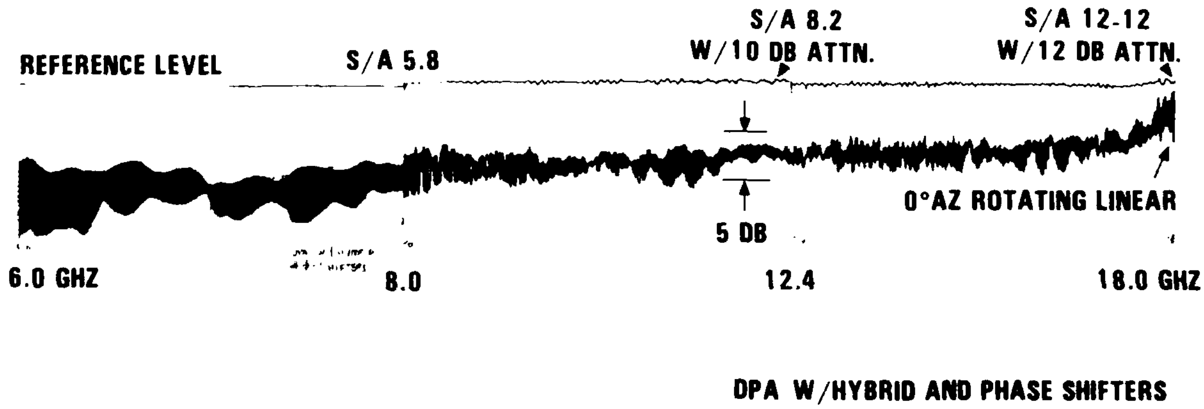

Figure 4. Dual Polarized Common Phase Center Array Boresight, Response to Rotating Linear Polarization

Mid-band array plane element patterns are given in Figure 5, with no change in incident signal or receiver settings so that plotted outputs are relative.

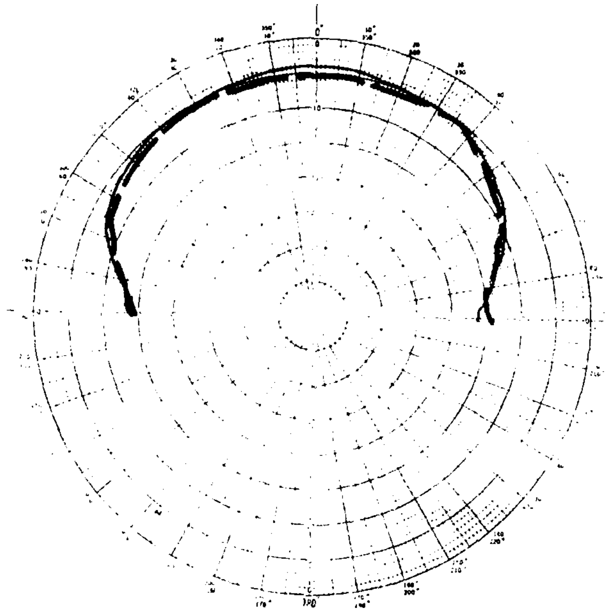

Figure 5. Array Element(s) Coverage (Mid-Band)

Similarly recorded patterns for the orthogonal plane are displayed in Figure 6.

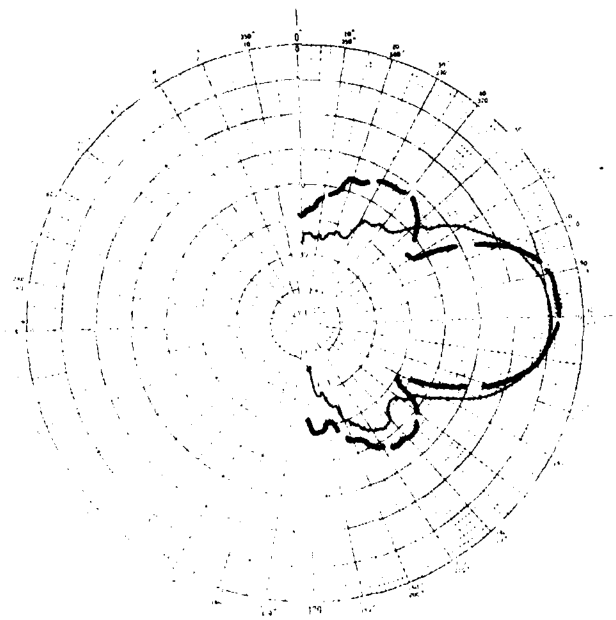

Figure 6. Elevation Coverage (Mid-Band)

Additional orthogonal plane beamwidth data is presented in Figure 7 showing elevation beamwidth tracking with frequency.

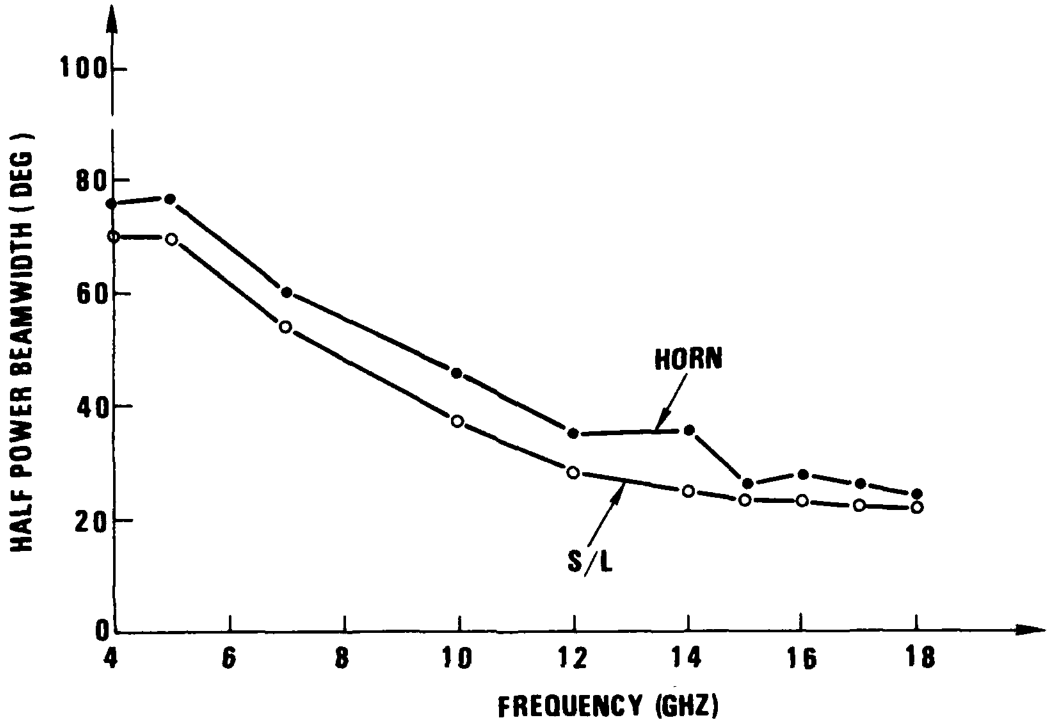

Figure 7. Orthogonal Plane Beamwidth Data (Elevation Beamwidth Tracking vs Frequency)

Derived gain data from Figure 2 is plotted in Figure 8. As can be seen, gain was typically well within 3 dB for the near-center, orthogonally polarized elements. For convenience, the data is identified as vertical and horizontal polarizations (i.e., test coordinates). Both passive and active matches were determined for the elements. Test results indicated an average passive match of 2/1 to 2.5/1 depending on the element and position within the array. Active match was determined as less than 2/1 over 90 percent of the band, with a noted singular maximum value of 3.1/1. Thus element efficiency was better than 80 percent.

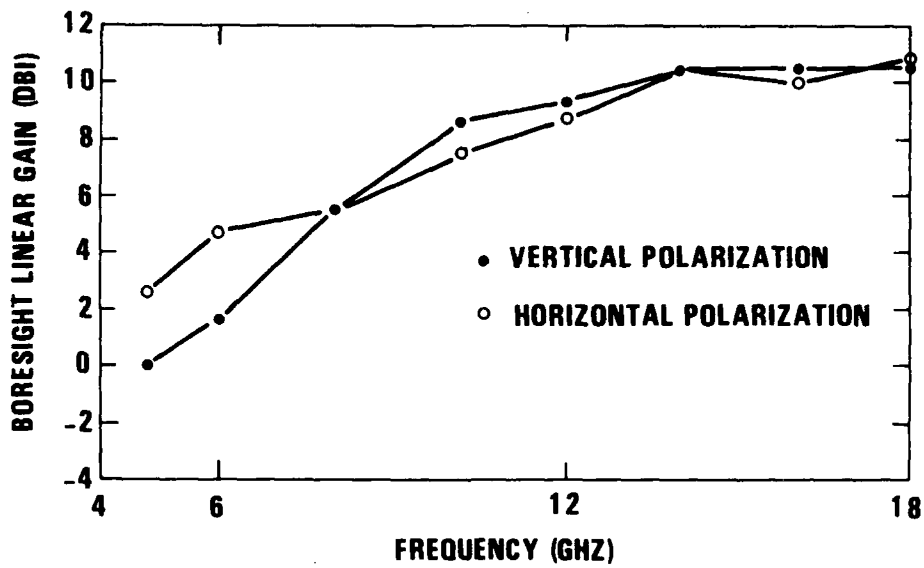

Figure 8. Boresight Element Linear Gains

4.0 CONCLUDING REMARKS

Significant advances in the state-of-the-art of array elements intended for use in EW systems applications have been presented.

As a result of these efforts, the EW system's engineer is afforded a new design dimension. Dual-polarized, continuous-coverage systems can be configured with confidence to cover the widest possible bandwidths with the fewest number of antennas for those applications where size and installation space are premium commodities.

ACKNOWLEDGEMENTS

The author gratefully acknowledges the supportive discussions with members of the Antenna and Microwave Department, Raytheon Company, Electromagnetic Systems Division, during the development of the antenna. Also, the empirical techniques applied by A. Roy and B. Lopez in developing the antenna elements are gratefully acknowledged.

A RAPID-TUNING HIGH-POWER POD-MOUNTED VHF ANTENNA SYSTEM

BY

BRYAN HODGSON

SECTION HEAD

ADVANCED ANTENNA CONCEPTS

ANTENNA DIVISION

AMERICAN ELECTRONIC LABORATORIES, INC.

MONTGOMERYVILLE, PENNSYLVANIA

SUMMARY

This paper describes a high-power jamming antenna system. The incorporation of a microprocessor in the RF coupler gives the system a very rapid frequency-hopping capability, enabling it to be time-shared between a number of threats. The antenna is electrically very small (approaching one-twentieth of a wavelength at the lowest operating frequency), but gives good omni-directional patterns up to 70 MHz. The system has an instantaneous bandwidth of approximately 1 percent, and a maximum efficiency of 40 percent.

I. INTRODUCTION

A high power pod-mounted VHF antenna system has been developed that operates over the 20-100 MHz band and has the capability of switching between frequencies in a fraction of a second. The system consists of an antenna, a coupler and a microprocessor-based controller.

The antenna system has been designed so that two identical systems can be installed under the radome of an Integrated Electronics Equipment Pod (Podpak III). This severe size constraint has resulted in a unique antenna configuration, that is best described as an elongated conical monopole over a ground plane. The other two parts of the "system" are the coupler and its associated microprocessor controller (see Figure 1).

II. FEATURES

The primary features of the system are:

- o High power handling capability (600 watts C.W.)
- o Microprocessor-based controller ensures maximum system flexibility
- o Rapid tuning capability (high power to high power in 45 milliseconds minimum)
- o Compact size (the coupler and controller occupy 2.0 cu. ft.)
- o Light weight - airborne system weight is 25 lbs.
- o Compact configuration - Two systems can be installed in a Podpak III
- o Digitized tuning process
- o Wide bandwidth (coupler operates over the 20-100 MHz band with input VSWR better than 2.0:1)
- o Omnidirectional radiation pattern (all radiation patterns are substantially omnidirectional (±2 dB) over the frequency range 20-75 MHz)
- o Vertically polarized.

III. PURPOSE

This equipment was originally designed for installation in an airborne pod-mounted jammer. Its compact size combined with its fast switching speed makes it a state-of-the-art Antenna for High-Power VHF applications.

IV. THEORY OF OPERATION

The coupler consists of a series of inductors and a capacitor (each with an associated vacuum switch) arranged in a series-parallel combination. The antenna is connected to the output port of this coupler, which effectively places part of the inductor/capacitor combination in series with the antenna. At any frequency in the 20-100 MHz range, a predetermined setting of the switches controlling the inductors and capacitors will result in the input port of the coupler and antenna combination presenting a 50Ω impedance match to the transmitter.

Operation of the switches (which affect the amount of inductance or capacitance placed in series with the antenna) is controlled by an AEL-developed microprocessor-based controller.

The controller uses readily available microprocessor logic boards. The controller accepts input data relating to frequency of operation and, after reference to its internal memory, sets the switches controlling the inductive and capacitive elements, so that the input impedance to the antenna/coupler combination is adjusted to approximately 50Ω (the tuned input VSWR is less than 2.0:1 at all frequencies in the 20-100 MHz band).

A major advantage of the microprocessor approach, is the ability of the microprocessor to improve its performance by a repetitive "learning" process. The microprocessor memory contains a tuning algorithm which tells the processor how to adjust the tuning sequence, in the event that the stored "switch state" data does not give the required 2.0:1 VSWR. In this circumstance, the microprocessor will initiate a "tuning search" around the previously stored data, and, as has been found in practice, will rapidly locate the correct switch-state settings, and then set the switches to obtain the correct input VSWR. The "learning" part of the process occurs when the microprocessor memory is updated with the new switch-state data. Then, some short time later, when that same frequency is selected again, the corrected switch data is instantly available. A primary advantage of this microprocessor controlled coupler is the speed at which changes between frequencies can be made.

Figure 2 shows the retuning sequence. Prior to the start of the retuning process it is necessary to load the data relating to the new frequency into the microprocessor memory. The microprocessor will, upon receipt of this information, refer to its memory, and extract the stored data relating the settings of the relays (at this frequency) to give the required 50Ω input impedance for the antenna/coupler combination. This data is held in a temporary store until it is called for by the microprocessor.

The initial phase of the retuning sequence is the removal of the high power RF to the coupler. In a situation where solid state amplifiers are driving the antenna system, this can be achieved by removing the RF drive to the final high power amplifier stage. This only requires a bias level change in the intermediate power amplifier, and only takes microseconds to complete. A time of 1 millisecond has been allowed for this operation, and any other associated logic changes. In a second phase of the retuning process, several changes occur simultaneously: Initially the high/low power RF switch is set in the low power position, and the frequency synthesizer is set to the new frequency. (Note that the synthesizer is not an integral part of the antenna system, but the two have electrical interconnections in an overall system); at the same time the relay-state data is extracted from the temporary stores, and the relays are set to give the required VSWR at the coupler input. At this point a low power tuning signal (about 10 mW) at the new frequency is passed through the coupler into the antenna. The time period (20 milliseconds) allowed for this phase is dictated by the closing speed of the relays, and of the high/low power switch (both 20 milliseconds).

It is now necessary to check that the input VSWR of the system is below the required 2.0:1, and this is done by the low power VSWR detection circuit. A voltage out of the VSWR detection circuit is compared with a known voltage threshold. In the relatively unlikely event that the voltage is too high (that is, there is too much reflected power), the retuning process is stopped until a separate "tuning search" is successfully completed.

If the voltage out of the VSWR detection circuit is less than the threshold voltage, then the "tuning" part of the tuning sequence has been completed, and only switching of the RF power level remains to be done. A time of 1 millisecond has been allowed for the VSWR detection and other associated logic operations.

Assuming that the input VSWR of the coupler/antenna is acceptable, the high/low power switch can at this time be set back to the high power position, an operation taking 20 milliseconds. Then, all that remains to be done, in the retuning sequence, is the reapplication of the high power RF signal, a bias change operation for which 1 millisecond has been allowed.

As Figure 2 indicates, the total time for the retuning process, from high power to high power, is approximately 43 milliseconds.

V. MECHANICAL DESCRIPTION

The antenna system consists of three subassemblies: the antenna subassembly, the coupler subassembly and the microprocessor subassembly. In a non-flying configuration, the three subassemblies above are controlled by a cable-connected test box that can perform all the functions usually controlled by the aircraft, and which also contains built-in test equipment (BITE) and timing circuits.

The antenna subassembly can best be described as an elongated conical monopole (i.e., of elliptical shape when seen in horizontal cross-section) over a ground plane. This shape was mandated by the need to radiate vertically polarized energy from an (electrically) very small antenna -- two antennas are required to be installed inside (and under the radome of) a Podpak III. The antenna has an elliptical upper surface approximately 29" (major axis) by 12" (minor axis), and the conical sides support this upper ellipse surface approximately 6 inches above the ground plane. The ground plane is formed by the lower surfaces of the equipment boxes (amplifier, exciter, couplers, etc.) that are suspended from the pod's strong-back, directly above the antenna. Note that in the attached photographs showing the antenna/pod/wing configuration, the whole assembly has been inverted for convenience during the development. In an operational situation, the pod hangs below the wing on a pylon, and the antenna (inside its radome) is nearest to the ground. The overall effect of the equipment cases suspended above the antenna, is to form a ground plane that is 13 inches wide by approximately 9 feet long.

The feed point of the antenna at the cone apex lies on the ground plane center line, and passes through the ground plane, to the feed point of the adjacent coupler subassembly. The antenna-to-coupler mechanical coupling is flexible enough to allow some relative lateral and longitudinal movement between the two components, and is also a quick-disconnect point between the antenna and coupler, allowing one to be removed without the other.

The coupler subassembly occupies a box approximately 13"x17"x5½" on the opposite side of the ground plane from the antenna. This box contains (on the top side of a shelf approximately 13"x17") the switches, coils and relays necessary to perform the impedance adjustments that are the most vital part of the whole system. The layout of the coils and switches has been very carefully planned to eliminate all possible stray inductive and capacitive pickups, and to keep mutual coupling between RF coils to a minimum. The developmental coupler contains a pair of fans to circulate ambient air.

The microprocessor subassembly, a single printed circuit board approximately 12"x15", occupies the space on the bottom side of the 13"x17" shelf within the coupler box. The microprocessor board also receives ambient air cooling from the two installed fans. This choice of location, within the coupler box, has resulted in a very compact automated coupler. The leads from the external connectors to the microprocessor board, and from the microprocessor board to the switches, are kept at a minimum length.

A fourth subassembly, though not an integral part of the antenna system, is the test box. A test box is necessary during the development phase of the antenna system, to generate the signals that the antenna system would ordinarily receive from the aircraft, and to permit alignment and preparation of an antenna system for in-flight use. The test box can therefore, upon receipt of a frequency input at its keyboard, generate the 12-bit word that the system would normally receive from the aircraft, and then indicate, on an LED display, the time that the system takes to switch to the new frequency. The test box also generates the voltages needed by the system, for operation in the absence of aircraft power supplies. The test box is supplied with 115V 60-cycle power.

VI. TEST PROGRAM

In order to make the test program as realistic as possible, AEL has constructed a full-scale mockup of an aircraft wing, with a pylon and pod. (See Figure 3). The wing mockup (20 feet long) and the pod mockup (12 feet long) are installed on an azimuth-over-elevation antenna positioner on a test tower adjacent to the Antenna Test Laboratory. The wing mockup can be rotated through 360 degrees in azimuth, and can be tilted 45 degrees in elevation. The signal transmitted from the antenna/coupler is received on a log-periodic antenna at the other end of the 150 foot range. The antenna-positioner controls and all the necessary receivers and data-recording equipment are installed behind a viewing window in the Test Laboratory.

In the course of the test program, the resultant radiation patterns of the antenna/wing combination were extensively measured. A series of conical cut patterns were recorded at 10 MHz intervals in the 20 - 100 MHz range. The results of the 20, 50 and 90 MHz measurements are shown in attached Figures 6, 7 and 8. The results clearly show the effects of wing resonances on the overall pattern shape.

General antenna/coupler efficiency measurements were made using both field strength and Wheeler Cap methods. The results corresponded to ±10%; the efficiency reaching a maximum value of 40% ± 5% at 70 MHz.

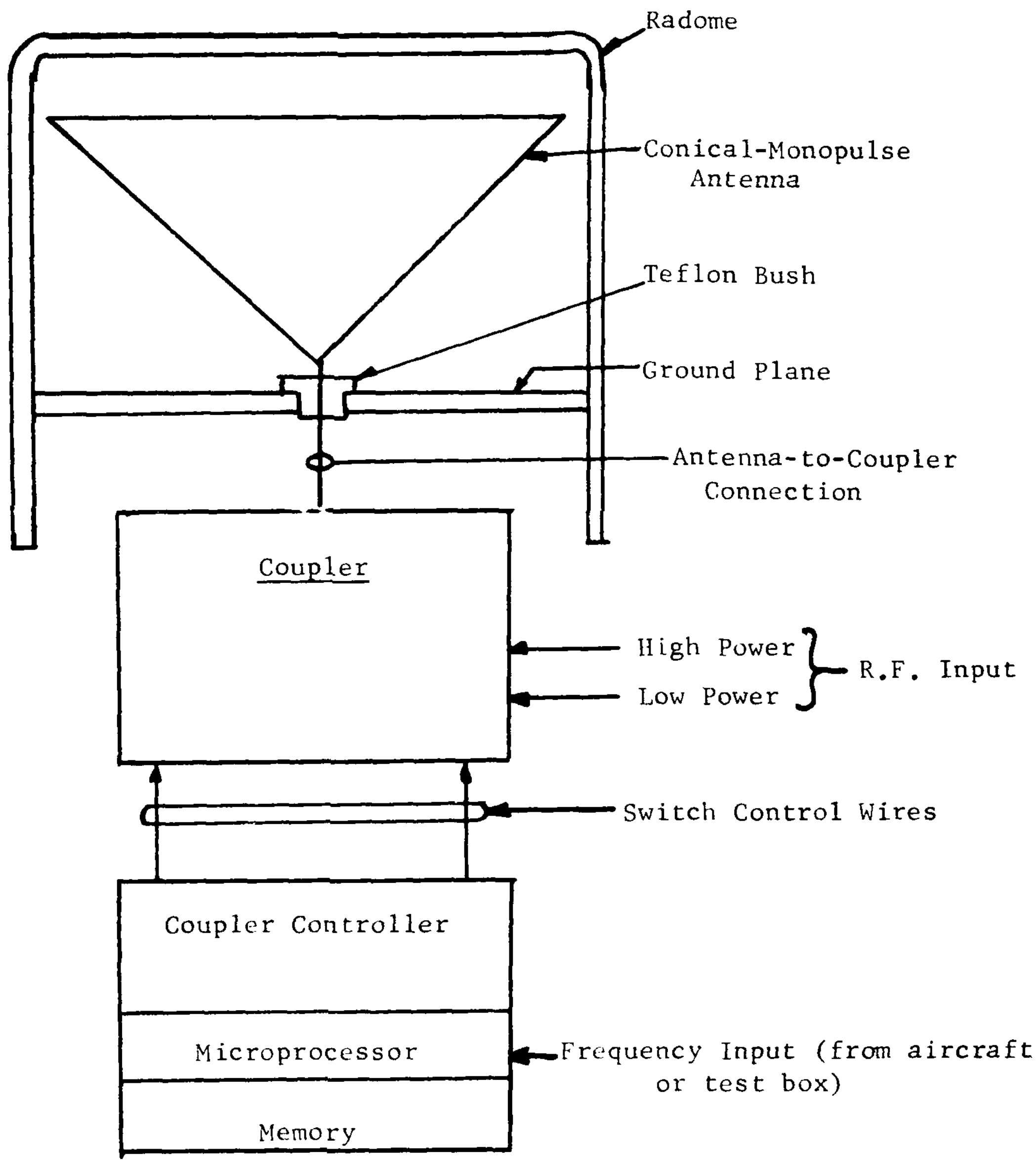

FIGURE 1: Schematic Layout of Microprocessor Controlled Coupler for High Power VHF Pod-Mounted Antenna

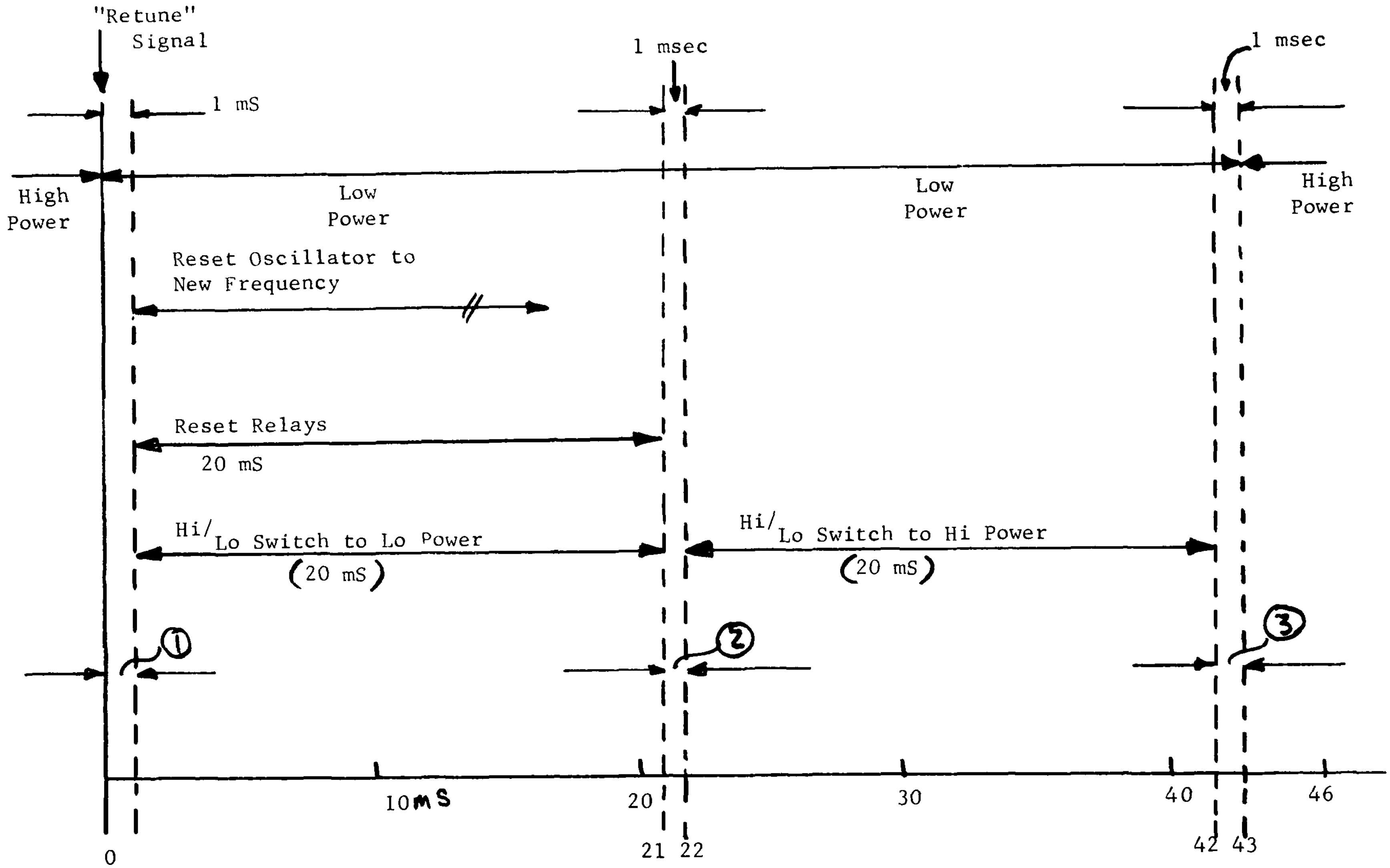

FIGURE 2: The Retuning Sequence

NOTES: 1. Take RF off
2. Check VSWR
3 Apply High Power RF

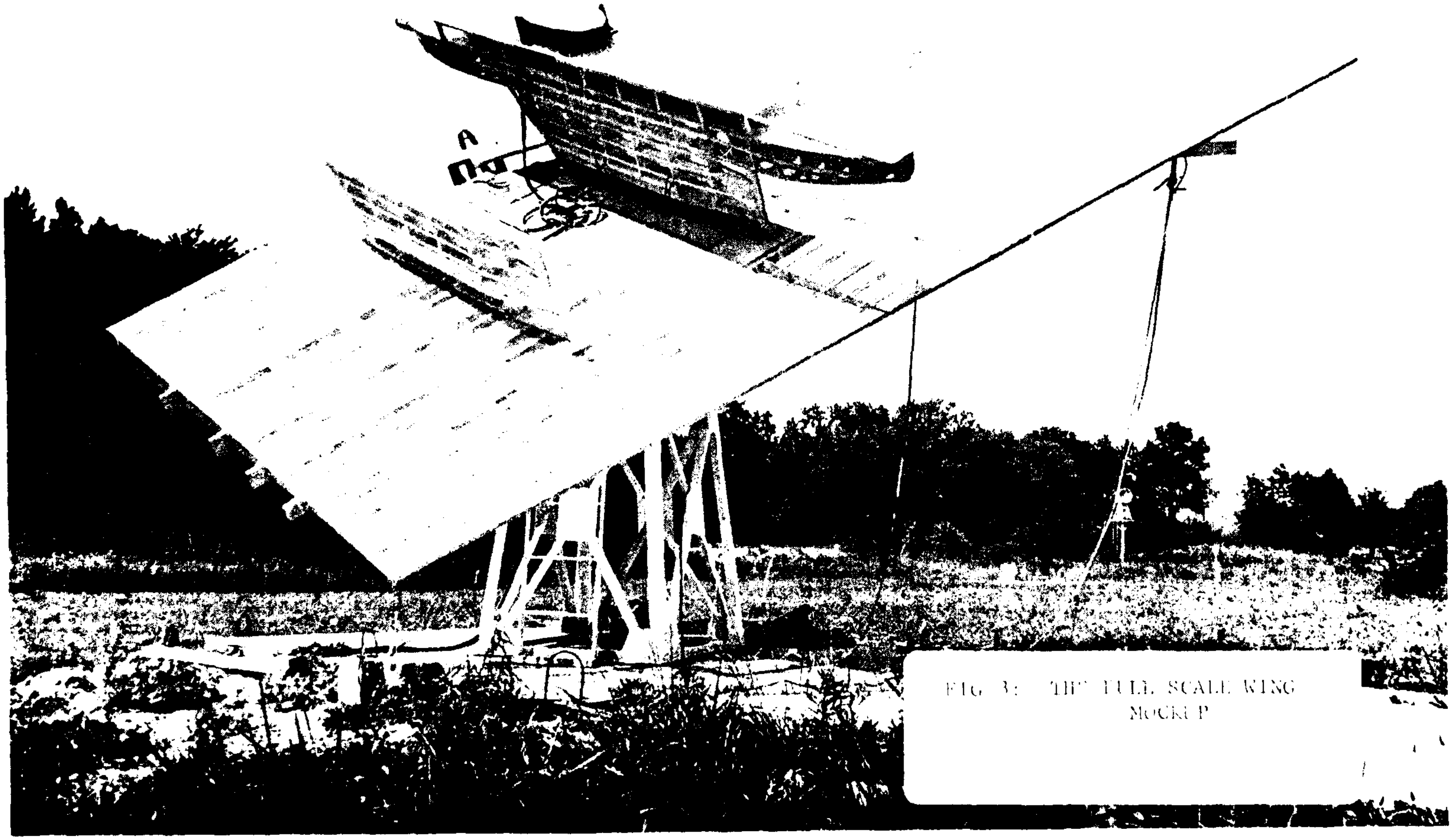

FIG. 3: THE FULL SCALE WING MOCKUP

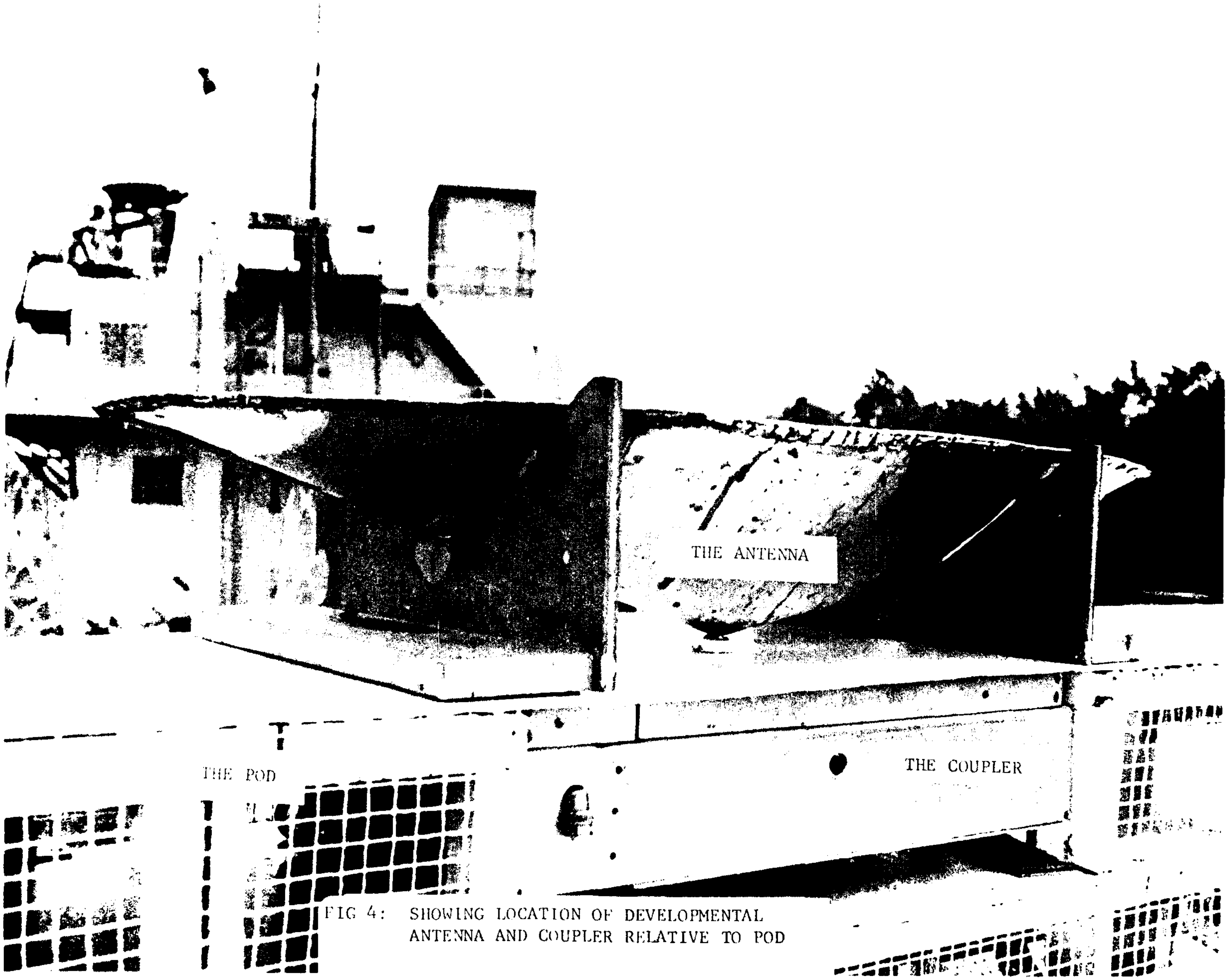

FIG 4: SHOWING LOCATION OF DEVELOPMENTAL ANTENNA AND COUPLER RELATIVE TO POD

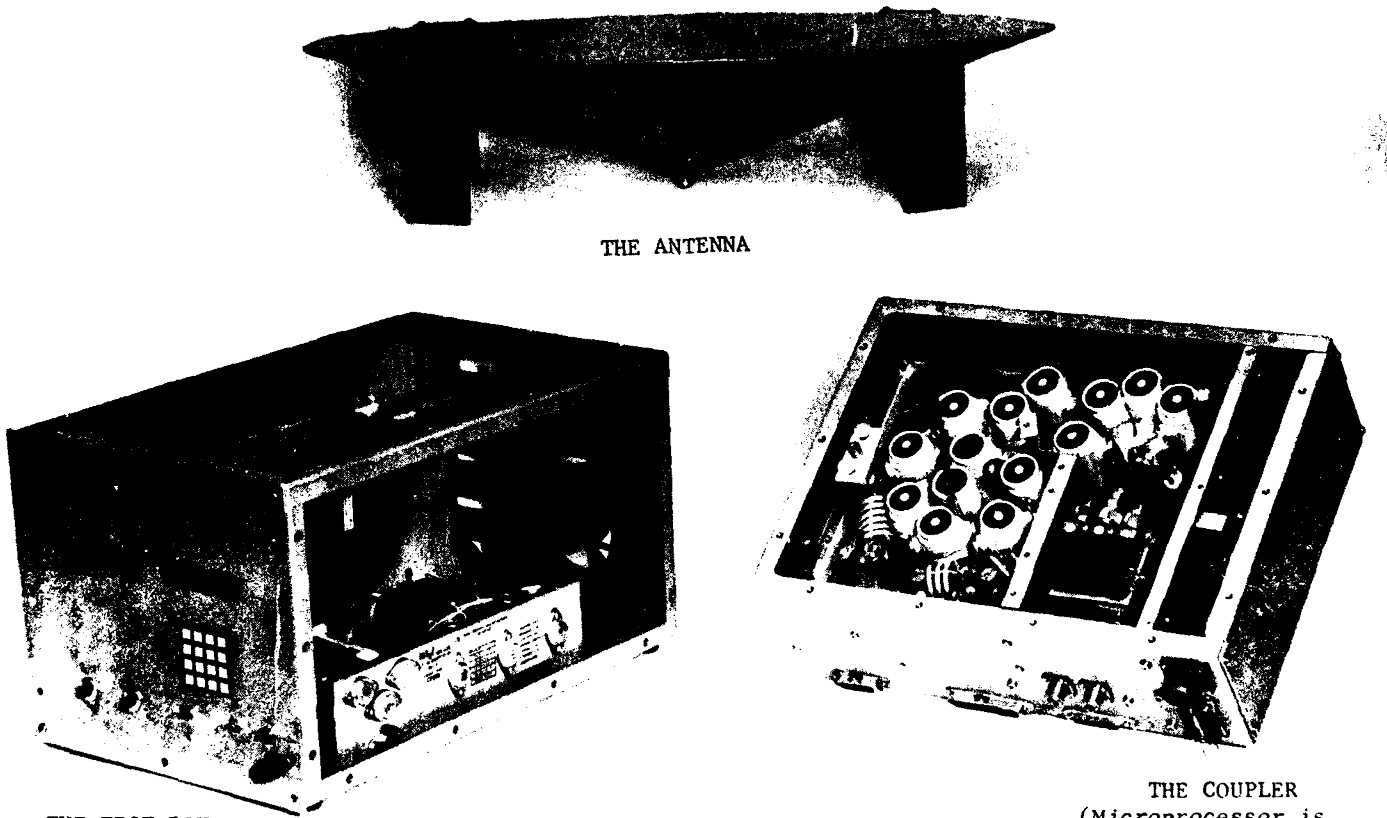

THE ANTENNA

THE TEST BOX

THE COUPLER
(Microprocessor is
below the relays)

FIG 5: THE VHF HIGH POWER ANTENNA SYSTEM

20MHZ.

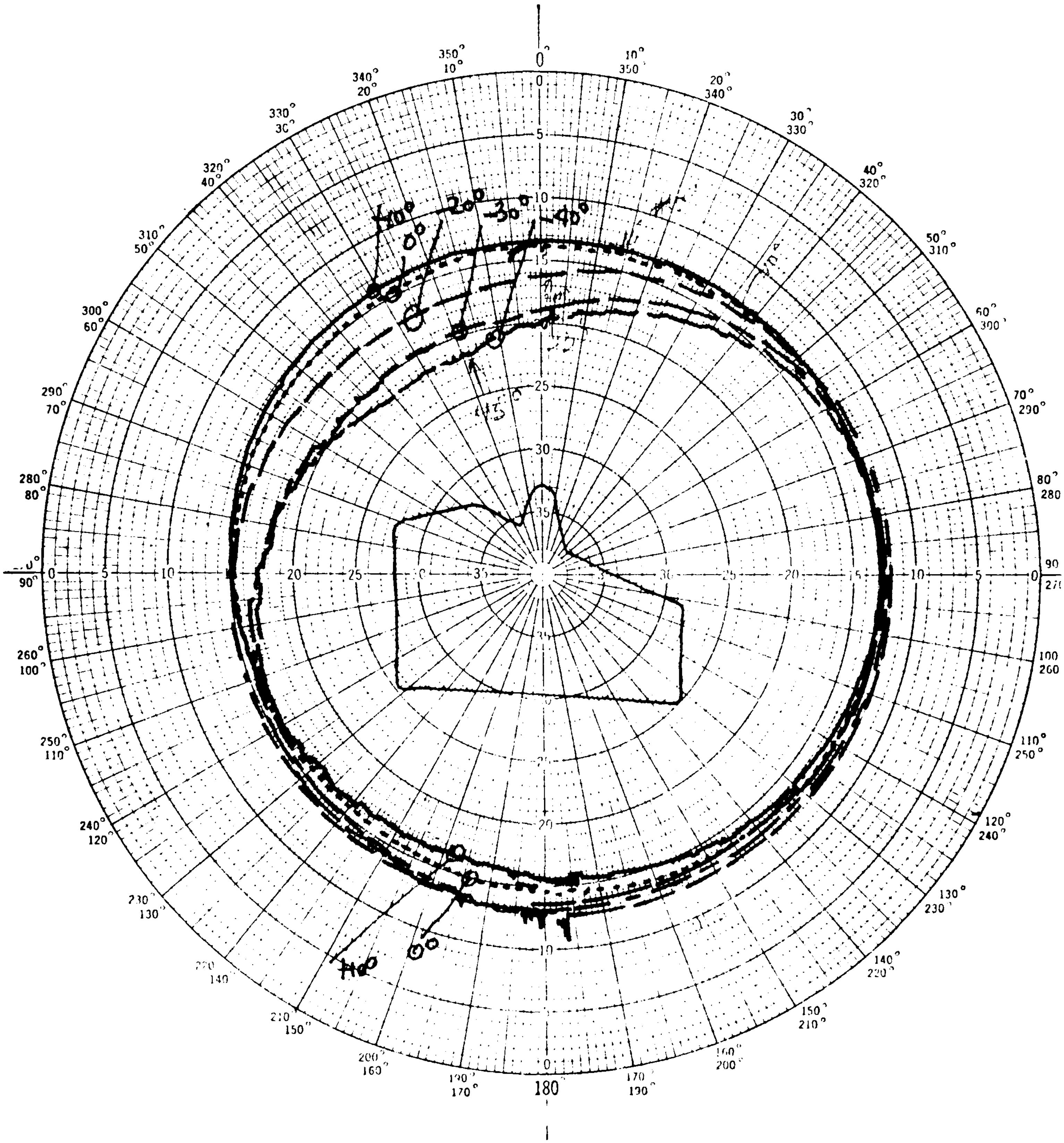

FIGURE 6: RESULTS AT 20 MHz

Polar Chart No. 127D
SCIENTIFIC-ATLANTA, INC.
ATLANTA, GEORGIA

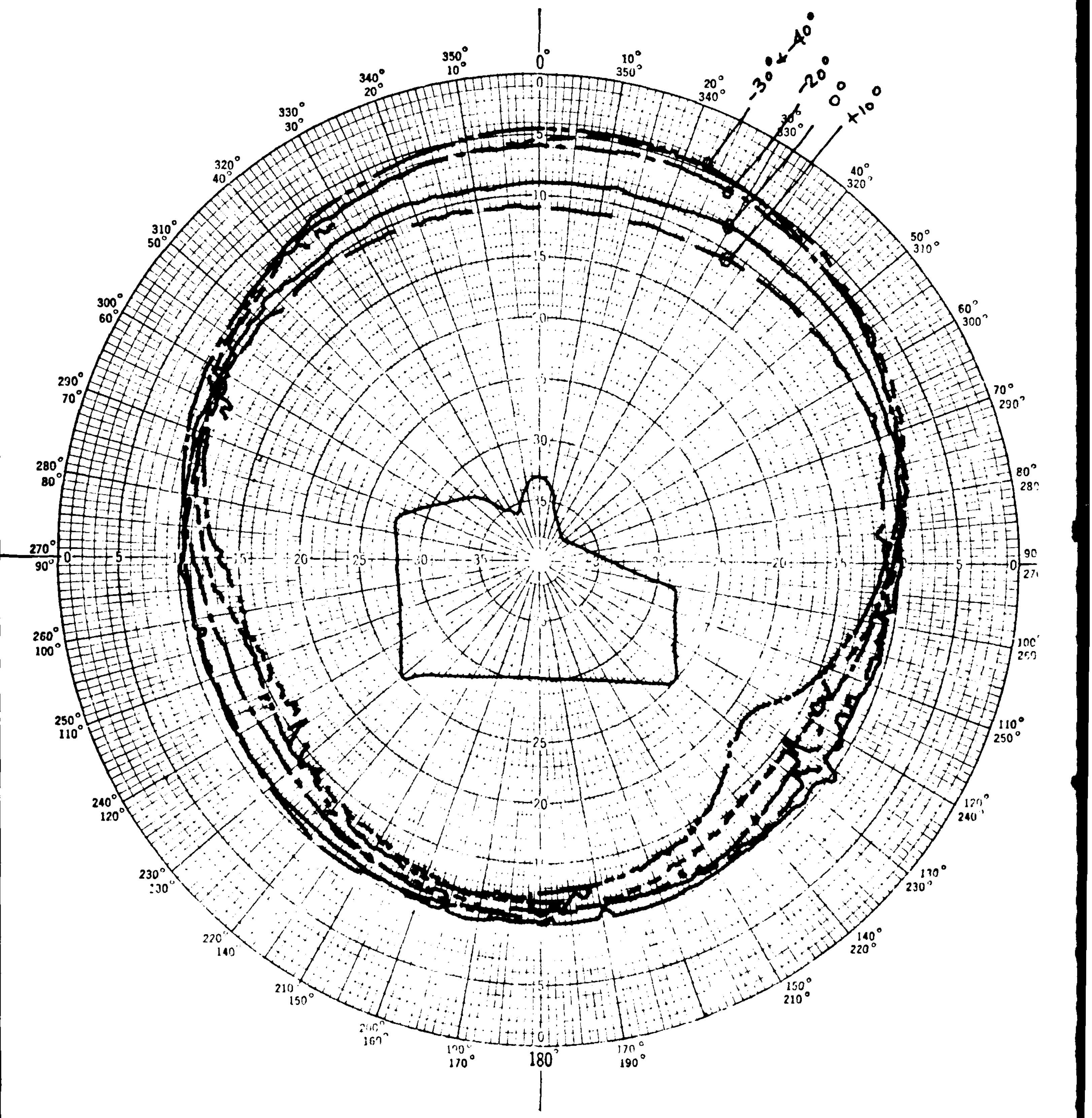

FIGURE 7: RESULTS AT 50 MHz

Polar Chart No. 127D
SCIENTIFIC-ATLANTA, INC.
ATLANTA, GEORGIA

90MHZ.

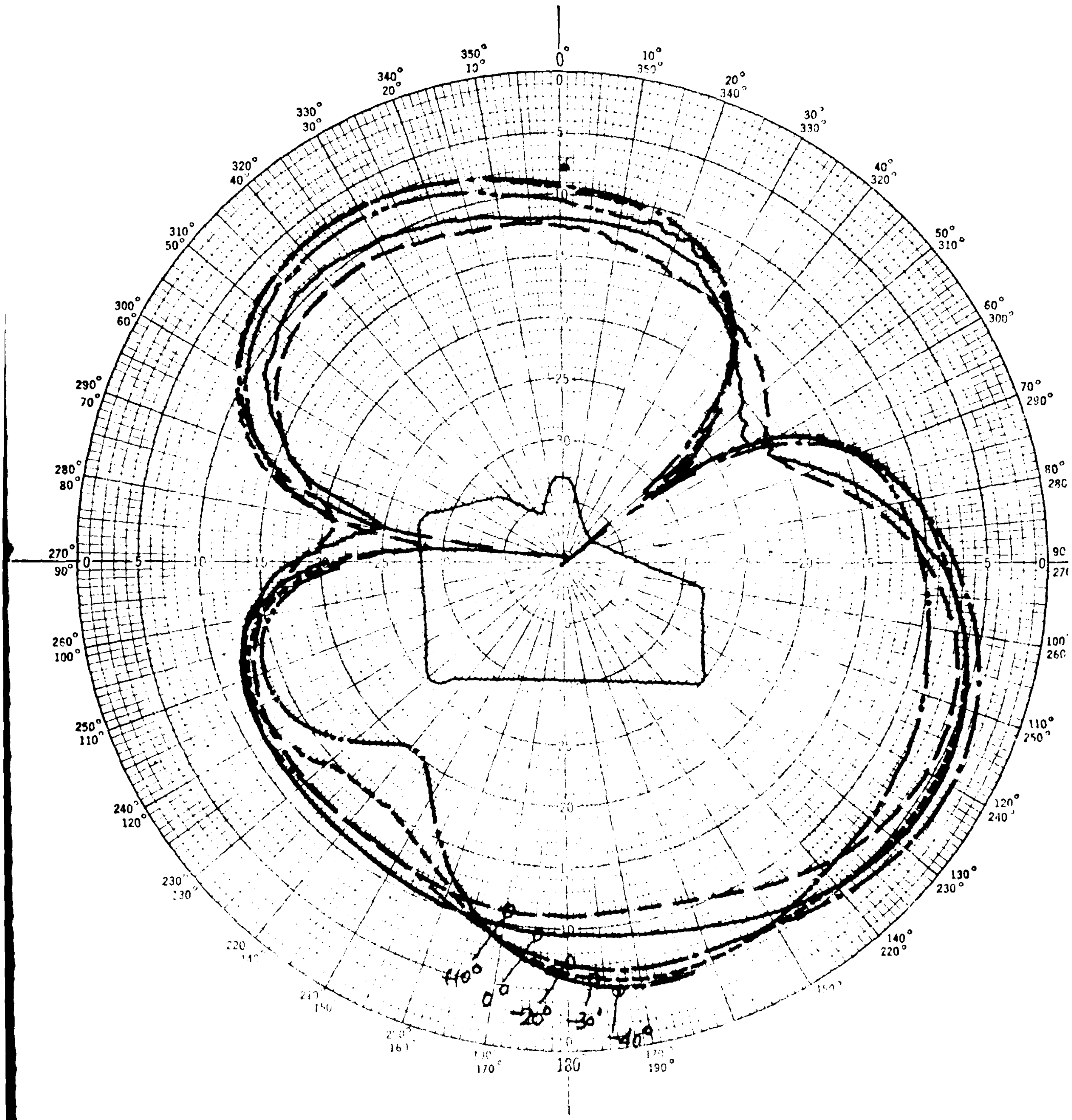

FIGURE [illegible] RESULTS AT 90 MHz

OMNIDIRECTIONAL TRANSMITTER COMBINING ANTENNA

by

Allen L. Davidson

MOTOROLA, INC.

Schaumburg, Illinois

Presented at:

THE 1981 ANTENNA APPLICATIONS SYMPOSIUM

UNIVERSITY OF ILLINOIS
ALLERTON PARK
MONTICELLO, ILLINOIS

September, 1981

ABSTRACT

Historically it has been difficult to combine transmitters which are closely spaced in frequency onto the same omnidirectional antenna. Two principal techniques have been used: cavity combining and transmission line hybrid combining. When using cavities, the minimum separation is limited by the amount of insertion loss that is acceptable and by the frequency stability of the cavities. In the 800 MHz land mobile frequency band, cavity combining has been used to combine transmitters as closely spaced as 0.5 MHz with 3 dB of insertion loss. When combining transmitters separated less than 0.5 MHz, hybrid combining has been used. When two transmitters are combined using this technique, half of the power [illegible] each is dissipated into a matched load. Further, each time the number of transmitters being combined is doubled, an additional 3 dB is added to the insertion loss.

A new technique has been developed which utilizes transmission line hybrids to combine the transmitters, but which does not suffer from large insertion loss. The power that was previously dissipated in the resistive load is radiated in a manner that produces an omnidirectional pattern. The antenna and network that accomplish this combine signals with 90 degree phase shifts. Measurements show that it is possible to combine 8 transmitters arbitrarily close in frequency with 35 dB of isolation between adjacent channels, less than 0.5 dB insertion loss, and with horizontal pattern circularity better than ± 3 dB.

INTRODUCTION

Land mobile communications are built around the concept of using a repeater. A mobile, portable, or control station transmits to the repeater where the signal is rebroadcast to other mobile, portable and control stations on a sec[illegible] frequency. This has placed a large demand for antenna space on the prime [illegible] sites in the major metropolitan areas. As a result, these sites have become [illegible] with many antennas for the land mobile service in addition to antennas [illegible] TV, and microwave communications. Figure 1 shows the land mobile antenna [illegible] on top of the Standard Oil Building in Chicago, Illinois. It is evident [illegible] the space is crowded, but there is still demand for more repeaters to be added to the site. There are a limited number of such prime sites; hence, the need for combining of transceivers onto the same antenna.

Figure 1 Land Mobile antennas on top of the Standard Oil Building in Chicago, Illi[illegible]

Satisfactory techniques exist for operating many receivers on the same antenna, however, this is not the case for transmitters. Therefore, this paper will describe the techniques which have been used in the past to combine transmitters, and the limitations in frequency spacing and insertion loss which minimize their performance. Then a new technique will be described which removes those limitations. This technique has negligable insertion loss, no practical limitation in frequency separation, and provides some additional benefits in terms of port-to-port isolation.

STANDARD TECHNIQUES

Two standard techniques have been used to combine transmitters onto a single antenna, cavity combining and hybrid combining. The first uses high Q band pass cavities, as shown in Figure 2, whose outputs are combined in a transmission line junction. The transmitted signal passes through the cavity and a length of cable to the junction. The length of the cable is adjusted to place a high impedance at that point to all other frequencies, and thus, the transmitted signals are routed to the coax feeding the antenna. Isolation is

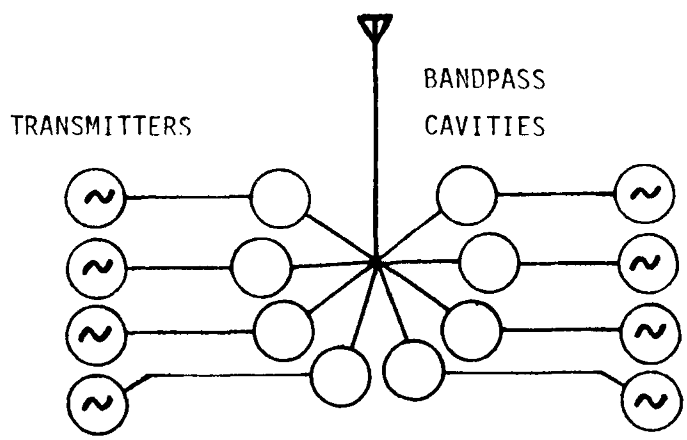

Figure 2 Eight transmitters combined using cavities and a junction.

determined by the power divided between the impedances of the 50 ohm antenna and the high impedances of the other cavities. This type of combining is, therefore, frequency sensitive because of the characteristics of the cavities.

Cavity combiners have been built using cavities with an unloaded Q of 10,000. The measured insertion loss of a single cavity from such a combiner is shown in Figure 3. With transmitter spacings of 0.5 MHz, an 8 cavity combiner has an insertion loss from the input to the cavity to the output of the junction of 2.9 dB. Isolation between transmitters is only 10 dB so circulators are required to provide acceptable decoupling between the transmitters.

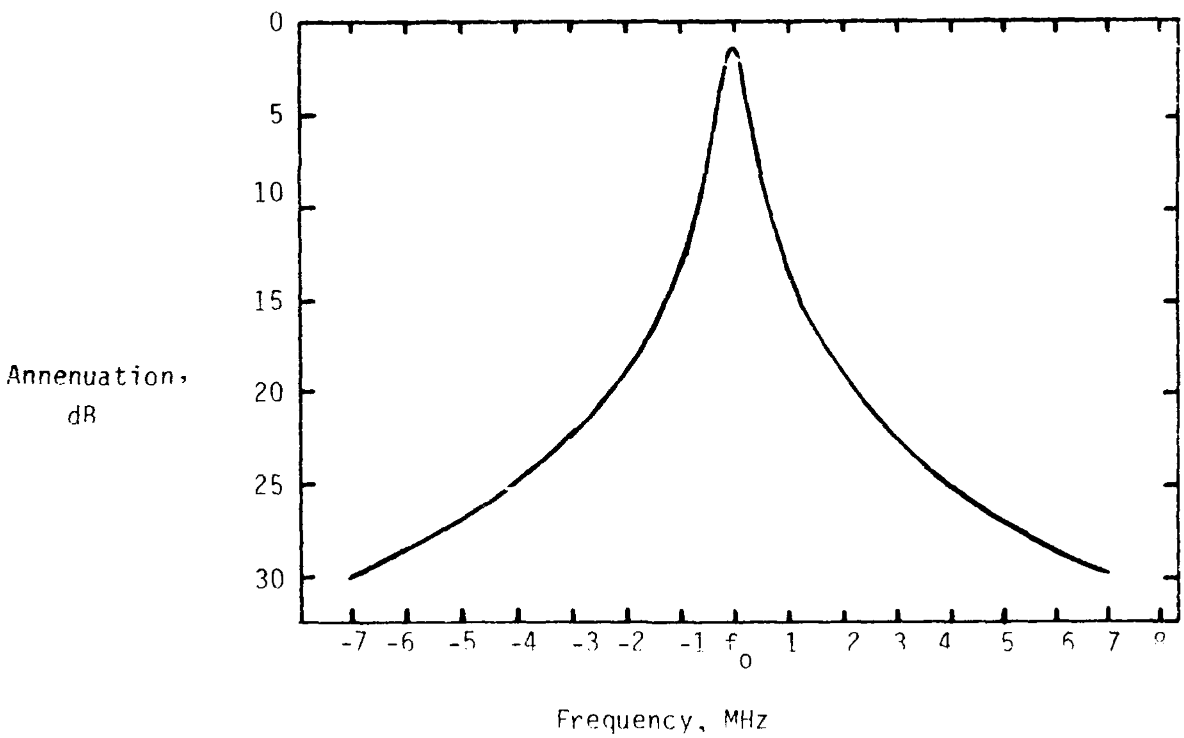

Figure 3 Measured frequency response of a single cavity tuned to the 820 MHz band.

The second technique, hybrid combining, uses 3 dB quadrature hybrids to combine pairs of transmitters. Pairs of hybrids are then combined in an

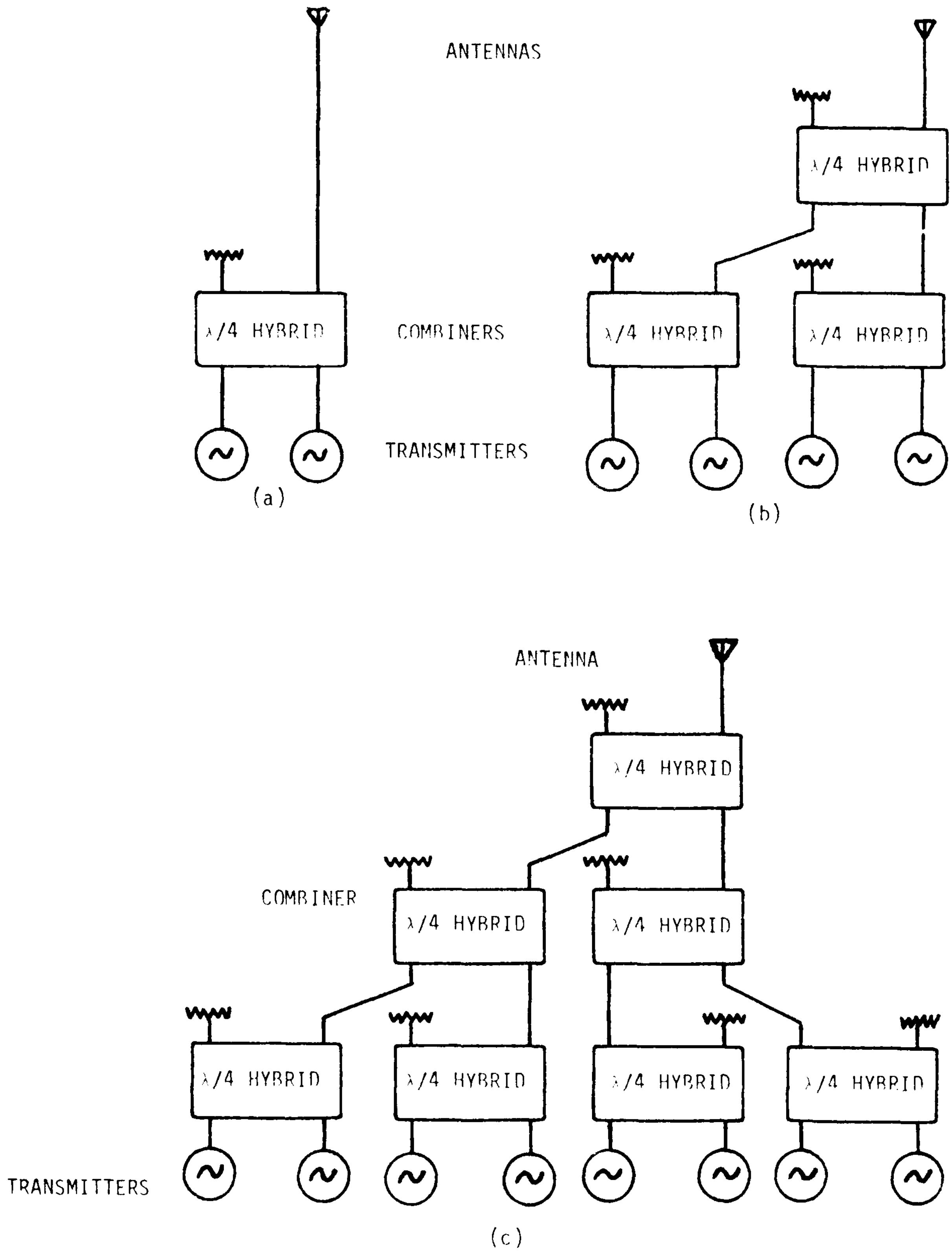

Figure 4 Transmitter combining using hybrids, (a) two transmitters, (b) four transmitters, (c) eight transmitters.

additional hybrid, and this procedure can be continued as shown in Figure 4. The technique is not frequency sensitive so the transmitters can be spaced as closely as desired. However, whenever a hybrid is used, there is a 3 dB loss because of half of the power is dissipated in a matched load on the fourth port of the hybrid. Also, there is about 1/4 dB insertion loss in the hybrid. So, to combine eight transmitters [illegible] technique produces close to 10 dB of loss. Isolation is limited by [illegible] lation in the hybrids and by the VSWR of the antenna to about 20 dB.

TRANSMITTER COMBINING ANTENNA

The limitations in isolation, insertion loss, and flexibility of assigning frequencies using the previously described techniques are evident. Hybrid combining suffers only from high insertion loss; therefore, improvements in this technique were investigated. In particular, if power that was dissipated in the loads could be radiated, this technique would yield a highly flexible approach.

Antenna for Four Transmitters

The circuit shown in Figure 5 has this property. There is one quarter wavelength hybrid added to the circuit that was shown previously, and the transmission lines feeding the hybrids have been crossed to produce a

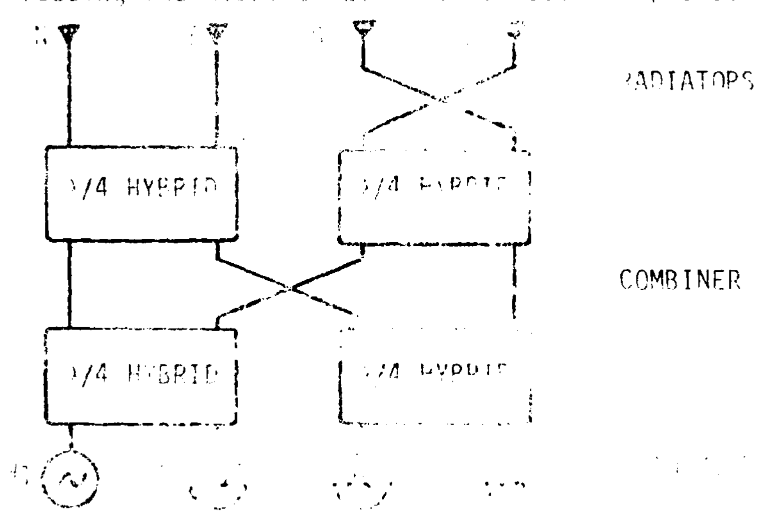

quadrature phase progression at the output. The transmission lines are also the same length, and radiators have been added so that none of the power will be dissipated in loads. If the radiator pattern is designed properly, the vector sum of all the patterns will produce an omnidirectional pattern. In particular, if the radiators are unidirectional, firing radially outward in a north, east, south, west progression and have a cos θ pattern with phase center at the origin, the desired pattern will result. Table 1 shows the phase progression for the signal from each transmitter, and Figure 6 illustrates the way the pattern from each radiator adds to form the composite.

TABLE 1

Transmitter Number	Phase at Radiator			
	N	E	S	W
1	0^0	90^0	180^0	90^0
2	90^0	180^0	90^0	0^0
3	90^0	0^0	90^0	180^0
4	180^0	90^0	0^0	90^0

The isolation for the transmitters is provided by the hybrids and must be maintained at the radiators. The radiator isolation takes two forms. First, there is coupling directly from radiator to radiator, and second, there is the contribution due to the VSWR. The limitation in the isolation between transmitters is produced by the vector sum of all three signals.

An array of vertically polarized corner reflectors was constructed and four hybrids were used to feed them as described in Figure 5. Measured VSWR of the radiators was under 1.5 to 1 at 820 MHz where all the measurements presented here were taken. The half voltage beam width was adjusted to 90 degrees. by varying the length of the sides of the corners making the overall diameter

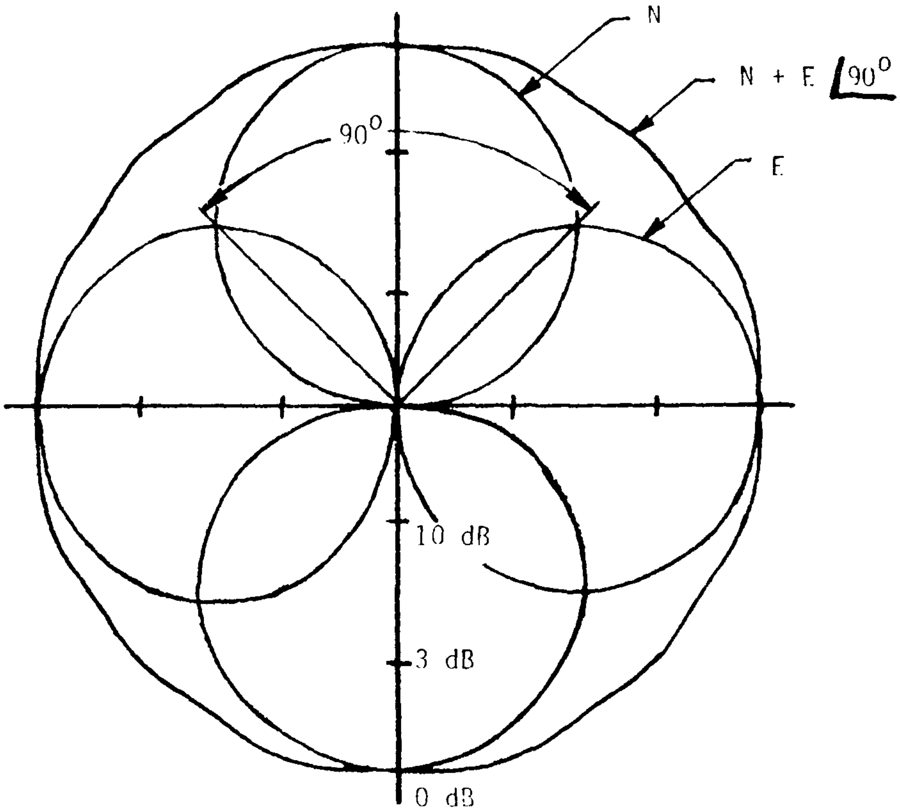

Figure 6 Pattern addition of separate radiators in a multitransmitter array of four.

of the array 18 inches The separate hybrids had isolation in excess of 25 dB and isolation between adjacent corner reflectors was over 20 dB. Insertion loss of the hybrid array was less than 0.5 dB from any transmitter port. The measured pattern of one of the corner reflectors is shown in Figure 7 with the composite pattern obtained by feeding one transmitter port. The other corner reflector patterns and composite patterns are essentially identical with appropriate rotation. The isolation from transmitter port to transmitter port to transmitter port was greater than 18 dB for all combinations.

Antenna for Eight Transmitters

It is desirable to expand this concept to more transmitters, and Figure 8

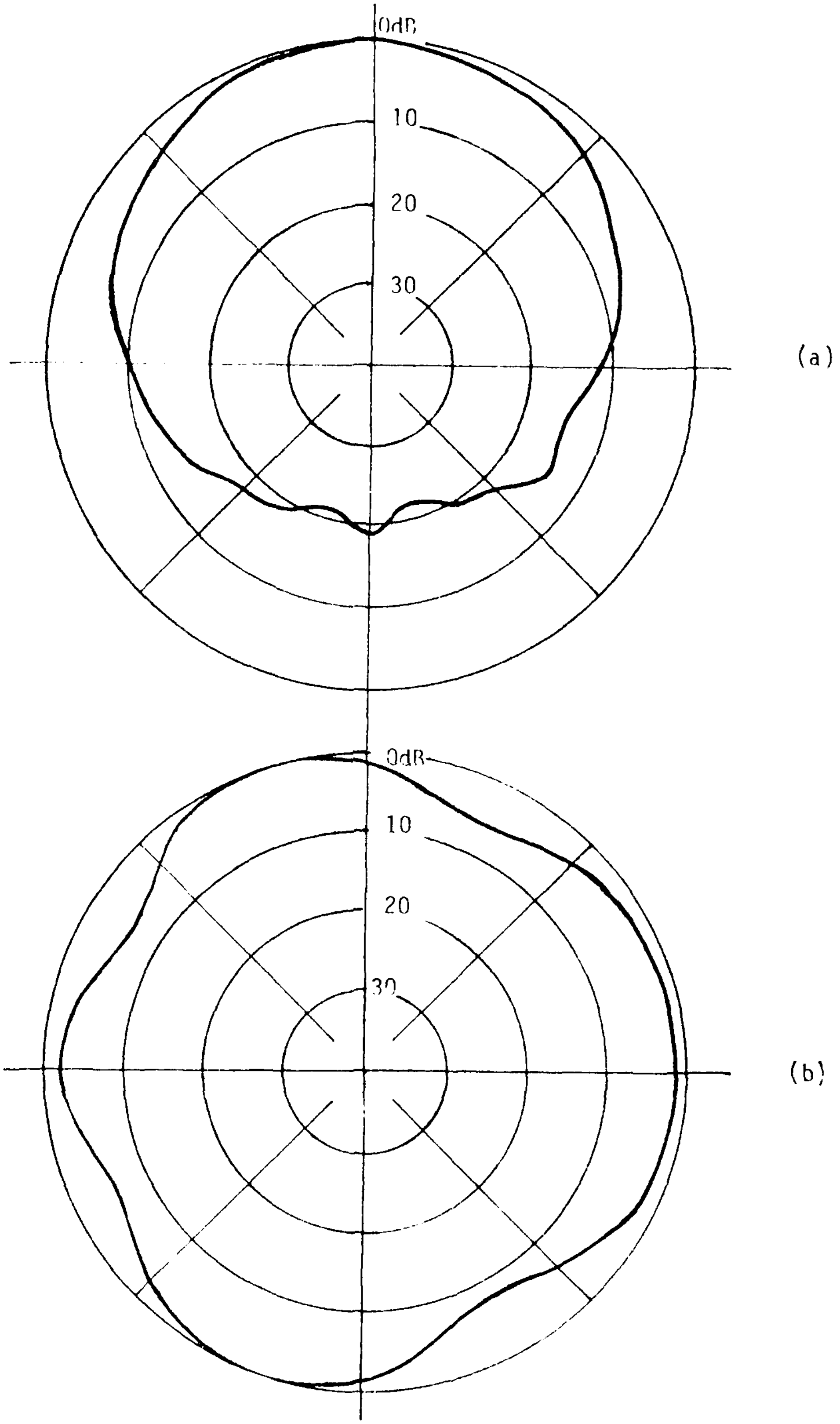

Figure 7 Measured patterns of four port multitransmitter antenna (a) element pattern, (b) composite pattern.

illustrates how the radiators can be interleaved to handle eight transmitters. In addition to the original set of radiators, another set has been added and rotated 45 degrees from the first. The two sets of radiators are fed by separate independent sets of hybrids. Pattern addition of each separate set of radiators occurs as shown previously in Figure 6.

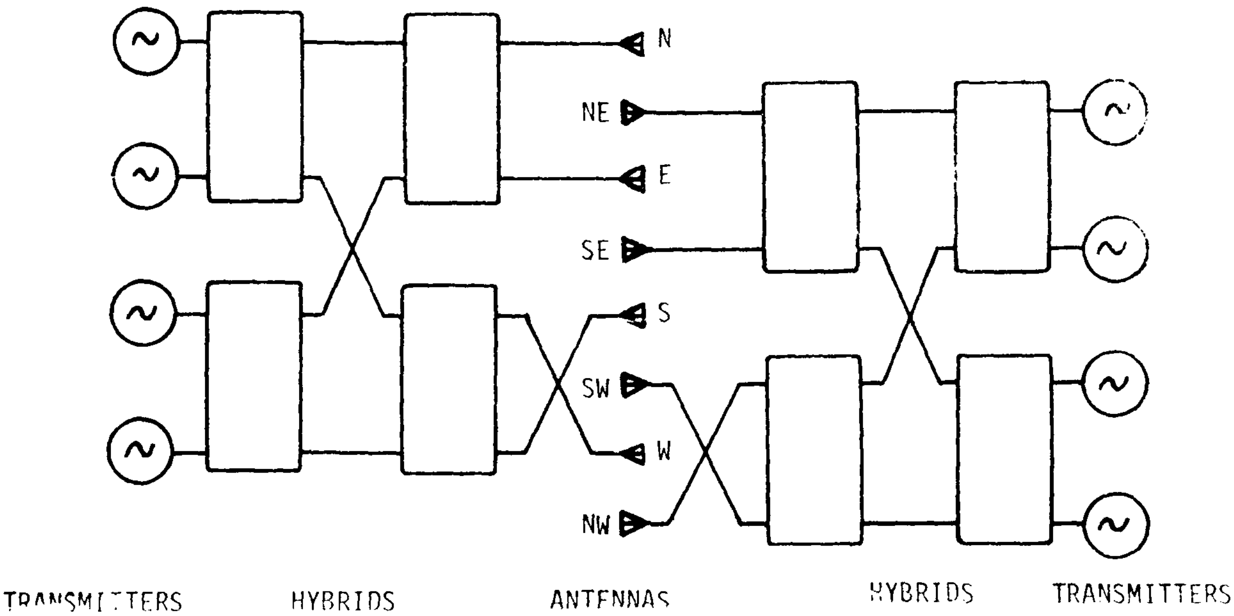

Figure 8 Eight antennas interleaved in eight multitransmitter antenna.

Again, an array of corner reflectors was assembled at 820 MHz whose measured VSWR into any radiator was less than 1.5 to 1. The overall diameter of the array was 40 inches after adjusting the half voltage beamwidths to 90 degrees. Two sets of 3 dB quadrature hybrids were attached, and the composite far field pattern shown in Figure 9 was measured while feeding one transmitter port. The other seven composite patterns were again virtually identical and the patterns of the corner reflectors were also very similar to that shown in Figure 7a.

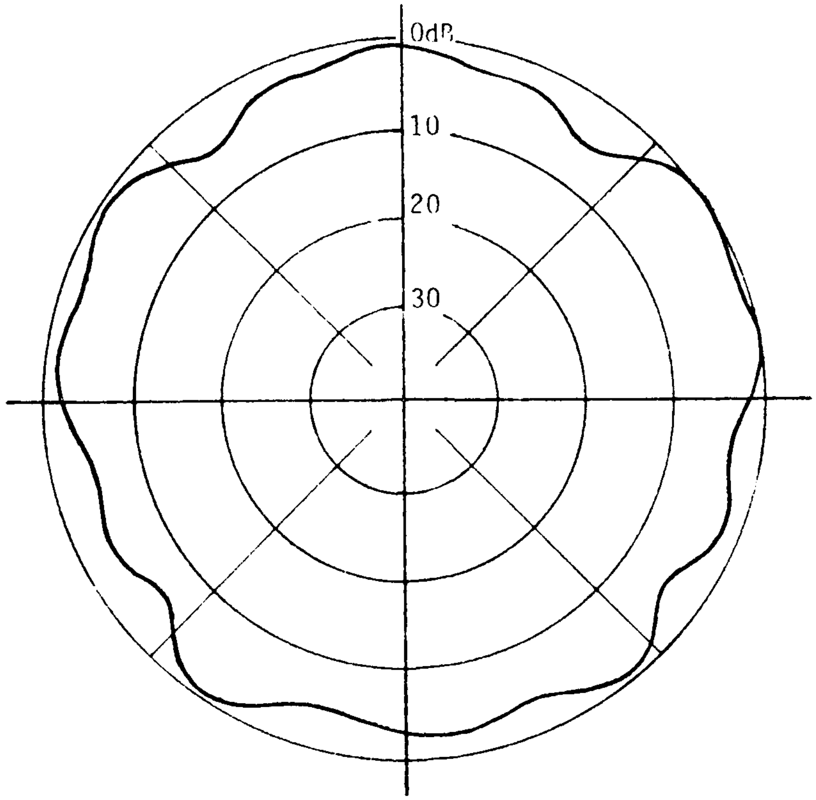

Figure 9 Composite pattern for eight multitransmitter antenna, measured with one transmitter exciting four radiators.

There is an interesting point to note regarding the isolation figures for the antenna shown in Table 2. Some of the figures are in excess of 35 dB as highlighted, while the minimum is 17 dB. The isolation in any single hybrid is only 25 dB and the isolation between radiators was measured at 20 dB. The high isolation occurs between transmitters feeding one set of hybrids and select transmitters feeding the other set. Isolation within the hybrids is not of importance in this case and the contribution due to the VSWR is also negligable. It can be shown that cancellation occurs between the signals coupled between the radiators at two of the ports of the second set of hybrids and adds at the other two. This fact can be used to provide high isolation for adjacent channel transmitters.

Antenna for Twenty Transmitters

Additional radiators can be interleaved in sets of four and 20 transmitters

TABLE 2

Measured isolation of eight multitransmitter antenna

Input Port	Output Port	Coupling, dB	Input Port	Output Port	Coupling dB
1	2	23.4	5	1	35.7*
	3	27.1		2	17.6
	4	18.0		3	38.8*
	5	36.0*		4	18.0
	6	38.7*		6	22.3
	7	18.0		7	35.0
	8	17.0		8	19.3
2	1	24.0	6	1	39.0*
	3	18.5		2	40.2*
	4	28.7		3	18.5
	5	17.6		4	18.0
	6	41.7*		5	23.2
	7	17.7		7	20.5
	8	41.2*		8	29.2
3	1	27.9	7	1	18.0
	2	18.0		2	17.7
	4	33.8		3	45.5*
	5	38.8*		4	45.2*
	6	18.5		5	34.8
	7	45.5*		6	20.3
	8	17.5		8	25.7
4	1	18.0	8	1	17.4
	2	28.8		2	42.0*
	3	34.1		3	17.5
	5	18.0		4	50.0*
	6	18.0		5	20.0
	7	45.2*		6	28.2
	8	52.7*		7	25.8

* Isolation greater than 35 dB where cancellation takes place in opposite hybrid matrix.

can be combined using this technique. A model scaled to 40% of the 820 MHz size was constructed and tested at 2050 MHz. Only 12 of the 20 radiators were included in the model to simplify the construction, and their configuration is shown in Figure 10. The radiators adjacent to the ones attached to the hybrids are there because their mutual coupling is important. This model was pattern tested to determine the shape of the composite horizontal pattern since the phase center of the radiators is quite far from the center of the array. The measured radiator pattern is shown in Figure 11a after it had been adjusted to have a 90 degree half voltage beam width. Some time was spent shaping this pattern to sharply roll off in amplitude past 90 degrees to try to minimize the nulls in the composite pattern shown in Figure 11b. Isolation between transmitter ports was maintained at the 20 dB level by keeping the radiator VSWR below 1.3 and the isolation between radiators greater than 25 dB. The hybrids had isolation greater than 25 dB.

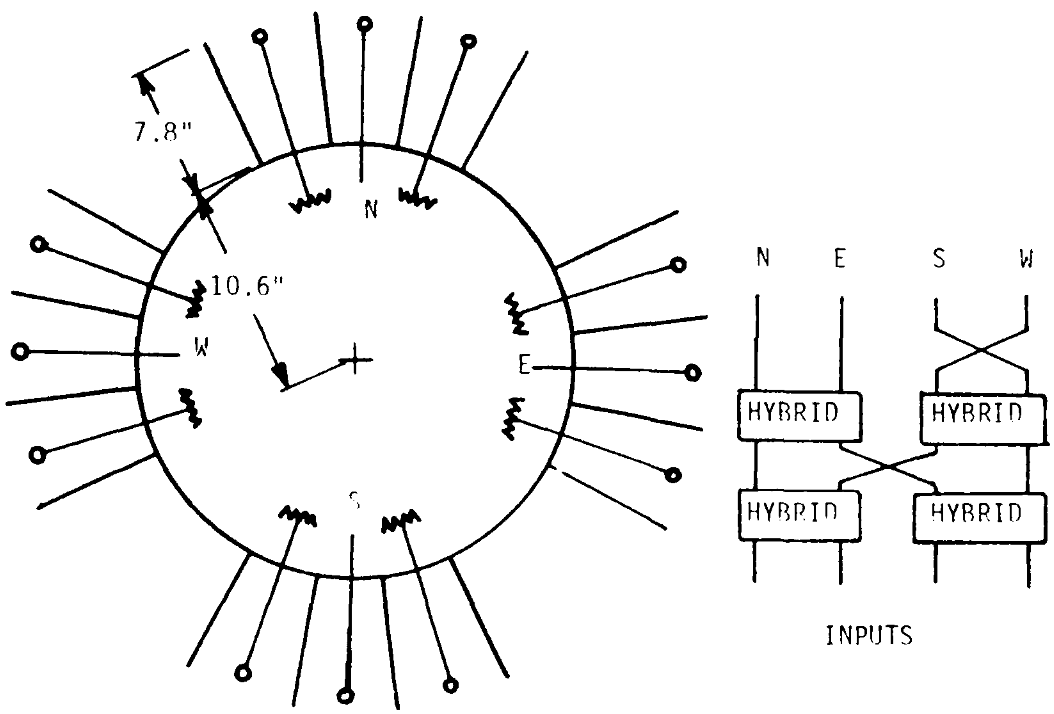

Figure 10 Top view of antenna tested in 20 multitransmitter configuration at 2050 MHz.

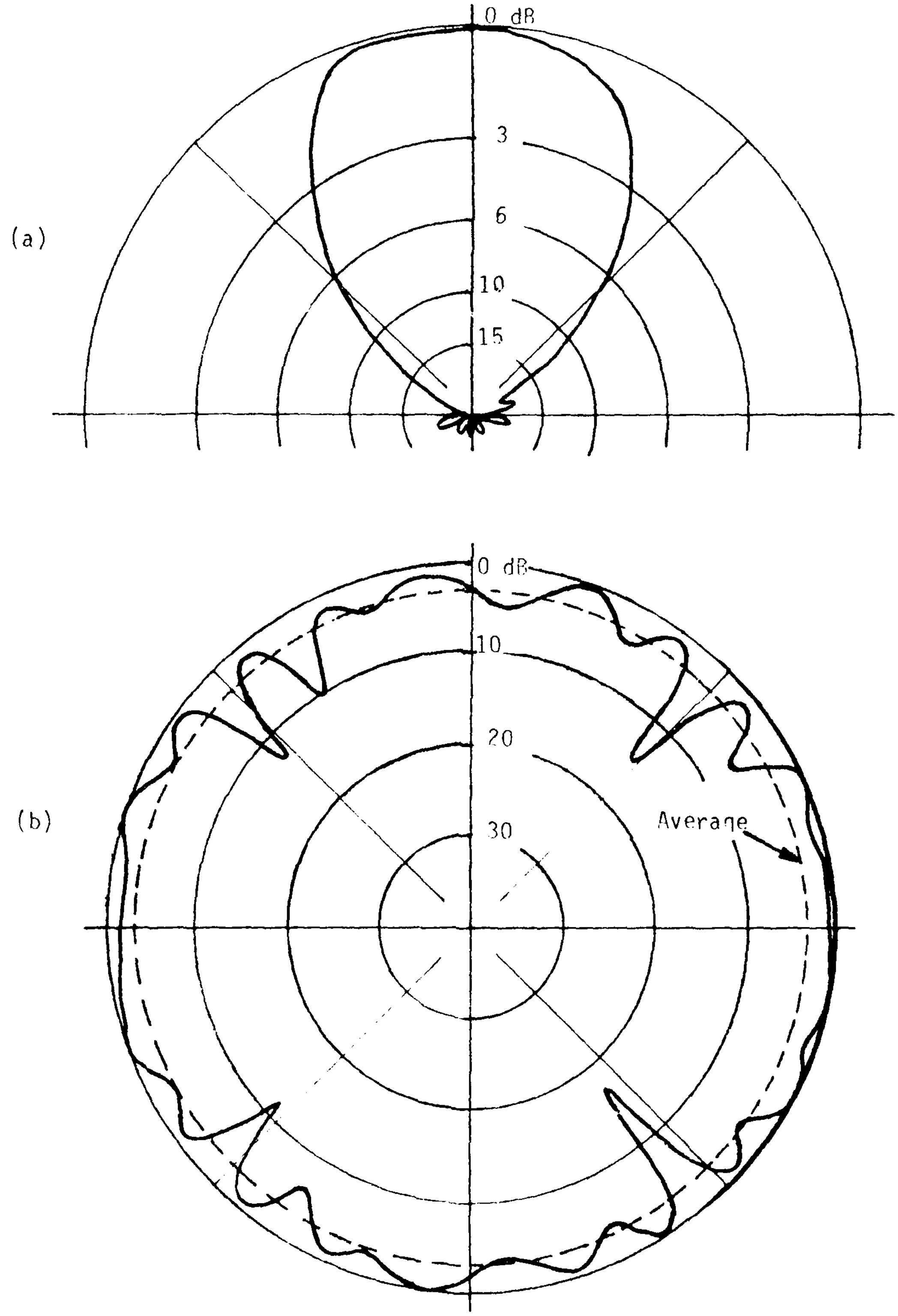

Figure 11 Measured patterns of antenna shown in Figure 10, (a) element pattern (linear voltage plot), (b) composite pattern (linear dB plot).

SYSTEM DESIGN

The multitransmitter antenna provides isolation between transmitter ports which can be made greater than 18 dB from any port to any other port. In addition, it has been shown that for the eight transmitter combiner adjacent channels can have isolation in excess of 35 dB. It is believed that the latter property carrier through to combiners for more transmitters. These properties are independent of the frequency of the transmitters.

Cavity combining, on the other hand, is highly frequency sensitive, providing more isolation to transmitters farther away from their center frequency. The two techniques can be combined to utilize the strengths of both to provide enhanced performance. Figure 12 shows schematically an eight transmitter combining antenna with cavity combiners attached to each port. The transmitter combining antenna provides 35 dB of isolation for all adjacent channels, and the cavities provide isolation greater than 15 dB for frequencies separated 1 MHz or more. For transmitters spaced 0.25 MHz or more, the combination provides isolation in excess of 35 dB for all transmitters.

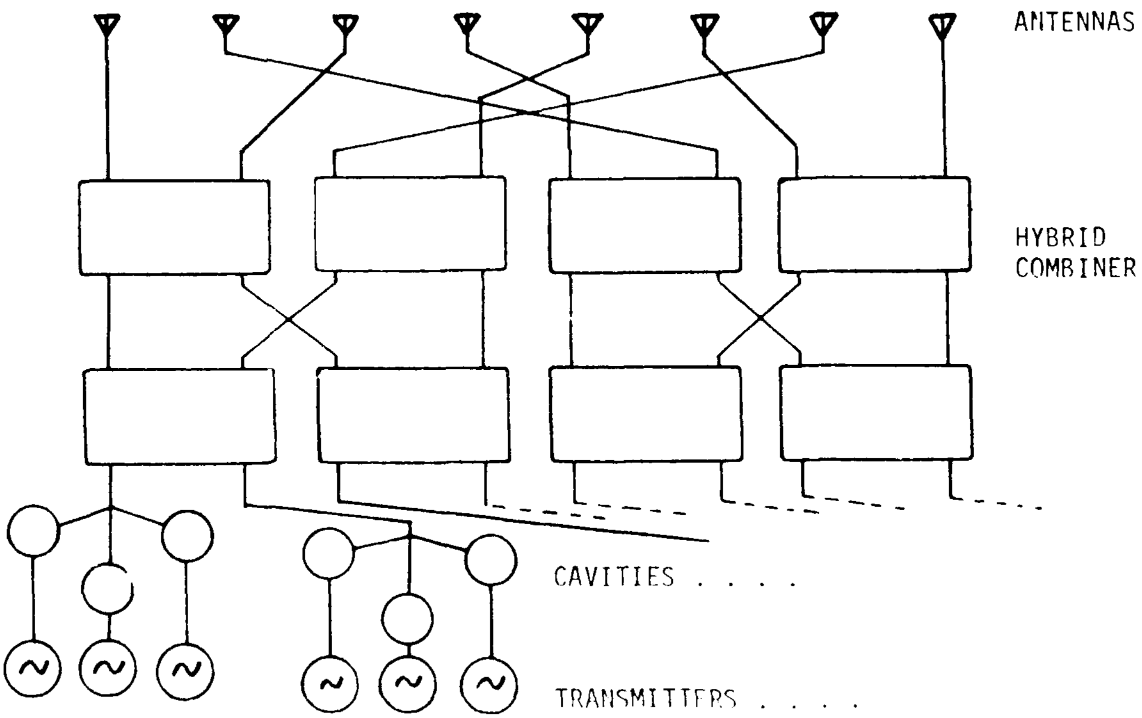

Figure 12 Eight multitransmitter anennna and cavity combining put together.

SUMMARY

A technique has been shown which permits the combining of many transmitters onto one antenna array while maintaining an omnidirectional horizontal pattern. It involves using quarter wave hybrids to combine the transmitters in a manner that produces a 90 degree phase progression on the outputs to feed the radiators in the array. The radiators are designed to produce a composite pattern which is omnidirectional while maintaining the isolation necessary for proper operation of the combiner. This technique can be combined with cavity combining, using the advantages of both techniques, to provide site designers with a powerful new tool.

REFERENCES

1. Allen L. Davidson, US Patent No. 4,213,132, Multiple Input Antenna System, issued September 16, 1980.

2. Richard S. Kommrusch, US Patent No. 4,101,901, Interleaved Antenna Array for Use in a Multiple Input Antenna System, issued July 18, 1978.

3. Allen L. Davidson and Ronald J. Wanat, US Patent No. 4,075,581, Stripline Quadrature Coupler, issued February 21, 1978.

4. Hiraku Mishima, Yoshio Ebine, and Kunio Watanabe, Base Station Antenna and Multiplexer for 800 MHz Band Land Mobile Telephone System, Review of the Electrical Communication Laboratories, Vol. 25, No. 11-12, November-December, 1977.

5. Henry Jasic, Antenna Engineering Handbook, pp. 23-8 to 23-13, McGraw Hill, 1961.

MULTIMODE PLANAR SPIRAL FOR DF APPLICATIONS

D. D. Connell
B. J. Lamberty
Boeing Aerospace Company
Seattle, Washington

I. INTRODUCTION

The several modes available in multi-arm log-spiral antennas can be useful in wide-angle direction-finding applications. The lowest order mode radiates a circularly-polarized sum beam, while all of the higher-order modes yield circularly-polarized difference beams. The radius to the active region of the antenna is directly proportional to the mode index so that the far-field pattern maximum of the difference beam occurs at larger angles as the mode index increases. Thus, by using the one basic sum (Σ) mode with the various difference (Δ) modes, different Δ/Σ slopes may be generated. Wider angle coverage and higher accuracy angle of arrival determination is thereby available than if only a single set of patterns were used. Also, this approach has the potential of combining wide-angle search capability with narrow-angle location accuracy using a single (circulary-polarized) antenna.

The present research was undertaken because the available data base on multi-arm spirals is sparse. Much has been published on two-arm structures, considerably less on four-arm varieties, and, to the authors' knowledge, very little for more than four arms. A moment-method technique was employed to calculate input impedance and radiation patterns at three frequencies (nominal and $\pm 10\%$), for all six modes of a self-complementary (30 degree armwidth) 6-arm planar spiral. Computations were also performed for non-self-complementary spirals for the two lowest-order modes. The calculated impedance values show excellent agreement with Deschamp's[1] analysis for N-arm complementary structures. Limited measurements on 15, 30, and 45-degree armwidth spirals showed self-complementary impedances consistently lower than computed values, as also observed by Deschamps. Measured radiation patterns show generally good agreement with computed patterns.

This work was performed using Independent Research and Development funding of The Boeing Aerospace Company 1980-1981.

II. BACKGROUND

For a rotationally-symmetric, N-arm antenna, it may be shown[2] that the set of excitation functions

$$v_{i,m} = V_o e^{j2m\pi(i-1)/N} \tag{1}$$

form a complete basis set, so that any arbitrary excitation must be a linear combination of these modes. $v_{i,m}$ represents the unit voltage on the i-th arm of the antenna, where arm 1 is taken as reference. The arms are fed in a phase progression of $2m\pi/N$ radians, where m is the mode index. m=1 yields a sum beam, while m=2,3,...,N-1 yield difference beams, all circularly polarized. The in-phase mode m=0 (or, equivalently, m=N) also gives a difference beam, but is essentially linear in polarization.

Prediction of the location of the active region is essential in determining where the outer radius of the spiral may be truncated. Atia has shown[3] that the phase velocity along a spiral arm is very nearly that of free space. By using this fact, and accounting for the arm-to-arm phase offset introduced by (1), the point at which adjacent arms are in phase may be easily calculated. This is the point where maximum radiation will occur. For a planar spiral, this approach predicts that the active region lies at a circumference of m wavelengths, as might be expected from physical reasoning. This result is fairly insensitive to spiral wrap angle variations.

The impedance of self-complementary structures has been predicted by Deschamps[1]. The admittance of a single arm with respect to common ground is:

$$Y_a = \sum_{i=1}^{N} Y_m e^{jm\theta(i-1)} \tag{2}$$

where

$$Y_m = \frac{4}{N\eta_o} \frac{\sin(\theta/2)}{\cos(m\theta)-\cos(\theta/2)} \tag{3}$$

and where: η_o is the impedance of the medium, m is the mode index, and $\theta = 2\pi/N$.

This result has been observed to yield impedance higher than measured values, and an empirical correction factor of 0.77 has been determined for six-arm structures[1].

For non-self-complementary structures, the impedance is no longer independent of arm shape. However, a general expression still exists to relate the impedance of the antenna to that of its complement[4]:

$$Z_1 Z_2 = Z_{sc}^2 \qquad (4)$$

where Z_1 and Z_2 are the impedances of the antenna and its complement, respectively, and Z_{sc} is the self-complementary impedance. For example, in a six-arm structure, the product of the 15° armwidth and 45° armwidth impedances must be equal to the square of the 30° armwidth impedance. Note that while the Z-notation has been retained, all impedances of truly frequency-independent antennas are purely real.

III. ANALYSIS AND MEASUREMENT

A. Method

The computations presented in this paper were performed by using the WIRANT computer code on a CDC Cyber 170/720. WIRANT is a moment-method code developed at Boeing in the early 1970's, and uses constant-current basis functions with point matching. The normal version of the code is (core) limited to approximately 200 straight-wire segments, but a recent modification by one of the authors has extended that capability to roughly 500 segments using an out-of-core matrix solution technique. The WIRANT wire-modeling approach is to outline the spiral arm with very fine wires, and to connect the inner and outer segments with another segment at each junction. This approach was chosen rather than one where the spiral arm segments are approximated by single wires whose diameters increase with the spiral radius, as in the code described by Atia[3]. This latter approach tends to limit the size of the spiral since the wire diameter can become a significant fraction of a wave-length at large spiral radii, which violates the thin-wire assumption inherent in the moments technique. Also, many practical spiral antennas are of the photo-etched variety and, hence, the arms are flat strips instead of round wires. While this generally makes no significant difference in the radiation patterns, input impedance predictions may not be valid using an expanding wire code. The wire outline technique has a further advantage in enabling the feed area to be modeled more accurately.

Multi-arm spirals are most conveniently fed by soldering the center conductors of N individual coaxial lines to a tab on the inner truncation radius of the spiral. Figure 1 shows one arm of one of the wire models used in the analysis, complete with a mesh representation of the feed tab. The tapered outer end of the arm represents the effect of truncation at a fixed radius. Only one arm of the structure is used as input; the other arms are represented by a rotational "imaging", causing the rank of the matrix (in the moments solution) to be equal to the number of segments on one arm only. The single segment extending from the origin to the tip of the feed tab in Figure 1 is the source segment; all arms are fed against the datum node at the origin. This configuration is valid for all but the in-phase mode. In this mode, the vector sum of the arm voltages is not zero and the antenna must be fed against an infinite ground plane, accounted for via imaging. This imaging requires the use of a few additional wire segments oriented perpendicular to the plane of the spiral. In all modes, the source segment is impressed with one volt, so that the input impedance is just the reciprocal of the current on this segment.

All of the spirals investigated were planar and had a wrap angle (α) of 83.7°. This angle was chosen for a one-turn expansion ratio of 2:1. The feed radius (inner truncation radius) was 0.1 wavelength at the nominal center frequency of 4 GHz. In an effort to conserve computer time, the outer truncation radius was tailored to the mode being investigated. In all cases, the outer circumference was at least twice the active zone circumference at midband.

B. Results

1) Input Impedance --- Spiral armwidth is the primary means of controlling input impedance. Figure 2 shows the computed arm impedance as a function of armwidth (δ) at 4 GHz for modes 1 and 2. The discontinuity at $\delta = 30^{\circ}$ (self-complementary) is because the narrower armwidth models could not be as finely gridded without violating certain wire-modeling guidelines. To bound the problem, the self-complementary case was run as both fine- and coarse-grid structures. The results at $\pm 10\%$ in frequency are similar but the discontinuity is larger at 3.6 GHz and smaller at 4.4 GHz. This indicates that some outer end effect is present, even with an outer truncation

circumference of 4 wavelengths (twice the circumference of the mode 2 active region). Deviation from true frequency-independence is also present at the inner truncation, as demonstrated by the increase in reactance with increasing armwidth.

The impedance calculated from equations (2) and (3) is also shown in Figure 2, and is in excellent agreement with the fine-grid model. Equation (4) was used to extrapolate the computed impedances of the large-δ spirals to those of their complements. For mode 1, it is seen that the agreement with the small-δ spiral impedance computations is excellent as far as the slope of the curves is concerned.

Agreement between extrapolation and direct computation of small-δ spiral impedance was better for mode 1 than for mode 2.

Figure 2 also shows the measured arm impedances for 15, 30, and 45 degree armwidth spirals. The spirals were photo-etched on .060" thick teflon/glass circuit board, with a .30" feed diameter and 12" outer diameter. They are fed via six 0.086" semi-rigid coaxial cables through a six-port beam forming network.[5] Flat RF absorber (AN-77) was placed approximately 10 inches behind the antenna to prevent scattering from the beam forming network and to simulate free-space conditions.

These data were obtained by inserting a dual directional coupler in one of the coaxial feed lines and phase-compensating the other five lines.

The short-circuit reference was established at the feed tab of the spiral, and swept-frequency measurements were made from 1 to 2 GHz. The outer circumference of the spiral was 4 wavelengths at 1.25 GHz. The measured values in Figure 2 represent the real part of the impedance at the center of the Smith Chart locus. The locus was generally within $\pm .07$ in reflection coefficient (Z_o = 50 ohms), and fairly well-centered on the real axis.

The experimental arm impedances are generally lower than the computed values, as observed by Deschamps. However, the most striking feature of the comparison is the difference in slope of the two curves. The measured values exhibit a lower slope and hence less sensitivity of impedance to arm-width than indicated by the computations. If the empirical correction factor of 0.77[1] is applied, the two curves are in close agreement for the 15^{o}

armwidth. (The correction factor is, incidentally, very close to that obtained by averaging the dielectric constant of the circuit board with that of free space). For wider armwidths, computed values are then lower than measured values. Since the spiral arms are modeled by a wire outline for computational purposes, it is reasonable to expect that a narrow arm is more accurately represented than a wide arm where the wires are further apart. This is suspected to be the case in Figure 2, since the error increases monotonically with armwidth once the empirical correction factor for the self-complementary case is applied.

Figure 3 shows the computed arm impedance as a function of mode index, for the self-complementary spiral at 4 and 4.4 GHz. The theoretical impedance from equations (2) and (3) is shown for comparison. The agreement is very good at 4.4 GHz; the 4 GHz curve is also in good agreement except for the value at m=2. This is probably caused by end reflections as discussed above. Note that the closed-form theoretical values are perfectly symmetric about m=3. This is because mode index pairs which are equally spaced on either side of mode 3 (180^o phase progression between arms) represent opposite senses of phase progression. For example, mode 2 phasing is 0,120,240,..., whereas mode 4 is 0,-120,-240,..., etc. Since impedance is independent of arm shape for self-complementary structures, the impedances of such mode pairs must be equal. The experimental values are shown for comparison and have been discussed above.

2) Radiation Patterns -- Computed radiation patterns for all six spiral modes are shown in Figures 4 through 6. The coordinate system is defined so that θ is the angle from antenna boresight, and ϕ is the cylindrical angle in the plane of the spiral. ϕ=0 coincides with the center of the feed tab of arm 1. Figure 4 shows θ-variable cuts at =0. The two traces on each pattern represent the maximum and minimum of the polarization ellipse, i.e., they represent the envelope which would be observed by rotating linear polarization. All patterns are normalized to their own maxima. Pattern integration indicates that all the difference modes have about the same directivity, while the sum mode directivity is on the order of 2 db higher.

The difference beam peak is observed to move further off boresight with increasing mode index, as would be expected from current rings of larger and larger diameter. Thus, the Δ, Σ -crossover point may be made to occur at variable θ-angles over an angular range of about 20 degrees. Patterns show that the difference beams suffer from increasing axial ratio with increasing mode index. This could be due in part to truncation effects, since any currents not radiated in the active region reflect from the arm end and travel inward, radiating the opposite sense polarization and contributing to high axial ratio. This phenomenon is very pronounced in the mode 5 pattern, where a vestigial lobe appearing on boresight. Comparison of the phases of the lobes (not shown) show that the minor lobe is indeed cross-polarized. This behavior is not evident in the lower-order difference modes since these modes are reflected as oppositely-polarized difference modes. Mode 5 (or, in general, the N-1 mode) is unique in that it is reflected as a cross-polarized sum beam.[6,7]

Figure 5 illustrates a similar set of patterns at ϕ=30 degrees. This angle was chosen since the fields must be periodic in 60^{o}, and hence represents a half-period. The patterns are not qualitatively difference from those of Figure 4. Note that in both figures, the in-phase mode (m=0) is essentially linearly polarized.

Figure 6 shows the ϕ-variation at fixed θ-angles. The value of θ was chosen for each mode to correspond to the beam peak location. Each pattern exhibits the 60-degree periodicity inherent in a six-arm structure. However, it is apparent that higher-order Fourier components are increasingly present as the mode index increases. The mode 4 pattern, for instance, shows a pronounced 12ϕ variation combined with the expected 6ϕ behavior; the higher-order components in the m=5 and 6 patterns are more complex and not readily identifiable (note, however, that the dominant polarization in the m=6 mode is nearly purely a 6ϕ variation). These irregular variations are not fully understood, but the end-reflection phenomenon is strongly suspected since it does introduce field components whose phase variation in ϕ differs from that of the initially-excited mode.

The computed patterns show generally good agreement with measured data. The experimental patterns are not shown for the sake of brevity. The primary area of disagreement is toward $\theta=90^{o}$ and greater, as would be expected since the computational model does not allow for radiation from feed lines, dielectric supports, etc.

Conclusions

Input impedance and radiation patterns have been computed using the method of moments, and compared to measured data for a 6-arm planar spiral antenna. The study was undertaken to evaluate potential use of this antenna for DF applications. The study showed that the WIRANT moments code can be used to accurately predict patterns and impedance of all possible modes in multiarm spirals.

The zero order mode is linearly polarized, the m=1 mode is a circularly polarized sum mode and all higher order modes are "circularly" polarized difference modes. Successively higher order difference modes have pattern peaks at successively larger angles off boresight, varying from about $\theta=25$ degrees for mode 2 to about $\theta=45$ degrees for mode 5. Also, successively higher modes have increasingly greater axial ratios.

Input impedance of the spiral antenna varies with mode and with arm width. Measured variation with armwidth was not as sensitive at that predicted by the computer model. The discrepancy is believed to be caused by a lack of sufficient detail in the wire model of the wider-arm spirals.

The multimode, multiarm spiral appears suitable for DF applications where broadband wide angle, high accuracy angle of arrival determination is a consideration.

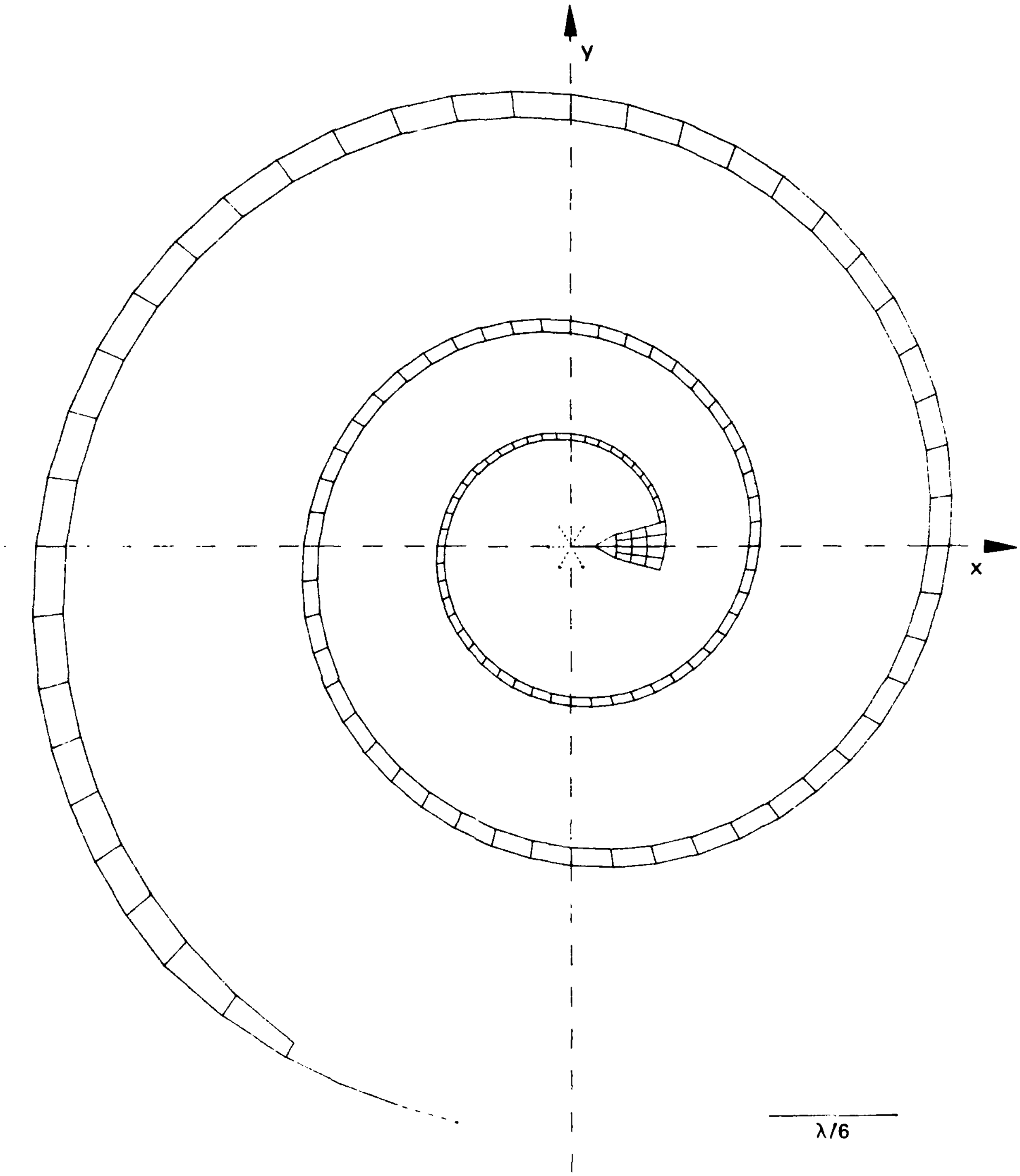

Figure 1. Wire Segment Model of One Arm of A 6-Arm Planar Spiral, $\alpha = 83.7^{0}$

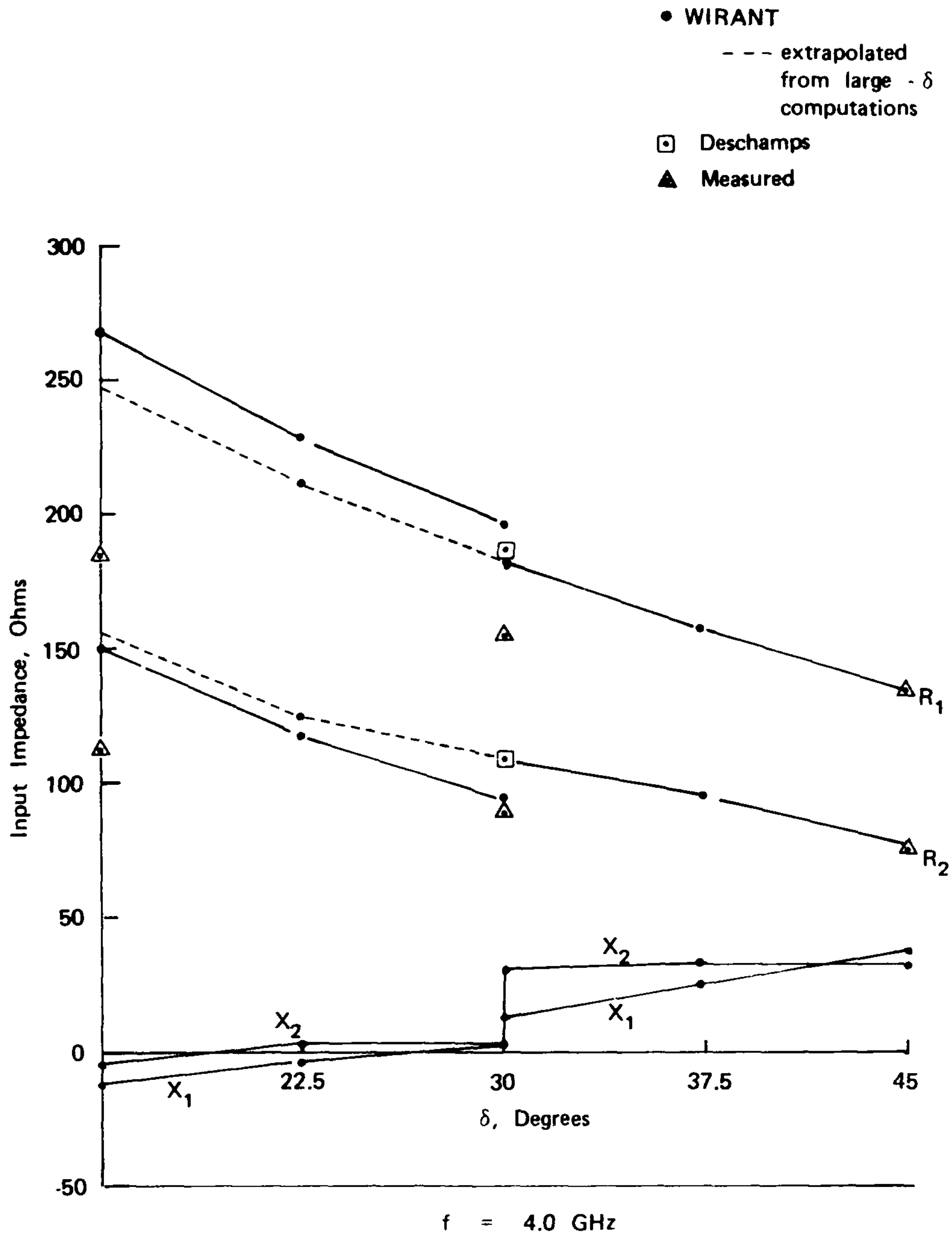

Figure 2. Computed and Measured Arm Input Impedance vs. Armwidth for 6-Arm Planar Spiral, α = 83.7^{o}, Modes 1 and 2

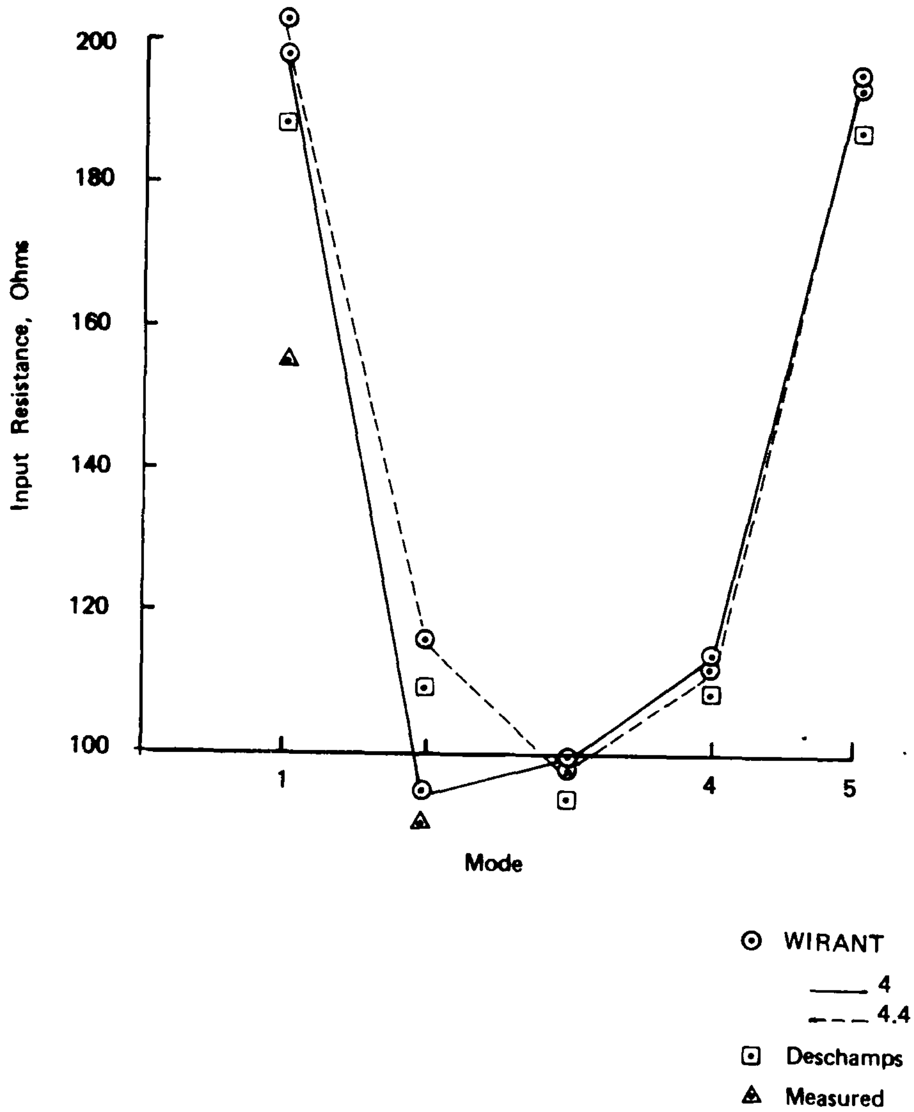

Figure 3. Computed and Measured Arm Input Resistance vs. Mode Index for 6-Arm Planar Spiral, $a = 83.7^{o}$, $\delta = 30^{o}$

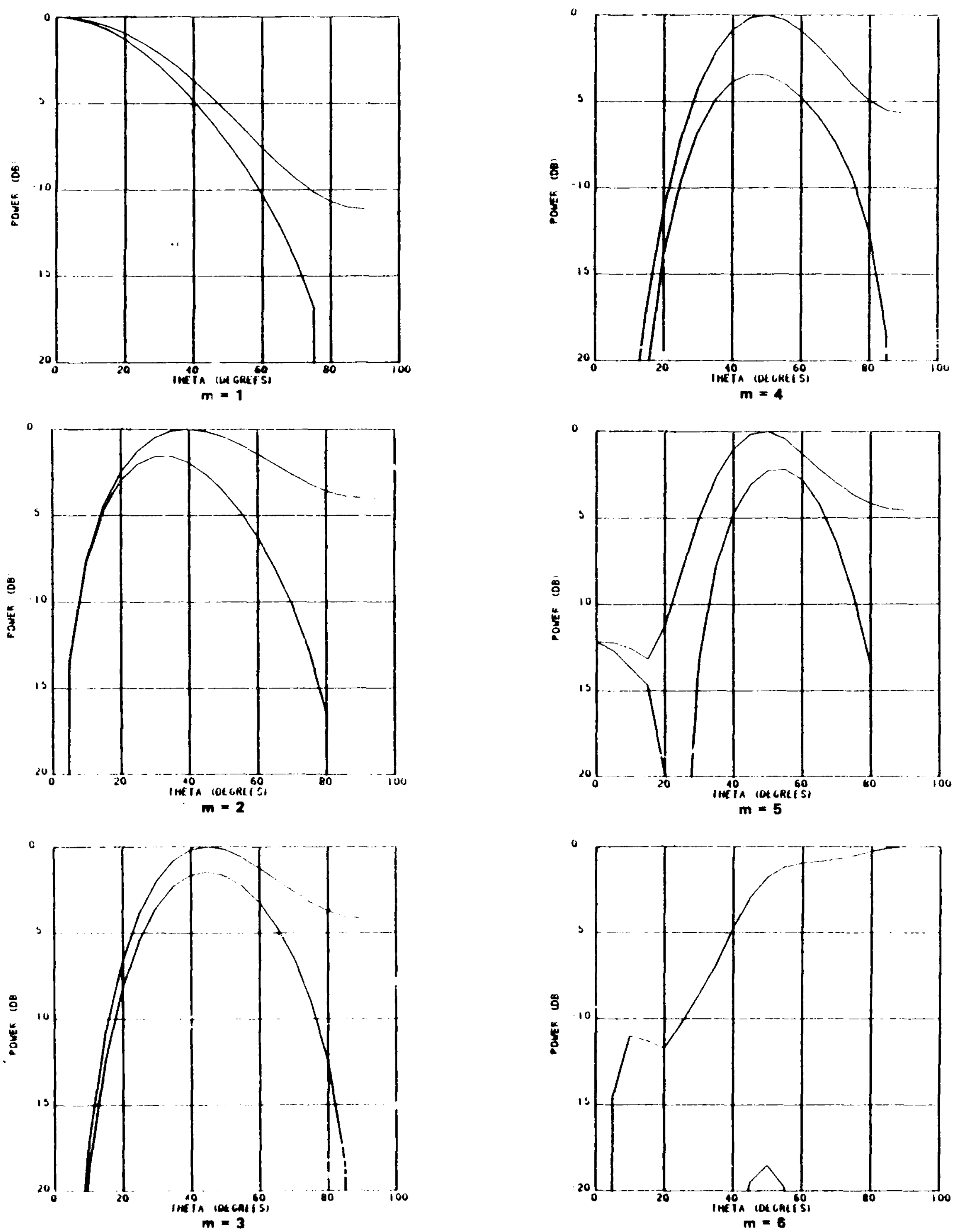

Figure 4. Radiation Patterns of 6-Arm Planar Spiral at $\phi = 0^o$, $a = 83.7^o$, $r_o = 0.1\lambda$, outer circumference = 4λ at 4 GHz, f = 4.4 GHz

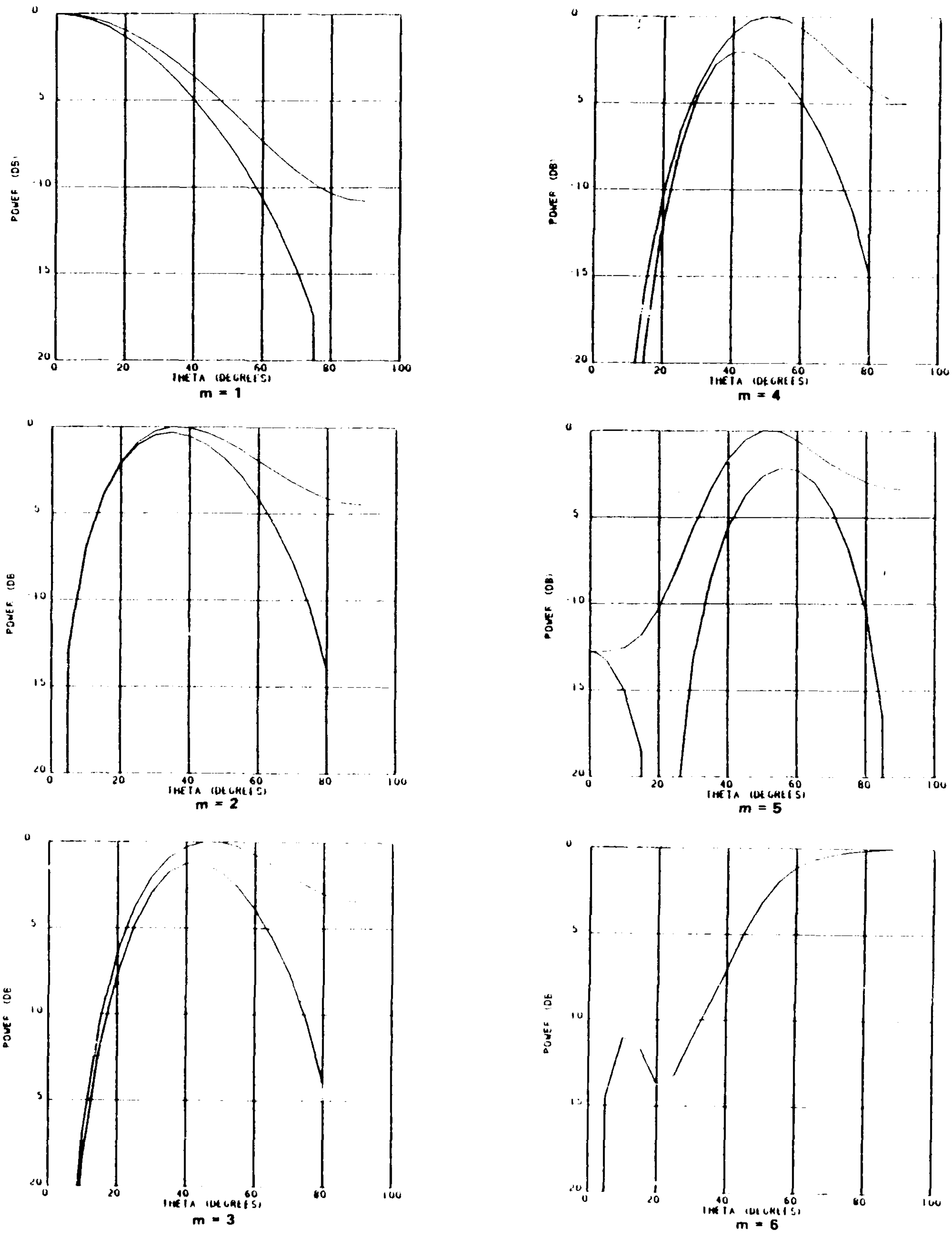

Figure 5. Radiation Patterns of 6-Arm Planar Spiral at $\phi = 30^o$.
$a = 83.7^o$, $r_0 = 0.1\lambda$, outer circumference = 4λ at 4 GHz, f = 4.4 GHz

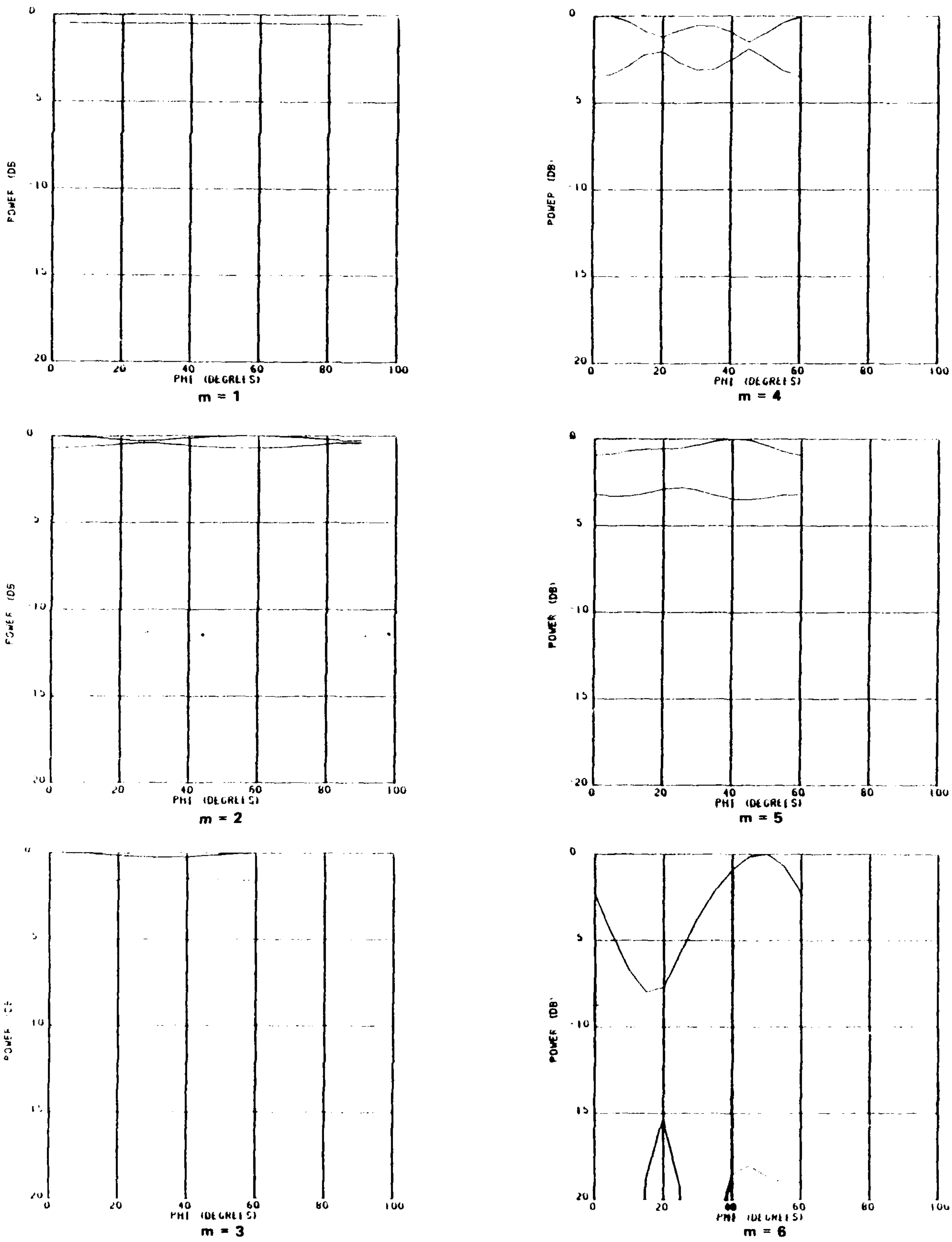

Figure 6. Radiation Patterns of 6-Arm Planar Spiral ϕ Variable; θ At or Near Difference Beam Peak

References:

1. Georges A. Deschamps, "Impedance Properties of Complementary Multi-terminal Planar Structures", IRE Trans. on Antennas and Propagation, Dec 1969, pp 5371-5378.

2. Ali E. Atia and Kenneth K Mei, "Analysis of Multiple-Arm Conical Log-Spiral Antennas", IEEE Trans. on Antennas and Propagation, May 1971, pp 320-331.

3. A. Atia, "Multiple-Arm Conical Log-Spiral Antennas", Ph.D Dissertation, University of California, Berkeley, 1969.

4. Victor H. Rumsey, "Frequency Independent Antennas", Academic Press, New York, 1966.

5. Craig G. Roberts, "Broad-Band Two-Channel Monopulse Tracking System", Technical Report ECOM-0181-E134, Electronic Defense Laboratories, Sylvania Electric Products, Mountain View, CA, Feb 1968, p. 50.

6. P. G. Ingerson, "Modulated Arm Width (MAW) Log-Spiral Antennas", Proceedings, 12th Annual Symposium, USAF Antenna Research and Development Program, Oct 13-15, 1970, Montecello, Ill.

7. O. K. Kim, and J. D. Dyson, "A Log-Spiral with Selectable Polarization", IEEE Trans. on Antennas and Propagation, Sept 1971, pp 675-677.

A Network Formulation for Phased Arrays-
Application to Log-periodic Arrays of
Monopoles on Curved Surfaces

Dr. Richard J. Coe
Dr. Donald E. Young

Boeing Aerospace Company
Seattle, Washington

ABSTRACT

An adequate matrix representation for the network parameters of virtually any array element geometry can be obtained through numerical modelling. Practical active or passive feed networks are also easily represented as a matrix of network parameters. Thus properties of the array (array element excitation, near and far field pattern, driving point impedance, gain, etc.) can be obtained from a solution of the connected networks. While the techniques involved are not new, there does not appear to have been extensive application of numerical modelling techniques to the complete antenna-feed subsystem. The power available in these techniques is illustrated, in this paper, by a numerical model of log-periodic arrays of driven monopoles interlaced with parasitic elements. The code has been implemented both as an interactive design tool on a minicomputer and on a larger system to handle several coupled arrays on surfaces of revolution.

The purpose of this paper is to describe the network formalism and present some comparison between computed and measured results. It will be demonstrated that when the parasitic element lengths of a log-periodic monopole array are adjusted properly, a backward slow-wave is developed on the structure. Typical plots of radiation pattern and impedance are presented. Results for several coupled arrays on a truncated cone are also given.

1.0 INTRODUCTION

In analysis, design and development of antennas, the antenna is often considered separately from its feed network and from the rest of the system of which it is a part. System performance specifications are often allocated over the various constituent subsystems. Traditionally the antenna allocations are translated into some of the following specifications on antenna performance: pattern, gain, coverage, polarization, bandwidth, VSWR and sidelobe level. Usually there is not a one-to-one correspondence between meeting specifications and system performance. Hence it is frequently advantageous to model an antenna together with several other components of the system to obtain an overall transfer function for the system. With recent advances in numerical techniques for the solution of electromagnetic field problems and improvements in computer technology it is possible to obtain accurate transfer functions from an incident field to a receiver through an antenna and other components of a reasonably complex system. The path may include aircraft response, antenna transfer function, coupler circuit and transmission lines. Several such end-to-end models have been used in calculating the pulse response of avionic systems on aircraft exposed to EMP. The approach is to combine the network representation of radiating systems with that of the transmission line or lumped element equivalent circuits of the rest of the system. For example, by considering the antenna and feed network as an entity, network parameters can be synthesized to provide prescribed maxima or nulls in the scattering pattern of any antenna. This is important in maintaining low radar cross-section of aircraft in military applications. In this paper, a combination of electromagnetic modelling techniques and network theory are used to calculate the performance of a log-periodic monopole array containing driven elements as well as parasitic elements. This is a particularly good example because the nature of the problem is that very accurate modelling of the radiating system is necessary and antenna performance cannot be separated from the properties of the feed. The performance of several log-periodic monopole arrays on a conducting conical surface are also obtained by representing the conical surface as a wire mesh.

2.0 NETWORK FORMALISM

An impedance matrix formulation of combined antenna and feed network is illustrated in Figure 1. Both antenna and feed are represented by multiport Thevenin equivalent networks. The open circuit impedance matrix is a convenient representation for arrays in which element currents become small upon open circuiting the antenna terminals. An array of dipoles is an example. The dual, a generalized Norton equivalent circuit with a short circuit admittance matrix, is more convenient for slots in which element voltages become zero upon short circuiting the terminals. The network to the left in Figure 1 is the generalized Thevenin equivalent circuit of an antenna array, which may be visualized as an array of dipoles with each feed point represented as a port of the network. The open circuit impedance matrix of the array is Z_A and the open circuit voltages induced on each element by an external incident field are represented by a column matrix V_R. The voltage at the accessible terminals of the antenna is represented by a column matrix, V_A, and the corresponding currents by I_A. The feed network can be similarly characterized as a Thevenin (or Norton) equivalent circuit as shown on the right of Figure 1. If there are sources in the feed network, they are represented by Thevenin open circuit voltages, V_T, in series with the terminals of a passive network represented by an open-circuit impedance matrix, Z_F. Usually an antenna is excited either as a transmitting antenna or a receiving antenna at a given time. In the transmitting mode, V_R is a null matrix and V_T is the only source term. Similarly in the receive mode, V_T, is null and V_R is the source.

A solution of the antenna-feed network consists of solving for currents at the accessible ports. With the port currents known, all the properties of interest in the antenna array can be calculated: antenna transmitting pattern, driving point impedance, scattering pattern, gain, and receiving effective height function.

Using the relations, $V_A = V_F$ and $I_A = -I_F$, it is readily shown that the port currents may be obtained from

$$I_F = \left[Z_A + Z_F\right]^{-1} V_R \qquad \text{(Receive Case)}$$
$$I_A = \left[Z_A + Z_F\right]^{-1} V_T \qquad \text{(Transmit Case)} \tag{1}$$

Once I_F or I_A are known, the other properties of the antenna may be calculated. For example, in the transmit case the terminal currents, I_A, may be used together with the current distribution on the elements (or the element patterns) to calculate the near or far fields of the array. The antenna gain may be obtained directly from the far field pattern and power into the feed network without performing the usual pattern integration. Network and mismatch losses are automatically included in the result. Similarly the driving point impedance may be obtained from the feed port voltage to current ratio. The active impedance of an element, i, is the ratio $V_A(i)/I_A(i)$. In the receiving mode, the currents $I_A = -I_F$ may be used to calculate the scattering pattern of the antenna. The ratio of open circuit voltage at the feed port to the field incident on the antenna is the effective height function of the array. Methods for representing array antennas and detailed examples of solutions will be given in the following section.

3.0 APPLICATION TO A LOG-PERIODIC MONOPOLE ARRAY WITH PARASITIC ELEMENTS

The intent of this section is to illustrate the application of network techniques to antenna-feed system modelling. The antenna-feed system discussed is a log-periodic monopole array in which a parasitic monopole, shorted at its base, is located between each base-fed driven element. The configuration is that investigated empirically by Barbano (Ref. 1) but generalized to allow different sets of scaling parameters for driven and parasitic elements. The model was extended to several coupled arrays of log-periodic monopoles on the surface of a conducting cone.

The exact image form of the Isbell Log-Periodic Dipole Array (LPDA) does not exist because of the method of reversing the phase of the feeder lines at adjacent elements. It has been shown that the k-β diagram of a log-periodic dipole array fed by a transmission line without phase reversal (a configuration which does image) has no solution in the backward slow-wave region (Ref. 2) and therefore is not capable at Pseudo frequency independent performance. Other ways of feeding log-periodic monopole arrays (LPMA) have been developed which do support a slow backward wave (Ref. 2 and 3). However, LPMA's are in general more sensitive to design parameters than LPDA's. Indeed the performance of the LPMA with parasitics is extremely sensitive to design parameters.

3.1 ARRAY GEOMETRY

Geometry of an LPMA interlaced with parasitic elements will be defined as shown in Figure 2. The parasitic array has an envelope defined by the angle, α_p, and the envelope of the driven array by α_D. The algorithm for generating the distance R(N) is R(N) = R(N-1)τ. Odd numbered elements are the driven elements, the longest of which is located at $R(1) = K_{LOW}/\tau$ where K_{LOW} has been termed the low frequency truncation constant. $K_{LOW} = 0.25\lambda$ (i.e., it is the length of an element in wavelengths which approximately defines the low frequency edge of the active region). The first driven element is chosen as the next longer element to assure that the active region is well inside the array. The distances from the apex are generated, starting with R(1), by the recursive relation

$$R(N) = R(N-1)\,\tau$$

The corresponding lengths are obtained from

$$L(N) = R(N) \cdot \tan(\alpha_D), \quad N_{ODD}$$

$$L(N) = R(N) \cdot \tan(\alpha_P), \quad N_{EVEN}$$

The process is terminated when the length of the parasitic element becomes

$$L(N_{EVEN}) < K_{HIGH}\,\tau$$

where $K_{HIGH} = 0.19\lambda$. Because the test is applied to the parasitic element, the number of elements outside the active region is greater at the high frequency end than the low frequency end of the array. This is to accommodate the increased directivity in the backward direction and possibly higher coupling to parasitic elements in that direction. A unit cell of the LPMA geometry consists of two elements. To satisfy scaling rules, the height to diameter ratio is a constant from cell to cell. However, the parasitic element height to diameter ratio may be different from the driven element ratio.

3.2 IMPEDANCE MATRIX OF LPMA

Obtaining an impedance matrix for an LPMA which could be used to predict design parameters of an LPMA with parasitic elements was somewhat challenging. For most applications involving monopole arrays (i.e. all elements driven or parasitic element arrays in which the interelement spacing is not too small), available theoretical treatments for self and mutual impedance are entirely adequate. We have found the integral equation method of T.T. Wu (Ref. 4) to give good results for the self-impedance terms. The induced EMF method using sinusoidal current distributions generally provides adequate values for mutual impedance. Computer implementations of these models provide good accuracy without incurring excessive computation time. Unfortunately these codes were found to be inadequate in calculating design parameters of an LPMA with parasitic elements. The inaccuracies increased as the scaling parameter, τ, approached unity (i.e. as the interelement spacing became small). The difficulty was not experienced for an LPMA consisting entirely of driven elements—even for closely spaced elements. In an attempt to resolve the issue, measurements were made of the self- and mutual-impedance of monopoles. Measurements were made over a wide range of monopole heights, height to diameter ratios, and interelement spacings. A typical measurement of self-impedance is compared in Figure 3 with calculations from the Wu model. Also shown are calculations obtained from a wire antenna moment method code

(WIRANT). In general, all three models agree well. Some difference is to be expected because of approximations in modelling particularly of the antenna base region in the models. Measured and computed mutual impedance as a function of element separation are shown in Figure 4 for three different heights which characterize the active region of an LPMA. Again all three models (empirical, EMF method, WIRANT) yield results in essential agreement.

Some other assumptions inherent in the impedance model were investigated experimentally. One of these is that the (open circuit) mutual impedance between monopoles imbedded in an array is well approximated by the mutual impedance between isolated elements. This is a common assumption based upon the fact that currents induced on a monopole open-circuited at its base are small relative to the near resonant currents of the loaded monopole. A measurement of mutual impedance between monopoles of height $.22\lambda$ separated by $.1\lambda$ was compared with a similar measurement with an open circuited monopole midway between them. The difference was negligible. The effect of an adjacent element on self impedance was also measured. This result is shown in Figure 5 as a function of the separation of the adjacent element. The solid curves are the measured self-impedance when the second monopole was removed. Maximum variation in amplitude of self impedance is about $\pm$ 2 ohms (or $\pm$ 5%). The maximum change in phase due to the presence of an adjacent open-circuited element is $\pm 7^{\circ}$. These are very small errors but are significant due to the nature of the array current distribution.

The net result of the experimental effort is that the theoretical models, the moment method code, and the empirical model yield very consistent results. It was observed experimentally that performance of the LPMA with parasitic elements is very sensitive to the length of the parasitic elements (or angle, α_p) and to interelement spacing. This provides a clue that even small errors in calculated impedance parameters may be significant. Ordinary log periodic dipole antennas are not usually considered to be high Q devices. However an essential ingredient in log-periodic operation is approximately 180° phase reversal of feeder voltage between adjacent elements. For electrically small interelement spacing this suggests the possibility of large stored energy in the vicinity of the elements. In the log-periodic monopole array with parasitic elements large phase differences with respect to the free space propagation phase occur when the structure is adjusted to support a backward slow-wave which is necessary for true log-periodic performance. As a result of these considerations, it was decided to include scattering from open circuited elements in computing the open-circuit impedance matrix. This was done by modelling the entire active region with the WIRANT code. The short-circuit admittance matrix was obtained by successively placing one-volt sources at each base segment with all other base segments grounded to the image plane. The open-circuit impedance matrix was then obtained by inversion. The resulting antenna impedance matrix when combined with the parasitic element LPMA feed network matrix, yielded results in excellent agreement with experiment. With the resulting code, design parameters could be predicted accurately. Calculated radiation patterns, input impedance, active element impedance and current distribution along the array were in good agreement with measurement. The code was extended to include several coupled arrays of LPMA's on conducting truncated cones and cylinders. The conducting surfaces were included in the antenna impedance code by wire mesh modelling of these surfaces.

3.3 IMPEDANCE MATRIX OF FEED LPMA WITH PARASITIC ELEMENTS

A network representation of the feed for an LPMA with alternate elements parasitic is shown in Figure 6. Driven elements are connected to a transmission line of characteristic impedance, R_o, and propagation constant, γ . Parasitic elements are terminated in short circuits. For convenience, the feed port (port '0') of the transmission line is taken to be at the apex of the LPMA and the opposite end of the line is terminated in its characteristic impedance. It is also convenient to feed the transmission line with a Thevenin source impedance equal to the characteristic impedance of the line. The Thevenin equivalent representation of the feed is obtained by finding the open circuit voltages at driven element ports and the impedance matrix of the reduced feed network (i.e., the feed port is imbedded) with the voltage source, V_o, short circuited. The Thevenin equivalent of the more general case of mismatched feed can also be obtained. This is most easily obtained by writing the admittance matrix of the network without the feed port imbedded, taking the inverse and then applying the Thevenin theory. The somewhat less general case being considered provides better insight into the phase relationships which exist between ports. The open circuit voltages vector is given by

$$V = \begin{bmatrix} V_1 \\ V_2 \\ \cdot \\ V_n \end{bmatrix} \qquad V_n = \begin{cases} \frac{V_o}{2} e^{-\Gamma_n} & n \text{ odd} \\ 0 & n \text{ even} \end{cases} \tag{1}$$

where r_n is the distance of the N^{th} port from the apex of the LPMA. Similarly, the impedance matrix of the reduced network is

$$Z = \begin{bmatrix} Z_{11} & Z_{12} & Z_{1n} \\ Z_{21} & Z_{22} & \\ \cdot & \cdot & \cdot \\ \cdot & \cdot & \cdot \\ Z_{n1} & \cdot & Z_{nn} \end{bmatrix} \qquad (2)$$

where

$$Z_{ij} = \frac{R_o}{2} \quad e^{-\gamma |r_i - r_j|} \qquad \text{i and j odd}$$

$$Z_{ij} = 0 \qquad \text{i or j even}$$

3.4 PATTERN, GAIN AND IMPEDANCE CALCULATIONS

RADIATION PATTERN

Antenna patterns were calculated in the moment method code by computing the reaction between a distant source produ·. ·g an incident plane wave and the computed current distribution on the array elements. It will be useful to have a simple analytic expression for gain in terms of the base currents on the elements. This will be used to define a performance function for optimizing design parameters. The coordinate system for pattern calculations is oriented as shown in Figure 7 with the positive Z-axis in the direction of the maximum for a slow backward wave. The vector potential of this current distribution has only an x component whi:h may be written

$$A_x = \sum_{n-1}^{NL} \int \frac{I_n(x)}{4\pi |r - r_n|} e^{-j\bar{k} \cdot (\bar{r} - \bar{r}_n)} dx$$

where $r_n = x_n i_x + z_n i_z$ is the position of an element of current and $I_n(x)$ is the current on the n^{th} element. Using far field approximations and, assuming quarter wavelength monopoles with a sinusoidal distribution, the far field pattern becomes

$$E_\theta = \frac{-j Z_o}{2} \frac{e^{-jkr}}{r} \frac{\cos\theta \cos\phi \cos\left[\frac{\pi}{2} \sin\theta \cos\phi\right]}{1 - \sin^2\theta \cos^2\phi} F(\theta)$$

(5)

$$E_\phi = \frac{-j Z_o}{2} \frac{e^{-jkr}}{r} \frac{\sin\phi \cos\left[\frac{\pi}{2} \sin\theta \cos\phi\right]}{1 - \sin^2\theta \cos^2\phi} F(\theta)$$

where $F(\theta) = \sum_{n=1}^{NL} I_n e^{jk Z_n \cos\theta}$

is the array factor.

PERFORMANCE FUNCTION - ANTENNA GAIN

In order to optimize parameters of an array it is desirable to have a single measure of performance. The antenna gain in the backward direction is one measure. In order to include impedance mismatch, the antenna gain is defined as the ratio of the radiation intensity to the average available power

$$G = \frac{r^2 P(\theta=0, \phi=0)}{\frac{1}{4\pi} P_{AVAIL}} \tag{1}$$

The radiation intensity, u, may be written

$$U = \frac{60}{4\pi} \left| \sum_{n=1}^{NL} I_n \, e^{-jkr_n} \right|^2 \tag{2}$$

where the distance of each element from the apex, r_n, has been substituted for $-z_n$.

For an array of monopoles above a perfectly conducting half space, the available power is

$$P_{AVAIL} = \frac{1}{2} \, I^2 \, R_o$$

where R_o is the characteristic impedance of the transmission line which is equal to the source impedance (see Figure 8). For a Thevenin source V_o

$$I = \frac{V_o}{2 \, R_o}$$

and

$$P_{AVAIL} = \frac{1}{2} \; \frac{V_o^2}{4 \; R_o^2} \; R_o = \frac{V_o^2}{8 \, R_o} \tag{3}$$

Substituting (2) and (3) in (1)

$$G = 480 \, \frac{R_o}{V_o} \left| \sum_{n=1}^{NL} f_n \, e^{-jk\,r_n} \right|^2 \tag{4}$$

3.5 INPUT IMPEDANCE

It will be assumed that the NL port network of Section 3 has been solved for NL currents at the ports of the feed network which are connected to monopoles. The problem is to find the impedance at the input port which is imbedded in the formulation of Section 3. Referring to Figure 8, currents $I_1, I_2 \ldots I_{NL}$ are known and the impedance $Z_{IN} = \frac{V_o}{I_o}$ is to be expressed in terms of the known currents. For the NL+1 port network of Figure 1

$$V_o = \sum_{n=0}^{NL} Z_{ok} I_k = Z_{oo} I_o + \sum_{n=1}^{NL} Z_{ok} I_k \tag{1}$$

where $Z_{oo} = R_o$ is the characteristic impedance of the transmission line and the mutual impedances between the 0^{th} port and the n^{th} port are

$$Z_{ok} = R_o e^{-\gamma R_k} \tag{2}$$

Now write

$$I_k = \left[- \frac{I_k}{V_s} \right] V_s \tag{3}$$

The quantity $\left[-I_k/V_s\right]$ is the monopole current due to a unit Thevenin voltage source ($V_s = 1$) at the input to feed network. This is the quantity which has been determined by the method of Section 3. The next step is to express V_s in terms of V_o and I_o.

$$V_s = V_o + I_o R_o \tag{4}$$

Substituting (3) and (4) in (1) yields

$$V_o = R_o I_o - (V_o + I_o R_o) \sum_{n=0}^{N} Z_{ok} \left[- \frac{I_k}{V_s} \right] \tag{5}$$

Let $\Gamma = \sum_{n=0}^{NL} Z_{ok} \left[- \frac{I_k}{V_s} \right]$ and solve (5) for V_o/I_o; the result is:

$$Z_{in} = \frac{V_o}{I_o} = R_o \frac{1 - \Gamma}{1 + \Gamma} \tag{6}$$

Equation (6) expresses the input impedance referenced to the apex of the LPMA in terms of quantities which can be calculated from solutions of the reduced network of Section 3.2.

4.0 RESULTS

Several codes were developed to calculate performance of monople arrays on conducting surfaces. The first of these was written for interactive computer aided design and was implemented on a mini-computer. The impedance matrix was generated using the theoretical models discussed in Section 3.0. The feed subroutine provided the option of calculating the impedance matrix of a phase reversing feed for a log periodic dipole array (LPDA), a log-periodic monopole array with differential feed (LPMA) or a log-periodic array with alternate elements parasitic (parasitic LPMA). This code was then implemented on the Cyber machine and coupled with the WIRANT code to calculate the antenna impedance matrix and to calculate antenna patterns. Initial verification of the code was to compare results for an LPDA with Carrel's (Ref. 5) calculations. These results are shown in Figure 9. While Carrel used a different model for element impedance, the results are seen to be in excellent agreement. The calculated current distribution for an LPDA design with similar configuration to Carrel's is shown in Figure 10. Note that the envelope angle, α_p, for the parasitic elements is larger than the corresponding angle, α_D, for the driven elements. This is characteristic of optimized parasitic LPMA's and is usually necessary to generate a backward wave. The current distribution has the phase distribution of a backward wave and a magnitude which tends to have lower current amplitudes in the parasitics than the driven elements. Calculations are shown for theoretical element impedances and for WIRANT impedances. For these relatively small values of τ, both models give nearly the same results.

An experimental model of a parasitic LPMA was constructed as shown in Figure 11. The design parameters are $\tau = .95$, $\alpha_D = 14^o$, α_p adjustable, $\Omega_D = 10$ and $\Omega_p = 8.9$. This differs from the Carrel parameters in that the interelement spacing is much smaller. The length to diameter ratio of the parasitic elements is different (smaller than) the ratio for the driven elements. The measured current distribution, with parasitics adjusted for best impedance match shown in Figure 12. Characteristics of the current distribution are very similar to those of Figure 10. The transmission line characteristic impedance was 72 ohms. The measured input impedance normalized to 50 ohms is shown in Figure 13 over a frequency band corresponding to two periods of the array. Also shown are a few calculated points using the WIRANT version of the code. The VSWR circle is slightly larger for the calculated impedances. It will be noted that parasitic LPMA's are not as well matched to the line as LPDA's. Measured and computed patterns are compared in Figure 14. The computed pattern is the H-plane pattern of the antenna. The measured pattern, with a necessarily finite ground plane, is a conic through the beam maximum, 63° from the normal to the ground plane. The WIRANT version gives better null definition. The measured beam width is also somewhat broader.

A computer model for several LPMA's distributed circumferentially around the surface of a cone was also developed. The configuration is shown on Figure 15. The angular displacement is uniform and the elements are fed with a uniform phase progression at some multiple of $2\pi/N$ radians per element. This produces circular polarization along the axis of the cone. The surface of the cone was modeled with a wire mesh and was truncated outside the active region of the arrays. Other aspects of the code were similar to its counter part on a flat ground plane. The construction of the WIRANT model is such that the effects of the conducting cylinder and mutual impedances between elements on the same array and in different arrays are all taken into account. Note that the cone maintains the frequency independent geometry. An experimental model was constructed on a solid metal cone. The arrays were fed by a Butler type feed network capable of either $2\pi/N$ or $4\pi/N$ radians phase shift between adjacent arrays. The active input impedance measured at one of the arrays over about an octave in frequency is shown in Figure 16. Calculated impedances covering a frequency range equal to the scaling parameter τ^2 are also shown. All impedances have been referenced to the tip of the cone. A little thought will show that this is the only point about which impedances will repeat in successive frequency intervals corresponding to the period of the array. The period is τ^2 since a similarity cell of the geometry contains two elements. Some calculated patterns are compared with measurements in Figure 17. The two patterns with a peak along the axis of the cone are the E and H plane patterns for a $2\pi/N$ mode. The patterns with a null on axis are $4\pi/N$ patterns. Fairly good agreement is obtained between measured and calculated patterns. Experimental patterns have nulls in the backward direction due to tower blockage.

5.0 CONCLUSIONS

The purpose of this paper was to illustrate that rather complex electromagnetic field problems can be accurately solved simultaneously with the networks connected to them. The result demonstrated is a code which can be used as a design tool for determining dimensions to satisfy some performance criteria. The particular example is extremely sensitive to small variations in the design parameters. For example a 0.1° change in angle of the parasitics was found to have a significant effect on the impedance plot and value of the maximum VSWR. It follows that this particular configuration is susceptible to tolerance errors. Indeed it was only after attention to tolerances in the manufacturing process that good agreement between calculated and measured results was obtained. This paper also illustrates that careful experimental evaluation of the various numerical/ theoretical models is indispensable.

The code structure employed in this model has been adapted to more general conformal phased arrays. Feed and antenna immittance matrix subroutines are user defined. Typically, antenna equivalent circuits are obtained from theoretical models or moment method codes. Antenna element patterns on complex structures have also been obtained from Geometrical Theory of Diffraction (GTD). One application of this code was to predict the pattern of a ring array of microstrip patches on a missile of cylindrical cross-section with various appendages. The element pattern of a patch in this geometry was obtained from GTD and input in tabular form to the array pattern code. Currently these codes are being implemented on the CRAY1 where it is anticipated that conformal phased arrays with several thousand elements and their feed networks can be accommodated.

REFERENCES

1. Barbano, Normand, "Log Periodic Dipole Array with Parasitic Elements Technical Memo EDL-M623, Sylvania Electric Products, Inc., Mountain View, CA. January 1964.

2. Hudock, E. and P. E. Mayes, "Nearfield Investigation of Uniform Periodic Monople Arrays," IEEE Transactions on Antennas and Propagation, Nov. 1965 pp. 840-855.

3. Green, Philip B. and Paul E. Mayes, "50Ω Log-Periodic Monopole Array with Modulated - Impedance Microstrip Feeder," IEEE Transactions on Antennas and Propagation, March 1974 pp. 332-334.

4. Wu, Tai Tsun, "Theory of the Diplole Antenna and the Two Wire Transmission Line," J. Math Phys., July - August 1964, pp. 550 574.

5. Carrel, Robert, "An Analysis of the Log-Periodic Dipole Antenna, Presented at the 10th Annual Symposium on the USAF Antenna Research and Development Program, 4 October 1960.

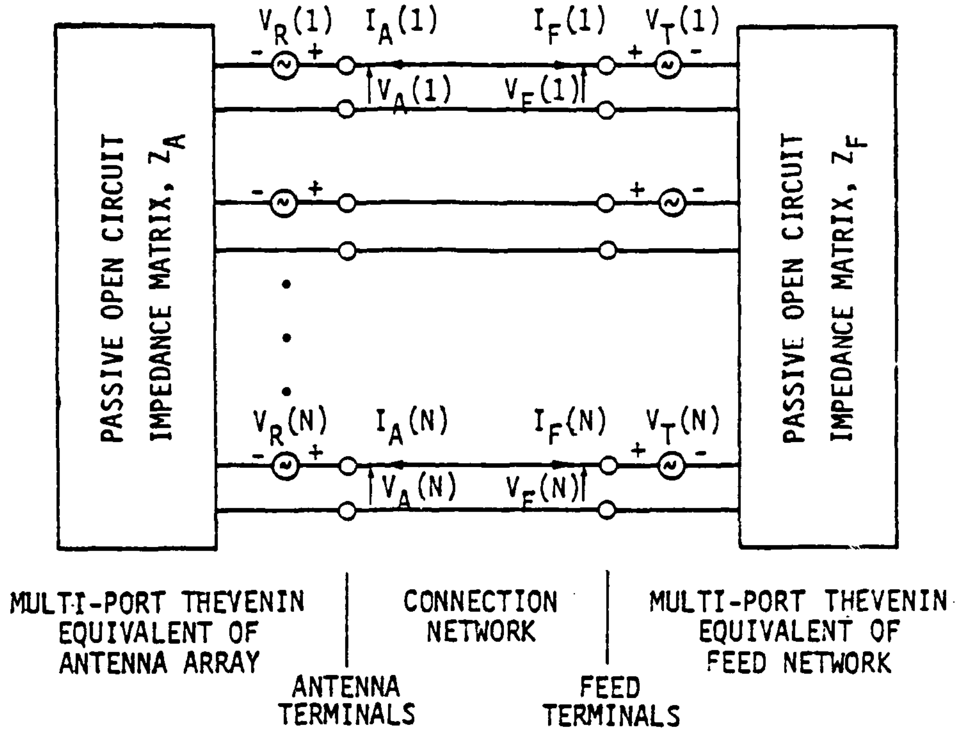

FIGURE 1 THEVENIN EQUIVALENT CIRCUIT OF ANTENNA AND FEED NETWORK

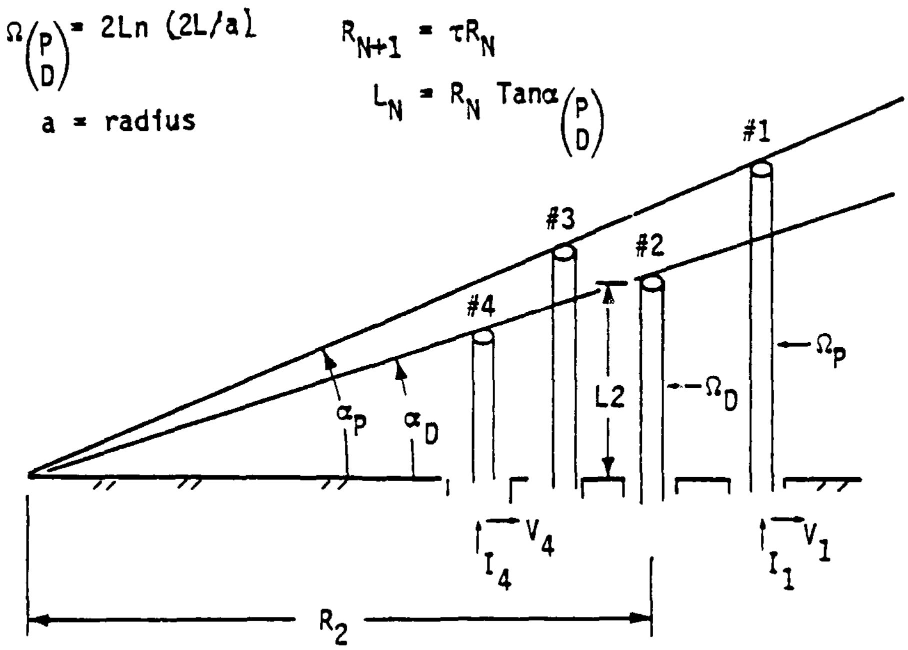

FIGURE 2 GEOMETRY OF LPMA INTERLACED WITH PARASITIC ELEMENTS

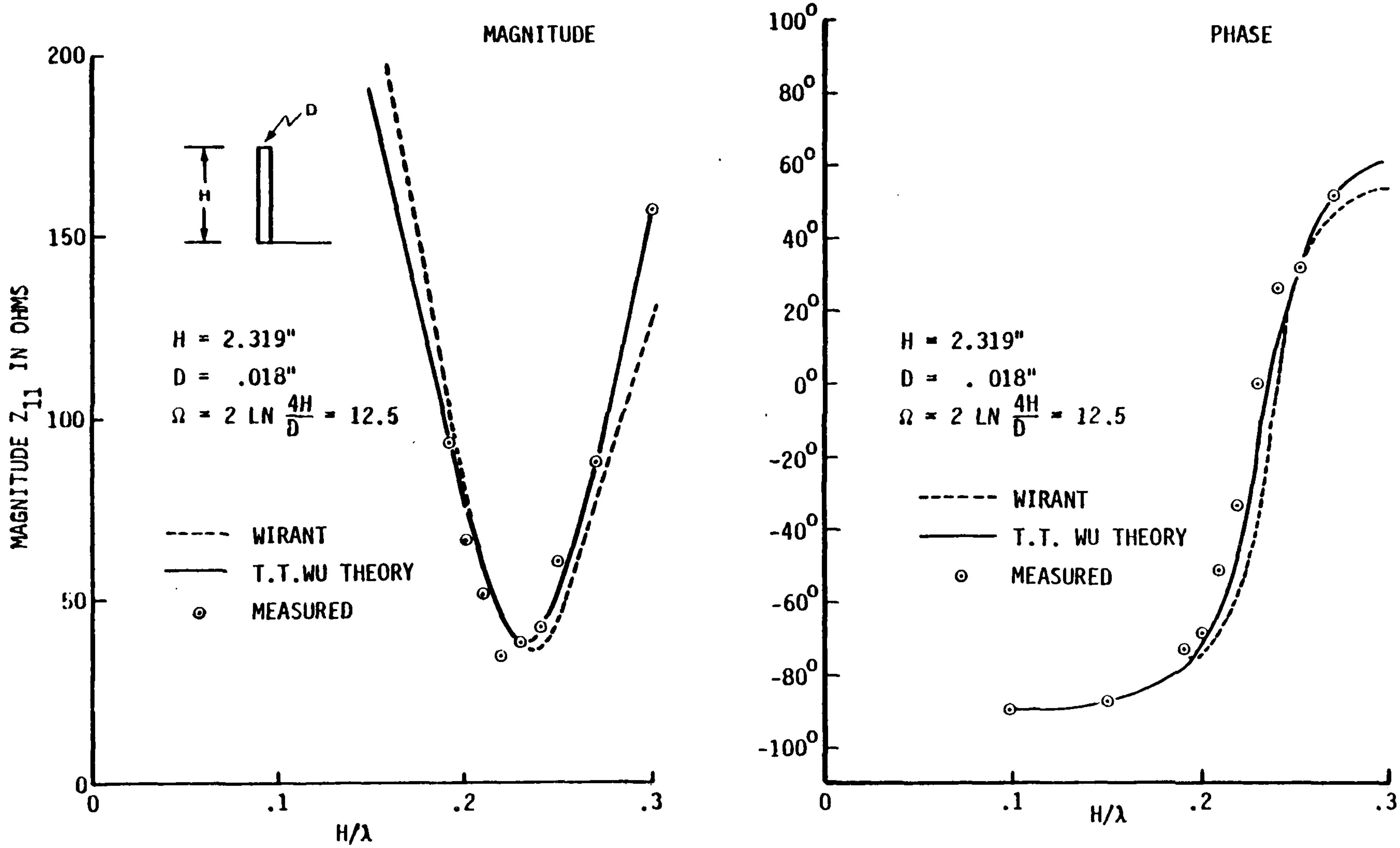

FIGURE 3 COMPARISON OF THEORETICAL AND MEASURED SELF-IMPEDANCE OF MONOPOLE

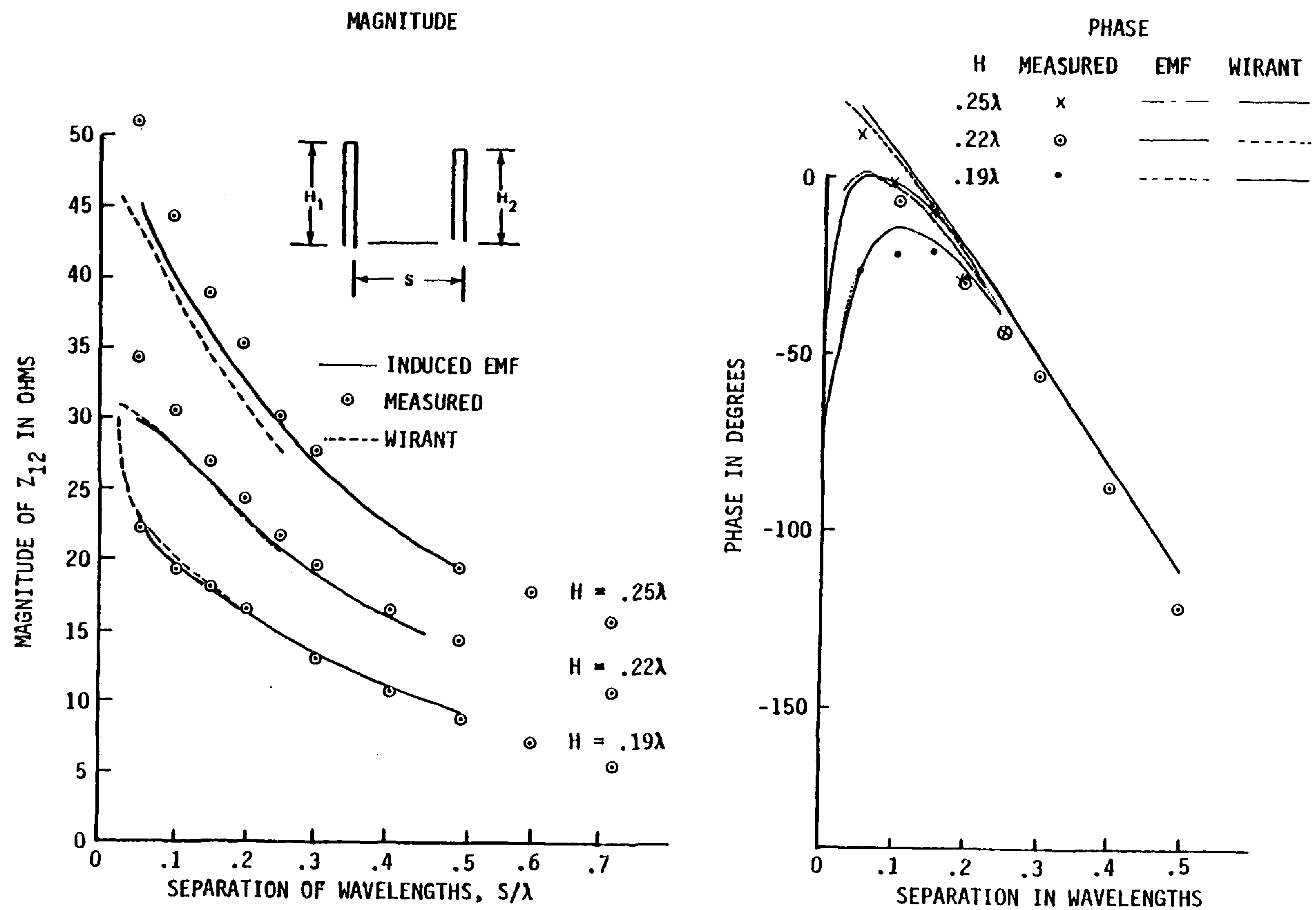

FIGURE 4 COMPARISON OF THEORETICAL AND MEASURED MUTUAL IMPEDANCE BETWEEN MONOPOLES AS A FUNCTION OF SEPARATION

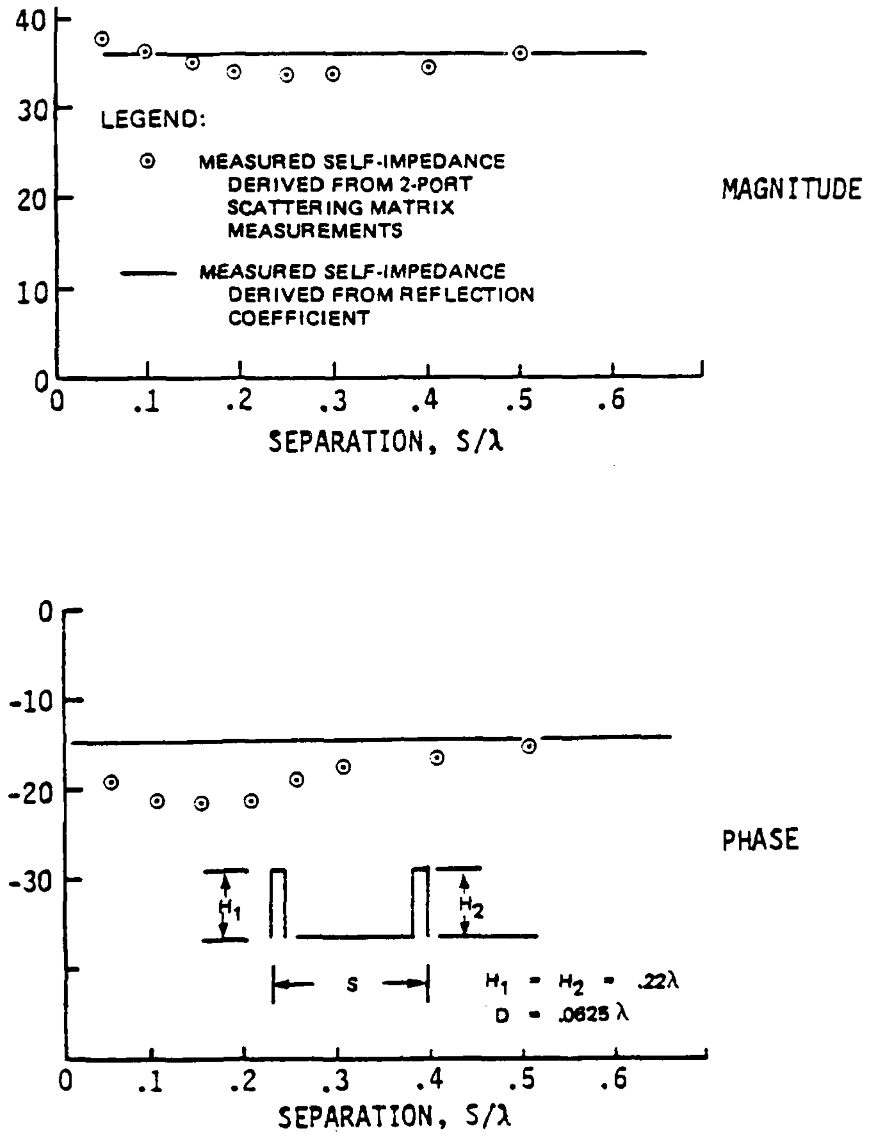

FIGURE 5 EFFECT OF A NEARBY OPEN-CIRCUITED ELEMENT ON THE SELF IMPEDANCE OF A MONOPOLE

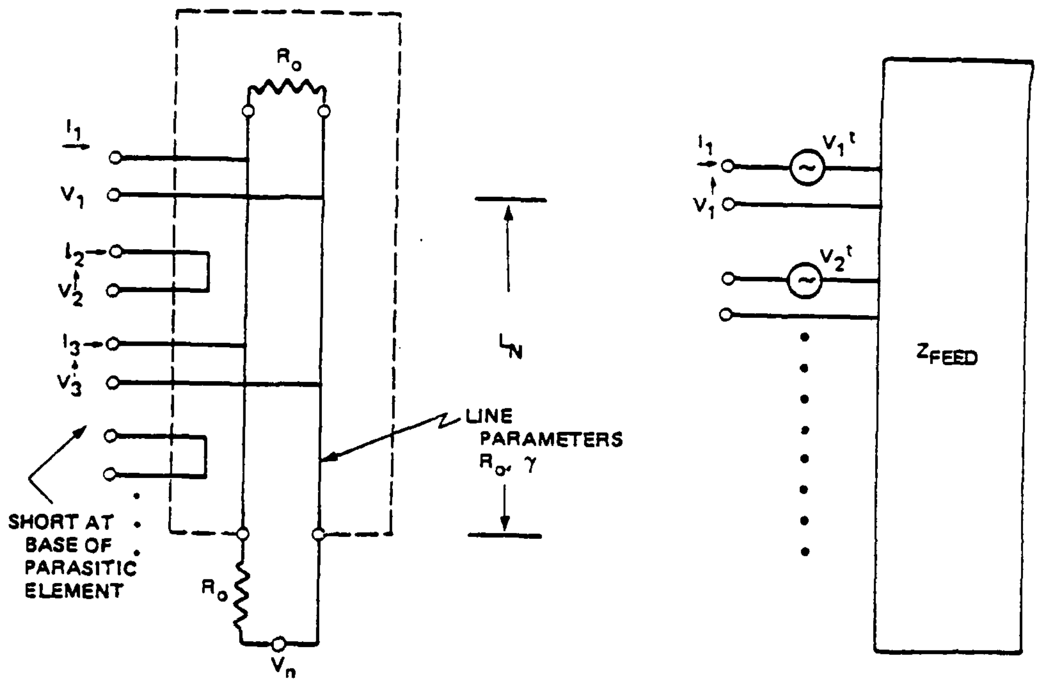

FIGURE 6 FEED NETWORK FOR LOG PERIODIC MONOPOLE

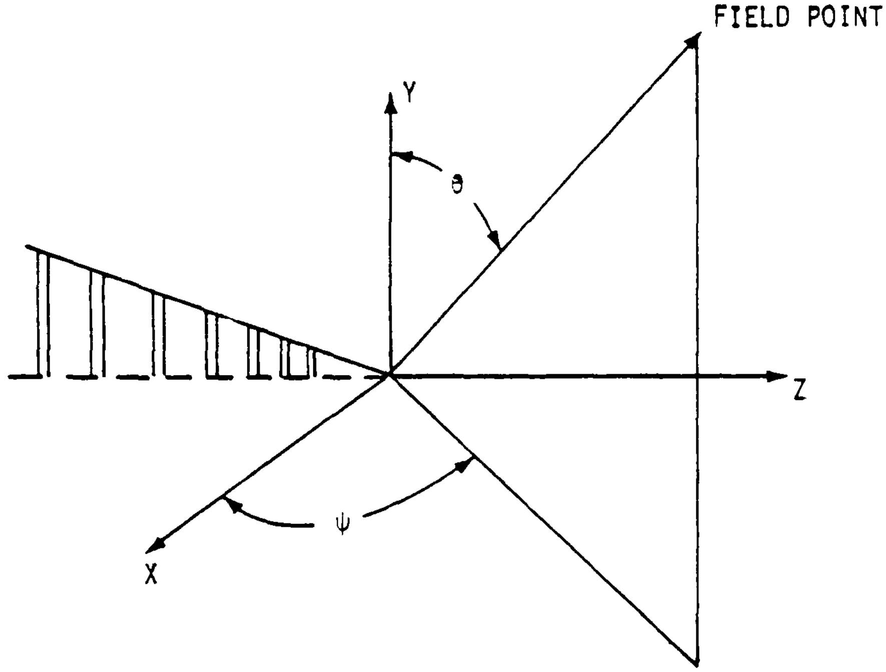

FIGURE 7 COORDINATE SYSTEM FOR PATTERN CALCULATIONS

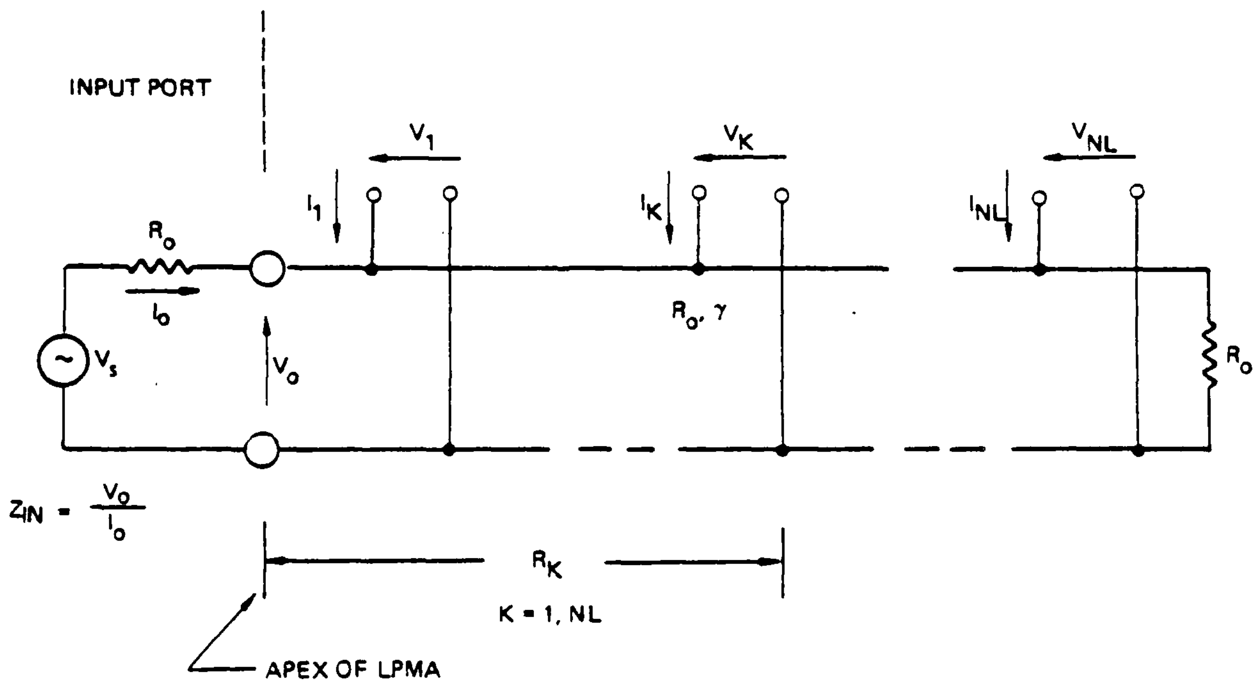

FIGURE 8 NETWORK FOR DETERMINING INPUT IMPEDANCE OF LPMA

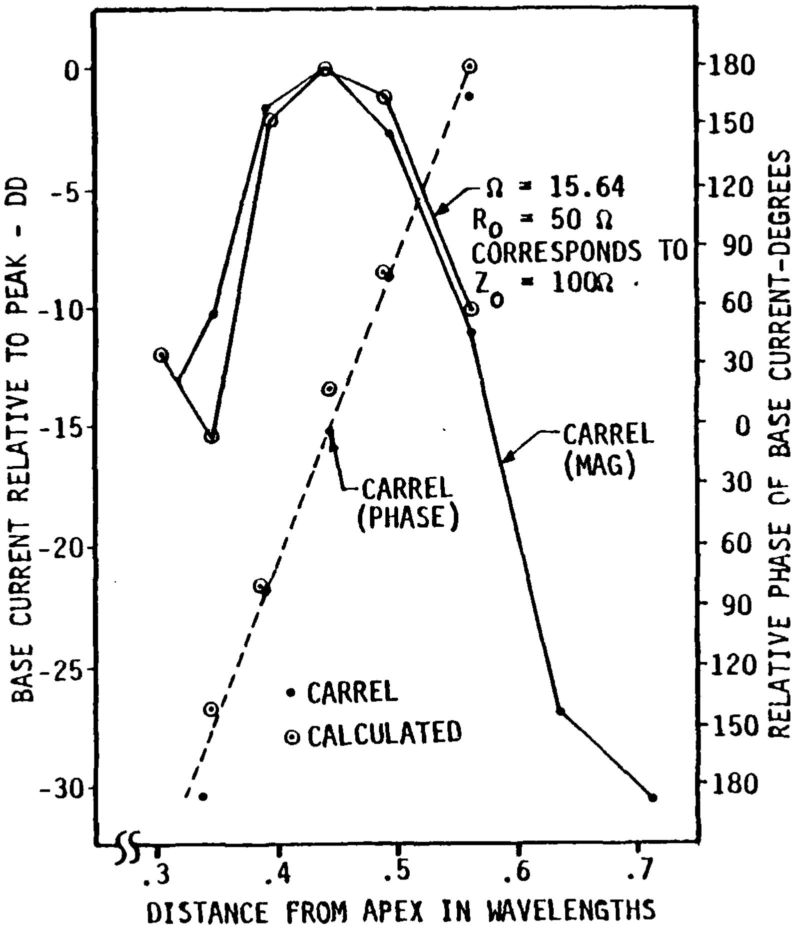

FIGURE 9 COMPARISON OF CALCULATED CURRENT DISTRIBUTION ON LOG PERIODIC DIPOLE ARRAY WITH THOSE OF CARREL

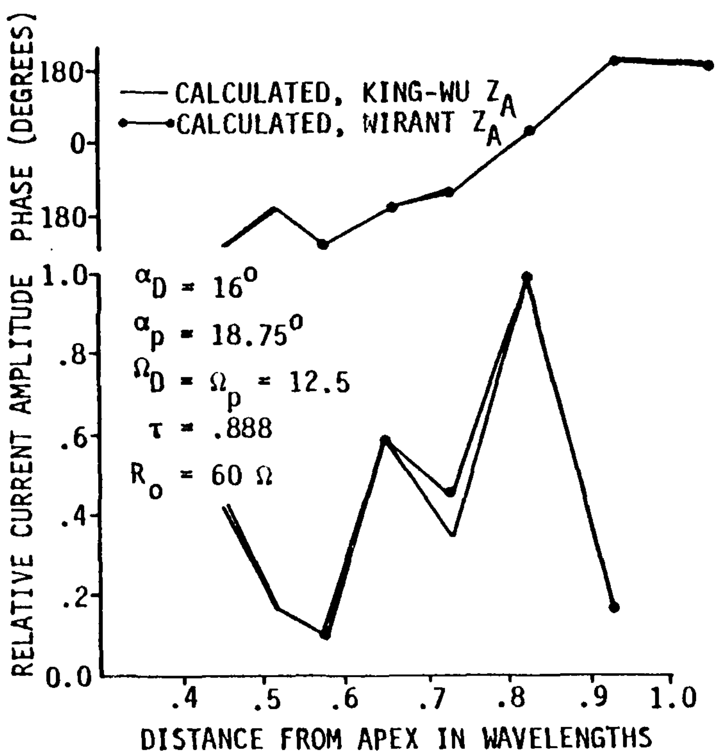

FIGURE 10 COMPARISON BETWEEN THEORETICAL MODELS OF LPMA ON FLAT CONDUCTING PLANE

ELEM	X	L	d	W
1	2.000	1.755	.082	
2	2.370	1.847		.028
3	2.760	1.944	.091	
4	3.171	2.047		.037
5	3.602	2.154	.101	
6	4.057	2.268	.112	.046
7	4.536	2.387	.112	
8	5.040	2.513		.056
9	5.571	2.645	.124	
10	6.129	2.784		.068
11	6.717	2.931	.137	
12	7.335	3.085		.081
13	7.986	3.247	.152	

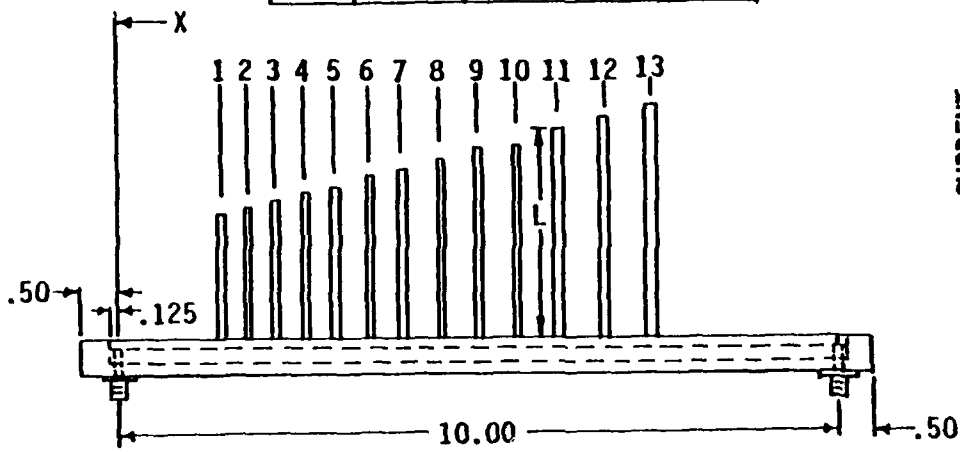

FIGURE 11 EXPERIMENTAL LPMA ON FLAT CONDUCTING SHEET

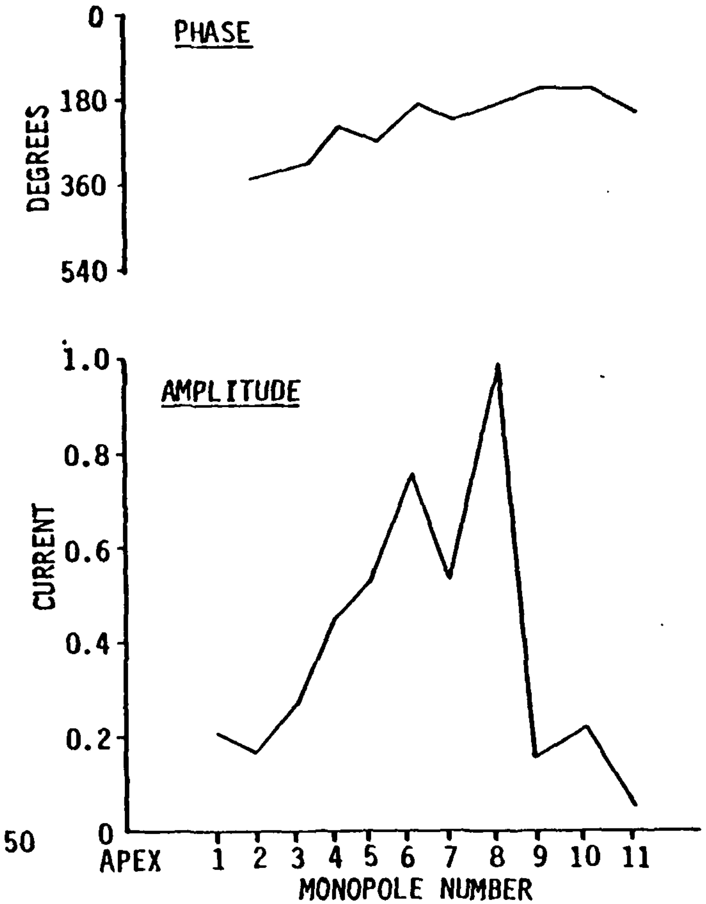

FIGURE 12 MEASURED CURRENT DISTRIBUTION OF LPMA

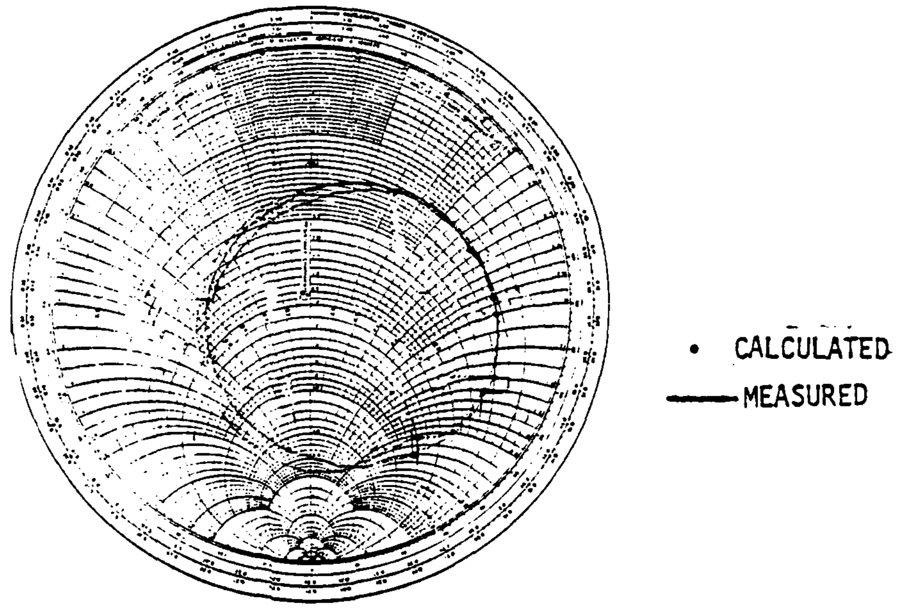

FIGURE 13 COMPARISON OF MEASURED AND COMPUTED IMPEDANCE OF LPMA ON FLAT IMAGE PLANE

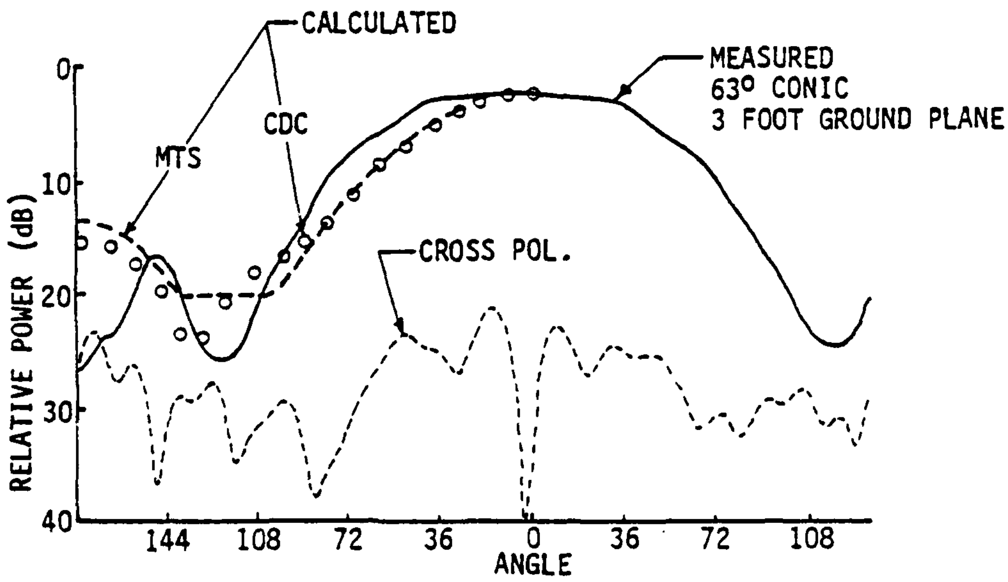

FIGURE 14 MEASURED AND CALCULATED PATTERN OF LPMA ON FLAT CONDUCTING SHEET

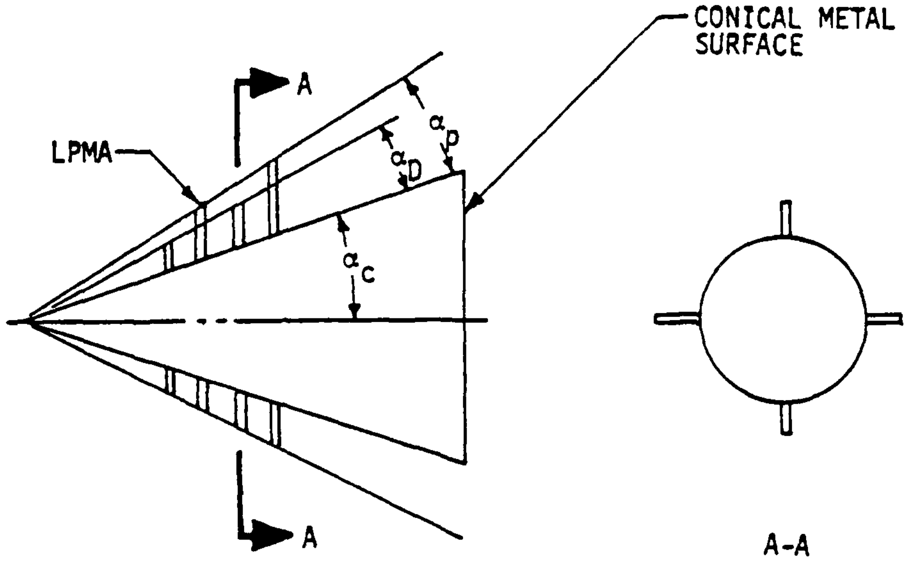

FIGURE 15 GEOMETRY OF LPMA'S ON CONDUCTING CONE

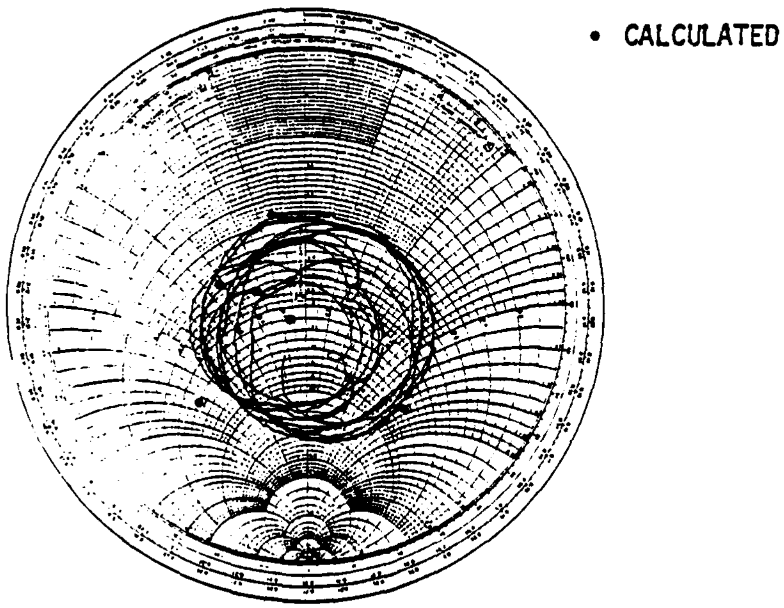

FIGURE 16 MEASURED AND COMPUTED ACTIVE IMPEDANCE OF LPMA ON CONE

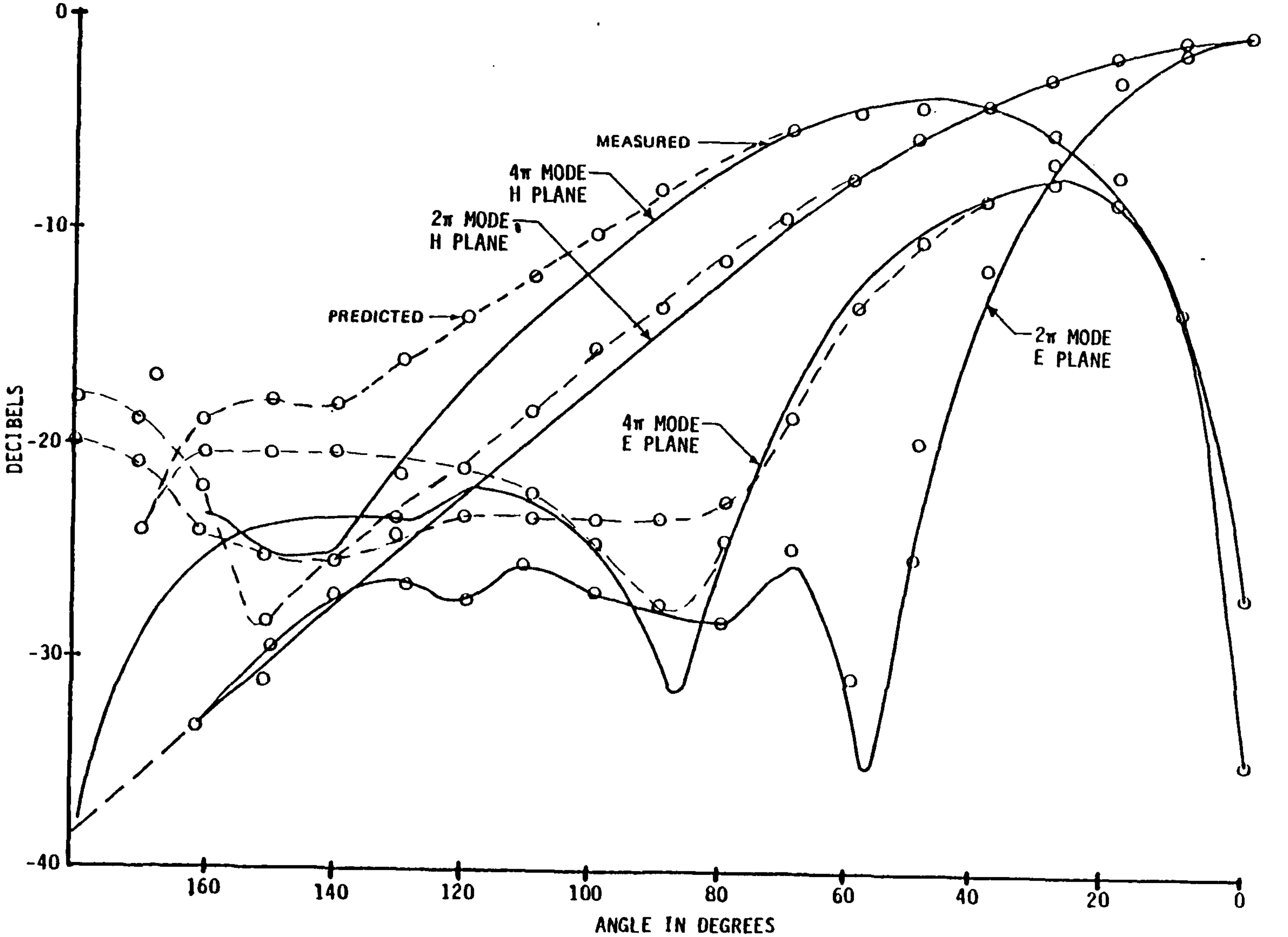

FIGURE 17 COMPARISON OF MEASURED AND CALCULATED PATTERNS OF 8 LPMA'S DISTRIBUTED UNIFORMILY ON CONICAL SURFACE

THE IMPEDANCE OF THE GUYED QUARTER WAVE MONOPOLE

By

Steven M. Wright and Paul W. Klock
Department of Electrical Engineering
University of Illinois, Urbana Illinois
and
J. Dane Jubera
Harris Corporation, Quincy Illinois

1 INTRODUCTION

The quarter wave monopole has been the subject of considerable time and effort by many researchers. Currently this antenna finds wide use as the radiator for many AM broadcast stations. Unfortunately, a problem arises when one of these simple monopoles is constructed; the input impedance is often significantly different than predicted by theory. This difference is the subject of this study.

AM broadcast towers are typically of open tower construction, supported by several sets of guy wires, and insulated from ground by a ceramic insulator. They are erected over a substantial ground screen, typically 120 quarter wave radials. A quarter wave tower in the broadcast band will vary in height from approximately 50 to 200 meters. Individual towers can vary in many details, however. Because of these variations, the input impedance of the towers can vary greatly from one to another, requiring matching networks at the base of each antenna. These networks, known as antenna coupling units (ACU), can be very costly. In addition, there is a growing interest in reactively controlled arrays for the broadcast band. Accurate knowledge of the impedance behavior of the antenna is critically important in the design of such an array. Clearly, accurate input impedance predictions would save the manufacturer considerable design time and cost by allowing tighter design windows to be used in the ACU at each antenna.

A three-part study was undertaken in an attempt to determine the cause of the impedance variations seen in the antennas. First, a general study was made of broadcast antennas, hoping to see a clear variation from the theoretical model which could cause the observed differences. Several areas were examined, including the feed region, guy wires, and the ground screen. Second, an experiment was performed to study the effect of guy wires on the input impedance of the tower. Third, a brief examination was made of the presently used theoretical techniques for predicting the input impedance. Two well-known moment method programs were acquired, and used to predict the input impedance of the antenna used in the experimental stage. This report summarizes the initial study, and discusses the results of the experiment. Complete results of the study can be found elsewhere [1].

2 AVAILABLE BROADCAST TOWER IMPEDANCE DATA

Many researchers have experimentally measured the characteristics of the monopoles. These measurements can basically be divided into two groups. The first group contains carefully controlled laboratory measurements of simple monopoles over ideal grounds. The second consists of experiments in the field on existing towers. This section compares the results of these measurements to the theoretical predictions.

One carefully conducted and documented study of the monopole was performed by Mack [2]. His report details the precautions taken to remove the effect of the finite ground plane and the feed region. In this manner his data should provide a check for the theoretical predictions for an ideal monopole over an infinite ground plane. Basically, his method consisted of extending the center conductor of a very narrow coaxial transmission line through a hole in a large ground plane. The outer conductor of the coaxial cable connected flush with the ground plane, which was many wavelengths across at the frequencies used. Measurements were made with slotted line techniques from beneath the ground plane. His results are in excellent agreement with the theoretical results in Table 1, which were obtained from a moment method program using piecewise sinusoidal, subsectional expansion and basis functions. For comparison to further theoretical results, it should be noted that at 90 degrees Mack's monopole had a height to radius (H/A) ratio of 35.6. Broadcast towers have an H/A on the order of one to two hundred. Based on the excellent agreement indicated in Table 1, Table 2 was compiled with resonant and quarter wavelength information for monopoles with H/A in the range used in broadcast towers. The same moment method program was used to obtain the data in both Tables 1 and 2.

TABLE 1.

IMPEDANCE DATA FOR MACK'S MONOPOLE

	Resonant height degrees	Resonant resistance	90 degree impedance
Measured	83.4	37.2	48.7 + j18.9
Theory	83.6	37.0	49.6 + j13.8

TABLE 2.

IMPEDANCE DATA FOR MONOPOLES WITH DIFFERENT H/A

H/A	Resonant height in degrees	Resonant resistance	90 degree impedance
360	86.11	35.91	41.74 + j21.99
180	85.55	35.94	42.95 + j21.86
120	85.15	35.99	43.93 + j21.40
90	84.83	36.06	44.83 + j21.40
45	83.96	36.51	48.04 + j19.39

A set of impedance measurements made on three typical broadcast towers was provided by the Harris Corporation [3]. The towers varied in height from 49 meters to 120 meters, but were virtually identical in every other respect. All had 120 radials approximately equal in length to the tower height. Each was constructed of triangular tower sections 6.1 meters long, having a face of 1.1 meters, with the bottom 1.5 meters of each tower tapering into the base insulator.

Impedance data for the antennas are given in Table 3. The towers are referred to by their geographical locations, in the Iranian cities of Birjand, Damghan, and Khash. The data in Table 3 were obtained by linear interpolation between the measured points.

TABLE 3.

IMPEDANCE DATA FOR SEVERAL AM BROADCAST TOWERS

	H/A approximate	Resonant Height degrees	Resonant Resistance	90 degree impedance
Birjand	225	73	32	64 + j101
Damghan	165	77	33	55 + j70
Khash	90	75	29	55 + j75
WWJ	92	80	35	53 + j52

Comparing Tables 2 and 3, the differences between the measured and theoretical values for the impedance of the towers are readily apparent. At resonance the physical height of the tower is approximately ten degrees below what would be expected for a cylindrical monopole of similar shape, and the resistance is somewhat lower. At 90 degrees, the impedance is considerably different than predicted by the simple theory, in both the resistive and reactive components. In short, the broadcast towers have apparent lengths much longer th their physical lengths.

Additional impedance data for a broadcast tower were found in an article by Morrison and Smith, in which they detail the measurements they made on the WWJ tower in Detroit, Michigan [4]. The WWJ tower is a 122 meter, uniform cross section square tower, approximately 2 meters on a side. The lower 6.7 meters of the tower tapered into the base insulator. Unlike the antennas in Iran, the WWJ tower had only one set of four guys, attached approximately half way up the tower. An H/A of 120 was used for purposes of comparison. No effort was made to determine the equivalent radius for a cylindrical tower, due to the difficulty in determining the effect of the open, tapered tower. However, it is noted from Table 2 that a fairly large error in H/A does not have a significant effect on the theoretical predictions of 90 degree and resonant impedance values, or resonant length. Data for the resonance and 90 degree height of the WWJ tower are included in Table 3. It can be seen that this tower also has an apparent length longer than its physical length. The resonance comes at a shorter length than predicted by theory, and the 90 degree impedance is considerably higher than predicted. However, the variations are not nearly so marked as those for the Iranian towers.

Based on the consistent results in the above studies, it was concluded that one or more factors not included in the theoretical models is significantly affecting the impedance of the broadcast tower. Thus the next stage of the project was to study several possible causes of the observed variation from the simple theory.

3 FACTORS AFFECTING THE IMPEDANCE OF THE BROADCAST ANTENNA

Several possible explanations for the observed impedance variations were studied. Theoretical work by Wait and Pope [5], along with experimental work by Maley, King, and others [6-10], conclusively demonstrated that the ground systems typically used in broadcast antennas would not change the 90 degree impedance more than a few ohms. Brown and Woodward [11] performed a series of experiments from which they concluded that base regions of demensions found in broadcast installations would not significantly affect the input impedance either. In addition, several other factors, including the effect of the open tower, and the depth of the tower galvanizing, were studied by Klock. All of these factors were found to have little effect.

Another difference between broadcast antennas and the idealized model is the guy wires. Investigations of their effect could not be found in the literature. However, there were several indications that the effect of the guys was important [1]. For example, a lengthening effect due to guy wires would help explain why the resonant impedance is lower for the Iranian towers than for the tower at WWJ. As mentioned earlier, the latter tower had only one set of guys, attached at the middle of the tower, as compared to several sets on the Iranian towers.

Because of these indications of the importance of the guy wires, and the lack of available data, it was decided to construct an antenna and make measurements in order to determine the effect of the guy wires.

4 EXPERIMENT TO DETERMINE THE EFFECT OF GUY WIRES

4.1 Antenna Location and Configuration

The antenna was located at the Monticello Field Station of the University of Illinois. This site had been previously used for radio location experiments, and already had a suitable ground screen installed. A large ground screen, with a radius of approximately 65 meters was made of 23 by 23 centimeter square mesh of ten gauge copper wire. The screen was buried at a depth of eight centimeters. At the center of this screen was an octagonal screen of eight by eight centimeter square copper mesh. This section measured 7.3 meters from the center to each side, and covered a concrete pad of the same dimensions. A sketch of the antenna site is included as

Figure 1.

Although the dimensions of the ground plane would have allowed a full scale model of a broadcast tower, a three section push-up mast was used. The mast had a full height of 14.66 meters, being a quarter wavelength at 5.113 mHz. This was roughly a five to one scale to the center of the broadcast band. In addition, measurements were made with the tower at a length of 10.44 meters, a quarter wavelength at 7.180 mHz. The dimensions of the tower at both heights are shown in Figure 2.

Unfortunately, because the tower did not have a uniform radius, the proper H/A to use for theoretical analysis was somewhat arbitrary. It was decided to use the bottom 6.1 meter section of the tower to determine the H/A, primarily because of the importance of the feed region on the impedance characteristics. In addition, Hallen has calculated the effective radius of a square tower to be .5902 times the length of one side [12]. Based on these factors, an H/A of 348 was used in all theoretical analyses of the shorter tower, and an H/A of 488 for the longer tower.

Metallic guy wires were made from stranded galvanized steel wire, approximately ten gauge. Only one set of guys was metallic, and they were attached to a guy ring approximately seven centimeters from the top of the monopole. Less than seven centimeters of wire seperated the top insulators from the tower, so that any top loading was insignificant. Three guys were used, seperated at 120 degree angles to each other. The wires came off the tower at an angle of 45 degrees, and were cut into three sections by insulators. Each

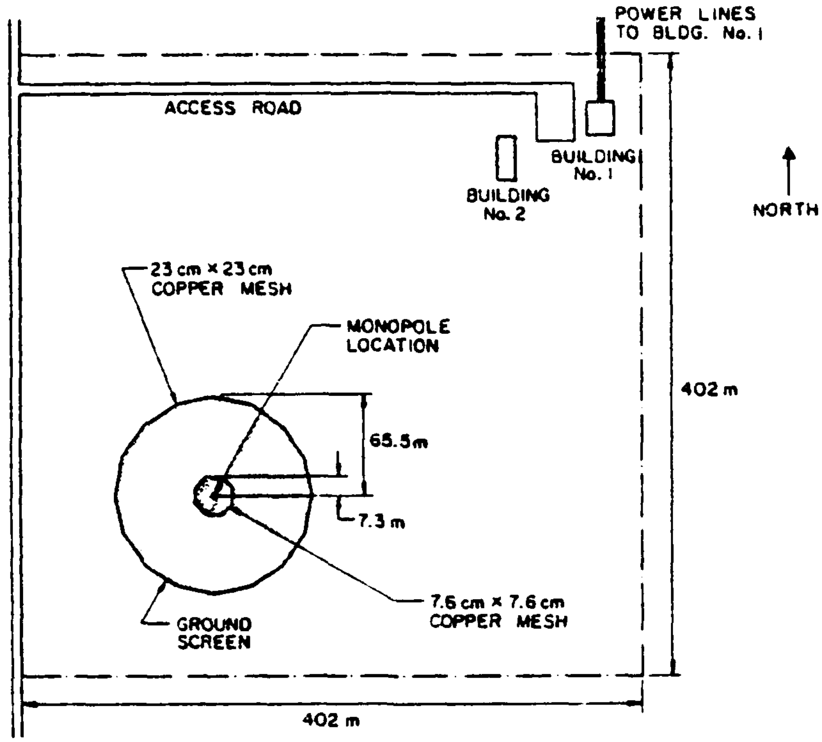

Figure 1. Antenna site.

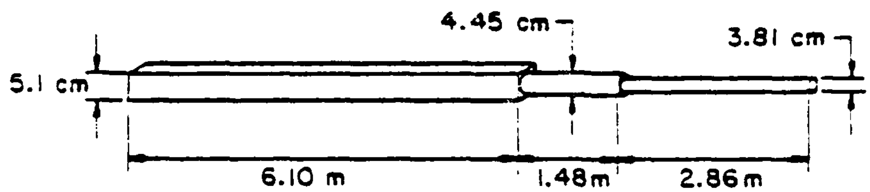

(a) 10.44 meter tower.

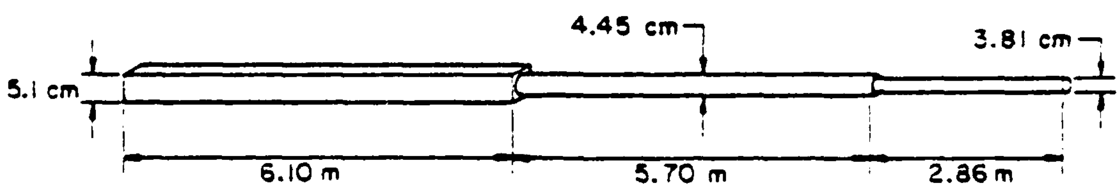

(b) 14.66 meter tower.

Figure 2. Dimensions for monopoles.

section was less than half the height of the tower. This geometry is illustrated in Figure 3.

Insulators were roughly four centimeters long, with approximately one centimeter seperating the loops of each guy wire. The guys were attached so that they were interlaced, putting the insulators under a compression. The insulators roughly scaled to those used in the broadcast band, which typically are fifteen to thirty centimeters long.

4.2 Experimental Equipment and Measurement Technique

Impedance measurements were made with a GR 1606-A impedance bridge. A GR bridge oscillator was used as the exciter because of its high power output. A Collins receiver served as the detector.

Impedance curves were obtained by maintaining a constant tower height and sweeping the frequency. The impedance was measured as an unknown at the end of 1.5 meters of Belden RG-8/U type 8327 FR-1 50 ohm coaxial cable. Raw data was referred to the antenna by transforming the measurement down the transmission line.

In addition, a correction factor was used to account for the leads connecting the transmission line to the antenna and the bridge. Figure 4 is a sketch of the antenna feed region, showing the connection to the antenna. The inductance of the clip leads was measured, and the electrical length of the line was determined on the basis of the measurement of several known impedances. The only problem occurred in measuring the impedance of the antennas just

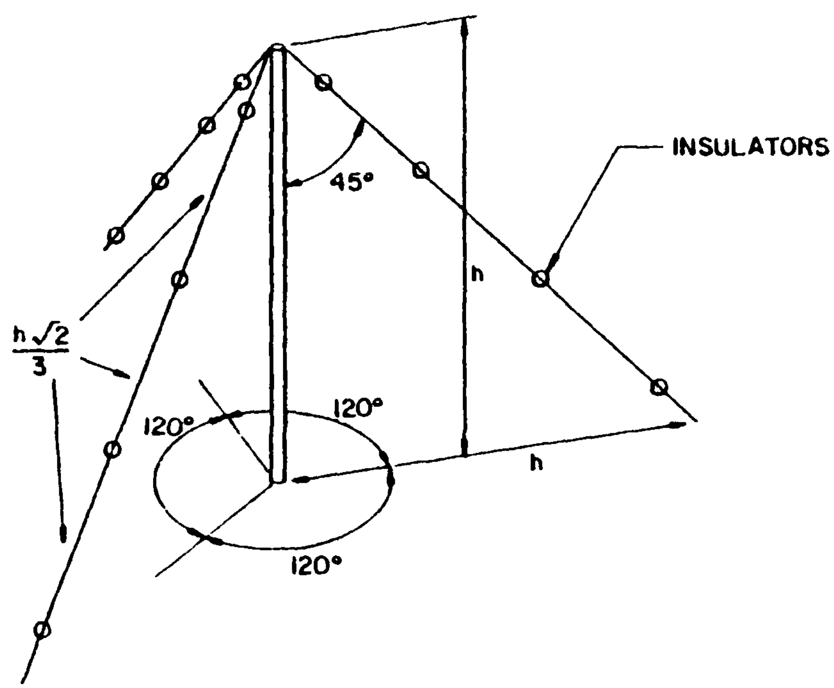

Figure 3. Geometry for monopole with one set of guy wires.

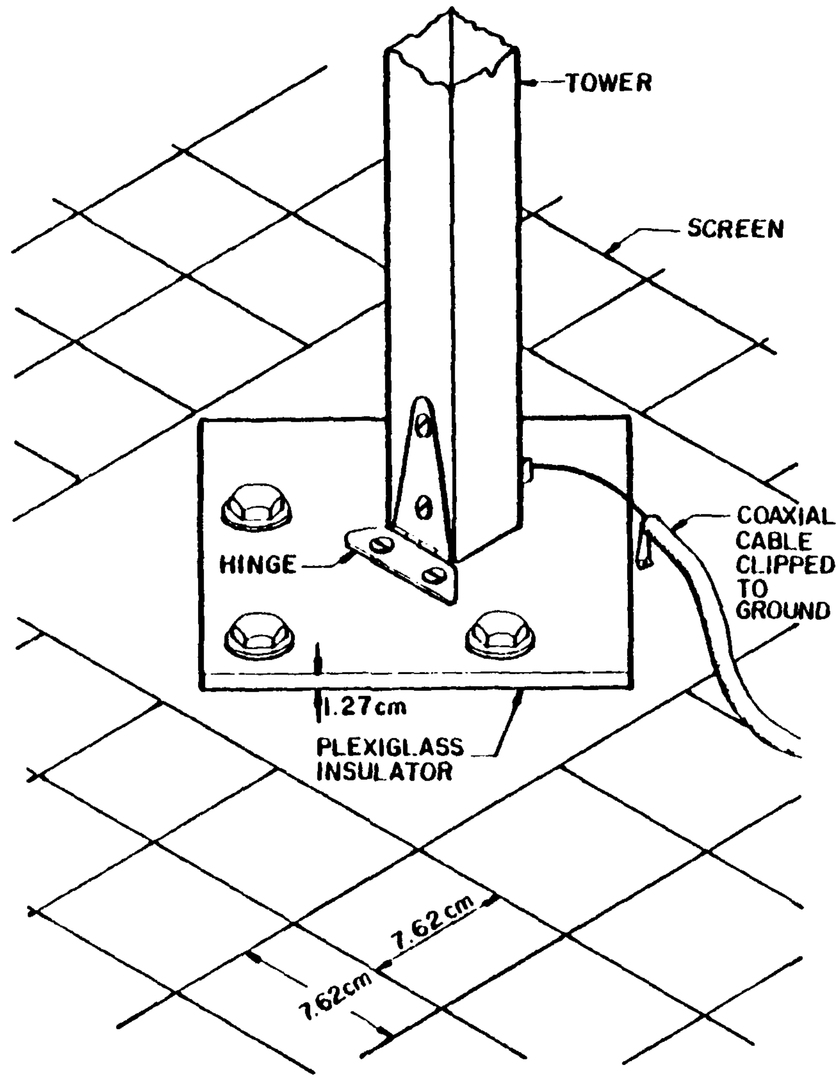

Figure 4. Antenna feed region.

below the half wave resonance. When the magnitude of the reactance became large enough, the bridge had to be set to the "high" setting for reactance. This caused inaccuracies which showed up in the impedance curves. Fortunately, only one or two data points for each antenna required this setting.

4.3 Experimental Results

Four configurations of the antenna were measured: 10.44 meter monopole with and without metallic guys, and 14.66 meter monopole with and without metallic guys. The experiment was repeated with separate tower heights to provide a check on the data, and also to provide more information to help determine the cause of any irregularities.

Results will be presented as impedance curves. As before, theoretical results for antennas without metallic guys were obtained from a moment method program using piecewise sinusoidal, subsectional expansion and basis functions. The theory assumes a cylindrical monopole with an infinite p.e.c. ground plane.

4.3.1 Monopoles with Dielectric Guys

The initial measurements were made on the 10.44 meter monopole, without metallic guy wires. Dielectric guys, consisting of nylon cord or rope, were used for support. The results are compared in Figures 5a and 5b to the theoretical impedance for a monopole with

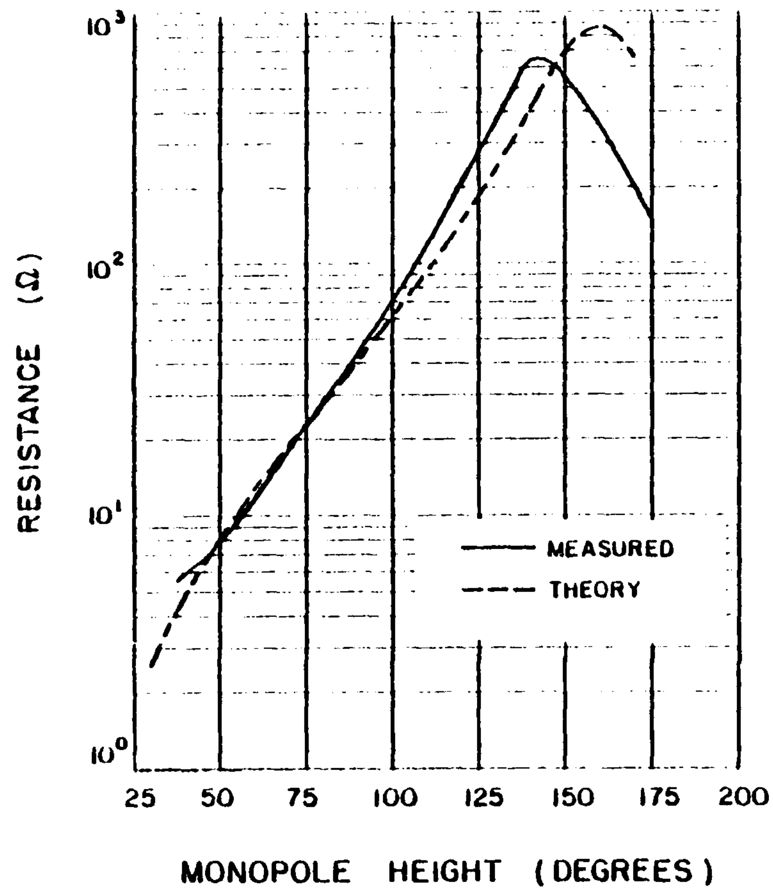

(a) Resistance.

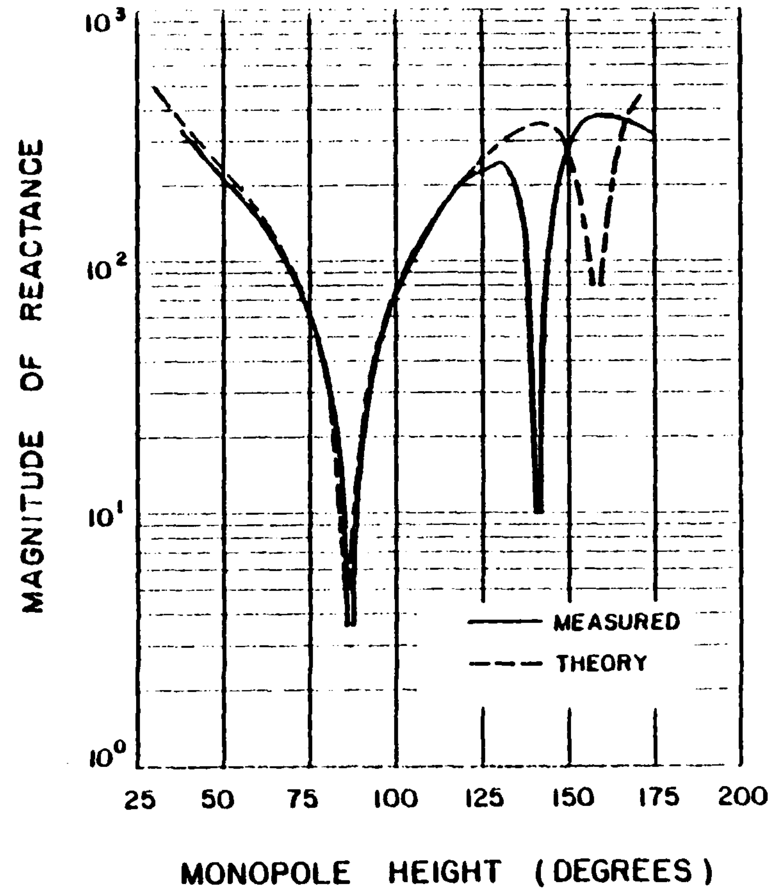

(b) Reactance.

Figure 5. Comparison of measured and uncorrected theoretical impedance for 10.44 meter non-guyed monopole.

an H/A of 348. It is immediately apparent that the results begin to significantly differ from theory at lengths greater than 100 degrees. The divergence from theory above 100 degrees was seen in all four antenna configurations. It is interesting to note that the theoretical reactance curve is somewhat steeper than the measured curve. This can be corrected by assuming a smaller equivalent H/A, but this is unjustified. It can also be corrected by allowing for the effect of a shunt capacitance in the feed region. While the effect of a small shunt capacitance will be of little importance near resonance, it will become important away from resonance where the magnitude of the impedance increases.

In order to check this possibility, the base capacitance was measured by cutting off the lower ten centimeters of the antenna, and measuring the impedance in exactly the same way as for the entire antenna. In order to improve accuracy, several capacitors in the same range as the measured base capacitance were also measured with the same equipment. These capacitors were then remeasured on a GR "twin-T" type bridge, which allows very accurate measurements of high impedances. The value of the base capacitance was adjusted based on the two sets of measurements of the known devices. The resulting value for the base capacitance was 14.3 picofarads.

Before proceeding, it is worthwhile to discuss the validity of such a measurement. It is not clear exactly what is being measured, or even the meaning of "base capacitance." Mack had a simple geometry, and was able to determine the base capacitance not included in the theoretical model. However, the geometry used in this experiment was not as simple. Certainly varying the H/A of an analysis accounts for some capacitance in the feed region. In addition, the moment method analysis brings in another complication by varying the size of the feed region as the number of subsections is varied. Therefore, exactly what part of the base capacitance needs to be accounted for is unclear, and should certainly be the subject of further study.

Obviously there is a precedent for measuring the capacitance of the base of a monopole over ground. Mack, and Brown and Woodward did so in their experiments [2,11], and Schelkunoff discussed the base capacitance in detail [13]. However, it is felt that at the present time measuring the base capacitance as done here should be viewed as an engineering approximation. The validity is perhaps best established by referring to the precedent set by others, and by the agreement with theory which results from taking it into account.

Figures 6a and 6b compare the results for the 10.44 meter monopole to the theoretical curves. The theoretical results have been corrected by including the 14.3 picofarad base capacitance in parallel with the input to the tower. Numerical data for the resonant heights and 90 degree impedance can be found in Table 4. Agreement is found to be very good with this factor included in the theory. It appears that this is the major reason for the divergence from the theoretical curves seen in Figures 5 a and b. Therefore, from now on this factor will be included in the theoretical analysis.

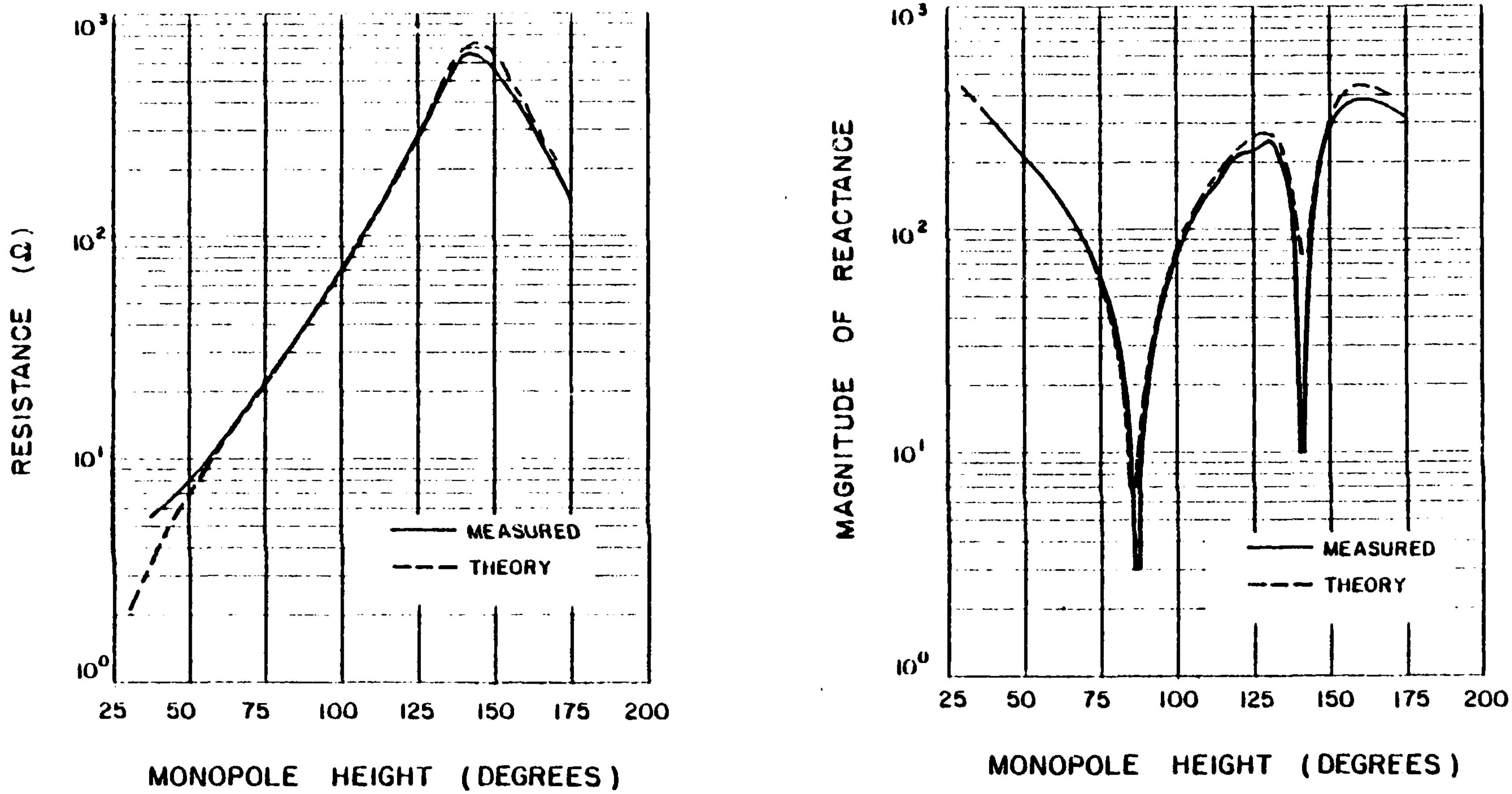

(a) Resistance.

(b) Reactance.

Figure 6. Comparison of measured and corrected theorectical impedance for 10.44 meter non-guyed monopole.

TABLE 4.

IMPEDANCE DATA FOR MONOPOLES WITH AND WITHOUT GUY WIRES

		Quarter Wave			Half Wave	
	r_{res}	90° Impedance	res. length (degrees)	Δ res. length (degrees)	res. length (degrees)	Δ res. length (degrees)
10.44 meter antenna						
No guys measured	37.8	44.0 + j16.5	86.9	3.7	141.2	4.8
With guys measured	34.7	48.8 + j40.8	83.2		136.4	
No guys theory	36.3	43.0 + j21.1	86.2	3.5	142.1	4.5
With guys theory	33.4	47.0 + j43.8	82.7		137.6	
14.66 meter antenna						
No guys measured	38.7	43.1 + j14.6	87.5	3.2	145.0	5.1
With guys measured	36.1	46.2 + j35.1	84.3		139.9	
No guys theory	36.2	42.2 + j21.4	87.0	3.5	147.1	4.2
With guys theory	33.6	44.9 + j40.9	83.5		142.9	

4.3.2 Towers with Metallic Guys

Before discussing the results of the measurements on towers with metallic guys, a short explanation of the theoretical model used is in order. Another moment method program was used, a thin-wire code written at the Ohio State University. This program also uses piecewise sinusoidal, subsectional expansion and testing functions. The geometry was modeled exactly as in Figure 4, with the mirror image of the antenna used instead of a ground screen. Figure 7 outlines the model for the monopole and one guy, along with their images. Thirteen unknowns were used on both the tower and each guy wire. This choice allowed one complete subsection between each insulator in the guy wires. As the sinusoidal expansion functions closely approximate the actual current on each guy section, increasing the number of subsections on each guy changed the results very little.

The capacitance of each insulator was measured on the GR "twin-T" bridge. Once measurements of the antenna were complete, the insulators were removed along with several centimeters of the guy wire as leads. Initially the capacitance of the insulators with the leads attached was measured. Then the insulator was removed leaving only the leads. The capacitance of the leads was measured, and the difference was taken as the value for the insulator. Three different types of insulators were used, all similar in size. One type was ceramic, one was plexiglass, and the third was another type of plastic. The same type of insulator was used at the same height

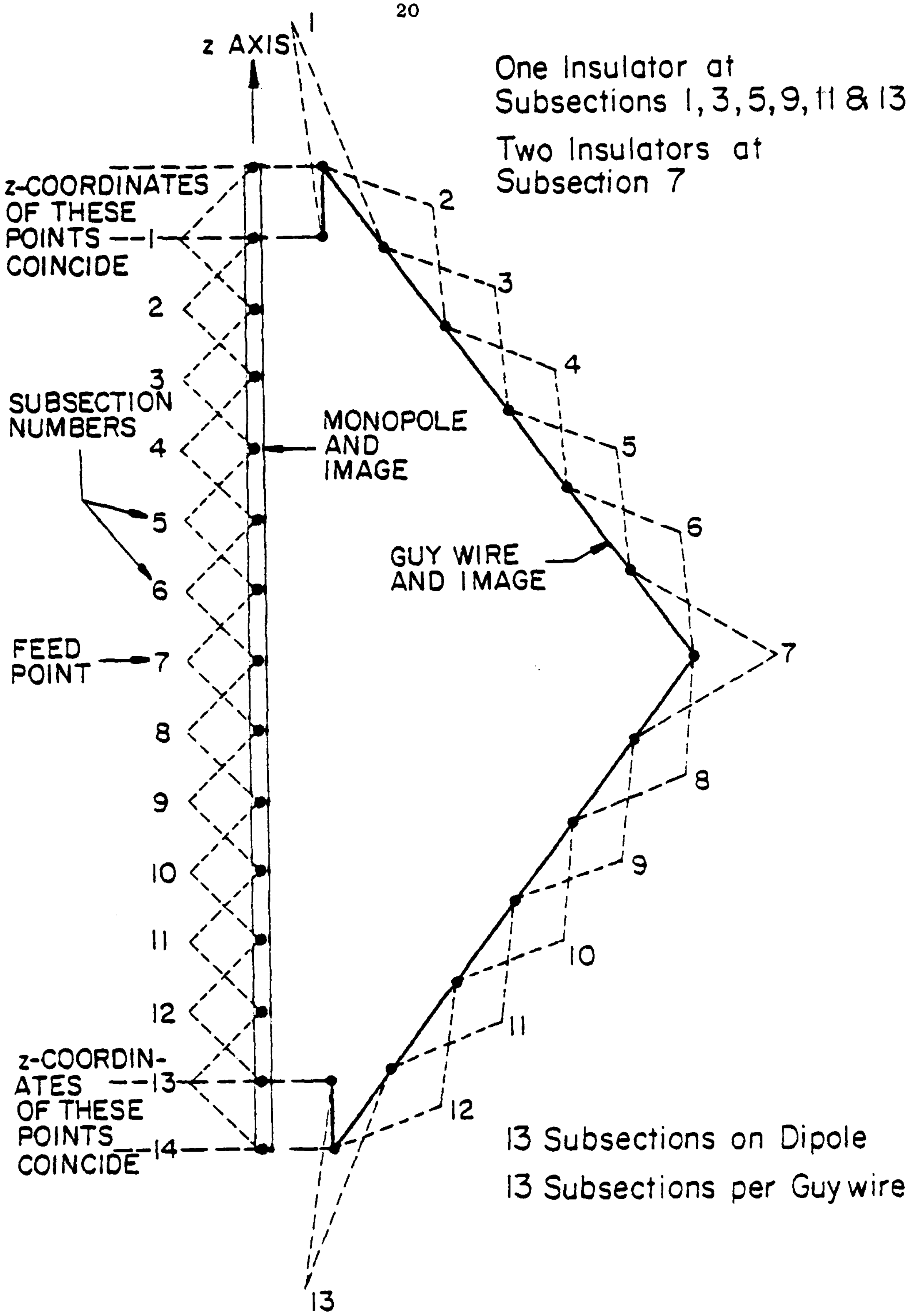

Figure 7. Input to moment method program for monopole with guy wires.

in all guys. The ceramic insulator (2.3 pF) was used at the top, the plastic (1.6 pF) in the middle, and the plexiglass (1.4 pF) at the lower section and at the bottom.

One final detail in the theory concerns the handling of the junction between the guy wires and the tower. One half of one subsection at the ends of each guy overlapped the tower, as shown in Figure 7. The overlapping subsections were separated from the tower by the radius of the cylindrical monopole used in the model. The endpoints of the overlapping subsections were at the same height as the middle point of the end subsections on the tower. This is pointed out here because it was discovered that these details can significantly affect the results from the moment method program. Further discussion of these sensitivities, along with some results which demonstrate the problem, can be found elsewhere [1].

As was the case with the dielectric guy wire supported monopoles, agreement between measurement and theory was very good. The results of the measurement for the 10.44 meter guyed tower are compared to the theoretical results in Figures 8a and 8b. The agreement is nearly the same as it was with the non-guyed tower; excellent below 100 degrees; and reasonable beyond that. Referring to Table 4, the theoretical prediction for the first resonant height was off by only half of a degree for the shorter tower, and only 0.8 degree for the longer tower. Considering the simple theory, it is felt that this is very good agreement. In addition, the 90 degree impedances are predicted closely by theory.

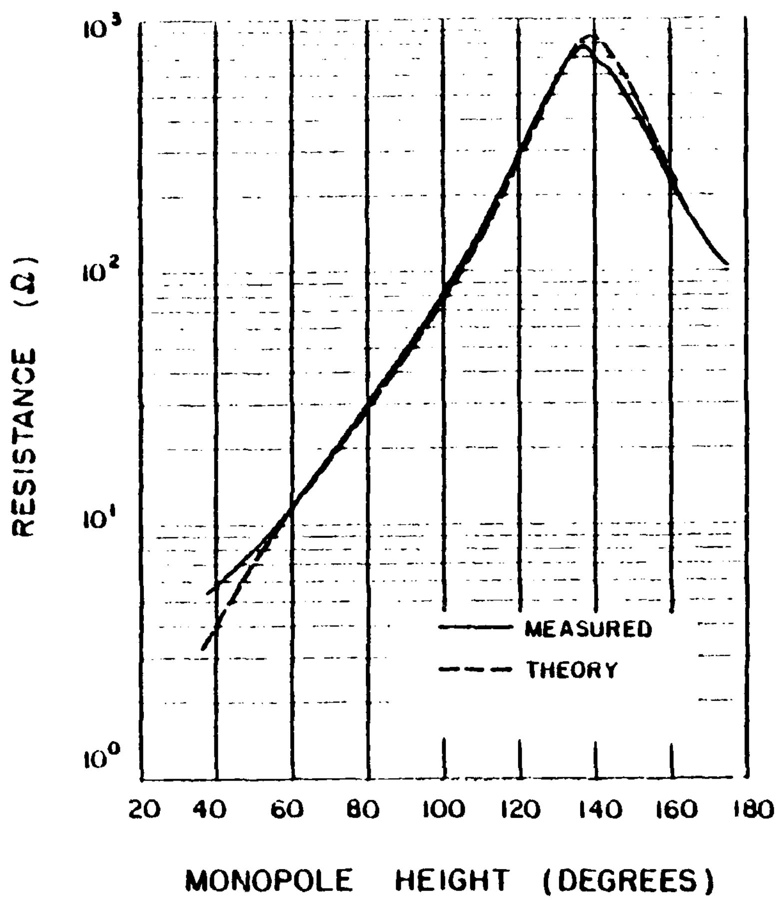

(a) Resistance.

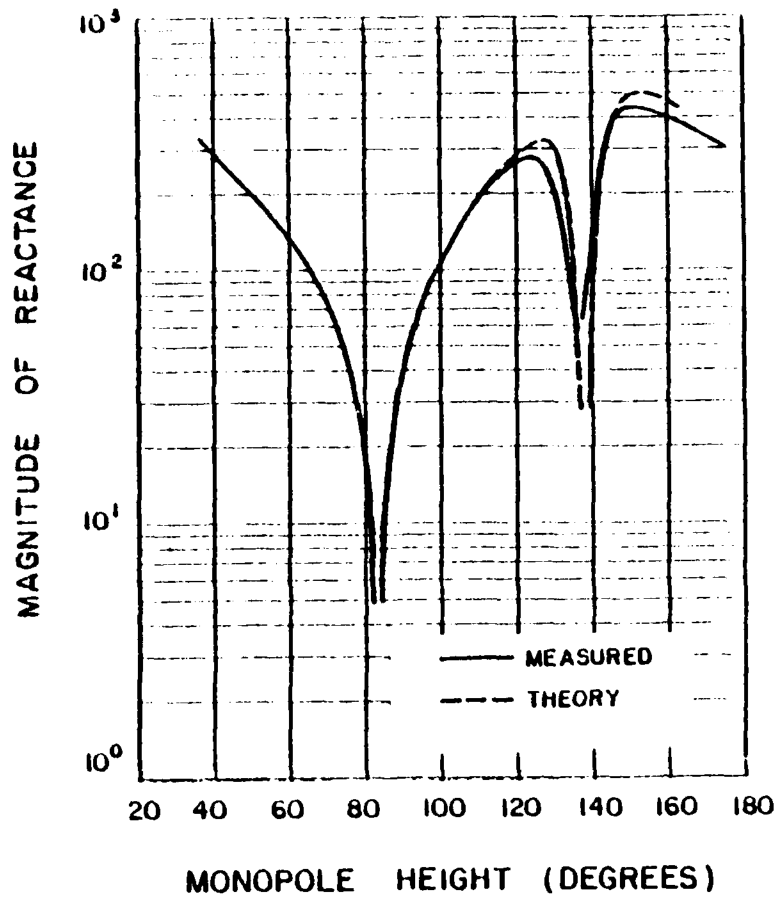

(b) Reactance.

Figure 8. Comparison of measured and theoretical impedance for 10.44 meter guyed monopole.

Probably the most interesting comparisons are between the guyed and non-guyed towers. Figures 9a and 9b compare these measurements for the 10.44 meter tower, and Figures 10a and 10b for the 14.66 tower. Referring to Table 4 again, it is seen that the first resonant height is lowered by about 3.5 degrees in both cases. The half wave resonance is depressed approximately 5 degrees. This agrees very well with the predicted shifts in the impedance seen in Table 4. Agreement is particularly good for the quarter wave resonance.

It is interesting to note that the effect of the guy wires is not just to shift the impedance curves, effectively lengthening the towers. Rather, both the resistance and reactance curves become steeper with the addition of the guy wires, more than can be accounted for by simply increasing the H/A by the increase in apparent length. In addition, the quarter wave resonant resistance is decreased, and the half wave resonant resistance is increased. All of these effects are predicted accurately by the theory, as shown in Figures 11 a and b.

4.4 Discussion of Results

As seen in the preceding section, the effect of the one set of guy wires used in the experiment was significant. The quarter wave resonant resistance and length were decreased, and the reactance at 90 degrees increased significantly. It is felt that this is the cause of the discrepancy between measured and theoretical results

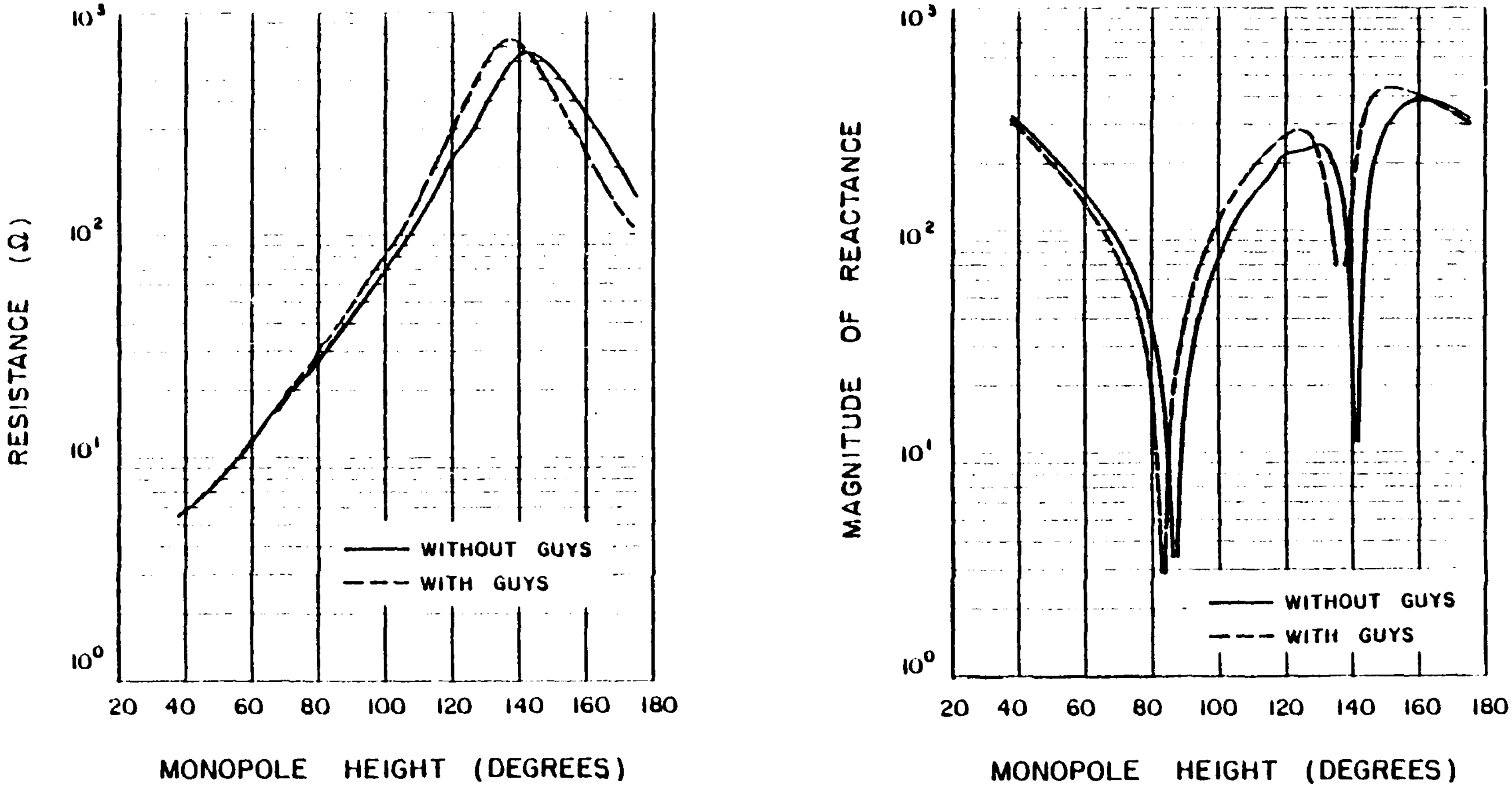

(a) Resistance.

(b) Reactance.

Figure 9. Comparison of measured impedance for 10.44 meter monopole with and without guy wires.

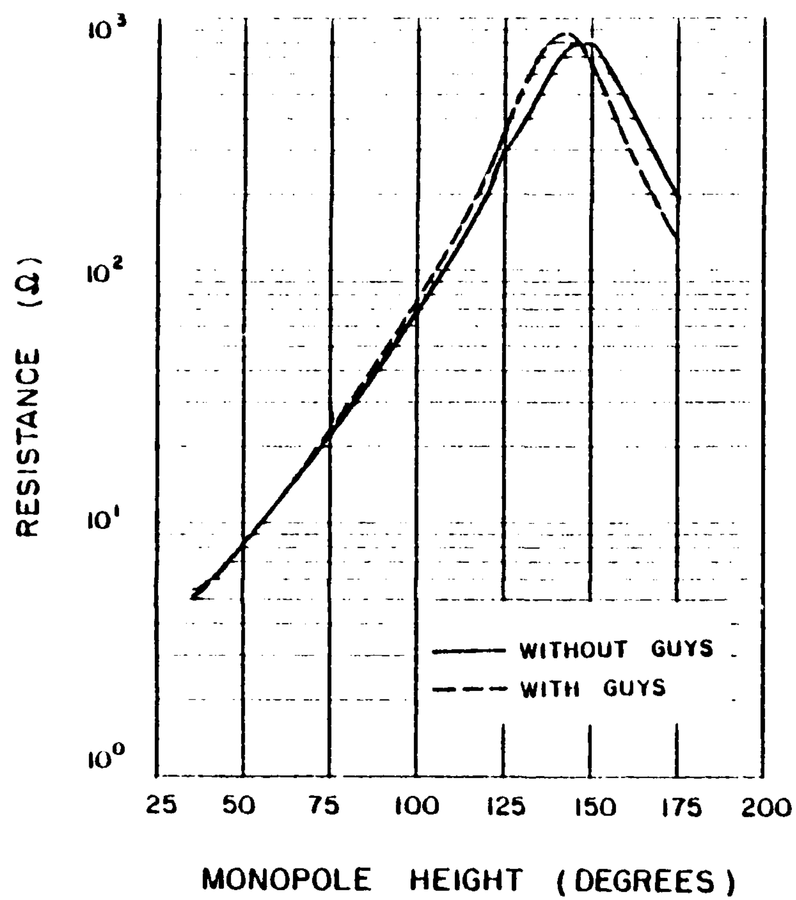

(a) Resistance.

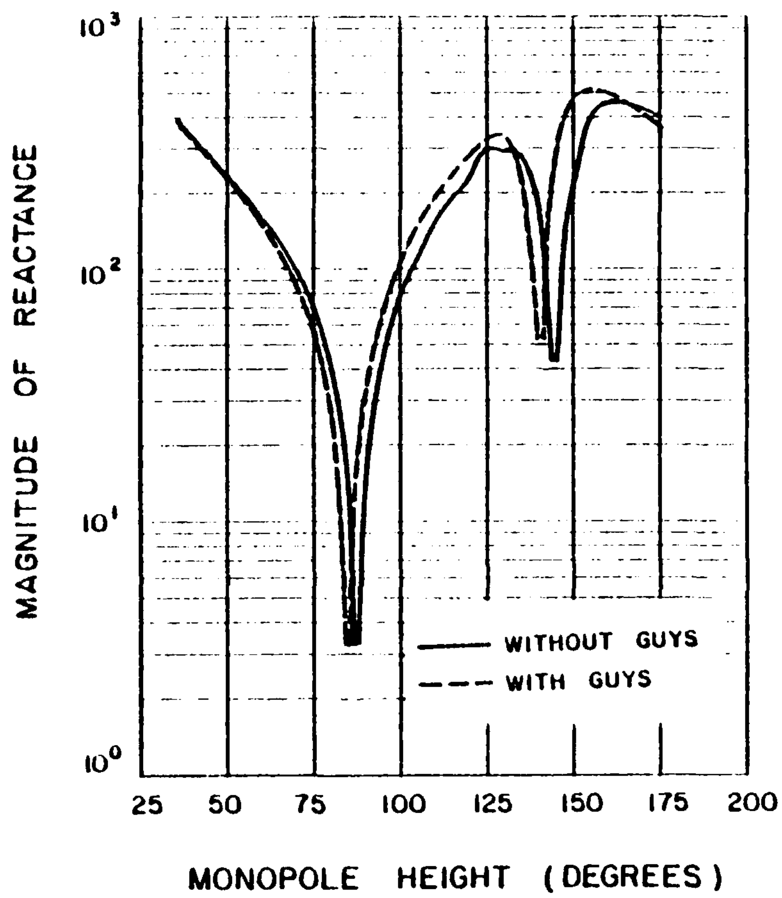

(b) Reactance.

Figure 10. Comparison of measured impedance for 14.66 meter monopole with and without guy wires.

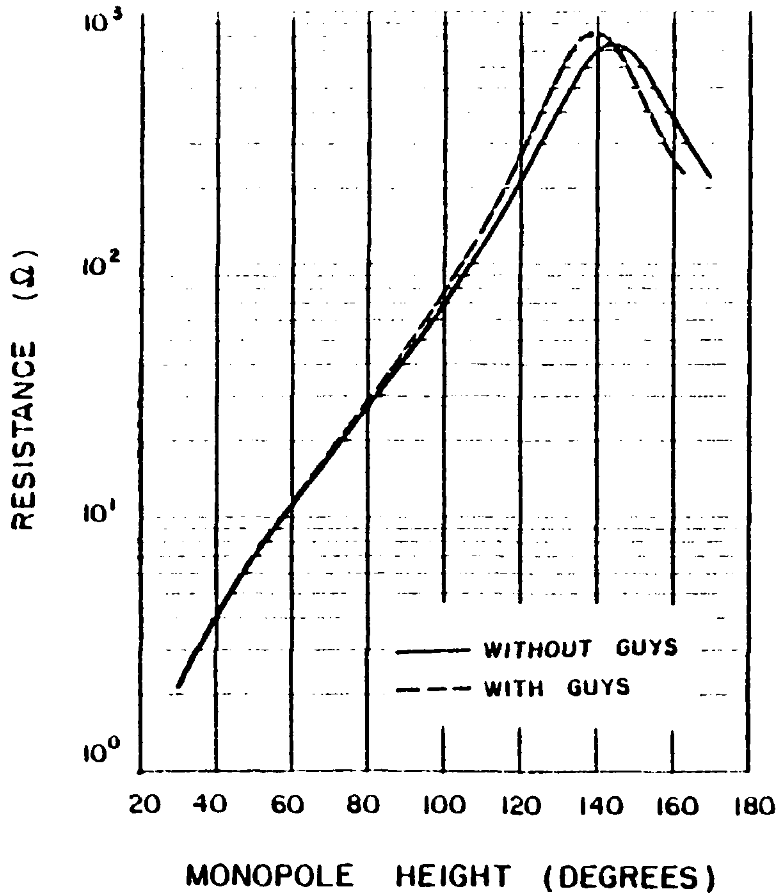

(a) Resistance.

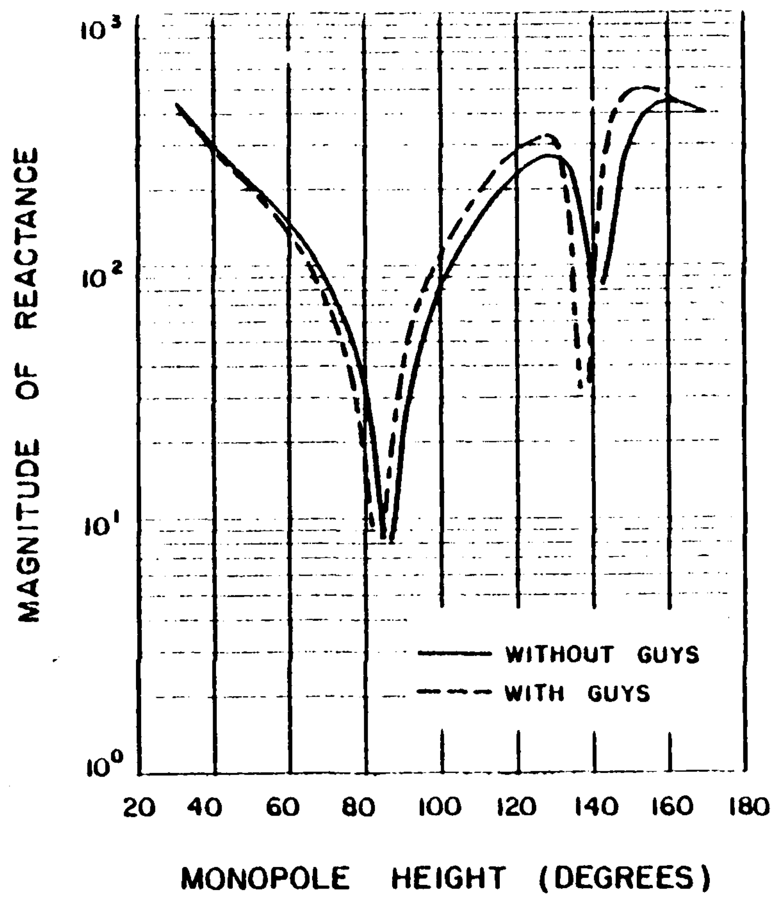

(b) Reactance.

Figure 11. Comparison of measured and theoretical impedance for 10.44 meter guyed monopole.

reported by others [3,4].

Because of the cost of computer time, an antenna with several sets of guy wires has not been analyzed. It is reasonable to assume that including more guy wires will increase the magnitude of the changes observed. Previous work by Klock supports this assumption. Another factor which can greatly change the effect of the guy wires is the capacitance of the insulators. To test their effect, a monopole with an H/A of 435, and one set of guys, just as in the experimental antenna, was analyzed using different capacitances for the guy wire insulators. All insulators were the same in any particular case. The results, given in Table 5, demonstrate that accurately measuring the capacitance of the insulators is an important step in predicting the input impedance.

TABLE 5.

EFFECT OF INSULATOR IMPEDANCE ON 90 DEGREE INPUT IMPEDANCE OF A GUYED MONOPOLE

Insulator impedance (ohms)	90 degree impedance
-j5,000	46.43 + j62.77
-j10,000	43.93 + j45.43
-j15,000	42.96 + j39.15
-j25,000	42.13 + j33.90

5 CONCLUSIONS

A study was made of the input impedance of the guy wire supported monopole, as commonly used in the AM broadcast band. Several studies were reported where the measured impedance of broadcast towers differed significantly from theoretical predictions.

The characteristics of the broadcast tower thought to be causing the discrepancy were examined. It was found that neither the feed region nor the ground system would significantly affect the input impedance of the typical tower installation. The guy wires had not been previously studied, but indications were that they could cause the observed impedance variations. Therefore, a monopole was constructed, and measurements were made to determine the effect of the guy wires.

It was found experimentally that the presence of metallic guy wires had a significant effect on the input impedance of the tower. Furthermore, the effect was accurately predicted by theoretical analysis with the method of moments. It was found that one set of guy wires at the top of the antenna lowered the quarter wave resonant height by more than three degrees, and also increased the ninety degree impedance significantly. The half wave resonant height was shifted downward by more than four degrees.

In order to improve the accuracy of the theory, several factors should be considered. First, the theory was based on a simple thin wire technique. Results have indicated that this is inadequate, particularly for dealing with junctions. Second, a more detailed study of the treatment of the feed region is needed. Finally, the measuring equipment and techniques used were somewhat crude and old, and could probably be greatly improved. Considering all of this, it is felt that the agreement between theory and experiment is quite good.

REFERENCES

[1] S. M. Wright, "Comparison of measured and theoretical impedance of the AM broadcast tower," Master's Degree Thesis, Univ. of Ill., Urbana Ill., 1981.

[2] R. B. Mack, "A study of circular arrays," Cruft Lab., Harvard University, Cambridge Mass., Tech. Reports 381-382, May 1963.

[3] G. Bingeman, Private Communication.

[4] J. F. Morrison and P. H. Smith, "The shunt excited antenna," Proc. IRE, vol. 25, pp. 673-697, June 1937.

[5] J. R. Wait and W. A. Pope, "The characteristics of a vertical antenna with a radial conductor ground system," Appl. Sci., vol. B-4, pp. 177-195, 1954.

[6] S. W. Maley and R. J. King, "Impedance of a monopole antenna with a circular conducting-disk ground system on the surface of a lossy half-space," J. Res. NBS, vol. 65D (Radio Prop.), No. 2, pp. 183-188, March-April 1961.

[7] S. W. Maley and R. J. King, "Impedance of a monopole antenna with a radial-wire ground system on an imperfectly conducting half-space, part I," J. Res. NBS, vos. 66D (Radio Prop.), No. 2, pp. 175-180, March-April 1962.

[8] S. W. Maley and R. J. King, "Impedance of a monopole antenna with a radial-wire ground system on an imperfectly conducting half-space, part II," Radio Sci. J. Res. NBS/USNC-URSI, vol. 68D, No. 2, pp. 159-165, Feb. 1964.

[9] S. W. Maley and R. J. King, "Impedance of a monopole antenna with a radial-wire ground system on an imperfectly conducting half-space, part III," Radio Sci. J. Res. NBS/USNC-URSI, vol. 68D, No. 3, pp. 297-301, March 1964.

[10] G. H. Brown, R. F. Lewis, and J. Epstein, "Ground systems as a factor in antenna efficiency," Proc. IRE, vol. 25, pp. 753-787, June 1937.

[11] G. H. Brown and O. M. Woodward, "Experimentally determined impedance characteristics of cylindrical antennas," Proc. IRE, vol. 33, pp. 257-262, April 1945.

[12] E. C. Jordan and K. G. Balmain, Electromagnetic Waves and Radiating Systems. New Jersey: Prentice Hall, 1968.

[13] S. A. Schelkunoff and H. T. Friis, Antennas Theory and Practice. New York: John Wiley and Sons, Inc., 1966.

ALTERNATE FORMULAS FOR NEAR-FIELD COMPUTATION

Paul E. Mayes
Electrical Engineering Department
University of Illinois
Urbana, IL 61801

In antenna analysis, the need often arises to evaluate the fields due to a known distribution of sources in an infinite homogeneous medium. The conventional approach is through the appropriate vector potential. Hence, the first step is to integrate over the volume occupied by the source. One differentiation is then required to find either $\underline{E}$ or $\underline{H}$ (depending on whether the source is electric or magnetic current) and a second differentiation is required to find the other. This procedure is not necessarily the best, particularly when numerical techniques are employed. Numerical integration followed by numerical differentiation is apt to consume a large amount of computer time in achieving the desired accuracy.

The alternate way of solving Maxwell's equations for the fields directly, without introducing potentials [1]-[3], deserves consideration. The procedure will be outlined here and some examples will be given to show that significant savings of time and effort are possible.

THE INHOMOGENEOUS EQUATIONS

Maxwell's equations can be written

$$\text{curl } \underline{E} = -j\omega\mu \ \underline{H} - \underline{K} \tag{1}$$

$$\text{curl } \underline{H} = j\omega\varepsilon \ \underline{E} + \underline{J} \tag{2}$$

where $\underline{E}$, $\underline{H}$, $\underline{K}$, $\underline{J}$ are the complex vector point functions which represent the time-harmonic electric field, magnetic field, magnetic source current density, and electric source current density, respectively, assuming $\exp(j\omega t)$ time dependence.

Since (1) and (2) are linear, it is permissible to consider the electric and magnetic sources independently. Considering $\underline{K} = 0$ first, taking the curl of (1) assuming the medium to be homogeneous in , and substituting for curl $\underline{H}$ from (2) yields

$$\text{curl curl } \underline{E} - k^2\underline{E} = -j\omega\mu \ \underline{J} \tag{3}$$

where $k^2 = \omega^2\mu\varepsilon$. By a vector identity valid in rectangular coordinates,

$$\text{grad div } \underline{E} - \nabla^2\underline{E} - k^2\underline{E} = -j\omega\mu \ \underline{J} \tag{4}$$

Taking the divergence of (2), assuming homogeneity in ε,

$$\text{div } \underline{E} = (-1/j\ \omega\varepsilon)\text{div } \underline{J} \tag{5}$$

whence (4) becomes

$$\nabla^2\underline{E} + k^2\ \underline{E} = (-1/j\omega\varepsilon\ )(\text{grad div } \underline{J} + k^2\underline{J}) = -\underline{S}_{JE} \tag{6}$$

where $\underline{S}_{JE}$ is a vector source function which can be used to find $\underline{E}$ when $\underline{J}$ is known.

To relate the magnetic vector to the electric current, take the curl of (2) and substitute using (1)

$$\text{curl curl } \underline{H} = \text{grad div } \underline{H} - \nabla^2\underline{H} = k^2\underline{H} + \text{curl } \underline{J} \tag{7}$$

and since div $\underline{H}$ = 0 when $\underline{K}$ = 0,

$$\nabla^2\underline{H} + k^2\ \underline{H} = -\text{curl } \underline{J} = -\underline{S}_{JH} \tag{8}$$

In a similar fashion it is possible to derive the following relations between fields and magnetic sources:

$$\nabla^2\underline{H} + k^2\ \underline{H} = (-1/j\omega\mu\ )(\text{grad div } \underline{K} + k^2\ \underline{K}) = -\underline{S}_{KH} \tag{9}$$

$$\nabla^2\underline{E} + k^2\ \underline{E} = \text{curl } \underline{K} = -\underline{S}_{KE} \tag{10}$$

Equations (6), (8), (9) and (10) are second-order, inhomogeneous, vector differential equations with source terms, $\underline{S}$, which can be evaluated by differentiating the functions that describe the given sources. The left-hand side involves the Helmholtz operator which also appears in the familiar relationship between vector potential, $\underline{A}$, and electric current density, $\underline{J}$,

$$\nabla^2\underline{A} + k^2\ \underline{A} = -\underline{J} \tag{11}$$

But whereas calculation of the field from $\underline{A}$ requires the vector differential operations

$$\underline{H} = \text{curl } \underline{A} \quad \text{and} \quad j\omega\varepsilon\ \underline{E} = \text{curl } \underline{H} - \underline{J} \tag{12}$$

after (11) is inverted, inversion of (6), (8), (9) and (10) gives expressions for $\underline{E}$ and $\underline{H}$ directly in terms of the appropriate source function. The solution of (11) which represents outgoing waves at infinity is well-known to be

$$\underline{A} = (1/4\ \pi) \int_V \underline{J}(\underline{r}')\ G(\underline{r},\underline{r}')\ dV' \tag{13}$$

where

$$G(\underline{r},\underline{r}') = \exp(-jk\,|\underline{r} - \underline{r}'|)/\ |\underline{r} - \underline{r}'| \tag{14}$$

V is the volume occupied by the source and $\underline{r}$ and $\underline{r}'$ are position vectors to the source and observation points, respectively. Comparing (6), (8), (9) and (10) with (11), the expressions for $\underline{E}$ and $\underline{H}$ are immediately obtained. For electric currents we have

$$\underline{E}(\underline{r}) = (1/j\omega\varepsilon\ 4\ \pi) \int_V [(\text{grad}'\ \text{div}' + k^2)\ \underline{J}(\underline{r}')]\ G(\underline{r},\underline{r}')\ dV' \tag{15}$$

$$\underline{H}(\underline{r}) = (1/4\ \pi) \int_V [\text{curl}'\ \underline{J}(\underline{r}')]\ G(\underline{r},\underline{r}')\ dV' \tag{16}$$

For magnetic currents

$$\underline{E}(\underline{r}) = (-1/4\ \pi) \int_V [\text{curl}'\ \underline{K}(\underline{r}')]\ G(\underline{r},\underline{r}')\ dV' \tag{17}$$

$$\underline{H}(\underline{r}) = (1/j\omega\mu\ 4\ \pi) \int_V [(\text{grad}'\ \text{div}' + k^2)\ \underline{K}(\underline{r}')]\ G(\underline{r},\underline{r}')\ dV' \tag{18}$$

Previously, these equations have been applied to the formulation of integral equations for scattering and antenna problems [4]-[6]. We now demonstrate that they can often be used to simplify the derivation of formulas for the exact fields of given sources. In cases where analytic integration is not possible, the evaluation of the fields is efficiently done numerically since only integration must be done numerically rather than both integration and differentiation.

NEAR FIELDS OF FILAMENTARY CURRENTS

The approximation is often used that the fields produced by currents flowing on thin wires are negligibly different if the current is concentrated in a filament along the axis of the wire. It is also common practice to approximate physical currents with functions that are discontinuous and/or that have discontinuous first derivatives. Equations (15)-(18) readily demonstrate that fields with higher-order singularities are produced by such currents. The calculation of near-fields of piecewise continuous filamentary currents often arises in the moment method of solving antenna and scattering problems involving thin wire structures. In these cases the current may take the general form

$$\underline{J}(x,y,z) = \sum_{q=1}^{Q} \hat{z}\ I_q(z)\ P(z;z_{q-},z_{q+})\ \delta(x)\ \delta(y) \tag{19}$$

where I (z) is a complex-valued function that describes the current amplitude and phase within the qth subinterval, $z_{q-} < z < z_{q+}$ where $P(z;z_{q-},z_{q+}) = 1$. For points outside the qth subinterval, $P(z;z_{q-},z_{q+}) = 0$. Applying (6) to (19)

$$-j\omega\varepsilon\ \hat{z}\cdot\underline{S}_{JE} = \delta(x)\ \delta(y) \sum_{q=1}^{Q} \{I_q(z_{q-})\ \delta'(z-z_{q-}) - I_q(z_{q+})\ \delta'(z-z_{q+}) + I_q'(z_{q-})\ \delta(z-z_{q-}) - I_q'(z_{q+})\ \delta(z-z_{q+}) + [I_q''(z) + k^2 I_q(z)]\ P(z;z_{q-},z_{q+})\} \tag{20}$$

The terms involving the Dirac delta $\delta(z-z\ )$ and its derivative $\delta'(z-z\ )$ arise from differentiating the discontinuous function $P(z;z_{q-},z_{q+})$ as a distribution.

The parallel component of the near-field of a dipole antenna with the often-used sinusoidal approximation for the current is very easily obtained from (20). In this case

$$I_q(z) = A_q \sin k(z-z_q) \tag{21}$$

where A_q and z_q are constants that assume different values for different sections of the antenna. In any case, we note immediately that

$$I_q'' + k^2 I_q = 0 \tag{22}$$

except at the junctions between subsections. Hence, the integration to find the near-field is a simple exercise.

$$4\pi k^2 E_2(\rho,z) = -j\eta \sum_{q=1}^{Q} \{-I_q(z_{q-})[\partial / \partial z'(\exp(-jkR)/R]\Big|_{z'=z_q} + I_q(z_{q+})[\partial / \partial z'(\exp(-jkR)/R]\Big|_{z'=z_{q+}} + I_q'(z_{q-})[\exp(-jkR)/R]\Big|_{z'=z_{q-}} - I_q'(z_{q+})[\exp(-jkR)/R]\Big|_{z'=z_{q+}}\} \tag{23}$$

It should be noted at this point that the near-fields of any current distribution which piecewise satisfies (22) is expressible as a summation of the fields of point sources with R^{-1} and R^{-2} singularities. As a result the near-field produced on the cylindrical surface a small distance from such a filamentary current will display maxima in the neighborhood of these point sources. The sources occur at points on the filament where the current or its derivative is discontinuous.

Let us now use the results obtained above to derive a well-known formula for the parallel component of the E-field of a centerfed thin linear dipole. In this case,

$$\begin{aligned} I_1(z) &= I_m \sin k(z+H) \\ I_1'(z) &= kI_m \cos k(z+H) \end{aligned} \qquad -H < z < 0$$

$$\begin{aligned} I_2(z) &= -I_m \sin k(z-H) \\ I_2'(z) &= kI_m \cos k(z-H) \end{aligned} \qquad 0 < z < H \tag{24}$$

It is apparent from these expressions that the current is everywhere continuous but that discontinuities in the derivative occur at $z = \pm H$ and $z = 0$. Substituting from (24) into (23), we obtain the result

$$\begin{aligned} E_z(\rho,z) = -j30I_m \{&\exp(-jkR_1)/R_1 + \exp(-jkR_2)/R_2 \\ &- 2\cos kH \exp(-jkr)/r\} \end{aligned} \tag{25}$$

where

$$R_1 = \sqrt{\rho^2 + (z-H)^2} \qquad R_2 = \sqrt{\rho^2 + (z+H)^2} \qquad r = \sqrt{\rho^2 + z^2} \tag{26}$$

What was a tortuous exercise involving some ingenious integration and subsequent differentiation when using the potential method [7] is a very simple procedure in which neither the integration nor the differentiation is complicated.

It is readily observed from the form of (25) that the point sources at $z = 0, \pm H$ produce singularities in only the imaginary part of the fields at those points. Figure 1 shows how $E_z(z)$ changes as the observer moves away from a half-wave filament with the sinusoidal current of Eq. (24). For this case ($kH = \pi/2$) the slope discontinuity at $z = 0$ disappears and the point sources occur only at the ends of the dipole. The effect of the point sources is quite pronounced at distances which correspond to a normalized radius from 0.01 to 0.15 and remain observable out to $\rho/\lambda = 0.2$.

Moment method solutions might be improved by avoiding basis functions that are discontinuous or that have discontinuous derivatives [8]. We have seen that computation of the near-fields is greatly simplified if the current is described in terms of functions that satisfy the one-dimensional wave equation. For these reasons, we investigate the near-field of a filamentary current having a spline distribution and compare the results with the near-fields of spatial pulses of rectangular and triangular shape.

For the rectangular pulse

$$\underline{J}(x,y,z) = \hat{z}\, P(z;-H,H)\, \delta(x)\, \delta(y) \tag{27}$$

we find

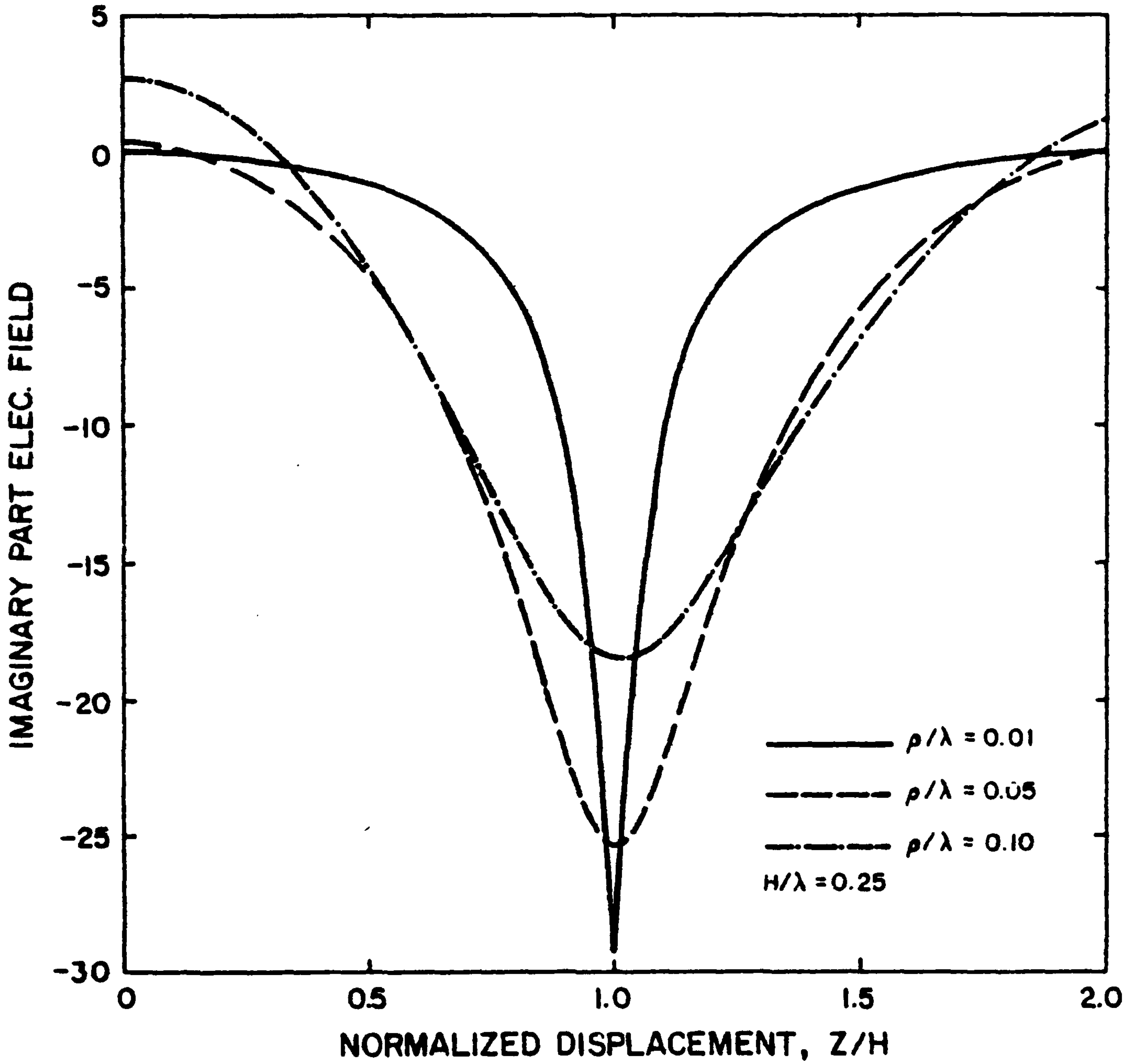

Figure 1a. Near field of sinusoidal current distribution.

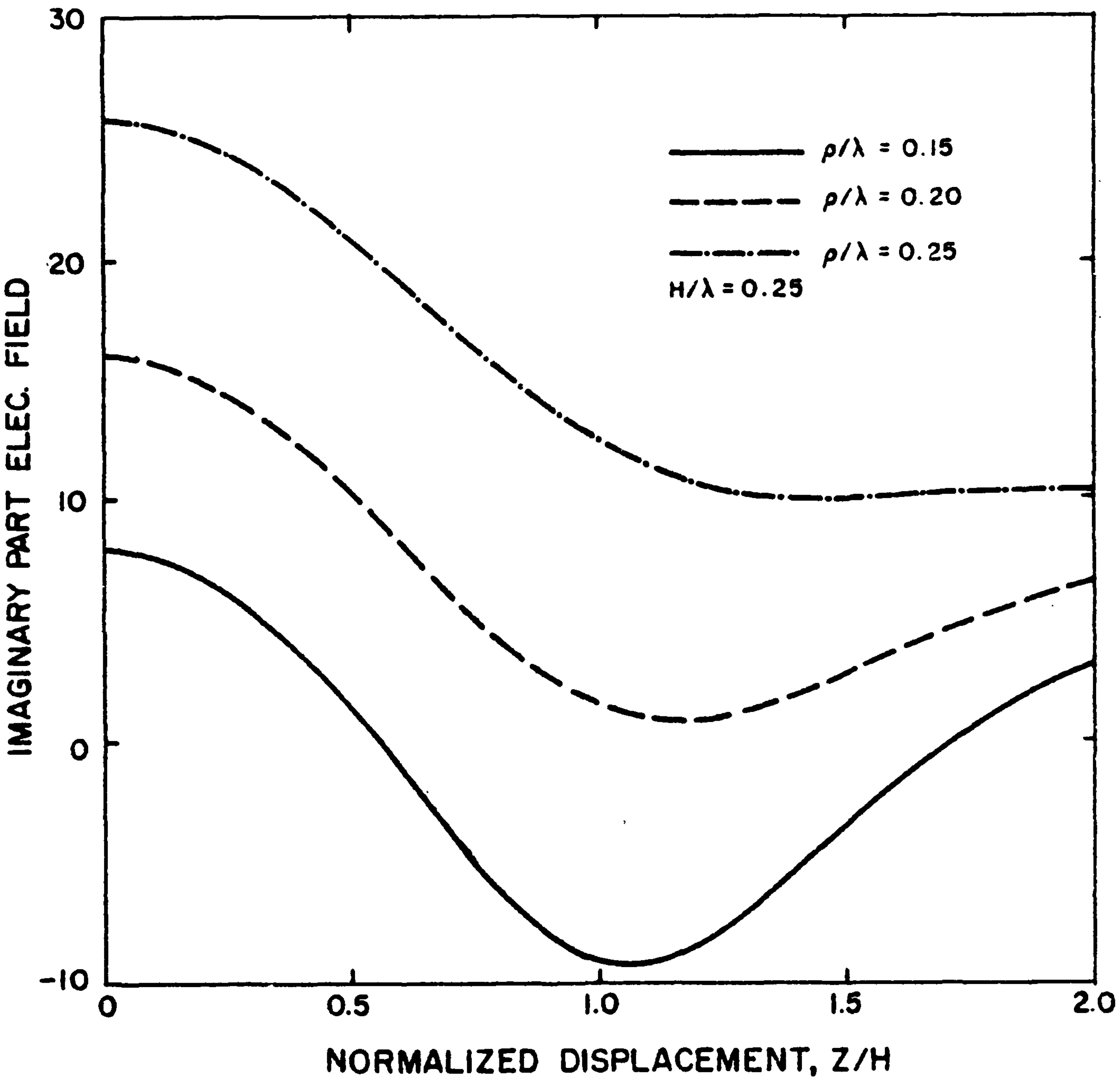

Figure 1b. Near field of sinusoidal current distribution.

$$j\omega\varepsilon\ 4\pi\ E_z(\rho,z) = (1+jkR_1)(z-H)(R_1)^{-3}\exp(-jkR_1) \tag{28}$$
$$-(1+jkR_2)(z+H)(R_2)^{-3}\exp(-jkR_2) + k^2 A_z(\rho,z;-H,H)$$

where

$$A_z(\rho,z;z_1,z_2) = \int_{z_1}^{z_2} \exp(-jkR)/R\ dz' \tag{29}$$

For the linear triangle,

$$\underline{J}(x,y,z) = \hat{z}\ [1-\ |z|/H]\ P(z;-H,H)\ \delta(x)\ \delta(y) \tag{30}$$

the field is

$$j\omega\varepsilon\ 4\pi\ E_z(\rho,z) = \{\exp(-jkR_1)/R_1 + \exp(-jkR_2)/R_2$$
$$-2\ \exp(-jkr)/r\}\ H^{-1} + k^2 A_z(\rho,z;-H,H) \tag{31}$$

Of course, the field of a short sinusoidal triangle is obtained by using (25) when kH is small. In each of the fields expressed in (25), (28) and (31), the singular terms attributable to function and/or slope discontinuities are readily observed.

A current pulse which has no discontinuities and which has a derivative with no discontinuities can be constructed using functions that are solutions of the one-dimensional wave equation. Let

$$\underline{J}(x,y,z) = \hat{z}\ I(z)\ P(z;-H,H)\ \delta(x)\ \delta(y) \tag{32}$$

where

$$I(z) = (A_- + B_-\ \exp(-jkz) + C_-\ \exp(jkz))\ P(z;-H,-pH)$$
$$+ (A + B\ \exp(-jkz) + C\ \exp(jkz))\ P(z;-pH,pH) \tag{33}$$
$$+(A_+ + B_+\ \exp(-jkz) + C_+\ \exp(jkz))\ P(z;pH,H)$$

and p is a constant between zero and one. The coefficients A, B, C are determined so that I(z) and its first derivative are continuous at $\pm$H and at $\pm$pH. Consequently only the last two terms of (21) are nonzero. Since the functions having B and C coefficients satisfy f"(z) + k f(z) = 0, we obtain

$$I''(z) + k^2 I(z) = k^2 [A_-\ P(z;-H,-pH)$$
$$+ A\ P(z;-pH,pH) + A_+\ P(z;pH,H)] \tag{34}$$

and the field produced by this type of current pulse is given by

$$j\omega\varepsilon\ 4\pi\ E_z(\rho\ ,z) = k^2 [A_-\ A_z(\rho,z;-H,-pH) \tag{35}$$

$$+ A\, A_z(\rho,z;-pH,pH) + A_+\, A_z(\rho,z;pH,H)]$$

Note that this formula contains no terms due to point sources and hence the field very close to a filament of this current will be a smoother function than that near a rectangular pulse (very bad since both function and derivative are discontinuous) or one of the triangular pulses (not so bad at the ends, but has a third peak in the center which the field of a rectangular pulse does not have).

The parallel E-field of a 0.2 wavelength rectangular pulse is shown in Figure 2 for a distance of 0.01 wavelength from the filament. The imaginary part is seen to vary greatly near the end of the pulse compared to the value at the center. The double peak of a 0.2 wavelength linear triangle pulse at the same distance is shown in Figure 3. In this case the field variation is somewhat less since only slope discontinuities occur. However, since a discontinuity is present at $z/H = 0$ as well as at $z/H = \pm 1$, the field attributable to this length source is not slowly varying at any point along its length.

The imaginary part of the parallel E-fields due to sinusoidal triangle pulses and exponential spline pulses at a distance of 0.001 wavelength for lengths of 0.02, 0.04 and 0.06 wavelengths are compared in Figures 4 and 5. These plots confirm the smoother behavior of the field of the spline pulse. In particular, the field of the spline pulse is seen to be almost constant for a significant part of the pulse width.

ANTENNA EXCITATION

An example of primary source for antennas is the magnetic frill which is described by a magnetic current density [9].

$$\underline{K} = -\hat{\phi}\ [\rho\ \ln(b/a)]^{-1}\ \delta(z)\ P(\rho;a,b) \tag{36}$$

when one volt is presumed impressed across the annular slot from inner radius, a, to outer radius, b. The electric field produced in a homogeneous medium by this source can be found from Equation (17).

$$4\pi\ \ln(b/a)\ E_z(\rho,z) = \int_0^{2\pi}\int_0^{\infty}[\delta\ (\rho'-a) - \delta(\rho'-b)]\ G(R)\ d\rho'\ d\phi' \tag{37}$$

where

$$G(R) = \exp(-jkR)/R$$
$$R = [\rho^2 + \rho'^2 - 2\rho\rho'\cos\phi' + z^2]^{1/2} \tag{38}$$

The integration on ρ' is easily performed, yielding

$$4\pi\ \ln(b/a)\ E_z(\rho,z) = \int_0^{2\pi}[\exp(-jkR_a)/R_a - \exp(-jkR_b)/R_b]\ d\phi' \tag{39}$$

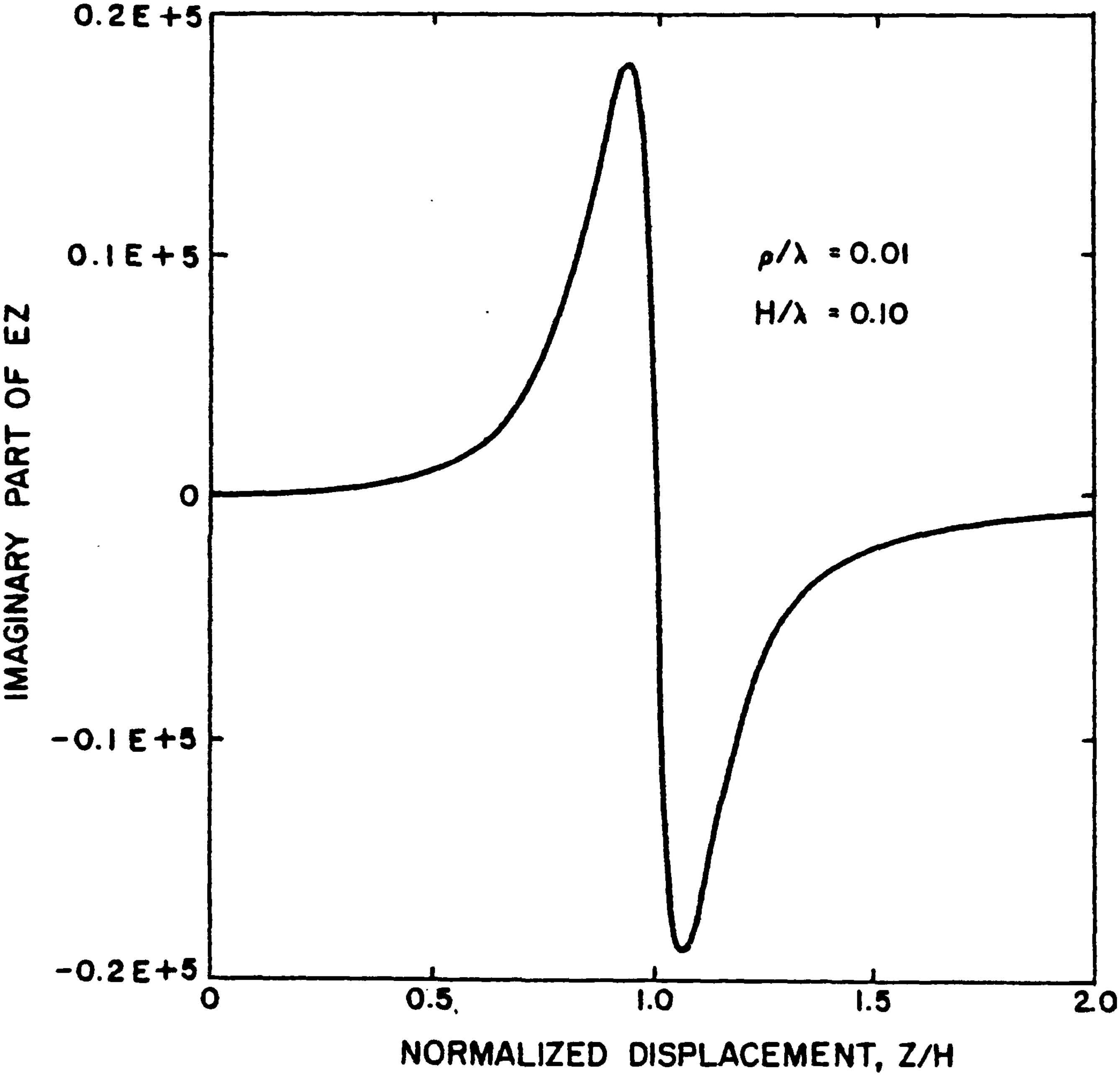

Figure 2. Near field of rectangular pulse.

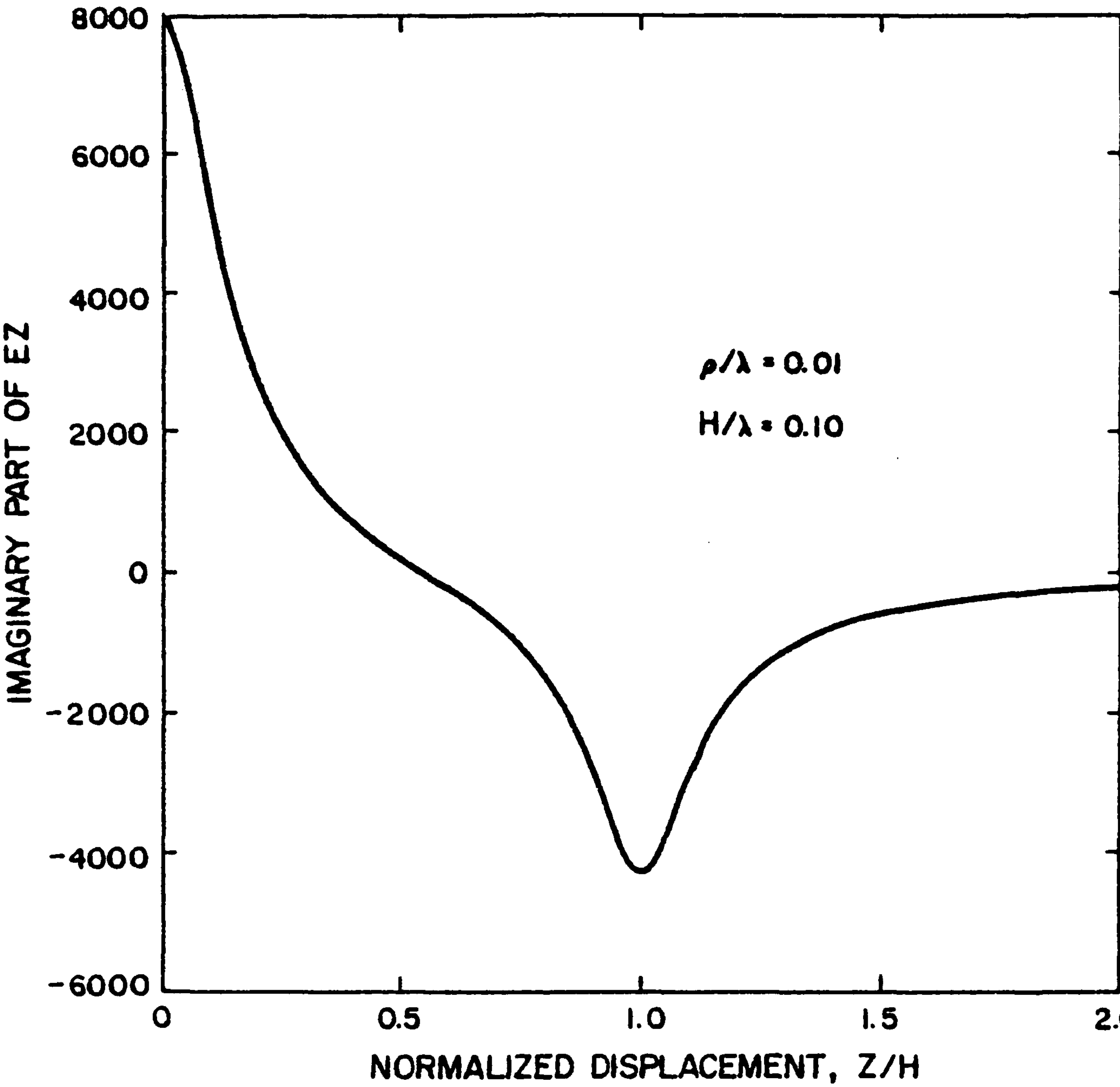

Figure 3. Near field of (linear) triangular pulse.

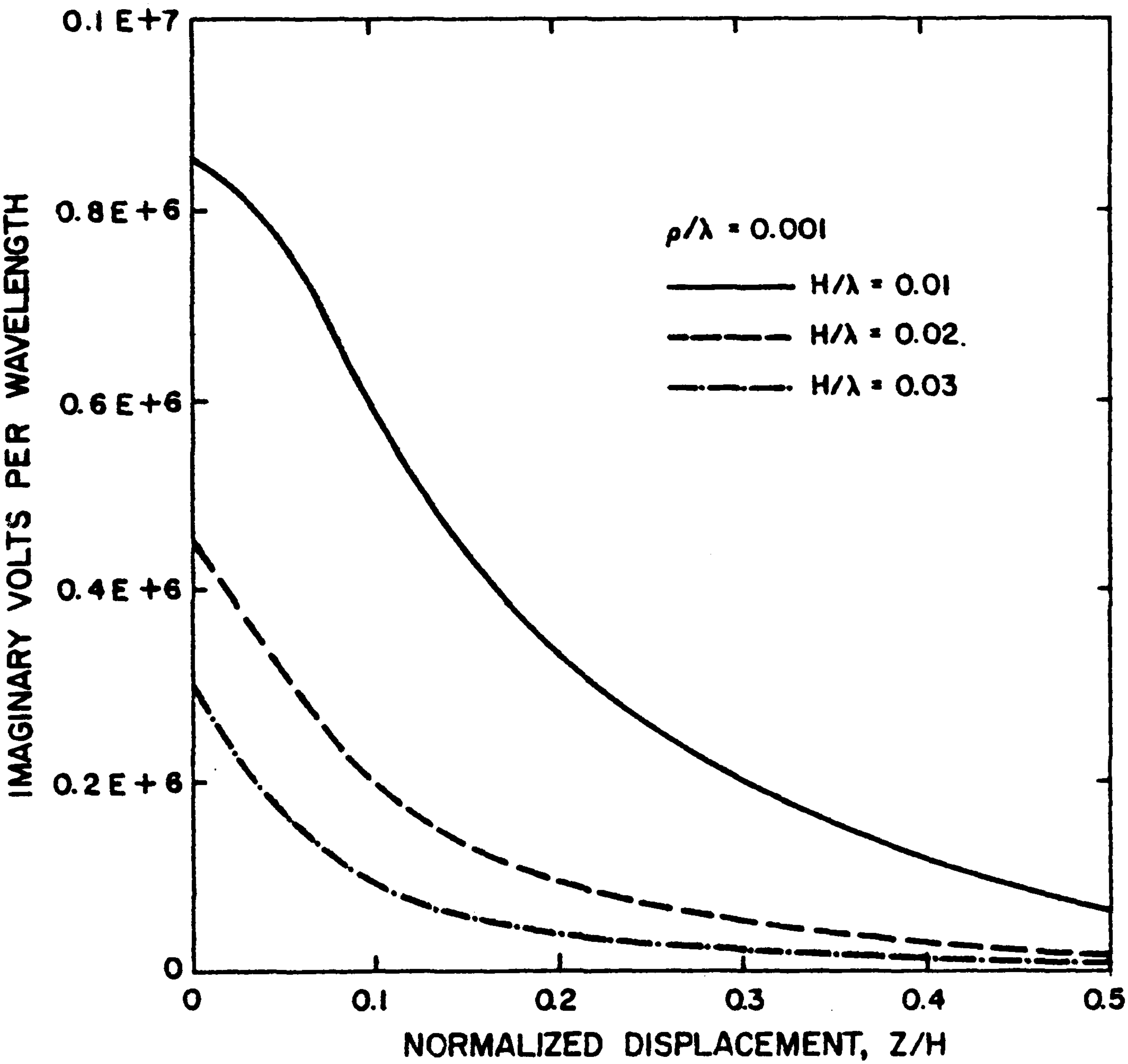

Figure 4. Near field of sinusoidal triangle pulse.

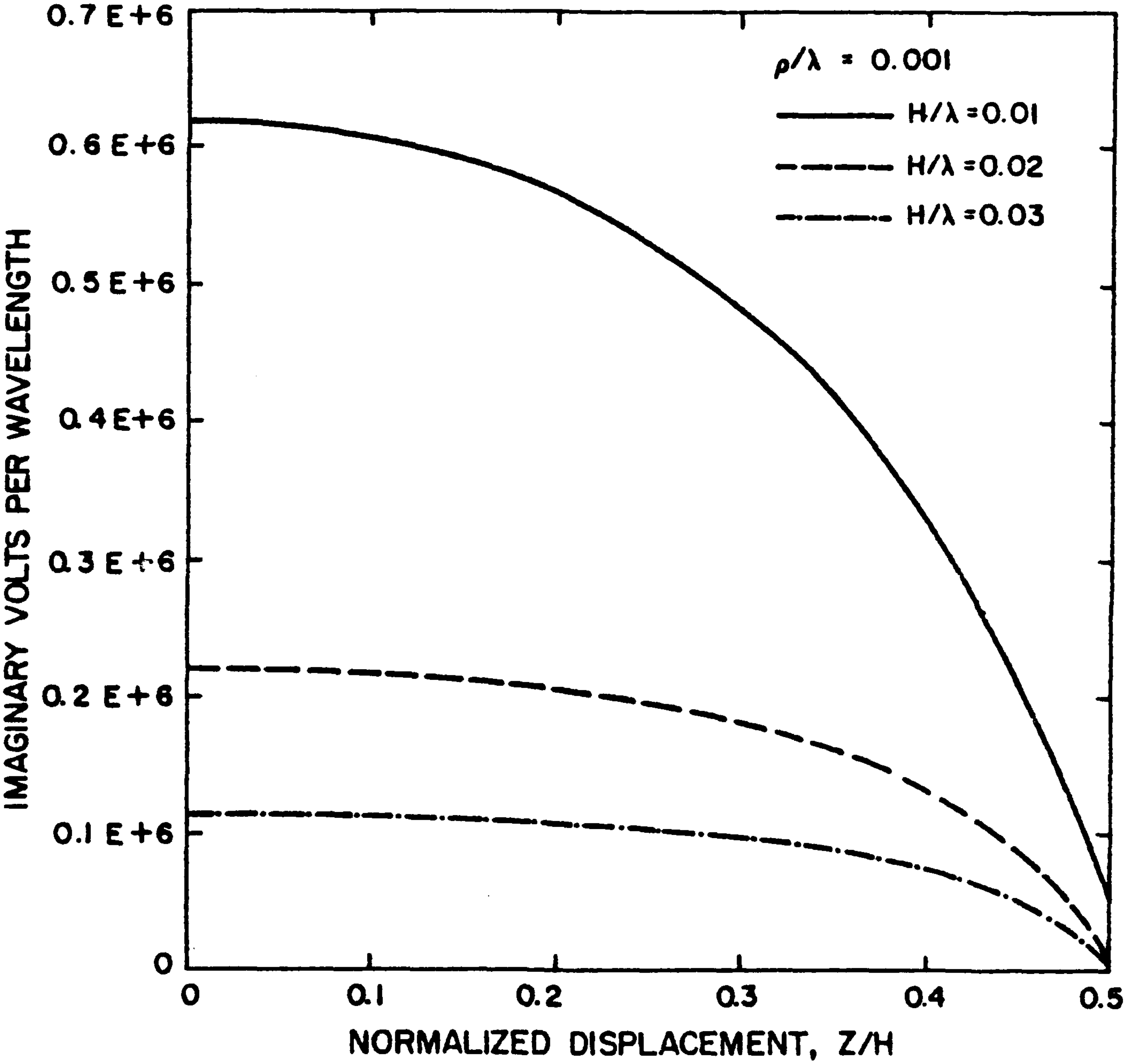

Figure 5. Near field of exponential spline pulse.

where $R_a = R|_{\rho'=a}$ and $R_b = R|_{\rho'=b}$

The numerical evaluation of (39) is much more readily done than the procedure which uses the vector potential [9] since no numerical differentiation is required. Figure 6 shows computed values of $|E_z/k|$ as a function of distance along the axis of the cylinder for several different values of ρ/a. Note that the field on the axis varies slowly as distance from the plane of the frill increases whereas the field on the antenna surface $\rho/a = 1$ is more highly peaked for small values of z/a. Once beyond z/a = 10, the fields in all cases are very nearly the same.

Although the frill is an appropriate source for cylindrical monopoles fed through a ground plane, a magnetic current ribbon conforms better to the geometry of a cylindrical dipole. In this case

$$\underline{K} = -\hat{\phi}\ (1/2w)\ P(z;-w,w)\ \delta(\rho-a) \tag{40}$$

for a one-volt source. The z-component of the incident field due to (40) is

$$2\pi E_z = -(a/w) \int_{-w}^{w}\int_{0}^{2\pi} [1+jkR_a)(\rho/a \cos \phi'-1)(R_a)^{-3} \exp(-jkR_a)]\ d\phi' dz' \tag{41}$$

where $R_a = [\rho^2 + a^2 - 2a\rho \cos \phi' + (z-z')^2]^{1/2}$

The results for the current ribbon as illustrated in Figure 7 are seen to be less peaked than those of the magnetic frill.

Computation of the near-fields of the magnetic frill or ribbon using the above formulas is readily done and gives a representation of the incident field which corresponds more closely to the physical situation than some popular approximations that are currently in use.

CONCLUSIONS

Some formulas have been presented for calculating the fields produced in a homogeneous medium by arbitrary distributions of electric or magnetic current. These formulas do not involve potential functions. Hence, no derivatives of potentials are required to find the fields. Rather, the differentiation is applied to the density functions which describe the given sources. The alternate viewpoint afforded by differentiating the current brings forcefully to attention the properties of source distributions that contribute to certain singular field behavior. This leads to consideration of alternate basis functions for use in the method of moments.

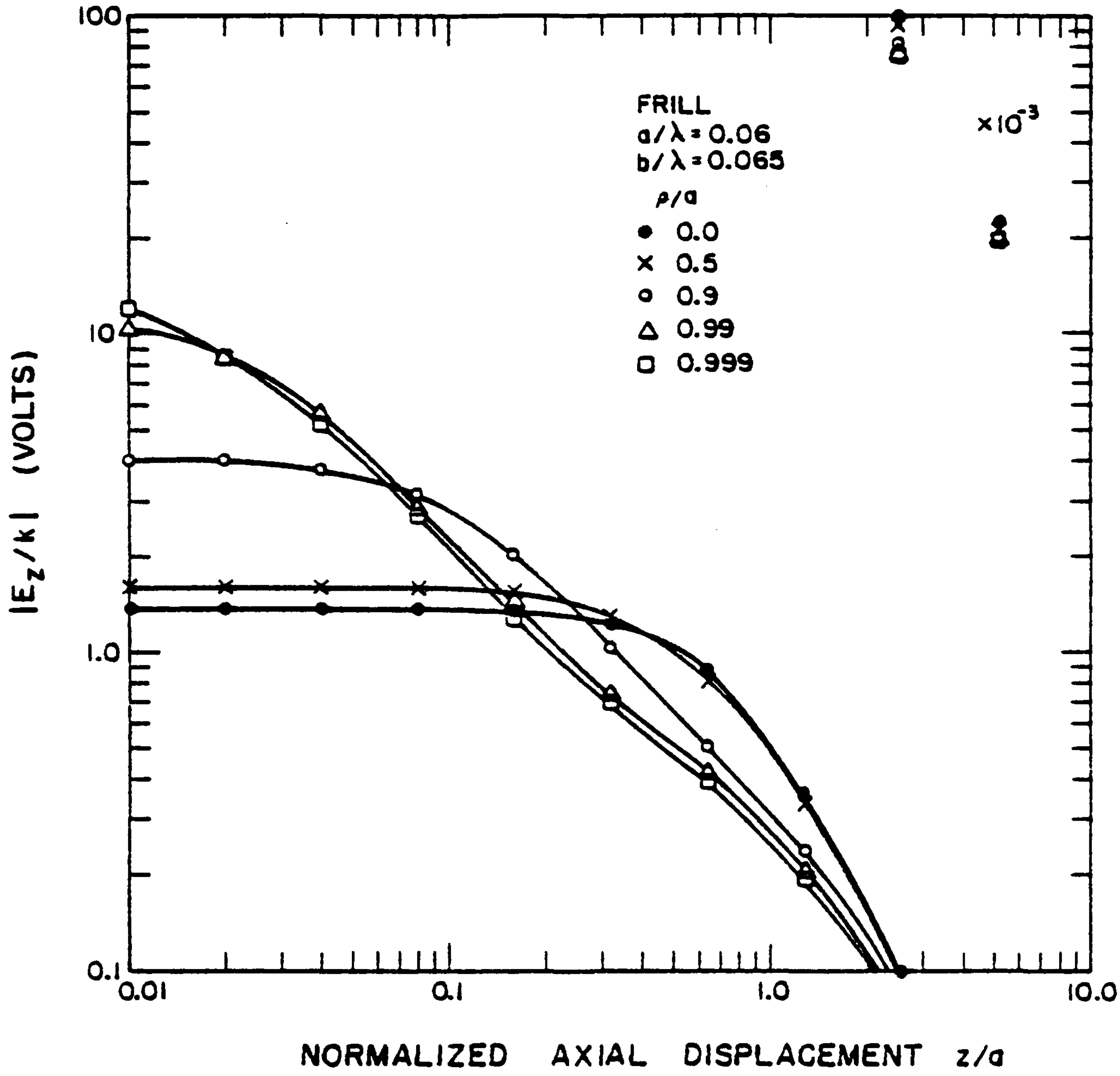

Figure 6. Magnitude of parallel component of electric field for a magnetic frill.

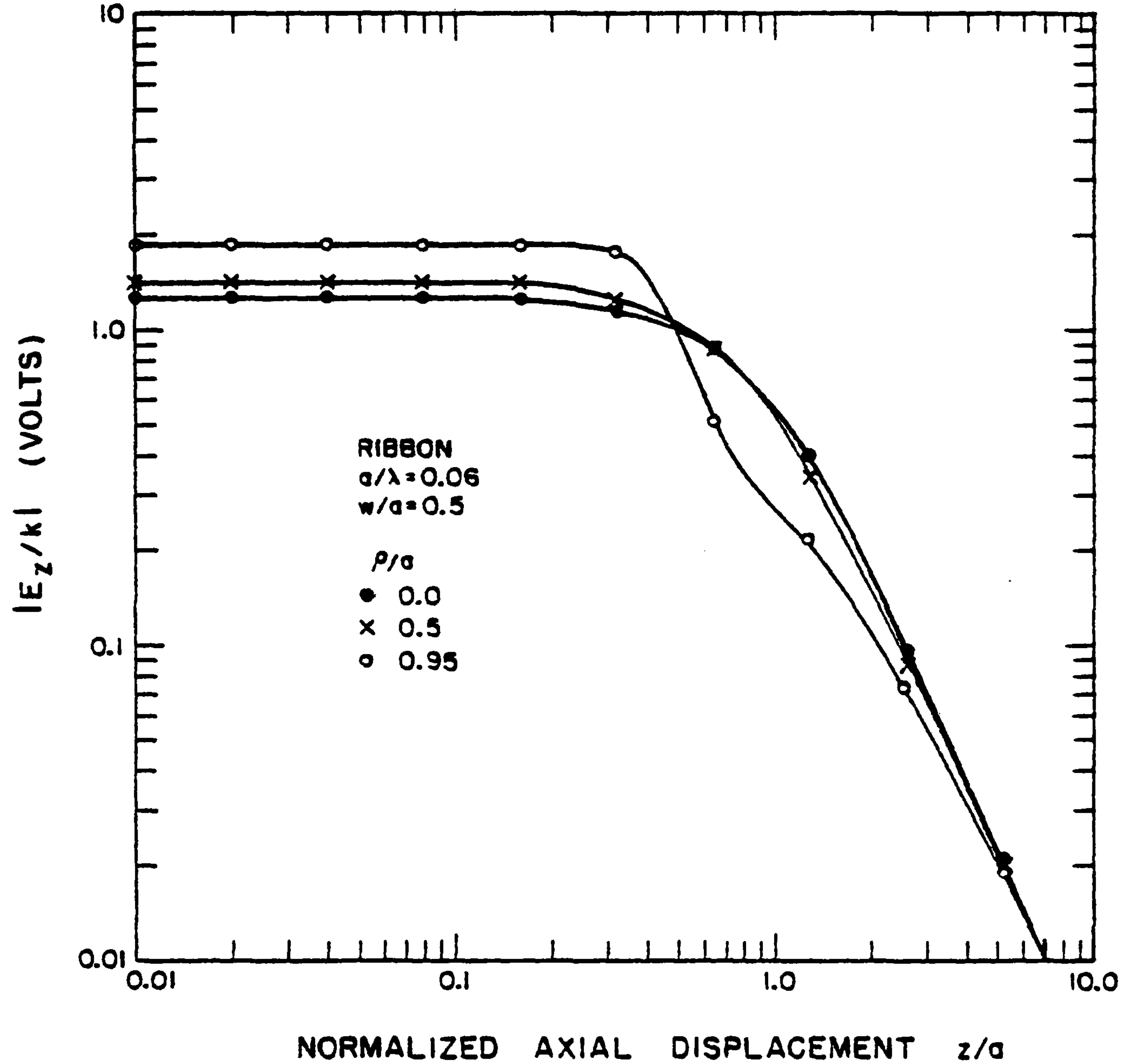

Figure 7. Magnitude of parallel component of electric field for a magnetic ribbon.

In several examples it has been demonstrated that the procedure presented here leads more straightforwardly to formulas for the fields. In those cases where analytic evaluation of the resulting integrals is not possible, the fields are found directly through numerical integration and no subsequent numerical differentiation is required. Although not necessarily producing a savings of effort for every current distribution, the technique provides a very useful alternative to the classical potential method.

ACKNOWLEDGMENT

The contributions of graduate students P. Simon, C. P. Wu, C. H. Tsao, K. W. England and D. Sali are gratefully acknowledged. Discussions with colleagues, particularly P. W. Klock, have also been very helpful. This work was supported in part by RCA Government Systems Division, Missile and Surface Radar, Moorestown, NJ 08057.

REFERENCES

[1] E. C. Jordan and K. G. Balmain, Electromagnetic Waves and Radiating Systems. New Jersey: Prentice-Hall, 1968, Sec. 10.01.
[2] R. E. Collin, Field Theory of Guided Waves. New York: McGraw-Hill, 1960, Sec. 1.5.
[3] S. Ramo, J. R. Whinnery and T. VanDuzer, Fields and Waves in Communication Electronics. New York: Wiley, 1965, Sec. 4.16.
[4] P. E. Mayes, "A new integral equation technique for electromagnetic scattering," presented at Fall Meeting, URSI, Williamsburg, Va., 1972.
[5] D. F. Hanson and P. E. Mayes, "The current source-function technique of electromagnetic scattering from a half-plane," Radio Science, vol. 13, pp. 49-58, 1978.
[6] J. Walsh and S. K. Srivastava, "Analysis of linear antenna systems: A different approach," Radio Science, vol. 15, pp. 913-921, 1980.
[7] Jordan and Balmain, op. cit., Sec. 10.09.
[8] R. Anders, "Criteria for the choice of optimal basis functions," in Proc. Inst. Elec. Eng. Int. Conf. Antennas and Propagation, Part I - Antennas, London, 1978, pp. 170-173.
[9] L. L. Tsai, "A numerical solution for the near and far fields of an annular ring of magnetic current," IEEE Trans. Antennas Prop., vol. AP-20, pp. 569-576, 1972.

EFFICIENT NUMERICAL EVALUATION OF ELECTROMAGNETIC FIELDS DUE TO RECTANGULAR PATCHES OF ELECTRIC CURRENT

P. W. Klock, D. Sall, and P. E. Mayes
Electromagnetics Laboratory
Department of Electrical Engineering
1406 West Green Street
University of Illinois
Urbana, IL 61801

1. INTRODUCTION

Many realizations of components in stripline involve abrupt changes in the geometry of the strip. Thus it is common for a step in the strip width to occur (Figure 1). Bends, tee and wye junctions are also frequently employed. To be able to accurately design stripline networks, data is needed for each of these discontinuities in the line as well as for the characteristics of the uniform line.

The problems of representing stripline discontinuities have received considerable attention in the years since 1965. A summary list of much of the published work is given in Gopinath [1]. Most of these papers employ static theory to obtain an equivalent circuit that produces approximately the same effect on stripline waves as the discontinuity in question. Some approaches deal with the electrostatic problem which is capable of yielding only a capacitive circuit element, thus ignoring any contribution which an inductive element might be required to make. Others consider separate electrostatic and magnetostatic problems, thus ignoring the interaction of the fields present in the dynamic case.

Consideration of dynamic integral equations has not been extensively applied to stripline discontinuity problems. It offers the possibility of computing more accurate data since it involves the solution for the time-harmonic fields that satisfy boundary conditions which closely correspond to the physical model. However, exact solutions cannot be expected. Rather, it is common to reduce the integral equation to a system of linear algebraic equations by means of the method of moments [2]. This technique must be used with care, however, since rapid

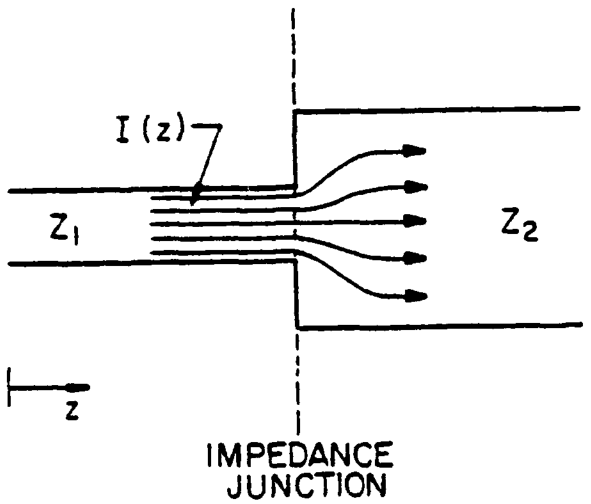

Figure 1. Stripline geometry in the vicinity of an impedance discontinuity.

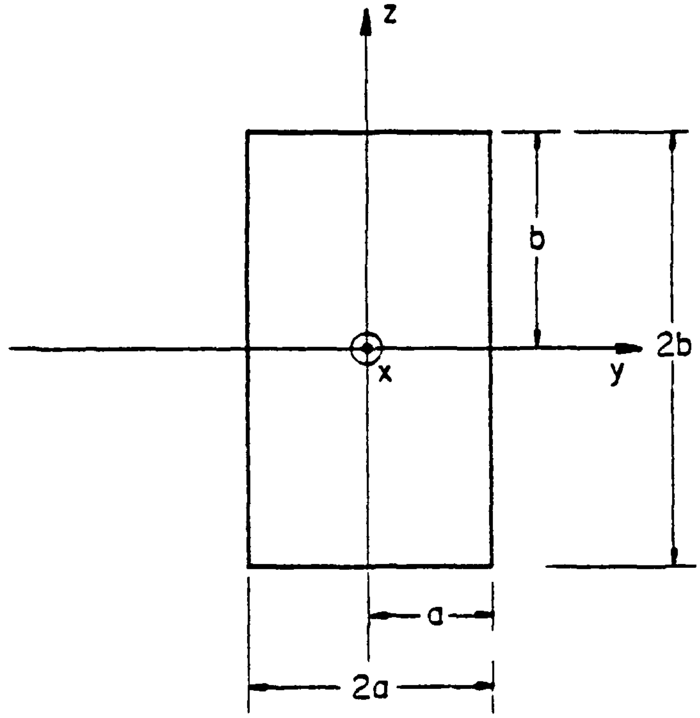

Figure 2. Patch geometry.

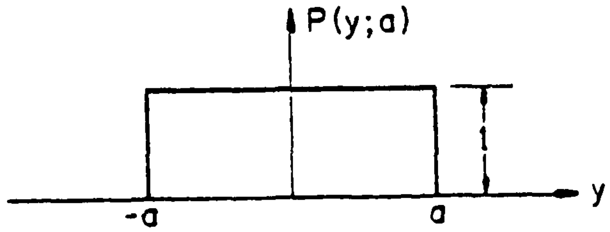

Figure 3. Pulse notation.

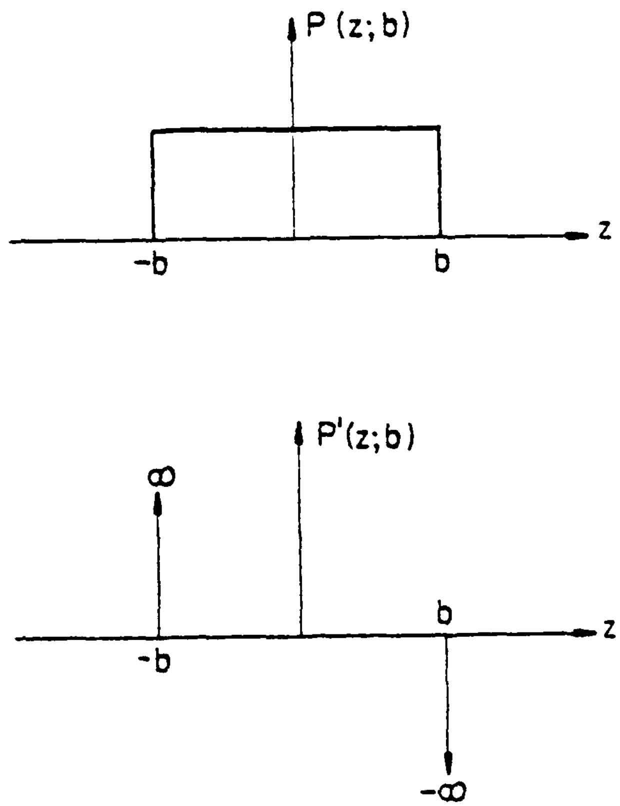

Figure 4. Derivative of a pulse.

convergence to an accurate result is not guaranteed. An important consideration in the success of the moment method is the proper choice of basis functions for representing the unknown current. Newman and Tulyathan [3] subdivide a microstrip antenna into rectangular subsections called "patches" and represents the current on each patch by a sinusoidal triangle function along the direction of current flow with a uniform distribution along the orthogonal direction. Wang, et al. [4] uses the same patch current distribution as Newman to describe the currents on scatterers. Richmond, et al. [5] expresses the electric field of the patch with a sinusoidal triangle current along both the direction of current flow and the orthogonal direction in terms of an exponential integral. The sinusoidal triangle current is frequently used because the electric field can be found easily with no surface integrals to evaluate. Glisson and Wilton [6] use uniform and linear triangle (rooftop) current patches to solve for the current on scattering strips and plates. Singh and Adams [7] use a nonrectangular patch with a sinusoidal triangle current in both the direction of current flow and the orthogonal direction.

Another crucial point in applying the moment method is the amount of computer time required to compute the fields due to the basis currents. The approach used by many authors to find the electric field due to the current on each patch is the potential method. With this technique, the current density vector is first integrated over the source region then differentiated with respect to the observation coordinates. If a moment method solution is desired, the impedance matrix elements are evaluated by an additional integration involving $\vec{E}$.

These procedures can be simplified by solving for the electric field directly from the current density vector as shown in Mayes [8], [9], Hanson and Mayes [10], and Walsh and Srivastava [11]. Analytical differentiation of the current is followed by an integration over the source region. This procedure not only reduces the effort but also exposes field singularities due to source discontinuities. The direct approach provides an early warning about possible numerical difficulties due to these singularities which are not as obvious when using the potential method.

This work addresses these two aspects of applying the moment method to solution of dynamic problems involving discontinuities in stripline. In particular, methods of computing the dynamic electric field produced by several subsectional basis currents are investigated. Each subsection is in the form of a flat rectangular area, or "patch," corresponding to subdivision of the portions of a stripline in the vicinity of a discontinuity. Three alternate forms are assumed for the current on each patch: (a) uniform, (b) sinusoidal triangle and (c) exponential spline. The fields produced by these currents involve intractable integrals. Such integrals can be accurately evaluated by a digital computer, but the process is very expensive. Nevertheless, computer programs were written for this purpose so that accurate values of the field would be known. Subsequently, the integrals have also been evaluated by employing various series representations of the integrands. Convergence of these series is compared and it is demonstrated that the field can be computed to a sufficient accuracy much more rapidly by a judicious choice of the series that is used.

2. CALCULATION OF E_z FOR A SPECIFIED CURRENT DISTRIBUTION

The patch under consideration lies in the x = 0 plane with z intercepts of b, -b and y intercepts of -a, a (Figure 2). The z-component of the electric field is now derived.

2.1 Uniform Current Distribution

The expression for uniform current as a function of y and z is given by

$$\vec{J} = \hat{z}\, J_{so}\, P(y;a)\, P(z;b)\, \delta(x) \tag{2.1}$$

The notation P(y;a) means a pulse function of y of unit height and half length a (Figure 3). The amplitude value J_{so} must be chosen by a normalizing technique. It is desired to have a current of one amp flowing across the middle of the patch at z = 0, thus, $J_{so} = \frac{1}{2a}$ which yields

$$\vec{J} = \frac{1}{2a} P(y;a)\, P(z;b)\, \delta(x) \tag{2.2}$$

The electric field can be found by solving Maxwell's Equations directly without the use of vector potentials. The result, given in Mayes [8], is

$$\vec{E} = \frac{1}{j4\pi\omega\varepsilon} \int_{V'} [\nabla'(\nabla'\cdot\vec{J}) + k^2\vec{J}]\, \frac{e^{-jk|\vec{r}-\vec{r}'|}}{|\vec{r} - \vec{r}'|}\, dV' \tag{2.3}$$

where the primed coordinates denote source points. To find the z component of $\vec{E}$

$$E_z = \hat{z}\cdot\vec{E} \tag{2.4}$$

For a current flowing in the $\hat{z}$ direction

$$\hat{z}\cdot[\nabla(\nabla\cdot\vec{J}) + k^2\vec{J}] = \frac{\partial^2}{\partial z^2} J_z + k^2 J_z \tag{2.5}$$

Inserting (2.5) into (2.4)

$$E_z = \frac{1}{j4\pi\omega\varepsilon} \int_{V'} \left[\frac{\partial^2}{\partial z'^2} J_z + k^2 J_z\right] \frac{e^{-jk|\vec{r}-\vec{r}'|}}{|\vec{r} - \vec{r}'|}\, dV' \tag{2.6}$$

where

$$|\vec{r} - \vec{r}'| = R = [(x - x')^2 + (y - y')^2 + (z - z')^2]^{1/2}$$

Evaluating (2.5) for the uniform current and substituting into (2.6) yields

$$E_z = \frac{1}{j4\pi\omega\varepsilon} \int_{V'} \frac{1}{2a} P(y';a)\ \delta(x')[\delta'(z' + b) - \delta'(z' - b)$$

$$+ k^2\ P(z';b)]\ \frac{e^{-jkR}}{R}\, dV' \tag{2.7}$$

where the pulse function was differentiated using the convention shown in Figure 4.

Equation (2.7) can be divided into three integrations

$$E_z = E_{z_1} + E_{z_2} + E_{z_3}$$

where

$$E_{z_1} = \frac{1}{j8\pi\omega\varepsilon a} \int_{V'} \delta(x')\ P(y';a)\ \delta'(z' + b)\ \frac{e^{-jkR}}{R}\, dV' \tag{2.8}$$

$$E_{z_2} = \frac{1}{j8\pi\omega\varepsilon a} \int_{V'} \delta(x')\ P(y';a)\ \delta'(z' - b)\ \frac{e^{-jkR}}{R}\, dV' \tag{2.9}$$

$$E_{z_3} = \frac{k^2}{j8\pi\omega\varepsilon a} \int_{V'} \delta(x')\ P(y';a)\ P(z';b)\ \frac{e^{-jkR}}{R}\, dV' \tag{2.10}$$

To evaluate (2.8) and (2.9), the following property of the Dirac delta function is used

$$\int_{-\infty}^{\infty} \delta'(x - x_o)\, f(x)\, dx = -f'(x_o) \tag{2.11}$$

Thus, the spherical wave kernel must be differentiated with respect to z'. Letting $w = e^{-jkR}/R$ and using the chain rule for composite functions

$$\frac{\partial w}{\partial z'} = \frac{\partial w}{\partial R}\frac{\partial R}{\partial z'} \tag{2.12}$$

where

$$\frac{\partial w}{\partial R} = \frac{-e^{-jkR}(1 + jkR)}{R^2}$$

$$\frac{\partial R}{\partial z'} = \frac{-(z - z')}{R}$$

Using (2.11) and (2.12) to evaluate (2.8) yields

$$E_{z_1} = j\,\frac{15}{2\pi a}\,\lambda \int_{-a}^{a} (z + b)\,\frac{e^{-jk[x^2+(y-y')^2+(z+b)^2]^{1/2}}}{[x^2 + (y - y')^2 + (z + b)^2]^{3/2}}$$

$$\cdot(1 + jk[x^2 + (y - y')^2 + (z + b)^2])\; dy' \tag{2.13}$$

where

$$\frac{1}{c\varepsilon} = 120\pi$$

Equation (2.9) is of the same form as (2.8) and can be found by inspection. Replacing b with -b and making a sign change gives

$$E_{z_2} = -j\,\frac{15}{2\pi a}\,\lambda \int_{-a}^{a} (z - b)\,\frac{e^{-jk[x^2+(y-y')^2+(z-b)^2]^{1/2}}}{[x^2 + (y - y')^2 + (z - b)^2]^{3/2}}$$

$$\cdot(1 + jk[x^2 + (y - y')^2 + (z - b)^2])\; dy' \tag{2.14}$$

Finally, E_{z_3} is simply given by

$$E_{z_3} = -j \frac{30\pi}{a\lambda} \int_{-b}^{b} \int_{-a}^{a} \frac{e^{-jk[x^2+(y-y')^2+(z-z')^2]^{1/2}}}{[x^2 + (y - y')^2 + (z - z')^2]^{1/2}} dy'dz' \tag{2.15}$$

2.2 Sinusoidal Triangle Current Distribution

The expression for a current density varying as a sinusoidal triangle in the z-coordinate and uniform in the y-direction is given by

$$\vec{J} = \hat{z} \frac{1}{2a\sin(kb)} \sin[k(b - |z|)] \; P(z;b) \; P(y;z) \; \delta(x) \tag{2.16}$$

where $J_{so} = 1/2a\sin(kb)$ to insure one amp of current flow at $z = 0$.

Using the procedure found in Mayes [8], E_z can be found to be

$$E_z = \frac{1}{j4\pi\omega\epsilon} \int_{V'} \delta(x') \; P(y';a) \; \frac{k}{2a\sin(kb)} [\delta(z' + b) + \delta(z' - b)$$

$$- 2\cos(kb) \; \delta(z')] \frac{e^{-jkR}}{R} dV' \tag{2.17}$$

The x' and z' integrations are trivial due to the properties of the delta function. The expression for E_z becomes

$$E_z = -j \frac{15}{a\sin(kb)} \left[\int_{-a}^{a} \frac{e^{-jkR_1}}{R_1} dy' + \int_{-a}^{a} \frac{e^{-jkR_2}}{R_2} dy' \right.$$

$$\left. -2\cos(kb) \int_{-a}^{a} \frac{e^{-jkR_3}}{R_3} dy' \right] \tag{2.18}$$

where

$$R_1 = [x^2 + (y - y')^2 + (z + b)^2]^{1/2}$$

$$R_2 = [x^2 + (y - y')^2 + (z - b)^2]^{1/2}$$

$$R_3 = [x^2 + (y - y')^2 + z^2]^{1/2}$$

2.3 Exponential Spline Current Distribution

The exponential spline current has a Gaussian shape along the z-coordinate and was chosen constant as a function of y. The general expression is given by

$$\vec{J} = \hat{z}\, J_{so}\, P(y;a)\, I(z)\, \delta(x) \tag{2.19}$$

where

$$I(z) = [A + Be^{-jkz} + Ce^{jkz}]\, P(z;Pb,b)$$

$$+ [D + Ee^{-jkz} + Fe^{jkz}]\, P(z;-Pb,Pb)$$

$$+ [G + He^{-jkz} + Ie^{jkz}]\, P(z;-b,-Pb)$$

The notation $P(z;Pb,b)$ denotes a pulse starting at Pb and stopping at b. J_{so} is determined only with the second pulse at $z = 0$ and is given by

$$J_{so} = \frac{1}{2a(D + E + F)}$$

The geometry of this current is shown in Figure 5.

The constants A-I can be calculated by enforcing boundary conditions on the function and its first derivative at the four boundaries. The constants A-C, E-I are expressed in terms of D, the dc value of the center pulse. As seen in Figure 5, the following boundary conditions must be satisfied

1. $M(b) = 0$
2. $M'(b) = 0$
3. $M(Pb) = Q(Pb)$
4. $M'(Pb) = Q'(Pb)$
5. $Q(-Pb) = T(-Pb)$

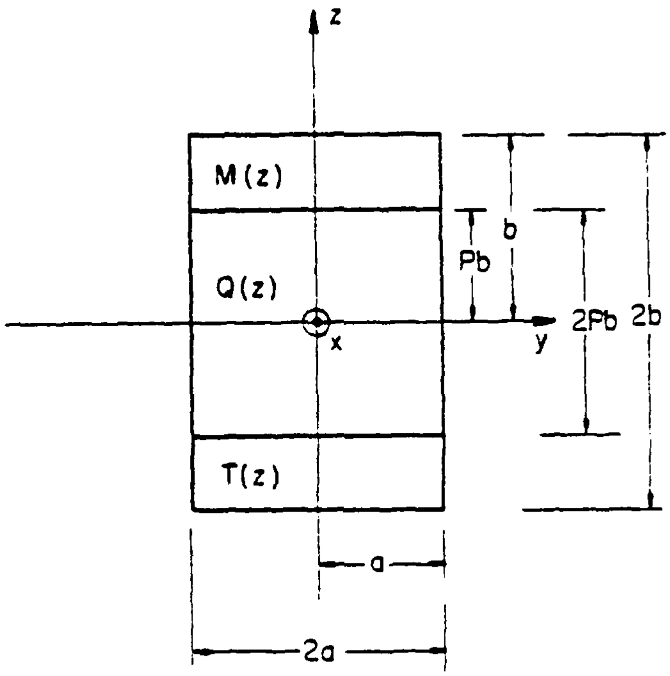

Figure 5. Pulse divisions for the exponential spline current distribution.

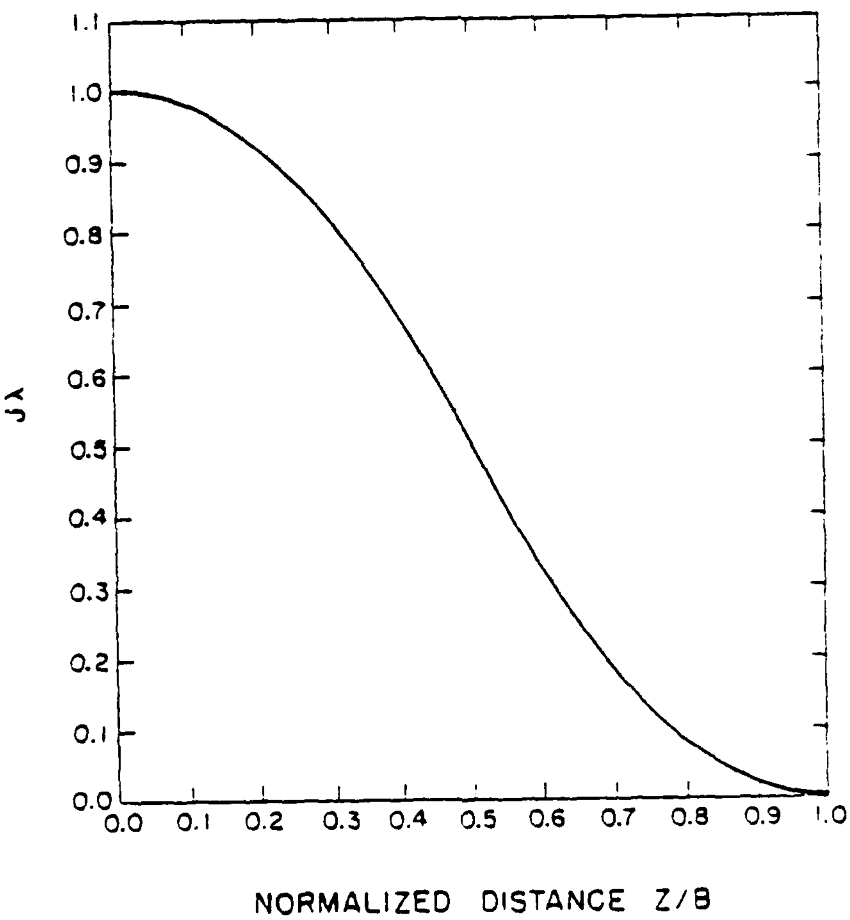

Figure 6. Exponential spline current distribution with $1/2a = 1$, $Pb = 0.5b$.

6. $Q'(-Pb) = T'(-Pb)$

7. $T(-b) = 0$

8. $T'(-b) = 0$

Applying conditions 1, 2, 7, and 8 immediately yields

$$B = -\frac{A}{2}e^{jkb} \tag{2.20}$$

$$C = -\frac{A}{2}e^{-jkb}$$

$$H = -\frac{G}{2}e^{-jkb}$$

$$I = -\frac{G}{2}e^{jkb}$$

Using conditions 3-6 and substituting in (2.20) produce a 4 × 4 matrix

$$\begin{bmatrix} 1 - \cos k(b - Pb) & -e^{-jk(Pb)} & -e^{jk(Pb)} & 0 \\ j\sin k(b - Pb) & e^{-jk(Pb)} & -e^{jk(Pb)} & 0 \\ 0 & e^{jk(Pb)} & e^{-jk(Pb)} & \cos k(b - Pb) - 1 \\ 0 & -e^{jk(Pb)} & e^{-jk(Pb)} & j\sin k(b - Pb) \end{bmatrix} \begin{bmatrix} A \\ E \\ F \\ G \end{bmatrix} = \begin{bmatrix} D \\ 0 \\ -D \\ 0 \end{bmatrix} \tag{2.21}$$

Evaluating (2.21) for A, E, F, and G by using Cramer's Rule and the following trigonometric identities

$$\cos\theta = \frac{e^{j\theta} + e^{-j\theta}}{2}$$

$$\sin\theta = \frac{e^{j\theta} - e^{-j\theta}}{j2}$$

$$\sin(\alpha + \beta) = \sin\alpha\cos\beta + \cos\alpha\sin\beta$$

$$\cos(\alpha + \beta) = \cos\alpha\cos\beta - \sin\alpha\sin\beta$$

$$\sin(2\theta) = 2\sin\theta\cos\theta$$

yields

$$A = G = Dw(b) \tag{2.22}$$

$$B = I = \frac{-D}{2}w(b)\ e^{jkb}$$

$$C = H = \frac{-D}{2}w(b)\ e^{-jkb}$$

$$E = F = \frac{D}{2}u(b)$$

where

$$w(b) = \frac{\sin(kPb)}{\sin(kPb) - \sin(kb)}$$

$$u(b) = \frac{\sin(kb - kPb)}{\sin(kPb) - \sin(kb)}$$

With the constants known, $J(z)$ can now be plotted (Figure 6). The expression for the current $I(z)$ in (2.19) can be written as

$$I(z) = M(z)\ P(z;Pb,b) + Q(z)\ P(z;-Pb,Pb) + T(z)\ P(z;-b,-Pb)$$

The functions $M(z)$, $Q(z)$, and $T(z)$ can be changed from complex exponentials to sinusoids by using (2.22)

$$M(z) = A[1 - \cos k(b - z)]$$

$$Q(z) = D + 2E\cos(kz)$$

$$T(z) = A[1 - \cos k(b + z)]$$

In evaluating (2.5) for the exponential spline current, several derivatives become trivial by using the following property of the delta function

$$x\delta(x - x_o) = x_o\delta(x - x_o)$$

Using equations (2.11) and (2.22), the second derivative of I(z) can be expressed as

$$\begin{aligned} I''(z) = &-k^2[Be^{-jkz} + Ce^{jkz}]\ P(z;Pb,b) \\ &-k^2[Ee^{-jkz} + Fe^{jkz}]\ P(z;-Pb,Pb) \\ &-k^2[He^{-jkz} + Ie^{jkz}]\ P(z;-b,-Pb) \end{aligned}$$

Substituting into (2.5) yields

$$\frac{\partial^2}{\partial z^2} J_z + k^2 J_z = \frac{k^2}{2a(D + E + F)} P(y;a)\ \delta(x)$$

$$\cdot[AP(z;Pb,b) + DP(z;-Pb,Pb) + GP(z;-b,-Pb)]$$

Using equation (2.6), E_z is given by

$$E_z = -j\frac{30\pi}{a(D + E + F)\lambda}\left[A\int_{Pb}^{b}\int_{-a}^{a}\frac{e^{-jkR}}{R}\,dy'dz' + D\int_{-Pb}^{Pb}\int_{-a}^{a}\frac{e^{-jkR}}{R}\,dy'dz'\right.$$

$$\left. + G\int_{-b}^{-Pb}\int_{-a}^{a}\frac{e^{-jkR}}{R}\,dy'dz'\right] \qquad (2.23)$$

where

$$R = [x^2 + (y - y')^2 + (z - z')^2]^{1/2}$$

and

$$\frac{1}{c\varepsilon} = 120\pi$$

3. CALCULATION OF E_y FOR A SPECIFIED CURRENT DISTRIBUTION

The y component of $\vec{E}$ can be evaluated by using the same techniques found in Chapter 2. To find Ey

$$E_y = \hat{y}\cdot\vec{E} \tag{3.1}$$

For a current flowing in the $\hat{z}$ direction

$$\hat{y}\cdot[\nabla(\nabla\cdot\vec{J}) + k^2\vec{J}] = \frac{\partial}{\partial y}\left(\frac{\partial J_z}{\partial z}\right) \tag{3.2}$$

Equation (3.2) is substituted into (2.3) to obtain

$$\vec{E} = \frac{1}{j4\pi\omega\varepsilon}\int_{V'} \frac{\partial}{\partial y'}\left(\frac{\partial J_z}{\partial z'}\right)\frac{e^{-jk|\vec{r}-\vec{r}'|}}{|\vec{r}-\vec{r}'|}\,dv' \tag{3.3}$$

Using (3.3), E_y will be evaluated for each current distribution.

3.1 *Uniform Current Distribution*

Equation (2.2) is differentiated as shown in (3.2) and substituted into (3.3) to yield

$$E_y = \frac{1}{j4\pi\omega\varepsilon}\int_{V'} \frac{1}{2a}\,\delta(x')[\delta(z'+b) - \delta(z'-b)]$$
$$\cdot[\delta(y'+a) - \delta(y'-a)]\,\frac{e^{-jk|\vec{r}-\vec{r}'|}}{|\vec{r}-\vec{r}'|}\,dv'$$

The integration is done by inspection,

$$E_y = -j\,\frac{15\lambda}{2\pi a}\left[\frac{e^{-jkR_1}}{R_1} - \frac{e^{-jkR_2}}{R_2} - \frac{e^{-jkR_3}}{R_3} + \frac{e^{-jkR_4}}{R_4}\right] \tag{3.4}$$

where

$$R_1 = [x^2 + (y + a)^2 + (z + b)^2]^{1/2}$$

$$R_2 = [x^2 + (y - a)^2 + (z + b)^2]^{1/2}$$

$$R_3 = [x^2 + (y + a)^2 + (z - b)^2]^{1/2}$$

$$R_4 = [x^2 + (y - a)^2 + (z - b)^2]^{1/2}$$

3.2 Sinusoidal Triangle Current Distribution

Equation (2.16) is differentiated as shown in (3.2) and substituted into (3.3) to yield

$$\begin{aligned}
E_y = -j \frac{15\lambda}{2\pi a \sin(kb)} \int_{V'} & \delta(x')[\delta(y' + a) - \delta(y' - a)] \\
& \cdot\{\sin(k(b - z'))[\delta(z') - \delta(z' - b)] \\
& - k \cos(k(b - z'))\, P(z';0,b)\} \frac{e^{-jkR}}{R}\, dv' \\
& - j \frac{15\lambda}{2\pi a \sin(kb)} \int_{V'} \delta(x')[\delta(y' + a) - \delta(y' - a)] \\
& \cdot\{\sin(k(b + z'))[\delta(z' + b) - \delta(z')] \\
& + k \cos\,(k(b + z'))\, P(z';-b,0)\} \frac{e^{-jkR}}{R}\, dv'
\end{aligned} \tag{3.5}$$

Replacing the cosine functions with complex exponentials and simplifying yields

$$E_y = -j \frac{15}{2a \sin(kb)} \left[\int_0^b \frac{e^{-jk(R_2+z'-b)}}{R_2} dz' + \int_0^b \frac{e^{-jk(R_2-z'+b)}}{R_2} dz' \right.$$

$$- \int_0^b \frac{e^{-jk(R_1+z'-b)}}{R_1} dz' - \int_0^b \frac{e^{-jk(R_1-z'+b)}}{R_1} dz'$$

$$- \int_{-b}^0 \frac{e^{-jk(R_2-z'-b)}}{R_2} dz' - \int_{-b}^0 \frac{e^{-jk(R_2+z'+b)}}{R_2} dz' \tag{3.6}$$

$$\left. + \int_{-b}^0 \frac{e^{-jk(R_1-z'-b)}}{R_1} dz' + \int_{-b}^0 \frac{e^{-jk(R_1+z'+b)}}{R_1} dz' \right]$$

where

$$R_1 = [x^2 + (y + a)^2 + (z - z')^2]^{1/2}$$

$$R_2 = [x^2 + (y - a)^2 + (z - z')^2]^{1/2}$$

3.3 Exponential Spline Current Distribution

Equation (2.19) is differentiated as shown in (3.2) and substituted into (3.3) to yield

$$E_y = -j \frac{15\lambda}{2\pi a(D + E + F)} \int_{V'} \delta(x')[\delta(y' + a) - \delta(y' - a)]$$

$$\cdot\{\delta(z' - Pb)[A + B\, e^{-jkz'} + Ce^{jkz'}]$$

$$+ \delta(z' + Pb)[D + E\, e^{-jkz'} + Fe^{jkz'}]$$

$$- \delta(z - Pb)[D + E\, e^{-jkz'} + Fe^{jkz'}]$$

$$- \delta(z' + Pb)[G + He^{-jkz'} + Ie^{jkz'}]$$

$$- jk[Be^{-jkz'} - Ce^{jkz'}]\, P(z';Pb,b)$$

$$- jk[Ee^{-jkz'} - Fe^{jkz}]\ P(z';-Pb,Pb)$$

$$-jk[He^{-jkz'} - Ie^{jkz'}]\ P(z';-b,-Pb)\} \frac{e^{-jkR}}{R}\, dv' \qquad (3.7)$$

The integrations involving the delta functions in all three space coordinates are easily evaluated. Using equation (2.22), the closed form expressions become

$$E_{y_1} = \{A[1 - \cos k(b - Pb)] - [D + 2E \cos kb]\}$$

$$\cdot\left[\frac{e^{-jkR_1}}{R_1} + \frac{e^{-jkR_2}}{R_2} + \frac{e^{-jkR_3}}{R_3} + \frac{e^{-jkR_4}}{R_4}\right] \qquad (3.8)$$

where

$$R_1 = [x^2 + (y + a)^2 + (z - Pb)^2]^{1/2}$$

$$R_2 = [x^2 + (y + a)^2 + (z + Pb)^2]^{1/2}$$

$$R_3 = [x^2 + (y - a)^2 + (z - Pb)^2]^{1/2}$$

$$R_4 = [x^2 + (y - a)^2 + (z + Pb)^2]^{1/2}$$

The remaining integral expressions are then added to E_{y_1} to give

$$E_y = E_{y_1} + jkB\left[\int_{Pb}^{b} \frac{e^{-jk(R_2+z')}}{R_2}\, dz' - \int_{Pb}^{b} \frac{e^{-jk(R_1+z')}}{R_1}\, dz'\right]$$

$$+ jkC\left[\int_{Pb}^{b} \frac{e^{-jk(R_1-z')}}{R_1}\, dz' - \int_{Pb}^{b} \frac{e^{-jk(R_2-z')}}{R_2}\, dz'\right]$$

$$+ jkE \left[\int_{-Pb}^{Pb} \frac{e^{-jk(R_2+z')}}{R_2} dz' - \int_{-Pb}^{Pb} \frac{e^{-jk(R_1+z')}}{R_1} dz' \right]$$

$$+ jkF \left[\int_{-Pb}^{Pb} \frac{e^{-jk(R_1-z')}}{R_1} dz' - \int_{-Pb}^{Pb} \frac{e^{-jk(R_2-z')}}{R_2} dz' \right]$$

$$+ jkH \left[\int_{-b}^{-Pb} \frac{e^{-jk(R_2+z')}}{R_2} dz' - \int_{-b}^{-Pb} \frac{e^{-jk(R_1+z')}}{R_1} dz' \right]$$

$$+ jkI \left[\int_{-b}^{-Pb} \frac{e^{-jk(R_1-z')}}{R_1} dz' - \int_{-b}^{-Pb} \frac{e^{-jk(R_2-z')}}{R_2} dz' \right]$$

where

$$R_1 = [x^2 + (y + a)^2 + (z - z')^2]^{1/2}$$

$$R_2 = [x^2 + (y - a)^2 + (z - z')^2]^{1/2} \tag{3.9}$$

4. EVALUATION OF THE FIELD

The integrals appearing in the expressions for the electric field are not expressible as a finite combination of the elementary functions. The evaluation of the integrals was performed by a number of different methods. First, the integrals were performed by numerical integration with tight error bounds so that one could have good "exact" results with which to compare other methods. Second, the integrals were performed by expanding exp(-jkR) in a Taylor's series and keeping only two or four terms. The resulting integrals after expanding are found in [12]. This is numerically efficient but not sufficiently accurate. More details can be found in a Master of Science thesis of the same title as this paper by D. Sall, 1981. Third, the integrals were performed by expanding exp(-jkR) by taking out exp(-jkr), and leaving exp[-jk(R - r)] for more rapid convergence as in [13]. This method is numerically efficient as well as accurate.

Figures 7 and 8 give E_z as a function of z and y, respectively, for a thin ribbon which was chosen so that the exact results in closed form for the sinusoidal triangle [14] might be used. Comparisons in all cases were done with numerical integration with extremely good results. Note the smoothness of the results near the end of the ribbon for the exponential spline. The physical field from a thin ribbon is unknown, but it is not like that resulting from the uniform or sinusoidal triangle currents.

Figures 9 and 10 show E_z as a function of z and y, respectively, for a square patch such as might be used as an expansion function. Note discontinuities near the edge of the patch. Expanded scales near the edge of the patch are used in Figures 11 and 12 for E_z as a function of z and y, respectively. Results of E_y may be found in the thesis.

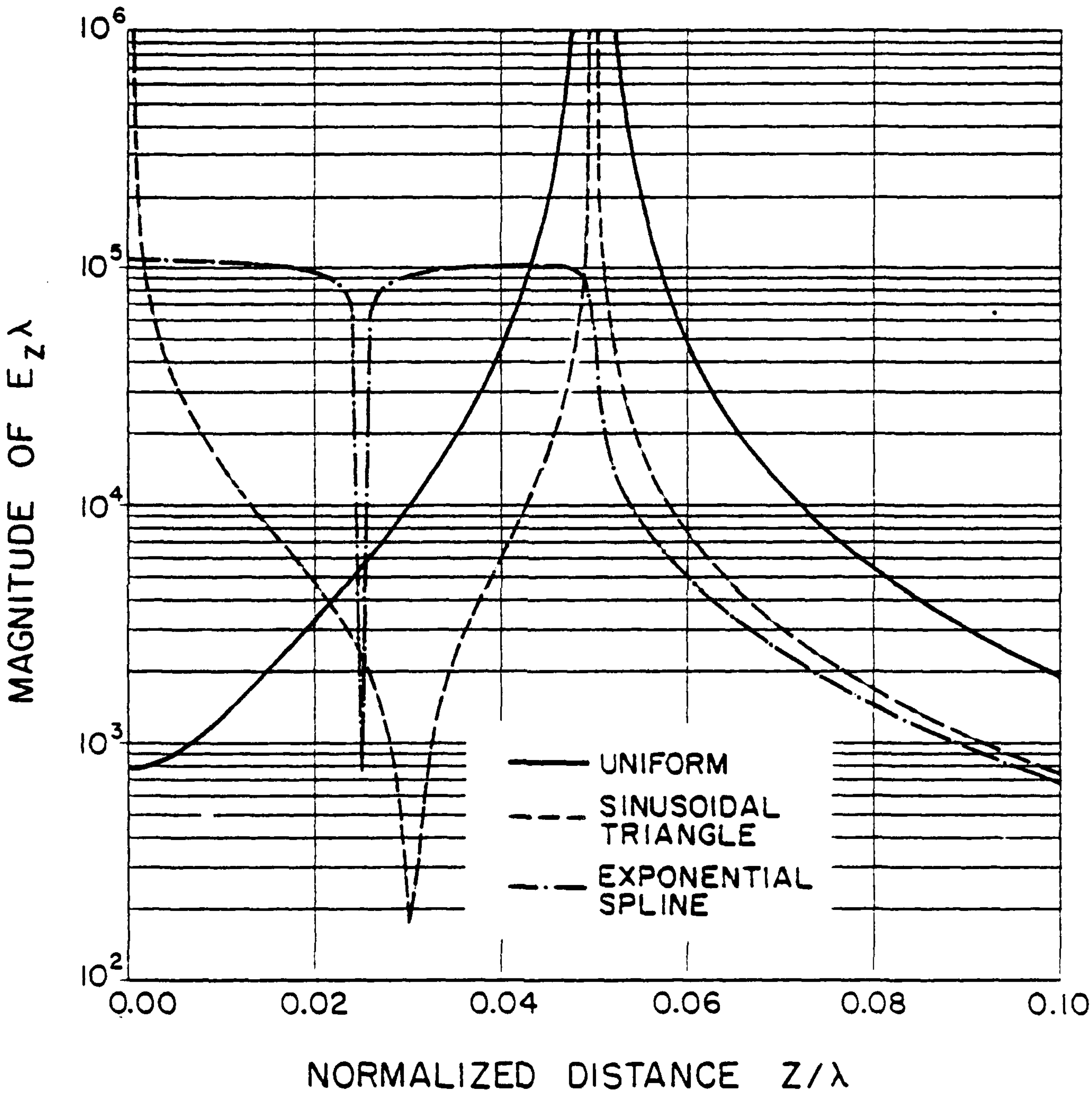

Figure 7. $E_z\lambda$ along the z-axis for a thin ribbon by expanding in powers of (R - r) with x/λ = 0.0, y/λ = 0.0, b/λ = 0.05, a/b = 0.001, and n = 0.5.

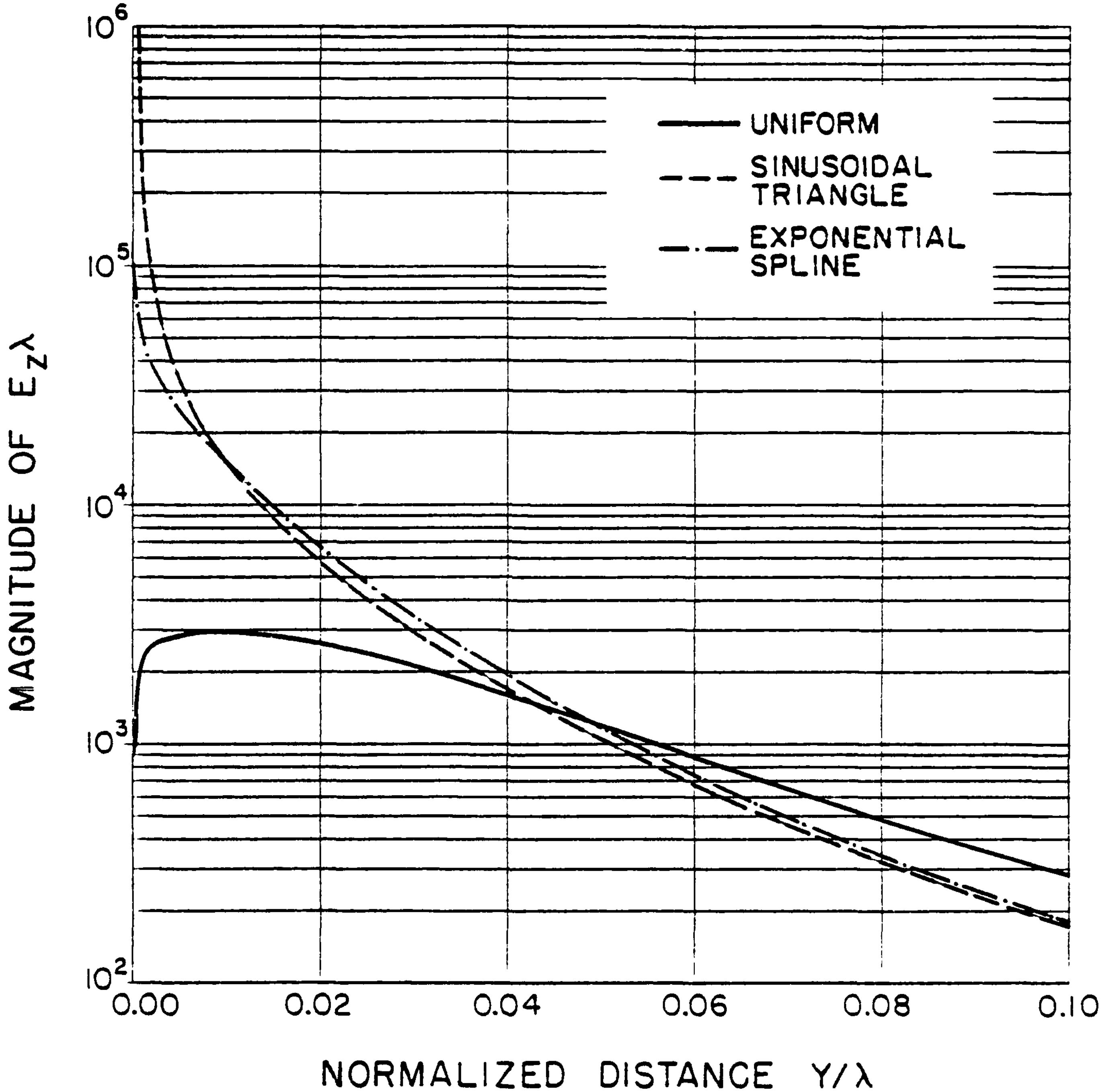

Figure 8. $E_z\lambda$ along the y-axis for a thin ribbon by expanding in powers of (R - r) with $x/\lambda = 0.0$, $z/\lambda = 0.0$, $b/\lambda = 0.0$, $a/b = 0.001$, and $n = 0.5$.

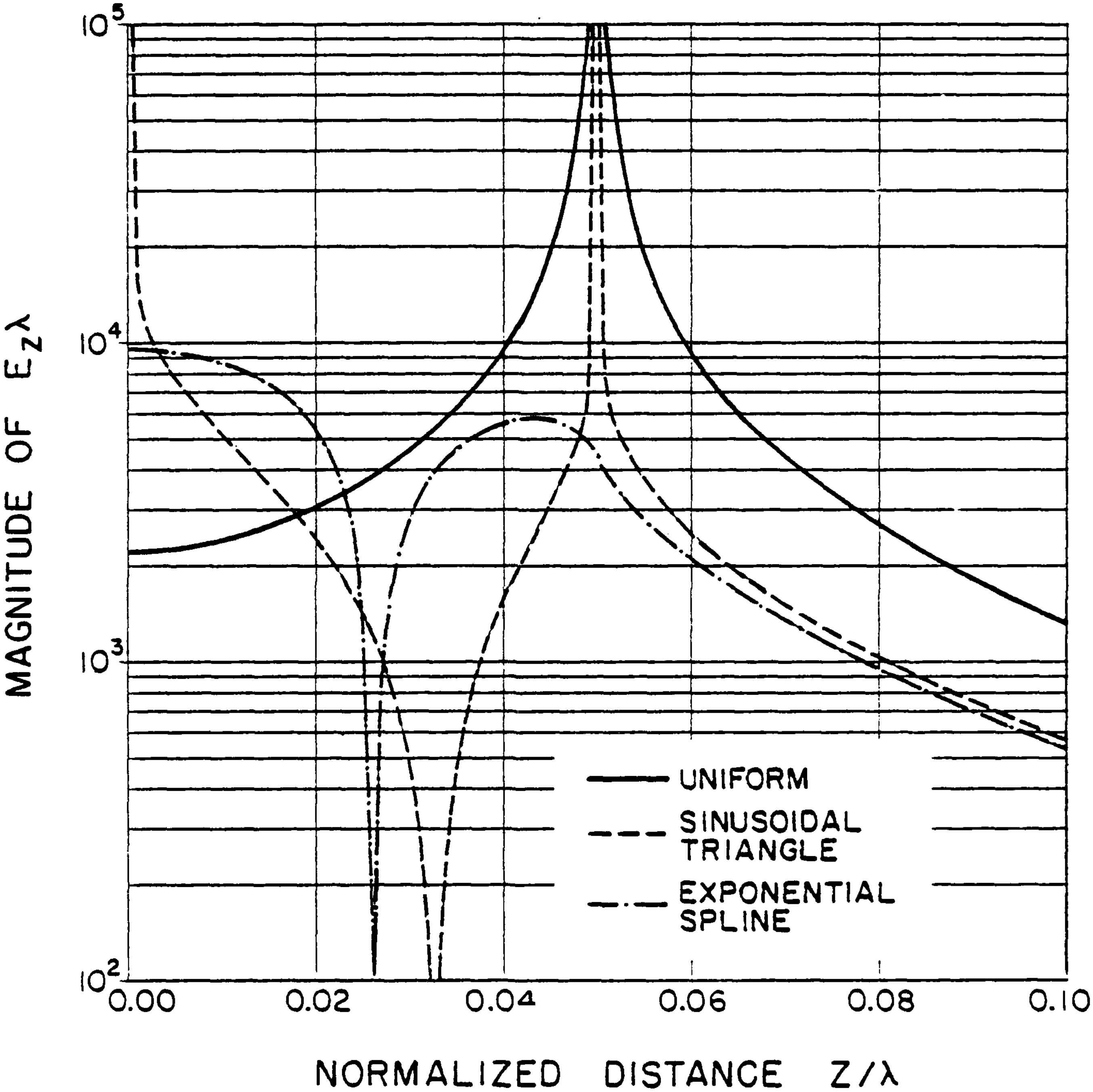

Figure 9. $E_z\lambda$ along the z-axis for a square patch by expanding in powers of (R - r) with $x/\lambda = 0.0$, $y/\lambda = 0.0$, $b/\lambda = 0.05$, $a/b = 1.0$, and $n = 0.5$.

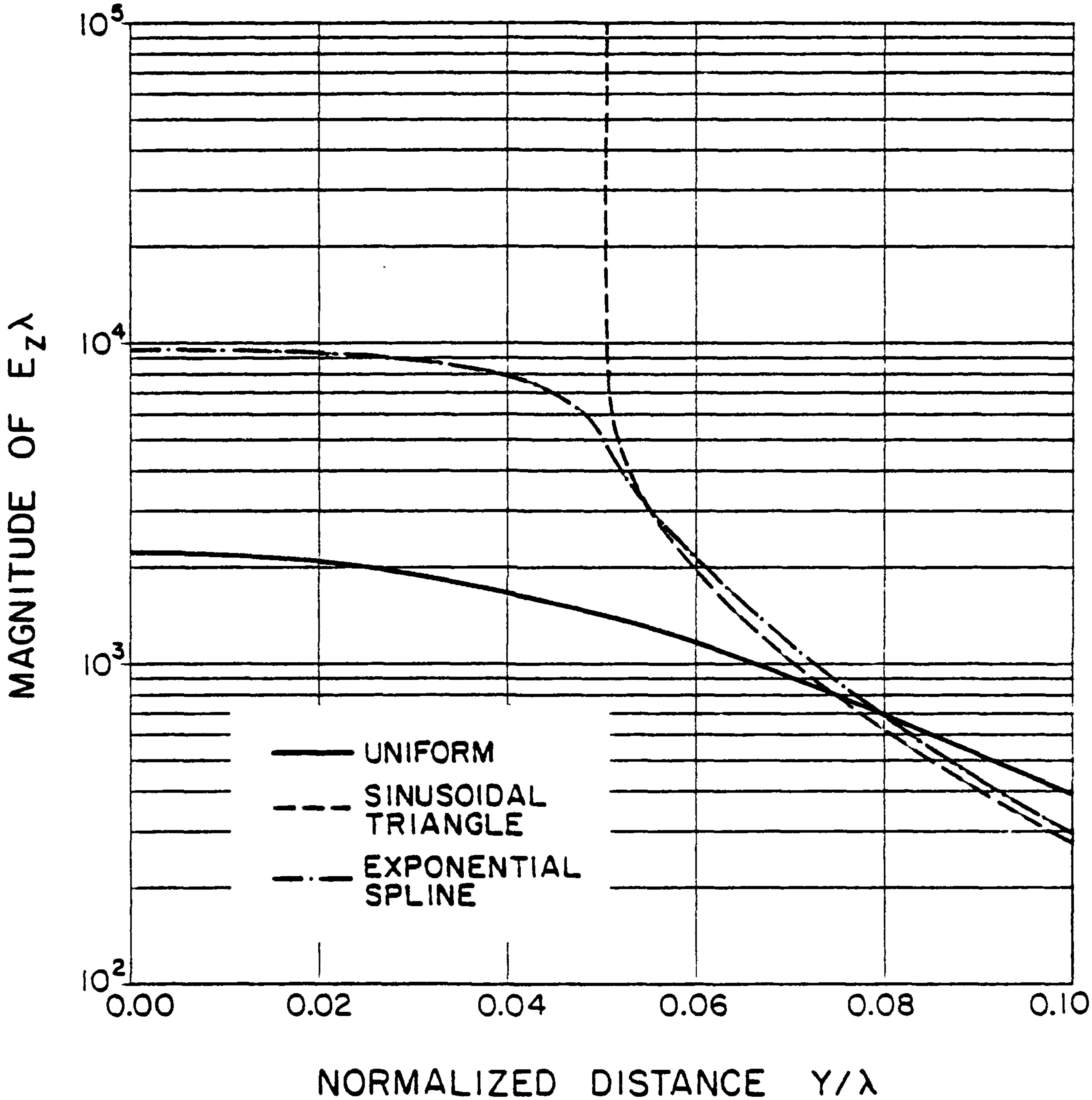

Figure 10. $E_z\lambda$ along the y-axis for a square patch by expanding in powers of $(R - r)$ with $x/\lambda = 0.0$, $z/\lambda = 0.0$, $b/\lambda = 0.05$, $a/b = 1.0$, and $n = 0.5$.

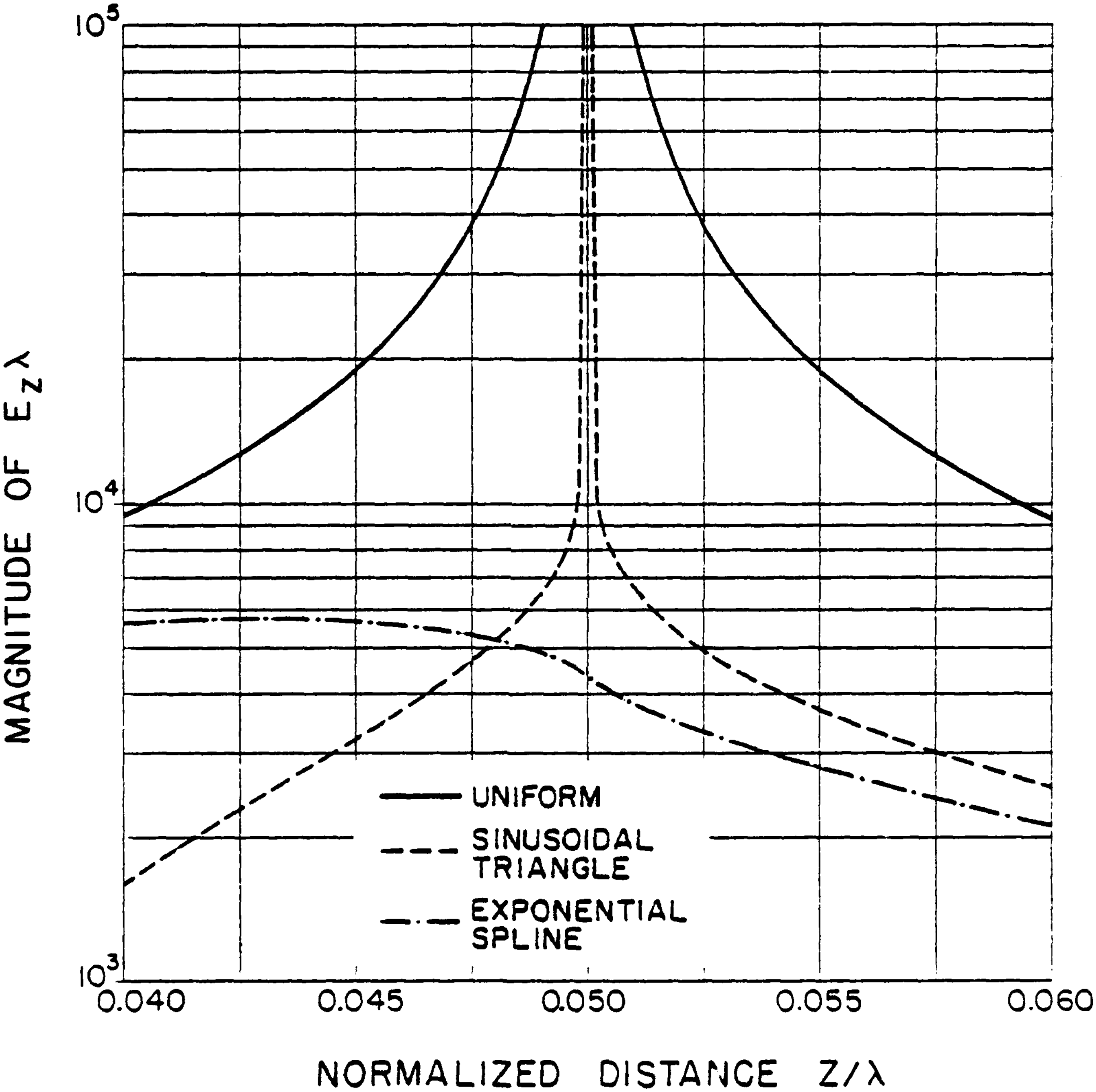

Figure 11. A magnified view of Figure 9 in the vicinity of the patch boundary.

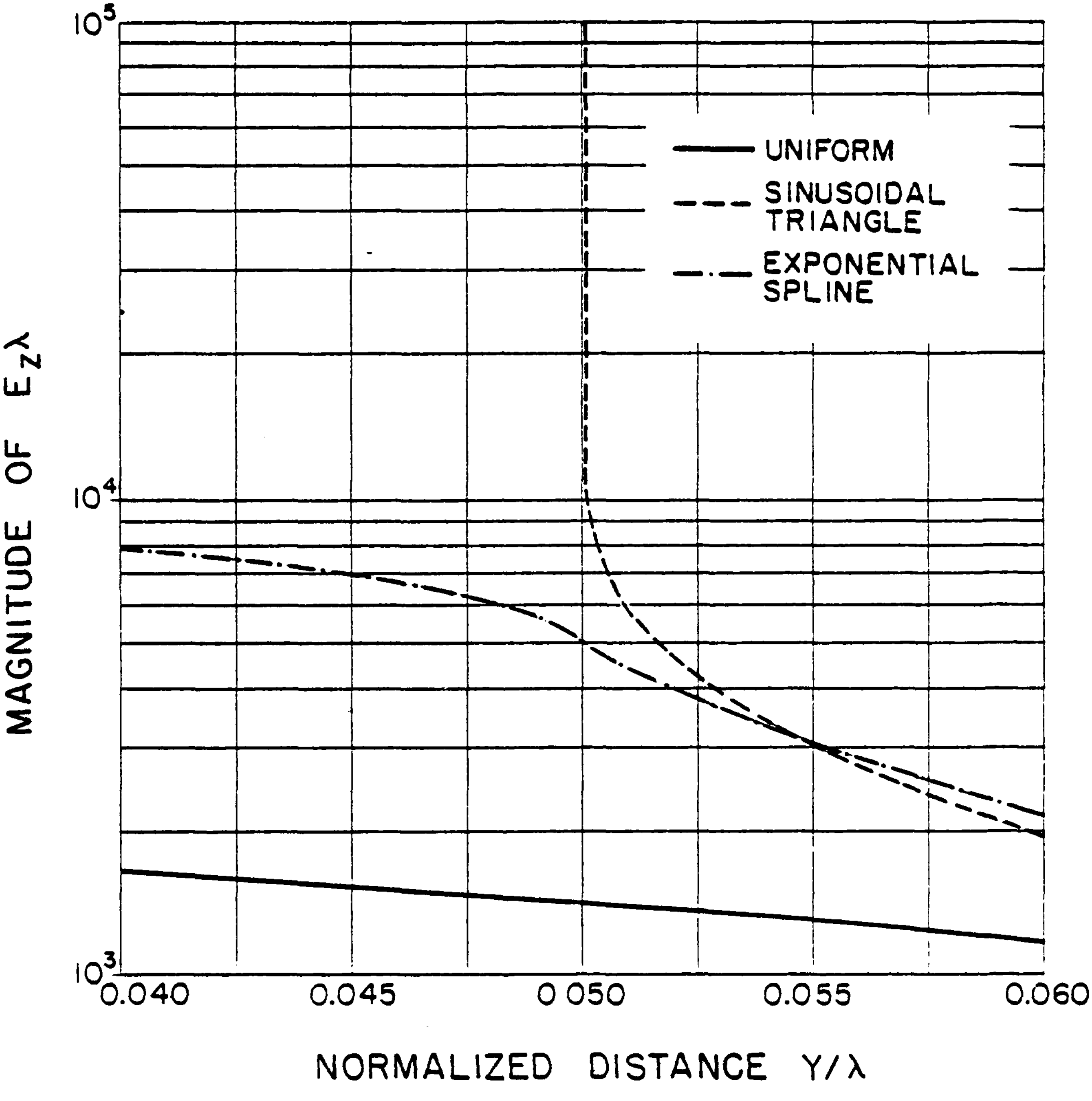

Figure 12. A magnified view of Figure 10 in the vicinity of the patch boundary.

The field from various current distributions on rectangular patches may be computed accurately and efficiently by the techniques given above. The choice of basis function for use in a moment method computation is still not fixed but certainly some function which would produce fields which are physically alike would seem appropriate.

REFERENCES

[1] A. Gopinath, "Modeling and characterization of microstrip parasitics," IEEE/MTT-S International Symposium, Orlando, Florida, May 3, 1979.

[2] R. F. Harrington, Field Computation by Moment Methods. New York: Macmillan, 1968.

[3] E. H. Newman and P. Tulyathan, "Analysis of Microstrip Antennas Using Moment Methods," IEEE Trans. Antennas Propagat., vol. AP-29, pp. 47-53, Jan. 1981.

[4] N. N. Wang, J. H. Richmond, and M. C. Gilreath, "Formulation for radiation and scattering from conducting surfaces," IEEE Trans. Antennas Propagat., vol. AP-23, pp. 376-381, May 1975.

[5] J. H. Richmond, D. M. Pozar, and E. H. Newman, "Rigorous near-zone field expressions for rectangular sinusoidal surface monopole," IEEE Trans. Antennas Propagat., vol. AP-26, pp. 509-510, May 1978.

[6] A. W. Glisson and D. R. Wilton, "Simple and efficient numerical methods for problems of electromagnetic radiation and scattering from surfaces," IEEE Trans. Antennas Propagat., vol. AP-28, pp. 593-603, Sept. 1980.

[7] Jitendra Singh and A. T. Adams, "A nonrectangular patch model for scattering from surfaces," IEEE Trans. Antennas Propagat., vol AP-27, pp. 531-534, July 1979.

[8] P. E. Mayes, "Electromagnetics without potentials: Near fields," to be published.

[9] P. E. Mayes, "A new integral equation technique for electromagnetic scattering," presented at Fall Meeting, URSI, Williamsburg, VA, 1972.

[10] D. F. Hanson and P. E. Mayes, "The current source-function technique of electromagnetic scattering from a half-plane," Radio Sci., vol. 13, pp. 49-58, 1978.

[11] J. Walsh and S. K. Srivastava, "Analysis of linear antenna systems: A different approach," Radio Sci., vol. 15, pp. 913-921, Sept.-Oct., 1980.

[12] I. S. Gradshteyn and I. M. Ryzhik, Table of Integrals, Series, and Products, 3rd Ed. New York: Academic Press, 1980.

[13] R. F. Harrington, "Matrix methods for field problems," Proc. IEEE, vol. 55, pp. 136-149, Feb. 1967.

[14] E. C. Jordan and K. G. Balmain, Electromagnetic Waves and Radiating Systems. New Jersey: Prentice-Hall, 1968.

SIMPLE FORMULAS FOR TRANSMISSION THROUGH PERIODIC METAL GRIDS OR PLATES*

S. W. Lee and G. Zarrillo

ABSTRACT

We give a simple, closed-form, approximate solution for the transmission coefficient of a normally incident electromagnetic plane wave through a screen made of periodic metal grids (inductive screen), or made of metal plates (the complementary capacitive screen). Explicit formulas are also presented for cascading screens and dielectric slabs. When compared with the exact solution, our approximate simple formulas show good numerical accuracy.

*This work was supported by NSF Grant ECS-80-07113.

+Lee and Zarrillo are with the Department of Electrical Engineering, University of Illinois, Urbana, IL 61801.

I. INTRODUCTION

This paper studies the transmission of electromagnetic waves through a thin screen made of periodic grids or plates shown in Figure 1. Such a screen finds application in diverse areas; it may be used as an antenna radome [1] - [5], as a microwave frequency selective surface [6] - [9], as a laser mirror [10] - [16], as a solar filter [17] - [20], and as an artificial dielectric [21] - [22]. Under the assumptions that the incident field is a plane wave and that the screen is of infinite size, the present transmission problem can be solved rigorously by the standard mode-matching technique [1] - [3], [19]. Unfortunately, the solution is contained in an infinitely large matrix equation, which must be truncated and inverted numerically with the aid of a computer. Hence, it is desirable to develop a simple closed-form solution to the transmission problem. Not only does the simple solution eliminate the need for a complex computer program, it also gives the explicit functional dependence of various design parameters, and allows one to isolate the "cause" and "effect."

Simple formulas for the transmission/reflection coefficient through the screen in Figure 1 have been reported in the literature. The earliest one was given by MacFarlane in 1946 [23]. Two of the most popular and useful formulas are given by Chen [3] and Ulrich [15]. Comparatively speaking, Chen's formula is more accurate while Ulrich's formula is simpler. In the present paper, we present a refined version which combines the merits of both Chen's and Ulrich's formulas. Furthermore, by using a scattering matrix approach, we extend the formula to cover the case of cascading several screens, which can be the screens shown in Figure 1, or dielectric slabs.

As expected, our simple formula has the following limitations: (i) The accuracy of the power transmission coefficient is within about 5% for most cases of practical interest. (ii) The formula is valid only when the incident direction of the plane wave is normal to the screen and the periodicity of the cells in the screen is less than one wavelength. (iii) When cascading, the separation between screens/dielectric slabs cannot be very small.

II. SINGLE SCREEN WITH ZERO THICKNESS

Let us consider the scattering problem sketched in Figure 1. The incident field from the lower half space is given by

$$\vec{E}^i(\vec{r}) = \hat{u}\, e^{-jkz} \quad , \quad \text{for } z < 0 \tag{1}$$

where the time factor $\exp(+j\omega t)$ has been suppressed, and $k = 2\pi/\lambda = \omega/c$ is the wavenumber. The unitary vector $\hat{u}$ satisfies the relation $\hat{u} \cdot \hat{u}^* = 1$ and $\hat{u} \cdot z = 0$. It specifies the polarization of the incident field, e.g., $\hat{u} = \hat{x}$ for a linearly polarized field, and $\hat{u} = (\hat{x} \pm j\hat{y})/\sqrt{2}$ for a circularly polarized field. The screen is made of metal periodic grids/plates, and it can be either of the following two types:

(i) Inductive screen (Figure 2a), which reflects at low frequencies and transmits at high frequencies (high-pass screen).

(ii) Capacitive screen (Figure 2b), which transmits at low frequencies and reflects at high frequencies (low pass screen).

Because of the periodic nature of the problem, we may represent the scattered field by a double Fourier series (Floquent space harmonics), namely,

$$\vec{E}(\vec{r}) = \begin{cases} \hat{u}\, Te^{-jkz} + \hat{u} \sum\limits_p \sum\limits_q T_{pq} Q_{pq}(x,y)\, e^{-j\gamma_{pq} z} \quad , & \text{for } z > 0 \\ \hat{u}\, Re^{+jkz} + \hat{u} \sum\limits_p \sum\limits_q R_{pq} Q_{pq}(x,y)\, e^{+j\gamma_{pq} z} \quad . & \text{for } z < 0 \end{cases} \tag{2}$$

The double summations in (2) are over the range

$$p,q = 0, \pm 1, \pm 2, \ldots, \text{ except } p = q = 0$$

They represent the so-called "grating lobes." The transverse variation of the (p,q)th grating lobe is

$$Q_{pq}(x,y) = \exp[-j \frac{2\pi}{a} (px + qy)] \quad ,$$

and its propagation constant is

$$\gamma_{pq} = [k^2 - (\frac{2\pi}{a})^2 (p^2 + q^2)]^{1/2} \quad .$$

Throughout this paper, we assume that the spacing a is small so that

$$(a/\lambda) < 1 \quad . \tag{3}$$

Hence, $\{\gamma_{pq}\}$ are all negative imaginary, and the fields of the grating lobes decay exponentially away from the screen. Thus, under condition (3), the quantities of practical interest are the transmission coefficient T and the (voltage) reflection coefficient R of the main beam. Their determinations are discussed below.

Circuit model. As long as the screen has zero thickness, ($\tau = 0$ in Figure 1) the scattering problem in Figure 1 can be exactly replaced by an equivalent transmission line problem sketched in Figure 3. The screen is described by a normalized shunt admittance 2Y. From the transmission line theory, it is a simple matter to show that

$$T = \frac{1}{1 + Y} \tag{4a}$$

$$R = \frac{-1}{1 + (1/Y)} = T - 1 \tag{4b}$$

which applies equally to the inductive (Figure 2a) and capacitive (Figure 2b) screens. From the Babinet principle [24], the coefficients of these two complementary screens are related as follows:

$$T_{cap} = -R_{ind} \quad , \quad R_{cap} = -T_{ind} \quad . \tag{5}$$

From here on, we concentrate on the inductive screen. Let us write the coefficients in polar form

$$T_{ind} = |T_{ind}|\, e^{j\theta_1} \quad , \quad R_{ind} = |R_{ind}|\, e^{j\theta_2} \quad . \tag{6a}$$

Because of the conservation of energy

$$|T|^2 + |R|^2 = 1 \tag{7}$$

and the fact $Y_{ind} = -j|Y_{ind}|$, it may be shown that

$$\cos\theta_1 = |T_{ind}| \quad , \quad 0 \le \theta_1 \le (\pi/2) \tag{6b}$$

$$\theta_2 = \theta_1 + (\pi/2) \quad , \quad (\pi/2) \le \theta_2 \le \pi \quad . \tag{6c}$$

As a check, for $c = 0$ in Figure 2a (a perfect conducting plane), we have from (8) that $\theta_1 = \pi/2$ and $\theta_2 = \pi$, as expected.

Approximate formulas for admittance. The scattering problem in Figure 1 can be formulated exactly in terms of an infinite set of linear equations [1] - [3]. After truncating the infinite set of equations at a large finite number (say 50), it may be numerically solved with the aid of a computer. We call such a solution the "exact solution." By matching the extensive data that we have generated from the exact solution, the following approximate formula for the admittance is obtained:

$$Y_{ind} = Y_{cap}^{-1} \simeq (-j)(\beta - \beta^{-1}) \frac{[(\frac{a}{c}) + \frac{1}{2}(\frac{a}{\lambda})^2]}{\ln \csc(\frac{\pi}{2}\frac{\delta}{a})} \quad , \quad \text{(LZLO)} \tag{8a}$$

where

$$\beta = (1 - 0.41 \frac{\delta}{a})/(a/\lambda) \quad , \quad \delta = (a - c)/2 \quad . \tag{8b}$$

Note that Y_{ind} depends only on two parameters: a/λ and c/a, and it is independent of the polarization parameter $\hat{u}$. The particular functional form in (8) is inspired by the work of Ulrich [15]. It is interesting to note that a total transmission ($Y_{ind} \to 0$ and $T_{ind} = 1$) occurs at

$$\frac{a}{\lambda} = 1 - 0.41(\frac{\delta}{a}) \quad . \tag{9}$$

For most practical screens, $(\delta/a) \leq 0.3$. Hence, total transmission occurs when a is slightly less than one wavelength.

<u>Other formulas in the literature</u>. Based on Marcuvitz's solution [26] for a one-dimensional periodic grid, Ulrich [15]* presents an approximate formula for Y_{ind}, namely,

$$Y_{ind} \simeq (-j)(\beta_1 - \beta_1^{-1}) \frac{1}{\ln \csc(\frac{\pi}{2} \frac{\delta}{a})} \quad , \quad \text{(Ulrich)} \tag{10a}$$

where

$$\beta_1 = (1 - 0.27 \frac{\delta}{a})/(a/\lambda) \quad . \tag{10b}$$

When compared with our formula in (8), we note the factor in the square bracket in (8a) is absent in (10a), and β in (8b) is slightly different from β_1 in (10b). Another approximate formula is given by Chen [3], namely,

*A factor 2 in the denominator is missed in Eq. (13) of [15].

$$Y_{ind} \simeq (-j)2\left\{\sqrt{(\frac{\lambda}{a})^2 - 1}\left[\frac{\cos(\frac{\pi c}{a})}{1-(\frac{2c}{a})^2}\right]^2 - \frac{1}{\sqrt{(\frac{\lambda}{a})^2 - 1}}\left[\frac{\sin(\frac{\pi c}{a})}{(\frac{\pi c}{a})}\right]^2\right.$$

$$\left. + \left[\sqrt{2(\frac{\lambda}{a})^2 - 1} - \frac{1}{\sqrt{2(\frac{\lambda}{a})^2 - 1}}\right]\left[\frac{\cos(\frac{\pi c}{a})}{1-(\frac{2c}{a})^2}\right]^2\left[\frac{\sin(\frac{\pi c}{a})}{(\frac{\pi c}{a})}\right]^2\right\} . \quad \text{(Chen)} \qquad (11)$$

In references [7], [8], Arnaud, Pelow, and Anderson give a formula similar to Ulrich's, namely,*

$$Y_{ind} \simeq (-j)\frac{1}{2(\frac{a}{\lambda})\ \ell n[\csc(\pi\frac{\delta}{a})]} \quad , \quad \text{(APA)} \quad . \qquad (12)$$

The argument of the cosecant function in (12) differs from that in (10a) by a factor of 2.

Numerical results. Results for the transmission coefficient T as a function of a/λ for an inductive screen with zero thickness is presented in Figures 4 to 7. The "exact" solution is the numerical solution based on the analysis of [1] - [3]. Four approximate solutions are calculated from (4a) with Y given in (8a), (10a), (11), or (12). We note that for $(c/a) \geq 0.7$, both LZLO's and Chen's solutions have good accuracy. For $(c/a) < 0.7$ (small aperture size), all simple formulas are no longer reliable.

*Equations (1) and (2) of [7] contain misprints. Our Eq. (12) above is obtained from Eqs. (2) and (12) of [8].

III. SINGLE INDUCTIVE SCREEN WITH FINITE THICKNESS

All of the formulas in Section II apply to an inductive or capacitive screen with zero thickness ($\tau = 0$ in Figure 1). When the thickness is not zero, the aperture section of an inductive screen may be considered as a square waveguide. The dominant mode in the waveguide is the TE_{10} mode whose propagation constant is

$$\Gamma = \begin{cases} +\sqrt{k^2 - (\pi/c)^2} , & \text{if } c > 0.5\lambda \\ -j\sqrt{(\pi/c)^2 - k^2} , & \text{if } c < 0.5\lambda \end{cases} \quad . \tag{13}$$

Based on one-mode approximation for the aperture field, Chen [3] found an approximate formula for the transmission coefficient of a thick inductive screen*, namely,

$$T_{thick} \simeq e^{jk\tau} \left[\frac{1}{1 + Y_{ind} - Z \tan(\Gamma\tau/2)} - \frac{1}{1 + Y_{ind} - Z \cot(\Gamma\tau/2)} \right] \tag{14a}$$

where

$$Z = j\left(\frac{\pi^2}{8}\right)\left(\frac{a}{c}\right)^2 (\Gamma/k) \quad . \tag{14b}$$

For numerical calculations, Y_{ind} given in (8) and (11) are used in (14). The results are presented in Figures 8 to 10. We note that (14) is fairly accurate. Two remarks about the thickness effect can be made:

*The exponential factor in (14) is missed in Eq. (7) of [3].

(i) When the TE_{10} mode in the square waveguide section of the screen is below cutoff ($c < 0.5\lambda$), (14a) is approximately equivalent to

$$T_{thick} \simeq T_{thin}\, e^{j(k-\Gamma)\tau} \tag{15}$$

or

$$|T_{thick}/T_{thin}|^2 \simeq -54.6 \frac{\tau}{\lambda} \sqrt{\left(\frac{\lambda}{2c}\right)^2 - 1} \;\; \mathrm{dB} \quad . \tag{16}$$

The numerical data in Table I demonstrate the accuracy of (16). It is observed from (15) and (16) that, when $c < 0.5\lambda$, the thickness effect introduces the TE_{10} mode attentuation in the transmission coefficient.

(ii) When $c > 0.5\lambda$, the total transmission ($T = 1$) of a thick screen occurs at a lower frequency than that of a thin screen. As an example, for $c/a = 0.7$, the total transmission of a thin screen occurs at $a/\lambda = 0.94$, which may be calculated from (9) or observed from the numerical curve in Figure 10. For the same screen with a finite thickness $\tau = 0.2a$, the total transmission occurs at $a/\lambda = 0.85$.

As a final remark, the formulas in (14) - (16) are applicable to an inductive screen, but not to a capacitive screen. In fact, when the screen is thick, relations in (4b), (5), and (6) are no longer valid.

TABLE I.

Ratio of $|T_{thick}/T_{thin}|^2$

a/λ	c/λ	τ/λ	Exact	From (14)	From (16)
0.3	0.21	0.06	-7.5 dB	-7.5 dB	-7.1 dB
0.3	0.24	0.06	-6.0	-6.0	-6.0
0.7	0.49	0.14	-1.28	-1.25	-1.6

IV. CASCADING SCREENS AND DIELECTRIC SLABS

In practical applications, we often cascade metal screens and dielectric slabs in order to obtain the desired transmission characteristics and/or mechanical strength. In this section, we provide a formula for calculating the transmission through such a cascade structure.

As sketched in Figure 11, let us assume that there are N (possibly different) sheets in cascading. For a typical nth sheet, its reference plane is located at $z = d_1 + d_2 + \ldots + d_{n-1}$. With respect to this reference plane, the sheet is symmetrical and its (transmission, reflection) coefficients are denoted by (T_n, R_n). If the sheet is a metal screen (inductive or capacitive), we may calculate its coefficient by the simple formulas in Sections II and III. If the sheet is a dielectric slab (Figure 12), its coefficients are given by the well-known expressions,

$$T_n = \frac{(1 - r^2)}{1 - r^2 \exp(-j2k'\tau)} e^{j(k-k')\tau} \tag{17a}$$

$$R_n = \frac{r[1 - \exp(-j2k'\tau)]}{1 - r^2 \exp(-j2k'\tau)} e^{jk\tau} \tag{17b}$$

where $k' = k\sqrt{\varepsilon}$, ε = relative dielectric constant of the slab, and

$$r = \frac{1 - \sqrt{\varepsilon}}{1 + \sqrt{\varepsilon}} \quad . \tag{18}$$

When the slab is lossy, ε has a negative imaginary part. The square root $\sqrt{\varepsilon}$ should also have a negative imaginary part.

The interaction among the N sheets can be accounted for by using the scattering matrices [26]. To be exact, the matrices are of infinite order. In the present paper, we use the so-called "one-mode interaction."

It means that only the main beam, not the grating lobes (the fields represented by the double summation in (2)), is used in calculating the interaction. This approximation is valid when the intersheet distances ($d_1, d_2, \ldots, d_{N-1}$) are small in terms of wavelength. As shown later by numerical example, good accuracy of the one-mode interaction is maintained for a surprisingly small d_n.

Using the one-mode interaction, our final results of (R,T) for the cascading structure in Figure 11 are

$$T = A - (BC/D) \tag{19a}$$

$$R = -(C/D) \quad . \tag{19b}$$

The coefficients (A,B,C,D) are calculated in the following steps. First, for each sheet, we determine a 2 × 2 scattering matrix $\bar{\bar{S}}_n$, where

$$\bar{\bar{S}}_n = \begin{bmatrix} T_n\left(1 - \dfrac{R_n^2}{T_n^2}\right) & \dfrac{R_n}{T_n} e^{j2k\ell_n} \\ -\dfrac{R_n}{T_n} e^{-j2k\ell_n} & \dfrac{1}{T_n} \end{bmatrix} \tag{20a}$$

$$\ell_n = d_1 + d_2 + \ldots + d_{n-1} \quad , \quad n = 2,3, \ldots, N \quad . \tag{20b}$$

Then

$$\begin{bmatrix} A & B \\ C & D \end{bmatrix} = \bar{\bar{S}}_N \bar{\bar{S}}_{N-1} \ldots \bar{\bar{S}}_3 \bar{\bar{S}}_2 \bar{\bar{S}}_1 \quad . \tag{21}$$

For the special case N = 2, (19) is simplified to become

$$T = \frac{T_1T_2}{1 - R_1R_2 \exp(-j2kd_1)} \tag{22a}$$

$$R = R_1 + \frac{T_1^2R_2}{1 - R_1R_2 \exp(-j2kd_1)} e^{-j2kd_1} \quad . \tag{22b}$$

We emphasize that in applying the formulas in (19) through (22), R_n is the reflection coefficient of the screen n in reference to the plane $z = d_n$ (Figure 11), namely, the ratio of the reflected and incident electric fields at $z = d_n$. One should not use reflection coefficients which refer to other planes. Another remark concerning the present cascading formula is in order. Within the approximation of the one-mode interaction, the final result in (19) is independent of the relative horizontal position of the screens. In other words, as long as the spacings d_1, d_2, ..., are maintained in Figure 11, (19) remains valid when screens are slid or rotated in their respective horizontal planes. In practical applications, sliding or rotating may be used for the suppression of higher-order space harmonics and/or the cross polarization.

Double Screen. Figures 13 to 15 show the transmission coefficients of a double inductive screen with interscreen spacing d = a, 0.5a, and 0.2a. We note that the present "one-mode" formula in (22) is accurate only when $d > 0.5a$. It is interesting to note that in both Figures 13 and 14, the transmission curves have a second peak at a frequency lower than the usual peak at $a \simeq \lambda$ as predicted by (9). This peak at the lower frequency can be predicted by the relation

$$\text{Arg.}[R_1R_2 \exp(-j2kd_1)] = 2n\pi \quad , \quad n = 0, \pm 1, \ldots \quad . \tag{23}$$

Under the condition in (23), the transmission coefficient in (22a) becomes

$$T = \frac{T_1 T_2}{1 - |R_1 R_2|} \tag{24}$$

which usually is a local maximum. For the example in Figure 13, this peak occurs at $a = d_1 = 0.423\lambda$ where $R_1 = R_2 = 0.879 \exp(j151.5°)$, and (23) is indeed satisfied.

Thin Double Screen Approximated by Thick Single Screen. When the spacing d_1 of a double screen is small, the present "one-mode" formula in (22) is no longer accurate, as seen from Figure 15. However, such a double screen can be well-approximated by a single screen with its thickness τ equal to d_1. This approximation holds well for $a < \lambda$ (Figure 15). In conclusion, in cascading two identical screens, (22) applies when spacing d_1 is large, and the thick screen approximation applies when d_1 is small.

Single Screen on Dielectric Slab. The "one-mode" formula in (22) remains reasonably accurate for spacing $d_1 = 0.1a$ (Figure 16). However, it fails to predict the rapid oscillation near $a \simeq \lambda$ when d_1 is reduced to zero (Figure 17).

Cascading complementary screens: The two screens (both of zero thickness) in Figure 2 are complementary, i.e., when one properly lies on top of the other, they form an infinite screen with no perforation. Their transmission and reflection coefficients are related in the manner described in (4). Now, let us consider the two cascading complementary screens. The transmission coefficient of the composite screen is obtainable from (22a) and (5), namely,

$$T = \frac{-T_{ind}R_{ind}}{1 + T_{ind}R_{ind}\exp(-j2kd_1)} \quad . \tag{25}$$

For given dimensions a and c, there exists a "resonance" wavelength λ_o

$$|Y_{ind}| = 1 \quad , \quad \text{when } \lambda = \lambda_o \quad . \tag{26a}$$

Substitution of (26a) into (4a) gives

$$T_{ind} = 0.707e^{j45^o} \quad , \quad R_{ind} = 0.707e^{j135^o} \quad . \tag{26b}$$

Let us choose the spacing between the screens such that

$$d_1 = \frac{1}{2}n\lambda_o \quad , \quad n = 1,2,3,\ldots \quad . \tag{27}$$

Under the conditions in (26) and (27), we calculate T from (25) with the result

$$T = 1 \quad , \quad \text{when } \lambda = \lambda_o \quad . \tag{28}$$

Thus, the composite screen has a sharp transmission peak at $\lambda = \lambda_o$. Based on the exact numerical solution, we have determined the resonance wavelength λ_o as a function of a and c, and the result may be presented in a simple formula, i.e.,

$$\frac{a}{\lambda_o} \simeq 1.502 - 1.266\frac{c}{a} \quad . \tag{29}$$

For example, when c/a = 0.7, (29) predicts that the resonance defined in (26) occurs at a = 0.616 λ_o, which agrees extremely well with the exact solution in Figure 18. Making use of (29) in (27), we obtain the interscreen spacing necessary for resonance:

$$\frac{d_1}{a} = \frac{n}{3.004 - 2.532(c/a)} \quad , \quad n = 1,2,3,\ldots \quad . \tag{30}$$

In summary, when (29) is satisfied, a single inductive or a single capacitive screen has a transmission coefficient $|T| = 0.707$ (3 dB transmission loss). When we cascade two complementary screens whose geometry satisfies (29) and (30), the transmission coefficient is $T = 1$ (total transmission). In Figure 18, we plot T of a composite screen with $c/a = 0.7$, and d_1 given by (30) with $n = 1$, 2, and 3. As predicted by (29), total transmission occurs at $a/\lambda = 0.616$. For $n = 1$ (smallest spacing d_1), the resonance curve is relatively broad. For $n = 3$, the curve is sharper, and has three other peaks with $|T|$ equal to -8.5, -1.8, and -3.8 dB.

REFERENCES

[1] C. C. Chen, "Transmission through a conducting screen perforated periodically with apertures," IEEE Trans. Microwave Theory Tech., vol. MTT-18, pp. 627-632, 1970.

[2] S. W. Lee, "Scattering by dielectric-loaded screen," IEEE Trans. Antenna Propagat., vol. AP-19, pp. 656-665, 1971.

[3] C. C. Chen, "Transmission of microwave through perforated flat plates of finite thickness," IEEE Trans. Microwave Theory Tech., vol. MTT-21, pp. 1-6, 1973.

[4] B. A. Munk, R. J. Luebbers, and R. D. Fulton, "Transmission through a two-layer array of loaded slots," IEEE Trans. Antennas Propagat., vol. AP-22, pp. 804-809, 1974.

[5] C. H. Tsao and R. Mittra, "A spectral-iteration approach for analyzing scattering from frequency selective surfaces," IEEE Trans. Antennas Propagat., to be published in 1981.

[6] G. H. Schennum, "Frequency-selective surfaces for multiple frequency antenna," Microwave J., vol. 16, pp. 55-57, 1973.

[7] J. A. Arnad and F. A. Pelow, "Resonant-grid quasi-optical diplexers," Bell Syst. Tech. J., vol. 54, pp. 263-283, Feb. 1975.

[8] I. Anderson, "On the theory of self-resonant grids," Bell Syst. Tech. J., vol. 54, pp. 1725-1731, Dec. 1975.

[9] V. D. Agrawal, and W. A. Imbriale, "Design of dichroic Cassegrain Subreflector," IEEE Trans. Antenna Propagat., vol. 27, pp. 466-473, 1979.

[10] R. Ulrich, T. J. Bridges, and M. A. Pollack, "Variable metal mesh coupler for far infrared lasers," Appl. Opt., vol. 11, pp. 2511-2516, 1970.

[11] E. J. Danielewicz, T. K. Plant, and T. A. DeTemple, "Hybrid output coupler for optically pumped far infrared lasers," Opt. Commun., vol. 13, pp. 366-369, 1975.

[12] R. A. Wood, N. Brignall, C. R. Pidgeon, and F. Al-Berkdar, "An optically pumped waveguide laser with mesh reflectors," Opt. Commun., vol. 14, pp. 301-303, 1975.

[13] D. T. Hodges, F. B. Foote, and R. D. Reel, "Efficient high-power operation of the CW far-infrared waveguide laser," Appl. Phys. Lett., vol. 29, pp. 662-664, 1976.

[14] E. J. Danielewicz and P. D. Coleman, "Hybrid metal mesh dielectric mirrors for optically pumped far infrared lasers," Appl. Opt., vol. 15, pp. 761-767, 1976.

[15] R. Ulrich, "Far infrared properties of metallic mesh and its complementary structure," Infrared Phys., vol. 7, pp. 37-55, 1976.

[16] M. R. Schubert, M. S. Durschlag, and T. A. DeTemple, "Diffraction limited CW optically pumped lasers," IEEE J. Quantum Electronics, vol. QE-13, pp. 455-459, 1977.

[17] C. M. Horwitz, "A new solar selective surface," Opt. Commun., vol. 11, pp. 210-212, 1974.

[18] J. C. C. Fan, F. J. Bachner, and R. A. Murphy, "Thin-film conducting grids as transparent heat mirrors," Appl. Phys. Lett., vol. 28, pp. 440-442, 1976.

[19] R. C. McPhedran and D. Maystre "On the theory and solar application of inductive grids," Applied Physics, vol. 14, pp. 1-20, 1977.

[20] "Study Plan for a SPS concept definition study," Tech. Rept. SSD-79-0092, Rockwell International, April 1979.

[21] S. B. Cohn, "Dielectric properties of a lattice of anisotropic particles," J. Appl. Phys., vol. 27, pp. 1106-1107, 1956.

[22] W. F. Richards and Y. T. Lo, "Anisotropy, birefringence, and dispersion in artificial dielectrics," Electromagnetics Lab. Tech. Rept. 77-17, University of Illinois, Urbana-Champaign, IL, 1977.

[23] G. G. MacFarlane, "Quasi-stationary field theory and its application to diaphragms and junctions in transmission lines and wave guides," J. IEE, pt. 3A, 93, pp. 703-719, 1946.

[24] M. Born and E. Wolf, Principles of Optics, 2nd ed., New York: Pergamon Press, 1964.

[25] N. Marcuvitz, Waveguide Handbook, M.I.T. Rad. Lab. Ser., No. 10, New York: McGraw-Hill, 1951.

[26] R. Mittra and S. W. Lee, Analytical Techniques in the Theory of Guided Waves. New York: Macmillan, 1971.

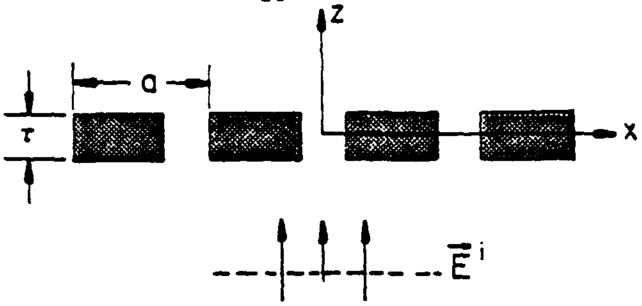

Figure 1. A metal screen illuminated by a normally incident plane wave.

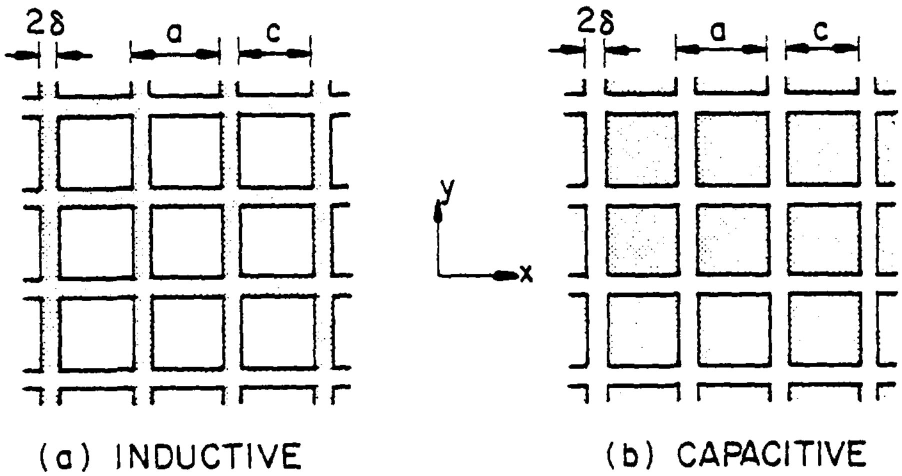

Figure 2. Two types of metal screens (top view).

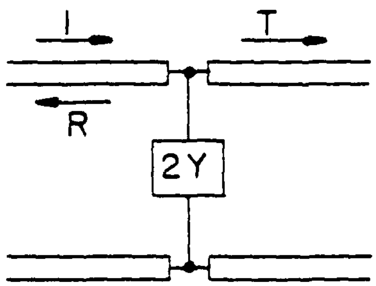

Figure 3. Transmission line model for the scattering problem in Figure 1 when $\tau = 0$.

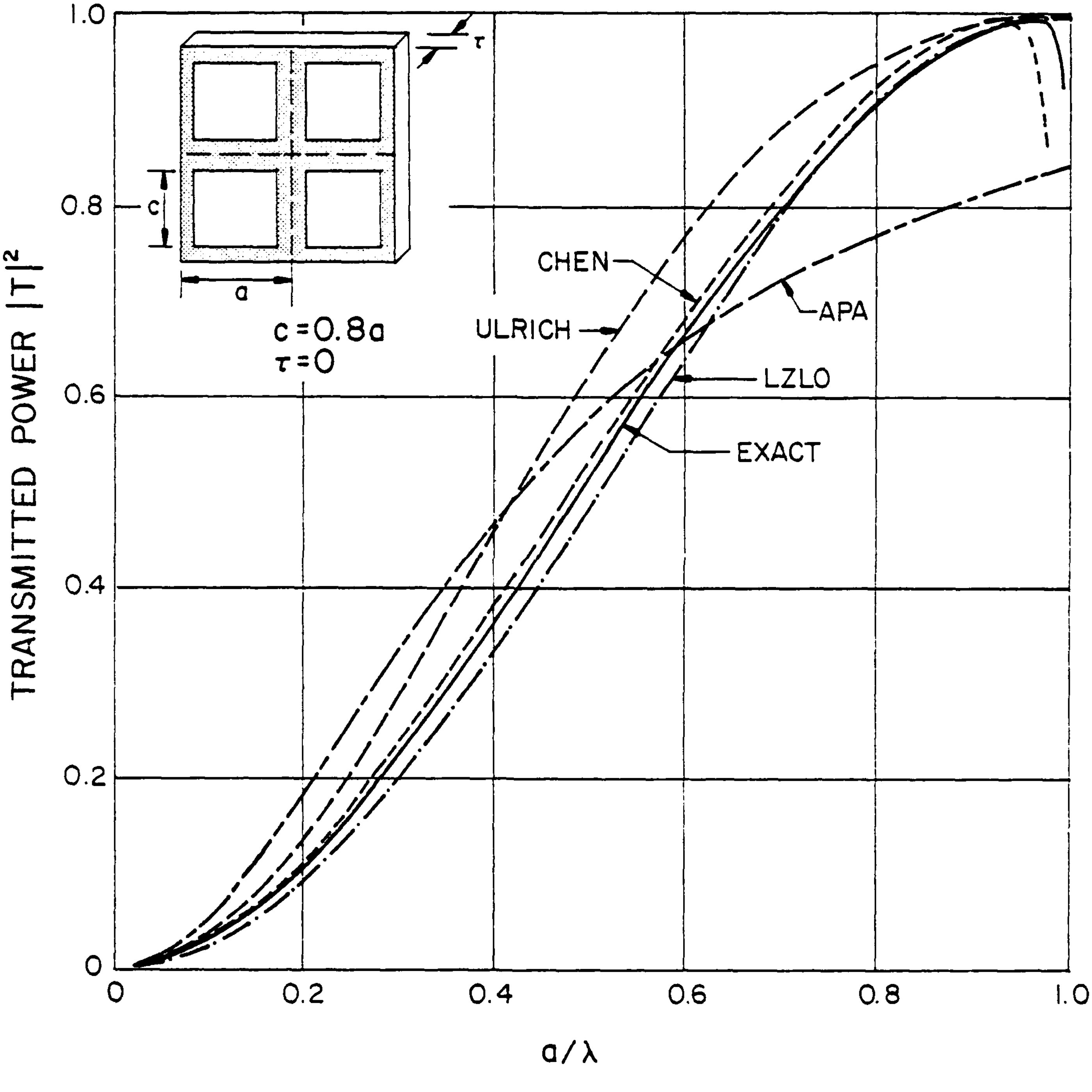

Figure 4. Power transmission coefficient $|T|^2$ of an inductive screen illuminated by a normally incident plane wave. The screen aperture dimension is c = 0.8a and its thickness τ is zero.

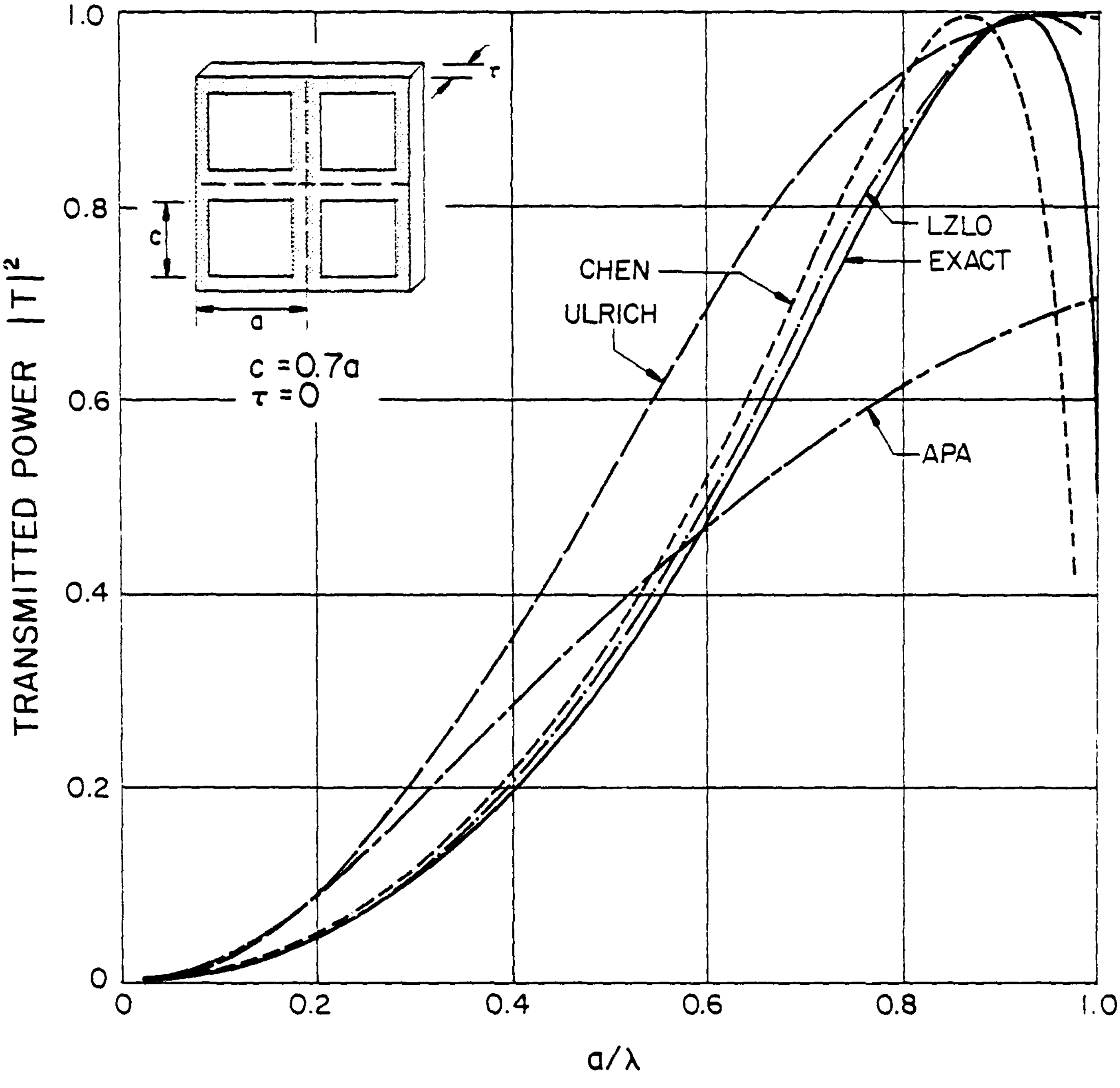

Figure 5. Power transmission coefficient $|T|^2$ of an inductive screen illuminated by a normally incident plane wave. The screen aperture dimension is c = 0.7a and its thickness τ is zero.

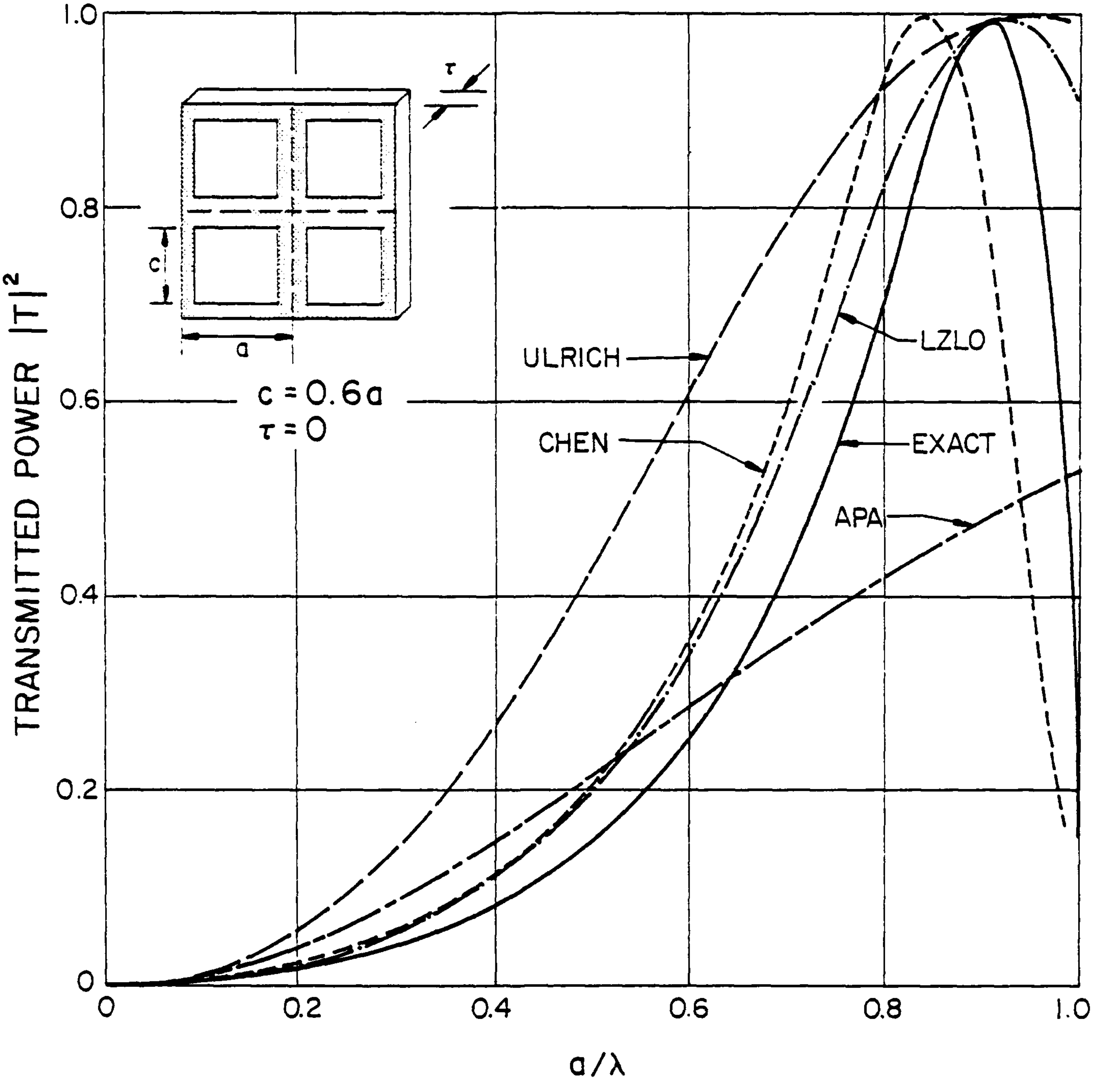

Figure 6. Power transmission coefficient $|T|^2$ of an inductive screen illuminated by a normally incident plane wave. The screen aperture dimension is $c = 0.6a$ and its thickness τ is zero.

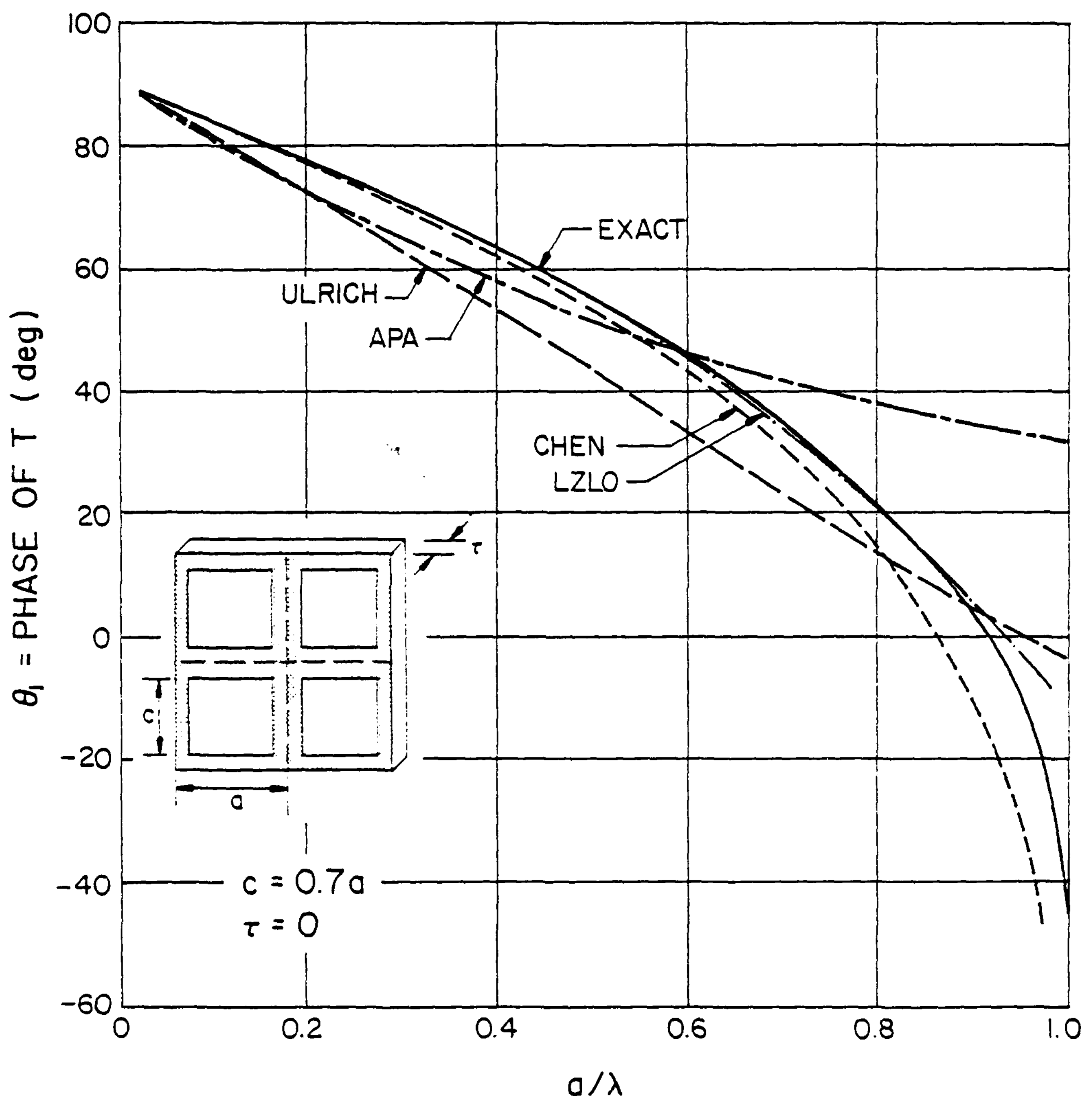

Figure 7. Phase of transmission coefficient T of an inductive screen illuminated by a normally incident plane wave. The screen aperture dimension is $c = 0.7a$ and its thickness τ is zero.

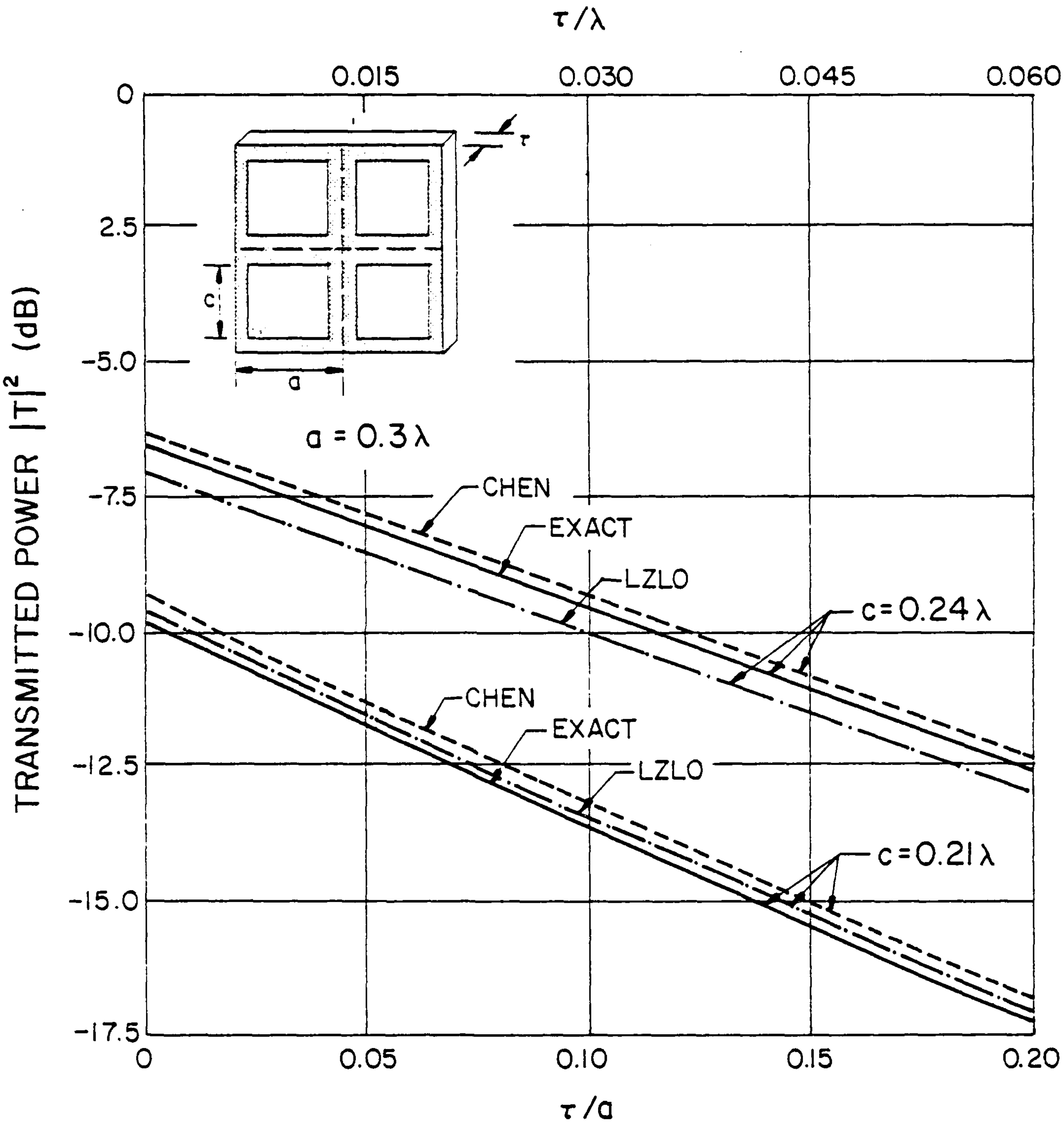

Figure 3. Power transmission coefficient $|T|^2$ of an inductive screen as a function of screen thickness τ.

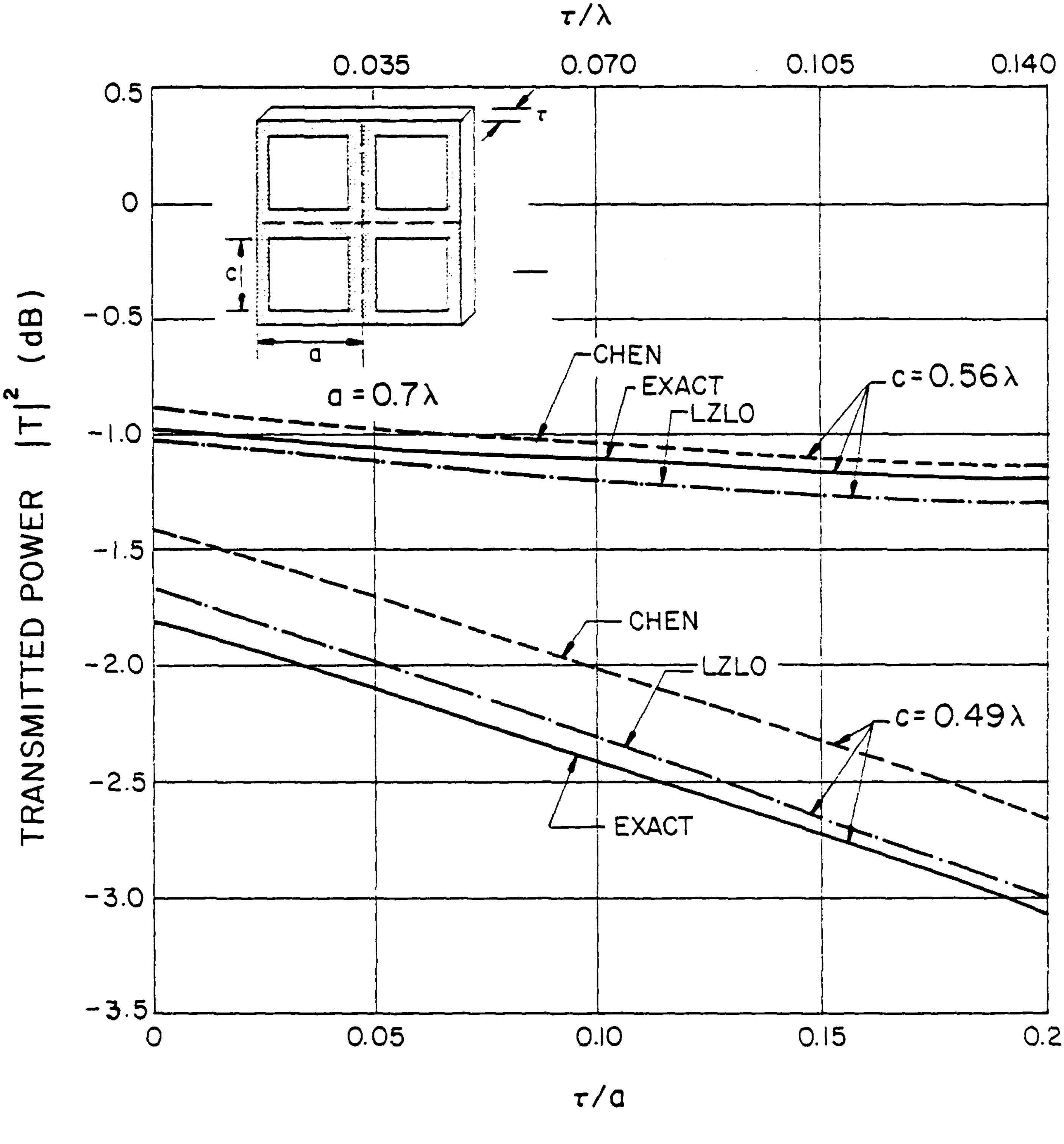

Figure 9. Power transmission coefficient $|T|^2$ of an inductive screen as a function of screen thickness τ and $a = 0.7\lambda$.

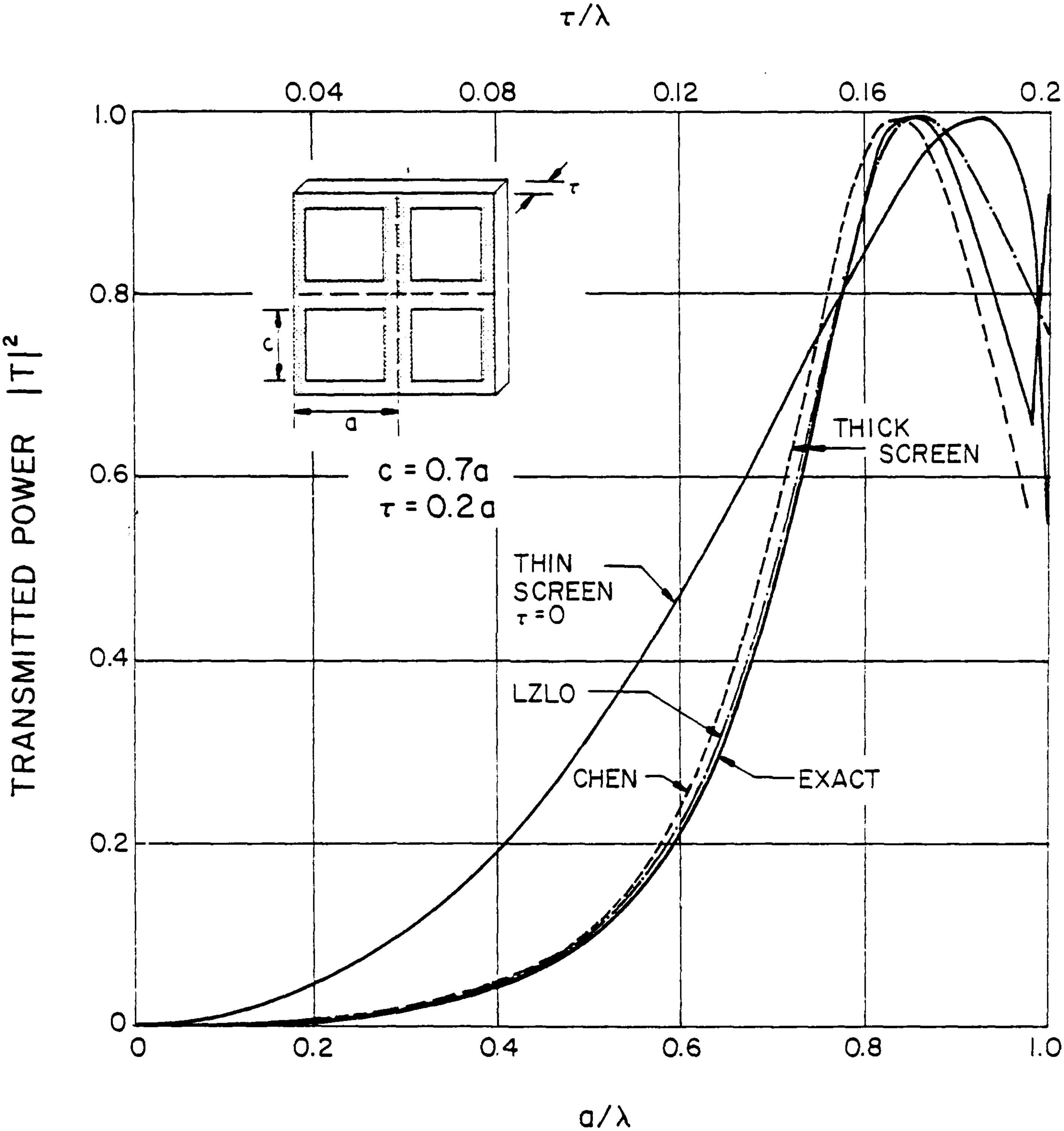

Figure 10. Power transmission coefficient $|T|^2$ of an inductive screen as a function of a/λ.

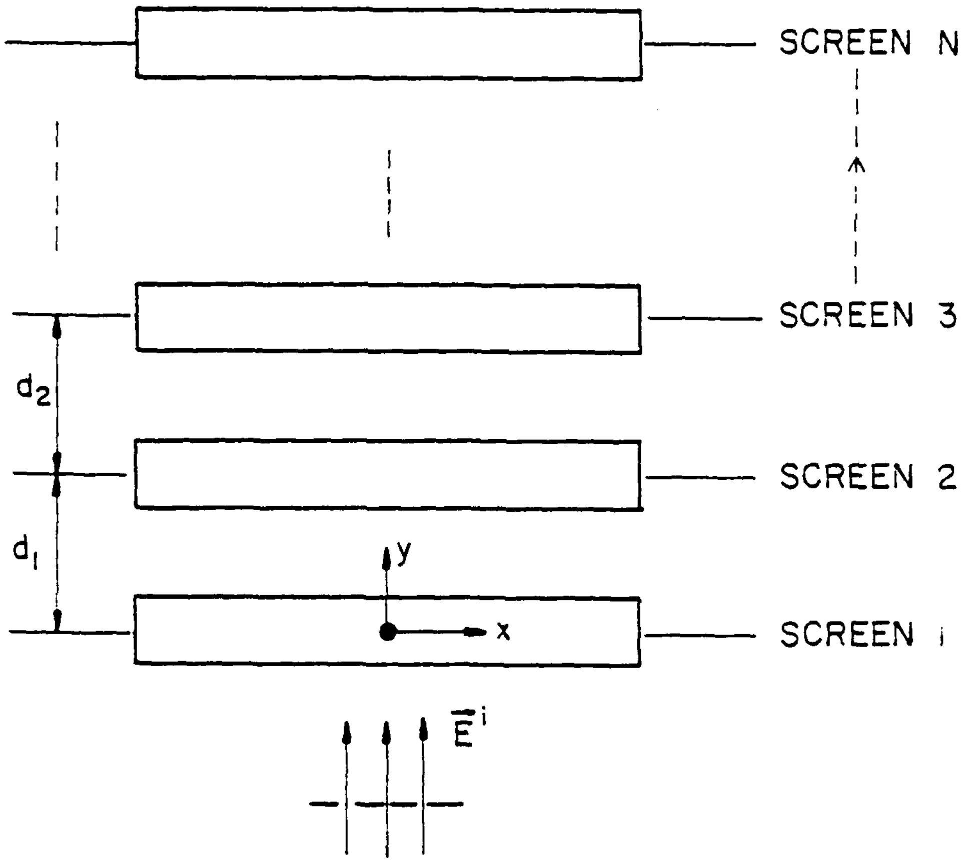

Figure 11. Cascading of N sheets of metal screens/dielectric slabs.

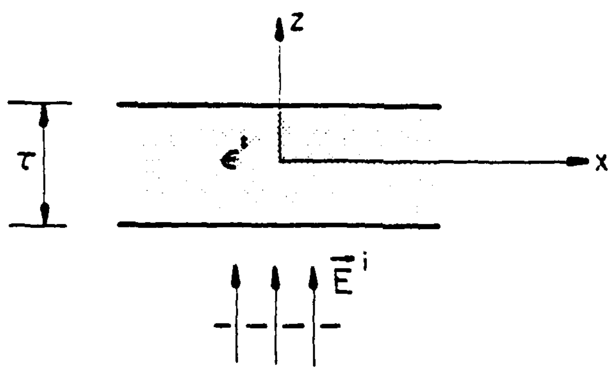

Figure 12. Transmission through a dielectric slab.

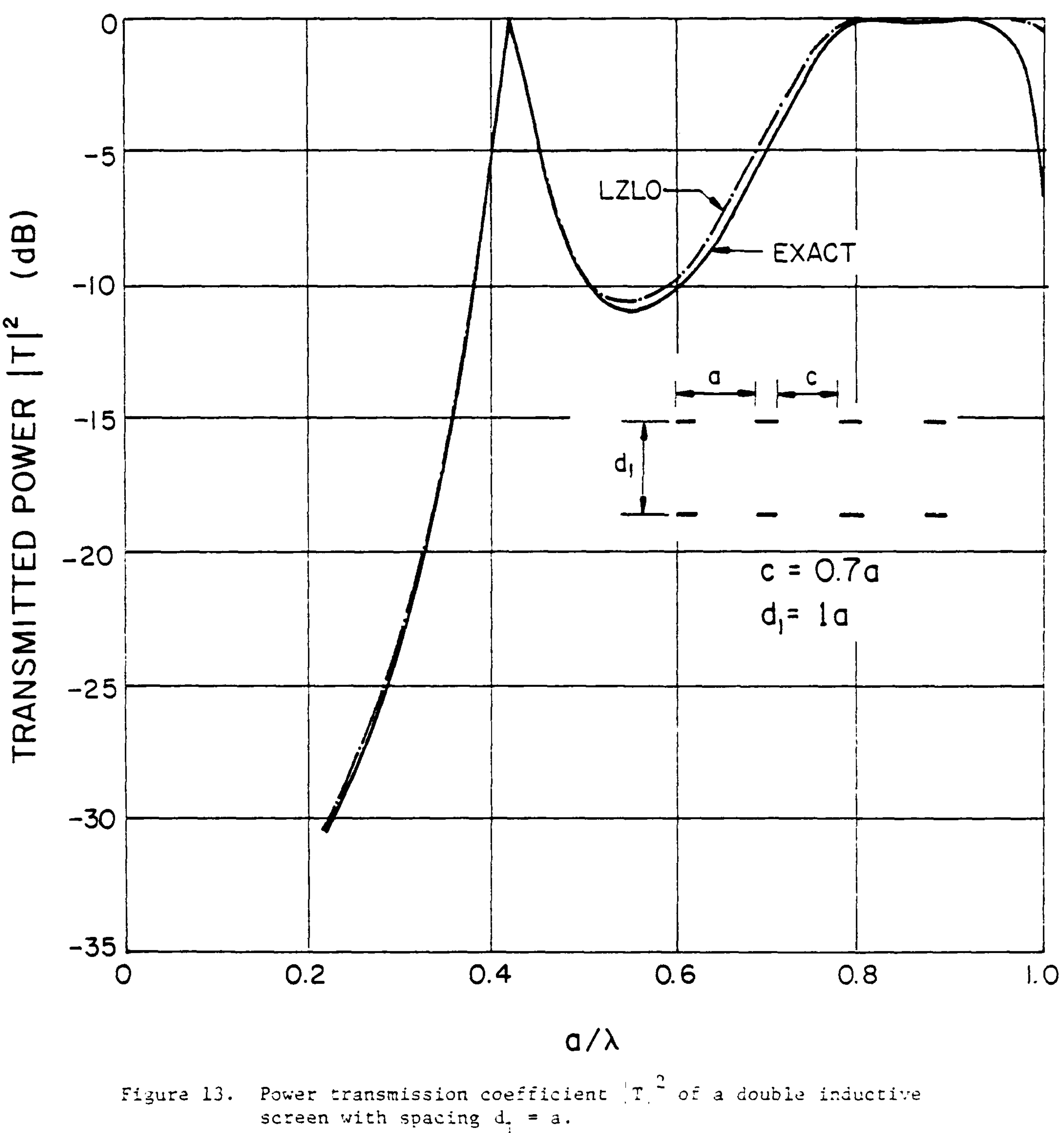

Figure 13. Power transmission coefficient $|T|^2$ of a double inductive screen with spacing $d_1 = a$.

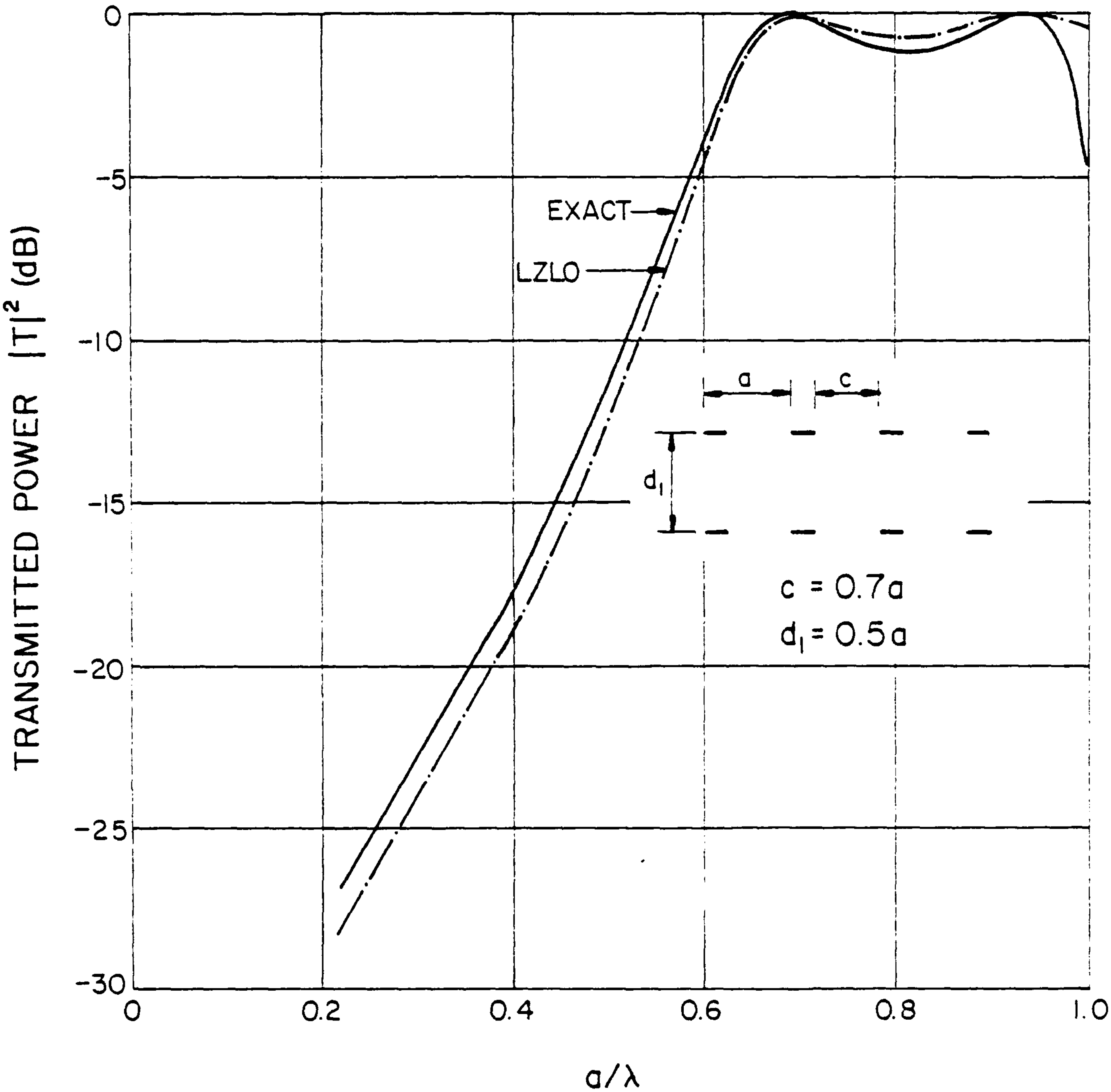

Figure 14. Power transmission coefficient $|T|^2$ of a double inductive screen with spacing $d_1 = 0.5a$.

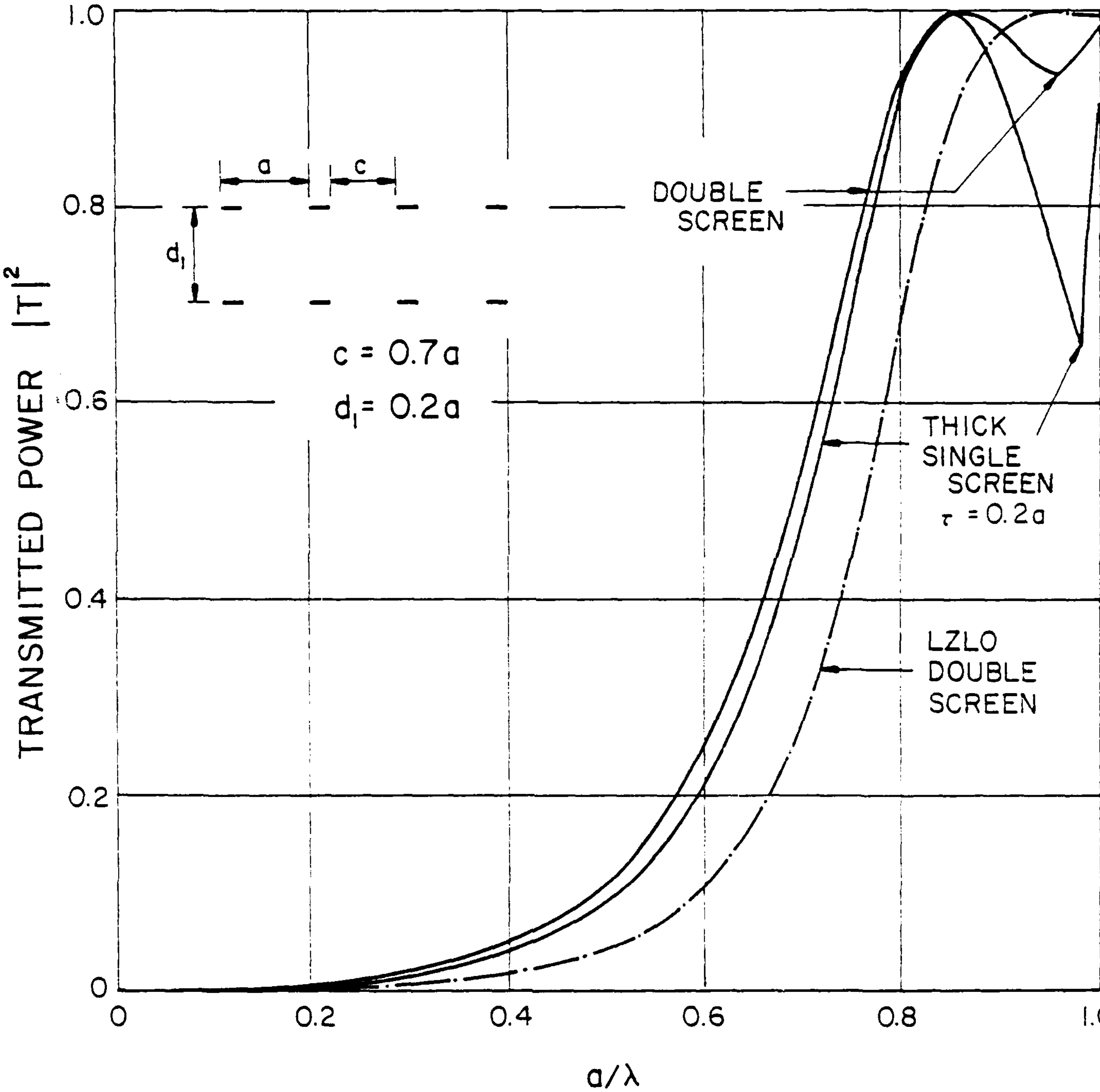

Figure 15. Power transmission coefficient $|T|^2$ of a double inductive screen with spacing d_1 = 0.2a and a thick single screen with τ = 0.2a.

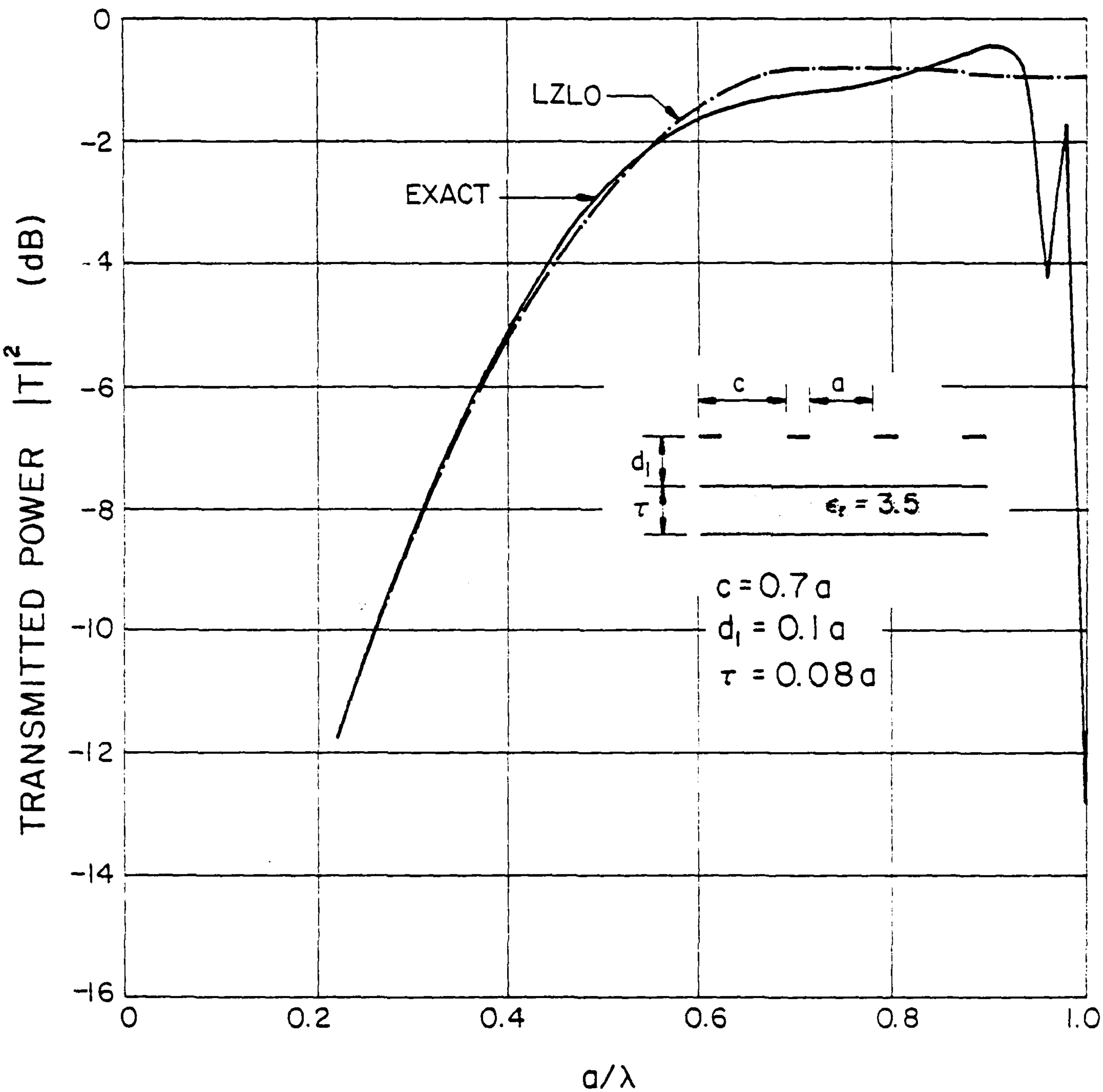

Figure 16. Power transmission coefficient $|T|^2$ of an inductive screen and a dielectric slab with spacing $d_1 = 0.1a$.

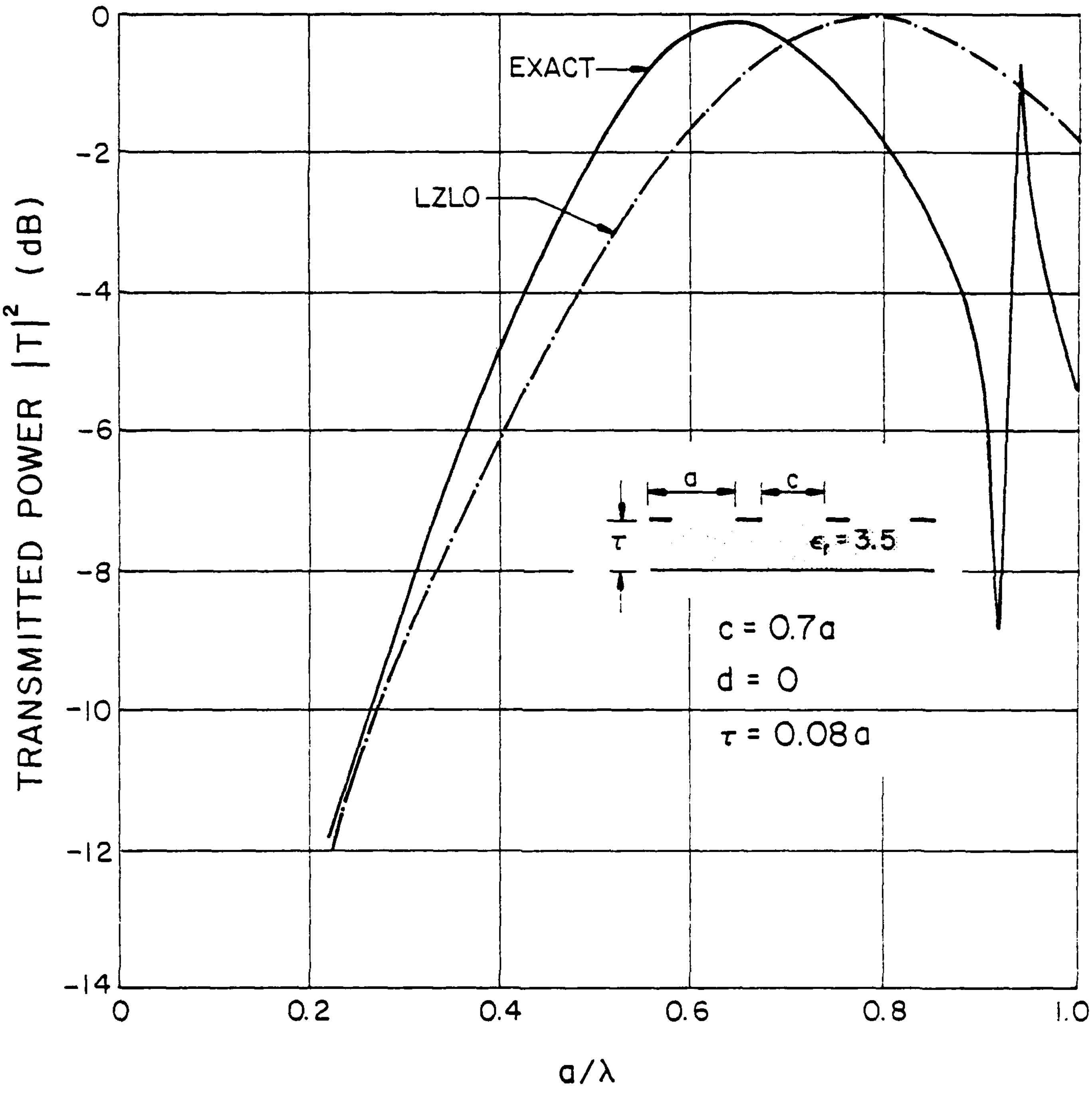

Figure 17. Power transmission coefficient $|T|^2$ of an inductive screen and a dielectric slab with spacing $d_1 = 0$.

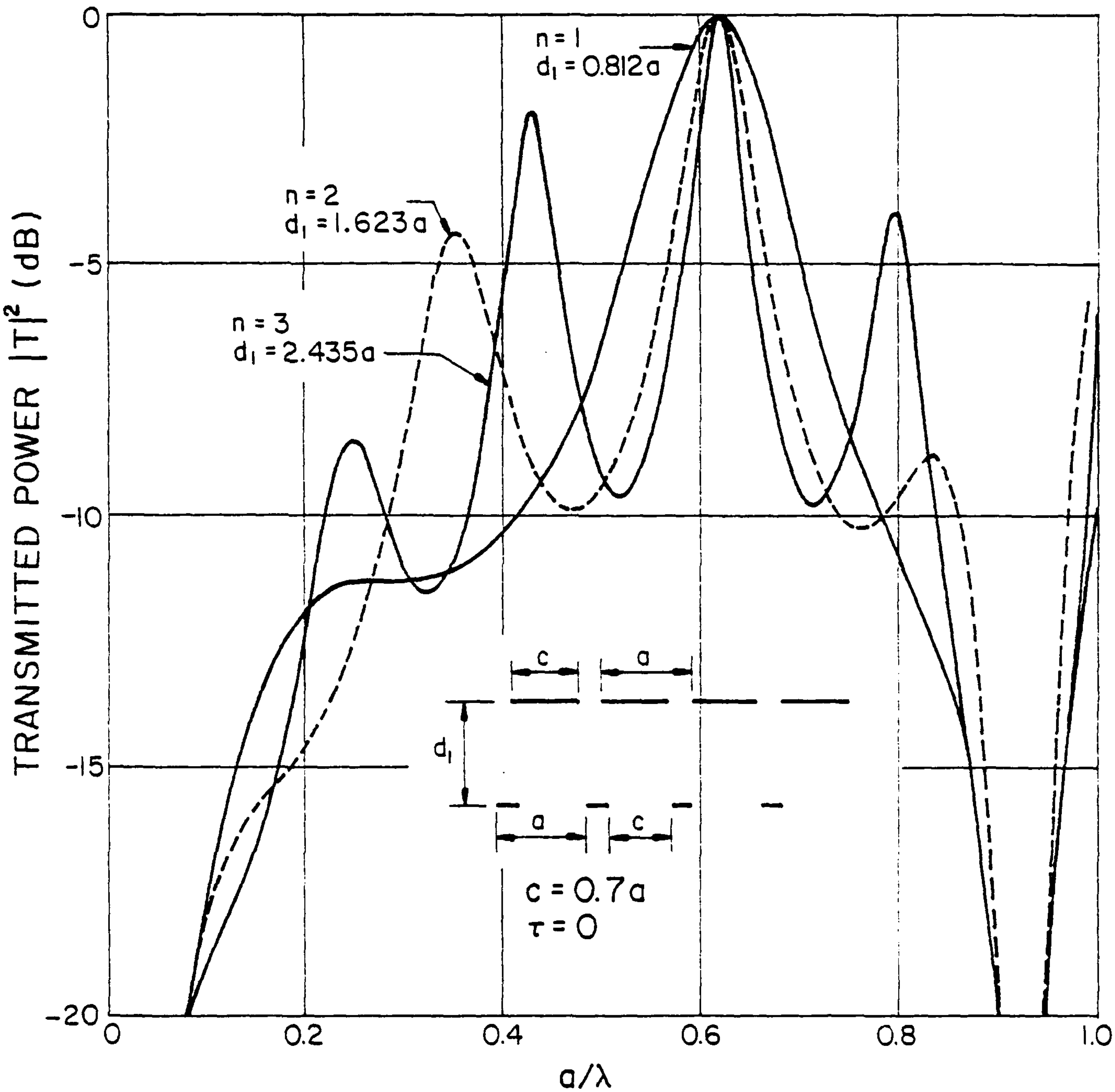

Figure 13. Power transmission coefficient $|T|^2$ of a double screen made of an inductive screen and its complementary capacitive screen.

Lockheed

MISSILES
& SPACE
COMPANY,
INC.

An Algebraic Synthesis Method for RN^2 Multibeam Matrix Network

G.G. Chadwick, W. Gee, P.T. Lam, J.L. McFarland
Lockheed Missiles & Space Co., Inc.
Sunnyvale, CA 94086

Multibeam antenna systems are rapidly gaining popularity; particularly, in the satellite and spaceborned applications. Up to now, multiple feed networks are generally the Butler matrix type and usually have an even number of radiating elements or beams. Lockheed Missiles & Space Company (LMSC) Space System Division (SSD) have in the past 4-5 years been heavily engaged in the analysis and development of the RN^2 triangular [1,2,3] subarrays for multiple beam application as well as a multiple beam design to be located at the focal point of a Cassegrainian reflector system for an adaptive [4] antenna system.

The original mathematical formulations of the RN^2 feeding matrix [1] are greatly simplified in this paper to render this work physically realizable and user oriented. A step-by-step algebraic synthesis procedure is given to obtain the overall RN^2 matrix network required to form independent and orthogonal sets of beams to occur in real space. An illustrative design example of a 27 beam matrix (R=3, N=3) including actual test result of the hardware implementation are given.

[1] J.McFarland; "Derivation of the Feeding Matrix for the $3N^2$ Multiple Beam Array Family"; LMSC D522569; dated April 1978.

[2] J.McFarland; "The RN^2 Multiple Beam Array Family and Beam Forming Matrix"; IEEE/APS International Symposium, June 1979, Seattle, Washington.

[3] W.Gee, J.McFarland; "A Generalized Algebraic Synthesis Procedure of an RN^2 Multibeam Matrix Network"; LMSC D714648, in preparation.

[4] G.G.Chadwick, J.Charitat, W.Gee, C.C.Hung, and J.McFarland; "Adaptive Antenna/Receiver-Processor System"; 1980 Antenna Applications Symposium, Sept 1980, Monticello, Illinois.

Acknowledgement

The authors wish to thank Dr. R. Haight for his continuing interest and encouragement of this work for multiple beam antenna applications. Also appreciation is due to Haj Honda and the technicians for the physical hardware implementation and testing of the 27 beam matrix network. Thanks is also expressed to Kaiija Clark for her help in getting the manuscript out.

Figure 1 depicts the RN^2 beam forming matrix, taken from the appendix, which applies for all R and N if a solution exists.

This paper is broken into 3 sections. Section 1 is a step-by-step algebraic procedure. Section 2 covers an example of a 27 element, 27 beam antenna under development at LMSC.

1.0 Step-by-step procedure

1.1 Choose R

R physically represents the number of input (or output) ports of the $[V_o]$ matrix.

1.2 Choose N

N physically represents the number of input (or output) ports of the $[T]$ matrix.

1.3 Determine if a Solution Exists

A solution exists if $N(R+1)/2$ = integer.

1.4 If a solution exists, continue. If a solution does not exist, choose either:

- another value for N

or

- another value for R.

Keep in mind that the solution sought will contain RN^2 elements and RN^2 orthogonal multiple beams.

1.5 Mapping of Beam Space and Array Space

Once N and R are determined, both beam space and array space must be mapped onto the infinite isoceles triangular grid. From the procedure outlined in the appendix, beam space and array space have been mapped for R ranging from 2 to 5 and N ranging from 2 to 4. The results are given by Figures 2A through 10B.

1.6 Choose Any Complete Array Set

From the array map, a complete set of array elements must be chosen. A complete set is defined by the following

FIGURE 1

THE MULTIPLE-BEAM FORMING MATRIX FOR THE RN^2 MULTIPLE BEAM ARRAY FAMILY

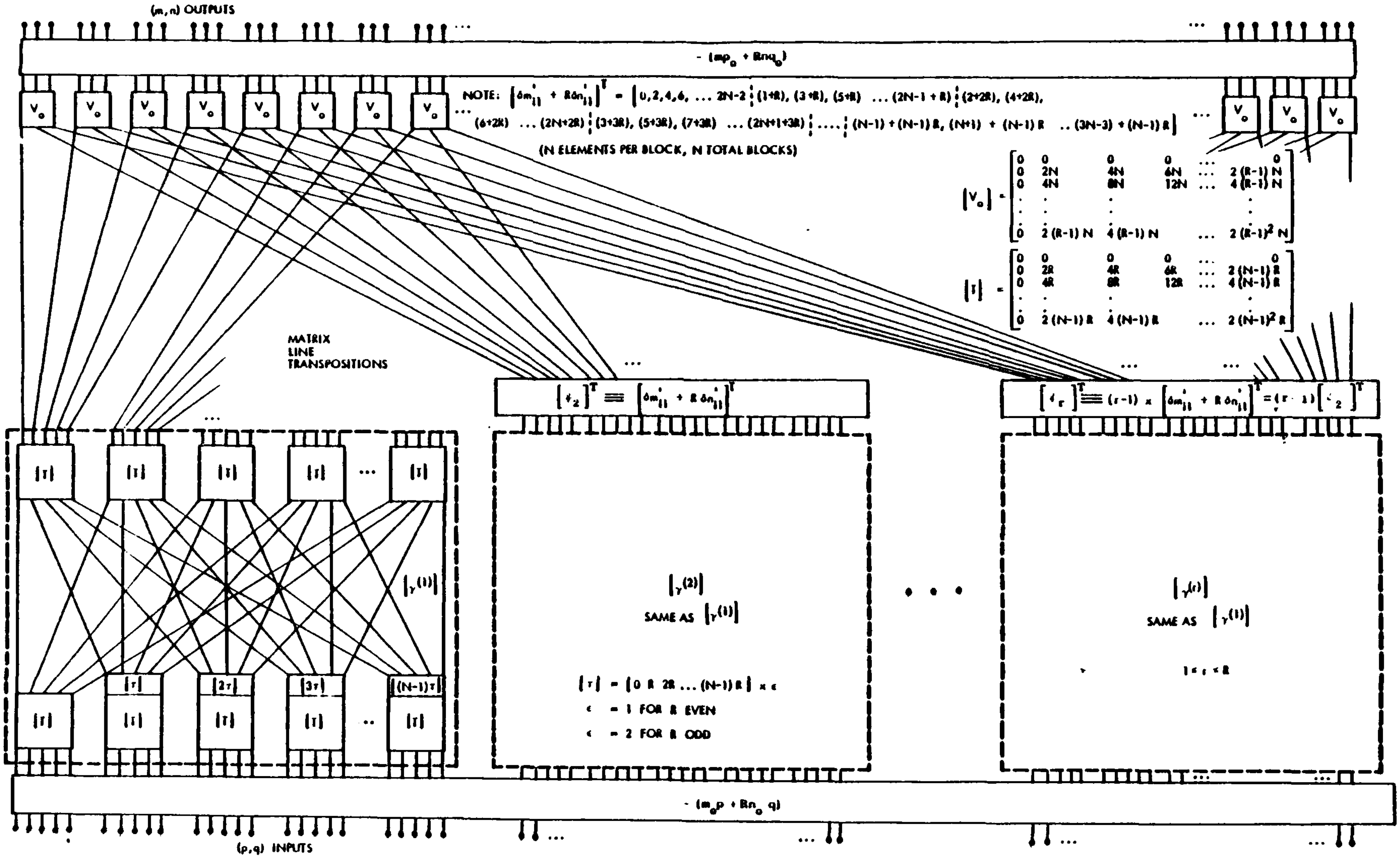

element names:

$$\begin{array}{ccccc} 11, & 12, & 13, & \ldots & 1R \\ 21, & 22, & 23, & \ldots & 2R \\ 31, & 32, & 33, & \ldots & 3R \\ \vdots & & & & \vdots \\ N^21, & N^22, & N^23, & \ldots & N^2R \end{array}$$

The array chosen need not be contiguous, but must be a complete array set.

1.7 Choose Any Complete Beam Set

In a similar manner, a complete set of beams are chosen to be called the main beams of interest. A complete beam set is defined by the following beam names:

$$\begin{array}{ccccc} 11, & 12, & 13, & \ldots & 1N^2 \\ 21, & 22, & 23, & \ldots & 2N^2 \\ 31, & 32, & 33, & \ldots & 3N^2 \\ \vdots & & & & \vdots \\ R1, & R2, & R3, & \ldots & RN^2 \end{array}$$

It should be pointed out that any complete set of beams is just as valid a set of real beams as any other. Distinctly different sets chosen from array space obviously yield distinctly different arrays; however, such is not the case in beam space because all complete sets in beam space are really one in the same set of beams. That is, grating lobes exist in beam space whether we like it or not, and in choosing one beam contained in a complete set in beam space, one also necessarily chooses all beams with the same ij name (ij=11,12, 13,...21,22,23,...etc). Such is not the case for the array, since array space is truncated, whereas beam space is an infinite series.

Thus for a given N and R, all array solutions produce beams with the same grating lobe boundaries; that is the spatial coverage of all array solutions is identical, although the radiation patterns will be different in general.

1.8 Establish (m,n) Coordinates

Using the 11 element location as the origin, $(m_{11},n_{11})=(0,0)$, record the (m,n) coordinates for the 11,12,13,...1R element positions (read from the array space map) giving (m_{11},n_{11}), $(m_{12},n_{12}),\ldots(m_{1R},n_{1R})$. Similarly, do likewise for the element positions 21,22,..2R; 31,32,..3R;...$N^2$1,$N^2$2,..N^2R. Record (m_{21},n_{21}), $(m_{22},n_{22}),\ldots.(m_{N^2R},n_{N^2R})$.

1.9 Establish (p,q) Coordinates

Using the 11 beam position as the origin, $(p_{11},q_{11})=(0,0)$, record the (p,q) coordinates for the 11,12,13,...1N^2 beam positions (read from the beam space map), giving (p_{11},q_{11}), $(p_{12},q_{12}),\ldots(p_{1N^2},q_{1N^2})$. Do likewise for the remaining beam positions 21,22,...2N^2; 31,32,...3N^2;...R1,R2,..RN^2. Record $(p_{21},q_{21}),(p_{22},q_{22}),\ldots(p_{RN^2},q_{RN^2})$.

1.10 Choose (m_o,n_o)

With respect to the physical array x,y coordinate system, $(m_o d_x,n_o d_y)$ represents the array position at which all phase fronts are at zero phase. This may or may not be important to the user depending upon the application. The coordinate of the center of gravity of the complete array may, for example, be used for (m_o,n_o) as the best array phase center.

1.11 Choose (p_o,q_o)

With respect to the u',v' beam coordinate system, $(p_o\Delta u'/2,q_o\Delta v')$ represents the coordinates that correspond to the array broadside. In other words, the relative placement of the multiple beams are fixed with respect to one another, but their absolute location is determined by the choice of (p_o,q_o).

1.12 Compute the Output Phasors

With reference to figure 1, the fixed output phasors are given by:

$$-(mp_o+Rnq_o).$$

Each output port has a unique (m,n) coordinate; thus given m,n,p_o,q_o, and R (all known) the fixed output phasors are readily calculated and the calculated value of phase shift is inserted into the output line of the particular (m,n) element under consideration. Carry this out for all (m,n) elements.

1.13 <u>Compute the Input Phasors</u>

Again, referring to Figure 1, the fixed input phasors are given by:

$$-(m_op+Rn_oq).$$

Each input port has a unique (p,q) coordinate; thus given p,q,m_o,n_o, and R (all known) the fixed input phasors are calculable and are inserted into the input lines. Carry this out for all (p,q) beams.

1.14 <u>Compute the $[\psi_2]$ Phasors</u>

The output of $[\gamma(r)]$, the r^{th} gamma matrix is given by

$$(r-1)[\psi_2].$$

The equation for $[\psi_2]$ is given in Figure 1. These computed values of phase shift are inserted at the output of the r^{th} gamma matrix. Carry this out for all r, where $1 \leq r \leq R$.

1.15 <u>Compute the $[\tau]$ Phasors</u>

The $[\tau]$ phasors are given by

$$\epsilon[0 \quad R \quad 2R \quad 3R \quad \ldots \quad (N-1)R]$$

in which

$\epsilon=1$ for R even,
$\epsilon=2$ for R odd.

The gamma matrices are all identical, hence only $[\gamma_o^{()}]$ need be considered. Place at the output of the ℓ^{th}

lower $[T]$ matrix the phasors

$$(\ell-1)[\tau]$$

in which $1 \leq \ell \leq N$.

The matrix is now totally characterized, mathematically; however, it may be further simplified by collecting and summing phasors that are common to a given line, or by adding or subtracting a fixed phase value at any common terminal plane.

The $[V_o]$ and $[T]$ matrices are given by the expressions in Figure 1. Their physical implementation may require certain input and/or output phasors that may cancel some of the fixed phasors that are already there. Some circuit simplification procedures are discussed in Section 2.

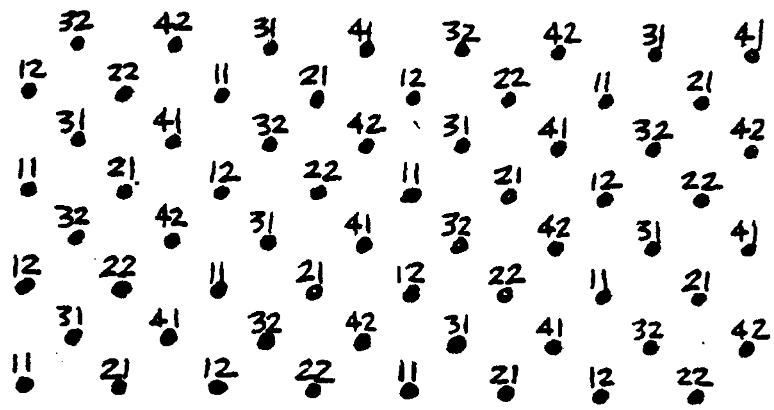

Figure 2A Array Space for R=2, N=2

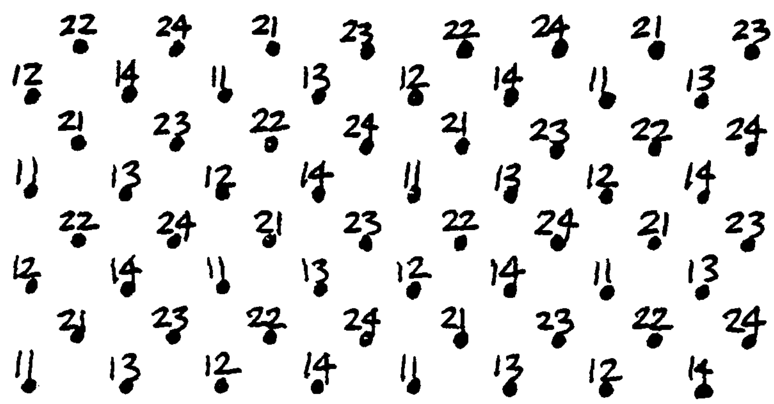

Figure 2B Beam Space for R=2, N=2

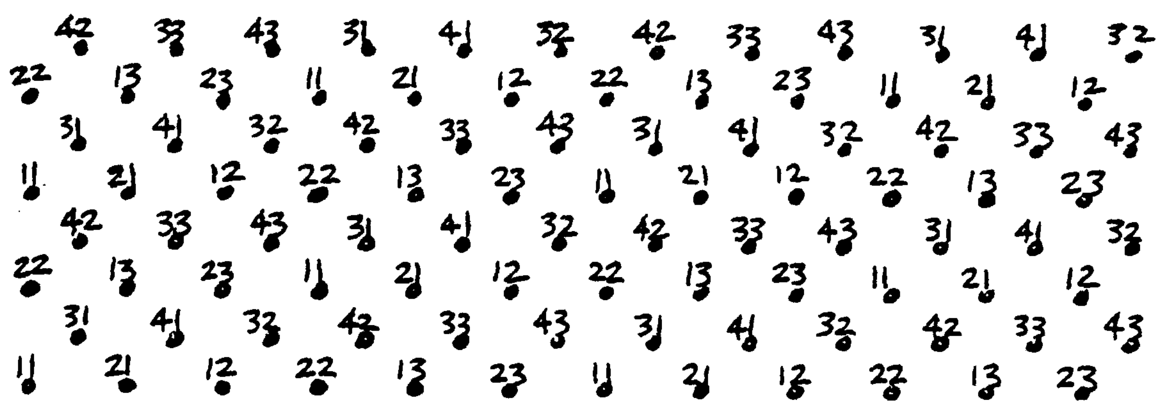

Figure 3A Array Space for R=3, N=2

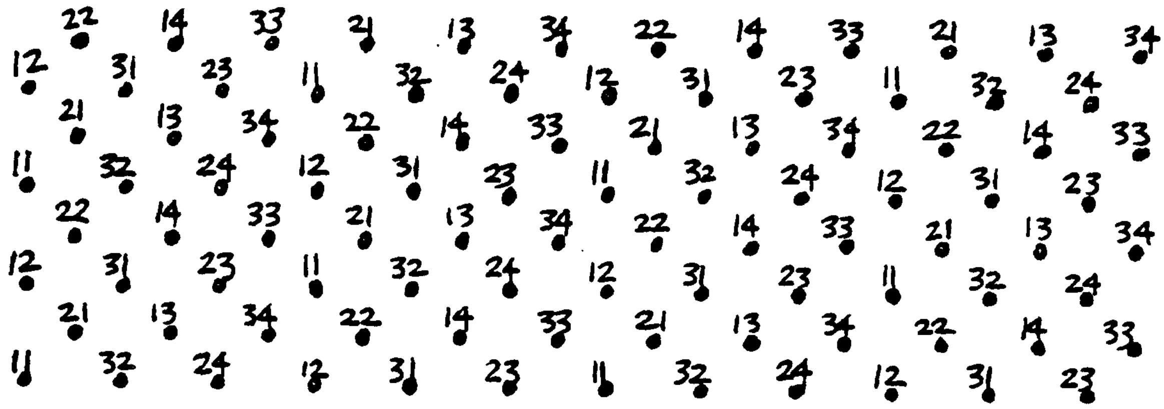

Figure 3B Beam Space for R=3,N=2

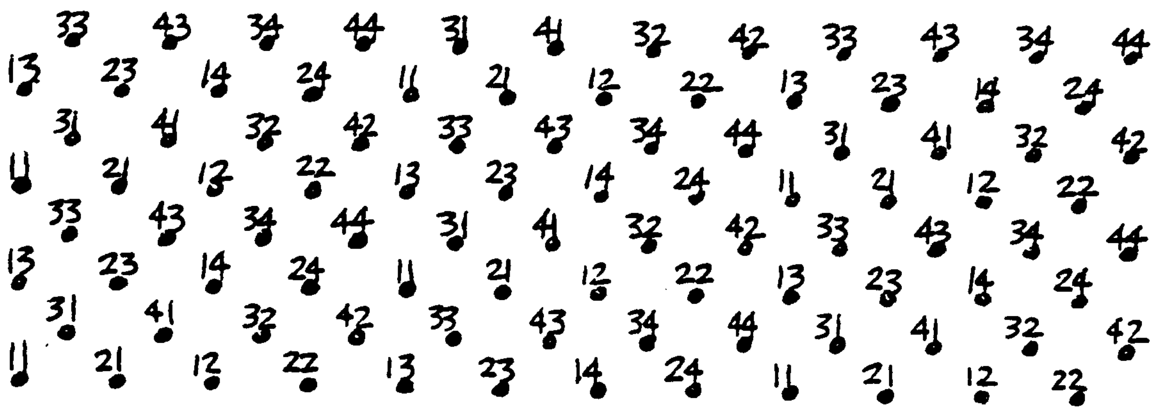

Figure 4A Array Space for R=4,N=2

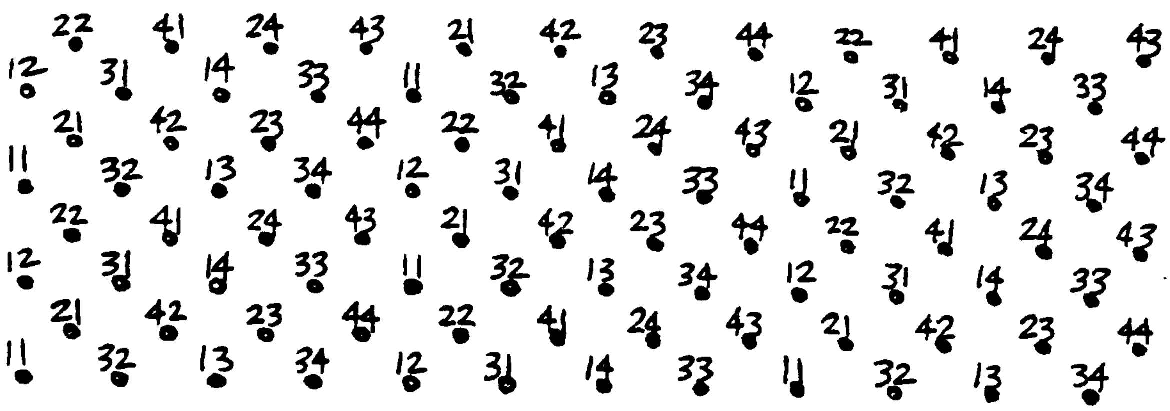

Figure 4B Beam Space for R=4,N=2

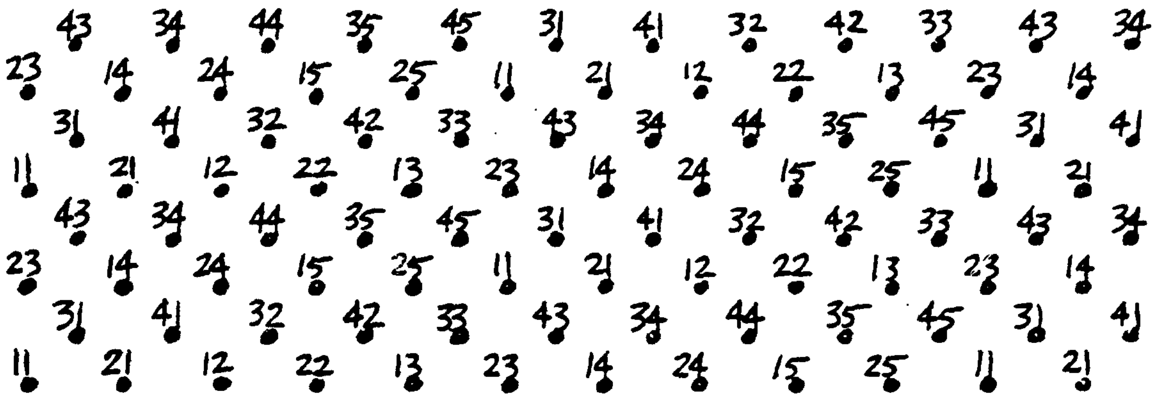

Figure 5A Array Space for R=5,N=2

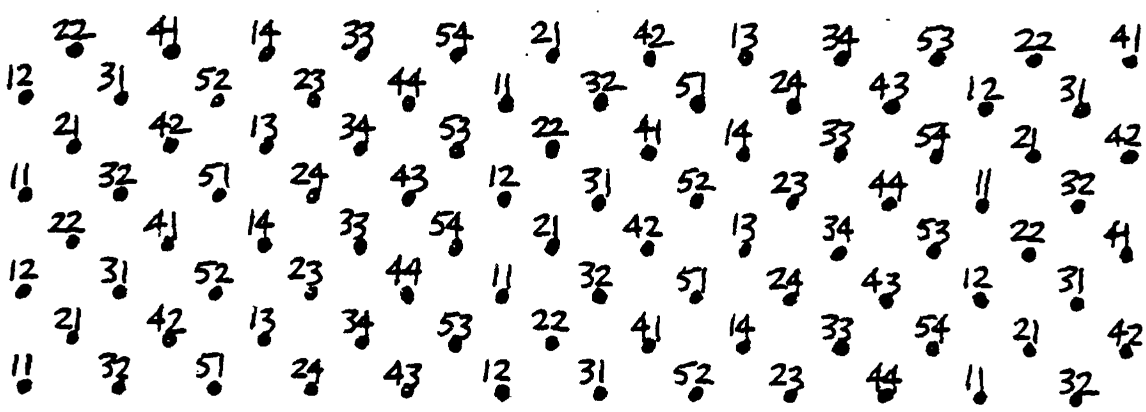

Figure 5B Beam Space for R=5,N=2

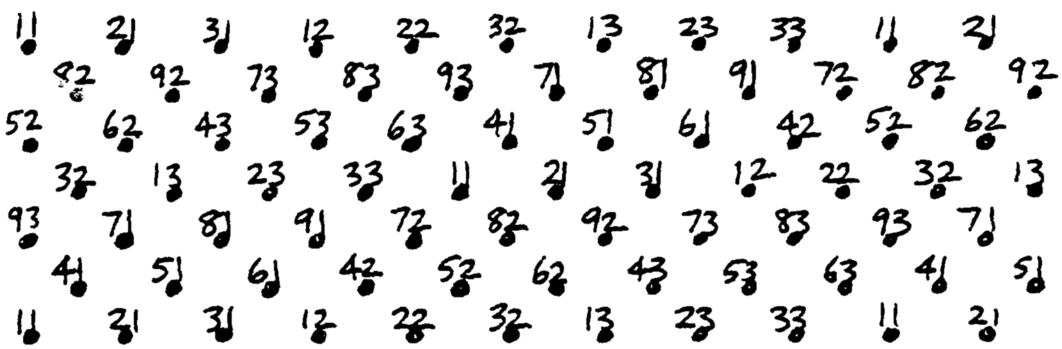

Figure 6A Array Space for R=3,N=3

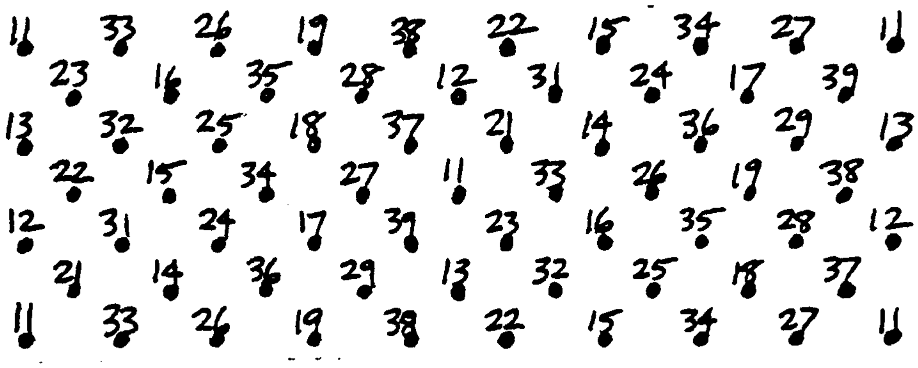

Figure 6B Beam Space for R=3, N=3

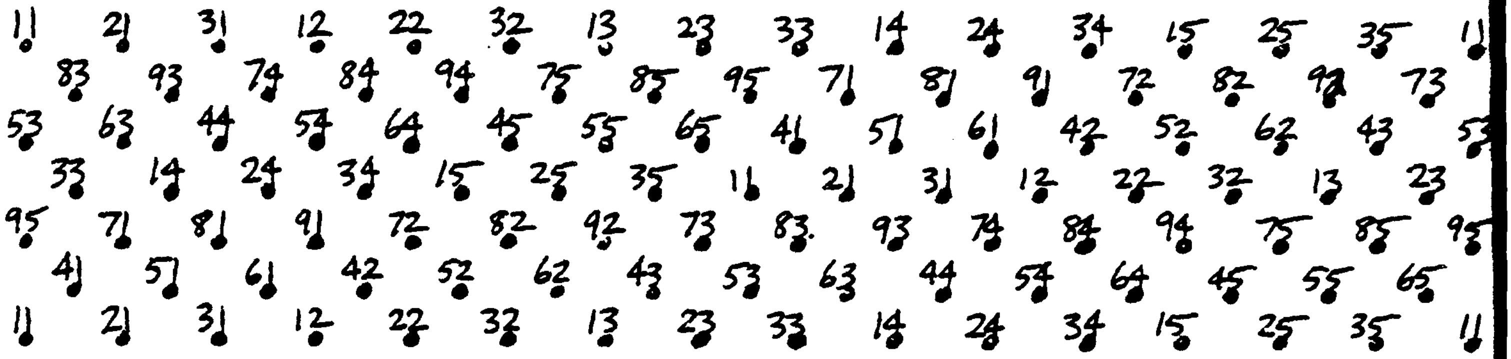

Figure 7A Array Space for R=5, N=3

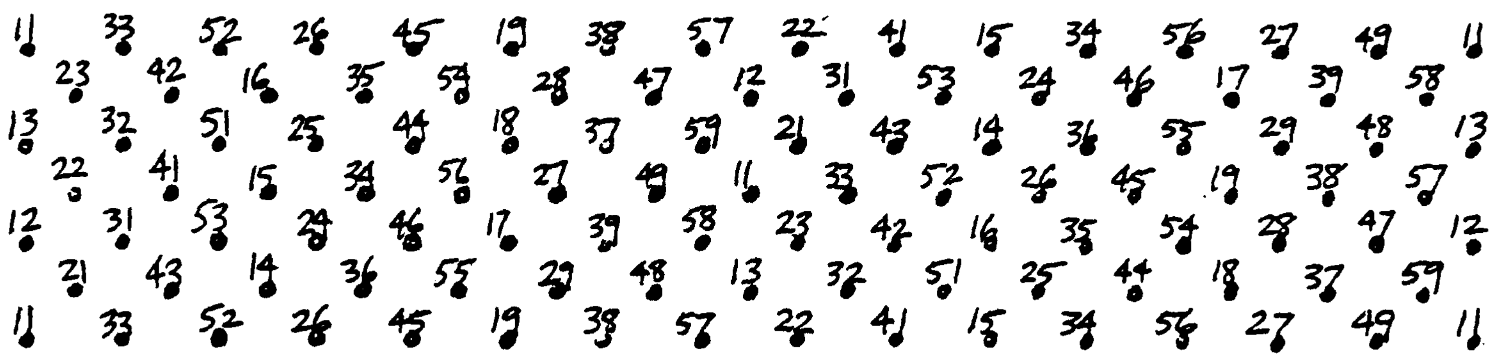

Figure 7B Beam Space for R=5, N=3

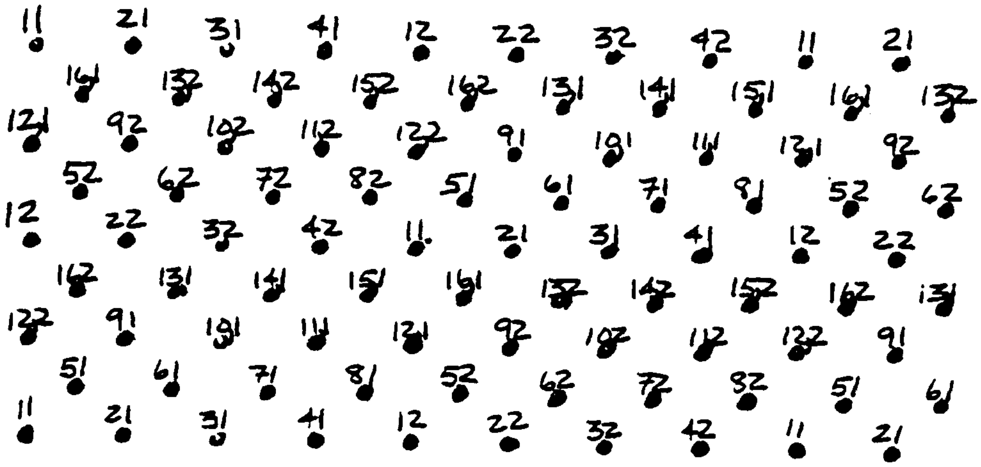

Figure 8A Array Space for R=2,N=4

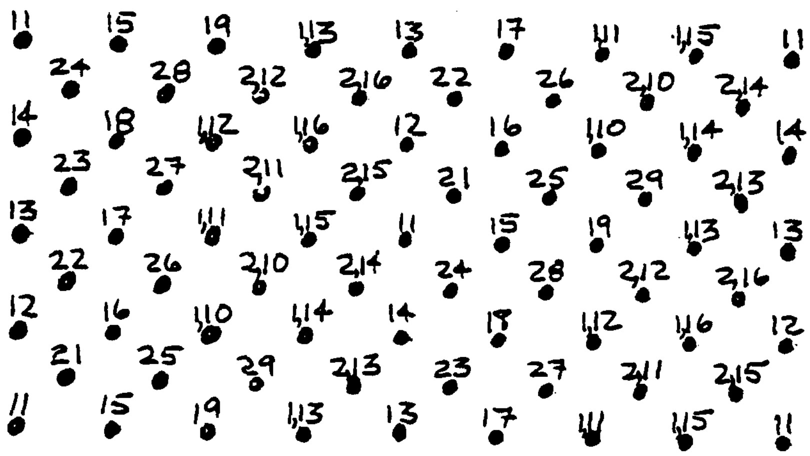

Figure 8B Beam Space for R=2,N=4

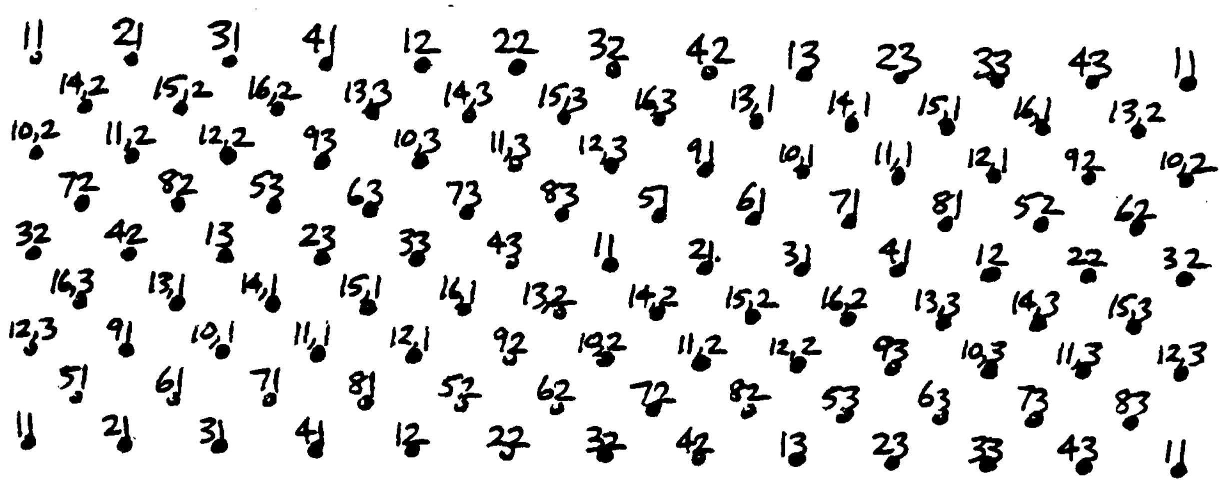

Figure 9A Array Space for R=3,N=4

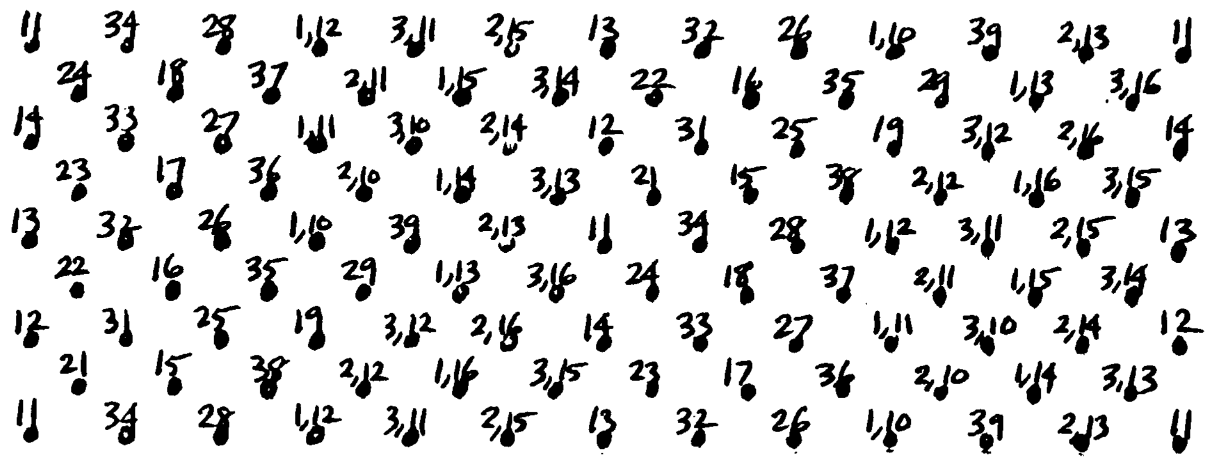

Figure 9B Beam Space for R=3, N=4

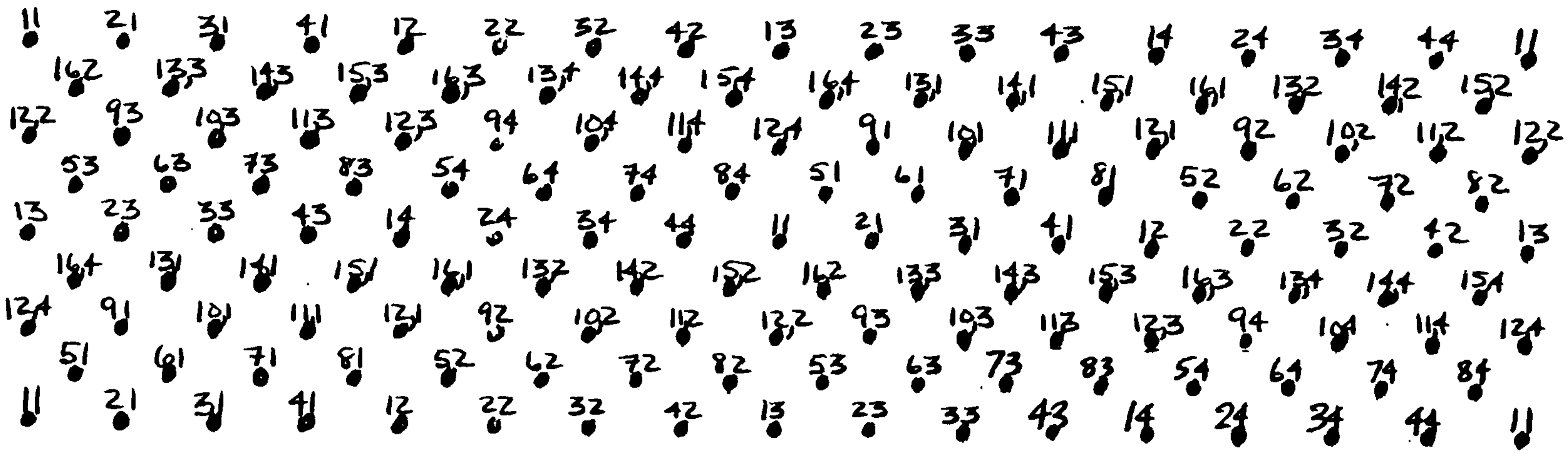

Figure 10A Array Space for R=4, N=4

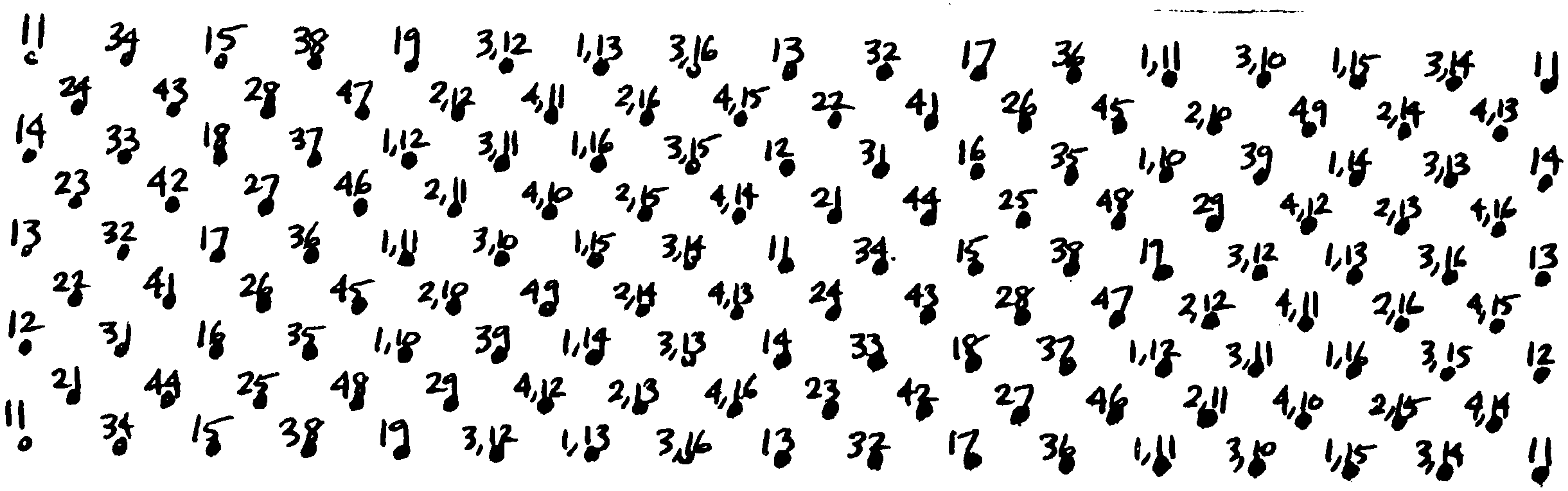

Figure 10B Beam Space for R=4, N=4

2.0 Example: R=3,N=3 27 Element Array

Figures 6A and 6B depict the mapping of array space and beam space, respectively, for the case R=3, N=3.

In accordance with step 1.6 of the previous section, a complete array set is chosen to be the hexagonally shaped array depicted by Figure 11A. The corresponding beam set is chosen as being shaped identically with the array shape (this will always be possible), and is given by Figure 11B.

(m_o, n_o) was chosen as (0,1/3) since this represents the center of gravity of the array; as such, it is the best phase center.

(p_o, q_o) was also chosen as (0,1/3) since the field-of-view of interest for this application was conical; consequently, the best approximation to a conical field-of-view was realized.

The (m,n) and (p,q) coordinates were calculated in accordance with the procedure given in Section 1, as well as the input and output phasors, $[\Psi_2]$, and $[\tau]$.

Thus the entire matrix was synthesized and is summarized by Figure 12.

The total phase shift through the matrix was checked for all (p,q) beam positions and all (m,n) element locations, resulting in the correct phase. It is concluded that the procedure as outlined in this paper yields the correct matrix for the array chosen.

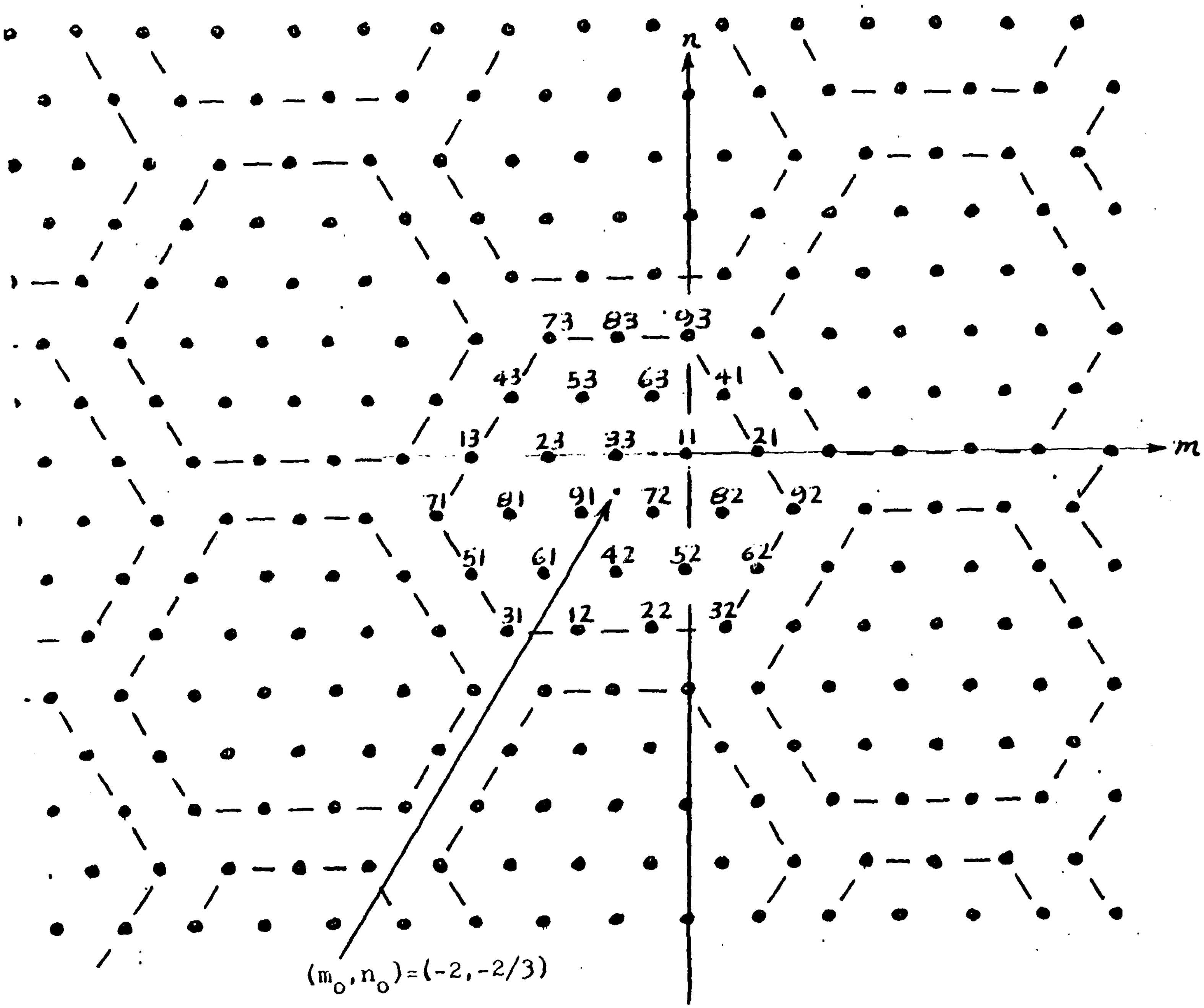

FIGURE 11A Array Space for R=3, N=3

Note: all hexagonal clusters has identical labeling

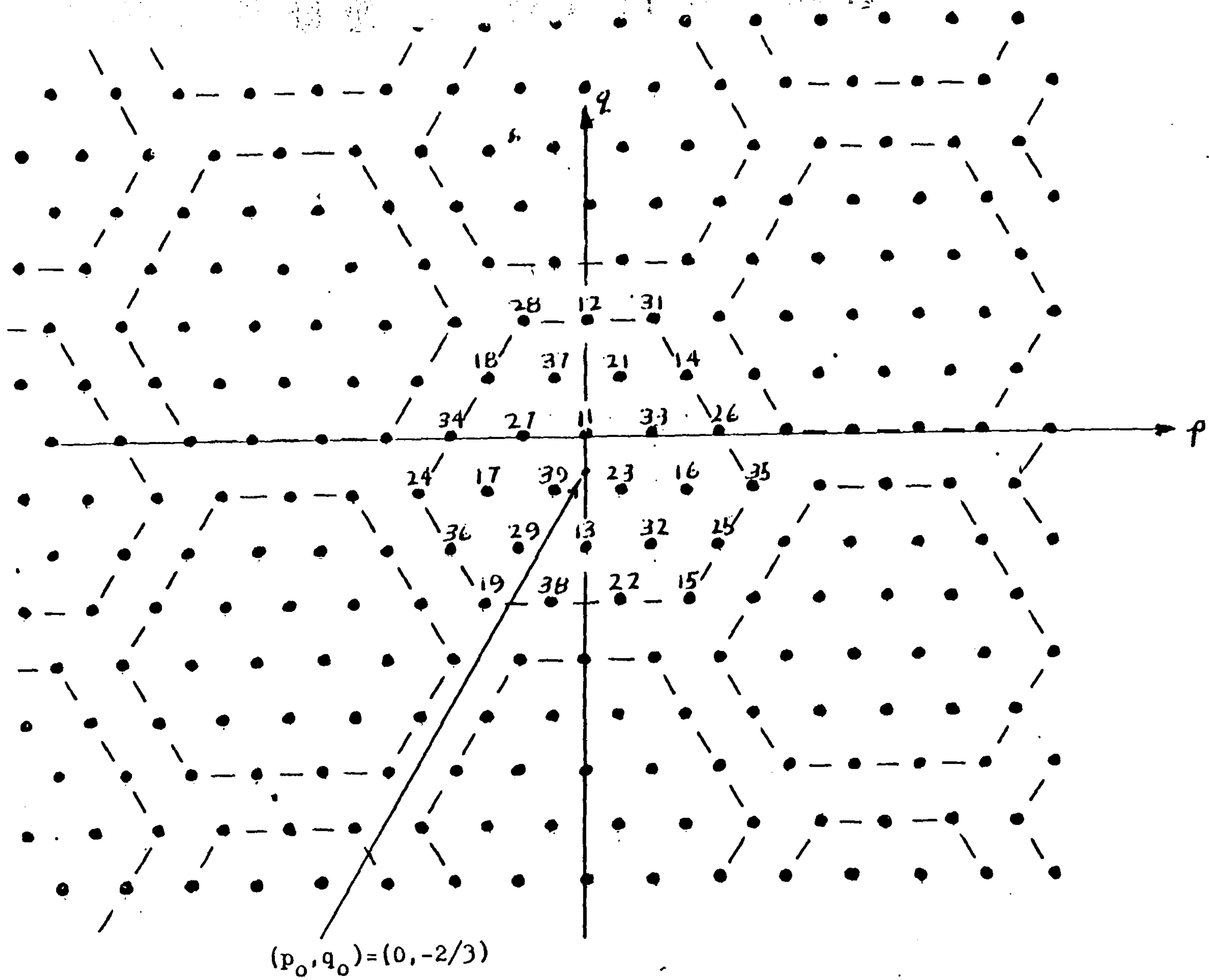

FIGURE 11B Beam Space for R=3, N=3

Note: all hexagonal clusters have identical labeling

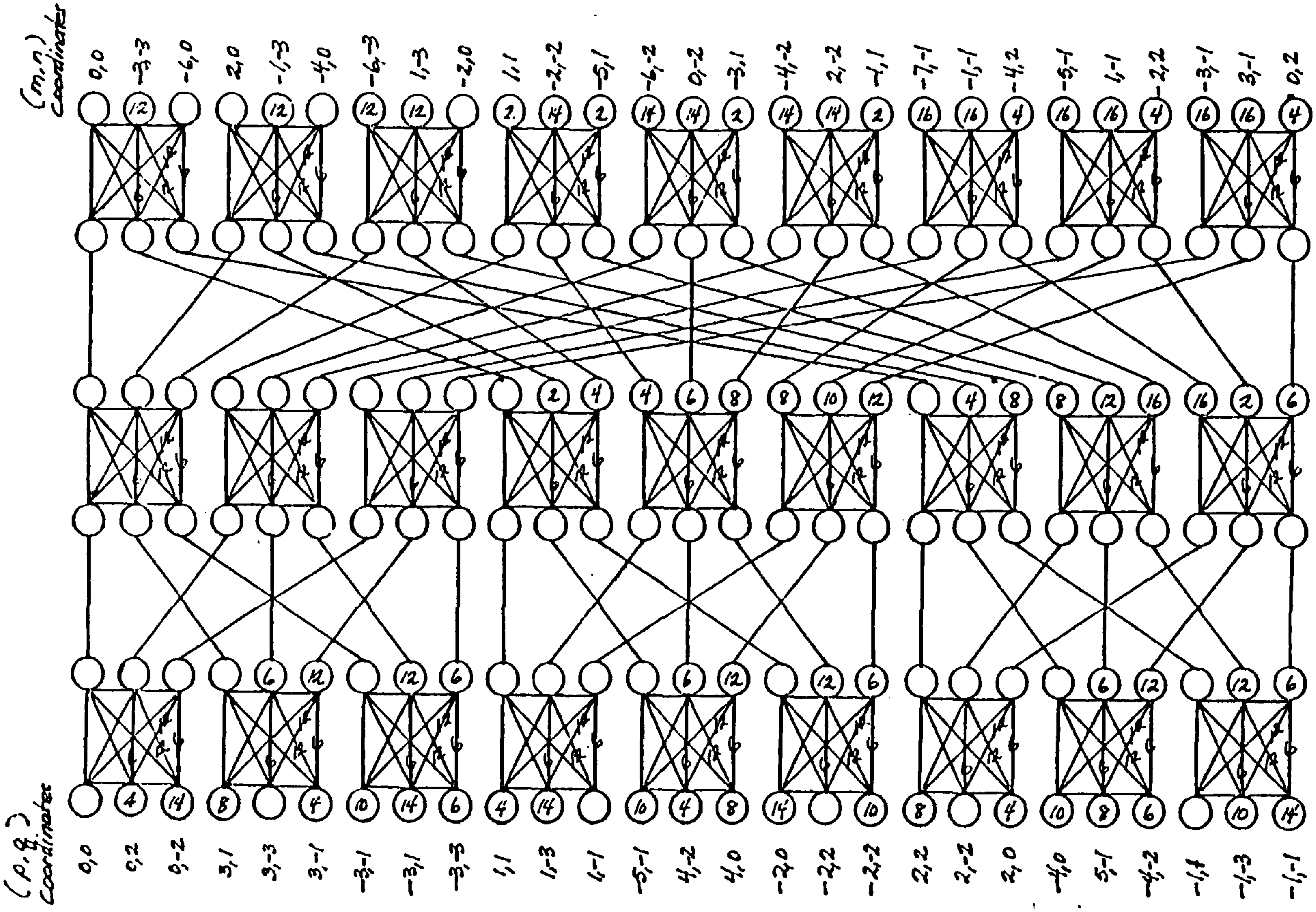

FIGURE 12
MATRIX FOR R=3, N=3

APPENDIX

THE RN^2 MULTIPLE BEAM ARRAY FAMILY AND THE BEAM FORMING MATRIX

J.L. MC FARLAND

LOCKHEED MISSILES & SPACE COMPANY, INC.
SUNNYVALE, CA.

ABSTRACT

THIS PAPER DERIVES A FAMILY OF LOSSLESS TRIANGULARLY SPACED ORTHOGONAL MULTIPLE BEAM ARRAYS AND THE BEAM-FORMING MATRIX REQUIRED TO PHASE IT. APPRECIABLE FREEDOM IS AVAILABLE TO THE USER IN CHOOSING THE NUMBER OF ELEMENTS (BEAMS) AND THE ARRAY SHAPE.

AN ARBITRARY NUMBER OF EQUAL AMPLITUDE ISOTROPIC SOURCES ARE ASSUMED TO LIE SOMEWHERE ON AN ISOSCELES TRIANGULAR PLANAR GRID STRUCTURE. THE ELEMENTS NEED NOT BE CONTIGUOUS. THE RESULTING ARRAY SHAPE IS CONSIDERED ARBITRARY AND NOT NECESSARILY SINGLY CONNECTED.

ORTHOGONALITY CONDITIONS ARE IMPOSED UPON THE M ELEMENT ARRAY SO AS TO PRODUCE M INDEPENDENT SIMULTANEOUS LOSSLESS MULTIPLE BEAMS.

THE REQUIRED ORTHOGONAL PHASE OF THE (m,n) ELEMENT FOR THE (p,q) BEAM BECOMES:

$$\phi_{mn}^{pq} = \frac{\pi}{NR}\,(m'p' + Rn'q') \tag{1}$$

WHERE $(m',n') = (m-n_o\,,\ n-n_o)$; $(p',q') = (p-p_o, q-q_o)$; (m_o,n_o) = THE ARRAY COORDINATE AT WHICH THE OUTPUT PHASE FRONT OF ALL BEAM POSITIONS IS ZERO ; AND (p_o,q_o) = THE BEAM PEAK COORDINATE CORRESPONDING TO THE ARRAY BROADSIDE.

PERMISSIBLE ARRAY SOLUTIONS ARE GIVEN BY :

$$\frac{\Delta m_A}{2NR} + \frac{\Delta n_A}{2N} = I\ (0,\ \pm 1,\ \pm 2,\ \text{ETC.}) \tag{2}$$

THAT IS, THE NUMBER OF ELEMENTS AND THE ARRAY SHAPE MUST BE SUCH THAT THE ARRAY CAN BE TRANSLATED IN THE (m,n) DOMAIN REPEATEDLY BY $(\Delta m_A, \Delta n_A)$, SATISFYING (2) FOR ALL THE VALUES OF THE INTEGER I , AND THEREBY COVERING, ONLY ONCE, ALL POSSIBLE ELEMENT LOCATIONS ON THE INFINITE TRIANGULAR GRID STRUCTURE.

THE SYNTHESIS OF THE MULTIPLE BEAM-FORMING MATRIX IS CARRIED OUT, FOR ANY R, ANY N THAT SATISFIES (2). NUMEROUS MEMBERS OF THIS FAMILY OF MULTIPLE BEAM ARRAYS ARE DEPICTED. A LIMITED AMOUNT OF DATA IS DISCUSSED.

This is a reprint of a paper given at a Poster Session in June 1979, IEEE/AP-S International Symposium, at Seattle, Washington.

METHODOLOGY

- DEFINE POSTULATED BEAM SPACE AND ARRAY SPACE.
- FROM GRATING LOBE CONDITION, DERIVE REQUIRED PHASE DISTRIBUTION.
- FROM ORTHOGONALITY, DEDUCE ARRAY MAPPING CONDITION (DISTRIBUTION OF RN^2 ELEMENTS AND BEAMS).
- DEFINE THE FORM OF POSTULATED OVERALL MATRIX (UNITARY).
- DEDUCE THE FORM OF THE "REFERENCE" MATRIX BY IMPOSING DIAGONALIZATION CONDITIONS AS THE RECEIVED WAVEFRONT PROPAGATES TOWARD THE INPUT PORTS.
- DEDUCE THE CHANGE IN THE "REFERENCE" MATRIX REQUIRED TO ACCOMMODATE ANY SOLUTION, I.E., DEDUCE GENERAL SOLUTION.
- ILLUSTRATE ARRAY/BEAM SOLUTIONS, DATA, AND GENERAL CIRCUIT.

COORDINATE SYSTEM FOR ARRAY ELEMENTS AND ORTHOGONAL BEAMS (ISOCELES TRIANGULAR GRID)

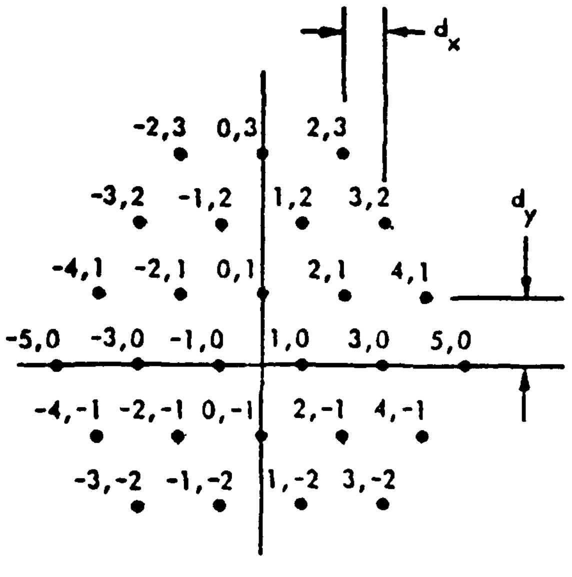

FIG. 1 APERTURE COORDINATES (m,n) VALUES SHOWN

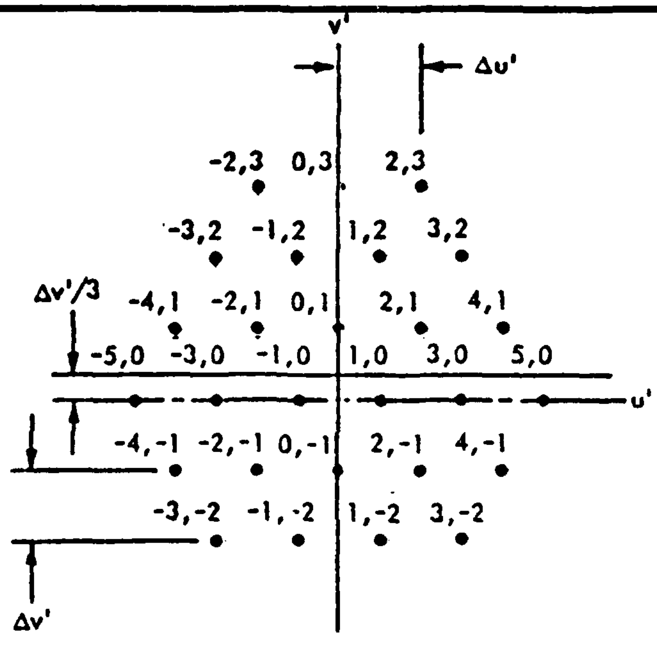

FIG. 2 BEAM COORDINATES (p,q) VALUES SHOWN

ORTHOGONAL MULTIPLE BEAM PHASE DISTRIBUTION FOR UNIFORMLY ILLUMINATED ARRAY ON AN ISOCELES TRIANGULAR GRID

THE FAR-FIELD RADIATION PATTERN FOR A UNIFORMLY ILLUMINATED ARRAY OF ISOTROPIC POINT SOUCRES IS GIVEN BY EQUATION (1)

$$E^{p,q}(u', v') = \frac{1}{N_e} \sum^{mn} e^{-j\Phi^{pq}_{mn}} e^{jk(d_{x_{mn}} u' + d_{y_{mn}} v')} \quad N_e \text{ TOTAL ELEMENTS} \tag{1}$$

WHERE

Φ^{pq}_{mn} $\triangleq$ PHASE OF THE mn^{th} RADIATOR THAT PRODUCES THE pq^{th} BEAM

k = $\frac{2\pi}{\lambda}$, λ = FREE SPACE WAVELENGTH

$d_{x_{mn}}$ = x COORDINATE OF THE mn^{th} RADIATOR = md_x (SEE FIG. 1)

$d_{y_{mn}}$ = y COORDINATE OF THE mn^{th} RADIATOR = nd_y

mn = VALUES OF m AND n (INTEGERS) THAT SPECIFY THE mn^{th} ELEMENT LOCATION

u' = $\cos\alpha_x = \sin\theta\cos\phi$, $v' = \cos\alpha_y = \sin\theta\sin\phi$

POSTULATE AN ORTHOGONAL SYSTEM OF REGULARLY SPACED MULTIPLE BEAMS IN WHICH THE PEAK OF THE pq^{th} BEAM IS DEFINED AS (u'_{pq}, v'_{pq}) AND IS GIVEN BY:

$$u'_{pq} = p\frac{\Delta u'}{2} \qquad v'_{pq} = q\,\Delta v' \qquad \text{(SEE FIG. 2)}$$

EQUATION (1) CAN BE REWRITTEN AS:

$$E^{pq}(u', v') = \sum^{mn} e^{j\left[mkd_x(u'-u'_{pq}) + nkd_y(v'-v'_{pq})\right]} \tag{2}$$

FROM WHICH IT FOLLOWS THAT:

$$\Phi^{pq}_{mn} = \left[mkd_x \frac{\Delta u'}{2} p + nkd_y \Delta v' q\right] \tag{3}$$

TRANSLATING THE BEAMS AND/OR APERTURE PHASE IN WHICH:

$$(u', v') \text{ Broadside} = \left(p_o \frac{\Delta u'}{2}, q_o \Delta v'\right), \text{ or } (p,q) \text{ Broadside} = (p_o, q_o)$$

AND (m_o, n_o) = APERTURE COORDINATE AT 0° PHASE FOR ALL BEAMS, THE REQUIRED PHASE BECOMES:

$$\boxed{\Phi^{pq}_{mn} = (m-m_o)\,kd_x \frac{\Delta u'}{2}(p-p_o) + (n-n_o)\,kd_y \Delta v' (q-q_o)} \tag{4}$$

E^{pq} IS A FOURIER SERIES IN (u',v'), AND, THUS, IS PERIODIC REQUIRING $R = \Delta p_A / \Delta q_A$

$$\Phi_{mn}^{pq} = S\,(m'p' + Rn'q')$$

WHERE $\quad S = kd_x \Delta u'/2 \;, \; R = d_y \Delta v' / \left[d_x \, (\Delta u'/2) \right] \geq 1$ (5)

$$(m',n') = (m-m_o \,,\, n-n_o) \;,\; (p',q') = (p-p_o, q-q_o)$$

$E^{p,q}\,(u',v')$ = FOURIER SERIES IN TWO VARIABLES; THUS THE GRATING LOBE PERIODICITY CONDITION IS:

$$\Delta\phi_i = 2\pi l_1 \,,\; (l_1 = 0, \pm 1, \pm 2, \text{ETC.}) \tag{6}$$

WHERE $\quad l_1 = l_1\,(m,n,p,q)$ (7)

AND ϕ_i = INTERELEMENT PHASE SHIFT

$\Delta\phi_i$ = CHANGE IN ϕ_i FOR OBSERVATION POINT CHANGING FROM MAIN BEAM TO ANY GRATING LOBE

$$\phi_i = \frac{\partial\phi}{\partial m}\,\Delta m + \frac{\partial\phi}{\partial n}\,\Delta n \;,\; \Delta\phi_i = \frac{\partial\phi_i}{\partial p}\,\Delta p_A + \frac{\partial\phi_i}{\partial q}\,\Delta q_A \;; \tag{8}$$

THUS $\quad \Delta\phi_i = \dfrac{\partial^2\phi}{\partial p\,\partial m}\,\Delta m \Delta p_A + \dfrac{\partial^2\phi}{\partial q\,\partial n}\,\Delta n \Delta q_A = S\,(\Delta m \Delta p_A + R \Delta n \Delta q_A) = 2\pi l_1$, FROM (6), (9)

WHERE $\quad (\Delta p_A, \Delta q_A) = (p,q)\Big|_{\text{ANY GRATING LOBE}} - (p,q)\Big|_{\text{MAIN BEAM}} \;;$

$$(\Delta m, \Delta n) = (m,n)\Big|_{\text{ANY ELEMENT}} - (m,n)\Big|_{\text{FIXED REFERENCE ELEMENT}}$$

THE ADJACENT GRATING LOBE DIRECTIONS ARE SHOWN IN FIGS. 3 AND 4.

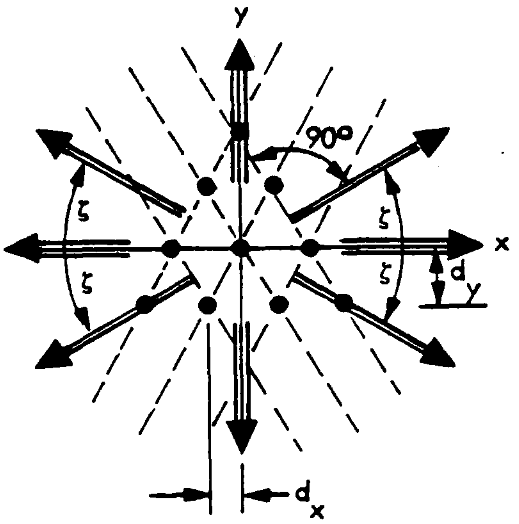

FIG. 3 APERTURE SPACE

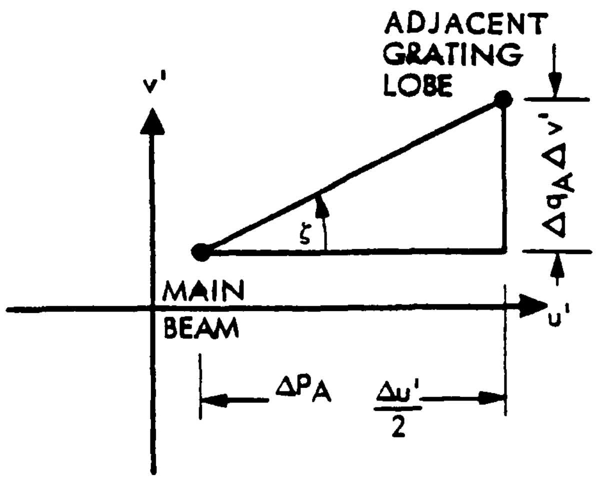

FIG. 4 BEAM SPACE

FROM FIGS. 3 AND 4, IT IS SEEN THAT ALONG THE LINES $v' = \pm u' \tan\zeta$:

$$\left| \tan\zeta \right| = \left| \frac{-1}{d_y/d_x} \right| \text{ (SEE FIG. 3) , AND } \left| \tan\zeta \right| = \left| \frac{\Delta q_A \, \Delta v'}{\Delta p_A \, (\Delta u'/2)} \right| \text{ (SEE FIG. 4)} \qquad (10)$$

THUS:

$$\frac{d_y \, \Delta v'}{d_x \, (\Delta u'/2)} = \boxed{\left. \frac{\Delta p_A}{\Delta q_A} \right|_{v' = \pm u' \tan\zeta} = R \text{ FROM (5)}} \qquad (11)$$

GRATING LOBE PERIODICITY ESTABLISHES THE REQUIRED PHASE ϕ_{mn}^{pq}

I_1 OF (9) MUST TAKE ON ALL INTEGER VALUES ($\pm$) ALONG BOTH u' AND v' , AND ALONG THE LINES $v' = \pm u' \tan\zeta$. EVALUATING (9) FOR $I_1 = 1$, $\Delta q_A = 0$:

$$S = \left. \frac{2\pi}{\Delta m \Delta p_A} \right|_{\substack{\Delta q_A = 0 \\ I_1 = 1}} = \frac{2\pi}{\alpha} \, , \qquad (12)$$

WHERE α = INTEGER INDEPENDENT OF $\Delta m, \Delta n, \Delta p_A, \Delta q_A$

SUBSTITUTING (12) INTO (9) GIVES (13):

$$\Delta m \, \Delta p_A + R \, \Delta n \Delta q_A = \alpha I_1 \qquad (13)$$

FROM ARRAY GEOMETRY:

$$(\Delta m \pm \Delta n) = 2 I_2 \text{ , WHERE } I_2(\Delta m, \Delta n) = \pm \text{ INTEGER} \qquad (14)$$

EVALUATING (13) ALONG THE LINE $v' = u' \tan\zeta$ AND USING (11) AND (14) GIVES:

$$\left. 2R \, I_2(\Delta m, \Delta n) \, \Delta q_A \right|_{v' = u' \tan\zeta} = \alpha I_1 \, (\Delta m, \Delta n, \Delta p_A, \Delta q_A) \qquad (15)$$

NOW

$$\left. \Delta q_A \right|_{v' = u' \tan\zeta} = N I_3 \, (\Delta p_A, \Delta q_A) \, ,$$

WHERE N = FIXED PARAMETER (INTEGER)

$I_3 = \pm$ INTEGER (16)

$$2\,RN\,I_3\,(\Delta p_A,\Delta q_A)\;I_2\,(\Delta m,\Delta n) = \alpha I_1\,(\Delta m,\Delta n,\Delta p_A,\Delta q_A) \quad ; \tag{17}$$

HENCE $\alpha = 2RN$; (9) BECOMES (18)

$$\frac{\Delta m \Delta p_A}{2NR} + \frac{\Delta n \Delta q_A}{2N} = I_1 \tag{19}$$

(19) MUST HOLD FOR ALL $(\Delta m, \Delta n)$ INCLUDING $(\pm 1, \pm 1)$, AND ALL $(\Delta p_A, \Delta q_A)$;
(19) THUS FINALLY BECOMES

$$\boxed{\frac{\Delta p_A}{2NR} + \frac{\Delta q_A}{2N} = I}\;, \text{ WHERE } \quad I = 0\ ,\ \pm 1\ ,\ \pm 2\ ,\ \text{ETC.} \tag{20}$$

ALL GRATING LOBES ARE GIVEN BY :

$$\Delta q_A = N\,I_q \quad , \quad \Delta p_A = NR\,I_p \quad , \tag{21}$$

WHERE I_p AND I_q ARE BOTH EVEN INTEGERS $(\pm)$ OR BOTH ODD INTEGERS $(\pm)$. FOR (20) TO REPRESENT THE GRATING LOBE SERIES, EITHER R OR I/R MUST BE AN INTEGER. BOTH CASES ARE THE SAME SOLUTION WITH p AND q INTERCHANGING ROLES; THUS, LET R BE AN INTEGER.

FROM (18) AND (12) : $S = \frac{\pi}{NR}$; (22)

THE REQUIRED PHASE BECOMES :

$$\boxed{\phi_{mn}^{pq} = \frac{\pi}{NR}\,(m'p' + R\,n'q') \quad \text{AND} \quad (\Delta u,\ \Delta v) = (2\pi/NR,\ \pi/N)\quad ,} \tag{23}$$

WHERE $\Delta u,\ \Delta v = kd_x \Delta u'\ ,\ kd_y \Delta v'$ (24)

RN^2 BEAMS IN p,q SPACE AND RN^2 ELEMENTS IN m,n SPACE COVER THE SAME LATTICE

DEFINE E_{ij} = i^{th} BEAM EVALUATED AT j^{th} BEAM PEAK $(i = 1,2,3 \ldots)$ $(j = 1,2,3 \ldots)$; THEN THE MATRIX :

$$\left[E_{ij}\right] \text{ IS AN IDENTITY} \quad , \tag{25}$$

WHERE

$$\left[E_{ij}\right] = \begin{bmatrix} E_{11} & E_{12} & \cdots \\ E_{21} & E_{22} & \cdots \\ \vdots & & \end{bmatrix} ,$$

$$E^{pq}(u_{rs}, v_{rs}) = \frac{1}{N_e} \sum^{mn} e^{\,j\left[m\,(r-p)\frac{\pi}{NR} + n\,(s-q)\frac{\pi}{N}\right]} \begin{array}{l} = 1 \ \text{FOR } p,q = r,s \\ = 0 \ \text{OTHERWISE} \end{array} \tag{26}$$

WHERE (r, s) IS ANY (p, q) CONTAINED IN THE BEAM SET.

IT FOLLOWS THAT (IN UNITS OF π/NR RADIAN) THE MATRIX OF PHASES:

$$[p]\,[m]^T + R\,[q]\,[n]^T \tag{27}$$

CORRESPONDS TO A UNITARY MATRIX IN WHICH $[m]$, $[n]$, $[p]$, AND $[q]$ ARE COLUMN MATRICIES FOR THE COMPLETE SETS OF (m,n) AND (p,q) COORDINATES. ALL BEAM SPACE IS EXHAUSTED BY (20) FOR RN^2 BEAMS; FURTHER, SINCE (25) IS A SQUARE MATRIX, THERE ARE RN^2 ELEMENTS IN THE ARRAY.

ALL ARRAY SPACE MUST BE EXHAUSTED BY :

$$\boxed{\frac{\Delta m_A}{2NR} + \frac{\Delta n_A}{2N} = I} , \quad (I = 0, \pm1, \pm2 \ldots) \tag{28}$$

THAT IS, THE NUMBER OF ELEMENTS AND THE ARRAY SHAPE MUST BE SUCH THAT IT CAN BE TRANSLATED IN THE (m,n) DOMAIN REPEATEDLY BY $(\Delta m_A, \Delta n_A)$ SATISFYING (28) FOR ALL VALUES OF THE INTEGER I , AND THEREBY COVERING , ONLY ONCE , ALL POSSIBLE ELEMENT LOCATIONS ON THE INFINITE TRIANGULAR GRID STRUCTURE.

A SOLUTION EXISTS ONLY IF :

$$\frac{N}{2}(R+1) = \text{INTEGER} \tag{30}$$

THUS THE LATTICE OF THE BEAMS IN (p,q) SPACE IS IDENTICAL TO THE LATTICE OF THE ELEMENTS IN (m,n) SPACE.

FIG. 5 FORM OF MATRIX [M]

N^2 BLOCKS OF R PORTS FED BY R BLOCKS OF N^2 PORTS

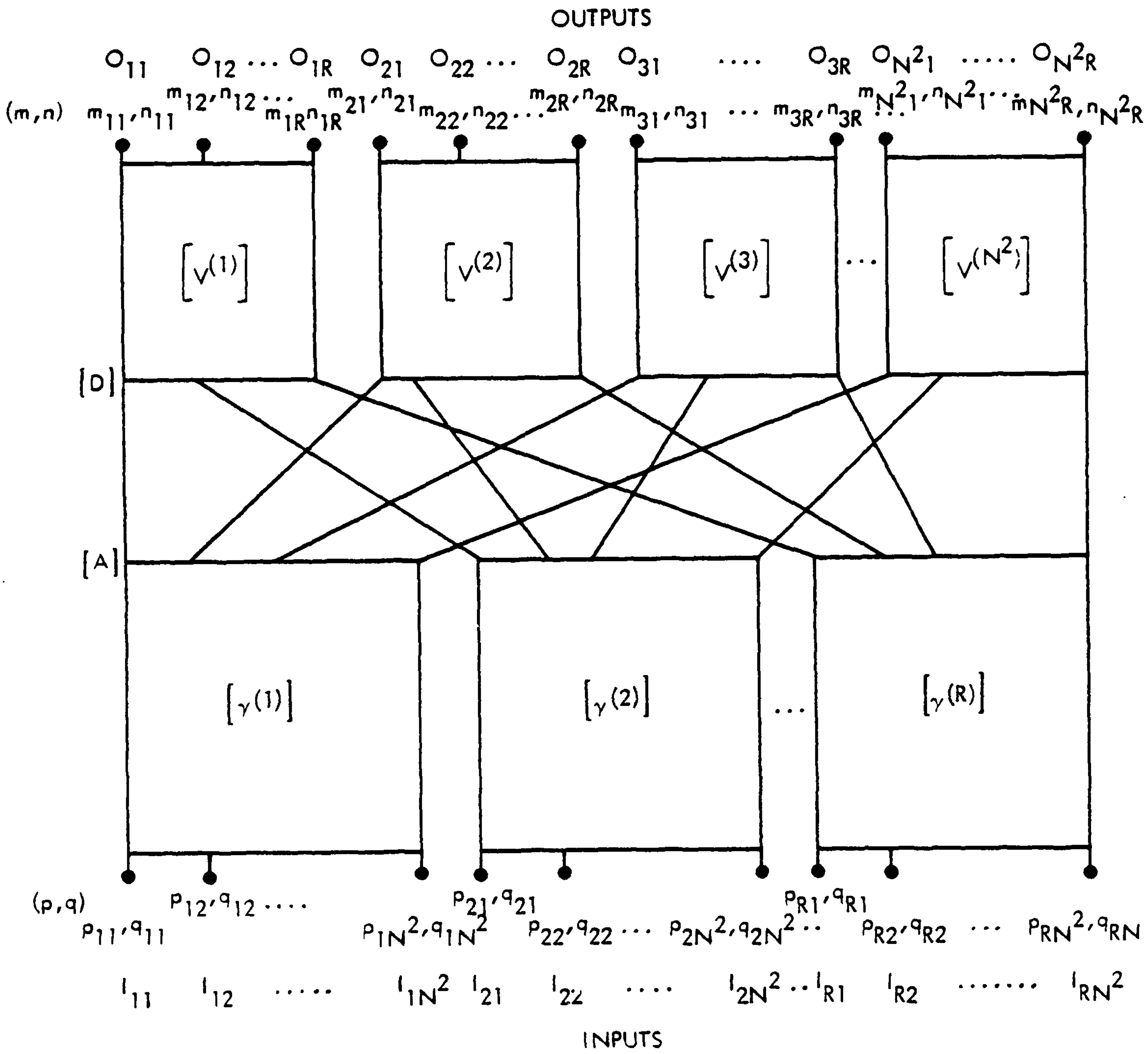

MATRIX TRANSFORMATION ELIMINATES m_o, n_o, p_o, q_o

UNLESS SPECIFIED OTHERWISE, MATRICIES ARE PHASE ONLY IN UNITS OF $\frac{\pi}{RN}$ RADIANS

OUTPUT $0 = (m-m_o)\ (p-p_o) + R\,(n-n_o)\ (q-q_o)$ FOR 0° INPUTS AT I (31)

$$0 = -\ (mp_o + Rnq_o)$$
$$- \left\{ m_o\ (p-p_o) + Rn_o\ (q-q_o) \right\}$$
$$+\ (mp + Rnq)$$

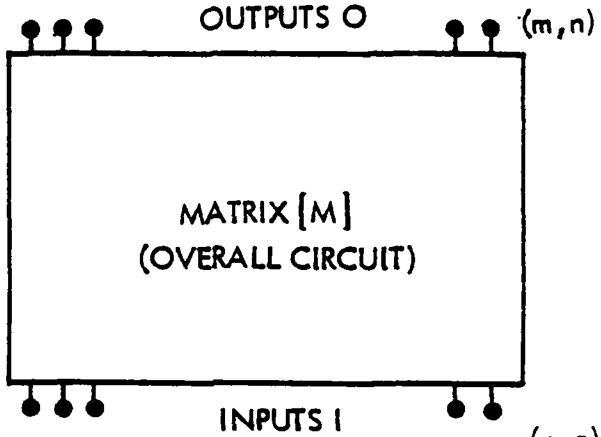

Fig. 6

EQUIVALENT TO:

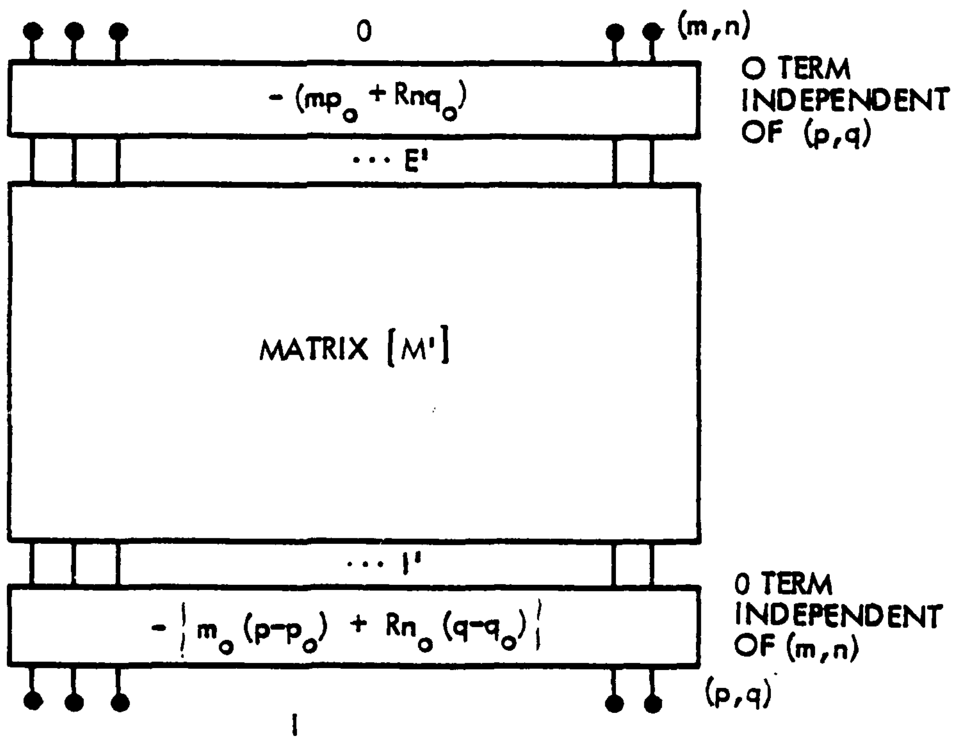

WHERE $\boxed{\text{OUTPUT } E' = mp + Rnq}$ FOR 0° INPUTS AT I' (32)

Fig. 7

MATRIX TRANSFORMATION CONVERTS (m,n) AND (p,q) TO $(\Delta m, \Delta n)$ AND $(\Delta p, \Delta q)$ (ELIMINATES $m_{11}, n_{11}, p_{11}, q_{11}$)

$$\text{OUTPUT } E' = mp + Rnq \text{ FOR } 0^\circ \text{ INPUTS AT } I' \tag{33}$$

$$E' = (m-m_{11})\,p_{11} + R\,(n-n_{11})\,q_{11} + m_{11}p + Rn_{11}q + (m-m_{11})\,(p-p_{11}) + R\,(n-n_{11})\,(q-q_{11}) \tag{34}$$

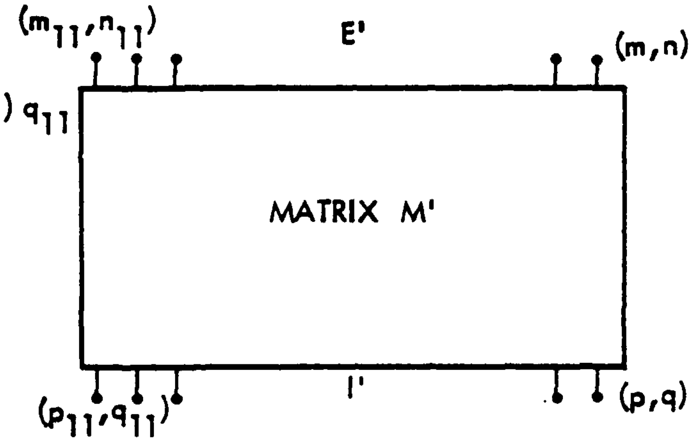

FIG. 8

EQUIVALENT TO:

$$\Delta m = m-m_{11} \tag{35}$$

$$\Delta n = n-n_{11} \tag{36}$$

$$\Delta p = p-p_{11} \tag{37}$$

$$\Delta q = q-q_{11} \tag{38}$$

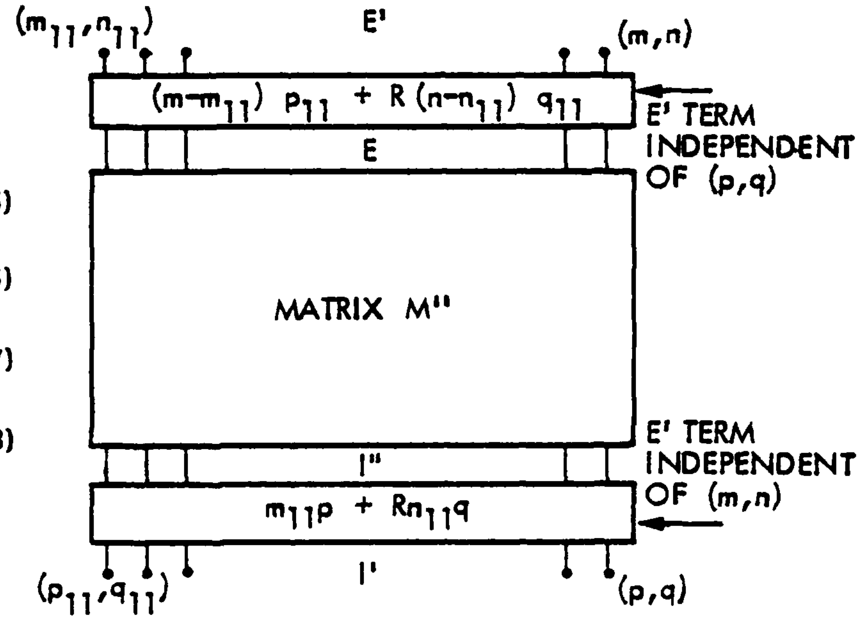

FIG. 9

WHERE $\boxed{\text{OUTPUT } E = \Delta m\Delta p + R\Delta n\Delta q}$ FOR 0° INPUTS AT I'' (39)

THE SCATTERING MATRIX [S] OF A $2RN^2$ PORT JUNCTION IS OF RANK $2RN^2$. LET THE FIRST RN^2 PORTS BE CONSIDERED INPUTS, THE SECOND RN^2 PORTS THE OUTPUTS.

FURTHER, POSTULATE THAT ALL INPUT PORTS ARE COMPLETELY MATCHED AND ISOLATED FROM ONE ANOTHER IF THE OUTPUT PORTS ARE TERMINATED IN THEIR RESPECTIVE CHARACTERISTIC IMPEDANCES. LIKEWISE, POSTULATE THE SAME SITUATION TO BE TRUE FOR THE OUTPUT PORTS.

FINALLY, POSTULATE THAT THE NETWORK IS LOSSLESS. IT THEN FOLLOWS THAT THE SCATTERING MATRIX IS OF THE FORM:

$$[S] = \left[\begin{array}{ccccc|ccccc} 0 & 0 & \cdots & & 0 & & & & & \\ 0 & 0 & \cdots & & 0 & & & & & \\ \cdot & \cdot & \cdots & & 0 & & & [M] & & \\ \cdot & \cdot & \cdots & & \cdot & & & & & \\ 0 & \cdot & \cdots & & 0 & & & & & \\ \hline & & & & & 0 & 0 & \cdots & & 0 \\ & & & & & 0 & 0 & \cdots & & 0 \\ & & [M^T] & & & \cdot & \cdot & \cdots & & 0 \\ & & & & & \cdot & \cdot & \cdots & & \cdot \\ & & & & & 0 & \cdot & \cdots & & 0 \end{array}\right] \tag{30a}$$

WHERE $[M]$ AND $[M^T]$ ARE SQUARE MATRICES OF RANK RN^2.

SINCE $[S]$ IS UNITARY, $[M]$ AND $[M^T]$ ARE ALSO UNITARY.

THE REMAINING PART OF THIS PAPER IS TO DETERMINE THE MATRIX $[M]$ AND TO SYNTHESIZE THE NETWORK REQUIRED.

THE EQUIVALENCE OF $[S]$ UNDER A SIMILARITY TRANSFORMATION IS USED TO SIMPLIFY THE SYNTHESIS OF THE NETWORK; i.e.

$$[S'] = [P]^T [S][P] \tag{30b}$$

WHERE $[P]$ IS A DIAGONAL MATRIX OF PHASE SHIFTS DUE TO A CHANGE IN TERMINAL PLANES AT WHICH THE NETWORK IS OBSERVED.

MATRIX DEFINITIONS

$$[\Delta m]^T = [\Delta m_1 \;\; \Delta m_2 \ldots \Delta m_{N^2}] \;,\quad [\Delta n]^T = [\Delta n_1 \quad \Delta n_2 \ldots \Delta n_{N^2}] \qquad (40)$$

$$[\Delta m_i]^T = [\Delta m_{i1} \;\; \Delta m_{i2} \ldots \Delta m_{iR}] \;,\quad [\Delta n_i]^T = [\Delta n_{i1} \;\; \Delta n_{i2} \ldots \Delta n_{iR}] \qquad (41)$$

$$\Delta m_{ij} = m_{ij} - m_{11} \quad \Delta n_{ij} = n_{ij} - n_{11} \;,\quad (\Delta m_{11} \,,\, \Delta n_{11}) = (0,0) \qquad (42)$$

$$[\delta m_i]^T = [\delta m_{i1} \;\; \delta m_{i2} \ldots \delta m_{iR}] \;,\quad [\delta n_i]^T = [\delta n_{i1} \;\; \delta n_{i2} \ldots \delta n_{iR}] \qquad (43)$$

$$\delta m_{ij} = m_{ij} - m_{i1} \;,\quad \delta n_{ij} = n_{ij} - n_{i1} \quad (\delta m_{i1} \,,\, \delta n_{i1}) = (0,0) \qquad (44)$$

$$[\Delta p_r]^T = [\Delta p_{r1} \;\; \Delta p_{r2} \ldots \Delta p_{rN^2}] \;,\quad [\Delta q_r]^T = [\Delta q_{r1} \;\; \Delta q_{r2} \ldots \Delta q_{rN^2}] \qquad (45)$$

$$[\Delta p]^T = [\Delta p_1^T \;\; \Delta p_2^T \ldots \Delta p_R^T] \;,\quad [\Delta q]^T = [\Delta q_1^T \;\; \Delta q_2^T \ldots \Delta q_R^T] \qquad (46)$$

$$\Delta p_{rk} = p_{rk} - p_{11} \;,\quad \Delta q_{rk} = q_{rk} - q_{11} \;;\quad (\Delta p_{11} \,,\, \Delta q_{11}) = (0,0) \qquad (47)$$

$$[\delta p_r]^T = [\delta p_{r1} \;\; \delta p_{r2} \ldots \delta p_{rN^2}] \;,\quad [\delta q_r]^T = [\delta q_{r1} \;\; \delta q_{r2} \ldots \delta q_{rN^2}] \qquad (48)$$

$$\delta p_{rk} = p_{rk} - p_{r1} \;,\quad \delta q_{rk} = q_{rk} - q_{r1} \;;\quad (\delta p_{r1} \,,\, \delta q_{r1}) = (0,0) \qquad (49)$$

$$[E_i] = [E_{i1} \;\; E_{i2} \ldots E_{iR}] \;,\quad [D_i] = [D_{i1} \;\; D_{i2} \ldots D_{iR}] \qquad (50)$$

$$[E_i^{rk}] \;,\quad [D_i^{rk}] = [E_i] \;,\quad [D_i] \quad \text{FOR INPUT } p_{rk} \,,\, q_{rk} \text{ ONLY} \qquad (51)$$

$$\left[E_i^k\right] = \begin{bmatrix} E_i^{1k} \\ E_i^{2k} \\ \vdots \\ E_i^{Rk} \end{bmatrix}, \quad \left[D_i^k\right] = \begin{bmatrix} D_i^{1k} \\ D_i^{2k} \\ \vdots \\ D_i^{Rk} \end{bmatrix}; \quad \left[E_i^k\right], \left[D_i^k\right], \; R \times R \tag{52}$$

$$\left[A_i^{(\;)}\right] = \begin{bmatrix} A_i^{j1} \\ A_i^{j2} \\ \vdots \\ A_i^{jN^2} \end{bmatrix}, \quad (N^2 \times N^2) \tag{53}$$

$$\left[A_i^{ji}\right] = \text{RESPONSE } \left[A_i\right] \text{ FOR INPUT } p_{ji}, \; q_{ji} \text{ ONLY} \tag{54}$$

$$\left[A_i\right] = \left[A_{i1} \; A_{i2} \ldots A_{iN^2}\right] \tag{55}$$

$$\left[\delta m'_{i1}\right]^T = \left[\delta m'_{11} \; \delta m'_{21} \ldots \delta m'_{N^2 1}\right], \quad \left[\delta n'_{i1}\right]^T = \left[\delta n'_{11} \; \delta n'_{21} \ldots \delta n'_{N^2 1}\right] \tag{56}$$

$$\delta m'_{i1} = m_{i1} - m_{11}, \quad \delta n'_{i1} = n_{i1} - n_{11} \tag{57}$$

FOR N AND/OR R NOT PRIME, $[T]$ AND/OR $[V_o]$ ARE COMPOSED OF ELEMENTARY MATRICIES ζ_M AND ζ_K

DEFINE $[\zeta_n]$ = OVERALL MATRIX BELOW

n PORTS = MK PORTS

FIG. 10

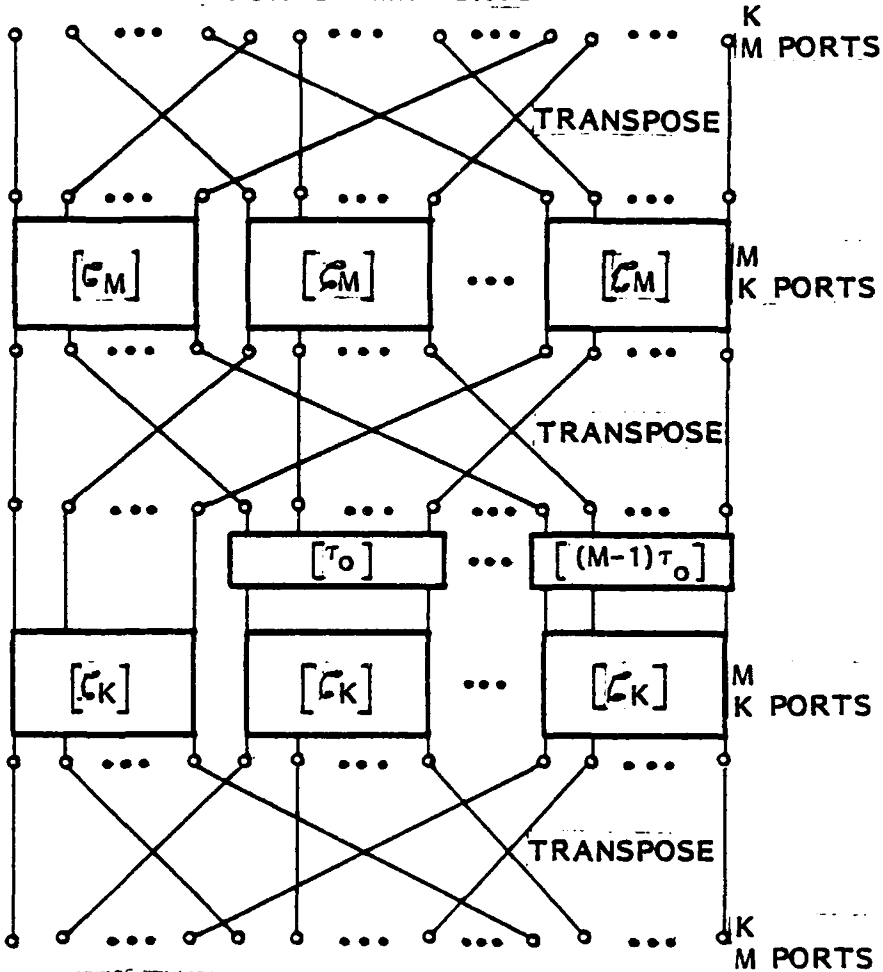

NOTE: THE FIXED PHASORS $[(M-1)\ \tau_o]$ MAY BE DELETED PROVIDED M & K DO NOT CONTAIN A COMMON FACTOR; HOWEVER, THE INPUT AND/OR OUTPUT LINE TRANSPOSITIONS MUST CHANGE.

DEFINE "STANDARD" FORM OF PORT: $[\zeta_\ell] \equiv \begin{bmatrix} 0 & 0 & 0 & \cdots \\ 0 & 2\pi/\ell & 4\pi/\ell & \cdots \\ 0 & 4\pi/\ell & 8\pi/\ell & \cdots \\ 0 & 6\pi/\ell & 12\pi/\ell & \cdots \\ \vdots & \vdots & \vdots & \end{bmatrix}$ RAD

- $[\ _n]$ WILL BE IN STANDARD FORM IF $[\zeta_M]$ AND $[\zeta_K]$ ARE, PROVIDED $[\tau_o]$ = $[0\ \ 2\pi/n\ \ 4\pi/n\ \ 6\pi/n\ \ldots\ 2\pi(K-1)/n]$ RAD

$[V_o^i]$, THE REMAINING PART OF $[V^i]$ SEPARATES BEAMS INTO ORTHONORMAL SETS

DEFINE BEAM SETS SUCH THAT

$$(p,q)_{SET\ r} = (p,q)_{SET\ 1} + (r-1, r-1) \tag{59}$$

$$r = 1,2,3 \ldots R; \qquad \Delta p_{rk} = \Delta p_{1k} + r-1, \qquad \Delta q_{rk} = \Delta q_{1k} + r-1 \tag{60}$$

THEN

$$E_{ij}^{rk} = E_{ij}^{1k} + (r-1)\ (\Delta m_{ij} + R\,\Delta n_{ij}) \tag{61}$$

OR

$$E_{ij}^{rk} = E_{ij}^{1k} + (r-1)\ (\delta m_{ij} + R\,\delta\, n_{ij}) + (r-1)\ \left\{ m_{i_1} - m_{11} + R\ (n_{i_1} - n_{11}) \right\} \tag{62}$$

NOTE:

$$E_{ij}^{1k} = \Delta m_{ij}\ \Delta p_{1k} + R\,\Delta n_{ij}\ \Delta q_{1k} \text{ IS INDEPENDENT OF THE BEAM SET.} \tag{63}$$

PLACE

$$(r-1) \left\{ m_{i1} - m_{11} + R\,(n_{i_1} - n_{11}) \right\} \text{ AT INPUT TO } V^i \text{ COUPLER ;} \tag{64}$$

SPECIFY

$$\boxed{\left[\delta m_i + R\,\delta n_i\right]^T = \left[0 \quad 2N \quad 4N \quad 6N \ \ldots\right];\ \text{VIZ.,}} \tag{65}$$

$$\text{R EVEN :} \quad \left[\delta m_i\right]^T = \left[0 \quad 2N \quad 4N \ \ldots\ 2\,(R-1)\,N\right] \tag{66}$$

$$\left[\delta n_i\right]^T = \left[0 \quad 0 \quad 0 \ \ldots \quad 0\right] \tag{67}$$

$$\text{R ODD:}\quad \left[\delta m_i\right]^T = \left[0 \quad 2N \quad 4N \ldots (R-1)\,N \;\vdots\; N \quad 3N \quad 5N \ldots (R-2)\,N\right] \tag{68}$$

$$\left[\delta n_i\right]^T = \left[0 \quad 0 \quad 0 \ldots \quad 0 \;\vdots\; N \quad N \quad N \ldots \quad N\right] \tag{69}$$

MODULO 2RN

THEN

$\boxed{\left[V_o\right] \text{ IS UNITARY AND DIAGONALIZES } \left[D_i^k\right] :}$

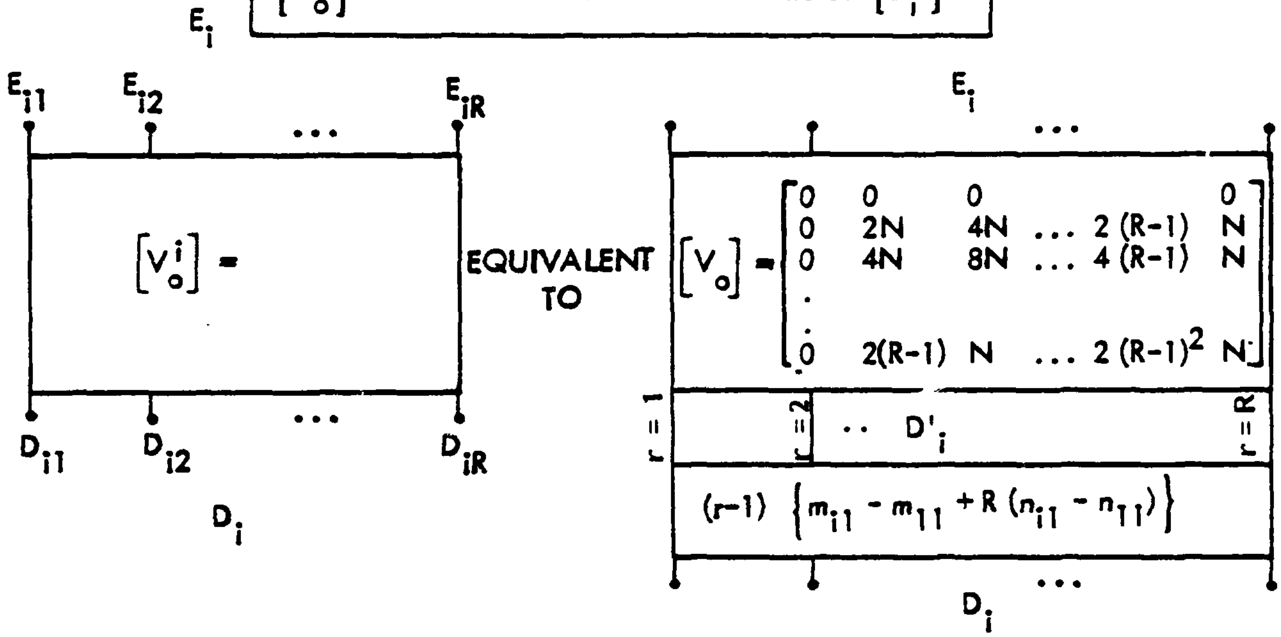

(70)

$$\left[D_i^k\right] = \left[E_i^k\right]\left[V^i\right]^{-1} = \text{DIAG}\begin{bmatrix} D_{i1}^{1k} & & & \\ & D_{i2}^{2k} & & \\ & & \ddots & \\ & & & D_{iR}^{Rk} \end{bmatrix} \tag{71}$$

WHERE

$$D_{ij}^{jk} = \delta m'_{i1}\ \delta p_{jk} + R\,\delta n'_{i1}\ \delta q_{jk}\ , \text{ SAME FOR ALL SETS } (j = 1,2 \ldots R) \tag{72}$$

$\left[\gamma_o^{(\ )}\right]$, THE REMAINING PART OF $\left[\gamma^{(r)}\right]$ IS INDEPENDENT OF THE SET

SINCE $A_{ji} = D_{ij}$, IT FOLLOWS THAT (73)

$$\left[A_i^{(\ )}\right] = \left[\delta p_j\right]\left[\delta m'_{i1}\right]^T + R\left[\delta q_j\right]\left[\delta n'_{i1}\right]^T \tag{74}$$

$$A_{ji}^{jk} = \delta m_{i1}\ \delta p_{jk} + R\delta n_{i1}\ \delta q_{jk} \tag{75}$$

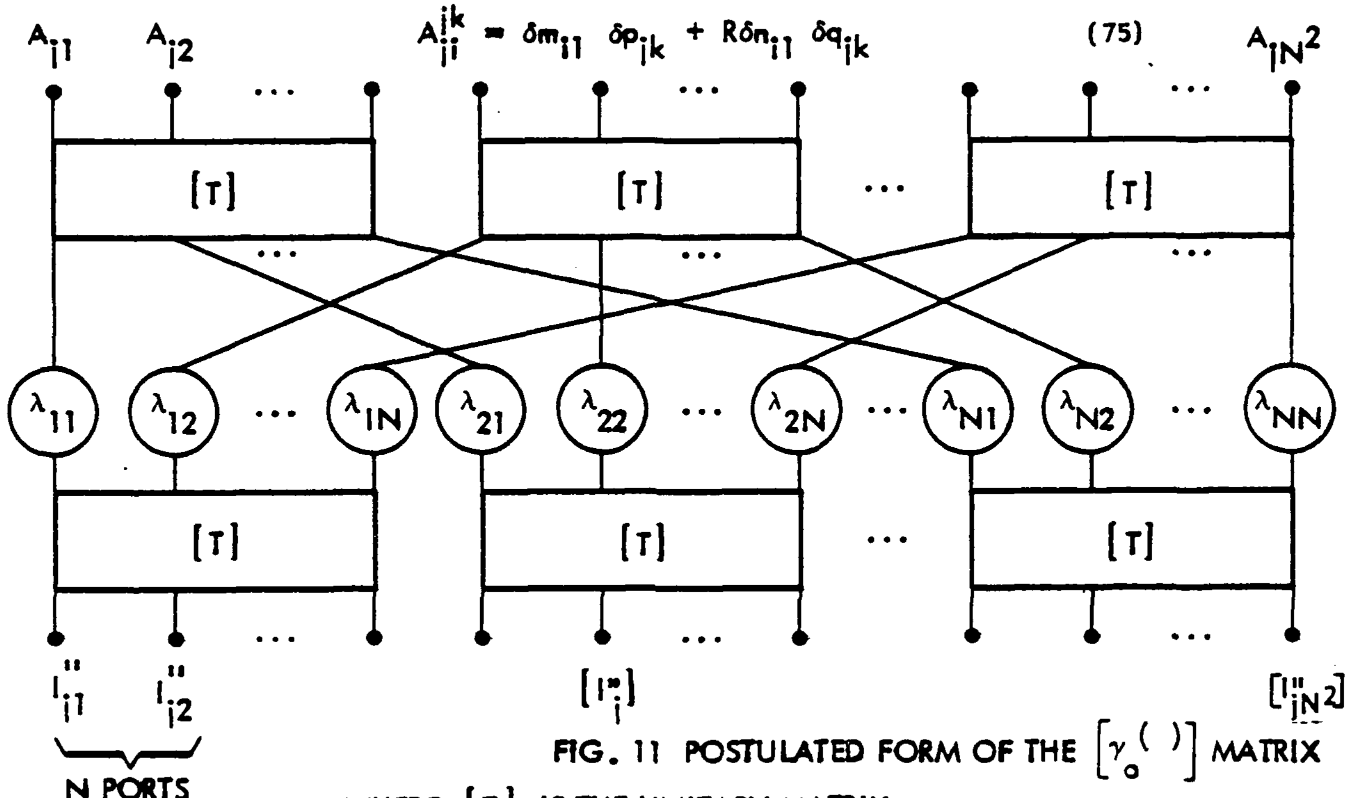

FIG. 11 POSTULATED FORM OF THE $\left[\gamma_o^{(\ )}\right]$ MATRIX

WHERE [T] IS THE UNITARY MATRIX:

$$[T] \triangleq \begin{bmatrix} T_1 \\ T_2 \\ T_3 \\ \vdots \\ T_N \end{bmatrix} = \begin{bmatrix} 0 & 0 & 0 & 0 \ \dots & 0 \\ 0 & 2R & 4R & 6R \ \dots & 2(N-1)\,R \\ 0 & 4R & 8R & 12R \ \dots & 4(N-1)\,R \\ \vdots & \vdots & \vdots & \vdots & \vdots \\ 0 & 2(N-1)\,R & 4(N-1)\,R & 6(N-1)\,R & 2(N-1)^2\,R \end{bmatrix} \tag{76}$$

AND λ_{xy} ARE FIXED PHASE SHIFTS

MATRIX FORM OF $\left[\gamma_o^{(\ )}\right]$ CIRCUIT

IT CAN BE SHOWN THAT $\left[A_i^{(\ )}\right]$ FOR THE POSTULATED CIRCUIT IS:

$$\boxed{\left[A_i^{(\ )}\right] = \left[F\right] + \left[F\right]^T + \left[L\right]} \tag{77}$$

WHERE

$$[F] \triangleq \left[\begin{array}{c|c|c|c} T_1' & T_1' & \cdots & T_1' \\ \hline T_2' & T_2' & \cdots & T_2' \\ \hline \vdots & & \cdots & \vdots \\ \hline T_N' & T_N' & & T_N' \end{array}\right], \text{ AN } N^2 \times N^2 \text{ MATRIX;} \tag{78}$$

$$\left[T_n'\right] \triangleq \begin{bmatrix} T_n \\ T_n \\ \vdots \\ T_n \end{bmatrix}, \text{ AN } N \times N \text{ MATRIX; } 1 \le n \le N \tag{79}$$

$$\left[T_n\right] = \left[0 \quad 2R\,(n-1) \quad 4R\,(n-1) \quad 6R\,(n-1) \ldots 2R\,(N-1)\;(n-1)\right] \quad 1 \times N \text{ MATRIX} \tag{80}$$

$$[L] \triangleq \left[\begin{array}{c|c|c|c} \lambda_{11}' & \lambda_{12}' & \cdots & \lambda_{1N}' \\ \hline \lambda_{21}' & \lambda_{22}' & \cdots & \lambda_{2N}' \\ \hline \vdots & \vdots & \cdots & \\ \hline \lambda_{N1}' & \lambda_{N2}' & \cdots & \lambda_{NN}' \end{array}\right], \text{ AN } N^2 \times N^2 \text{ MATRIX;} \tag{81}$$

$$\left[\lambda_{xy}'\right] \triangleq \begin{bmatrix} \lambda_{xy} & \lambda_{xy} & \cdots & \lambda_{xy} \\ \lambda_{xy} & \lambda_{xy} & \cdots & \lambda_{xy} \\ \vdots & \vdots & & \vdots \\ \lambda_{xy} & \lambda_{xy} & & \lambda_{xy} \end{bmatrix}, \text{ AN } N \times N \text{ MATRIX} \tag{82}$$

THE "REFERENCE" SOLUTION IS DEFINED

EQUATING EXPRESSIONS FOR $\left[A_i^{(\ )}\right]$ YIELDS :

$$\left[\left[\delta p_j\right]\left[\delta m'_{i1}\right]^T\right] + \left[\left[R\delta n'_{i1}\right]\left[\delta q_j\right]^T\right]^T = \left[F\right] + \left[F\right]^T + \left[L\right] , \qquad (83)$$

SUGGESTING THAT, TO WITHIN AN ADDITIVE MATRIX OF FORM $\left[L\right]$:

$$\left[\delta p_j\right] = \left[R\delta n'_{i1}\right] , \quad \left[\delta q_j\right] = \left[\delta m'_{i1}\right] \quad \text{INDEPENDENT OF } i \text{ AND } j . \qquad (84)$$

FROM NUMERICAL VALUES OF $\left[F\right]$ AND $\left[L\right]$, A SOLUTION IS :

R EVEN OR ODD

| ← N ELEMENTS → |
TYPICAL

(85)

$$\left[\delta p_j\right]^T = \left[0\ \ 0\ \ 0\ \ \ldots\ 0 \,\vdots\, R\ \ R\ \ R \ldots R \,\vdots\, 2R\ \ 2R\ \ldots\ 2R \,\vdots\, \ldots \,\vdots\, (N-1)R\ \ (N-1)R \ldots (N-1)R\right]$$

FOR ALL j (86)

$$\left[\delta n'_{i1}\right]^T = \left[0\ \ 0\ \ 0\ \ \ldots\ 0 \,\vdots\, 1\ \ 1\ \ 1 \ldots 1 \,\vdots\, 2\ \ 2\ \ldots\ 2 \,\vdots\, \ldots \,\vdots\, (N-1)\ \ (N-1) \ldots (N-1)\right]$$

FOR ALL i

$$\left[\delta m'_{i1}\right]^T = \left[0\ \ 2\ \ 4\ \ 6 \ldots (2N-2) \,\vdots\, 1\ \ 3\ \ 5\ \ 7 \ldots (2N-1) \,\vdots\, 2\ \ 4\ \ 6\ \ 8 \ldots 2N \,\vdots\, \ldots\right.$$

$$\left.\ldots \,\vdots\, (N-1)\ \ (N+1)\ \ (N+3)\ \ (N+5) \ldots (3N-3)\right] \quad \text{FOR ALL } i \qquad (87)$$

FOR R ODD : $\left[\delta q_j\right]^T = \left[\delta m'_{i1}\right]^T$ FOR ALL i AND j (88)

FOR R EVEN : $\left[\delta q_j\right]^T = \left[0\ \ 2\ \ 4\ \ 6 \ldots (2N-2) \,\vdots\, 0\ \ 2\ \ 4\ \ 6 \ldots (2N-2) \,\vdots\, \ldots \,\vdots\, 0\ \ 2\ \ 4\ \ 6\ \ (2N-2)\right]$ (89)

FOR ALL j .

WHERE

FOR R EVEN $\lambda_{xy} = R(x-1)(y-1)$, FOR R ODD $\lambda_{xy} = 2R(x-1)(y-1)$ (90)

DEFINE THIS SOLUTION AS THE "<u>REFERENCE.</u>"

THE TOTAL MATRIX $\left[\Delta p\right]\left[\Delta m\right]^T + R\left[\Delta q\right]\left[\Delta n\right]^T$ IS UNITARY . (91)

THE MODIFIED REFERENCE MATRIX PRODUCES ALL SOLUTIONS

DEFINE (m,n) AND (p,q) AS ELEMENT/BEAM COORDINATES OF REFERENCE SOLUTION RELATIVE TO SOME ARBITRARY ORIGIN. (m_A,n_A) AND (p_A,q_A) CORRESPOND TO ANY OTHER SOLUTION.

ALL SOLUTIONS ARE GIVEN BY THE PAIR OF EQUATIONS :

$$\left\{ \begin{array}{l} \dfrac{\Delta m_A}{2NR} + \dfrac{\Delta n_A}{2N} = I_1 \ (0, \pm 1, \pm 2, \text{ETC.}) \\ \\ \dfrac{\Delta p_A}{2NR} + \dfrac{\Delta q_A}{2N} = I_2 \ (0, \pm 1, \pm 2, \text{ETC.}) \end{array} \right\} \qquad (92)$$

IN WHICH

$$(m_A,n_A) = (m,n) + (\Delta m_A,\Delta n_A) \qquad (93)$$

$$(p_A,q_A) = (p,q) + (\Delta p_A,\Delta q_A) \qquad (94)$$

IT IS EASY TO SHOW THAT THE NECESSARY CHANGE IN THE REFERENCE MATRIX TO ACCOMMODATE ANY SOLUTION IS GIVEN BY ADDING AT THE OUTPUT:

$$\Delta m_A \ (p_{11}-p_o) + R\,\Delta n_A \ (q_{11}-q_o) \qquad (95)$$

AND ADDING AT THE INPUT:

$$\Delta p_A \ (m_{11}-m_o) + R\,\Delta q_A \ (n_{11}-n_o) \qquad (96)$$

THE GENERAL SOLUTION IS GIVEN BY ADDING ALL INPUT AND OUTPUT PHASES TO BECOME (THE SUBSCRIPT A IS NOW DROPPED) :

$$\text{OUTPUT:} \quad m\ (p_{11}-p_o) + Rn\ (q_{11}-q_o) - (m_{11}p_{11} + R\,n_{11}q_{11}) \qquad (97)$$

$$\text{INPUT:} \quad p\ (m_{11}-m_o) + Rq\ (n_{11}-n_o) + (m_o\,p_o + R\,n_oq_o) \qquad (98)$$

ONE IS FREE TO CHOOSE ORIGINS IN BOTH THE (m,n) AND (p,q) DOMAINS SEPARATELY AND ARBITRARILY. (m,n) AND (p,q) REFER TO ANY SOLUTION.

FIG. 12 (Δm, Δn) COORDINATES FOR N = 2, R = 3

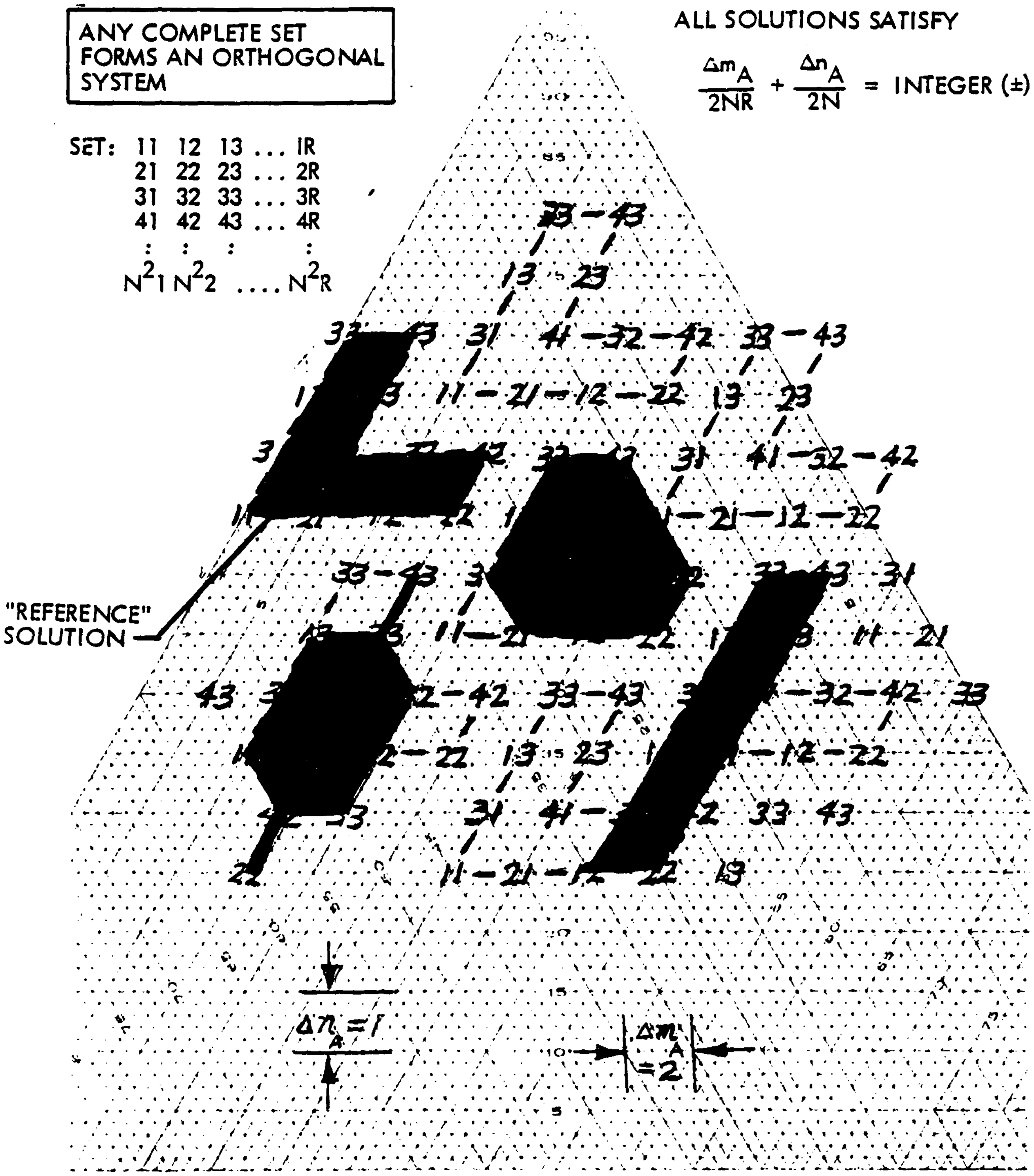

SOME COMPLETE SETS DEPICTED

FIG. 13 $(\Delta p, \Delta q)$ COORDINATES FOR N = 2, R = 3

ANY COMPLETE SET FORMS AN ORTHOGONAL SYSTEM

SET:	11	12	13	14 ...	$1N^2$
	21	22	23	24 ...	$2N^2$
	31	32	33	34 ...	$3N^2$
	:	:	:		:
	R1	R2	R3	....	RN^2

ALL SOLUTIONS SATISFY

$$\frac{\Delta p_A}{2NR} + \frac{\Delta q_A}{2N} = \text{INTEGER } (\pm)$$

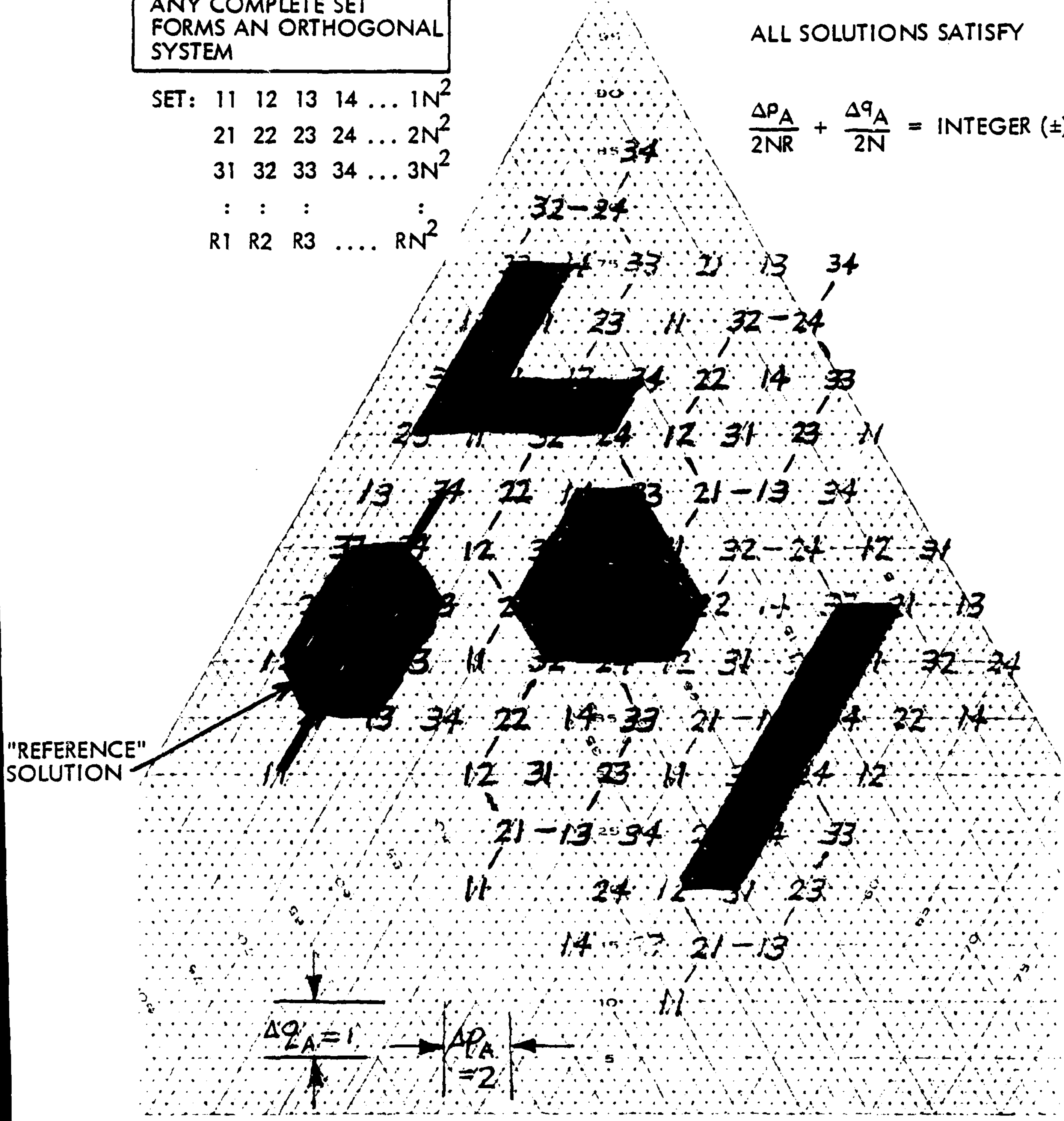

SOME COMPLETE SETS DE[illegible]CTED

FIG. 14 EXAMPLES OF THE RN^2 FAMILY THAT ARE DIAMOND-, PENTAGON-, OR HEXAGON-SHAPED

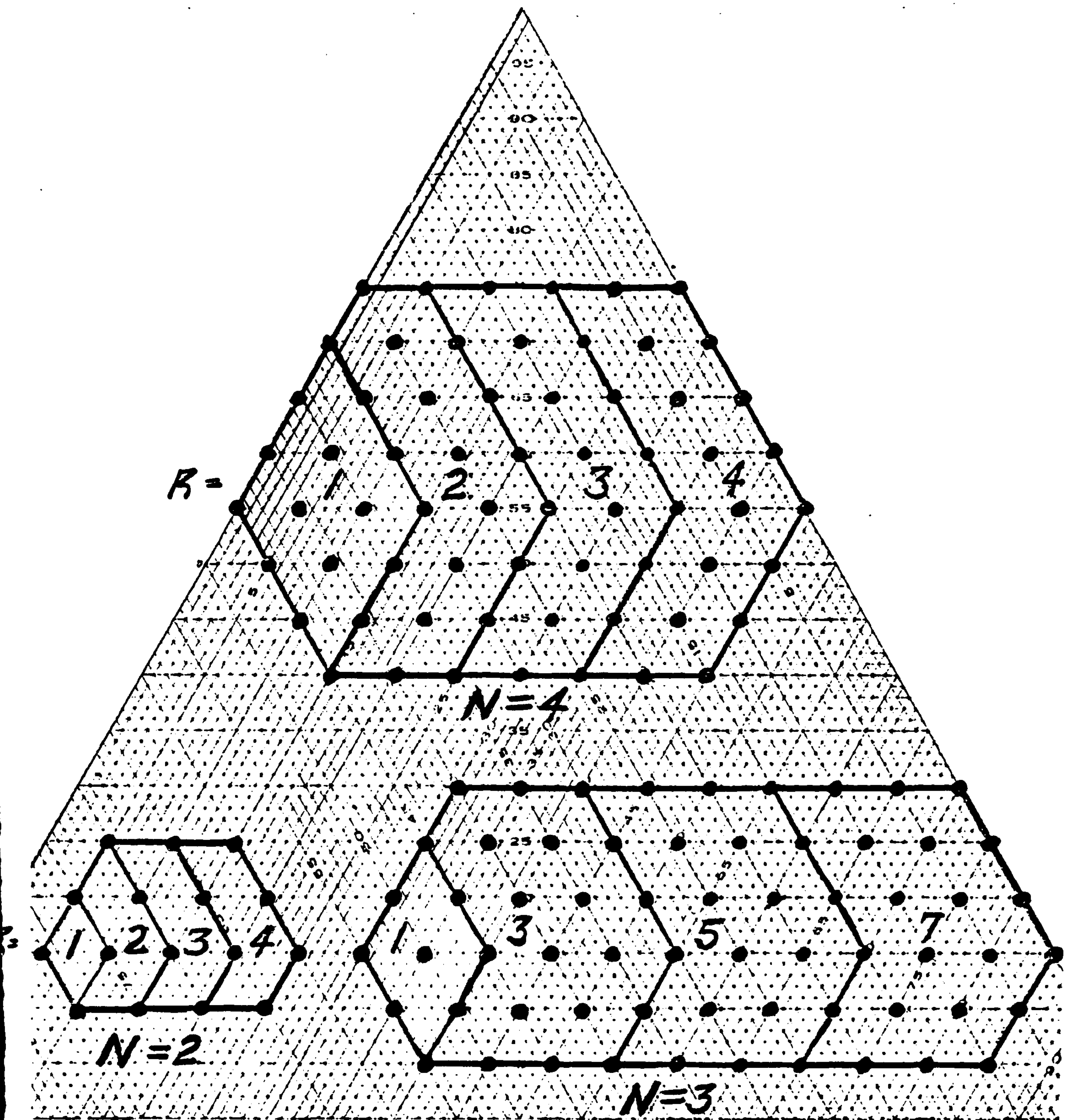

FIG. 15 EXAMPLES OF ORTHOGONAL RN^2 MULTIPLE BEAM ARRAYS (R = 3, N = 2)

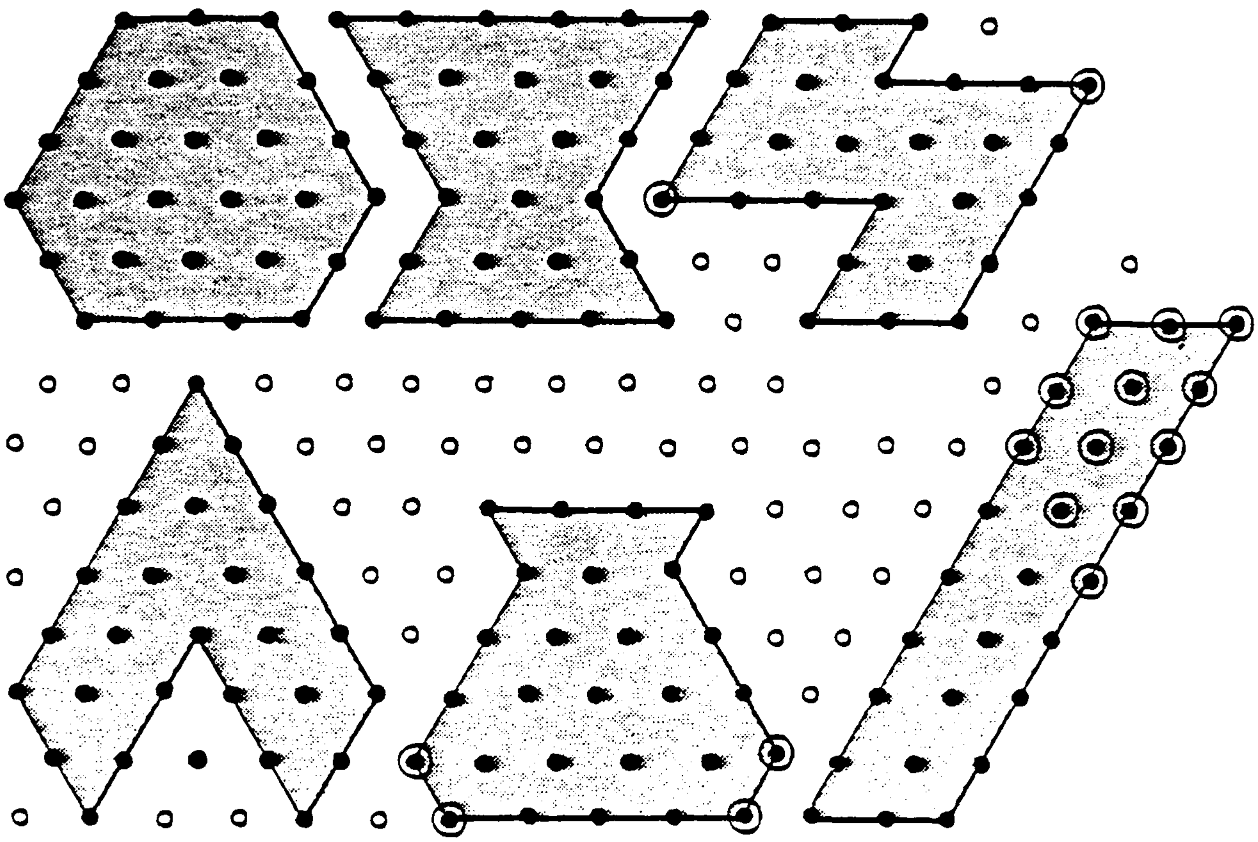

FIG. 16 MULTIPLE-BEAM CYLINDRICAL ARRAYS FORMED FROM PLANAR ARRAYS USING THE RN^2 FAMILY

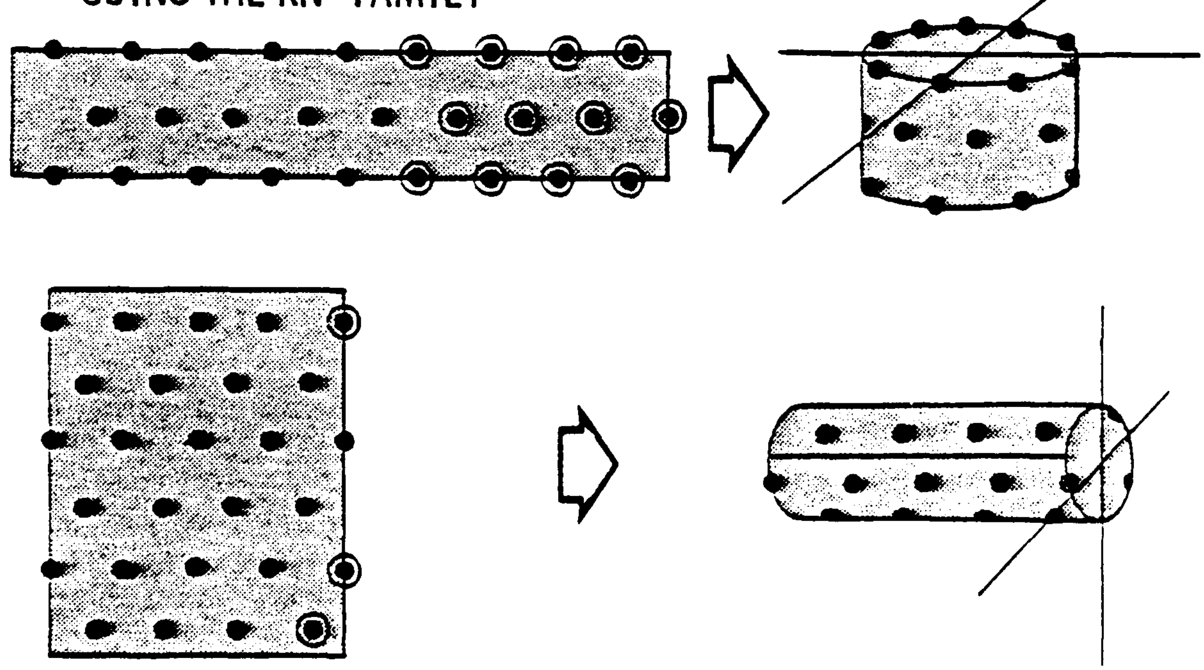

FIG. 17 TYPICAL ANTENNA PATTERN FOR HEXAGON ARRAY (R = 3, N = 4)

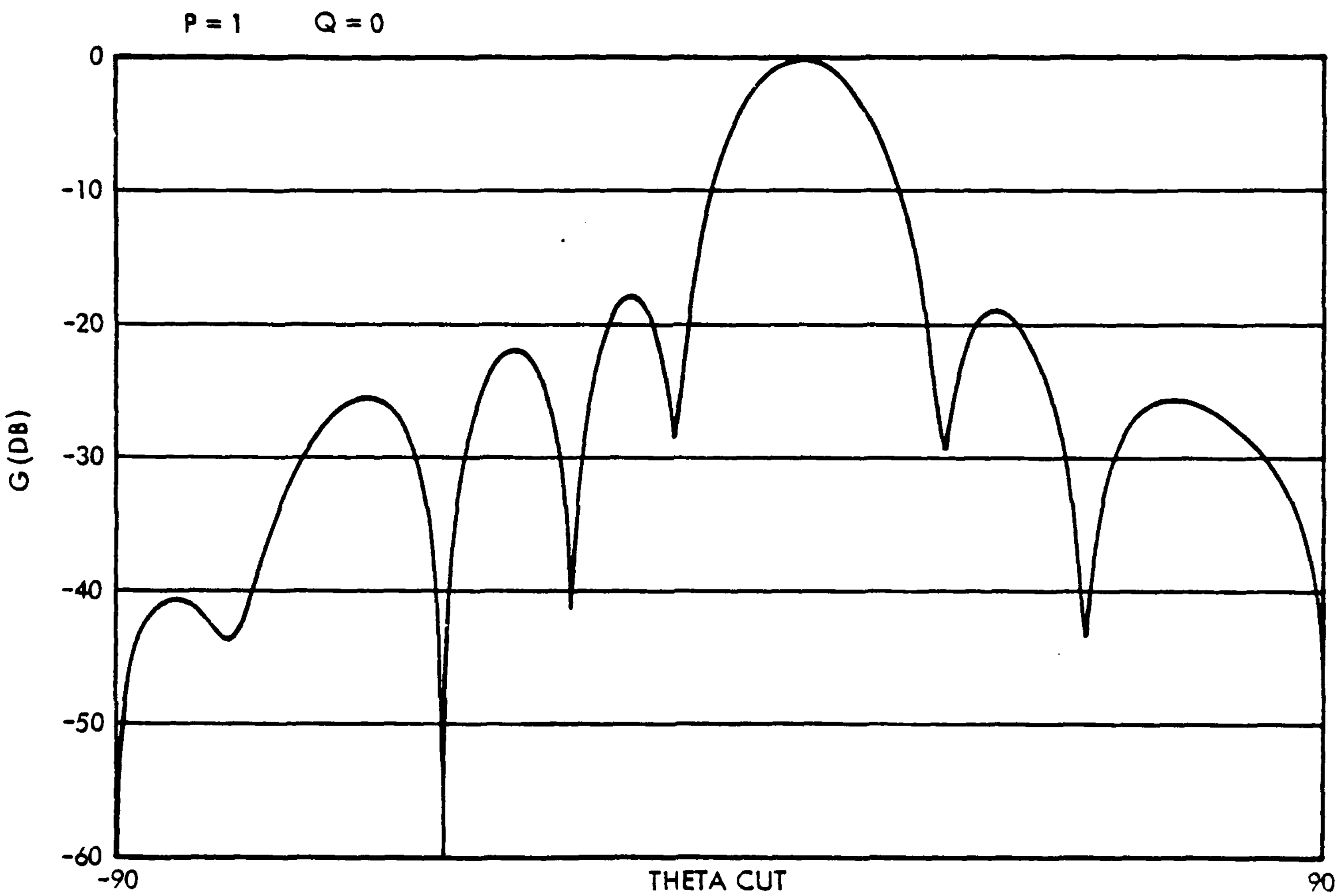

NOTE: 48 ELEMENTS AT 100 MHZ

FIG. 18 CROSSOVER LEVEL BETWEEN THREE BEAMS FOR DIAMOND-, PENTAGON-, OR HEXAGON-SHAPED ARRAYS

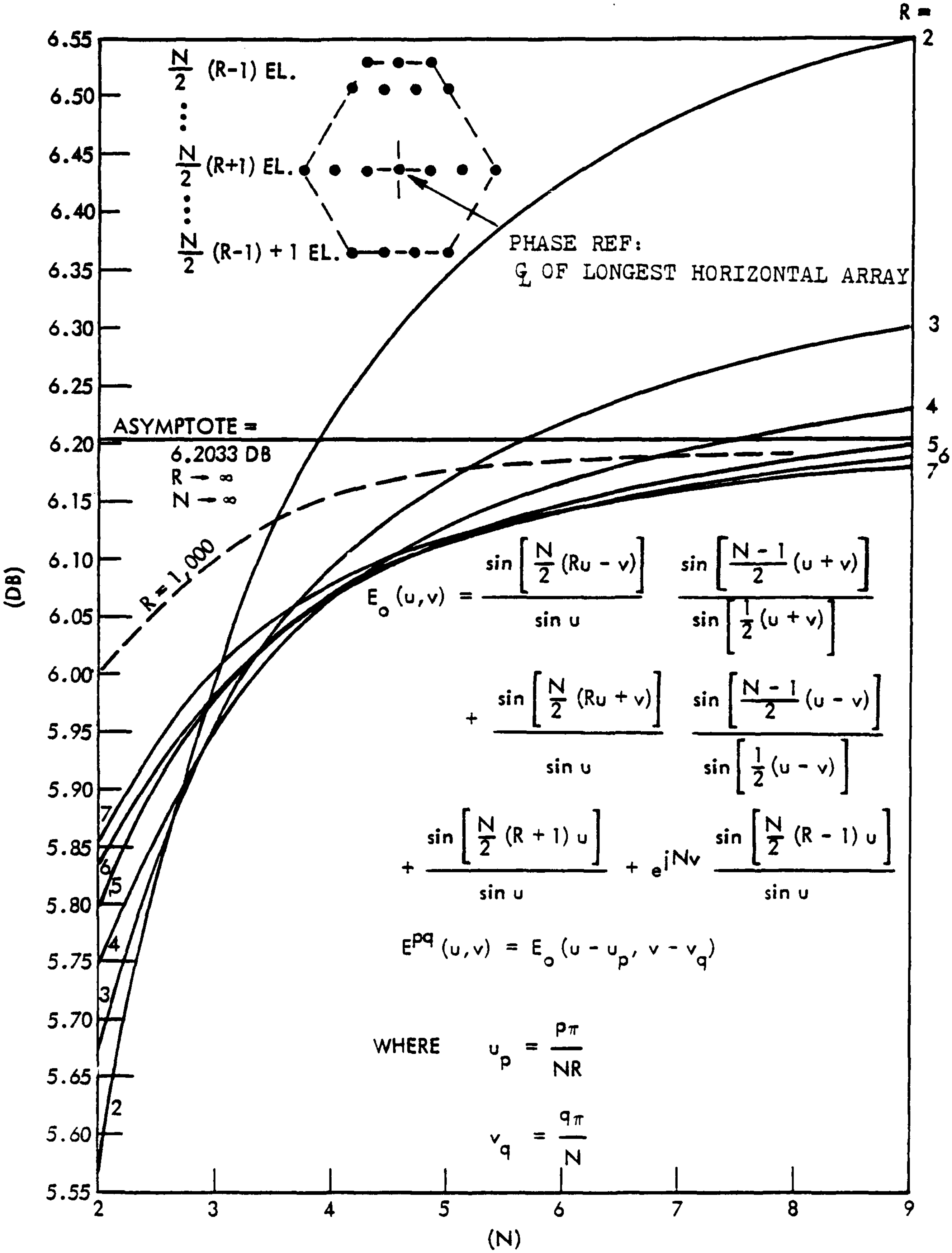

FIG. 19 CROSSOVER LEVEL BETWEEN TWO BEAMS FOR DIAMOND-, PENTAGON-, OR HEXAGON-SHAPED ARRAYS

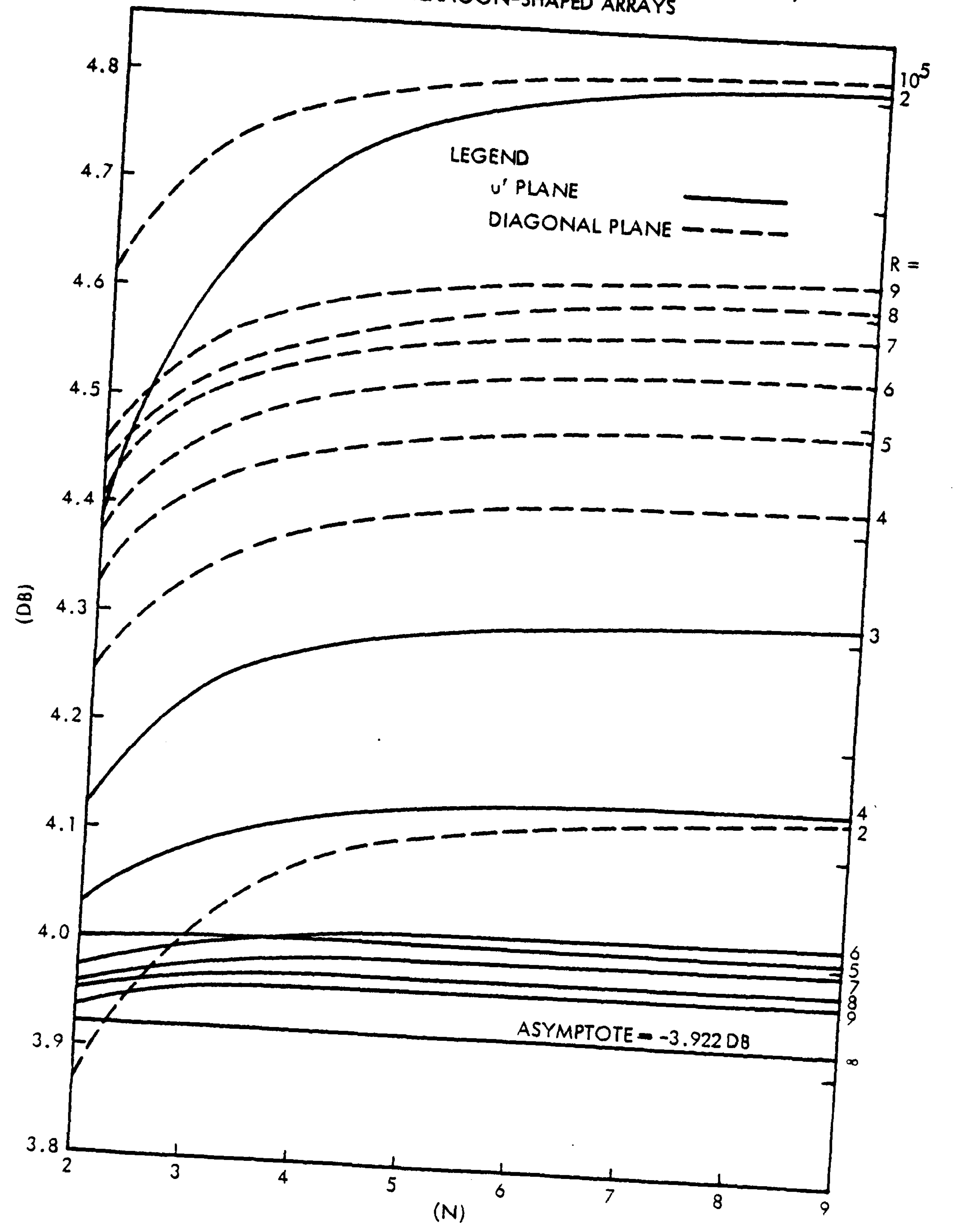

FIG. 20 THE GENERAL MULTIPLE-BEAM FORMING MATRIX FOR THE RN^2 MULTIPLE BEAM ARRAY FAMILY

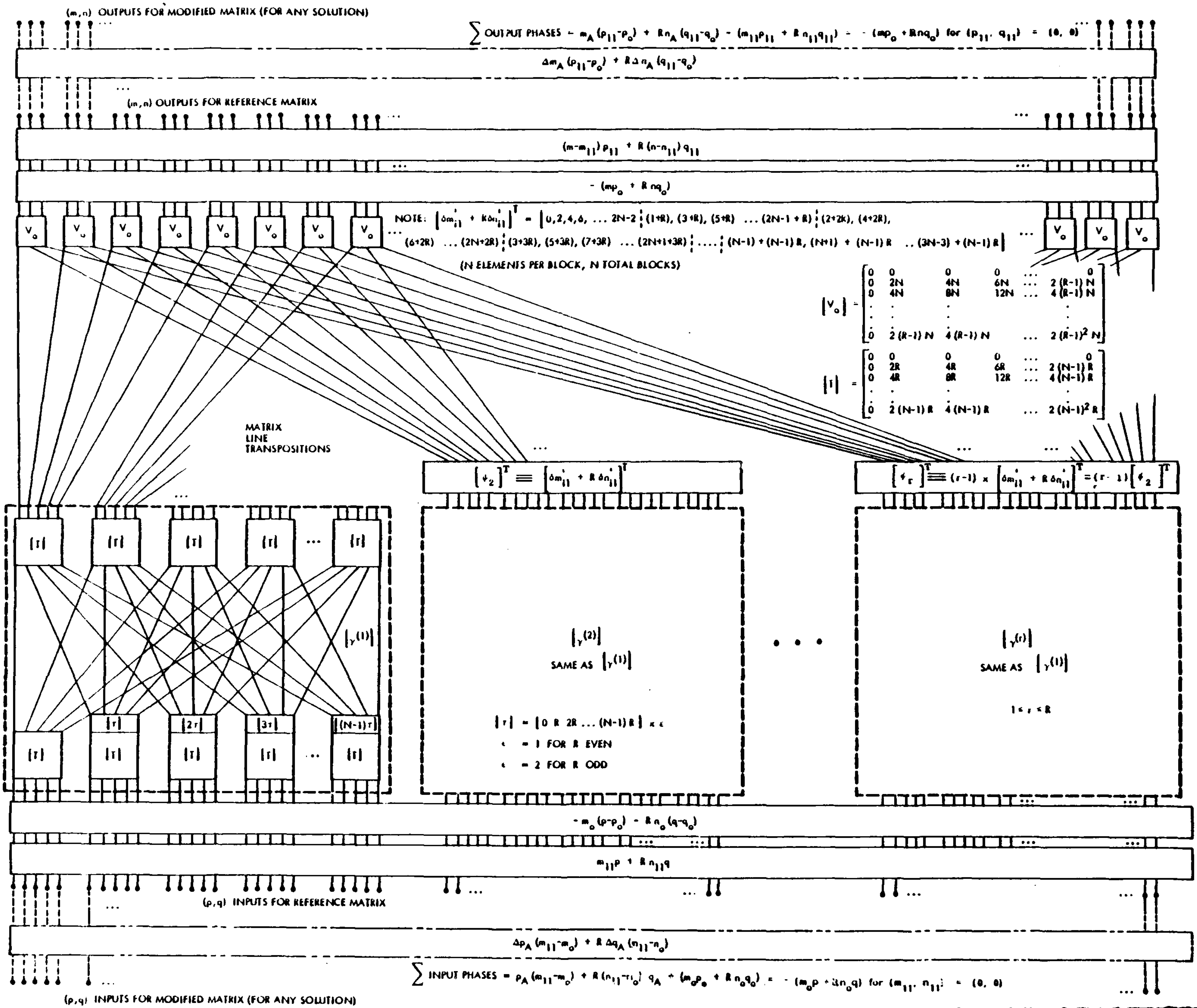

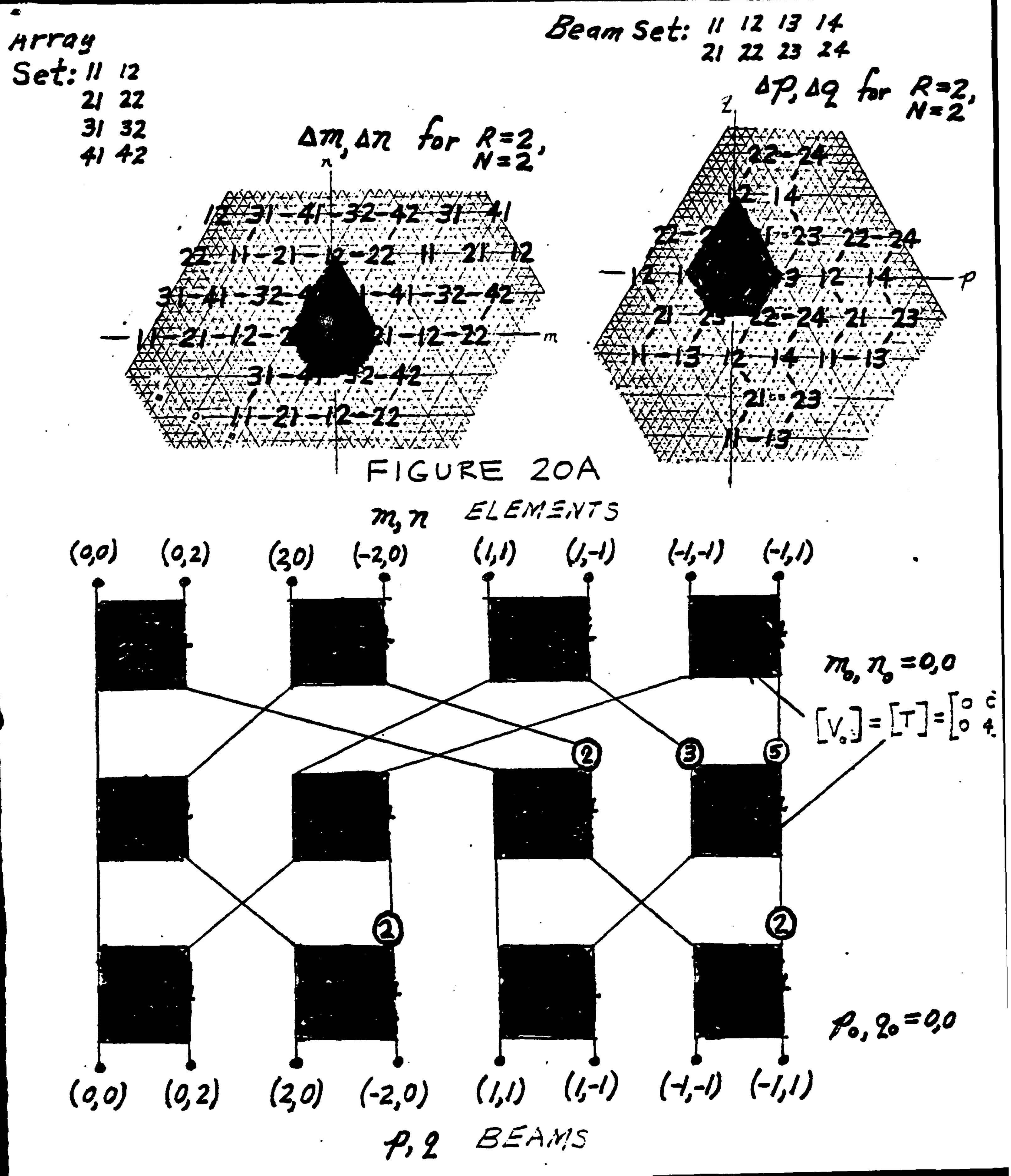
Array Set: 11 12
21 22
31 32
41 42
Beam Set: 11 12 13 14
21 22 23 24
Δm, Δn for R=2, N=2
Δp, Δq for R=2, N=2
FIGURE 20A
m, n ELEMENTS
(0,0) (0,2) (2,0) (-2,0) (1,1) (1,-1) (-1,-1) (-1,1)
m₀, n₀ = 0,0
[V₀] = [T] =
p₀, q₀ = 0,0
(0,0) (0,2) (2,0) (-2,0) (1,1) (1,-1) (-1,-1) (-1,1)
p, q BEAMS

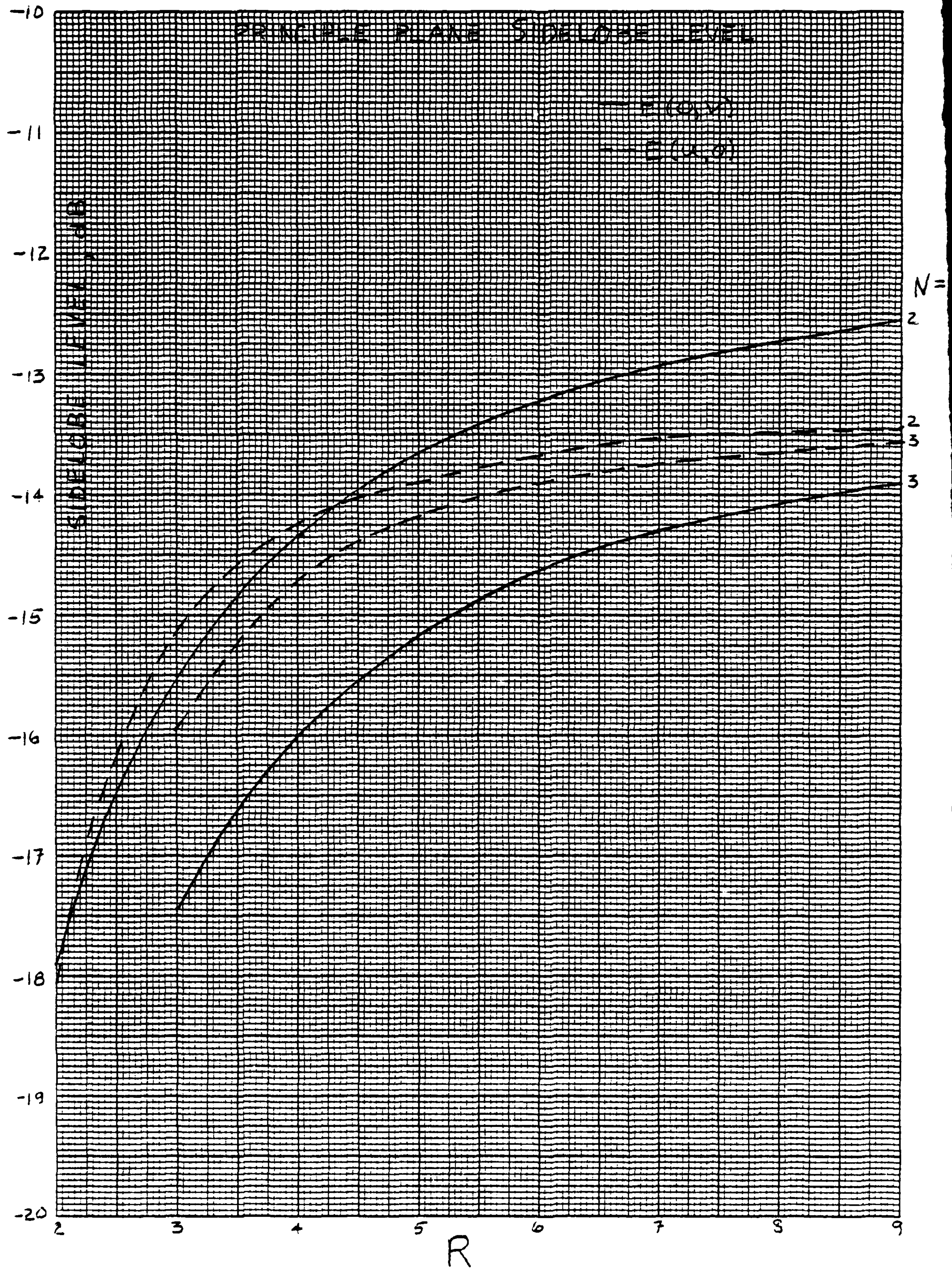

PRINCIPLE PLANE SIDELOBE LEVEL
— E(0,v)
- - - E(u,0)
SIDELOBE LEVEL, dB
-10
-11
-12
-13
-14
-15
-16
-17
-18
-19
-20
N=
2
2
3
3
2
3
4
5
6
7
8
9
R

WITH NO LOSS IN GENERALITY, DEFINE ORIGINS IN THE (m,n) DOMAIN AND (p,q) DOMAIN SUCH THAT

$$(m_{11},n_{11})=(0,0) \quad \text{and} \tag{99}$$

$$(p_{11},q_{11})=(0,0). \tag{100}$$

MOREOVER, CONSTANT PHASE TERMS IN (97) AND (98) MAY BE IGNORED. (97) AND (98) BECOME, IN VIEW OF (99) AND (100):

$$\Sigma \text{OUTPUT PHASORS}= -(mp_o+Rnq_o) \tag{101}$$

$$\Sigma \text{ INPUT PHASORS}= -(m_op+Rn_oq) \tag{102}$$

THUS, FIGURE 20 GIVES THE MATRIX FOR ANY SOLUTION. IF N AND/OR R IS NOT A PRIME NUMBER, THE CIRCUIT FOR [T] AND/OR [V] IS GIVEN BY USING THE MATRIX DECOMPOSITION, REITERATIVELY IF NECESSARY, GIVEN BY FIGURE 20A, UNTIL M AND K ARE PRIME NUMBERS.

IF IS WORTHWHILE MENTIONING THAT, ONCE A SOLUTION FOR THE OVERALL MATRIX IS OBTAINED, THE MATRIX MAY BE USED BACKWARDS BY SIMPLY INTERPRETING (m,n) AS (p,q) AND VICE VERSA. THE ROLES OF (m_o,n_o) AND (p_o,q_o) ALSO INTERCHANGE IN THE :ROCESS, AS WELL AS (m_{11},n_{11}) AND (p_{11},q_{11}). IN OTHER WORDS, THE INPUTS AND OUTPUTS MAY INTERCHANGE ROLES, RESULTING IN ANOTHER EMBODIMENT OF THE OVERALL MATRIX: R BLOCKS OF N^2 PORTS FED BY N^2 BLOCKS OF R PORTS (AS OPPOSED TO THE CONFIGURATION OF FIGURE 5). THIS IS NOT TO SAY THAT FOR A GIVEN DESIGN OF THE MATRIX, IT MAY BE SIMPLY FLIPPED OVER AND YIELD IDENTICAL RESULTS; IT IS RATHER TO SAY THAT, BY APPROPRIATE INTERPRETATION OF THE INTERCHANGING OF (m,n) AND (p,q) ROLES, IT CAN BE MADE TO YIELD IDENTICAL RESULTS.

EXAMPLES AND PROCEDURE OUTLINED

FOR A GIVEN N AND R SATISFYING (30), THE REFERENCE SOLUTION MAY BE USED TO GENERATE AN INFINITE GRID OF ELEMENT COORDINATES FROM WHICH ANY COMPLETE SET OF ELEMENTS MAY BE CHOSEN. LIKEWISE FOR THE BEAM COORDINATES.

FOR EXAMPLE, PLACING ELEMENT 11 AT THE ORIGIN, USING (43) AND (44), TOGETHER WITH (66) THROUGH (69), ELEMENTS 11,12,13,...1R ARE GIVEN BY:

(R EVEN): $(0,0),(2N,0),(4N,0),(6N,0),\ldots [(R-1)2N,0]$

(R ODD) : $(0,0),(2N,0),(4N,0),(6N,0),\ldots [(R-1)N,0]$
$(N,N),(3N,N),(5N,N),\ldots [(R-2)N,N]$

NOW, USING (86) AND (87), ELEMENTS 21,22,23,...2R ARE THE SAME AS 11,12,13,...1R BUT TRANSLATED BY (2,0).

FOR $I \leq N$, THE I1,I2,...IR ELEMENTS ARE THE SAME AS FOR I=1 BUT TRANSLATED BY $[2(I-1),0]$.

FOR I RANGING FROM 1 TO N, DEFINE THESE ELEMENTS AS SUBSET 1.

SUBSET 2 IS IDENTICAL TO SUBSET 1 BUT TRANSLATED BY (1,1), SUBSET 3 IS THE SAME AS SUBSET 1 BUT TRANSLATED BY (2,2), AND SO ON UP TO AND INCLUDING SUBSET N, WHICH IS THE SAME AS SUBSET 1 BUT TRANSLATED BY $[(N-1),(N-1)]$.

THE COMPLETE SET OF ALL ELEMENTS IS THE UNION OF ALL N SUBSETS.

NOW USING THE DEFINITIONS OF (48) AND (49), (43) AND (44) WITH EQUATIONS (84) THROUGH (89), THE BEAM COORDINATES 11,12,13,...1N ARE GIVEN BY

$(0,0),(0,2),(0,4),\ldots [0,2(N-1)]$ for R=EVEN OR ODD

FOR $N < J \leq 2N$, THE 1J BEAM COORDINATES ARE THE SAME AS THOSE GIVEN ABOVE EXCEPT TRANSLATED BY (R,1) FOR R ODD OR BY (R,0) FOR R EVEN.

FOR $(n-1)N < J \leq nN$ WHERE $n \leq N$, THE 1J BEAM COORDINATES ARE THE SAME AS FOR 11,12,...1N EXCEPT TRANSLATED BY $[(n-1)R,n-1]$ FOR R ODD OR $[(n-1)R,0]$ FOR R EVEN.

DEFINE THE UNION OF ALL OF THE ABOVE BEAM COORDINATES AS SUBSET 1. BEAM SUBSET r, WHERE 1 r R, IS GIVEN BY (59) BY TRANSLATING SUBSET 1 BY $(r-1,r-1)$. THE UNION OF ALL R SUBSETS FORMS THE COMPLETE BEAM SET.

ALL ARRAY SPACE OR ALL BEAM SPACE ON THE INFINITE TRIANGULAR GRID IS THEN EXHAUSTED (USED) BY APPLYING (92) TO THE COMPLETE SET DEFINING THE REFERENCE SOLUTION. FOR EXAMPLE, BY TRANSLATING THE REFERENCE SOLUTION COMPLETE SET BY $(2NRI_1, 2NI_2)$ WHERE I_1 AND I_2 TAKE ON ALL $\pm$ INTEGER VALUES, HALF OF SPACE IS EXHAUSTED; THE REMAINING HALF SPACE IS COVERED BY TRANSLATING THE PREVIOUS HALF SPACE BY (NR,N).

ONCE ALL ARRAY SPACE HAS BEEN "MAPPED" ACCORDING TO THE ABOVE PROCEDURE, ONE IS FREE TO CHOOSE ANY COMPLETE SET FROM THE EXISTING COORDINATE POSITIONS. THE FACT THAT THE "REFERENCE" SOLUTION WAS USED TO MAP THE SPACE IS OF NO FURTHER CONSEQUENCE. FIGURES 12 AND 13 ARE EXAMPLES FOR R=3,N=2. SOME COMPLETE SETS ARE DEPICTED SHADED.

DISTINCTLY DIFFERENT SETS CHOSEN FROM ARRAY SPACE OBVIOUSLY YIELD DISTINCTLY DIFFERENT ARRAYS; HOWEVER, SUCH IS NOT THE CASE IN BEAM SPACE BECAUSE ALL COMPLETE SETS IN BEAM SPACE ARE REALLY ONE IN THE SAME SET OF BEAMS. THAT IS, GRATING LOBES EXIST IN BEAM SPACE WHETHER WE LIKE IT OR NOT, AND IN CHOOSING ONE BEAM CONTAINED IN A COMPLETE SET IN BEAM SPACE, ONE ALSO NECESSARILY CHOOSES ALL BEAMS WITH THE SAME ij NAME (ij=11,12,13,...,21,22,23,...etc). SUCH IS NOT THE CASE FOR THE ARRAY, SINCE ARRAY SPACE IS TRUNCATED, WHEREAS BEAM SPACE IS AN INFINITE SERIES.

THUS FOR A GIVEN N AND R, ALL ARRAY SOLUTIONS PRODUCE BEAMS WITH THE SAME GRATING LOBE BOUNDARIES; THAT IS THE SPATIAL COVERAGE OF ALL ARRAY SOLUTIONS IS IDENTICAL, ALTHOUGH THE RADIATION PATTERNS WILL BE DIFFERENT IN GENERAL.

PROCEDURE

1. CHOOSE R.
2. CHOOSE N.
3. FORM THE INFINITE LATTICE OF $(\Delta m, \Delta n)$ COORDINATES BY THE PROCEDURE GIVEN.
4. CHOOSE AN ORIGIN AT THE 11 POSITION.
5. CHOOSE ANY <u>COMPLETE</u> SET OF ELEMENT LOCATIONS.
6. CHOOSE (m_o, n_o), THE APERTURE COORDINATE AT WHICH ALL MULTIPLE BEAM PHASE FRONTS HAS ZERO PHASE.
7. FORM THE INFINITE LATTICE OF $(\Delta p, \Delta q)$ COORDINATES BY THE PROCEDURE GIVEN.
8. CHOOSE AN ORIGIN AT THE 11 POSITION.
9. CHOOSE (p_o, q_o), THE (p,q) COORDINATE CORRESPONDING TO BROADSIDE TO THE ARRAY.
10. LABEL (p,q) COORDINATES AT INPUT.
11. LABEL (m,n) COORDINATES AT OUTPUT.
12. COMPUTE THE OUTPUT PHASE SHIFTS OF FIGURE 20: $-(mp_o+Rnq_o)$
13. COMPUTE THE INPUT PHASE SHIFTS OF FIGURE 20: $-(m_op+Rn_oq)$
14. COMPUTE $[\tau]$ AND $[\delta m'_{i1}+R\delta n'_{i1}]$ OF FIGURE 20.
15. FILL IN THE VALUES OF ALL PHASE SHIFTS OF FIGURE 20.
16. REPLACE $[T]$ AND $[V_o]$ MATRICES BY THE NETWORK EQUIVALENTS.
17. SUM ALL PHASORS COMMON TO A GIVEN LINE.
18. ADD OR SUBTRACT ANY FIXED PHASE SHIFT ALL THE WAY ACROSS THE MATRIX AT ANY TERMINAL PLANE TO CANCEL AS MANY PHASORS AS POSSIBLE.
19. IF PHASE RELATIONSHIPS BETWEEN FAR-FIELD BEAMS IS UNIMPORTANT, DELETE INPUT PHASE SHIFTERS $-(m_op+Rn_oq)$.
20. IF IT IS UNIMPORTANT AS TO WHERE THE FAR-FIELD BEAMS ARE BIASED, DELETE THE OUTPUT PHASE SHIFTERS $-(mp_o+Rnq_o)$.

OPTIMIZATION OF THE DIRECTIVITY OF A PARABOLIC REFLECTOR ANTENNA

by

Roland A. Gilbert and Y. T. Lo
University of Illinois, Urbana, IL

INTRODUCTION

Reflector antennas are perhaps the most widely used antennas in radar, radio astronomy, satellite communications, etc. Much has been done in the area of pattern analysis for these antennas; however, little has been published on directive gain optimization. One of the pioneering works in optimizing the directive gain of the parabolic reflector antenna was done by Silver [1]. He selected a feed aperture distribution of a particular type with one degree of freedom and computed the gain of the antenna by varying the parameter in the feed aperture function until the maximum gain was obtained. Not only is his result restricted, but his hit-and-miss searching method is very costly for more than one degree of freedom.

In this paper, the maximum directive gain of a parabolic reflector antenna is found in a very general way and the optimum feed aperture distribution which maximizes the directive gain for a given F-number and feed aperture size is then found. Also to be discussed is the sensitivity of the optimum gain to variations in the feed aperture distribution.

STATEMENT OF THE PROBLEM

In practice, the geometrical optics approximations can generally be applied to the analysis of the parabolic reflector antenna assuming that the size of the reflector aperture is large in terms of the wavelength of the signal transmitted or received. The maximum directive gain for an aperture with equal phase is obtained when the reflector aperture distribution is uniform. It is a well-known problem that the reduction of spill-over and the aperture efficiency constitute two opposing factors in designing reflector antennas. Oftentimes, the design of reflector antennas is based on a rule of thumb that limits the reflector aperture illumination taper to about -10dB. Clearly a more rigorous analytic investigation is needed.

The directive gain of the parabolic reflector antenna is considered in the following way. A circular feed aperture of radius a is placed at the focus of the reflector as shown in Figure 1. It is assumed that the feed aperture has N degrees of freedom, or N modal fields, available for optimization, i.e.

$$f(\rho) = \sum_{n=0}^{N-1} a_n Q_{2n}(\rho) \tag{1}$$

where

$Q_{2n}(\rho)$ is the modal field which for convenience will be chosen to be the Zernike polynomial [2] which is given by

$$Q_{2n}(\rho) = \sum_{k=0}^{n} \frac{(-1)^k (2n-k)!\,\rho^{2(n-k)}}{k!\,[(n-k)!]^2}$$

a_n is a modal coefficient.

The scalar far-field of the feed whose radius is normalized to 1 becomes

$$E_{feed}(R) = j k a^2 (1+\cos\psi) e^{-jkR} \int_0^1 f(\rho) J_0(ka\rho \sin\psi)\rho\, d\rho \tag{2}$$

$$= \frac{ja(1+\cos\psi)e^{-jkR}}{2R} \sum_{n=0}^{N-1} (-1)^n a_n \frac{J_{2n+1}(ka\sin\psi)}{\sin\psi}$$

where

R is the distance from the center of the feed aperture to a point on the reflector surface; therefore R is a function of the angle ψ as shown in Fig. 1;

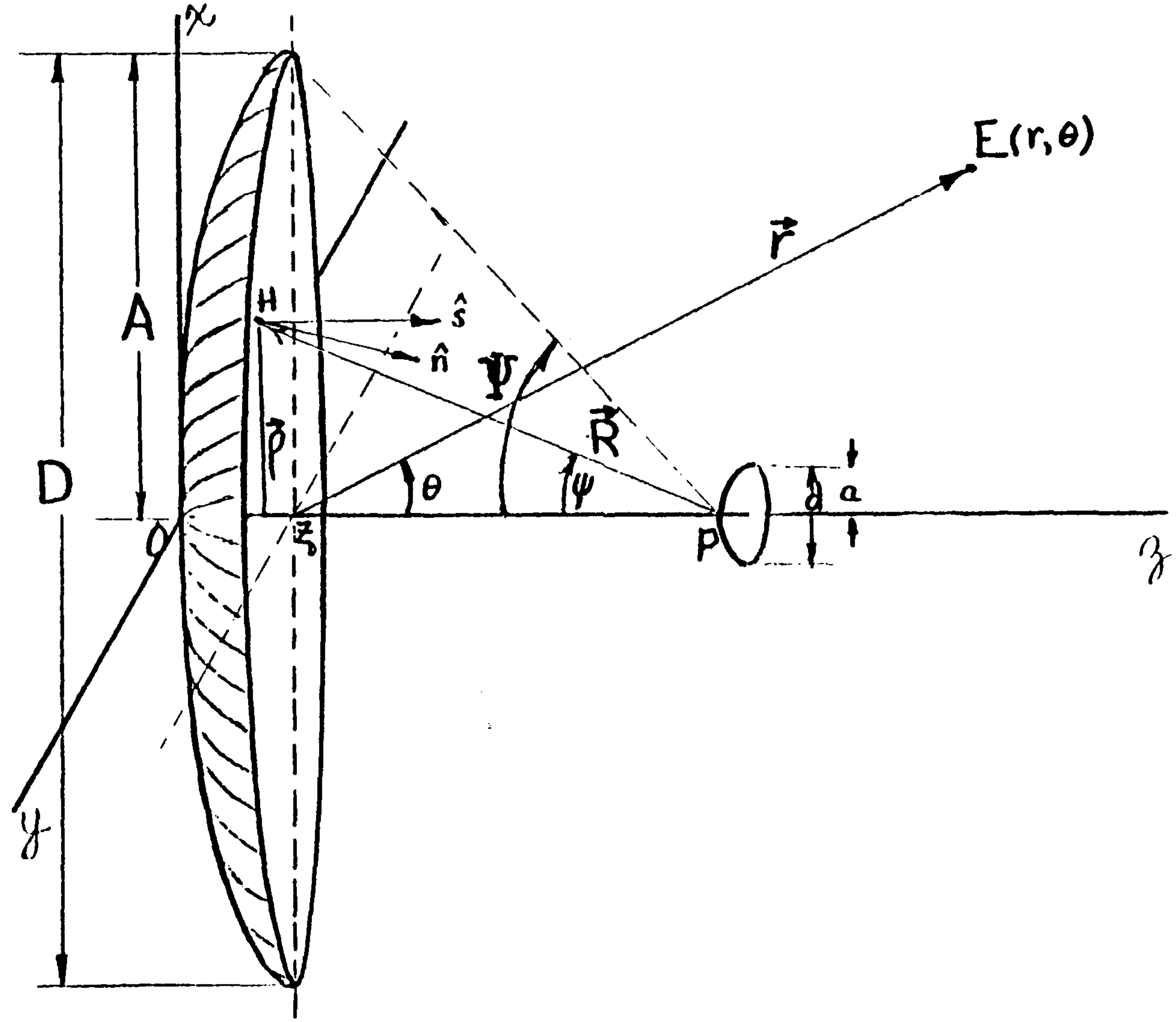

Figure 1 : Parabolic reflector antenna

k $= 2\pi/\lambda$;

a is the radius of the feed aperture;

ρ is the distance from the center of the feed to a point on its aperture; and

$J_m(\cdot)$ is the m^{th} order Bessel function of the first kind.

By letting $\varepsilon A = R \sin\psi$, and $F = f/2A$ where

A is the radius of the reflector aperture;

f $= \overline{OP}$ is the focal length of the reflector;

F is the F-number of the reflector; and

ε is the normalized distance of a point in the reflector aperture from the center of the aperture, $0 \leq \varepsilon \leq 1$,

then the reflector aperture distribution is given by

$$E_{\substack{\text{reflector}\\ \text{aperture}}}(\varepsilon) = \frac{jae^{-jk(f+z_0)}}{A} \sum_{n=0}^{N-1} (-1)^n a_n \frac{J_{2n+1}\left[ka \frac{\varepsilon/2F}{1+(\varepsilon/4F)^2}\right]}{\varepsilon\left[1+(\varepsilon/4F)^2\right]} \tag{3}$$

where z_0 is the disk depth as shown in Fig. 1. Once the reflector aperture distribution is known, the far-field of the antenna is given by

$$E(r,\theta) = -kaAe^{-jk(f+z_0+r)}(1+\cos\theta) \sum_{n=0}^{N-1} (-1)^n a_n \int_0^1 \frac{J_{2n+1}\left[\frac{ka(\varepsilon/2F)}{1+(\varepsilon/4F)^2}\right] J_0(\varepsilon kA\sin\theta)\,d\varepsilon}{\left[1+(\varepsilon/4F)^2\right]} \tag{4}$$

$$= \langle a\, V(\theta) \rangle$$

where

r is the distance from the center of the reflector aperture to an observation point in space;

$>$ and $<$ are the commonly used bra-ket notation for column and row vectors.

There is no closed form expression for the above integral, thus the far-field must be evaluated numerically.

The maximum directive gain can be expressed in terms of a Hermitian quadratic form [3]-[4]:

$$\underset{\{a\}}{\mathrm{Max}}\ G = \underset{\{a\}}{\mathrm{Max}}\ 4\pi \frac{\langle a D a^* \rangle}{\langle a B a^* \rangle} \tag{5}$$

where

D is a semi-definite Hermitian matrix; and

B is a positive definite Hermitian matrix.

The numerator $\langle a\ D\ a^* \rangle$ represents the power in the axial direction of the reflector. The denominator, $\langle a\ B\ a^* \rangle$, represents the total power radiated by the feed of the antenna. A typical element D_{ij} of D is given by

$$D_{ij} = V_i^*(\theta=0)\ V_j(\theta=0) \tag{6}$$

where

$$V_i^*(\theta=0) = -2kaAFe^{-jk(f+z+r)}(-1)^i \int_0^{2\tan^{-1}(1/4F)} J_{2i+1}(ka\sin\psi)\,d\psi \tag{7}$$

The total power radiated by the feed is determined by summing the power radiated by the feed over all space. Thus

$$\langle a B a^* \rangle \propto \int_{4\pi} E^*_{feed}(R,\psi)\, E_{feed}(R,\psi)\, d\Omega \tag{8}$$

A typical element B_{ij} of B becomes

$$B_{ij} = (-1)^{i+j} a^2 \pi \int_0^{\pi/2} (1+\cos^2\psi) \frac{J_{2i+1}(ka\sin\psi)\, J_{2j+1}(ka\sin\psi)\, d\psi}{\sin\psi} \tag{9}$$

The optimum solution, $a^*\rangle$, of (5) as given in Lo [3] is found as follows:

$$a^*\rangle = B^{-1} V^*(\theta=0)\rangle \tag{10}$$

Since B is a positive definite symmetric matrix, finding B^{-1} with sufficient numerical accuracy presents no problems numerically. Once the modal coefficients are found, then the directive gain is readily determined.

The question of interest, now, is how sensitive is the gain of the antenna to variations in the modal amplitude vector $a^*\rangle$. Obviously this question cannot be simply answered. For a small feed aperture, the optimum solution could be of super-gain. In that case, the solution would be of no practical value.

COMPUTATIONAL RESULTS

The maximum directive gain, as given by Eq. (5), can be written as

$$G_{max} = 16\pi^2 F^2 (2A/\lambda)^2 g_{max} \tag{11}$$

where g_{max} is the maximum gain factor for a given F-number and feed aperture size and is independent of the reflector size. The gain factors for a number of modes, F-numbers, and feed aperture sizes are given in Table 1. Some interesting observations can be made. First, looking at the maximum gain factors as the number of modes increases, one sees that for about 6 or 7 modes, the gain factors are close to their optimum values. Moreover, this is the case for a fewer number of modes as the feed aperture becomes smaller. It is not necessary to take too many modes. As a matter of fact, there is question as to the accuracy of the gain factors computed for 7 or 8 modes for the case where the feed diameter is 1.5λ. The problem of super-gain occurs for a smaller number of modes as the feed diameter decreases. Also

Table 1: Table of gain factors for various antenna parameters

Number of modes	Diameter of feed in wavelengths			
	d = 3.0	d = 2.5	d = 2.0	d = 1.5
		F = 0.30		
1	0.0333	0.0088	0.0017	0.0788
2	0.0345	0.0591	0.3979	0.5182
3	0.3423	0.5307	0.5200	0.5182
4	0.5323	0.5307	0.5374	0.5440
5	0.5483	0.5563	0.5622	0.5662
6	0.5710	0.5753	0.5783	0.5802
7	0.5836	0.5854	0.5865	0.5872
8	0.5889	0.5894	0.5897	0.5898
		F = 0.35		
1	0.0218	0.0049	0.0067	0.1022
2	0.0284	0.0977	0.3604	0.3786
3	0.3497	0.4047	0.3890	0.3973
4	0.4110	0.4194	0.4295	0.4357
5	0.4398	0.4435	0.4447	0.4450
6	0.4458	0.4454	0.4451	0.4450
7	0.4463	0.4469	0.4476	0.4482
8	0.4512	0.4523	0.4516	0.4538
		F = 0.40		
1	0.0129	0.0037	0.0147	0.1187
2	0.0324	0.1319	0.3117	0.2878
3	0.3181	0.3187	0.3142	0.3246
4	0.3344	0.3399	0.3420	0.3417
5	0.3438	0.3424	0.3420	0.3423
6	0.3463	0.3480	0.3496	0.3508
7	0.3545	0.3552	0.3555	0.3556
8	0.3560	0.3558	0.3557	0.3556

interesting to note is that the optimum gain factors for a given F-number are about the same for 6, 7, or 8 modes for different size feed apertures.

Another observation is that the optimum gain factors for the different F-numbers are not the same. The smaller the F-number, the larger the optimum fain factor. Since the objective of the optimization is to obtain a uniform reflector aperture distribution, then for a given reflector size, the directive gain of the antenna should be similar for various F-numbers. To show this, consider a reflector diameter of 25λ with $d=3.0\lambda$ and 6 modes: $G_{F=0.30}=37.05$ dB, $G_{F=0.35}=37.32$ dB, and $G_{F=0.40}=37.38$ dB. There is only a small difference between these directive gains. The larger the F-number, only slightly larger is the gain. This is expected since it is more difficult to illuminate uniformly the reflector for a wider aperture angle Ψ (Fig. 1).

The feed aperture distributions, reflector aperture distributions, and associated far-field patterns are presented in Figures 2-7 for various F-numbers, number of modes used, and feed aperture diameters while keeping the same reflector aperture diameter of 25λ. For the sake of comparison, the directive gains obtained by Silver using his cosine feed far-field pattern function are shown in Table 2 together with the optimum gains obtained for a 3.0λ feed aperture size using the optimization procedure above.

In Figures 8-9 is a comparison of the reflector illuminations, and far-field patterns of the reflector of Silver's pattern function and the optimum aperture illuminations. In Fig. 9, one can see that the beamwidth of the 6-mode pattern is about 2.5 degrees less than Silver's.

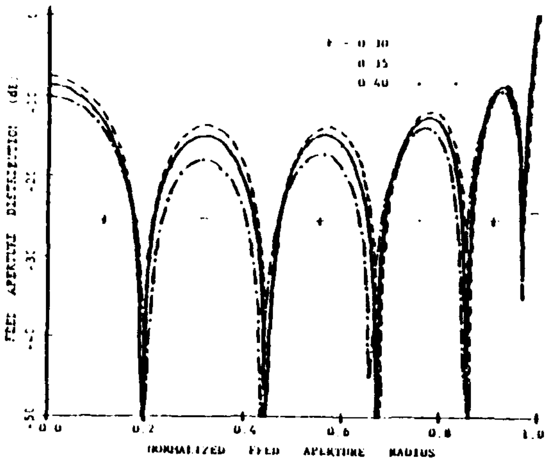

Figure 2: Optimum feed aperture distribution for a feed of 3λ diameter, 4 modes, and F=0.30, 0.35, and 0.40. Phase changes are indicated on the graph.

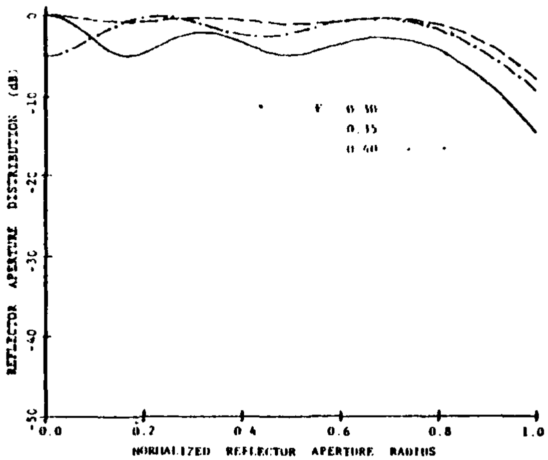

Figure 3: Reflector illuminations produced by the feeds in Fig. 2.

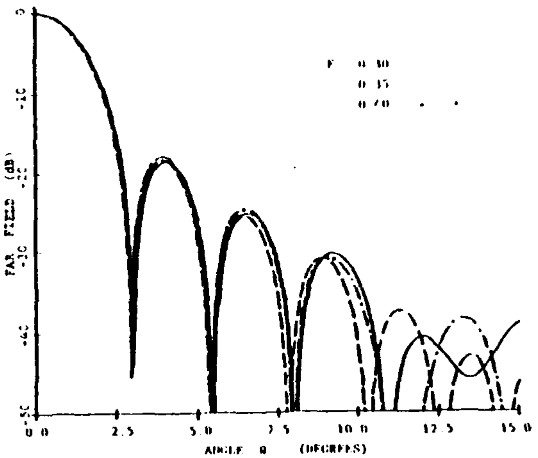

Figure 4: Far-field pattern of a 25λ diameter reflector for the feed shown in Fig. 2. The computed directive gains are $G_{F=0.30}$ = 37.05 dB, $G_{F=0.35}$ = 37.32 dB, and $G_{F=0.40}$ = 37.10 dB.

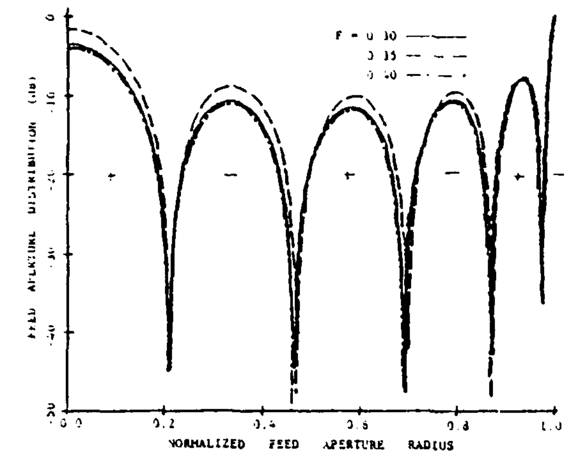

Figure 5: Optimum feed aperture distributions for a feed of 2λ diameter, 6-modes, and F = 0.30, 0.35, and 0.40. Phase is indicated on graph.

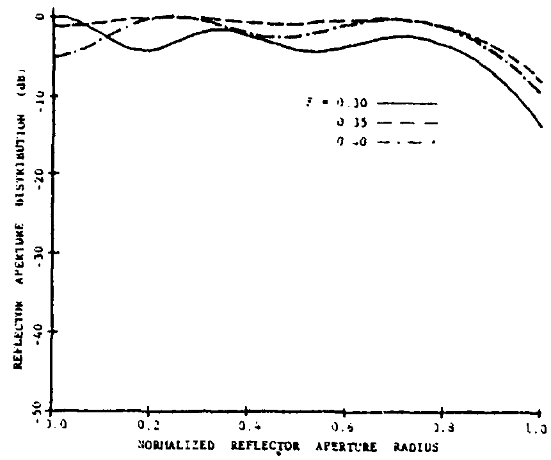

Figure 6: Reflector illumination produced by the feeds in Fig. 5.

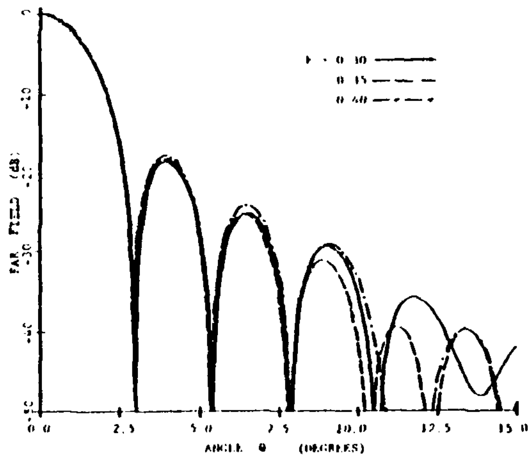

Figure 7: Far-field patterns of a 25λ diameter reflector for feeds shown in Fig. 5. The computed directive gains are $G_{F=0.30}=37.11$ dB, $G_{F=0.35}=37.11$ dB, $G_{F=0.40}=37.42$ dB.

TABLE 2

Comparison of the maximum directive gains obtained by Silver with the optimum directive gains for various F-numbers.

F = 0.30	F = 0.35	F = 0.40
G_{Silver} = 35.91 dB	G_{Silver} = 36.57 dB	G_{Silver} = 36.84 dB
G_{max} = 37.05 dB	G_{max} = 37.32 dB	G_{max} = 37.38 dB

Silver's far-field pattern has lower sidelobes than the optimum pattern; however, it is stressed again that the optimization objective is to obtain the maximum directive gain only.

SENSITIVITY ANALYSIS

The decision to use a given number of modes is dictated by the ability to meet the required tolerance specifications. Figures 10-13 show the probability of the gain factors to be within 1% of the maximum gain factor v.s. the modal amplitude error for various number of modes, M. The data were obtained by introducing random errors uniformly distributed in a range of $\pm$ maximum percent for each element of the modal amplitude vector. Six hundred trials were computed for each case with a given maximum percent error and the cases in which the deviation of the gain factors from the maximum values were within 1% of the maximum gain factor were counted. Hence the probability of being within 1% of the maximum gain factor for a given maximum percent error in the

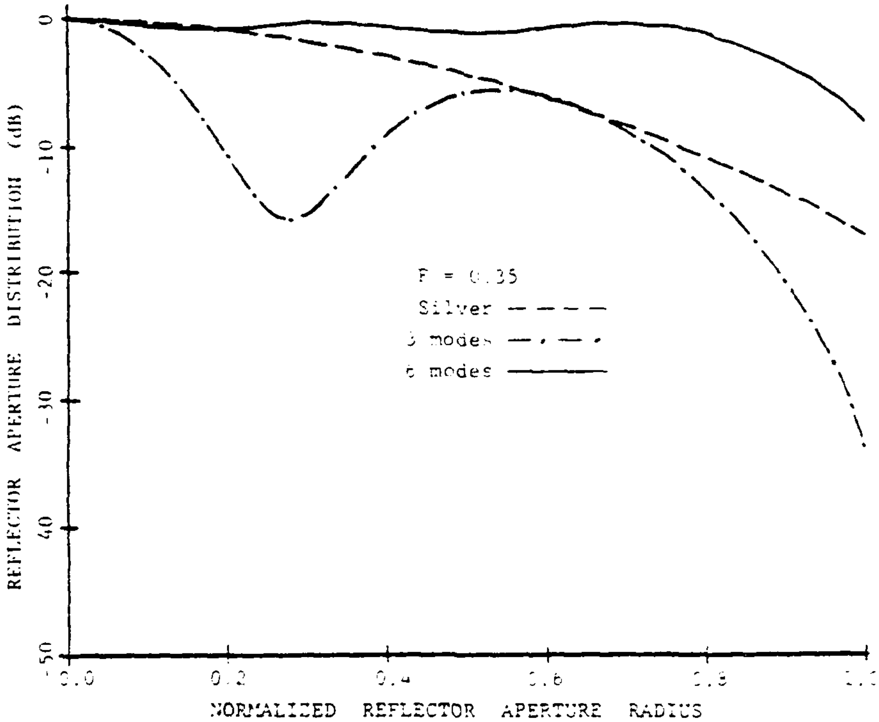

Figure 8: Comparison of the reflector illuminations of Silver's pattern function and the optimum aperture illuminations obtained from 6-modes and 3-modes and an F-number of 0.35 with a 3λ feed diameter.

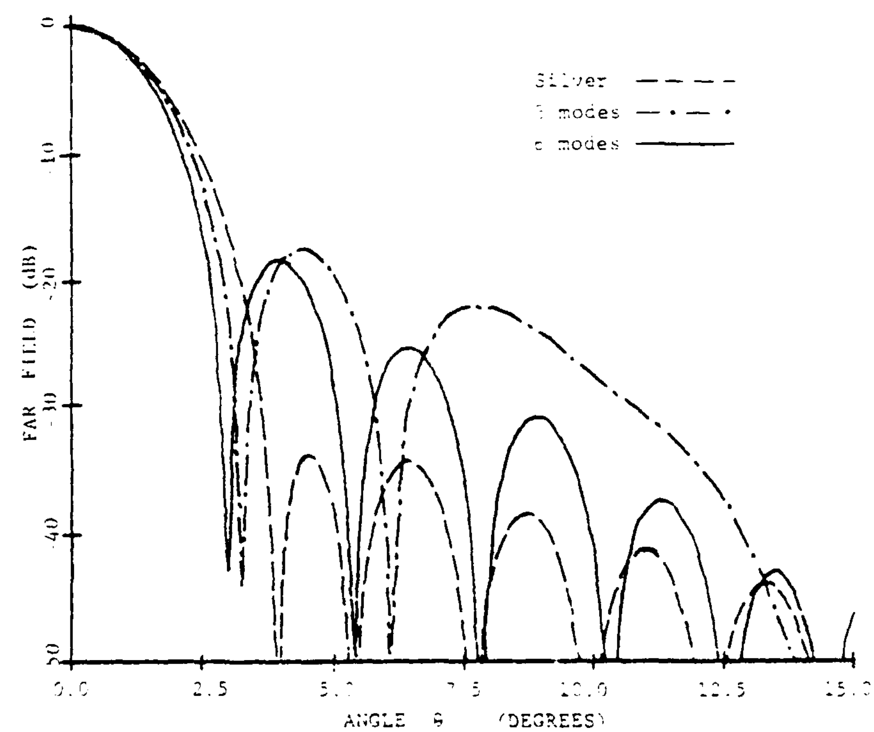

Figure 9: Far-field patterns produced by a reflector aperture of 25λ diameter for F = 0.35. The computed directive gains are G_{SILVER} = 36.57 dB, $G_{6\text{-}modes}$ = 37.32 dB, and $G_{3\text{-}modes}$ = 36.26 dB.

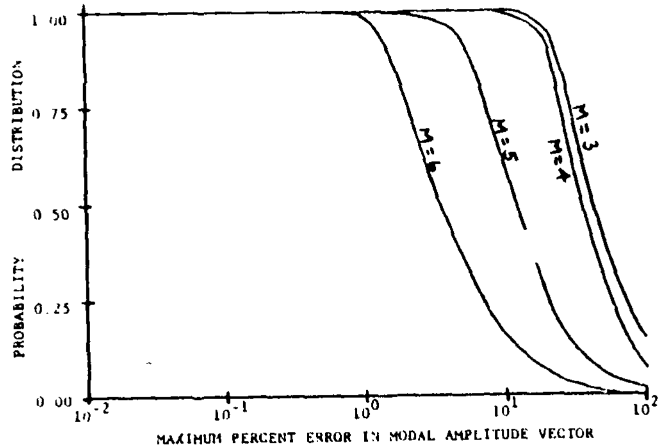

Figure 10: Probability density distribution of being within 1% of the maximum gain factor v.s. the largest allowed error which is uniformly distributed between the ± maximum percent error allowed in the modal amplitude vector for the feed of a parabolic reflector antenna of a 3λ diameter, with F = 0.35. M on each curve above represents the number of modes used.

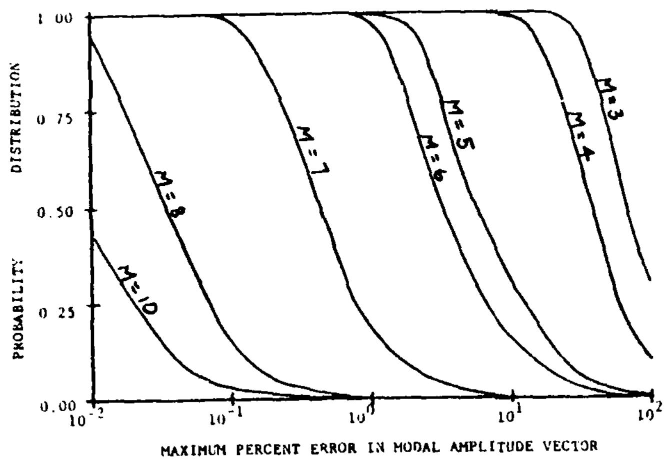

Figure 11: Probability density distribution of being within 1% of the maximum gain factor v.s. the largest allowed error which is uniformly distributed between the ± maximum percent error allowed in the modal amplitude vector for the feed of a parabolic reflector antenna of a 2.5λ diameter, with F = 0.35. M on each curve above represents the number of modes used.

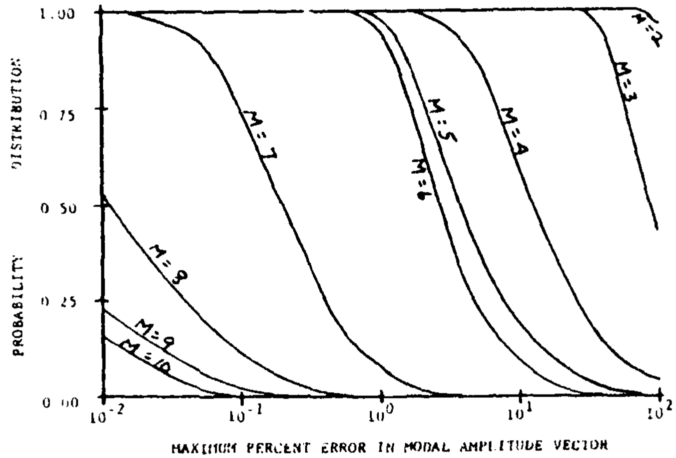

Figure 12: Probability density distribution of being within 1% of the maximum gain factor v.s. the largest allowed error which is uniformly distributed between the ± maximum percent error allowed in the modal amplitude vector for the feed of a parabolic reflector antenna of a 2.0λ diameter, with F = 0.35. M on each curve above represents the number of modes used.

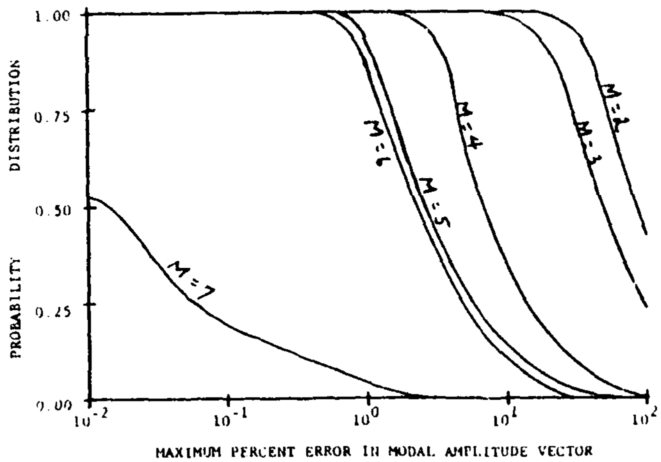

Figure 13: Probability density distribution of being within 1% of the maximum gain factor v.s. the largest allowed error which is uniformly distributed between the ± maximum percent error allowed in the modal amplitude vector for the feed of a parabolic reflector antenna of a 1.5λ diameter, with F = 0.35. M on each curve above represents the number of modes used.

modal amplitude vector is given by the ratio of the number of trials counted above to the total number of trials. Also obtained with the above computations, but not shown here, were the probability distribution curves for the cases of being within 2%, 3%, etc. of the maximum gain factor. Obviously, by relaxing the tolerance on the directive gain, the maximum allowable error on the modal amplitudes can be increased.

Comparing plots in Fig. 10-13, it is seen that as the size of the feed aperture decreases, the sensitivity of the gain factor to errors in the modal amplitude vector increases. For example, for $d=3\lambda$, $M=5$, a 1% maximum error in the modal vector would give nearly 100% probability for the directive gain to be within 1% of its maximum value, whereas a 10% error would reduce the probability to about 60%. Comparing the plots for, say, $M=7$ $d=2\lambda$ in Fig. 12 to that for $M=7$ and $d=1.5\lambda$ in Fig. 13, it is seen that with a 0.1% error in the modal amplitude vector, the probability would reduce from about 75% to 20%. In other words, for a given number of modes and given tolerance, the feed aperture must be sufficiently large in order to have a good chance to keep the directive gain within 1% of its maximum.

In order to give a physical picture of the relationship between the maximum error in the modal amplitude vector and the feed aperture distribution, the feed aperture distributions obtained from the modal amplitude vectors that include the error variations could be plotted. Thus an envelope of the aperture distribution would be found that represents the maximum modal amplitude error and it would provide the actual error bounds needed to synthesize the feed distribution. Due to the unavailability of computing facilities, the maximum error envelope curve of the feed aperture distribution will not be shown here.

CONCLUSION

In this paper, the maximum directive gains for parabolic reflector antennas with various feed sizes and F-numbers were found. In addition the sensitivity of the directive gain to variations in the modal amplitudes was also considered for a few typical cases. Also, the optimum feed aperture distributions along with their resulting reflector aperture distributions and far-field patterns were presented for some of the above cases. In order to compare these results with some known results, the optimum directive gains obtained were compared with the gains obtained using Silver's best gain cosine feed pattern functions.

REFERENCES

[1] S. Silver, Microwave Antenna Theory and Design, McGraw-Hill Book Company, Inc., New York, 1949. MIT Radiation Laboratory Series, vol. 12, Chap. 12

[2] M. Born and E. Wolf, Principles of Optics, New York: Pergamon Press, 1959.

[3] Y. T. Lo, S. W. Lee, and Q. H. Lee, "Optimization of Directivity and Signal-to-noise Ratio of an Arbitrary Antenna Array," IEEE Trans. Antennas and Propagation, vol. AP-19, No. 4, July 1971.

[4] Y. T. Lo, "Optimum Feed for Parabolic Reflectors," Technical Report, Eindhoven Univ. of Technology, June 1973.

AN ANALYSIS OF ANNULAR, ANNULAR SECTOR, AND CIRCULAR SECTOR MICROSTRIP ANTENNAS

J. D. Ou, W. F. Richards
Department of Electrical Engineering
University of Houston
Houston, TX 77004

Y. T. Lo
Department of Electrical Engineering
University of Illinois
Urbana, IL 61801

In this paper we present the results of an analysis of three types of microstrip antenna elements, the annular, annular sector, and circular sector microstrip antennas. The method of analysis used is the same as that which has been reported in detail elsewhere [1,2] for the rectangular and the circular disk elements. The reader is referred to those works for a fuller discussion of the methods used. However, a brief discussion of the salient features of the method is included here.

DESCRIPTION OF THE METHOD OF ANALYSIS

When the thickness of the printed circuit board from which the antenna is made is small compared to a wavelength (on the order of a few thousandths to a few hundredths), then the microstrip antenna can be thought of as on open circuited parallel plate waveguide. Of course, the "open circuit" is not an "ideal" open since (once hopes) the antenna radiates. However, for such thin antennas, as far as the *shape* of the distribution of the fields under the patch element is concerned, the open circuit can be assumed to be an ideal open. This ideal open is modelled as a wall of magnetic conductor joining the edge of the patch to the ground plane thus forming a *closed cavity*. It is important to make a distinction here, it is claimed that only the *shape* of the "internal" field distribution for the cavity and that for the actual antenna are approximately the same. However,

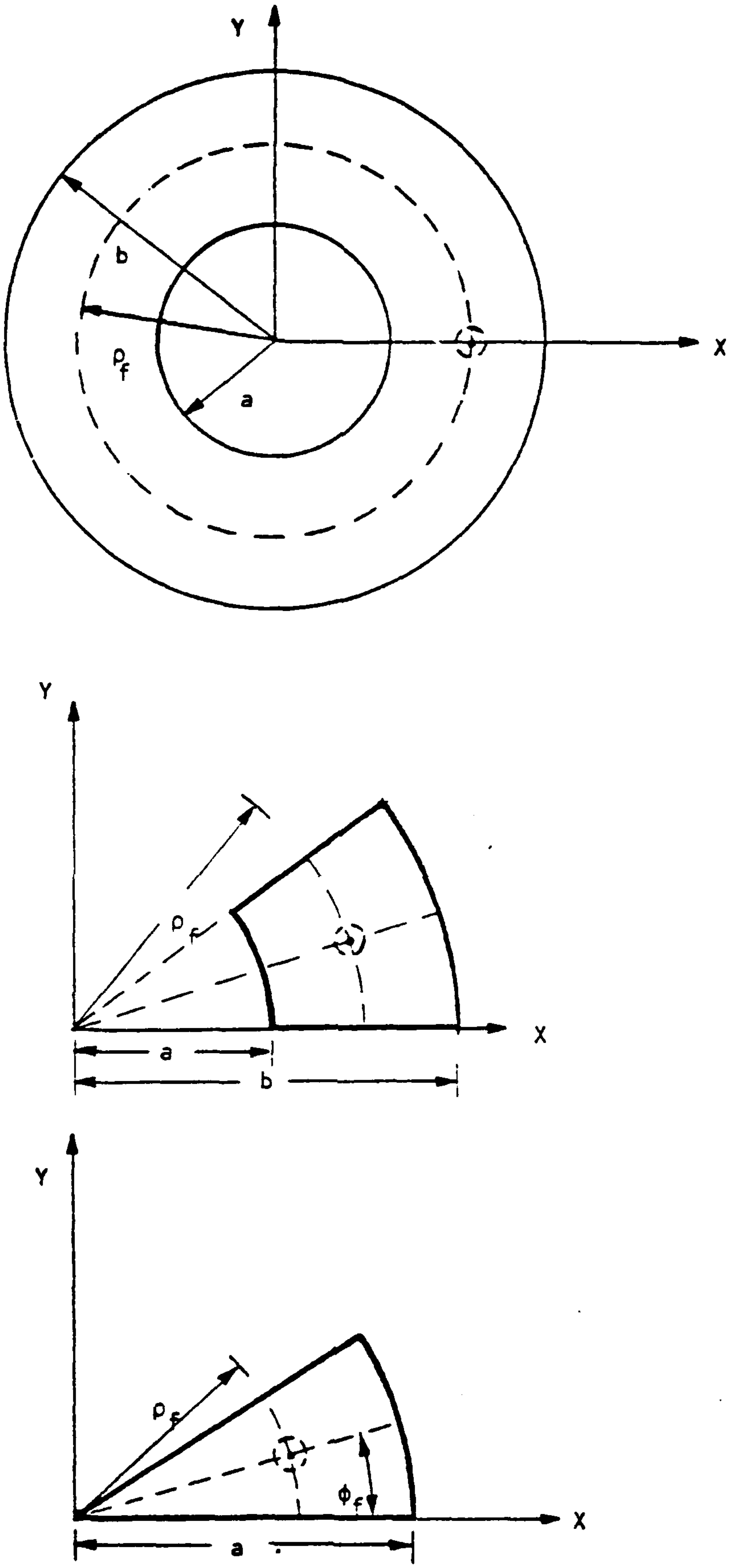

Figure 1. Illustrations of the three types of antennas analyzed which, from top to bottom, are the annular, annular sector, and circular sector microstrip antennas.

the *amplitude, i.e.*, the coefficient that multiplies this distribution, differs significantly between that for the cavity and that for the actual antenna.

The reason for the similarity in shape of the field distribution can be explained as follows. The electric current flowing on the bottom (dielectric) side of the patch and perpendicular to the edge of the patch must be very small for thin antennas. It must equal the rather small current "diffracted" around the edge of the patch that flows on the top side of the element. Thus, the component of magnetic field tangential to the edge of the patch must also be small. Since the antenna is very thin, the magnetic fields everywhere in the surface joining the patch edge to the ground plane must be small. The assumption that the tangential component of magnetic field on that surface is zero (i.e., the introduction of a magnetic wall), then, only introduces a slight error in the calculated shape of the internal field distribution.

On the other hand, that the amplitudes of the internal fields of the cavity and the antenna must differ can be seen from the following considerations. If (u_1,u_2,z) represents a point in a cylindrical coordinate system where z is the height of this point above the ground plane, and $\Psi_{mn}(u_1,u_2)$ are the z-independent resonant modes of the cavity, then the electric field in the cavity due to a filamentary, z-independent, unit electric current at (u_1',u_2') is given by

$$E(u_1,u_2) = j\omega\mu \sum_{m=0}^{\infty} \sum_{n=0}^{\infty} \frac{\Psi mn(u_1,u_2)\Psi mn(u_1',u_2')}{k^2 - k_{mn}^2} \quad , \tag{1}$$

where the k_{mn}'s are the resonant wave numbers. Two things emerge from equation (1). The first is that in the vicinity of a resonant frequency of the antenna, all other terms in the series except for the resonant term are relatively small and can be neglected without causing a great deal of error. The second is that the coefficient of the resonant term,

$$\frac{1}{k^2 - k_{mn}^2}$$

has a *magnitude* that is critically dependent on the imaginary part of the wave number, k. This parameter, of course, is

$$k = \omega\sqrt{\mu\varepsilon}\ (1 - j\delta)^{1/2} \approx \omega\sqrt{\mu\varepsilon}\ (1 - j\frac{\delta}{2}) \qquad (2)$$

where μ is the permeability of the dielectric and ε is the permittivity of the dielectric, and δ is the dielectric loss tangent. Thus, although the *shape* of the distribution, described approximately by the single resonant term which varies as $\Psi_{mn}(u_1,u_2)$ is not strongly dependent on this imaginary part, the *amplitude* is.

The imaginary part of k is proportional to the loss tangent of the dielectric within the cavity. The loss tangent is equal to the reciprocal of the quality factor, Q, of the cavity. Since the actual antenna looses power to the radiated field and to heating of the metallic cladding of the printed circuit board, the quality factor of the antenna is clearly much less than that of the idealized cavity. Since the shape of the internal fields of the actual antenna is about the same as that of the idealized cavity, the *form* of equation (1) is sensibly retained to express the internal fields of antenna. However, the wave number, k, must be modified in (1) since it accounts only for the power lost to heating of the dielectric. The reciprocal relationship between cavity Q and dielectric loss tangent clearly suggests that (1) be modified by introducing an *artificially lossy* dielectric into the cavity with "effective loss tangent" equal to the reciprical of the *antenna* quality factor.

The problem becomes, then, how to calculate the antenna quality factor. In order to do this, the power loss associated with the antenna due to all mechanisms, radiation, surface wave, and heating of the dielectric and metal cladding must be estimated as well as the total energy stored in the antenna.

To compute the radiated power, the most significant loss mechanism for a practical antenna, one first can think of removing the metal patch by introducing an equivalent magnetic surface current and an electric surface current at the surface between the patch edge and the ground plane, and the electric surface current induced in the *top* side of the patch as illustrated in figure 2. However, the electric surface currents are both fairly small and can be neglected for thin antennas. The radiated fields can then be computed in terms of the remaining magnetic current. But this magnetic current is simply the cross product of the electric field and the patch edge normal. The dominant term of equation (1) is used to supply the required electric field at the edge of the patch.

The power lost in the surface wave can be estimated using similar approximations as those used for finding the radiated power. However, since this loss is so small for thin antennas, it is normally neglected.

The power lost to heating of the metal cladding can be approximated using the usual perturbation approach, namely, by first finding the induced current in a perfectly conducting cladding and then using these known currents to compute the power loss in the finitely conductive metal. The power lost in the dielectric, of course, is computed directly from the internal electric fields and the actual dielectric loss tangent. In both of these computations, the electric field is again assumed to be given by the dominant term of (1).

The average stored energy is approximately the energy stored in the internal fields. The latter can be found by doubling the electric stored energy since in the vicinity of a resonance, the energy stored in the electric and magnetic fields are approximately the same. The electric field used in the computation of this energy is again assumed to given by the dominant term of (1).

Thus, all required quantities to compute the antenna quality factor are now available. But a problem seems to remain. The imaginary part of k is still unknown since the Q and hence the effective loss tangent are not known. Then

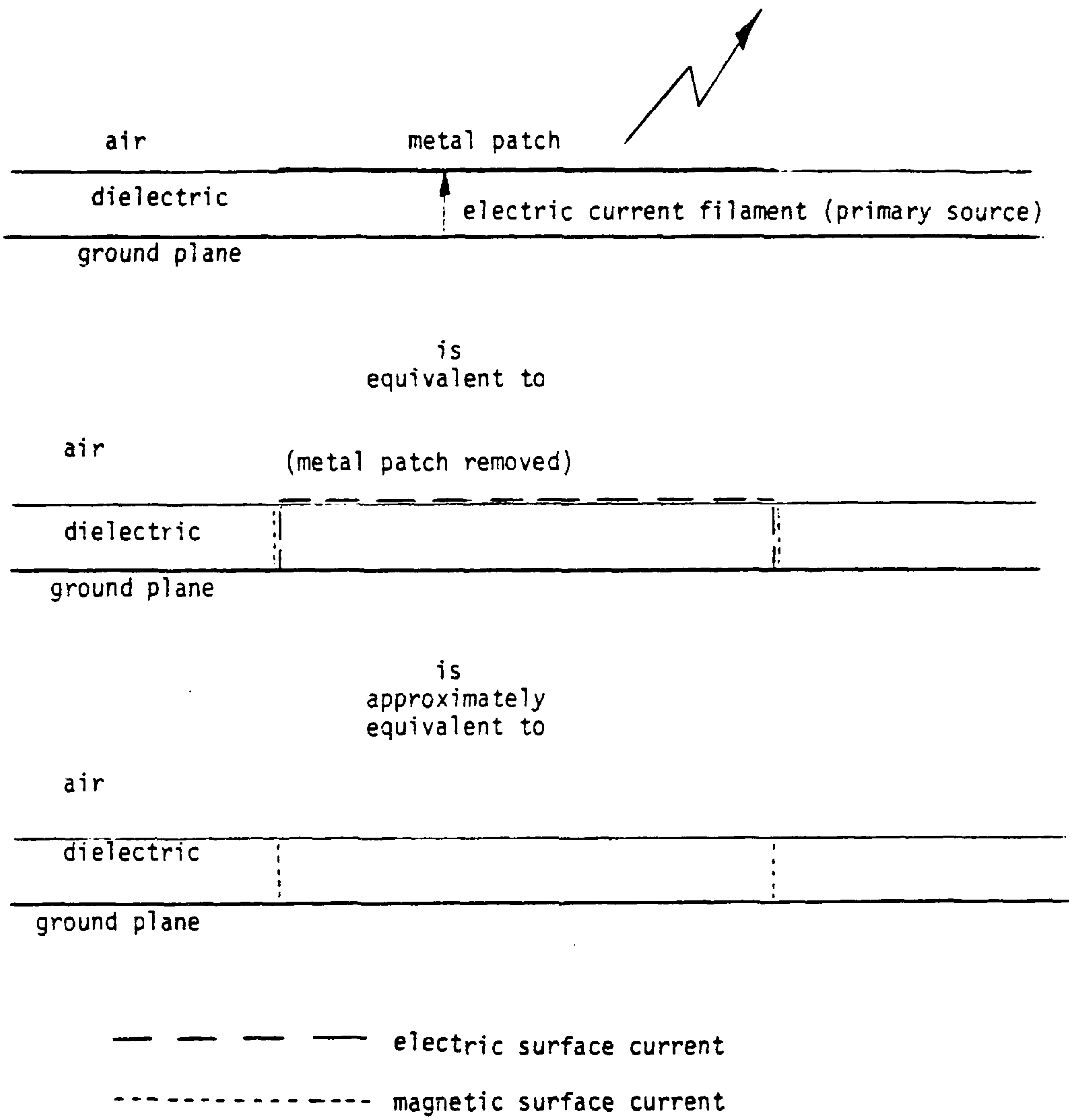

Figure 2. A cross-sectional view of a microstrip antenna shown with its primary source (top), its equivalent secondary sources with the patch removed (middle), and its approximate equivalent with the electric currents neglected.

the electric field computed in (1) is also unknown. THus, how can Q be determined? The answer is simply that the unknown factor of

$$\frac{1}{k^2 - k^2_{mn}}$$

cancels out in the expression for Q since it is proportional to the *ratio* of the stored energy to the total power. Said another way, the Q is dependent (approximately) only on the *shape* of the field distribution and *not* its *amplitude*.

Once the Q has been determined, the k in (1) is replaced by a modified, "effective wave number", k', given by

$$k' = \omega\sqrt{\mu\varepsilon}\ (1 - j\frac{1}{Q})^{1/2} \approx \omega\sqrt{\mu\varepsilon}\ \ (1 - j\frac{1}{2Q}).$$

From the modified form of (1), the driving point and even multi-port impedance parameters of an antenna with one or more ports can be computed. The only additional complication is the fact that the filamentary current which was assumed to obtain (1) must now be replaced with a current distribution with a finite surface area in order to obtain the correct inductance associated with the antenna feed. What we did in this investigation was to assume that the current was uniformly distributed over a small cylindrical surface. The width of this surface, called the "feed width", was determined empirically for a single frequency and feed point and used with good results for all other frequencies and feed points.

Rather than present the somewhat lengthy and tedious equations which represent the detailed implementation of the procedure described above, we simply indicate that the Ψ_{mn}'s required for the specific structures studied involved various combinations of Bessel and Neumann functions of fractional order. All power and energy computations were done in "closed form" except for the computation of the radiated power which required a numerical integration.

THEORETICAL AND EXPERIMENTAL RESULTS

The normalized resonant frequencies for a variety of differently shaped antennas are listed in tables 1-4. The parameter definitions and denormalizing factors are given in the tables. The table is useful because a large number of different shapes have identical resonant frequencies. That is, the resonant frequency of a mode of one shape, can have the same resonant frequency of a different mode of another shape. It is also clear from comparison between the measured and calculated impedances that the resonant frequencies are reasonably accurately predicted from this table although a firm conclusion is impossible since the actual dielectric constant of the antennas and its nominal value may not be the same.

Figures 3-5 are the Smith Chart Plots of both the measured and computed impedances for some of the antennas that were measured. The antennas were constructed from one sixteenth inch thick, Fiberglass reinforced, PTFE printed circuit board with a nominal dielectric constant of 2.55. The measurements were made on an automated network analyzer at Harry Diamond Laboratory without the benefit of a large ground plane and an anechoic chamber. Nevertheless, the predicted and measured results agree quite well and confirms our expectation that the method used in the aforementioned references works equally well for these classes of antennas.

Since at least some of these antennas have already found application, a method of analyzing them is needed. We believe that the results show that this method provides an accurage solution to the problem for such thin antennas.

Table 1. The normalized resonant frequencies of disk and circular sector microstrip antennas.

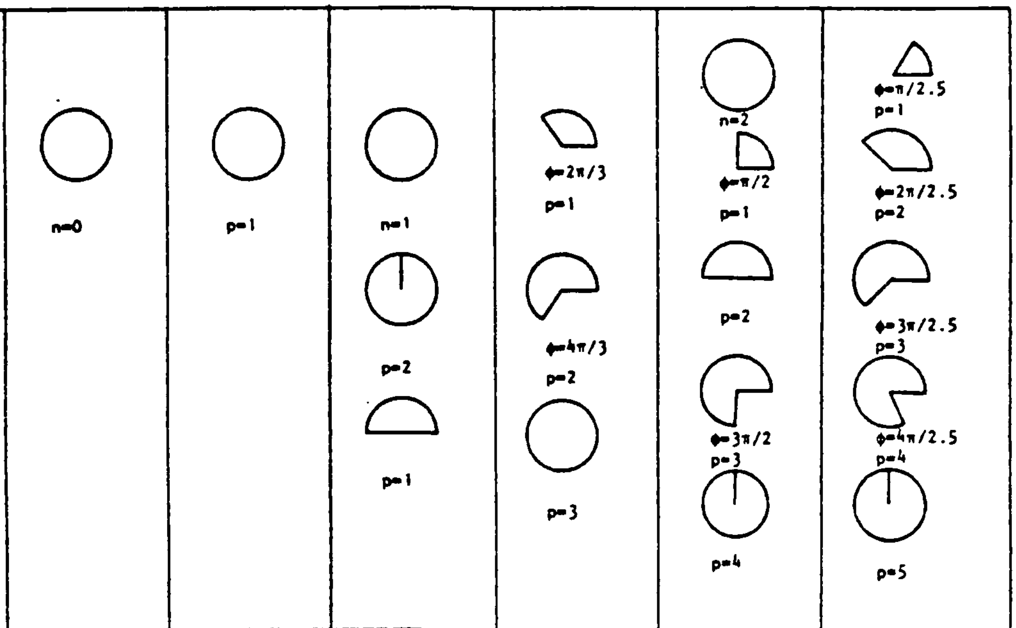

m \ ν	0	0.5	1	1.5	2	2.5
1	0	1.16556	1.84118	2.46053	3.05424	3.63230
2	3.83170	4.60422	5.33143	6.02929	6.70612	7.36701
3	7.01559	7.78989	8.53631	9.26139	9.96946	10.66356
4	10.17347	10.94994	11.70601	12.44526	13.17037	13.38336

Table 2. The normalized resonant frequencies of disk and circular sector microstrip antennas.

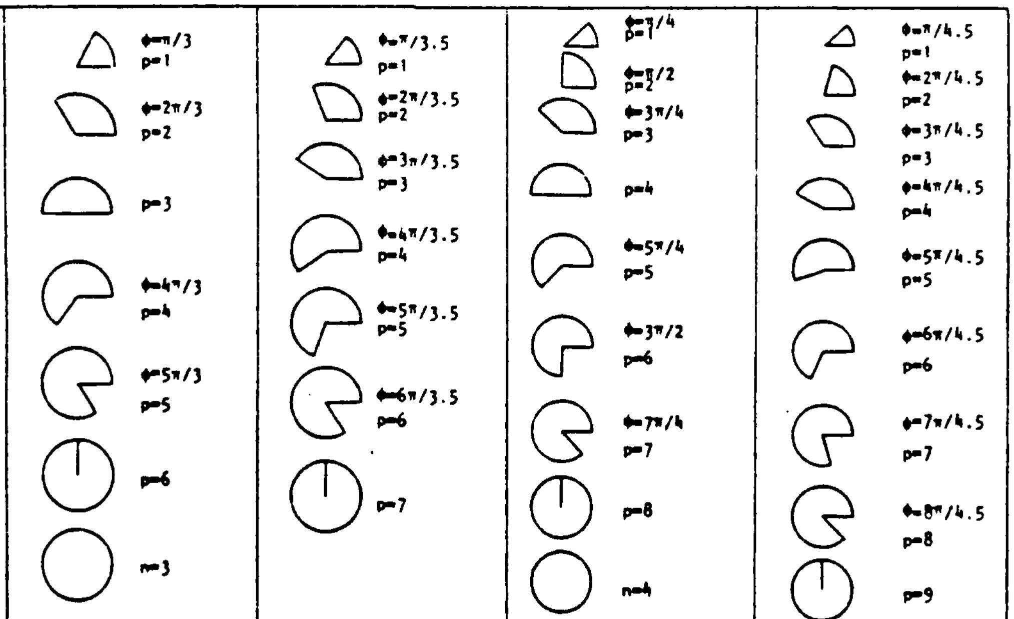

m \ ν	3	3.5	4	4.5
1	4.20119	4.76219	5.31754	5.86841
2	8.01523	8.65312	9.28239	9.90430
3	11.34529	12.01825	12.68191	13.33792
4	14.58585	15.27907	15.96410	16.64179

For both tables, the modal fields are proportional to $J_\nu(k_{mp}\rho)\cos(m\phi)$. The denormalizing factor is $c/(2\pi a\sqrt{\varepsilon_r})$ where ε_r is the relative permittivity, c is the speed of light in a vacuum, and a is the radius of the antenna. The parameter, $\nu = n$ for the circular disk and $\nu = p\pi/\phi_o$ for the sectoral antenna where ϕ_o is the sectoral angle and k_{mp} is the resonant wave number.

Table 3. The normalized resonant frequencies of annular and annular sector microstrip antennas.

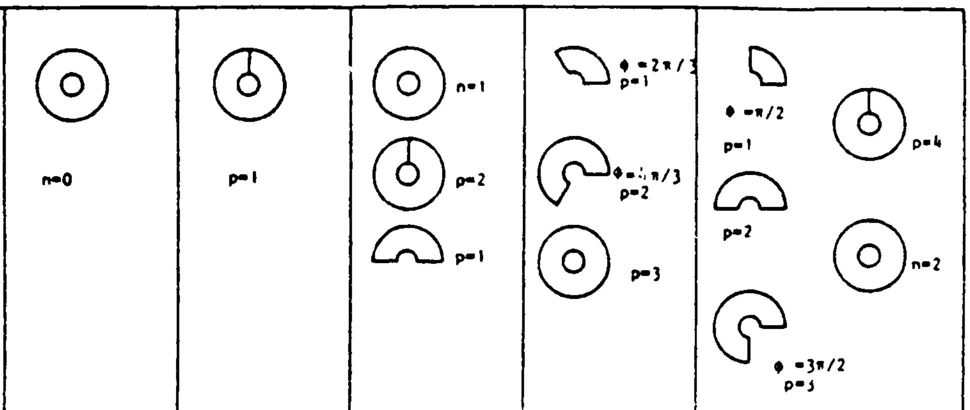

λ	m \ ν	0	0.5	1	1.5	2
λ = 2	1	0	0.33952	0.67733	1.01150	1.34060
	2	3.19657	3.21820	3.28247	3.38796	3.53129
	3	6.31231	6.32257	6.35321	6.40402	6.47471
	4	9.44442	9.45119	9.47133	9.50433	9.55158
λ = 2.5	1	0	0.29463	0.58471	0.86636	1.13695
	2	2.15645	2.18356	2.26364	2.39312	2.56640
	3	4.22309	4.23567	4.27330	4.33569	4.42238
	4	6.30657	6.31474	6.33923	6.37992	6.43665
λ = 3	1	0	0.26067	0.51362	0.75321	0.97743
	2	1.63561	1.66669	1.75776	1.90233	2.09009
	3	3.17884	3.19318	3.23611	3.30730	3.40667
	4	4.73309	4.74730	4.77493	4.82030	4.88506

Table 4. The normalized resonant frequencies of annular and annular sector microstrip antennas.

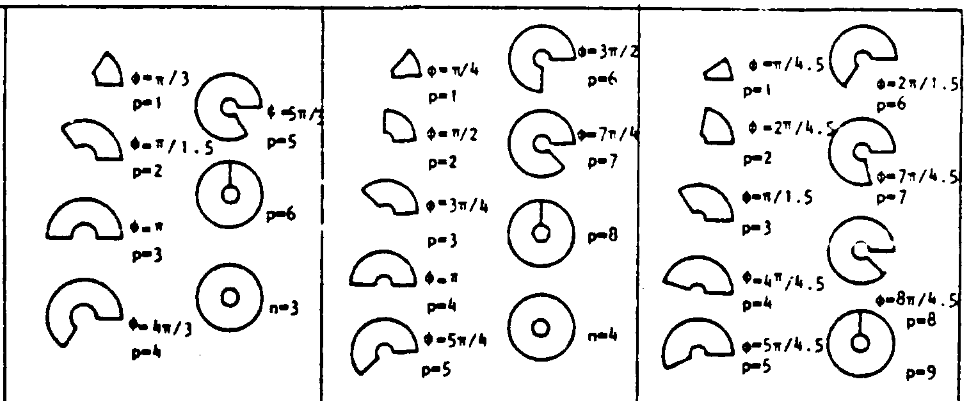

λ	m \ ν	3	4	4.5
λ = 2	1	1.97800	2.58761	2.83152
	2	3.92005	4.41822	4.69302
	3	6.67380	6.94614	7.10825
	4	9.68421	9.86760	9.97786
λ = 2.5	1	1.64327	2.11284	2.33039
	2	3.01411	3.54103	3.81551
	3	4.66643	5.00039	5.19909
	4	6.59744	6.81965	6.95321
λ = 3	1	1.38803	1.76922	1.95449
	2	2.54219	3.01972	3.25069
	3	3.68720	4.06812	4.23021
	4	5.06762	5.32232	5.47692

For both tables, the modal fields are proportional to $J_\nu(k_{mp}\rho)N'_\nu(k_{mp}b) - J'_\nu(k_{mp}b)N_\nu(k_{mp}\rho)$. The denormalizing factor is $c/(2\pi b\sqrt{\epsilon_r})$. The parameter, λ, is the ratio of the outer radius, a, to the inner radius, b. See tables 1 and 2 for the description of the other parameters.

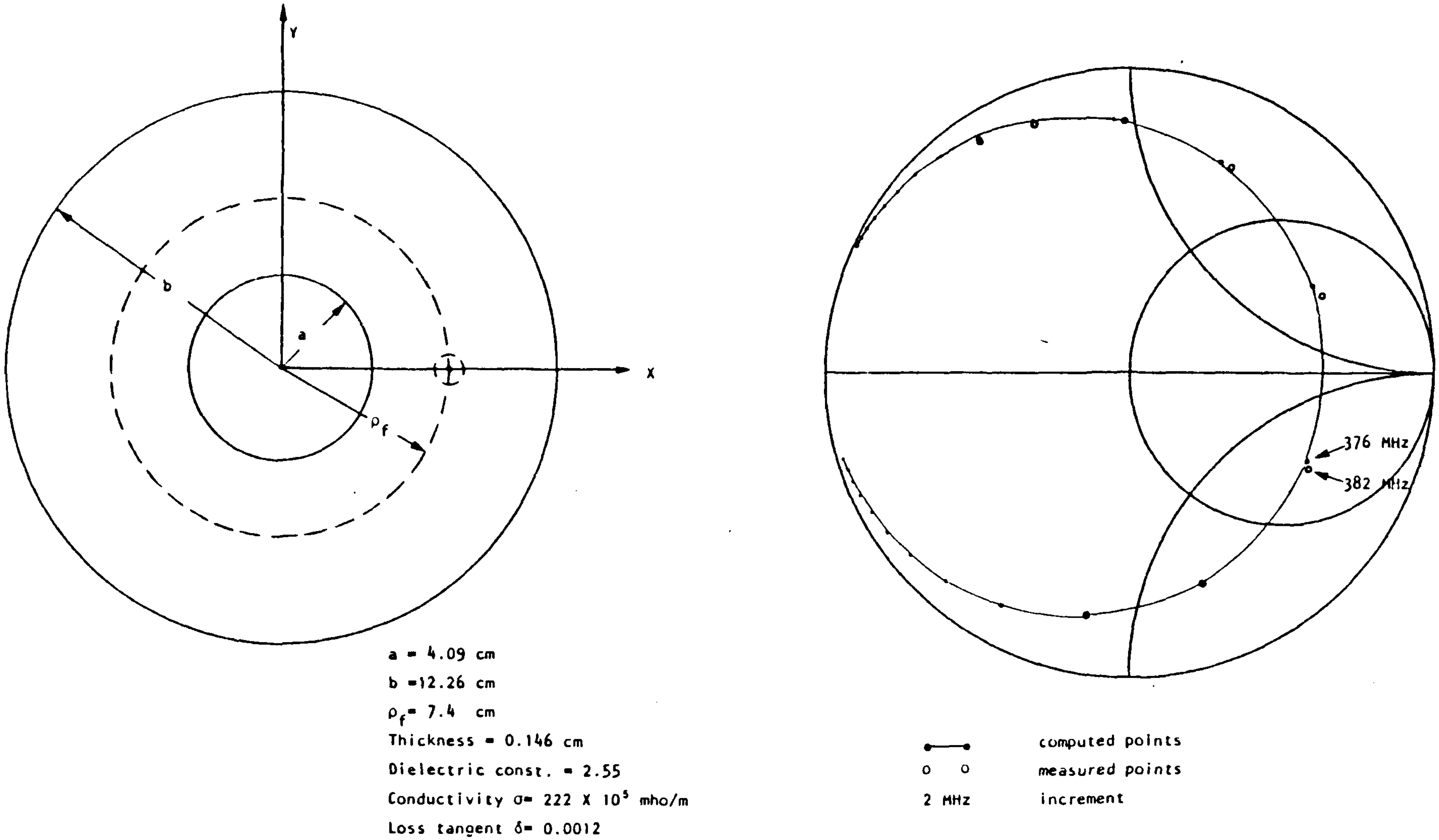

Figure 3. The measured and computed input impedance for the annular microstrip antenna.

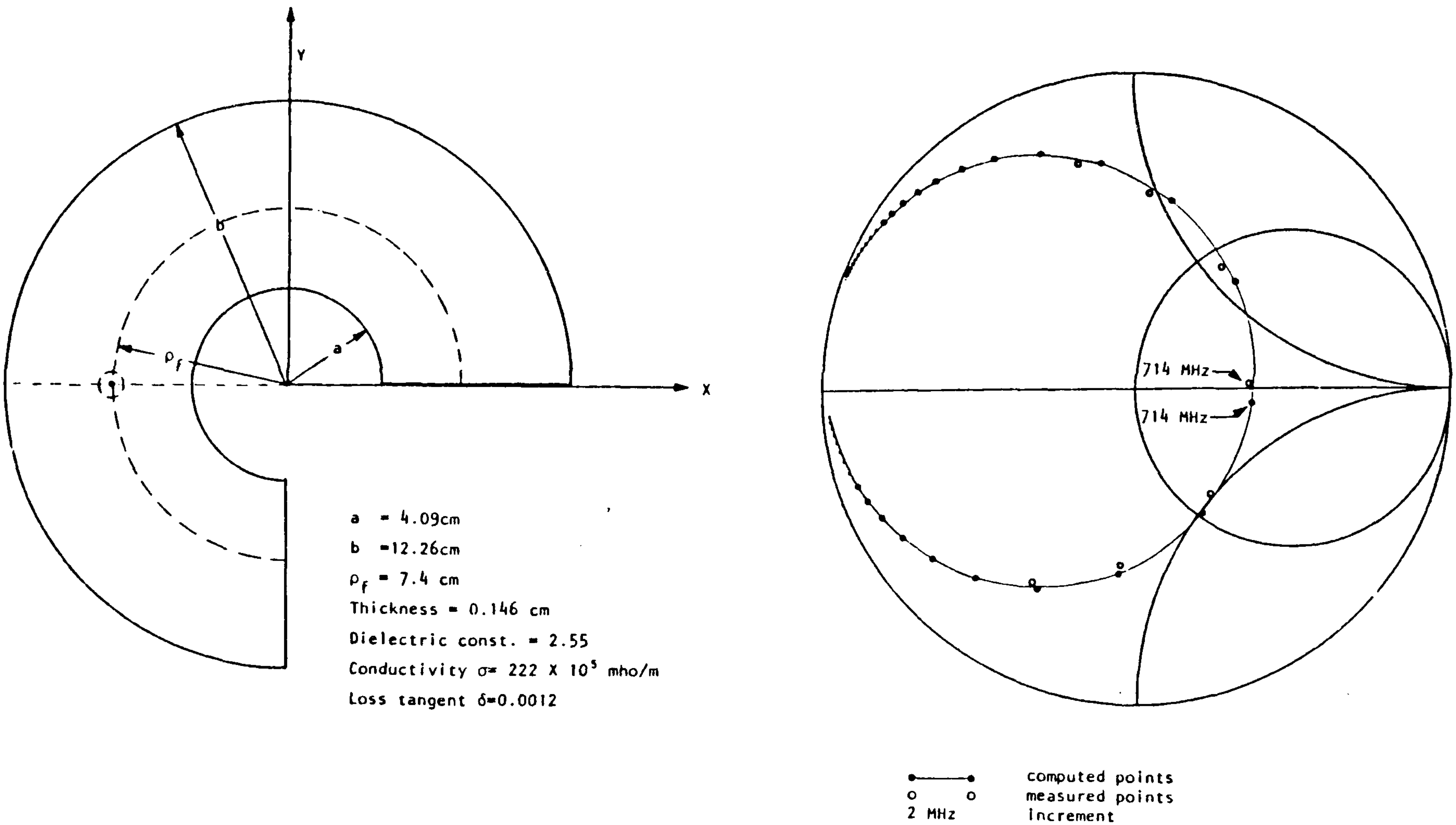

Figure 4. The measured and computed input impedance for the annular sector microstrip antenna.

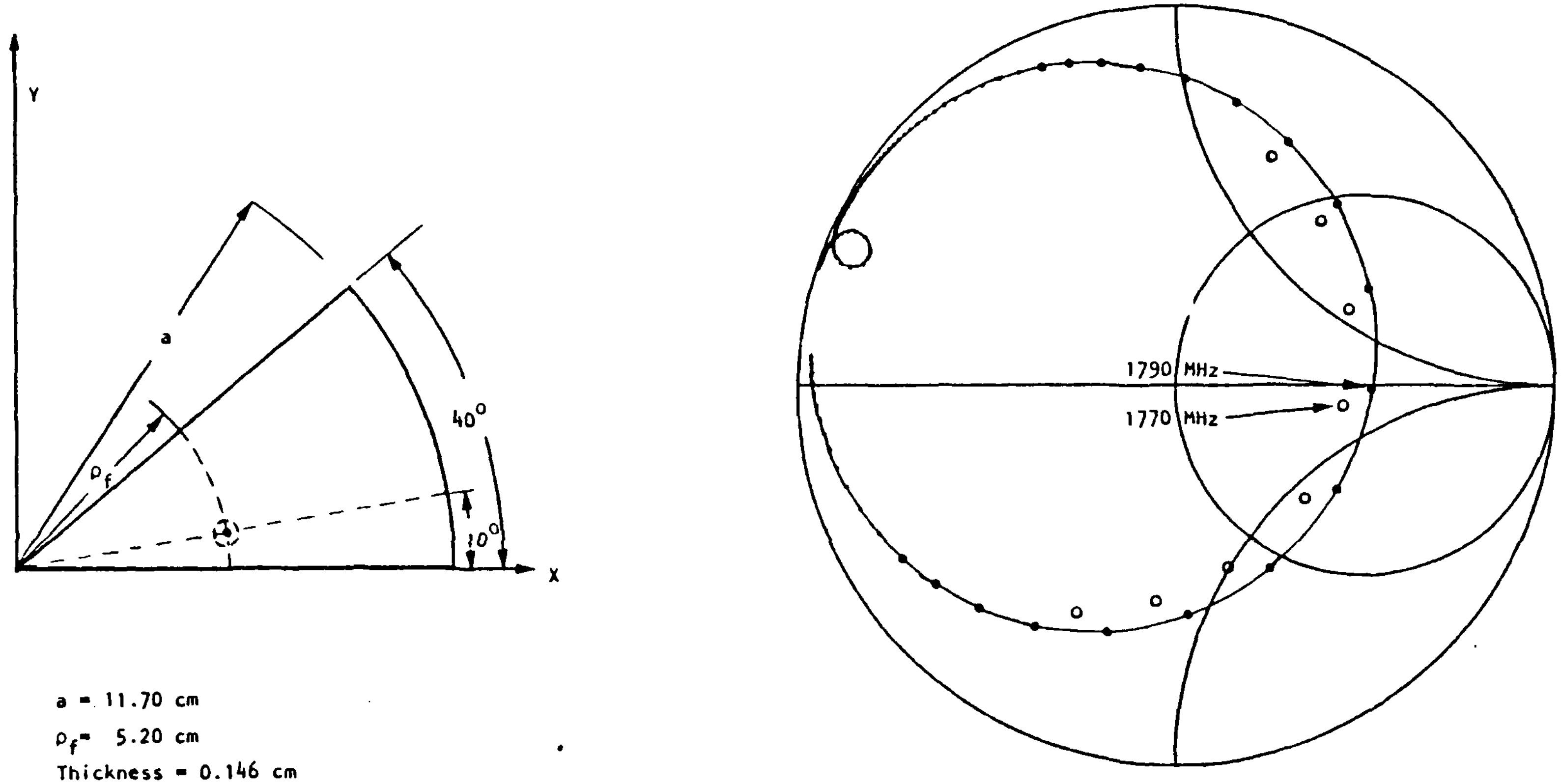

a = 11.70 cm
ρ_f = 5.20 cm
Thickness = 0.146 cm
Dielectric const. = 2.55
Conductivity σ = 222 X 10^5 mho/m
Loss tangent δ = 0.0012

●——● computed points
o o measured points
5 MHz increment

Figure 5. The measured and computed input impedance for the circular sector microstrip antenna.

ACKNOWLEDGEMENT

We are very grateful to Fred Farrar and Art Sindoris at Harry Diamond Laboratory for providing both the antennas and the measurement facilities for this project. Without their efforts, we could not have carried out the experimental part of this work.

REFERENCES

1. Y. T. Lo, D. Solomon, W. F. Richards, "Theory and Experiments on Microstrip Antennas," IEEE Transactions on Antennas and Propagation, Vol. AP-27, No. 2, March 1979, pp. 137-145.

2. W. F. Richards, Y. T. Lo, D. D. Harrison, "An Improved Theory for Microstrip Antennas and Applications," IEEE Transactions on Antennas and Propagation, Vol. P-29, No. 2, pp. 38-46.

Microstrip Dipoles on Cylindrical Structures[*]

N. G. Alexopoulos
Electrical Engineering Department
University of California at Los Angeles
Los Angeles, CA 90024

P. L. E. Uslenghi
Department of Information Engineering
University of Illinois at Chicago Circle
Chicago, IL 60680

N. K. Uzunoglu
Department of Electrical Engineering
National Technical University of Athens
Athens TT-147, Greece

[*] Research supported by U. S. Army Research contract DAAG29-79-C-0050

1. Abstract

An electric dipole tangent to the outer surface of a dielectric layer which coats a metallic cylinder is considered. Exact expressions are obtained for the electromagnetic field produced by the dipole, both inside the coating layer and in the surrounding free space. Asymptotic results are derived for a cylinder whose diameter is large compared to the wavelength. Arrays of elementary dipoles are discussed.

2. Introduction

Microstrip antennas and arrays have received increasing attention in the scientific literature during the past few years, largely as a consequence of advances in printed circuit technology. The state of the art, in both theoretical and experimental studies, is summarized in the book by Bahl and Bhartia [1] and in the special issue [2], which contains two exhaustive review papers on these subjects [3,4]. The geometries of microstrip antennas are not conducive to easy analytical treatment; for example, rectangular and triangular microstrip patch antennas may be studied by combining function-theoretic methods with ray-tracing techniques [5,6,7]. Therefore numerical treatments, based e.g. on the moment method [8], have been extensively adapted, especially for computation of input impedance and mutual impedance [9,10].

Although most studies carried out so far have dealt with planar substrates, from a practical viewpoint it is very important to consider the case of printed antennas and arrays on curved surfaces, especially on portions of cylinders, cones or spheres. Together with a companion work on spherical structures [11], this paper presents a detailed study of dipoles on a dielectric-coated cylindrical structure. The exact field produced by an electric dipole tangent to the outer surface of the coating layer is given in Section 3; the results are specialized to the radiated far field and to the surface field. An asymptotic analysis for the radiated equatorial field due to a longitudinal dipole is given in Section 4, for a thin substrate and a cylinder whose diameter is large compared to the wavelength. Preliminary results for arrays of such longitudinal dipoles are presented in Section 5. The time-dependence factor $\exp(-i\omega t)$ is omitted throughout.

3. Exact Solution

Consider an infinitely long, perfectly conducting cylinder of radius $\rho = a$ coated by a uniform layer of constant thickness $D = b - a$, permittivity $\varepsilon\varepsilon_o$ and permeability μ_o, and immersed in free space (see fig. 1).

Let us introduce a cylindrical coordinate system ρ,ϕ,z with the z axis on the axis of the cylinder. The primary source is an electric dipole located at $\underline{r}_o \equiv (\rho_o,\phi_o,z_o)$ where $\rho_o \geq b$, and whose electric dipole moment is

$$\underline{p} = \frac{4\pi\varepsilon_o}{k}\hat{c} \,, \tag{1}$$

where $\hat{c}$ is a unit vector and $k = \omega\sqrt{\varepsilon_o\mu_o}$ is the free-space wavenumber. The source strength of Eq. (1) corresponds to an incident (or primary) electric Hertz vector

$$\underline{\Pi}_e = \frac{e^{ikR}}{kR}\hat{c} \,, \quad R = |\underline{r} - \underline{r}_o| \,, \tag{2}$$

where $\underline{r} \equiv (\rho,\phi,z)$ is the position of the observation point. It should be noted that with the primary source normalized as in Eqs. (1,2), the electric dyadic Green's function has dimensions of m^{-1}, whereas the field is measured in m^{-2}.

The total (incident plus scattered) electric field is given by:

$$\begin{aligned} \underline{E}(\underline{r}) &= 4\pi k \underline{\underline{G}}_e^{(I)}(\underline{r};\underline{r}_o) \cdot \hat{c}\ , \qquad a \le \rho \le b \\ &= 4\pi k \underline{\underline{G}}_e^{(II)}(\underline{r};\underline{r}_0) \cdot \hat{c}\ , \qquad \rho \ge b. \end{aligned} \tag{3}$$

The electric dyadic Green's functions $\underline{\underline{G}}_e^{(I)}$ in the coating layer and $\underline{\underline{G}}_e^{(II)}$ in the surrounding medium may be obtained by the method described by Tai [12], as amended in [13,14]. It should be noted that disagreements on the singular term which appears in Eq. (6) below (see e.g. [15]) are of no relevance here, because the $\hat{\rho}\hat{\rho}$ term does not contribute to the field generated by a dipole tangent to the cylinder (i.e., $\hat{c} \cdot \hat{\rho} = 0$).

After imposing the boundary conditions at the perfectly conducting surface $\rho = a$ and across the dielectric interface $\rho = b$, as well as the radiation condition at $\rho \to \infty$, it is found that:

$$\begin{aligned} \underline{\underline{G}}_e^{(I)}(\underline{r};\underline{r}_o) = \frac{i}{8\pi} \int_{-\infty}^{\infty} du \sum_{n=0}^{\infty} \frac{\tau_n}{\eta^2} \sum_{e,o} \Bigg(\Bigg\{ A_n \left[\underline{M}^{(1)}_{\substack{e\\o}n,\xi}(u,\underline{r}) + \alpha_n \underline{M}^{(3)}_{\substack{e\\o}n,\xi}(u,\underline{r}) \right] \mp \\ \mp C_n \left[\underline{N}^{(1)}_{\substack{o\\e}n,\xi}(u,\underline{r}) + \beta_n \underline{N}^{(3)}_{\substack{o\\e}n,\xi}(u,\underline{r}) \right] \Bigg\} \underline{M}^{(3)}_{\substack{e\\o}n,\eta}(-u,\underline{r}_o) + \\ + \Bigg\{ B_n \left[\underline{N}^{(1)}_{\substack{e\\o}n,\xi}(u,\underline{r}) + \beta_n \underline{N}^{(3)}_{\substack{e\\o}n,\xi}(u,\underline{r}) \right] \mp \\ \mp D_n \left[\underline{M}^{(1)}_{\substack{o\\e}n,\xi}(u,\underline{r}) + \alpha_n \underline{M}^{(3)}_{\substack{o\\e}n,\xi}(u,\underline{r}) \right] \Bigg\} \underline{N}^{(3)}_{\substack{e\\o}n,\eta}(-u,\underline{r}_o) \Bigg)\ , \end{aligned} \tag{4}$$

$$\underline{\underline{G}}_e^{(II)}(\underline{r};\underline{r}_o) = \underline{\underline{G}}_{eo}(\underline{r};\underline{r}_o) + \underline{\underline{G}}_{es}(\underline{r};\underline{r}_o)\ , \tag{5}$$

$$\underline{\underline{G}}_{eo}(\underline{r};r_o) = -k^{-2}\hat{\rho}\hat{\rho}\delta(\underline{r} - \underline{r}_o) + \underline{\underline{G}}_{eo}^{(\gtrless)}(\underline{r};\underline{r}_o), \quad (\rho \gtrless \rho_o)\ , \tag{6}$$

$$\begin{aligned} \underline{\underline{G}}_{eo}^{(>)}(\underline{r};\underline{r}_o) = \frac{i}{8\pi} \int_{-\infty}^{\infty} du \sum_{n=0}^{\infty} \frac{\tau_n}{\eta^2} \sum_{e,o} \Bigg[\underline{M}^{(3)}_{\substack{e\\o}n,\eta}(u,\underline{r}) \underline{M}^{(1)}_{\substack{e\\o}n,\eta}(-u,\underline{r}_o) + \\ + \underline{N}^{(3)}_{\substack{e\\o}n,\eta}(u,\underline{r}) \underline{N}^{(1)}_{\substack{e\\o}n,\eta}(-u,\underline{r}_o) \Bigg]\ , \quad (\rho > \rho_o)\ , \end{aligned} \tag{7}$$

$$\underline{\underline{G}}_{eo}^{(<)}(\underline{r};\underline{r}_o) = \frac{i}{8\pi}\int_{-\infty}^{\infty} du \sum_{n=0}^{\infty} \frac{\tau_n}{\eta^2} \sum_{e,o} \Big[\underline{M}^{(1)}_{\substack{e\\o}n,\eta}(u,\underline{r})\underline{M}^{(3)}_{\substack{e\\o}n,\eta}(-u,\underline{r}_o) + \tag{8}$$

$$+ \underline{N}^{(1)}_{\substack{e\\o}n,\eta}(u,\underline{r})\underline{N}^{(3)}_{\substack{e\\o}n,\eta}(-u,\underline{r}_o)\Big] , \quad (\rho < \rho_o),$$

$$\underline{\underline{G}}_{es}(\underline{r};\underline{r}_o) = \frac{i}{8\pi}\int_{-\infty}^{\infty} du \sum_{n=0}^{\infty} \frac{\tau_n}{\eta^2} \sum_{e,o} \Big\{ \Big[a_n \underline{M}^{(3)}_{\substack{e\\o}n,\eta}(u,\underline{r}) \mp$$

$$\mp c_n \underline{N}^{(3)}_{\substack{o\\e}n,\eta}(u,\underline{r})\Big] \underline{M}^{(3)}_{\substack{e\\o}n,\eta}(-u,\underline{r}_o) + \Big[b_n \underline{N}^{(3)}_{\substack{e\\o}n,\eta}(u,\underline{r}) \mp \tag{9}$$

$$\mp c_n \underline{M}^{(3)}_{\substack{o\\e}n,\eta}(u,\underline{r})\Big] \underline{N}^{(3)}_{\substack{e\\o}n,\eta}(-u,\underline{r}_o)\Big\} ,$$

where

$$\underline{M}^{(j)}_{\substack{e\\o}n,\eta}(u,\underline{r}) = \nabla \mathrm{x} \Big[Z_n^{(j)}(\eta\rho)\,\substack{\cos\\ \sin}(n\phi)\, e^{iuz}\hat{z} \Big] =$$

$$= e^{iuz}\Big[\mp \frac{n}{\rho} Z_n^{(j)}(\eta\rho)\,\substack{\sin\\ \cos}(n\phi)\hat{\rho} - \frac{\partial}{\partial\rho} Z_n^{(j)}(\eta\rho)\,\substack{\cos\\ \sin}(n\phi)\hat{\phi}\Big] , \tag{10}$$

$$\underline{N}^{(j)}_{\substack{e\\o}n,\eta}(u,\underline{r}) = \frac{1}{\sqrt{u^2+\eta^2}}\, \nabla \mathrm{x} \underline{M}^{(j)}_{\substack{e\\o}n,\eta}(u,\underline{r}) =$$

$$= \frac{e^{iuz}}{\sqrt{u^2+\eta^2}} \Big[iu \frac{\partial}{\partial\rho} Z_n^{(j)}(\eta\rho)\,\substack{\cos\\ \sin}(n\phi)\hat{\rho} \mp \frac{inu}{\rho} Z_n^{(j)}(\eta\rho)\,\substack{\sin\\ \cos}(n\phi)\hat{\phi} + \tag{11}$$

$$+ \eta^2 Z_n^{(j)}(\eta\rho)\,\substack{\cos\\ \sin}(n\phi)\hat{z}\Big] ,$$

$$\eta = \sqrt{k^2 - u^2} , \quad \xi = \sqrt{k_1^2 - u^2} , \quad k_1 = \varepsilon k = N^2 k , \tag{12}$$

$j = 1$ or 3, $Z_n^{(1)}(x) = J_n(x)$ and $Z_n^{(3)}(x) = H_n^{(1)}(x)$ are the Bessel function and the Hankel function of the first kind, $\delta(\underline{r} - \underline{r}_o)$ is the three-dimensional Dirac delta-function, $\tau_o = 1$ and $\tau_{n>0} = 2$, and the integral path along the real u-axis passes below the points $u = k$, $u = k_1$ and above the points $u = -k$, $u = -k_1$ (see fig. 2).

The various coefficients which appear in Eqs. (4) and (9) are given by (the prime means derivative with respect to the argument of the primed function):

$$\alpha_n = -\frac{J_n'(\xi a)}{H_b^{(1)\prime}(\xi a)} \quad , \quad \beta_n = -\frac{J_n(\xi a)}{H_n^{(1)}(\xi a)} \tag{13}$$

$$A_n = N\frac{\Gamma_{n\beta}}{\Gamma_{n\alpha}} B_n = \frac{2i\Gamma_{n\beta}}{\pi b\delta_n H_n^{(1)}(\eta b)} \ , \tag{14}$$

$$C_n = N\frac{\gamma_{n\alpha}}{\gamma_{n\beta}} D_n = \frac{2nu\gamma_{n\alpha}}{\pi k_1 b^2\delta_n H_n^{(1)}(\eta b)}\left(1 - \frac{\xi^2}{\eta^2}\right) \ , \tag{15}$$

$$a_n = -\frac{J_n(\eta b)}{H_n^{(1)}(\eta b)} + \frac{\xi^2\gamma_{n\alpha}}{\eta^2 H_n^{(1)}(\eta b)} A_n \ , \tag{16}$$

$$b_n = -\frac{J_n(\eta b)}{H_n^{(1)}(\eta b)} + \frac{\xi^2\gamma_{n\beta}}{N\eta^2 H_n^{(1)}(\eta b)} B_n \ , \tag{17}$$

$$c_n = \frac{\xi^2\gamma_{n\beta}}{N\eta^2 H_n^{(1)}(\eta b)} C_n \ , \tag{18}$$

where

$$\gamma_{n\alpha} = J_n(\xi b) + \alpha_n H_n^{(1)}(\xi b), \ \gamma_{n\beta} = J_n(\xi b) + \beta_n H_n^{(1)}(\xi b) \ , \tag{19}$$

$$\Gamma_{n\alpha} = -\frac{\partial\gamma_{n\alpha}}{\partial b} + \frac{\xi^2}{\eta^2}\gamma_{n\alpha}\frac{\partial}{\partial b}\ln H_n^{(1)}(\eta b) \ , \tag{20}$$

$$\Gamma_{n\beta} = -\frac{\partial\gamma_{n\beta}}{\partial b} + \frac{\xi^2}{\varepsilon\eta^2}\gamma_{n\beta}\frac{\partial}{\partial b}\ln H_n^{(1)}(\eta b) \ , \tag{21}$$

$$\delta_n = \Gamma_{n\alpha}\Gamma_{n\beta} - \left(\frac{nu}{k_1 b}\right)^2 \left(1 - \frac{\xi^2}{\eta^2}\right)^2 \gamma_{n\alpha}\gamma_{n\beta}. \tag{22}$$

The above formulas can be considerably simplified in particular case. Consider, for example, an axially-oriented dipole $(\hat{c} = \hat{z})$ located on the substrate $(\rho_o = b)$; the total electric field on the substrate and in the equatorial plane $z = z_o$ is:

$$[\underline{E}]_{\substack{\rho=\rho_o=b \\ z=z_o \\ \hat{c}=\hat{z}}} = \hat{z}\,\frac{-2}{\pi\varepsilon k^2 b} \sum_{n=0}^{\infty} \tau_n \cos n\,(\phi - \phi_o) \int_0^{\infty} du\,\gamma_{n\beta}\Gamma_{n\alpha}\xi^2\delta_n^{-1}. \tag{23}$$

In the more general case when the dipole at $\underline{r}_o = (b,\phi_o,z_o)$ is tangent to the substrate but not necessarily axially oriented, i.e.

$$\hat{c} = \hat{c}\cdot\hat{\phi}_o\hat{\phi}_o + \hat{c}\cdot\hat{z}\hat{z}\,, \quad \hat{c}\cdot\hat{\rho}_o = 0\,, \tag{24}$$

then the electric field at any point $\underline{r}$ in free space is:

$$\underline{E}(\underline{r}) = \underline{E}_{\perp}\,\hat{c}\cdot\hat{\phi}_o + \underline{E}_{||}\,\hat{c}\cdot\hat{z}\,, \tag{25}$$

where

$$\underline{E}_{\perp} = \frac{1}{\pi k b}\int_{-\infty}^{\infty} du\, k^2\eta^{-2} e^{-iuz_o} \sum_{n=0}^{\infty} \frac{\tau_n}{H_n^{(1)}(\eta b)} \sum_{e,o} \begin{matrix}\cos\\ \sin\end{matrix}(n\phi_o)\,\cdot$$

$$\cdot\left\{\left[-1 + \frac{\xi^2\gamma_{n\alpha}\Gamma_{n\beta}H_n^{(1)\prime}(\eta b)}{\eta\delta_n H_n^{(1)}(\eta b)} - \frac{n^2u^2\xi^2\gamma_{n\alpha}\gamma_{n\beta}}{\eta^2 k_1^2 b^2\delta_n}\left(\frac{\xi^2}{\eta^2} - 1\right)\right]\underline{M}^{(3)}_{\substack{e\\o}n,\eta}(u,\underline{r}) \pm\right.$$

$$\left.\pm\,\frac{inu\gamma_{n\beta}\xi^2}{\varepsilon k b\delta_n\eta}\left[\eta^{-1}\Gamma_{n\alpha} - \gamma_{n\alpha}\left(\frac{\xi^2}{\eta^2} - 1\right)\frac{H_n^{(1)\prime}(\eta b)}{H_n^{(1)}(\eta b)}\right]\underline{N}^{(3)}_{\substack{o\\e}n,\eta}(u,\underline{r})\right\}, \tag{26}$$

$$\underline{E}_{||} = \frac{1}{\pi\varepsilon b}\int_{-\infty}^{\infty} du\,\xi^2\eta^{-2} e^{-iuz_o} \sum_{n=0}^{\infty} \frac{\tau_n\gamma_{n\beta}}{\delta_n H_n^{(1)}(\eta b)} \sum_{e,o} \begin{matrix}\cos\\ \sin\end{matrix}(n\phi_o)\,\cdot$$

$$\cdot\left[-\Gamma_{n\alpha}\,\underline{N}^{(3)}_{\substack{e\\o}n,\eta}(u,\underline{r}) \pm \frac{inu}{kb}\left(\frac{\xi^2}{\eta^2}-1\right)\gamma_{n\alpha}\underline{M}^{(3)}_{\substack{o\\e}n,\eta}(u,\underline{r})\right]. \tag{27}$$

In the far field $(\rho \to \infty)$, the integrals in Eqs. (26-27) may be asymptotically evaluated by the method of stationary phase, the stationary point being at $u = k\cos\theta$, where $\theta = \arccos(z/r)$ is the usual polar angle in spherical coordinates. If we write the radiated field as

$$\left.\begin{aligned}\underline{E}_{\|}(\underline{r}) &= -k^2\frac{e^{ikr}}{kr}\underline{S}_{\|}(\hat{r}),\\ \underline{E}_{\perp}(\underline{r}) &= -k^2\frac{e^{ikr}}{kr}\underline{S}_{\perp}(\hat{r}),\end{aligned}\right\}(\rho\to\infty) \tag{28}$$

then the dimensionless far-field coefficients $\underline{S}_{\|}$ and $\underline{S}_{\perp}$ are

$$\begin{aligned}\underline{S}_{\|}(\hat{r}) &= S_{\|\theta}\hat{\theta} + S_{\|\phi}\hat{\phi}\\ &= \frac{2i}{\pi\zeta}\left(1-\frac{\cos^2\theta}{\varepsilon}\right)e^{-ikz_o\cos\theta}(A_\theta\hat{\theta}+A_\phi\hat{\phi}),\end{aligned} \tag{29}$$

$$\begin{aligned}\underline{S}_{\perp}(\hat{r}) &= S_{\perp\theta}\hat{\theta} + S_{\perp\phi}\hat{\phi}\\ &= \frac{2}{\pi\zeta}e^{-ikz_o\cos\theta}(B_\theta\hat{\theta}+B_\phi\hat{\phi}),\end{aligned} \tag{30}$$

where

$$\zeta = kb\sin\theta,$$

$$A_\theta = \sum_{n=0}^{\infty}\tau_n(-i)^n\frac{k\tilde{\gamma}_{n\beta}\tilde{\Gamma}_{n\alpha}}{\tilde{\delta}_n H_n^{(1)}(\zeta)}\cos n(\phi-\phi_o), \tag{32}$$

$$A_\phi = (\varepsilon-1)\frac{2\cot\theta}{\zeta}\sum_{n=1}^{\infty}(-i)^n n\frac{k^2\tilde{\gamma}_{n\alpha}\tilde{\gamma}_{n\beta}}{\tilde{\delta}_n H_n^{(1)}(\zeta)}\sin n(\phi-\phi_o), \tag{33}$$

$$B_\theta = \left(1 - \frac{\cos^2\theta}{\varepsilon}\right) \frac{2\cot\theta}{\zeta} \sum_{n=1}^{\infty} (-i)^n n \frac{k^2\tilde{\gamma}_{n\beta}}{\tilde{\delta}_n H_n^{(1)}(\zeta)} \left[k^{-1}\tilde{\Gamma}_{n\alpha} - \frac{\varepsilon - 1}{\sin\theta} \tilde{\gamma}_{n\alpha} \frac{H_n^{(1)'}(\zeta)}{H_n^{(1)}(\zeta)} \right] \sin n(\phi - \phi_o) , \tag{34}$$

$$B_\phi = \sum_{n=0}^{\infty} \frac{\tau_n(-i)^n}{H_n^{(1)}(\zeta)} \left[-1 + \frac{\varepsilon - \cos^2\theta}{\sin\theta} \cdot \frac{k\tilde{\gamma}_{n\alpha}\tilde{\Gamma}_{n\beta}H_n^{(1)'}(\zeta)}{\tilde{\delta}_n H_n^{(1)}(\zeta)} - \frac{n^2\cot^2\theta}{\varepsilon\zeta^2} (\varepsilon - 1)(\varepsilon - \cos^2\theta) \frac{k^2\tilde{\gamma}_{n\alpha}\tilde{\gamma}_{n\beta}}{\tilde{\delta}_n} \right] \cos n(\phi - \phi_o) , \tag{35}$$

and $\tilde{f} = (f)_{u=k\cos\theta}$. In particular, observe that $S_{||\theta}$ and $S_{||\phi}$ are even and odd functions of $(\phi - \phi_o)$, respectively, as it must be by reason of symmetry. Also, $S_{||\phi} = 0$ when $\varepsilon = 1$. If the cylindrical structure were absent, the dipole at the origin $(\rho_o = z_o = 0)$ and axially oriented $(\hat{c} = \hat{z})$ would yield $S_{||\theta} = \sin\theta$, $S_{||\phi} = 0$, as expected.

4. Asymptotic Expansions for Thin Substrate

We limit our considerations to the far field produced by a dipole on the substrate and parallel to the z axis, in the equatorial plane $\theta = \frac{\pi}{2}$, so that $S_{\|\phi} = 0$. We assume

$$kb \gg 1, \quad |k_1 D| \ll 1 \; ; \tag{36}$$

the second inequality means that the coating layer is electrically thin. Then

$$\begin{aligned} Z_n(k_1 a) &\simeq Z_n(k_1 b) - k_1 D Z_n'(k_1 b) \, , \\ Z_n'(k_1 a) &\simeq Z_n'(k_1 b) + k_1 D \left[1 - \frac{n^2}{(k_1 b)^2} \right] Z_n(k_1 b), \end{aligned} \tag{37}$$

where $Z_n = J_n$ or $H_n^{(1)}$; substitution into (32) yields, for $\theta = \pi/2$:

$$(S_{\|\theta})_{\theta=\frac{\pi}{2}} \simeq S = -\frac{2ikD}{\pi kb} \sum_{n=0}^{\infty} \frac{\tau_n (-1)^n \cos n(\phi - \phi_o)}{H_n^{(1)}(kb) - kDH_n^{(1)\prime}(kb)} \, . \tag{38}$$

Set:

$$\begin{aligned} \Phi &= \phi - \phi_o - \pi \\ \eta_o &= -ikD, \end{aligned} \tag{39}$$

and observe that η_o would be the relative surface impedance of a thin substrate with magnetic permeability equal to that of free space. Then:

$$S = \frac{2\eta_o}{\pi kb} \sum_{n=-\infty}^{\infty} \frac{(-1)^n e^{-i\frac{\pi}{2}n} \cos n\Phi}{H_n^{(1)}(kb) - i\eta_o H_n^{(1)'}(kb)}$$

$$= \frac{2i\eta}{\pi kb} \int_C \frac{e^{-i\frac{\pi}{2}\nu} \cos\nu\Phi}{\left[H_\nu^{(1)}(kb) - i\eta_o H_\nu^{(1)'}(kb)\right] \sin\pi\nu}\, d\nu \qquad (40)$$

where the contour C is along the real axis and just above it in the complex ν-plane, from $-\infty$ to $+\infty$. The integral in (40) is similar to the one studied by Goriainov [16] in relation to plane-wave scattering by a cylinder. Following [16], we set

$$e^{-i\nu\frac{\pi}{2}} = e^{i\nu\frac{3\pi}{2}} - 2ie^{i\nu\frac{\pi}{2}} \sin\pi\nu \qquad (41)$$

in the integrand of Eq. (40), so that

$$S = S_1 + S_2$$

where

$$S_1 = \frac{4\eta_o}{\pi kb} \int_C \frac{e^{i\nu\frac{\pi}{2}} \cos\nu\Phi}{M_\nu(kb)}\, d\nu\ , \qquad (42)$$

$$S_2 = \frac{2i\eta_o}{\pi kb} \int_C \frac{e^{i\nu\frac{3\pi}{2}} \cos\nu\Phi}{M_\nu(kb)\sin\pi\nu}\, d\nu\ , \qquad (43)$$

with

$$M_\nu(kb) = H_\nu^{(1)}(kb) - i\eta_o H_\nu^{(1)'}(kb). \qquad (44)$$

The integral S_1 has a stationary point, as is seen by using Debye's expansion for $H_\nu^{(1)}$ in (44); the integral S_2 does not have a stationary point. Assume

$$|\nu - kb| > |\nu^{1/3}|\ , \qquad (45)$$

then, in a region about the origin in the ν-plane (for details see, e.g. [17,18]):

$$S_1 \sim \eta_o \sqrt{\frac{2}{\pi kb}} \int_C d\nu \frac{\sqrt[4]{1 - (\frac{\nu}{kb})^2}}{1 - i\eta_o\sqrt{(\frac{\nu}{kb})^2 - 1}}$$

$$\cdot \left\{ \exp i \left[\nu(\frac{\pi}{2} + \Phi + \arccos\frac{\nu}{kb}) - \sqrt{(kb)^2 - \nu^2} + \frac{\pi}{4} \right] + \exp i \left[\nu(\frac{\pi}{2} - \Phi + \arccos\frac{\nu}{kb}) - \sqrt{(kb)^2 - \nu^2} + \frac{\pi}{4} \right] \right\}; \tag{46}$$

the first integral in (46) has a stationary point at $\nu_o = -kb\sin\Phi$, whereas the second integral has no stationary point. A stationary phase evaluation of S is therefore obtained by considering the stationary phase contribution due to the first term in the integrand of Eq. (46):

$$S \sim - \frac{2ikD\cos(\phi - \phi_o)}{1 - ikD\cos(\phi - \phi_o)} e^{-ikb\cos(\phi - \phi_o)} . \tag{47}$$

On the basis of Eq. (36 the denominator in (47) may be replaced by unity, so that

$$S \sim - 2ikD\cos(\phi - \phi_o) e^{-ikb\cos(\phi - \phi_o)} . \tag{48}$$

At the point of stationary phase, condition (45) is satisfied if

$$|\phi - \phi_o| < \frac{\pi}{2} - \sqrt{2}\,(kb)^{-4/3} , \tag{49}$$

which defines the region of free space into which direct radiation by the dipole occurs. Thus, Eq. (48) is valid in the "illuminated region" defined by (49), as shown in Fig. 3.

The far field in the penumbra and shadow regions, where inequality (49) does not hold, is obtained by letting

$$\nu = kb + mt \ , \qquad m = \left(\frac{kb}{2}\right)^{1/3} >> 1 \tag{50}$$

into Eq. (44), so that:

$$M_\nu(kb) \sim \frac{-i}{m\sqrt{\pi}} \left[w_1(t) + \frac{kD}{m} w_1'(t)\right] \ , \tag{51}$$

where $w_1(t)$ is Airy's function in Fock's notation [18]. The poles of (40) in the complex ν-plane are the zeros of $M_\nu(kb)$, i.e.:

$$\frac{w_1'(t_s)}{w_1(t_s)} = - \frac{m}{kD} \ . \tag{52}$$

Since this last ratio is large compared to unity,

$$t_s \simeq t_{os} - \frac{kD}{m} \ , \tag{53}$$

where the zeros $t_{os}(s = 1,2,\ldots)$ of $w_1(t_{os}) = 0$ are well tabulated.

Since $\mathrm{Im}\nu > 0$ at t_s, we may rewrite Eq. (40) as:

$$S \sim \frac{kD}{m} \left[f\left(\xi_+, \frac{kD}{m}\right) e^{ikb(\frac{\pi}{2} + \Phi)} + f\left(\xi_-, \frac{kD}{m}\right) e^{ikb(\frac{\pi}{2} - \Phi)} \right], \tag{54}$$

where

$$\xi_{\pm} = m\left(\frac{\pi}{2} \pm \Phi\right) \ , \tag{55}$$

and the generalized Fock function

$$f(\xi,\rho) = \frac{1}{\sqrt{\pi}} \int_\Gamma \frac{e^{i\xi t}}{w_1(t) + \rho w_1'(t)} \, dt \tag{56}$$

is well known, and can be evaluated e.g. by residues at the poles (53); the contour Γ starts at infinity in the angular sector $\pi > \arg t > \pi/3$, passes between $\nu = kb$ and the pole of the integrand nearest the origin (i.e. $t = t_1$), and ends at infinity in the angular sector $\pi/3 > \arg t > -\pi/3$ (see fig. 4).

The approximation (54) includes only the first two creeping waves, which complete less than one complete turn around the cylinder; the geometric interpretation of the two terms in Eq. (54) is shown in fig. 5.

5. Arrays of Longitudinal Dipoles

An axially oriented dipole at angular position ϕ_o on the substrate produces the far-field pattern of Eq. (48) in the illuminated portion of its equatorial plane. Consider an array of n such dipoles with angular separation α between dipoles, i.e. the total array angle is $(n - 1)\alpha$ (see fig. 6). The far-field point of observation is in the illuminated region of all dipoles if

$$-\frac{\pi}{2} + (n - 1)\alpha + \sqrt{2}(kb)^{-4/3} < \phi < \frac{\pi}{2} - \sqrt{2}(kb)^{-4/3}. \tag{57}$$

Under limitation (57), dipoles fed with equal amplitude and progressive phase shift β yield the pattern:

$$S_{total} = 2kD \frac{\partial}{\partial(kb)} \sum_{\ell=0}^{n-1} e^{-ikb\cos(\phi - \ell\alpha) + i\ell\beta}. \tag{58}$$

6. Concluding Remarks

The basic analysis for studying the behavior of printed circuit antennas on cylindrical structures has been presented herein. Numerical results pertaining to current distribution and other antenna characteristics for various substrate parameters will be presented.

References

[1] I. J. Bahl and P. Bhartia (1980), Microstrip Antennas, Artech House, Dedham, MA.

[2] IEEE Trans. Antennas Propag. (1981), special issue on microstrip antennas and arrays (D. C. Chang, editor), Vol. AP-29, No. 1.

[3] K. R. Carver and J. W. Mink (1981), "Microstrip antenna technology", IEEE Trans. Antennas Propag., AP-29, 2 - 24.

[4] R. J. Mailloux, J. F. McIlvenna and N. P. Kernweis (1981), "Microstrip array technology", IEEE Trans. Antennas Propag. AP-29, 25-37.

[5] D. C. Chang and E. F. Kuester (1981), "Total and partial reflection from the end of a parallel-plate waveguide with an extended dielectric slab", Radio Science 16, 1 - 13.

[6] D. C. Chang (1981), "Analytical theory of an unloaded rectangular microstrip patch", IEEE Trans. Antennas Propag., AP-29, 54-62.

[7] E. F. Kuester and D. C. Chang (1981), "Resonance and Q properties of isosceles triangular patch antennas of 60^{o} and 90^{o} vertex", National Radio Science Meeting, Los Angeles, CA.

[8] E. H. Newman and P. Tulyathan (1981), "Analysis of Microstrip antennas using moment methods", IEEE Trans. Antennas Propag., AP-29, 47-53.

[9] I. E. Rana and N. G. Alexopoulos (1981), "Current distribution and input impedance of printed dipoles", IEEE Trans. Antennas Propag., AP-29, 99 - 105.

[10] N. G. Alexopoulos and I. E. Rana (1981), "Mutual impedance computation between printed dipoles", IEEE Trans. Antennas Propag., AP-29, 106-111.

[11] N. G. Alexopoulos and P. L. E. Uslenghi (1981), "Microstrip dipoles on spherical structures", National Radio Science Meeting, Los Angeles, CA.

[12] C. -T. Tai (1971) Dyadic Green's Functions in Electromagnetic Theory, Intext, Scranton, PA.

[13] C. -T. Tai (1973), "Eigen-function expansion of dyadic Green's functions", Math. Note 28, AFWL, Kirtland AFB, NM.

[14] C. -T. Tai (1976), "Singular terms in the eigen-function expansion of dyadic Green's function of the electric type", Math. Note 65, AFWL, Kirtland AFB, NM.

[15] R. E. Collin (1981), "Dyadic Green's functions-Current views on singular behavior", session on Scattering and Diffraction, 20th General Assembly of the International Union of Radio Science, Washington, D.C.

[16] A. S. Goriainov (1958), "An asymptotic solution of the problem of diffraction of a plane electromagnetic wave by a conducting cylinder", Radiotekhinka i Elektronica 3, 23 - 39.

[17] G. N. Watson (1966), A Treatise on the Theory of Bessel Functions, 2nd ed., Cambridge University Press, Cambridge, England.

[18] J. J. Bowman, T.B.A. Senior and P.L. E. Uslenghi (1969), Electromagnetic and Acoustic Scattering by Simple Shapes, North-Holland, Amsterdam.

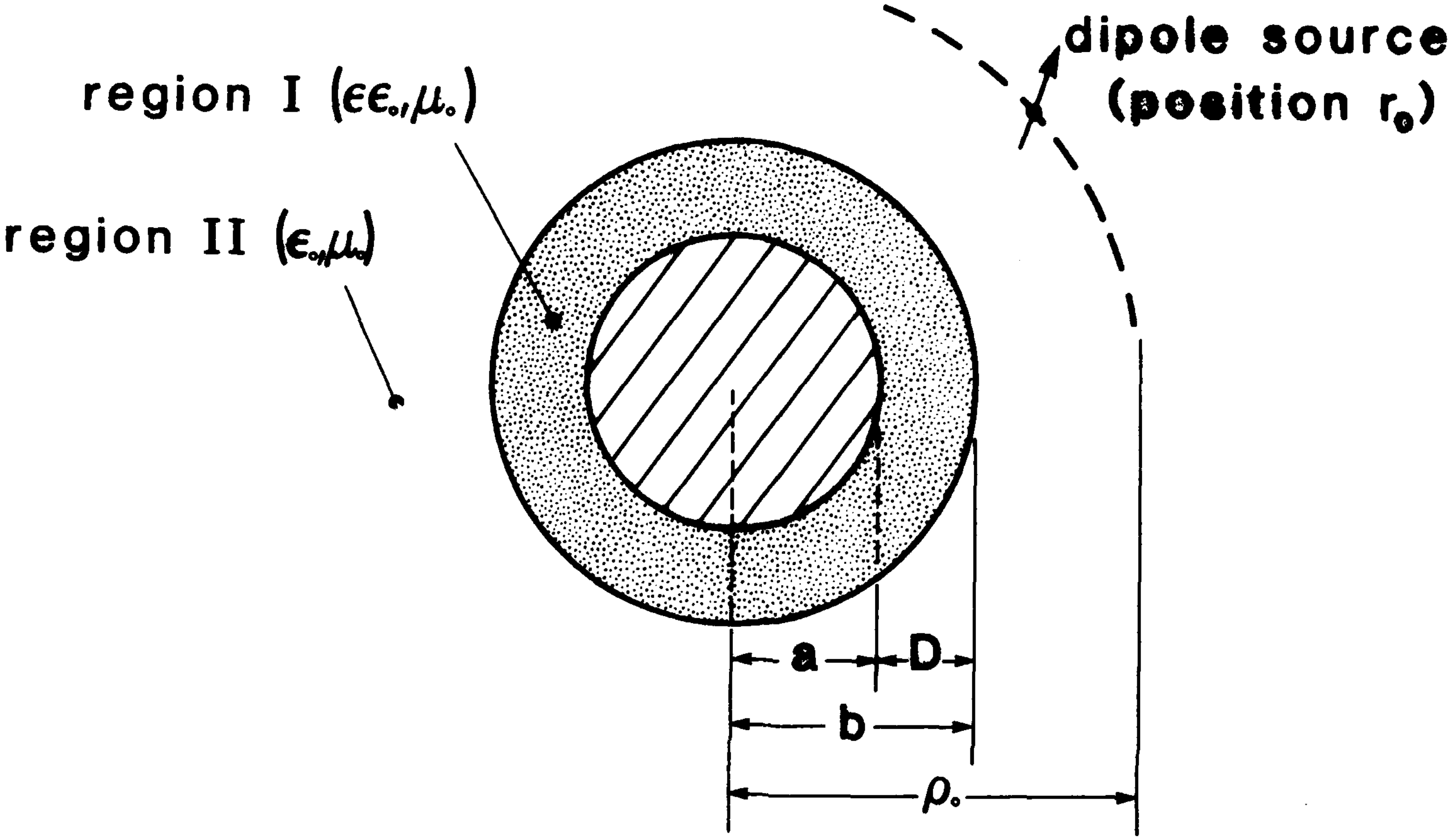

Figure 1 Geometry of the Problem

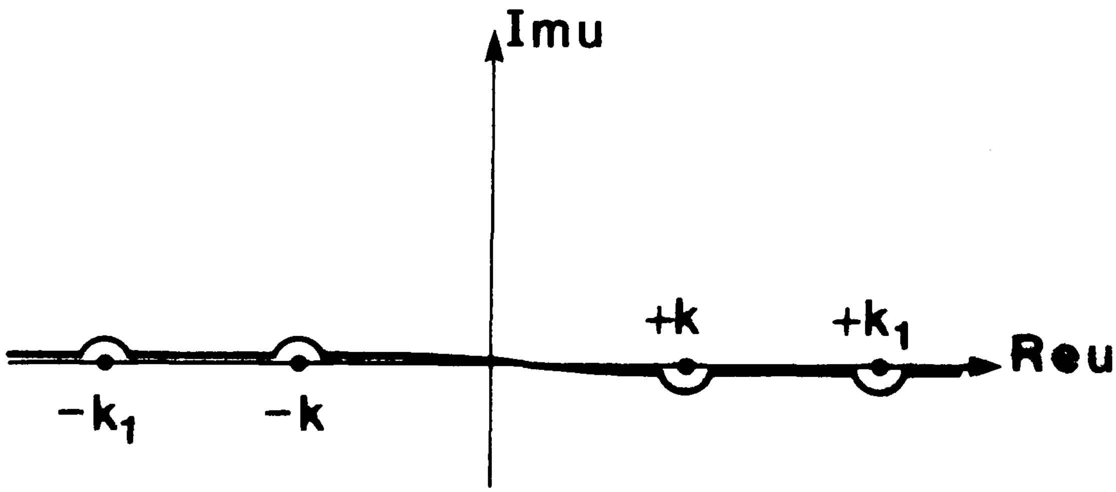

Figure 2 Path of Integration Along the Reu-axis

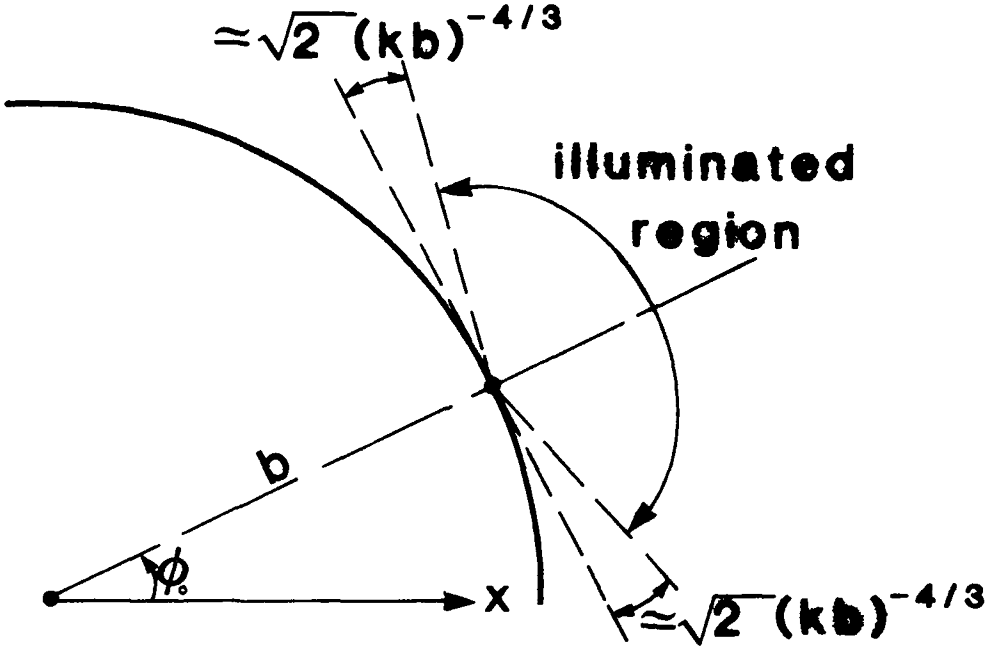

Figure 3 Geometric Interpretation of Condition (49)

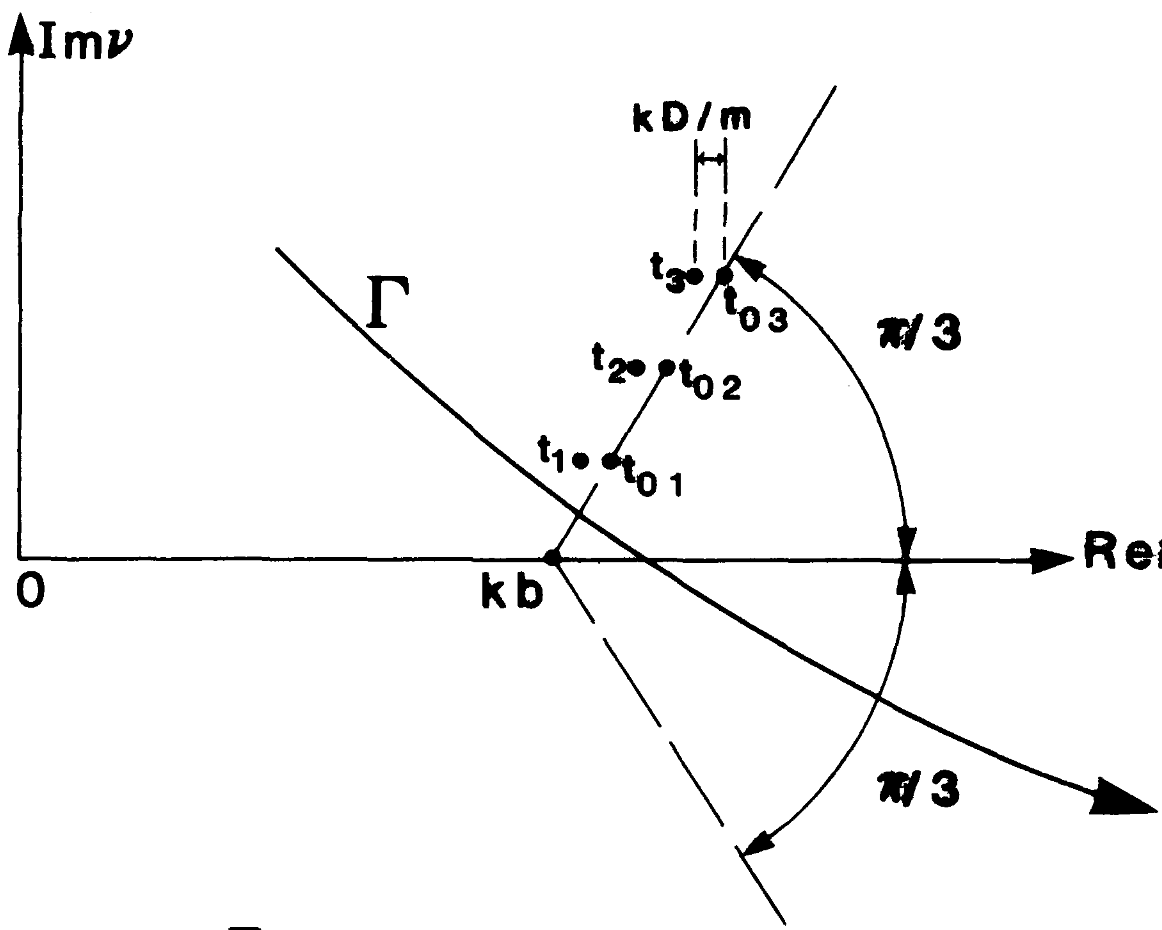

Figure 4 Contour Γ and Poles in the Complex ν-plane

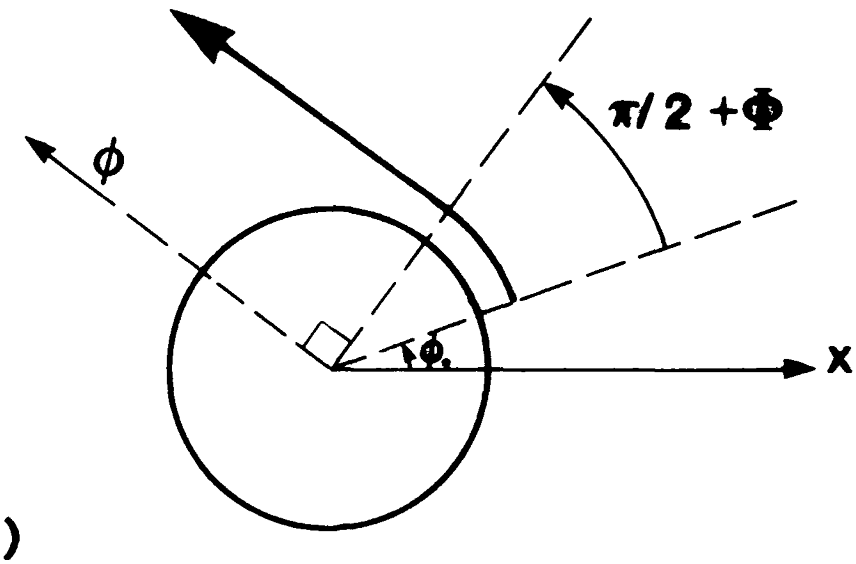

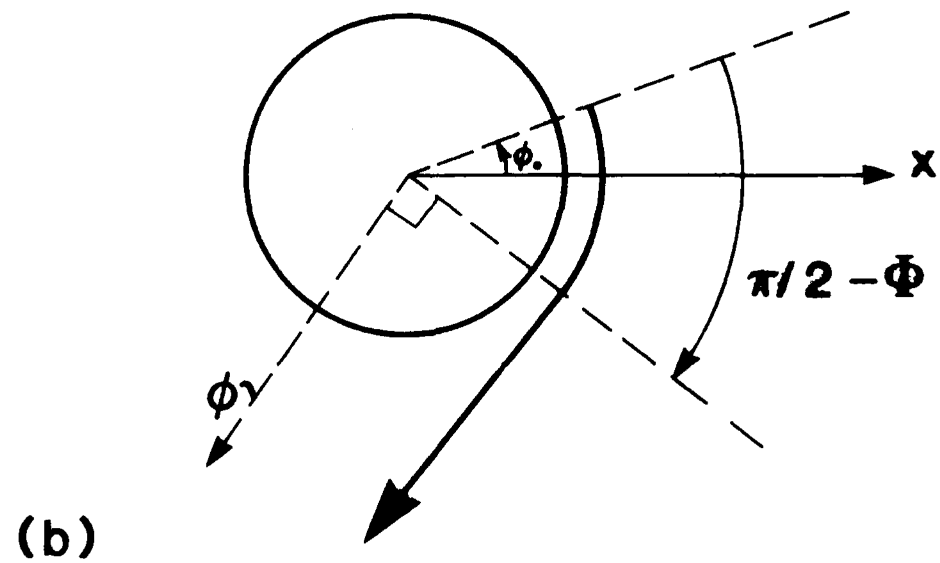

Figure 5 Geometric Interpretation of the Creeping-wave Terms in Equation (54); (a) $\xi=\xi_+$; (b) $\xi=\xi_-$

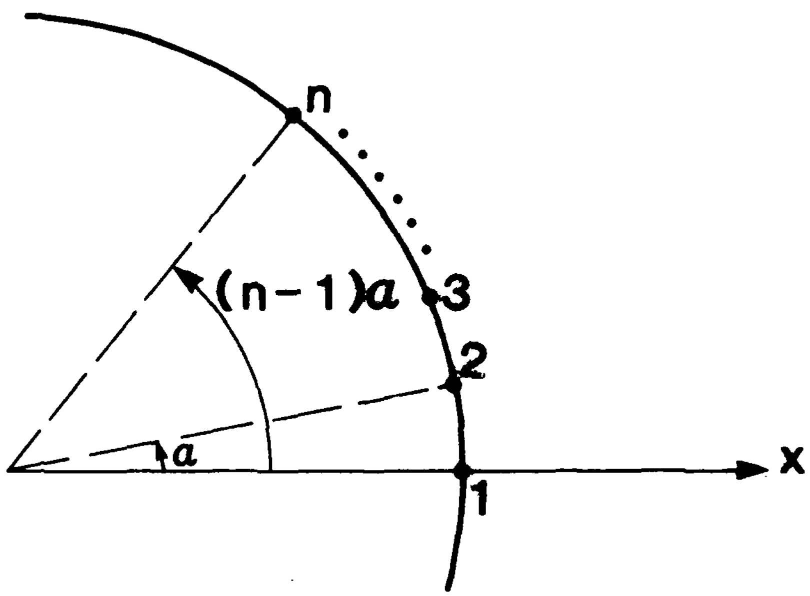

Figure 6 Geometry for Circumferential Array

PREPRINT
HDL-PP-81-RTA-2

August 1981

DESIGN OF MICROSTRIP LINEAR ARRAY ANTENNAS

by Morris Campi

U.S. Army Electronics Research
and Development Command
Harry Diamond Laboratories
Adelphi, MD 20783

Copies available from author

DESIGN OF MICROSTRIP LINEAR ARRAY ANTENNAS

Morris Campi

A computer code has been developed to be used as a tool for the design of microstrip linear array antennas. This code treats a rectangular "patch" element connected in series by a transmission line to form a traveling wave array. Included are provisions for sensitivity studies of the radiation patterns to array parameters such as (1) patch element conductance, (2) patch separation, (3) reflections, (4) individual element directivity, (5) insertion phase, (6) mutual coupling, (7) radiation efficiency, (8) terminating impedance, (9) dielectric constant, and (10) dissipative losses.

The code is interactive and presents a series of questions which, when answered, helps the engineer design an antenna for a specified main beam angle and side-lobe level. A constrained optimization routine is used to vary the conductances and related parameters to produce an aperture distribution close to the distribution needed for the type of side-lobe structure desired (such as Tchebyscheff, Taylor, and binomial). One major feature of this code is that it allows the engineer to vary any one or more of the design parameters and to observe the changes in the radiation pattern displayed on the user terminal screen. Once a design is established, the engineer is presented with the design data needed to fabricate the antenna.

Several antenna arrays were fabricated and tested. The results indicate that antennas can be accurately designed by this code for side-lobe levels in the 15- to 30-dB range. With additional improvements in certain subroutines, it is anticipated that the code can be used to design antennas with side-lobe levels lower than 30 dB.

1. INTRODUCTION

Microstrip antenna technology and design are currently being researched to meet the present and future needs of military radar and fuze system requirements. Configured either in single- or multiple-lattice structures, microstrip has the advantages of being easy to fabricate, low cost, lightweight, and geometrically conformable. When designed to have either a series or a corporate feed network, the lattices become antenna arrays that can be used for transmitting and receiving signals from microwave through millimeter frequencies into the lower regions of the near-millimeter-wave portion of the spectrum. However, the present state of the art is at the same stage of development as existed for waveguide slot array designs in the late 1950's and early 1960's. This stage was a "cut-and-try" period, where an empirical design would take from weeks to months of fabrication and testing before satisfactory results were obtained; even then, one was never sure of achieving the optimum design to meet the system's specific requirements.

Today, computer-aided design codes can be developed to help antenna engineers in their design of linear or phased array microstrip antennas. This report describes one such code that was developed from empirical data and a theoretical model (discussed in sect. 2 and 3). One major feature of this code is that it allows the designer to vary any one or more of the antenna design parameters and to observe the changes in the radiation pattern displayed at the computer terminal screen. This application alone provides the tool required by the engineer to determine in a matter of seconds the prime factors affecting his design, and to make parametric adjustments (sensitivity studies) to help understand and develop his final product. Once a design is established, the engineer is presented with a set of coordinate numbers that can be used to fabricate the antenna on a printed circuit board without the need for drawings or art layout, thus simplifying the process and reducing the time spent toward producing a final product from a computer design.

Some specific antennas were designed based on the models presently existing in the code. This paper discusses the results of the designs, along with remarks as to where improvements can be incorporated in the code to enhance its applicability.

2. MICROSTRIP LINEAR ARRAY ANTENNA

When a combination of two or more single microstrip patch elements are placed end to end, they form a linear series array. Like all other series arrays, the radiation characteristics are essentially those produced by the electromagnetic fields that illuminate the antenna aperture (the far-field radiation pattern is related to the Fourier transform of the aperture illumination). A constant illumination produces a $\sin^2 x/x$-like pattern in the far field, with 13.2 dB side lobes below the main beam. Other distributions will produce far-fielded patterns with other levels of side lobes, gains, and beam widths, each dictated by the antenna aperture distribution. Analysis of far-field measurements over the years has provided engineers with some very specific aperture distributions that satisfy their system requirements.

Control of the radiated power distribution in a corporate feed array is fairly simple. This is done by independently feeding each array element a prescribed power level to radiate, which, when combined with the other elements, forms the aperture illumination. As power is transmitted along a series-fed array, some power radiates from the first element and the rest continues, in like fashion, until all the elements radiate power accordingly. The aperture distribution in this case is determined by the radiation characteristics of each element and their relation to all the other element characteristics. Therefore, it becomes necessary to study the single-element characteristics along with the array neighbor-to-neighbor interactions in order that a linear series-fed array can be designed to propagate energy with a prescribed power distribution.

2.1 Single-Element Patch Model

The geometry of the single-element microstrip patch is shown in figure 1. It consists of a thin rectangular conducting plate positioned over a conducting ground plane separated by a thin layer of dielectric material, where the material thickness is much less than one wavelength. By use of inexpensive printed circuit technology the patch element is readily fabricated using etching techniques applied to metal-clad dielectric (usually Teflon, or Teflon impregnated with fiberglass sandwiched between thin copper plating).

The patch width, W, determines the electrical admittance of the element, and the dimension ℓ (nearly one-half wavelength) determines the frequency at which the element is resonant. At resonance, the element is an efficient radiator of electromagnetic energy. As such the element consists basically of two radiating slots perpendicular to the feed line and separated by a transmission line of very low impedance.[1] The resonant line length ℓ is slightly less than one-half wavelength because of phase modifications due to substrate thickness, fringing field capacitance, and the patch aspect ratio.

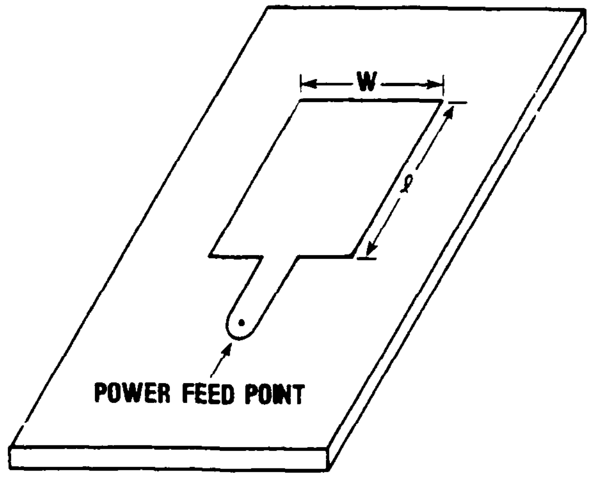

Figure 1. Geometry of microstrip patch element.

The fields radiating from these slots have components parallel to the ground plane which add in phase to give a maximum radiated field normal to the element.

2.2 Microstrip Element Conductance

Since the combined power radiated by the two slots of a patch is the same as that dissipated by a conductance, G, having across it the voltage V_O at the center of the slot, then

$$G = P/V_O^2\ , \text{ or } G = J/60\pi^2,$$

where

$$J = \int_0^\pi [\sin^{2}(\pi w \sin\phi/\tau_O)\ \mathrm{Cos}^3\phi/\sin^2\phi]d\phi \quad (1)$$

The integral J is solved by use of computer integration techniques. It is worth noting that for small values of patch width ($W/\lambda_O \ll 1$) the conductance can be approximated to

$$G = (1/45)(W/\lambda_O)^2 \quad (2)$$

[1]A. G. Derneryd, *IEEE Trans AP*, AP-24 (November 1976) 846-851

As the width increases to infinity the conductance approaches

$$G = (1/60)(W/\lambda_0) \quad . \tag{3}$$

In the intermediate range, $0.033 \leq W/\lambda_0 \leq 0.254$, conductance values have been measured and follow the relation[2]

$$G = 0.0162(W/\lambda_0)^{1.757}, \tag{4}$$

which is in fair agreement with equation (2).

2.3 *Insertion Phase*

Transmission line discontinuities produce phase shifts or delays in the propagation of energy down the transmission line. The impedance mismatch and line-to-patch-width aspect ratio at the entrance and exit ports of each microstrip patch produce phase delays to the propagating signal. And most importantly, mode structure and wave number along the longitudinal axis of the microstrip cavity can introduce a large insertion phase shift between input and output ports, in addition to the desired phase shift of 180 deg. This effect does not alter the resonance condition of the patch, but increases the effective phase delay to the following patch in the array, thus changing the composite radiation pattern. For example, if all the patch widths were equal, the resulting constant insertion phase of each patch would rotate the main lobe of the antenna pattern. However, most array designs require different sized element widths, causing unequal insertion phases to occur and modifying the pattern in even less desirable ways. One method used to compensate for the insertion phase is to foreshorten the transmission line lengths between the elements by an amount $\Delta \ell$ such that $\Delta \ell/\lambda_e = \phi_e/2\pi$, where ϕ_e is the insertion phase, and λ_e is the signal wavelength in the dielectric.* The reduction in length by this method will cause the patch separation to have the desired equal electrical path lengths, but unequal physical lengths.

2.4 *Mutual Coupling*

The proximity of one patch element positioned close to another in forming an array will cause coupling of the E- or H-fields, depending on the patch element plane orientation. The series-fed array aligns the E-fields to be oriented along the array direction. Published literature[3,4] and in-house experiments† indicate that E-plane coupling is about −17 dB for 0.1 λ_0 separation and decreases with increasing separation. These data were tabulated in a subroutine of the program and are used in designing an array.

3. COMPUTER MODEL

The computer program reported here was developed to provide design data for fabricating a linear series microstrip array antenna. The design is based on information provided by the user as he answers a series of questions that are displayed on the terminal screen. Figure 2 indicates the nature of the questions presented, along with the manner of response needed to satisfy the program input requirements. Although this figure shows five element options from which to choose, option 4 is the one used for designing microstrip arrays. There are also currently eight varieties of dielectric material and thicknesses from which to choose; they determine the transmission line width, once the characteristic impedance is designated.

The computations in this program normalize impedances (or admittances) to the line characteristic impedance/admittance as chosen. Distance is also dimensioned by normalizing to the wavelength of interest, as it is measured in the dielectric (or free space if so chosen). As such, the element separation need only be dimensioned as decimal parts of a wavelength. Actual design dimensions need not be determined until the antenna design is completed and resonant frequency is assigned.

The program also offers options for considering the effects of (a) reflections due to impedance mismatch at each element, (b) patch directivities

---

[2] *T. Metzler, Proceedings of the Workshop on Printed Circuit Antenna Technology, New Mexico State University, Las Cruces (October 1979), 20-1–20-16.*

**The effect of the dielectric is to change the wavelength dimension from the free space value λ_0 to the dielectric value λ_e by the relation $\lambda_e = \lambda_0/\sqrt{\epsilon_e}$, where ϵ_e is the material effective dielectric constant.*

[3] *P. P. Jedlicka and K. R. Carver, Proceedings of the Workshop on Printed Circuit Antenna Technology, New Mexico State University, Las Cruces (October 1979), 4/1-19.*

[4] *P. P. Jedlicka and K. R. Carver, IEEE Trans AP, **AP-29**, 1 (January 1981).*

†Data obtained from F. Farrar, Harry Diamond Laboratories.

due to the broadside gain of each element, (c) insertion phase, and (d) compensation for insertion phase. This capability and the others mentioned provide for a variety of parametric studies toward determining the causal relations of the antenna pattern peculiarities and sensitivity studies important in understanding the effect of manufacturing tolerances.

```
*ENTER ELEMENT OPTION:
  1—FOR OMNIDIRECTIONAL
  2—FOR HALF-WAVE DIPOLE, MAX AT THETA = 90
  3—FOR HALF-WAVE DIPOLE, MAX AT PHI = 90
  4—FOR MICROSTRIP PATCH, THETA POLARIZATION
  5—FOR MICROSTRIP PATCH, PHI POLARIZATION

*ENTER NUMBER OF ARRAY ELEMENTS IN
  I2 FORMAT
10
*DIELECTRIC MATERIAL ON FILE
ENTER 1   FOR FREE SPACE
ENTER 2   FOR 1/16 IN. TFE
ENTER 3   FOR 1/32 IN. TFE
ENTER 4   FOR 1/64 IN. TFE
ENTER 5   FOR 1/16 IN. PURE TEFLON
ENTER 6   FOR 1/32 IN. PURE TEFLON
ENTER 7   FOR 1/64 IN. PURE TEFLON
ENTER 8   FOR .005 IN. PURE TEFLON, 1/4 OZ. CU

*ENTER DIELECTRIC CONSTANT. (TEFLON
  FIBERGLASS:2.55)
  (PURE TEFLON:2.1)

*ENTER DESIRED BEAM ANGLE IN + OR — DEGREES
  FROM BROADSIDE (F—FORMAT)
POSITIVE, FOR ANGLES TOWARD THE FEED
NEGATIVE, FOR ANGLES TOWARD THE LOAD

*ENTER ALPHA VALUE IN DB PER UNIT DISTANCE
  USED IN LAMBDA

*ENTER CHARACTERISTIC IMPEDANCE IN OHMS
  DEFAULT TO 50. OHMS
```

Figure 2. Sample information request as displayed on terminal screen during antenna design.

If the conductance values of the array elements are unknown they will be calculated by the program after the power distribution taper is entered. Six power taper arrays are programmed and are available for use as subroutines as discussed in section 3.2. Other power distributions have to be entered manually.

3.1 *Optimization*

An algorithm contained in the program computes an initial estimate of the required element conductances which is then iteratively improved to provide precisely the desired power distribution. The optimization routine generates the calculated power distribution from the calculated radiated power of each element and compares it with that given as input data. The square of the difference is calculated, and the optimization routine varies the conductance values to minimize this difference. When completed, the power calculated to radiate from each element is in very good agreement with the input power data, and the conductance values generated are used for designing the array.

The antenna radiation pattern from the generated design can be displayed on the terminal screen as planar or polar plots displayed over any desired angular range.

3.2 *Power Distribution Subroutines*

The power distribution to be radiated over the antenna aperture may be inserted into the program either by use of a terminal keyboard or by use of those distributions already available in the program as subroutines. Those distributions are:

(a) Uniform
(b) Tchebyscheff
(c) Taylor
(d) Cosine square on a pedestal
(e) Binomial
(f) $(1 - x^2)^m$

The choice of any specific distribution must include tradeoffs between gain, beamwidth, and side-lobe levels—a decision usually dictated by system requirements. Here the computer code is particularly useful in displaying the design for each distribution, where comparisons of each feature may be explored with relative ease.

4. ANTENNA DESIGNS

Several arrays were designed using the computer to study specific parameters such as frequency, beam angle, mutual coupling, characteristic impedance, and overall performance of the antenna. Table 1 provides a brief synopsis of the designed arrays along with some of the measured results.

TABLE 1. DESIGN PARAMETERS AND MEASURED RESULTS OF ANTENNA DESIGNS

Design parameters	Antenna			
	MCX-1	MCX-2	MCX-3	MCX-4
Frequency band	X	S	S	S
No. of elements	10	14	12	12
Side-lobe level (dB)	−20	−25	−25	-25
Efficiency	80%	80%	80%	50%
Beam angle (broadside to feed)	25°	55°	35°	35°
Z_0 (ohms)	100	50	50	50
Measured results	**Antenna**			
	MCX-1	MCX-2	MCX-3	MCX-4
Gain	12 dBI	6 dBI	13 dBI	10 dBI
Side-lobe level (dB)	−15	−29	−16	−16
Beam angle	25°	55°	35°	35°
Impedance bandwidth (2:1 VSWR)	10%	21%	17%	25%

4.1 MCX-1

This antenna was designed to see how well it performed at X-band with 100 ohms as the termination and as the characteristic impedance of the feed line for the array elements. Figure 3 is a measured polar plot of the radiation pattern for this antenna at the design frequency. The 0 deg corresponds to broadside illumination. A cross polarization of about −25 dB is indicated by the dashed curve. Figure 4 shows the array pattern at three frequencies. The variation in amplitudes of the main beam is attributed to variations in the generator output rather than differences in the antenna gain at the measured frequencies. The side lobes are about 5 dB higher than designed, indicating a possible limitation of the computer model or the effects of mutual coupling between the array elements.

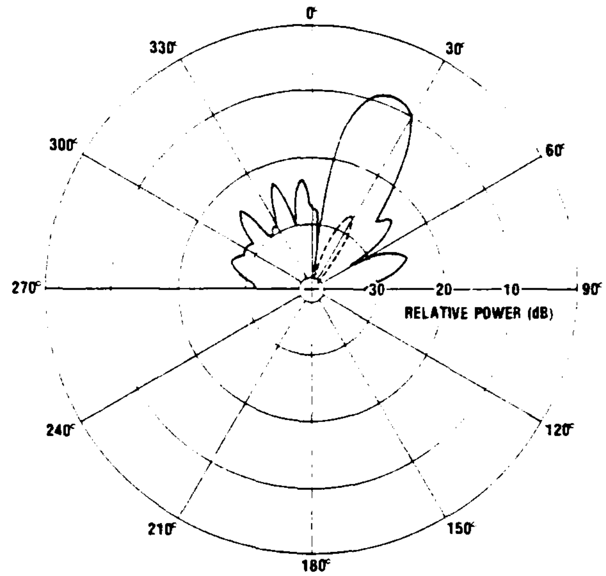

Figure 3. Polar plot of MCX-1 antenna showing main beam at 25 deg from broadside. Dashed curve is cross-polarization plot.

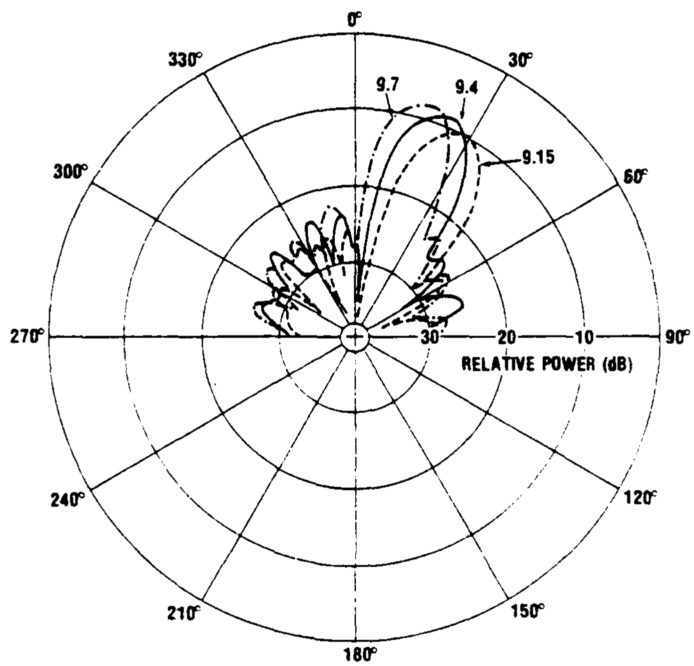

Figure 4. Polar plot of MCX-1 antenna showing main beam shift with frequency.

4.2 MCX-2

It was suspected that E-plane mutual coupling may cause the power that is coupled from adjacent elements to re-radiate and alter the aperture distribution, thereby producing higher side lobes than expected. To test this hypothesis, a 14-element S-band array was designed to produce a beam of about 55 deg from broadside (about 35 deg toward the antenna feed). This beam angle design would reduce the spacing between the patches so that the separation distance approaches 0.1 wavelength. The measured polar plot in figure 5 shows −28 dB side lobes, which is 3 dB better than the −25 dB design. This result indicates that mutual coupling is not the factor for causing the high side lobes shown in the previous design.

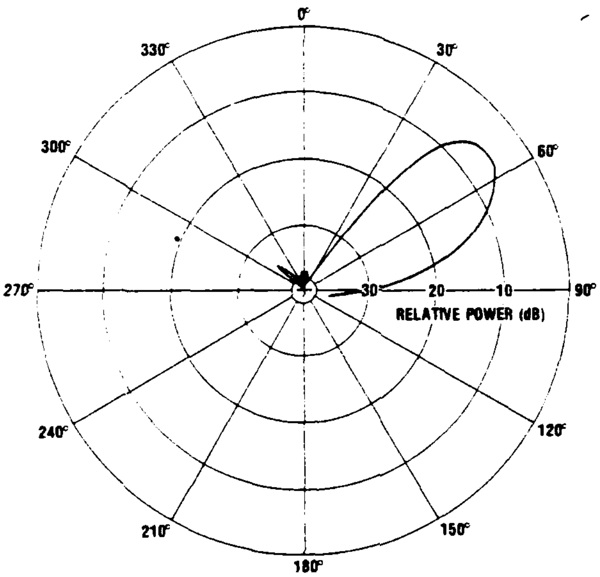

Figure 5. Polar plot of MCX-2 antenna with main beam at 55 deg from broadside.

4.3 MCX-3

The next antenna was designed to have a moderately wide beam angle, keeping the frequency characteristic impedance, efficiency, and antenna length the same as MCX-2. This antenna is a 12-element array with the beam designed to be 35 deg from broadside (aimed toward the feedpoint). Figure 6 shows the polar plot for this antenna design. Here again the side-lobe level is about 5 dB higher than designed. The separations between the array elements are sufficiently spaced to keep the mutual coupling to a minimum. Some of the element patch widths exceed the half-wavelength criteria, which produces cross-polarized multiple modes. Modes developed at other than the fundamental reduce the antenna capability for radiating fields at a desired polarization. To reduce this effect, a lower efficient antenna was designed that held all the other parameters constant.

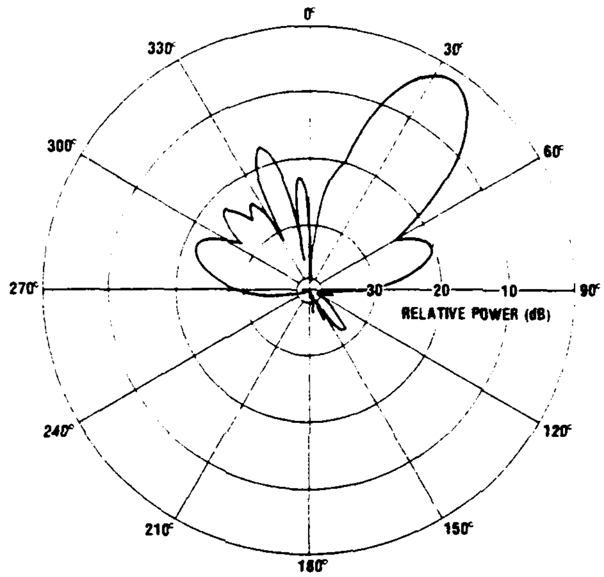

Figure 6. Polar plot of MCX-3 antenna showing main beam at 35 deg from broadside. High lobe on left may be due to termination reflections.

4.4 MCX-4

The definition of efficiency used here is the ratio of the total normalized radiated power to unity. The design of this antenna to 50-percent efficiency provided a gain of 10 dBI, a reduction of 3 dB from the previous 80-percent efficiency design. It is obvious by this 3-dB change in gain that the actual efficiencies differ from the theoretical designs.

Figure 7 shows the results of return loss measurements, indicating a 25-percent bandwidth over a 2:1 VSWR (corresponding to −9.6 dB).

5. CONCLUSIONS AND RECOMMENDATION

It has been shown that by use of a simple transmission line model of shunt conductance elements, along with present computer programming techniques, linear array microstrip antennas can now be simulated, designed, and studied in a short time and at a low cost. Measurements of resonant frequency and beam angle of all the antennas fabricated show excellent correlation with the design data submitted to the computer.

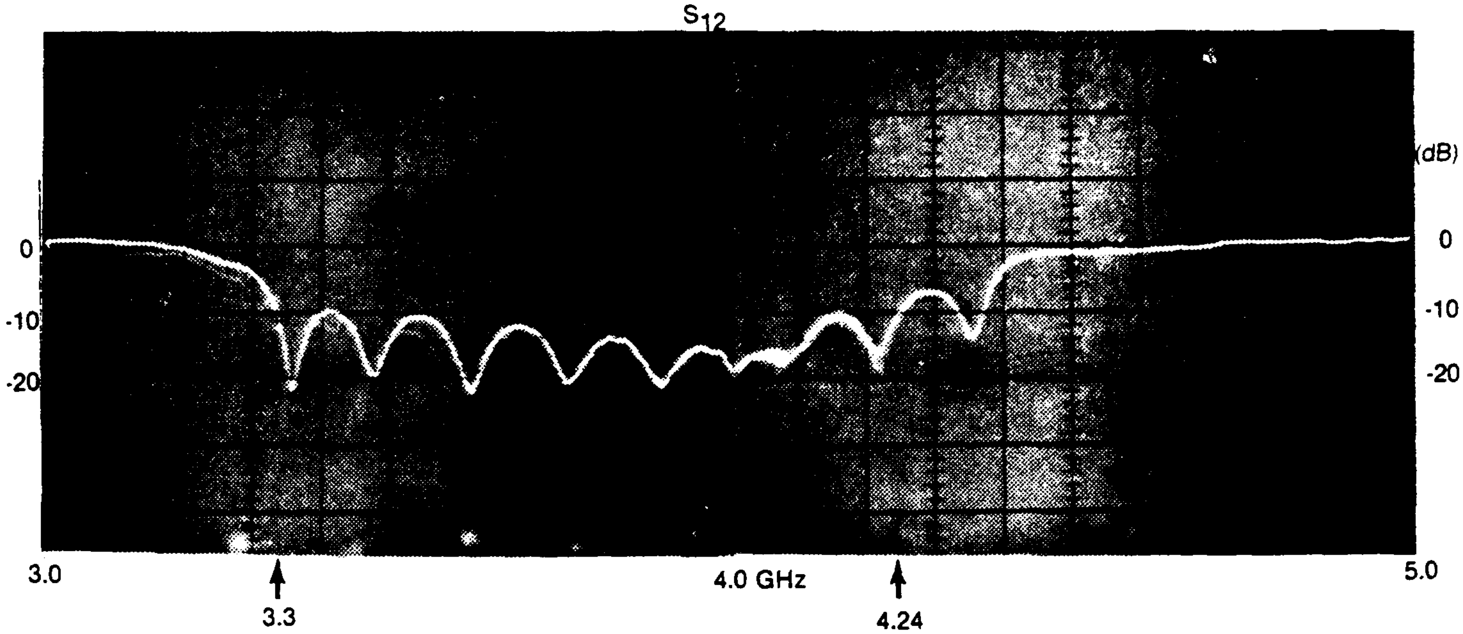

Figure 7. Network analyzer photograph of return-loss measurement for MCX-4 antenna. Measurement indicates 25-percent impedance bandwidth (VSWR, 2:1).

Cross-polarization of the fields and mutual coupling of the array elements appear to be minimal. Several antennas etched, using the same negative, have shown identical return-loss measurements and radiation patterns, indicating excellent reproducibility.

Although antennas designed by the present code may be adequate for many system applications, there is concern with regard to the disparity in the antenna side-lobe levels and the antenna efficiency. An improvement to the present code, in which the transmission line model is calculated by use of ABCD parameters showed increase computation accuracy. An ABCD parameter analysis should provide a more exacting fit to the desired characteristics, without the need for optimization, and a better prediction of antenna performance.

Additional work is needed in obtaining a better analytical model and data on the element values of conductance and insertion phase as a function of patch width, characteristic impedance, and loading. When incorporated with an ABCD parameter and transmission matrix calculations, this approach should improve the antenna side-lobe levels and the overall measured design performance. Additional information must be gathered to better describe the radiation pattern and directivity of a single patch element. Further, it would be desirable to design series arrays having elements of equal widths but with different characteristic impedance lines interspaced between them. This type of design would provide for a simpler means of phase shifting the array, since the insertion phase of each element is the same. Additionally, information about thick and low-loss substrates is needed so that arrays may be designed to 100 GHz, where most of the commonly used dielectrics have thicknesses approaching the dimensions of a wavelength.

Some of these aspects are under investigation, and the results are being implemented into the present code. It is expected that when all the data are incorporated, low side-lobe efficient antennas will be designed easily.

The conformal aspect of microstrip antennas has been so attractive that an entire industry and specialized antenna technology have developed because of it. Designing arrays for cylindrical and conical geometries might then be the next area for additional analysis and synthesis research.

HDL-PP-81-RT-1

(second printing)

August 1981

Conformal and Small Antenna Designs

By Howard S. Jones, Jr.

U.S. Army Electronics Research
and Development Command

Harry Diamond Laboratories

Adelphi, MD 20783

Select antennas are described that can be used effectively on conformal surfaces. Most of these antennas are compact, are electrically and physically small, and can be easily integrated into conical and cylindrical bodies. Edge-slot, microstrip, and dielectic rod radiator design techniques are employed in the development of these antennas. Critical design parameters, modes of radiation, empirical data, and theoretical considerations are discussed. The intrinsic properties and characteristics of selected dielectric materials are considered.

Several unique design configurations are illustrated. Performance data on prototype antenna models such as impedance, gain, polarization, radiation patterns, and bandwidth characteristics are presented. Salient features and advantages realized from the use of these design techniques are summarized.

1. INTRODUCTION

Over the past few years, there has been an increasing interest in the development and use of efficient antenna systems that have certain desirable characteristics and can be easily integrated into various shaped bodies, conforming to their outer surfaces. Equal attention has been given to the need for reducing the size of antennas, especially in cases where there are space limitations and the antennas must be conformal to surfaces. At first glance, satisfying these requirements would appear to be a formidable task because, despite the difficulties involved in achieving these goals, in most antenna systems there can be no sacrifice in electrical performance. However, antenna systems that can be designed to include these features can solve many problems and have numerous applications.

Antenna research work performed at the Harry Diamond Laboratories in recent years has been directed toward solving many of the difficult problems. Both theoretical and experimental studies on antenna designs and material development were fully exploited. Other investigations included the determination of certain overall system requirements, to effect optimum antenna performance that would result in improvements over conventional antennas. From this research effort, several unique conformal antenna designs were conceived that made possible some antenna systems that are compatible with a variety of body shapes.

This report summarizes much of the research and development effort involving certain basic design techniques that are applicable to conformal and small antennas. The results of the overall effort have made possible the antenna designs that are operational in the ultrahigh frequency (uhf) region through the millimeter wave frequency range.

2. EDGE-SLOT RADIATORS

The edge-slot radiator design approach is a unique method used for designing antenna systems that are functional and compatible with conformal surfaces.[1-4] The basic radiator is a thin structure usually in the form of a circular disk or a similar shape that consists of two parallel conducting surfaces separated by a low-loss dielectric material and fed from a coaxial line. When the radiator is incorporated into a body such as a cone or a cylinder, its outer edge is intended to coincide with the surface of the body. This outer edge is the radiating aperture. In the case of the circular disk, the radiating aperture is circumferential, and the radiation pattern is uniformly symmetrical around the body.

Although most of the emphasis is focused on the flat circular disk type radiator, there are modifications that include semicircular and wedge shapes, as well as other design configurations. Typical illustrations showing how the edge-slot radiators are effectively used in bodies of revolution are included in other sections of this report.

Some of the features of edge-slot antennas are as follows:

a. They can be integrated quite well into conformal bodies.

---

[1] *Daniel H. Schaubert, Howard S. Jones, Jr., and Frank Reggia, Conformal Dielectric-Filled Edge-Slot Antennas for Bodies of Revolution, Harry Diamond Laboratories HDL-TR-1837 (September 1977).*

[2] *F. Reggia and H. S. Jones, Conformal Edge-Slot Radiators, U.S. Patent 4,051,480 (27 September 1977).*

[3] *Daniel H. Schaubert, Howard S. Jones, Jr., and Frank Reggia, Conformal Dielectric-Filled Edge-Slot Antennas with Inductive-Post Tuning, IEEE Trans. Antennas Propag.,* **27** *(September 1979), 713-716.*

[4] *Dipak L. Sengupta and Luis F. Martins-Camelo, Theory of Dielectric-Filled Edge-Slot Antennas, IEEE Trans. Antennas Propag.,* **28** *(July 1980), 481-490.*

b. Antenna systems can be designed in several frequency bands.

c. Electronic scanning is possible.

d. The technique provides a simple means of construction at low cost.

e. Radiation patterns from edge-slot radiators have good azimuthal symmetry.

2.1 *Single Edge-Slot Radiator Characteristics*

In the previous section, a typical edge-slot radiator is described as a compact circular disk. This basic design operates at some fundamental frequency, depending on its diameter and the dielectric material characteristics. However, by placing inductive posts in certain positions across the parallel conducting plates, the antenna characteristic can be altered, particularly its impedance and frequency of operation. An example of the basic edge-slot radiator with inductive posts is shown in figure 1.

Two-element, four-element, and eight-element antennas are shown in figure 2. The number of elements in the radiator is determined by the number of rows of inductive posts.[1,3] Also, the frequency can be affected by a change in the number of posts in the row.

[1]*Daniel H. Schaubert, Howard S. Jones, Jr., and Frank Reggia, Conformal Dielectric-Filled Edge-Slot Antennas for Bodies of Revolution, Harry Diamond Laboratories HDL-TR-1837 (September 1977).*

[3]*Daniel H. Schaubert, Howard S. Jones, Jr., and Frank Reggia, Conformal Dielectric-Filled Edge-Slot Antennas with Inductive-Post Tuning, IEEE Trans. Antennas Propag.,* **27** *(September 1979), 713-716.*

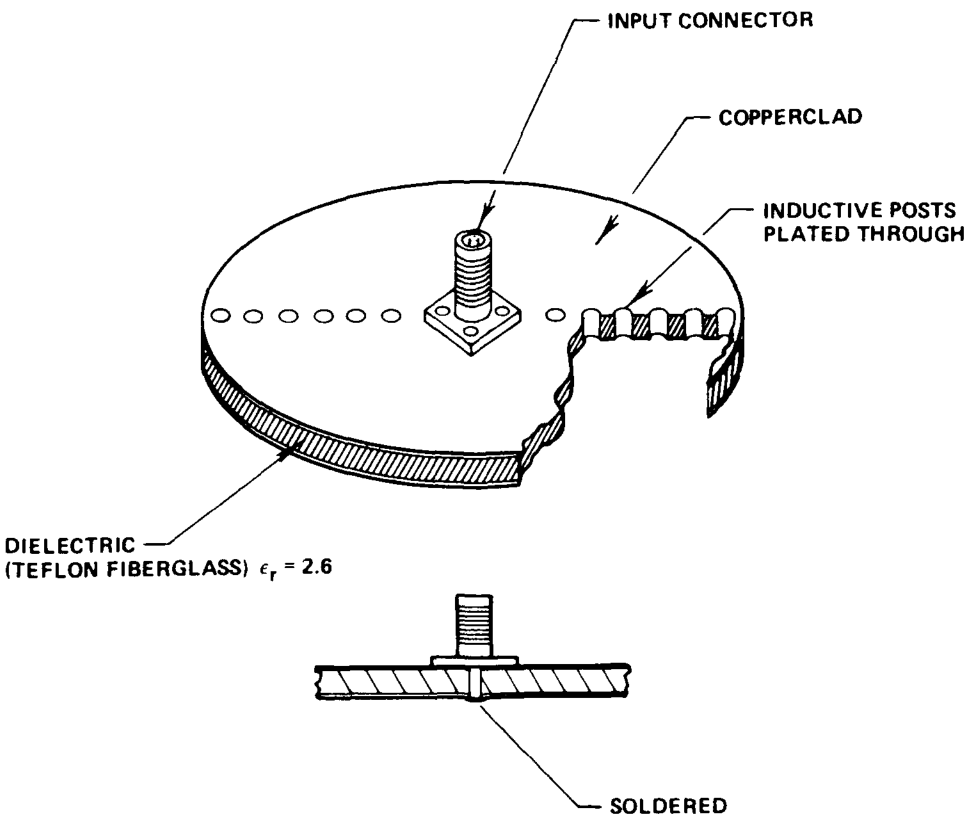

Figure 1. Single edge-slot radiator.

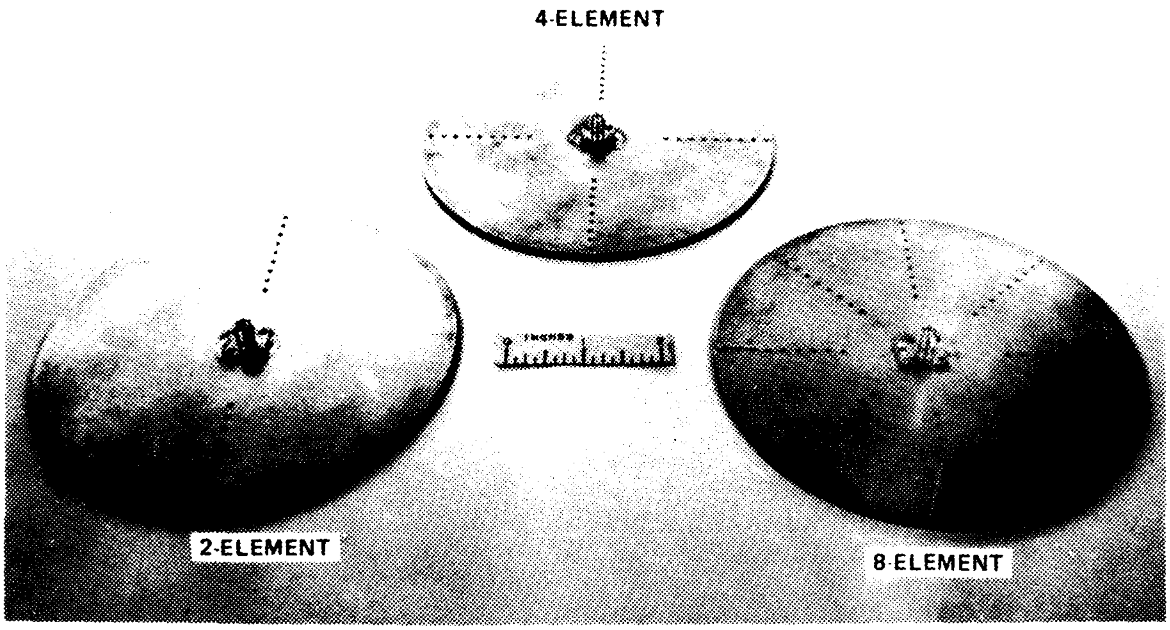

Figure 2. Two-, four-, and eight-element edge-slot radiators.

Data illustrating frequency characteristics as a function of the number of posts for multiple elements are shown in figure 3.

2.1.1 *Radiators in Bodies of Revolution*

When used with typical weapon configurations, the edge-slot antenna can be mounted conformally between portions of a conducting body of revolution. Because the aperture is very narrow and it couples strongly to the body, full advantage can be taken of the radiation properties of the antenna used on large and small structures. Furthermore, the rotational symmetry of the antenna and the body preserves the desired azimuthal symmetry of the radiation pattern. This symmetry can be seen in the patterns of an 8-in. (20.32-cm)-diameter, two-element edge-slot radiator mounted at the center of a 16-in. (40.64-cm)-long cylinder shown in figure 4.

2.1.2 *Material Characteristics*

In most cases, copperclad dielectric laminated materials (printed-circuit boards) were used to design the individual radiators. Typical dielectric materials used were low-loss Teflon fiberglass, epoxy glass, and silicone glass laminates. Also, polystyrene foam dielectric and selected inorganic dielectrics were used for certain experiments. The dielectric constant and the loss tangent of the materials were important design factors. Most of the materials lend themselves well to electroless copperplating techniques used to provide the parallel conducting surfaces and the plated-through holes for the inductive posts.

2.2 *Practical Edge-Slot Antenna Designs*

Because the edge-slot radiator can be easily integrated into conformal surfaces, it is used advantageously on both large and small bodies. The design technique is often sought for use to satisfy critical electrical and mechanical problems. In some designs, practically no additional space is needed for the antenna. The space saved is frequently used to package electronic circuitry. This area is also isolated from the external radiation fields of the antenna.

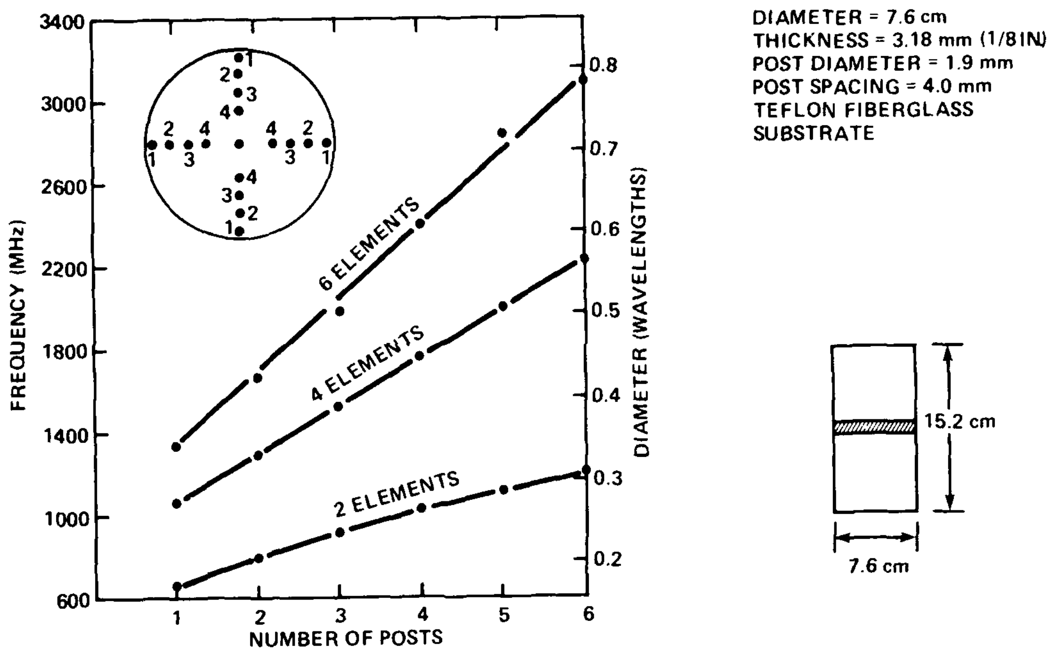

Figure 3. Frequency versus number of posts for multiple elements.

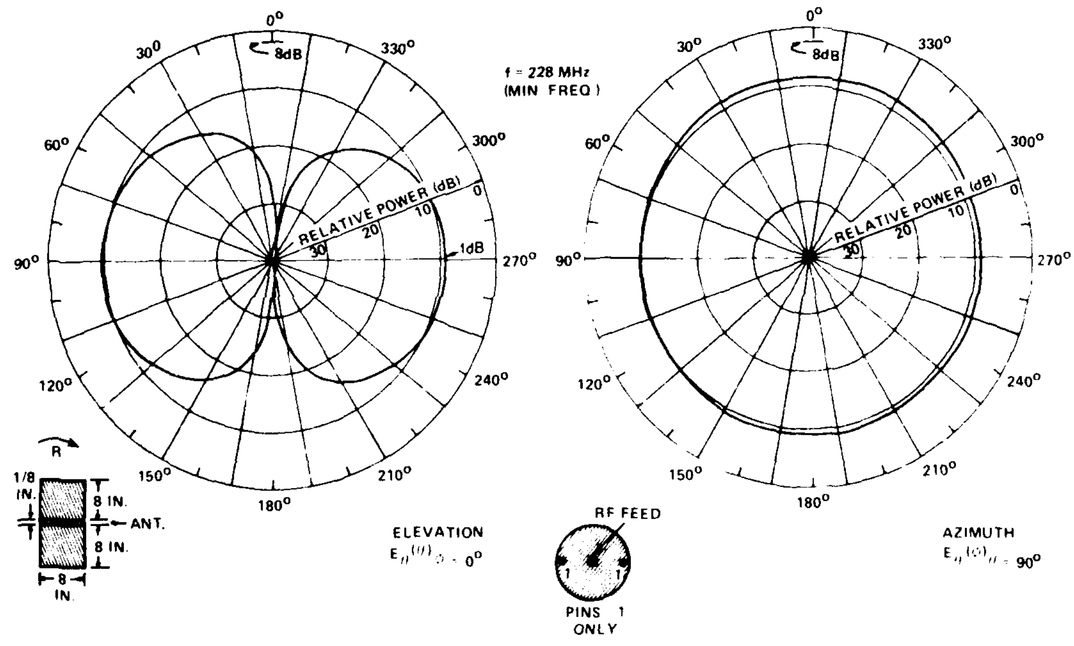

Figure 4. *Radiation patterns of dual element edge-slot radiator at center of 8-in.-diameter cylinder.*

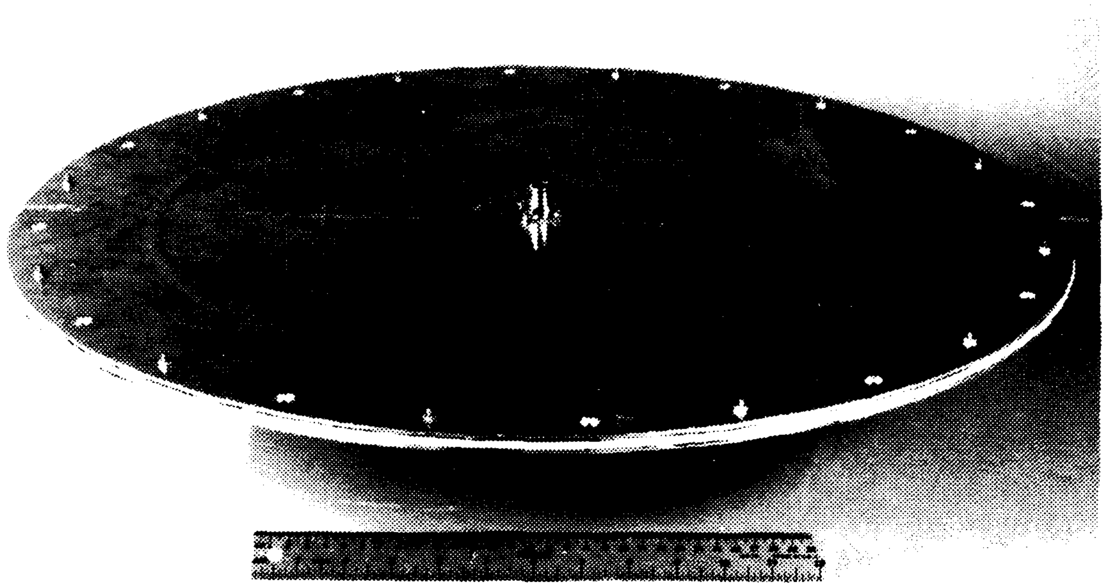

24.5 IN. DIAM.
24 ELEMENTS
FREQ. 1510 MHz
1/8 IN. TEFLON BETWEEN 1/8 IN. ALUMINUM

Figure 5. Edge-slot telemetry antenna for Honest John Missile.

2.2.1 *Large and Small Edge-Slot Radiators*

It is sometimes difficult to obtain the proper radiation coverage around a body (projectile or missile) employing conventional antenna designs. The inherent properties of the edge-slot radiator allow full symmetrical radiation coverage around both large and small bodies. A typical example is a 24.5-in. (62.23-cm) telemetry (TM) edge-slot antenna developed for use on an Honest John Missile for multiple launch rocket system (MLRS) tests. A photograph of this antenna is shown in figure 5. Radiation patterns taken in both azimuthal and elevation planes are shown in figure 6. This antenna satisfied all radiation pattern requirements. Also, there was no sacrifice in structural integrity, and the design was cost effective.

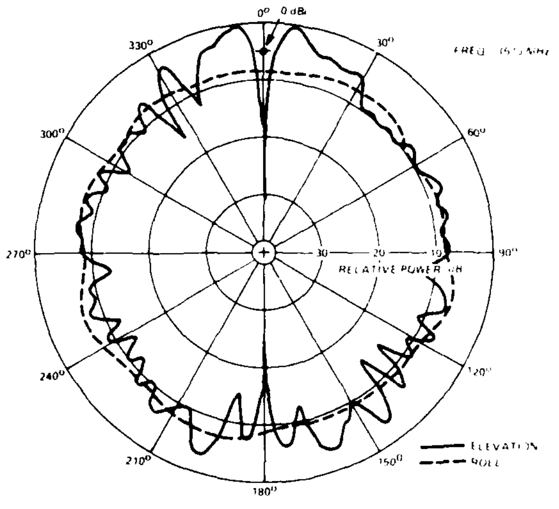

Figure 6. Radiation patterns of telemetry antenna for Honest John Missile.

The planar disk is not the only configuration for the edge-slot radiator. It can also be designed by using other shapes producing very good results. An example is the conical shape edge-slot antenna shown in figure 7. This four-element antenna is designed in the shape of a hollow nose cone (copperplated dielectric) for use on an 81-mm projectile. The feed is at the inside tip of the nose cone, and the aperture is at the base 3.33 cm from the apex. The space inside the nose cone is available for other circuitry.

Thirteen inductive posts separate the elements and give an operating frequency of 6330 MHz with an impedance bandwidth (voltage standing wave ratio—VSWR ≤ 2) of 150 MHz. Radiation patterns for this conical edge-slot antenna also are shown in figure 7. The peak gain is directed in the forward region.

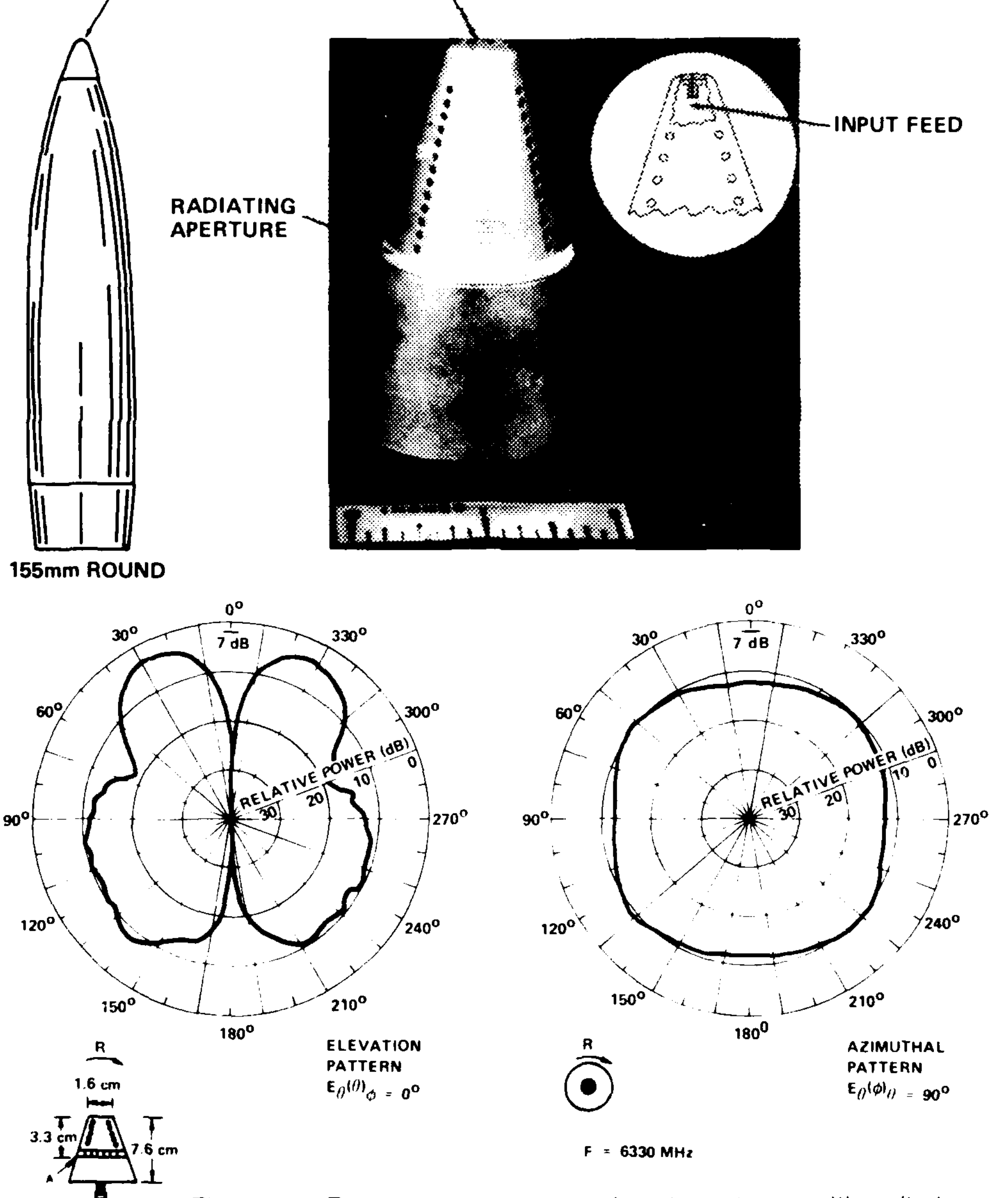

Figure 7. Four-element conical edge-slot antenna with radiation patterns for 155-mm projectile.

2.2.2 *Quadrature Edge-Slot Radiator*

Figure 8 shows a novel low-profile quadrature edge-slot antenna with polarization diversity and the capability of performing several functions.[5] It consists of four conformal parallel plate edge-slot radiators (one in each quadrant). Each radiator can be independently excited in any phase relationship for changing direction and polarization of the radiation field. The model shown in figure 8 is 2-1/2 in. (6.35 cm) high and has a 5-in. (12.7-cm) diameter; it can be designed to operate in the 600- to 700-MHz range. Also, shown in the figure is the same antenna designed into a hemispherical dielectric foam radome. Because the dielectric material has low-loss characteristics, there are only slight changes in the radiation patterns in the presence of the radome.

[5] *F. Reggia and H. S. Jones, Low Profile Quadrature-Plate UHF Antenna, U.S. Patent 3,987,458 (19 October 1976).*

2.3 Arrays of Edge-Slot Radiators

It has been shown that the frequency of an edge-slot radiator can be changed in a number of different ways.[1] Also, further investigations have indicated that diode devices can be effectively employed to perform similar functions for array designs.[2] These and other techniques used for designing multiple radiator systems have been developed. The advantages derived from the use of edge-slot radiators in arrays, especially for small diameter bodies, have been quite beneficial.

[1] *Daniel H. Schaubert, Howard S. Jones, Jr., and Frank Reggia, Conformal Dielectric-Filled Edge-Slot Antennas for Bodies of Revolution, Harry Diamond Laboratories HDL-TR-1837 (September 1977).*

[2] *F. Reggia and H. S. Jones, Conformal Edge-Slot Radiators, U.S. Patent 4,051,480 (27 September 1977).*

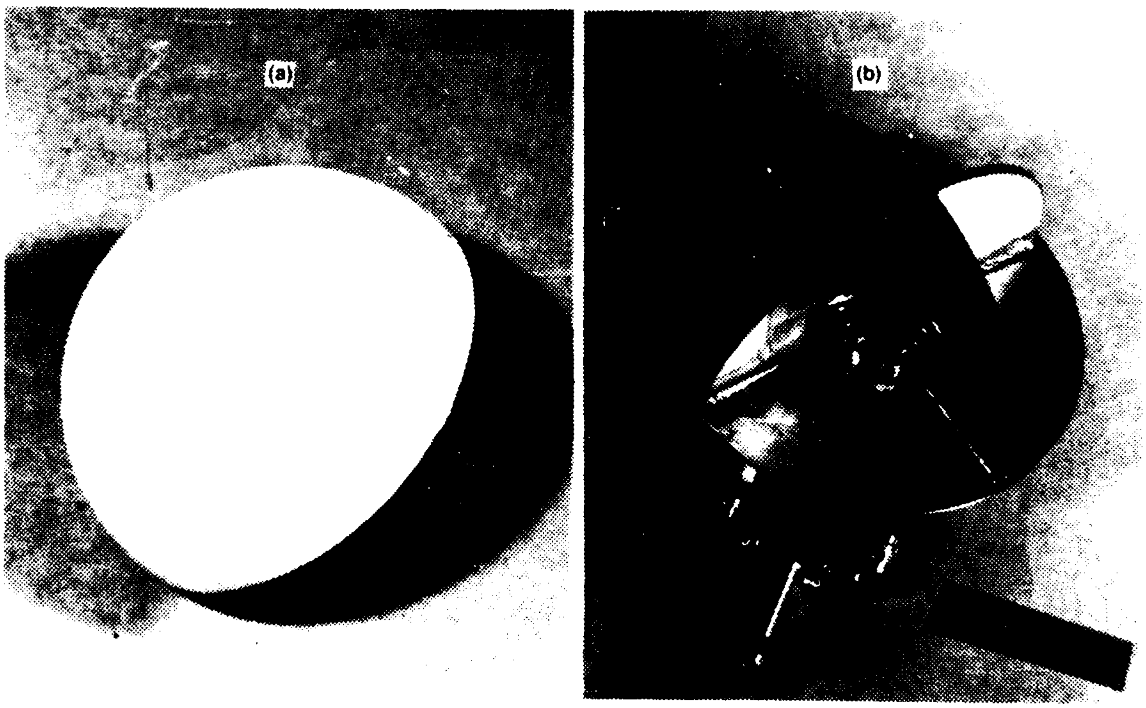

Figure 8. Multifunction low-profile quadrature edge-slot uhf antenna (a) with and (b) without radome.

2.3.1 *Parallel Fed Antennas*

Because edge-slot radiators are thin and can be placed close together without physical interference, they satisfy severe space requirements, while providing adequate radiation pattern coverage. Also, sometimes it is necessary to design an antenna for a particular operating frequency with certain bandwidth requirements. In several cases, these requirements were satisfied with an edge-slot antenna array fed in parallel. Figure 9(a) shows two edge-slot radiators fed in parallel. The antenna is incorporated into the forward section of a 40-mm projectile. It consists of eight elements and operates at 8300 MHz.

Radiation patterns of a single radiator and the two radiators working together, excited in phase and spaced one-half wavelength ($\lambda/2$) apart, are shown in figure 9(b). The impedance bandwidth (VSWR $\leqslant$ 2) of a single antenna on the 40-mm mockup was 1000 MHz (>12 percent).

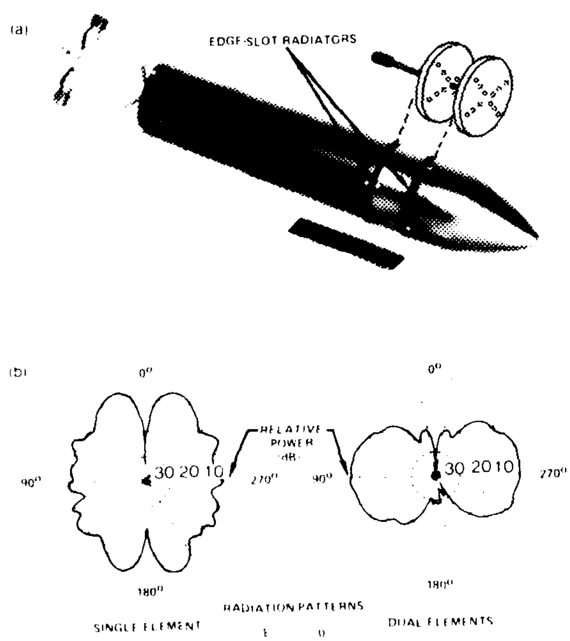

Figure 9. Edge-slot radiator system designed into 40-mm projectile body and radiation patterns.

Other edge-slot arrays containing as many as eight radiators have been developed using corporate feed structures. An array of edge-slot radiators currently being developed for use in a conical body is illustrated in figure 10. Despite the different diameters, each radiator can be designed to resonate at the same frequency. This type of antenna can be designed for use as a fixed angle system, monopulse array, or electronic scanned array.

Figure 10. Edge-slot array in conical body.

2.3.2 *Series-Fed Antennas*

Series-fed dielectric-filled edge-slot (SDE) antennas have been extensively investigated, and practical multifunctional designs have resulted.[6] A prototype design of an SDE antenna consisting of three radiators mounted in a 30.2-cm-long cylinder is shown in figure 11(a). The transmission and reflection characteristics of this three-radiator model are shown in the same figure. The dissipation maxima at 675, 790, and 875 MHz (fig. 11b) correspond to transmission minima and agree well with predicted operating frequencies for one-, two-, and three-post antennas. The radiation patterns of this multiradiator antenna are omnidirectional in the azimuthal plane. In the elevation plane, the patterns are controlled by the size of the cylinder and the locations of the antennas on the cylinder.

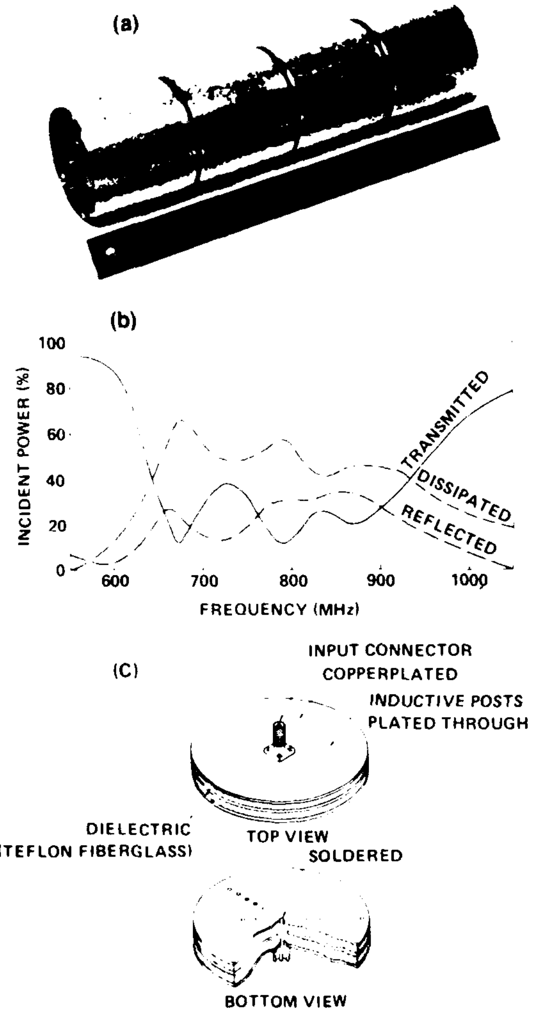

Figure 11. Series-fed antennas and transmission characteristics.

Another version of the series-fed antenna also is shown in figure 11(c). It depicts two radiators (each with six radiating sections) stacked together, fed in series, and terminated in a short circuit. By using a different number of posts in each radiator, a thin dual frequency antenna design with omnidirectional azimuthal radiation coverage is possible.[6]

3. MICROSTRIP ANTENNAS

Until recently, very little had been published on the theory of microstrip radiators. However, the design technique is being increasingly used. A considerable amount of experimental and development work has been done, and a number of unique antenna designs have been demonstrated.[7,8] Modifications can be made easily to enhance its performance. Notwithstanding the narrow bandwidth, these microstrip radiators have been widely used in microwave antenna systems. Microstrip antennas are attractive because they are low profile, compact, lighweight, rugged, and easy to fabricate, and they can be manufactured at low cost using printed-circuit techniques.

The basic microstrip radiator is a thin structure consisting of a rectangular conducting patch that is mounted over a parallel ground plane, excited by an inductive post fed from a coaxial line. The conducting patch is usually approximately $\lambda/2$ and separated from

[6]D. Schaubert and H. S. Jones, *Series-Fed, Dielectric-Filled, Edge-Slot Antenna, International Symposium Antennas and Propagation, Seattle, WA (1979).*

[7]Robert E. Munson, *Conformal Microstrip Antennas and Microstrip Phased Arrays, IEEE Trans. Antennas Propag.*, **AP-22** *(January 1974), 74-78.*

[8]John Q. Howell, *Microstrip Antennas, IEEE Trans. Antennas Propag.*, **AP-23** *(January 1975), 90-93.*

the ground plane by a thin low-loss dielectric material. Various widths (1/32, 1/16, and 1/8 in.—0.3, 0.6, and 1.2 mm) of copperclad dielectric laminated materials are commonly used in the construction of microstrip antennas. An illustration of the basic microstrip radiator is shown in figure 12.

3.1 *Quarter-Wavelength Microstrip Radiator*

Although much attention has been given to the $\lambda/2$ radiator, there are certain advantages realized from the use of the $\lambda/4$ radiator. One of the chief benefits is that it conserves space. The $\lambda/4$ microstrip radiator is shown in figure 13. It is short-circuited at one end and fed at the center near the short circuit. Impedance matching the microstrip radiator is fairly easy; various techniques are used. The radiation patterns obtained from both $\lambda/4$ and $\lambda/2$ radiators are very broad and therefore quite useful for many applications.

3.2 *Conformal Microstrip Antenna Designs*

The microstrip technique lends itself well to the design of conformal antennas. Because of the benefits derived from this design approach, extensive effort has gone into experimental research to develop antennas that are applicable to various weapon systems. As a result, several novel concepts and useful conformal antenna systems have been successfully designed. Illustrations and performance characteristics of some of these antennas integrated into different body configurations are included in the following sections.

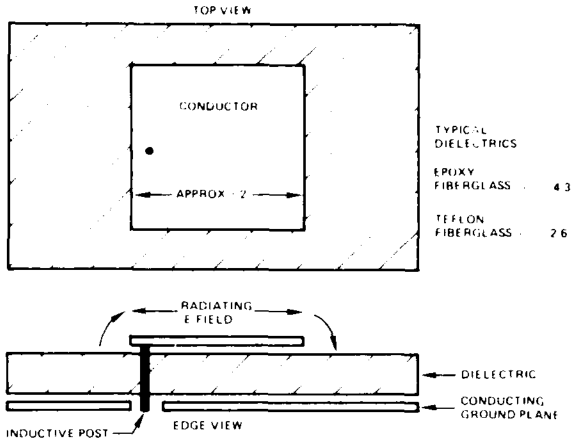

Figure 12. Basic microstrip radiator.

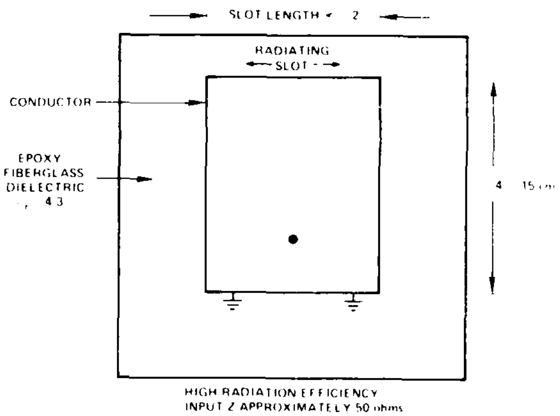

Figure 13. Quarter-wavelength microstrip radiator.

3.2.1 *Two-Element Microstrip Antenna*

The microstrip antenna is gradually replacing the cavity-backed slot, stripline, and waveguide cavity antennas because it requires less space, the construction cost is minimal, and there is very little sacrifice in performance. Furthermore, it can be easily designed into most conformal bodies that use low-loss dielectrics. An example of a two-element microstrip antenna design that replaced a cavity-backed slot antenna is shown in figure 14. The azimuthal radiation pattern is shown in the same figure. In this case, all system requirements were satisfied in addition to the benefits cited above.

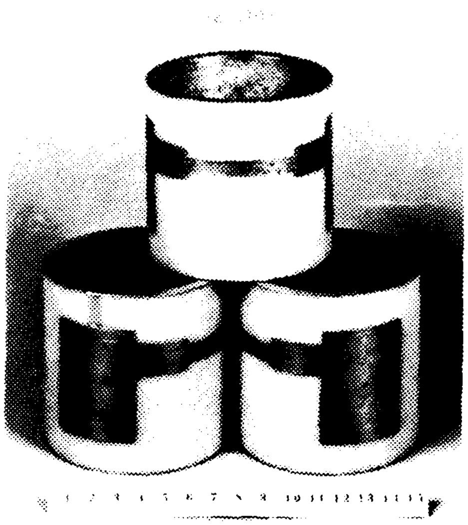

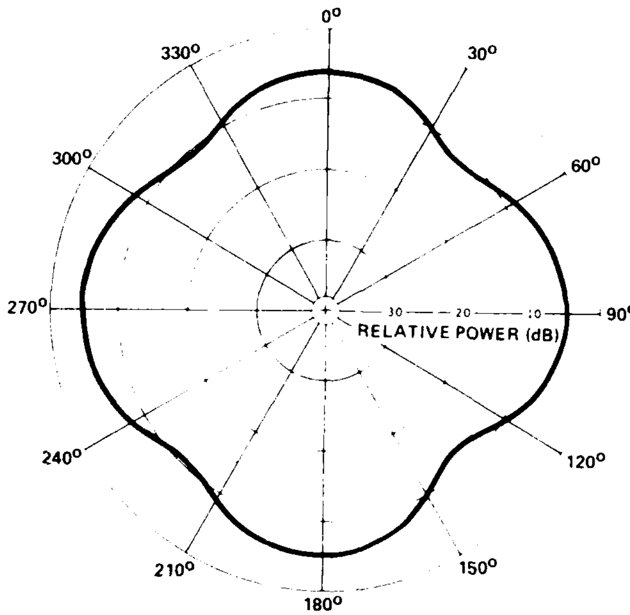

Figure 14. Two-element microstrip telemetry antenna and radiation pattern.

3.2.2 *Dual Frequency Microstrip Arrays*

A further indication of the exploitation and increasing use of microstrip radiators is observed in their successful application in the design of linear, planar, and conformal arrays. Results of recent investigations have shown that microstrip arrays can be integrated quite well into radome structures. Various flush-mounted design configurations that are compatible with their body structures have been demonstrated.

The flush-mounted piggyback microstrip antenna designed into a silicone fiberglass radome on a missile body is illustrated[9] in figure 15. Here, four dual linear arrays, one array in each quadrant, are designed into the radome (copperplated on the surface). Each of four elements of the array consists of two radiators, one mounted on top of the other in a piggyback fashion. The bottom radiator is a $\lambda/2$ design, and the top radiator is a $\lambda/4$ design. The dielectric radome has a 0.2-in. (0.5-cm)-thick wall, and the inside of the radome has complete copperplating, which provides the ground plane for the dual radiating elements. These elements that make up the array are excited in parallel from a corporate feed.

The $\lambda/4$ section of the dual radiator has plated-through holes along its bottom edge, which form the short circuit. An inductive post, which is also a plated-through hole, matches the bottom $\lambda/2$ radiator. In addition, it provides a passageway to feed the $\lambda/4$ radiator, as shown in figure 15. The elevation and azimuth plane radiation patterns of each radiator are shown in figure 16.

[9] *H. S. Jones, D. Schaubert, and F. Farrar, Flushmounted Piggyback Microstrip Antenna, U.S. Patent 4,162,499 (24 July 1979)*

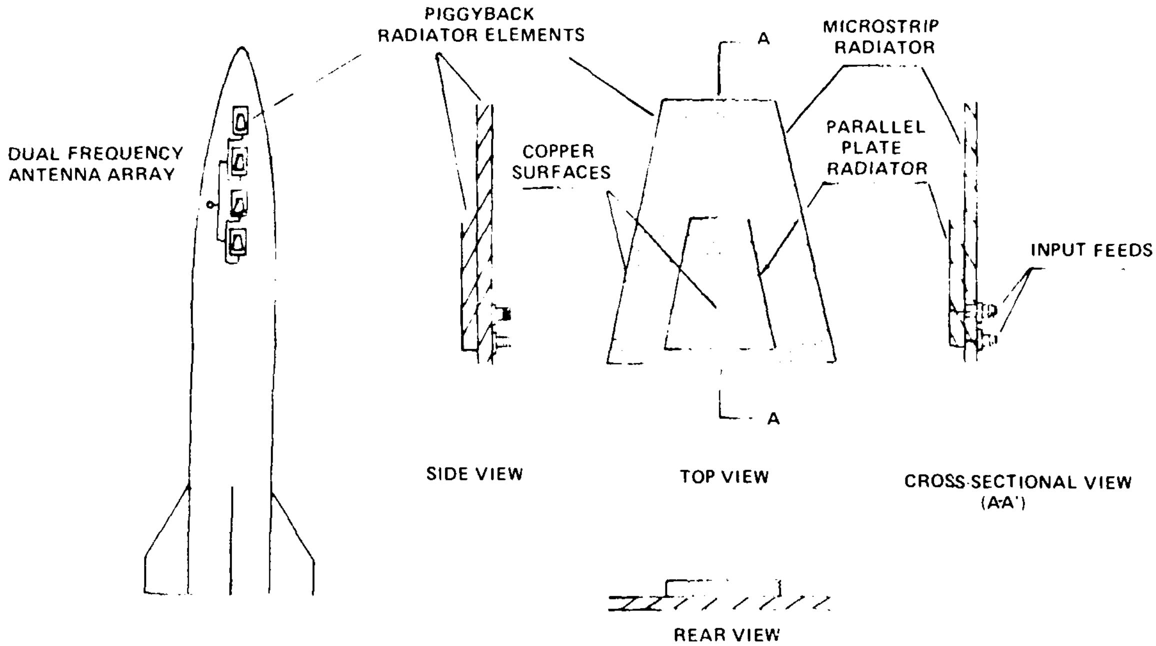

Figure 15. Piggyback microstrip radiator.

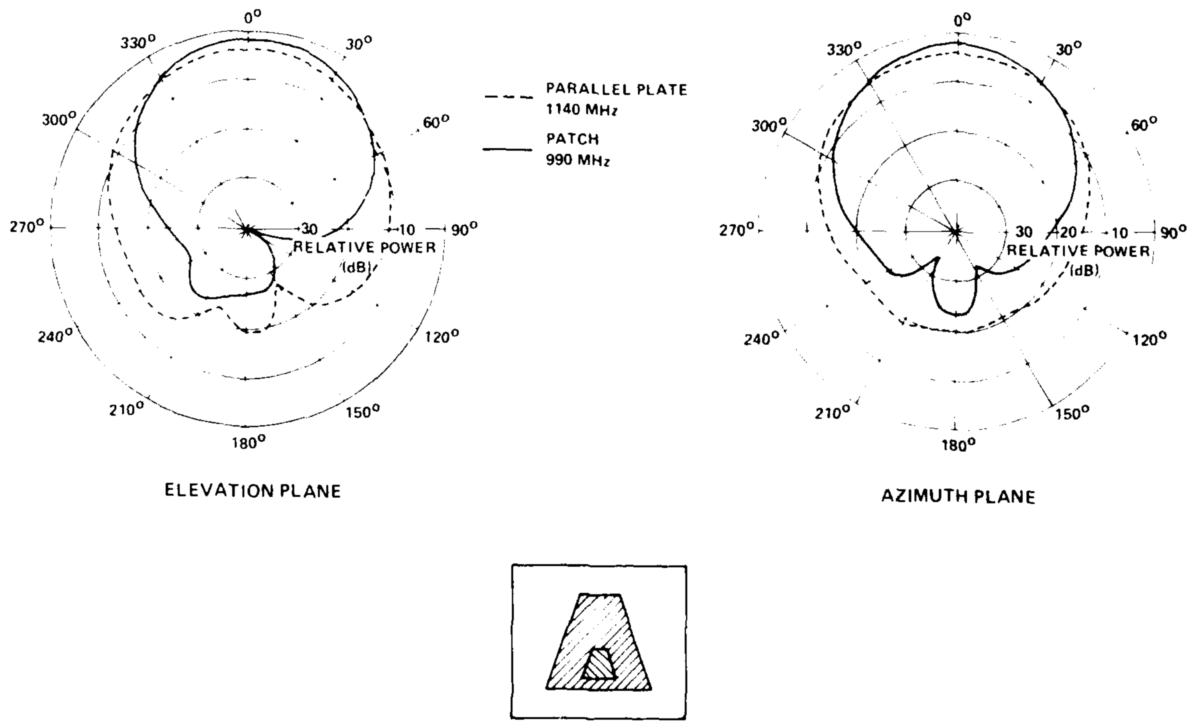

Figure 16. Radiation patterns of piggyback antenna.

The design of a dual frequency microstrip antenna integrated into a section of conical radome is shown[10] in figure 17. This antenna consists of two linear arrays; one has four radiators and the other has eight. All of the radiators are $\lambda/4$. Although the arrays operate in different frequency bands, they are physically separated far enough to minimize mutual coupling. Furthermore, the elements in one array are staggered with respect to those in the other. This staggering provides additional decoupling between arrays. Radiation patterns of the four-element array also are seen in figure 17.

3.2.3 *Multifunction Radome Antenna*

Dielectric radomes of various shapes and sizes are commonly used on the forward end of military weapons. They provide a sound and rugged aerodynamic structural housing, within which is located antenna systems, electronic hardware, and other devices. Efficient, functional antenna systems can be designed and constructed into these radomes without having their structural integrity destroyed. A concept was conceived and developed that makes full use of the dielectric radome in the design of a multifunction antenna system.[11,12]

A typical example of this design concept is shown in figure 18. Here, the parallel plate microstrip radiators are designed

[10] *H. S. Jones, Multifrequency Antenna Integrated into a Radome, U.S. Patent 4,101,895 (18 July 1978).*

[11] *H. S. Jones, Multi-Function Integrated Radome-Antenna System, U.S. Patent 4,010,470 (1 March 1977).*

[12] *H. S. Jones, A Novel Technique for the Design of Integrated Radome-Antenna Systems, Proceedings of 13th Symposium on Electromagnetic Windows (September 1976).*

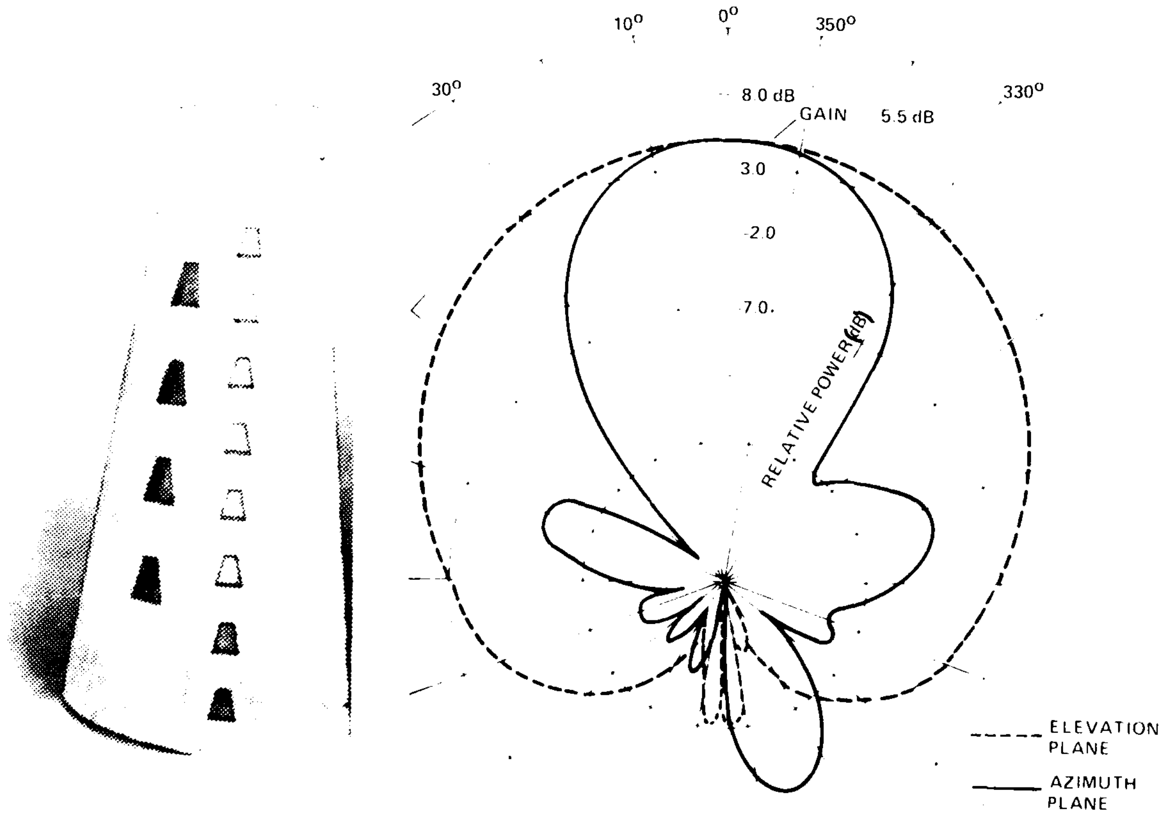

Figure 17. Dual frequency radome antenna with radiation pattern of four-element array.

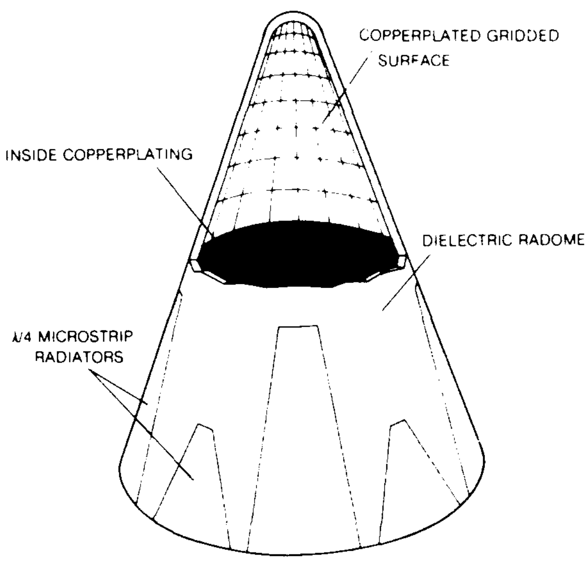

Figure 18. Multifunction integrated radome antenna system.

into the radome at the base and positioned at points around the circumference. These λ/4 radiators copperplated on the outer surface extend around the base connecting with the inside conducting surface (ground plane), where they are excited from a coaxial probe near the base. The parallel plate radiators are designed to operate in the uhf region.

The inside of the radome is completely copperplated except for the forward region of the cone, which is a conductive gridded surface. This dielectric loaded gridded region can be designed to act as a spatial filter. That is, it is transparent to transmission at certain frequencies; for example, at X-band, energy can be transmitted through the medium with minimum loss and distortion. Yet, at the low frequencies (uhf), this region is opaque to transmitted energy. These design features allow the radome antenna (fig. 18) to serve a variety of functions.

3.2.4 *Spiral Microstrip Antenna*

The spiral-slot antenna is an electrically small flush-mounted microstrip radiator designed for small-diameter missile or projectile applications.[13] High radiation efficiency is obtained by strongly coupling radio frequency (rf) currents to the body of a missile and exciting the dipole mode of radiation. When the antenna operates in the uhf band, an instantaneous bandwidth of approximately 2 percent is achieved. The spiral-slot antenna produces an axially polarized radiation field and a dipole radiation pattern with isotropic gain.

The antenna is fabricated from a copperclad tube of epoxy fiberglass dielectric. A thin rectangular sheet of conductor, wrapped in a spiral around the outer surface of a cylindrical tube of dielectric, forms the basic spiral-slot antenna. In figure 19, the spiral-slot antenna is shown in a typical application, mounted in the nose tip of a 2-m-long rocket. The radiation patterns from the antenna mounted on the body are shown in figure 20. The peak gain is about +1 dBi.

Main-polarized and cross-polarized radiation-pattern gains over a narrow frequency range are plotted in figure 21. The spiral-slot antenna displays a 3-dB gain bandwidth of 9 MHz or approximately 3 percent. The instantaneous impedance (VSWR = 2:1) bandwidth is 4 MHz or about 2 percent. The cross-polarized field component is at least 9 dB down and decreases to about 14 dB down at the design center frequency (238 MHz).

---

[13] *D. H. Schaubert, A. R. Sindoris, and F. G. Farrar, The Spiral Slot, a Unique Microstrip Antenna, Proceedings of 1978 Antenna Applications Symposium, University of Illinois, Monticello, IL (October 1978).*

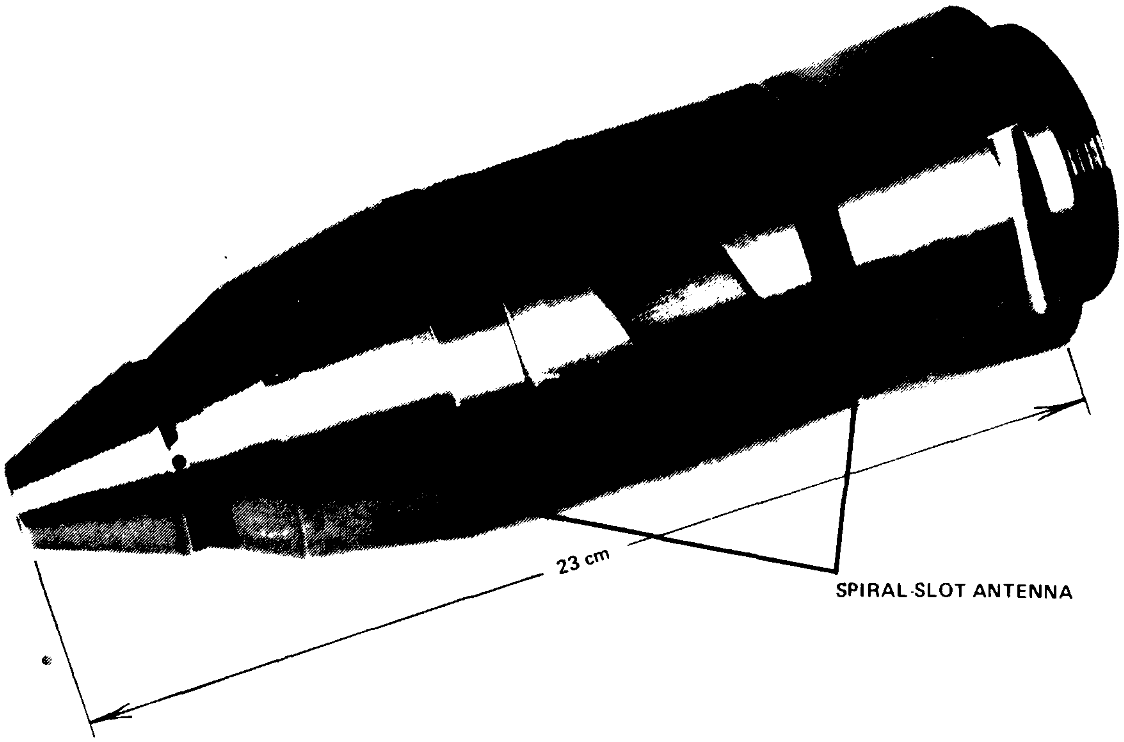

Figure 19. Spiral-slot antenna mounted in nose of 2-m-long rocket.

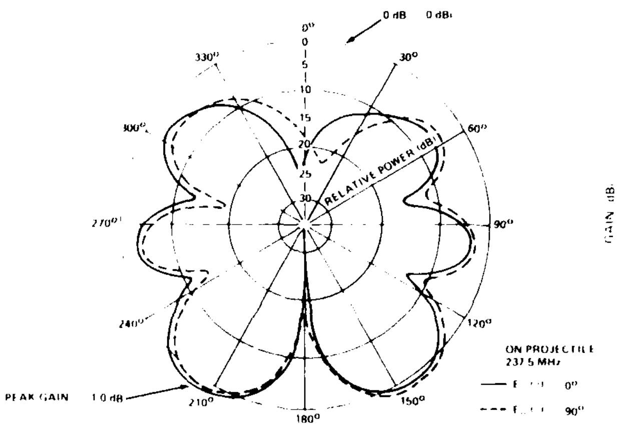

Figure 20. Radiation patterns of spiral-slot antenna in 2-m-long rocket.

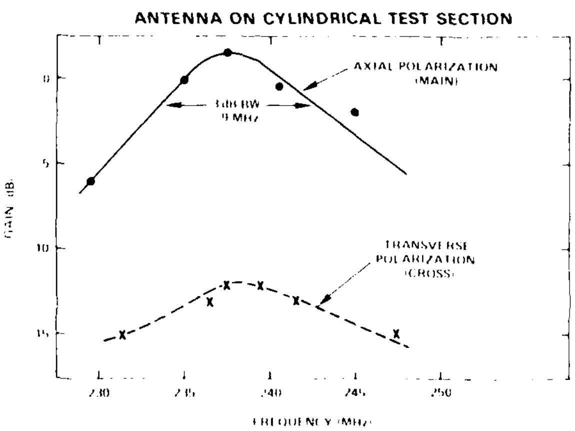

Figure 21. Gain-bandwidth (BW) characteristics of spiral-slot antenna.

4. DIELECTRIC ROD ANTENNAS

The theory of dielectric rod radiators is well known.[14] They are highly suited for use in military weapon systems to perform a variety of functions. These end-fired radiators have high gain, low side lobes, high decoupling between radiators, and in some cases broad bandwidth characteristics. They are efficient with good directivity and can be compactly designed into small apertures. Because of these and other features, dielectric rod radiators offer many advantages when used in the design of small and conformal antennas.

4.1 *Single Dielectric Rod Designs*

A considerable amount of research and development has been performed on dielectric rod radiators operating in the X-band region.[15] Although a number of different materials can be used as dielectric rod radiators, the material that is used most often is aluminum oxide (Al_2O_3). It has a dielectric constant of 9.0 and a loss tangent of 0.0011.

The use of waveguide is a simple and convenient means of launching a wave into the dielectric rod. In this case, the waveguide is operated in its dominant TE_{10} mode, and as the wave passes into the rod it is transformed into the hybrid mode of the rod.[15] A dielectric rod radiator design using X-band waveguide is shown in figure 22. The dielectric rod is tapered to a point at one end for matching to the waveguide. A more gentle taper is on the output end to provide a smooth transfer of the energy to space. The lossless dielectric foam seen in figure 22 is used to position the rod in the center of the waveguide. Shown in the same figure are elevation and azimuth plane radiation patterns taken at 9.0, 9.2, and 9.4 GHz.

[14] *D. F. Halliday and D. G. Kiely, Dielectric-Rod Aerials, IEEE J.,* **94** *(1947), Part IIIA, 610-618.*

[15] *Howard S. Jones, Jr., Design and Development of Dielectric Rod Antennas, Harry Diamond Laboratories HDL-TR-1640 (July 1973).*

4.1.1 *Decoupling Characteristics*

Because the energy tends to adhere to the rod, there is very little coupling of energy between rods placed close together.[16] Two radiators were used with three different orientations of their electric fields to determine the decoupling characteristics between radiators as a function of separation. The results of this experiment are shown in figure 23. Here, it is observed that when two rods are separated by only 1 in. (2.54 cm) and polarized in the same plane, the decoupling is greater than 30 dB. In one orientation as much as 70-dB decoupling is obtained.

4.1.2 *Coaxial-Fed Dielectric Rod Radiator*

Dielectric rod radiators can be designed simply and effectively by feeding the rod from a coaxial input; however, the bandwidth is narrow. In this case, a portion of one end of a cylindrical dielectric rod is metallized (or copperplated). The rod is fed from this enclosed metallized end by a coaxial line whose center probe extends into the dielectric. The other unbound end of the cylindrical rod is tapered to match the radiated energy to free space. An X-band dielectric rod radiator designed and constructed in this manner with its radiation pattern is shown in figure 24. This radiator is mounted in a circular ground plane and is housed in a small conical radome.

Another coaxial-fed dielectric rod radiator design that operates at 3.0 GHz is shown in figure 25. This small antenna was designed for use in a projectile nose cone conformal with its apex. The overall length of the antenna is about 2 in. (5.08 cm), and it provides broad radiation coverage in the forward direction.

[16] *H. S. Jones, Dielectric Rod Antenna System, U.S. Patent 3,858,214 (31 December 1974).*

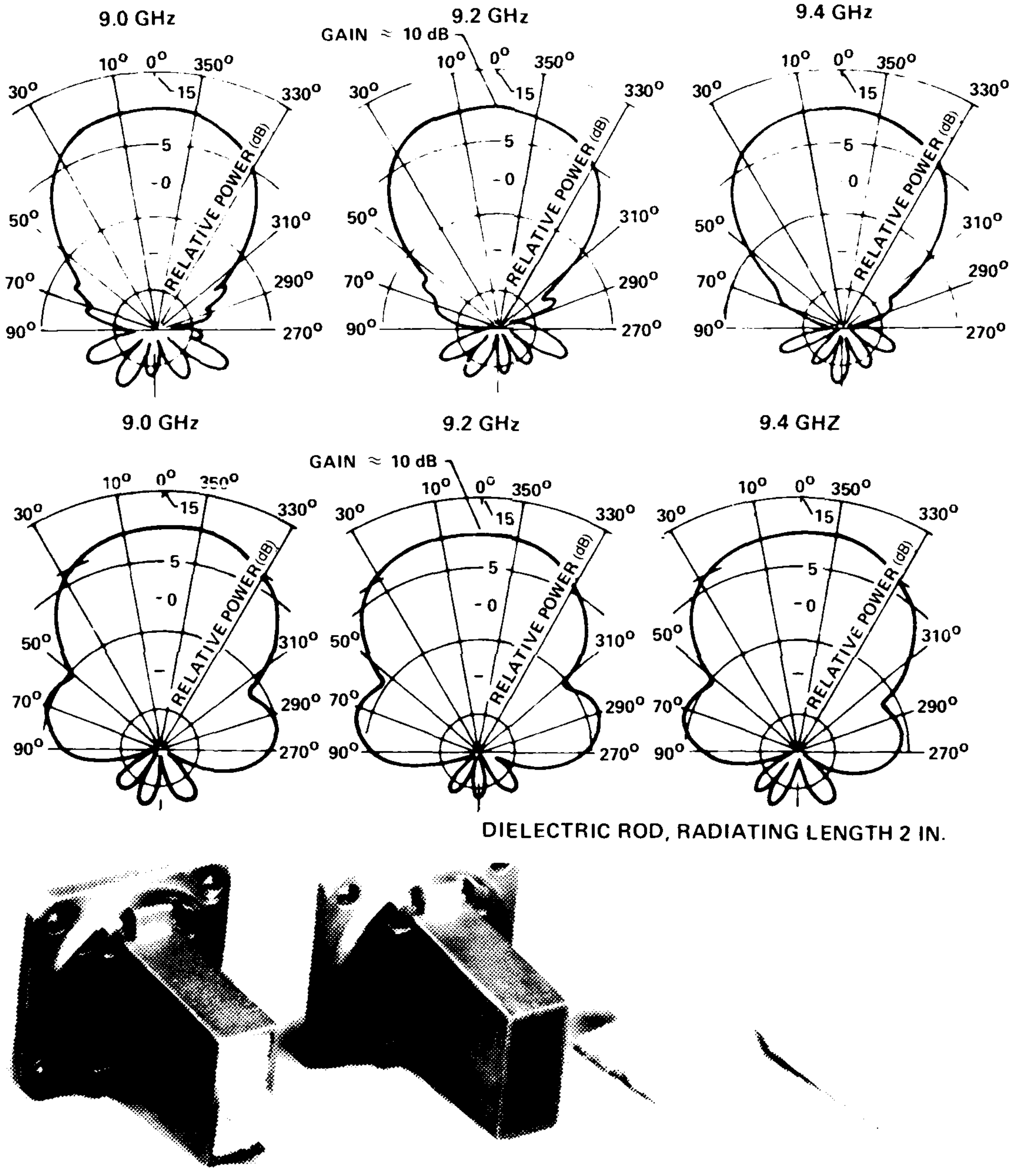

Figure 22. Single rod dielectric radiator and radiation patterns.

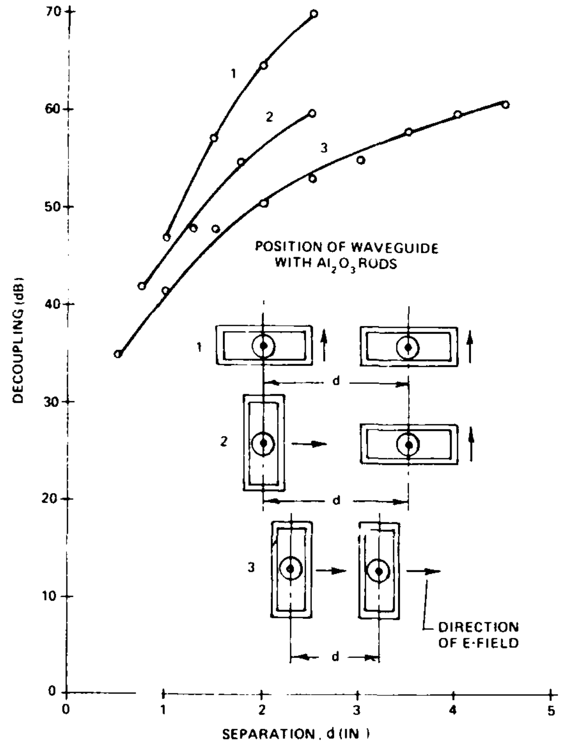

Figure 23. Decoupling as function of dielectric rod separation for three waveguide orientations.

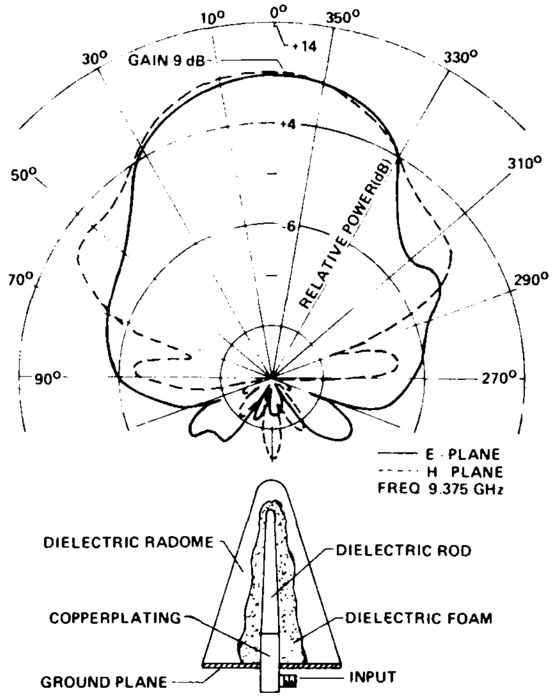

Figure 24. Radiation patterns of X-band coaxial-fed dielectric rod antenna in radome.

4.1.3 *Cylindrical Dielectric Rod Radiator*

The cylindrical dielectric antenna was designed to be small, compact, and capable of producing a radiation pattern with the null on axis. This antenna is a 1-in.-high dielectric (machinable glass) cylinder with a 1/16-in. (0.6-mm) wall with a solid base on one end and open on the other end. It is completely copperplated on the inside. On the outside, the base and only a small portion of the outer surface are copperplated. The copperplated dielectric structure is fed from coaxial line at the center of the base and is mounted in a 2-1/2-in. (6.35-cm) circular ground plane. Figure 26 sketches a prototype model. In the same figure are radiation patterns, one taken with a thin absorber over the ground plane and the other taken without the absorber. There are other versions of this antenna currently under investigation.

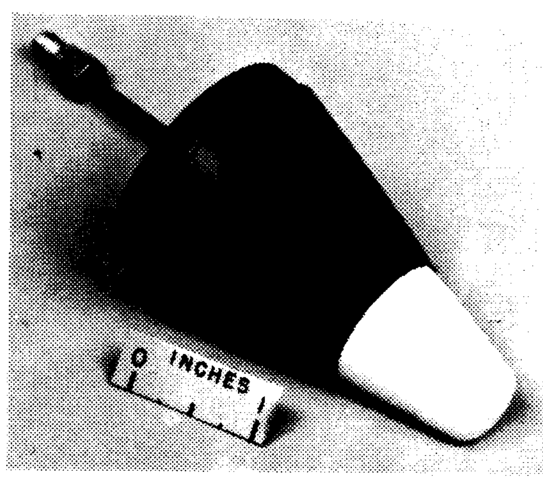

Figure 25. S-band dielectric rod radiator designed into small nose cone.

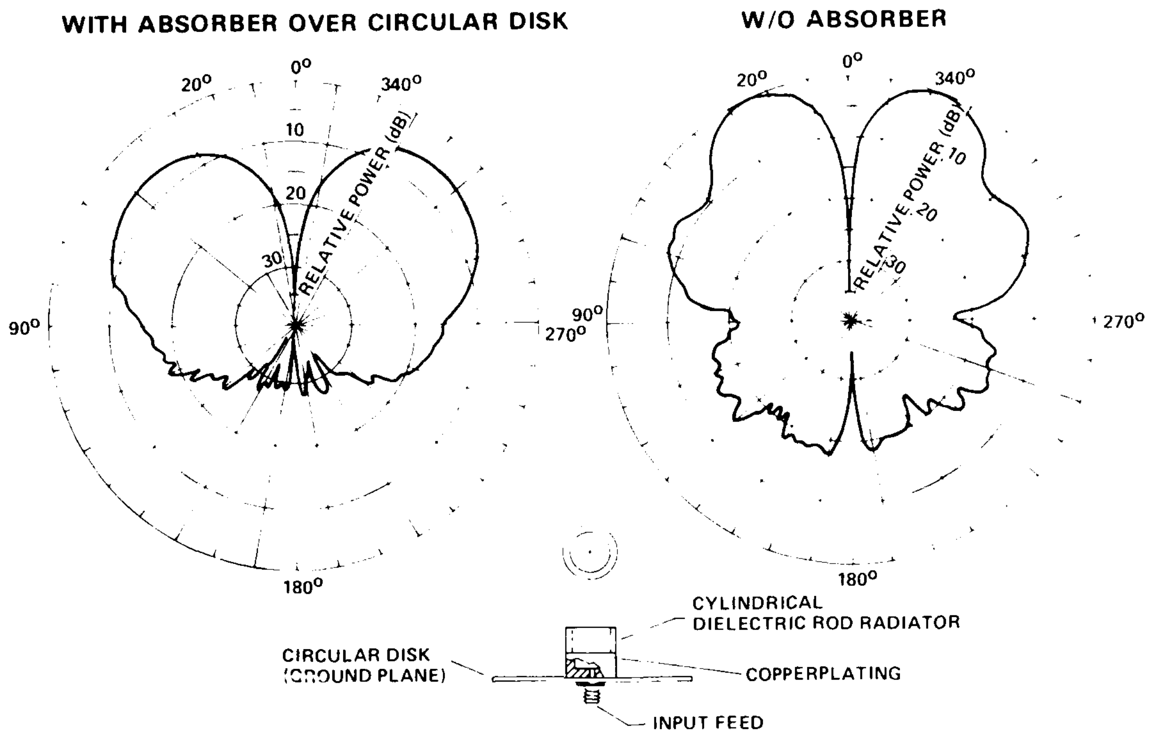

Figure 26. Radiation patterns of small cylindrical dielectric radiator.

4.2 *Dielectric Rod Monopulse Antenna*

A typical dielectric rod monopulse antenna is illustrated in figure 27 (p. 24). The antenna consists of a hybrid tee, a dual 90-deg twist to rotate the plane of polarization, and two H-plane tee junctions that support the four dielectric rods. These rods are separated approximately 1 in. The hybrid tee has two inputs: one feeds the two output channels in phase and the other feeds the output channels out of phase. Each of these outputs (through the twist section) feeds a pair of rods that are mounted in each series tee junction. This configuration allows each pair of rods to be excited in phase or out of phase with each other. Figure 28 (p. 25) shows the sum and difference patterns of the dielectric rod monopulse antenna taken in a ground plane.

4.3 *Millimeter Wave Dielectric Rod Radiators*

Single dielectric rod radiators launched from waveguide have been designed at 70 and 94 GHz. The experimental model of the 70-GHz radiator with its radiation patterns is shown in figure 29. This antenna uses a sapphire rod whose dielectric constant $\varepsilon_r = 8.6$ and loss tangent tan δ = 0.0014. The radiating length of the rod is 0.75 in. (1.905 cm) measured from the waveguide (RG98/U) aperture.

In the design of dielectric rods for operation at 94 GHz, two dielectric materials were used, TPX (ε_r = 4) and custom HiK (ε_r = 3.3). The radiating ends of the rods were designed in a pyramidal and tapered wedge

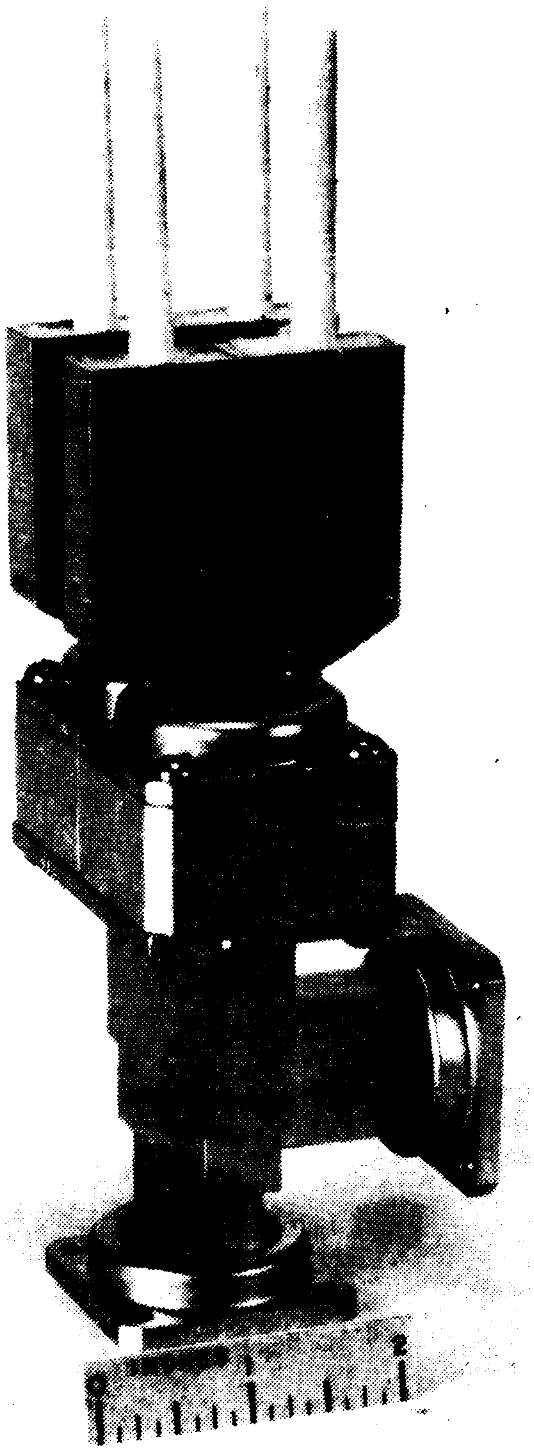

Figure 27. X-band dielectric rod monopulse antenna.

configuration (fig. 30, p. 27). The input ends were tapered to a point at the center to provide an optimum match to the waveguide. Radiation pattern characteristics of these dielectric rod radiators are shown in figure 31 (p. 28). The TPX wedge design had a peak gain of about 16 dB.

5. OTHER DESIGNS

In addition to the antennas that have been discussed, modifications and other antenna designs employ the same techniques and are useful and noteworthy. Several of these antennas were designed into a small dielectric nose cone that is commonly used on projectiles. These are typical examples of electrically and physically small antennas. In most cases, these antennas conform to the conical body and consume very little space. A selected group of these small compact antennas and a brief description of each are shown in figure 32 (p. 28).

6. CONCLUSION

The antenna techniques discussed here have many outstanding features. Each technique lends itself to the design of conformal and small antennas. Also, with these techniques, antennas can be designed in several frequency bands, an additional advantage. The antennas illustrated are efficient, functional, low cost, and capable of being used in a variety of applications.

There has been increasing interest in conformal and small antennas. For example, the continued use of microstrip radiators in planar, conformal, and phased arrays has been heavily emphasized. Further research and investigation into the use and exploitation of these and other techniques are continuing at the Harry Diamond Laboratories.

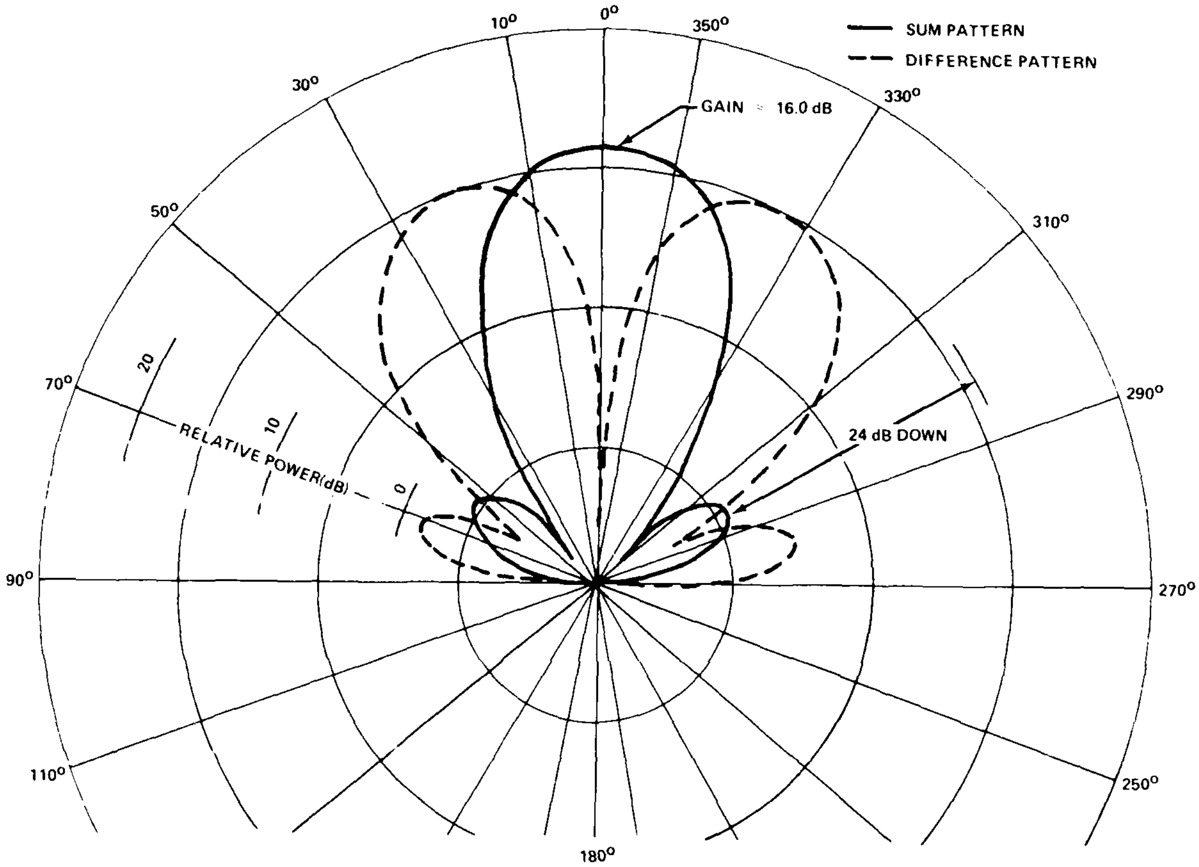

Figure 28. Radiation patterns of X-band dielectric rod monopulse antenna, taken in ground plane.

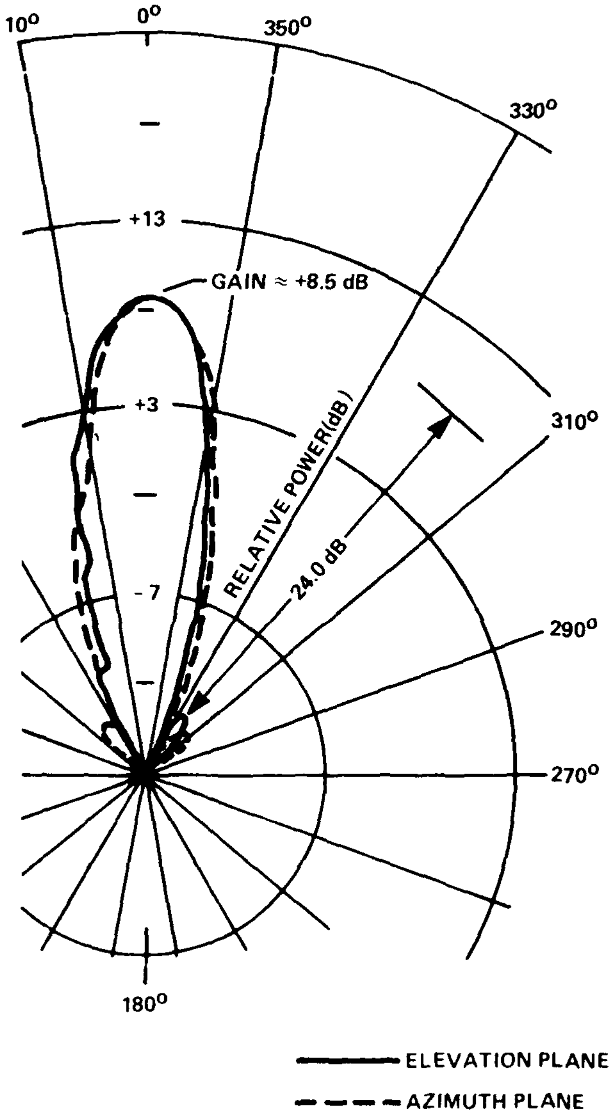

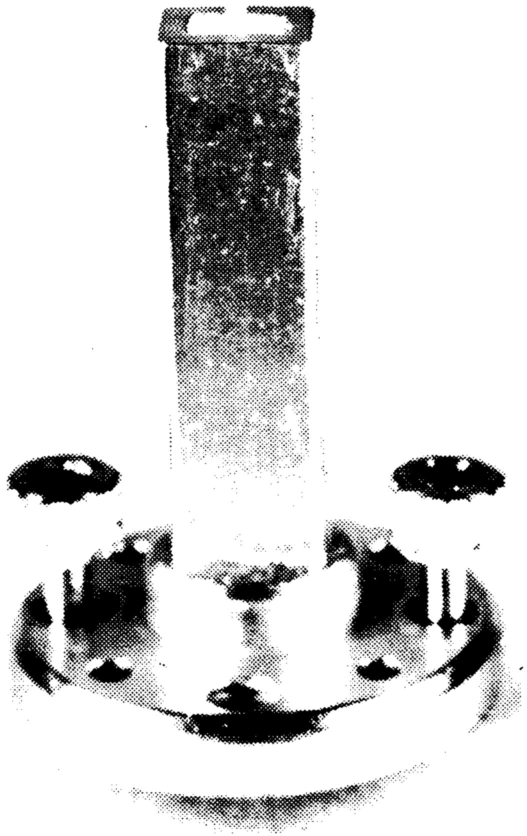

Figure 29. Millimeter wave dielectric rod radiator (70 GHz) with radiation patterns.

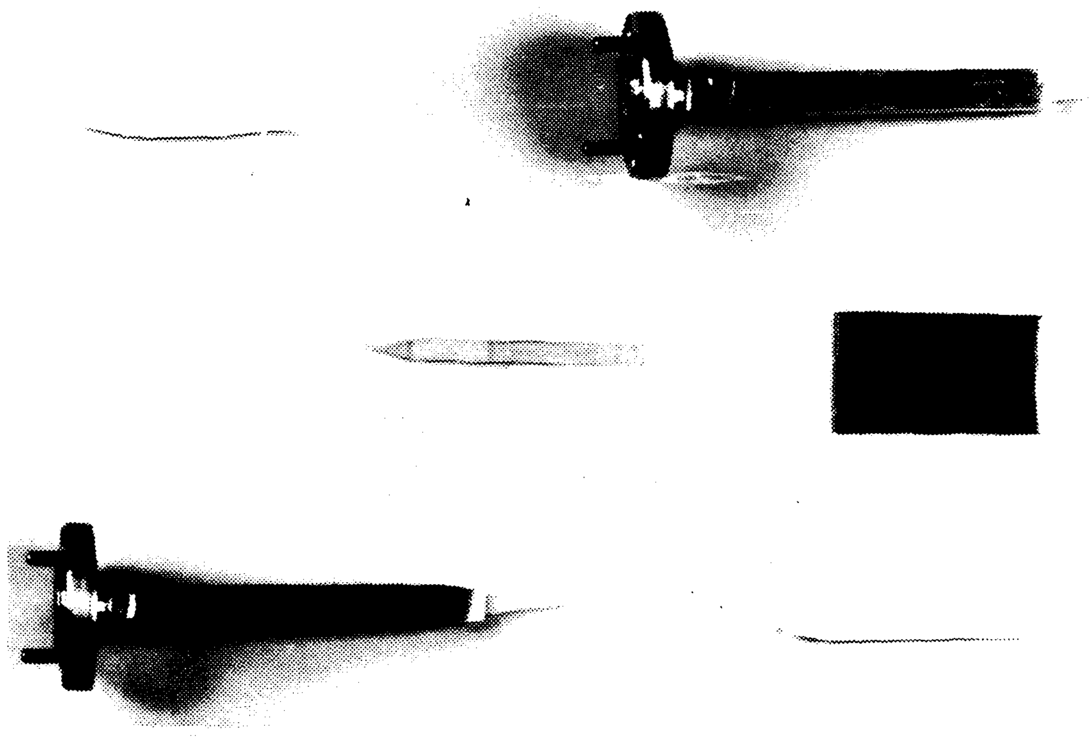

Figure 30. Millimeter wave dielectric rod radiators (94 GHz).

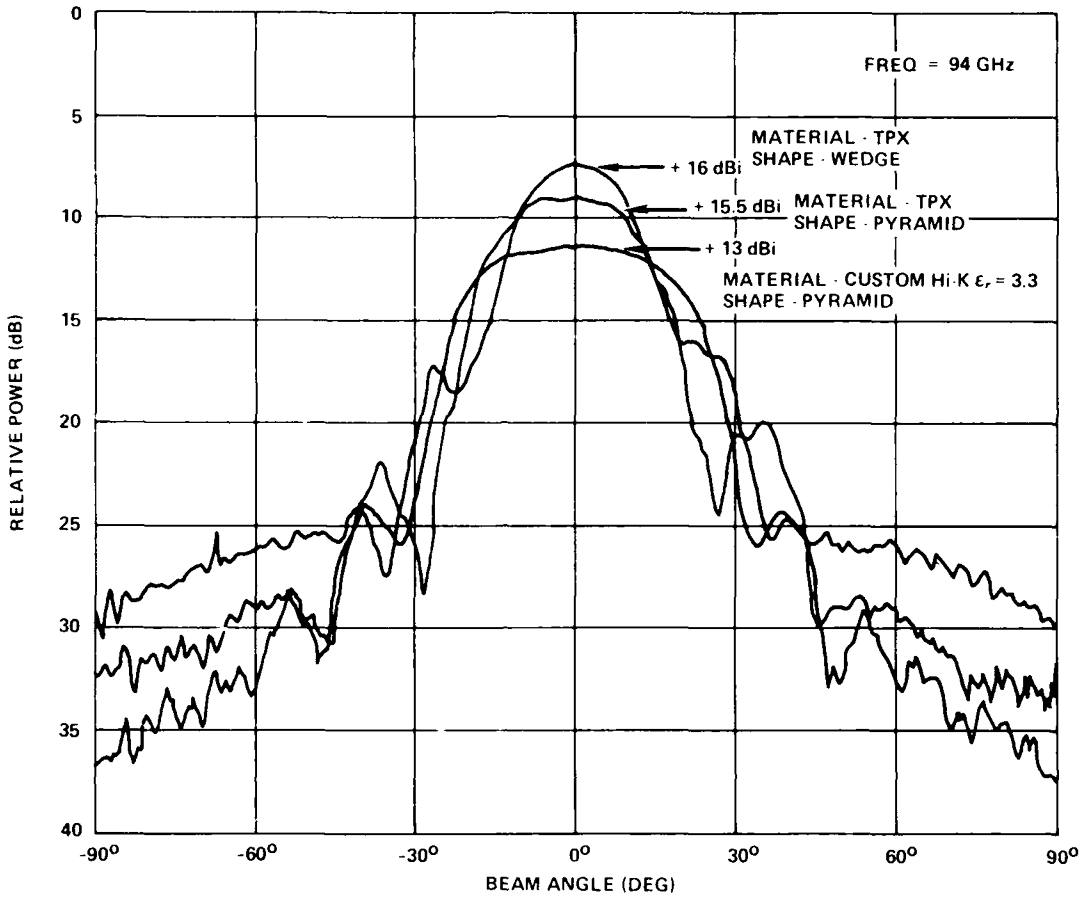

Figure 31. Radiation patterns of millimeter wave antennas (94 GHz).

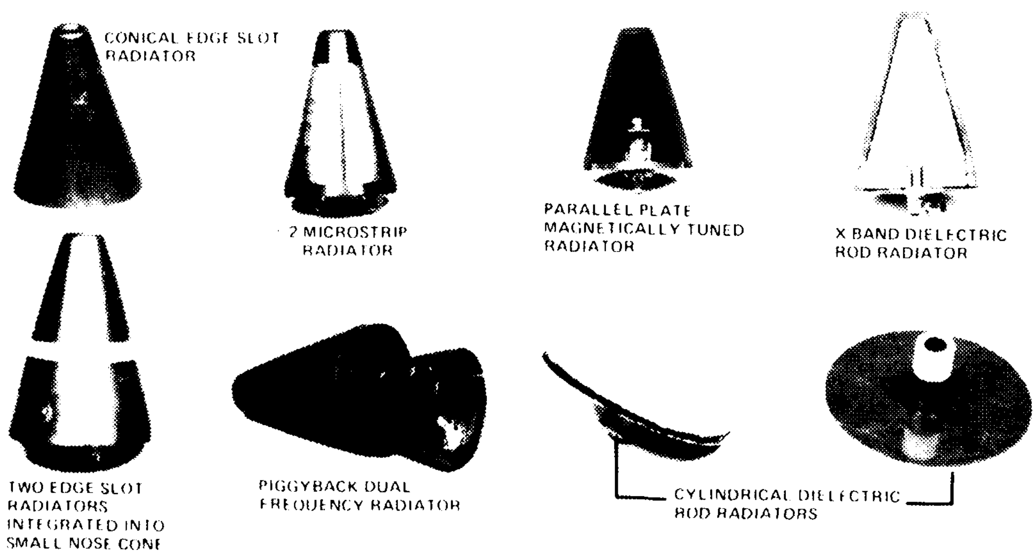

Figure 32. Small compact low-profile antennas.